

UC San Diego

UC San Diego Electronic Theses and Dissertations

Title

Seismic Response and Performance-Based Assessment of Multi-Span Bridge-Ground Systems

Permalink

<https://escholarship.org/uc/item/19g7k24h>

Author

Almutairi, Abdullah S E S E

Publication Date

2019

Peer reviewed|Thesis/dissertation

UNIVERSITY OF CALIFORNIA SAN DIEGO

Seismic Response and Performance-Based Assessment of Multi-Span Bridge-Ground Systems

A dissertation submitted in partial satisfaction of the
requirements for the degree of Doctor of Philosophy

in

Structural Engineering

by

Abdullah S E S E Almutairi

Committee in charge:

Professor Ahmed Elgamal, Chair
Professor John S McCartney
Professor Gilberto Mosqueda
Professor Peter Shearer
Professor P. Benson Shing

2019

Copyright

Abdullah S E S E Almutairi, 2019

All rights reserved

The Dissertation of Abdullah S E S E Almutairi is approved, and it is acceptable in quality and form for publication on microfilm and electronically:

Chair

University of California San Diego

2019

Dedication

To my parents, Sulaiman Almutairi and Haya Alrukaibi

To my wife Wadhah Alolaiyan

To my daughter Haya Almutairi

Epigraph

“The technical man must not be lost in his own technology. He must be able to appreciate life; and life is art, drama, music, and most importantly, people.”

Fazlur R. Khan

Table of Contents

Signature Page	iii
Dedication... ..	iv
Epigraph.....	v
Table of Contents.....	vi
List of Symbols	xviii
List of Figures	xxi
List of Tables	xxxvii
Acknowledgements	xliii
Vita.....	xlvi
Abstract of the Dissertation.....	xlviii
Chapter 1. Introduction and Literature Review	1
1.1. Motivation	1
1.2. Performance of Bridge Systems in Past Earthquakes	2
1.3. Influence of Soil-Structure Interaction on Bridge Seismic Response.....	3
1.4. Numerical Evaluation of Soil-Structure Interaction	4
1.4.1. Comprehensive Model Approach	4
1.4.2. Equivalent Substructure Approach.....	5
1.4.2.1. Soil Springs Approach	5
1.4.2.2. Foundation Matrix Approach.....	5
1.5. Damage Caused by Liquefaction	6

1.6.	Performance-Based Earthquake Assessment of Bridge Systems	7
1.7.	Objectives and Scope	8
1.8.	Outline	9
Chapter 2. Simplified Equivalent Static Analysis and Nonlinear Time History		
Analysis of Multi-Span Bridges.....15		
2.1.	Abstract.....	15
2.2.	Introduction.....	16
2.2.1.	Background.....	16
2.2.2.	Chapter Scope and Layout.....	17
2.3.	Salinas River Bridge	18
2.3.1.	Bridge Description and Geometric Configuration	18
2.3.2.	OpenSees Bridge FE Model and Mode Shapes	19
2.3.3.	Equivalent Static Analysis (ESA)	20
2.3.3.1.	ESA in the Longitudinal Direction.....	21
2.3.3.2.	ESA in the Transverse Direction.....	21
2.3.4.	Nonlinear Time History Analysis	22
2.3.4.1.	Maximum Displacement and Acceleration.....	22
2.3.4.2.	Response Time Histories	23
2.4.	Samoa Channel Bridge.....	24
2.4.1.	Bridge Description and Geometric Configuration	24
2.4.2.	OpenSees Bridge FE Model and Mode Shapes	25
2.4.3.	Equivalent Static Analysis (ESA)	26
2.4.3.1.	ESA in the Longitudinal Direction.....	26

2.4.3.2. ESA in the Transverse Direction	27
2.4.4. Nonlinear Time History Analysis	27
2.4.4.1. Maximum Displacement and Acceleration	28
2.4.4.2. Response Time Histories	28
2.4.5. Analysis of Samoa Bridge with Stiff Foundation Matrix	29
2.4.5.1. Mode Shape Analysis	30
2.4.5.2. Equivalent Static Analysis (ESA)	30
2.4.5.3. Nonlinear Time History Analysis	31
2.5. Eureka Channel Bridge	32
2.5.1. Geometric Configuration	33
2.5.2. OpenSees Finite Element Modeling	33
2.5.3. Mode Shape Analysis	34
2.5.4. Equivalent Static Analysis (ESA)	34
2.5.4.1. ESA in the Longitudinal Direction	34
2.5.4.2. ESA in the Transverse Direction	34
2.5.5. Nonlinear Time History Analysis	35
2.5.5.1. Maximum Displacement and Acceleration	35
2.6. Summary	36
2.7. Conclusions	37
2.8. Acknowledgements	38
Chapter 3. Effect of Abutment Modeling on the Bridge Seismic Response	102
3.1. Abstract	102
3.2. Introduction	102

3.3.	Bridge-Foundation model.....	103
3.4.	Abutment Models.....	104
3.4.1.	Roller Abutment.....	104
3.4.2.	SDC 2010-Sand Abutment	104
3.4.3.	HSR-HFD Abutment	105
3.5.	Abutment Model Comparison	105
3.5.1.	Mode Shape Analysis	106
3.5.2.	Pushover Analysis	106
3.5.3.	Nonlinear Time History Analysis	106
3.6.	Conclusions.....	106

Chapter 4. Implementation of the Performance-Based Earthquake Engineering

Framework for Multi-Span Bridge-Ground Systems 116

4.1.	Abstract.....	116
4.2.	Introduction.....	117
4.3.	Computational Framework	118
4.3.1.	Performance-Based Earthquake Engineering Framework	118
4.3.2.	Finite Element Computational Framework	119
4.3.3.	User-Interface for Nonlinear Bridge-Foundation Analysis	119
4.4.	Simulation Models	119
4.5.	Ground Profiles.....	120
4.5.1.	Bridge-Ground Case Study 1: Fixed-Base/Rigid Soil.....	120
4.5.2.	Bridge-Ground Case Study 2: Benchmark Soil Profile.....	120
4.6.	Ground Motions for PBEE Analysis.....	121

4.7.	Time History Results.....	121
4.8.	PBEE Results.....	122
4.9.	PBEE Application for Other Types of Civil Infrastructure.....	123
4.10.	Summary and Conclusions	123
4.11.	Acknowledgements.....	124
Chapter 5. Performance-Based Earthquake Assessment of Samoa Channel Bridge-Foundation System		137
5.1.	Abstract.....	137
5.2.	Introduction.....	137
5.3.	Computational Framework	139
5.3.1.	Performance-Based Earthquake Engineering Framework	139
5.3.2.	Finite Element Computational Framework	139
5.3.3.	User-Interface for Nonlinear Bridge-Foundation Analysis	139
5.4.	Finite Element Model.....	140
5.4.1.	Bridge Model	142
5.4.2.	Foundation Matrix.....	143
5.4.3.	Mode Shape Analysis	144
5.5.	Ground Motions	144
5.6.	Representative Time History Results.....	145
5.7.	PBEE Results.....	146
5.7.1.	Loss Models.....	146
5.7.2.	Hazard Models	147
5.8.	Summary and Conclusions	147

5.9.	Acknowledgements	148
Chapter 6. Seismic Response of Samoa Channel Bridge-Foundation System		
Subjected to Site-Specific Motions.....174		
6.1.	Abstract.....	174
6.2.	Introduction.....	174
6.3.	Bridge Model	175
6.4.	Specification of Ground Motion Input	176
6.4.1.	Uniform Hazard Spectra.....	176
6.4.2.	Hazard Deaggregation (Somerville and Collins 2002)	176
6.4.3.	Process for Selecting Ground Motions (Somerville and Collins 2002)	177
6.4.4.	Time Histories for 50% in 50 years (Somerville and Collins 2002).....	177
6.4.5.	Time Histories for 10% in 50 years (Somerville and Collins 2002).....	177
6.4.6.	Time Histories for 2% in 50 years (Somerville and Collins 2002).....	178
6.4.7.	Scaling of the Ground motions (Somerville and Collins 2002).....	178
6.5.	Nonlinear Time History Analysis	178
6.5.1.	Simulation of Seismic Demand (Engineering Demand Parameters)	179
6.5.2.	Primary EDP Used in Evaluation.....	179
6.5.3.	Variation of Bridge Column Drift Ratio	179
6.6.	Conclusions.....	179
6.7.	Acknowledgements	181
Chapter 7. Framework for Assessment of Bridge-Ground Response Due to		
Liquefaction-Induced Lateral Spreading201		
7.1.	Abstract.....	201

7.2.	Introduction.....	202
7.3.	Bridge-Foundation Model	204
7.4.	The Caltrans Simplified Method (Lateral spreading)	205
7.4.1.	Implementation of the Simplified Method to the Bridge Abutment Foundation	205
7.4.2.	Pile-pinning Effect	206
7.5.	Representative Bridge Response Due to Lateral Ground Displacement.....	206
7.6.	Performance-Based Earthquake Engineering Framework	207
7.7.	Lateral Displacements for PBEE Analysis	208
7.8.	PBEE Results.....	209
7.8.1.	Repair Cost and Time	209
7.8.2.	Hazard Curves.....	211
7.8.3.	Carbon Footprint of Repair Results	211
7.9.	Conclusions.....	211
7.10.	Acknowledgements	212
 Chapter 8. Sensitivity of Seismic Demands for Bridge-Ground Systems Subjected to Liquefaction-Induced Lateral Spreading		232
8.1.	Abstract.....	232
8.2.	Introduction.....	232
8.3.	Bridge-Foundation Model	234
8.4.	The Caltrans Simplified Method (Lateral spreading)	234
8.4.1.	Implementation of the Simplified Method to the Bridge Abutment Foundation	234

8.4.2. Effect of Liquefied Layer Shear Strength.....	235
8.4.3. Effect of Potential Retrofit Configurations.....	236
8.4.4. Effect of the Empirical Equations to Estimate the Demand Displacement .	236
8.5. PBEE Results.....	236
8.6. Summary and Conclusions	238
8.7. Acknowledgements.....	238
Chapter 9. Conclusions and Future Work.....	251
9.1. Summary.....	251
9.2. Conclusions.....	252
9.2.1. Seismic Response of Highway Bridges.....	252
9.2.2. Performance-Based Assessment	253
9.2.3. Practice-Oriented Lateral Spreading Analysis Approach.....	254
9.3. Future Work.....	255
References... ..	256
Appendix A. MSBridge: Multi-span Bridge Analysis.....	267
A.1. General Overview	267
A.2. Verification of MSBridge Response Mechanism	269
A.2.1. Pushover Analysis	269
A.2.2. Mode Shapes Analysis	270
A.2.3. Abutment Model	271
A.2.3.1. Elastic Abutment Model.....	272
A.2.3.2. Roller Abutment Model.....	272

A.2.3.3. SDC Abutment Model.....	273
Appendix B. Base Input Motions.....	279
Appendix C. Comparison of ESA and THA Results in the Transverse Direction...286	
C.1. Introduction.....	286
C.1.1. Purpose of Study	286
C.1.2. Salient Modeling Considerations	288
C.1.3. Layout.....	288
C.2. Typical Bent.....	289
C.2.1. ESA Comparison for MSBridge and wFrame	290
C.3. Case 1: Single Bent Model with Rigid Base and Linear Columns	290
C.3.1. Case 1 Description	290
C.3.2. Comparison of ESA and THA Results	290
C.4. Case 2: Single Bent Model with Linear Soil Springs and Linear Columns	291
C.4.1. Case 2 Description	291
C.4.2. Comparison of ESA and THA Results	291
C.5. Case 3: Single Bent Model with Rigid Base and Nonlinear Columns.....	292
C.5.1. Case 3 Description	292
C.5.2. Comparison of ESA and THA Results	292
C.6. Case 4: Single Bent Model with Linear Soil Springs and Nonlinear Colum ..	292
C.6.1. Case 4 Description	292
C.7. Case 5: Single Bent Model with Nonlinear Soil Springs and Nonlinear	
Columns	293
C.7.1. Case 5 Description	293

C.7.2. Transverse Pushover Loading	293
C.8. Case 6: Multi-bent Model with Nonlinear Soil Springs and Nonlinear Columns	294
C.9. Case 7: Multi-bent Model with End-bents	295
C.9.1. Case 7 Description	295
C.9.2. Comparison of ESA and THA Results	295
C.10. Case 8: Salinas River Bridge Model	295
C.10.1. Case 8 Description	295
C.10.2. Comparison of ESA and THA Results	296
C.11. Summary and Conclusions	297
C.11.1. Summary	297
C.11.2. Conclusions	297
Appendix D. Salinas Bridge Modeling Details	325
D.1. Column	325
D.2. Soil Springs	325
D.3. Deck and Bentcap	325
D.4. Abutment	326
Appendix E. Samoa Channel Bridge Modeling Details	331
E.1. Column	331
E.2. Foundation Matrix	331
E.3. Deck	332
E.4. Abutment	332
E.5. ESA	332

Appendix F. Eureka Channel Bridge Modeling Details	338
F.1. Column	338
F.2. Foundation Matrix.....	338
F.3. Deck	338
F.4. Abutment	338
 Appendix G. Column nonlinear fiber sections for the Samoa Channel Bridge and the Eureka Channel Bridge	 340
G.1. Section I.....	340
G.2. Section II	343
 Appendix H. PEER Performance-Based Earthquake Engineering (PBEE) Framework	 347
H.1. Theory and Implementation of PBEE Analysis.....	347
H.2. Efforts to Expand PBEE Framework	348
H.3. PBEE Quantities	349
H.4. PBEE Outputs.....	349
 Appendix I. PBEE for Pile-Supported Wharves	 362
I.1. Introduction.....	362
I.2. Characteristics of the Vertical-Pile-Supported Wharf	363
I.3. Numerical Modeling of the Wharf.....	363
I.4. Experimental-Based Damage States	364
I.5. Probabilities of Exceeding the Damage States	365
I.6. Repair Methods.....	365

Appendix J. Simplified Method for Lateral Spreading Load on Bridge Foundation..

.....373

J.1. Step-by-step Procedures373

J.2. Worked Example.....376

List of Symbols

B	Pile diameter
c	Cohesion
CF	Cubic foot
CWD	Crew working day
CY	Cubic yard
DM	Damage model
DS	damage state
DV	Decision variable
E	Elastic modulus
EA	Each
EDP	Engineering demand parameter
EF	Emission factor
f	Frequency
f_c'	unconfined concrete compressive strength
f_y	Steel yield strength
GAL	Gallon
H	Crust height
I	Section inertia
IM	Intensity measure
K	column lateral stiffness
K_{abt}	Abutment back wall stiffness
k_{max}	PGA modified by a class site
K_p	Passive soil pressure coefficient of the non-liquefied soil layer

k_w	Adjustment factor for a wedge-shaped failure surface
k_y	Slope yield acceleration
LB	Pound
LF	Linear foot
m	Mass
m_p	p-multiplier
MTD	Caltrans Memo to Designers
M_w	Moment magnitude
N_{60}	SPT blow count corrected for 60% hammer efficiency
$N_{1,60}$	SPT blow count N_{60} corrected for overburden pressure
p	Lateral soil force per unit length acting on the pile
P_{bw}	Abutment back wall passive pressure
PG	Performance Group
PGA	Peak Ground Acceleration
PGV	Peak Ground Velocity
PSDM	Probabilistic seismic demand model
Q	Repair quantity
R	Closest distance to fault
RCR	Repair Cost Ratio
RT	Repair Time
S_b	Diameter factor
SF	Square foot
SPT	Standard penetration test
S_r	Residual strength of soil

S_u	Undrained shear strength of soil
SRSS	Square root of the sum of squares
T_{DECK}	Deck thickness
TON	Ton = 2,000 LB
Var	Variance
ω	Angular frequency
W_L	Longitudinal abutment width
W_T	Transverse abutment width
y	Relative soil-pile displacement
z	Depth
γ	Unit weight of soil
ρ	Density of soil
\emptyset	Friction angle
δ	Pile-soil interface friction angle
λ	Lognormal distribution parameter (median)
β	Lognormal distribution parameter (standard deviation)
μ	Mean
σ	Dispersion
$\overline{\sigma'_v}$	Mean vertical effective stress
σ'_v	Effective vertical stress
σ_v	Total vertical stress

List of Figures

Figure 1.1. Caltrans seismic retrofit program.....	12
Figure 1.2. Soil springs in the equivalent pile analysis (MTD 20-15, Caltrans 2017)	13
Figure 1.3. Equivalent base spring for pile group foundation (Shamsabadi and Law 2010)	14
Figure 2.1. General layout of Salinas Bridge (Caltrans 2005)	54
Figure 2.2. Sectional details of Salinas Bridge: (a) deck; (b) Type I shaft cross-section	55
Figure 2.3. Salinas Bridge FE model created in MSBridge (dimensions in ft): (a) plan view; (b) elevation view; (c) close-up of 3D view; (d) side view of a bent (typical)	56
Figure 2.4. Salinas Bridge mode shapes: (a) first mode; (b) second mode; (c) third mode; (d) fourth mode; and (e) fifth mode	57
Figure 2.5. Acceleration response spectrum (ARS) curve employed in Caltrans (2005)	58
Figure 2.6. ARS curve employed in the ESA	58
Figure 2.7. Bridge deck maximum longitudinal displacement	59
Figure 2.8. Bridge deck maximum transverse displacement.....	59
Figure 2.9. Bridge deck maximum longitudinal acceleration	60
Figure 2.10. Bridge deck maximum transverse acceleration	60
Figure 2.11. Column top longitudinal response time histories of Column 1 of Bent 7 for Simulation 1 (ROCKS1N1): (a) acceleration; (b) displacement; (c) bending moment; (d) and base excitation.....	61
Figure 2.12. Column top longitudinal moment-curvature response of Column 1 of Bent 7 for Simulation 1	62
Figure 2.13. Deformed mesh (factor of 100) for Simulation 1 at the maximum displacement step (grey lines represent undeformed mesh): (a) entire bridge; (b) close-up of Bents 6, 7,	

and 8 (from left to right).....	63
Figure 2.14. Column top longitudinal response time histories of Column 1 of Bent 7 for Simulation 4 (ROCKS1N4): (a) acceleration; (b) displacement; (c) bending moment; and (d) base excitation.....	64
Figure 2.15. Column top longitudinal moment-curvature response of Column 1 of Bent 7 for Simulation 4	65
Figure 2.16. Deformed mesh (factor of 100) for Simulation 4 at the step of the maximum displacement (14 in @ 19.2 seconds) (grey lines represent undeformed mesh): (a) entire bridge; (b) close-up of Bents 6, 7, and 8 (from left to right)	66
Figure 2.17. Bridge configuration: (a) Samoa Channel Bridge, Eureka geotechnical array, Middle Channel Bridge and Eureka Channel Bridge (Map Data @ 2015 Google) and (b) photo of the Samoa Channel Bridge (http://www.strongmotioncenter.org)	67
Figure 2.18. Layout of instrumentation at Samoa Bridge (http://www.strongmotioncenter.org): (a) elevation view; (b) plan view	68
Figure 2.19. Elevation and bridge deck of Pier S-8 of Samoa Bridge	69
Figure 2.20. Samoa Bridge: (a) column detail of Piers S-8 and S-9; and (b) column detail of other piers except Piers S-8 and S-9	70
Figure 2.21. Samoa Bridge FE mesh created in MSBridge: (a) 3D view; (b) elevation view; (c) plan view.....	71
Figure 2.22. Mode shapes for Samoa Bridge: (a) first mode; (b) second mode; (c) third mode; (d) fourth mode; and (e) fifth mode	72
Figure 2.23. ARS curve employed in the ESA	73
Figure 2.24. Bridge deck maximum longitudinal displacement	74

Figure 2.25. Bridge deck maximum transverse displacement.....	74
Figure 2.26. Bridge deck maximum longitudinal acceleration.....	75
Figure 2.27. Bridge deck maximum transverse acceleration	75
Figure 2.28. Pier S-8 column top longitudinal response time histories for Simulation 1 (ROCKS1N1): (a) acceleration; (b) displacement; (c) bending moment; and (d) base excitation.....	76
Figure 2.29. Column top longitudinal moment-curvature response for Simulation 1: (a) Pier S-4; (b) Pier S-8; (c) Pier S-19	77
Figure 2.30. Deformed mesh (factor of 100) for Simulation 1 at the maximum displacement step (grey lines represent undeformed mesh): (a) entire bridge; (b) close-up of Bents 6, 7, and 8 (from left to right).....	78
Figure 2.31. Pier S-8 column top longitudinal response time histories for Simulation 4 (ROCKS1N4): (a) acceleration; (b) displacement; (c) bending moment; and (d) base excitation.....	79
Figure 2.32. Column top longitudinal moment-curvature response for Simulation 4: (a) Pier S-4; (b) Pier S-8; (c) Pier S-19	80
Figure 2.33. Deformed mesh (factor of 100) for Simulation 4 at the maximum displacement step (grey lines represent undeformed mesh): (a) entire bridge; (b) close-up of Bents 6, 7, and 8 (from left to right).....	81
Figure 2.34. Stiff foundation matrix employed (Caltrans, personal communications).....	81
Figure 2.35. Mode shapes for Samoa Bridge with stiff foundation matrix: (a) first mode; (b) second mode; (c) third mode; (d) fourth mode; and (e) fifth mode	82
Figure 2.36. Bridge deck maximum longitudinal displacement	83

Figure 2.37. Bridge deck maximum transverse displacement.....	83
Figure 2.38. Bridge deck maximum longitudinal acceleration.....	84
Figure 2.39. Bridge deck maximum transverse acceleration	84
Figure 2.40. Pier S-8 column top longitudinal response time histories for Simulation 1 (ROCKS1N1): (a) acceleration; (b) displacement; (c) bending moment; and (d) base excitation.....	85
Figure 2.41. Pier S-8 column top longitudinal moment-curvature response for Simulation 1	86
Figure 2.42. Deformed mesh (factor of 200) for Simulation 1 at the maximum displacement step (grey lines represent undeformed mesh): (a) entire bridge; (b) close-up of Bents 6, 7, and 8 (from left to right)	86
Figure 2.43. Pier S-8 column top longitudinal response time histories for Simulation 8 (ROCKS1P1): (a) acceleration; (b) displacement; (c) bending moment; and (d) base excitation.....	87
Figure 2.44. Pier S-8 column top longitudinal moment-curvature response for Simulation 8	88
Figure 2.45. Deformed mesh (factor of 200) for Simulation 8 at the maximum displacement step (grey lines represent undeformed mesh): (a) entire bridge; (b) close-up of Bents 6, 7, and 8 (from left to right)	88
Figure 2.46. Bridge configuration: (a) Samoa Bridge, Eureka Geotechnical Array, Middle Channel Bridge and Eureka Bridge (Map Data @ 2015 Google) and (b) photo of the Eureka Bridge (http://www.strongmotioncenter.org)	89
Figure 2.47. Layout of instrumentation at Eureka Bridge (http://www.strongmotioncenter.org): (a) elevation view; (b) plan view	90
Figure 2.48. Elevation and bridge deck for Pier E-6	91

Figure 2.49. Eureka Bridge FE mesh created in MSBridge: (a) 3D view; (b) elevation view; (c) plan view.....	91
Figure 2.50. Mode shapes for Eureka Bridge: (a) first mode; (b) second mode; (c) third mode; (d) fourth mode; and (e) fifth mode	92
Figure 2.51. ARS curve employed in the ESA	93
Figure 2.52. Bridge deck maximum longitudinal displacement	94
Figure 2.53. Bridge deck maximum transverse displacement	94
Figure 2.54. Bridge deck maximum longitudinal acceleration.....	95
Figure 2.55. Bridge deck maximum transverse acceleration	95
Figure 2.56. Pier E-7 Column top longitudinal response time histories for Simulation 2: a) acceleration; b) displacement; c) bending moment; d) base excitation ROCKS1N2	96
Figure 2.57. Column top longitudinal moment-curvature response for Simulation 2 (motion ROCKS1N2): (a) Pier E-6; (b) Pier E-7; (c) Pier E-13.....	97
Figure 2.58. Deformed mesh (factor of 100) for Simulation 1 (motion ROCKS1P2) at the maximum displacement step (grey lines represent undeformed mesh): (a) entire bridge; (b) close-up of Piers 6, 7, and 8 (from left to right)	98
Figure 2.59. Pier E-7 column top longitudinal response time histories for Simulation 9: (a) acceleration; (b) displacement; (c) bending moment; (d) base excitation ROCKS1P2	99
Figure 2.60. Column top longitudinal moment-curvature response for Simulation 9 (motion ROCKS1P2): (a) Pier E-6; (b) Pier E-7; (c) Pier E-13.....	100
Figure 2.61. Deformed mesh (factor of 100) for Simulation 9 (motion ROCKS1P2) at the	

maximum displacement step (grey lines represent undeformed mesh): (a) entire bridge; (b) close-up of Piers 6, 7, and 8 (from left to right)	101
Figure 3.1. Finite element mesh: (a) 3D view, (b) elevation view (dimensions are in ft)	110
Figure 3.2. General scheme of the Roller Abutment Model	110
Figure 3.3. General scheme of the longitudinal response of the Abutment Model	111
Figure 3.4. Definition of the SDC 2010-Sand Abutment Model (after Caltrans 2010).....	111
Figure 3.5. SDC 2010-Sand abutment longitudinal response	112
Figure 3.6. Definition of the HSR-HFD Abutment Model (Shamsabadi <i>et al.</i> 2007, 2010; Shamsabadi 2019)	112
Figure 3.7. HSR-HFD abutment longitudinal response	113
Figure 3.8. First five mode shapes of the studied bridge model.....	114
Figure 3.9. Longitudinal abutment response from the pushover analysis.....	115
Figure 3.10. Demand model of longitudinal relative deck-back wall displacement	115
Figure 4.1. MSBridge user-interface.....	128
Figure 4.2. Finite element mesh: (a) 3D view, (b) elevation view	128
Figure 4.3. Modeling of column and pile: (a) column cross-section; (b) fiber discretization; (c) core concrete; (d) cover concrete; (e) reinforcing steel; and (f) moment-curvature response	129
Figure 4.4. Soil layer properties for case 2 (benchmark)	130
Figure 4.5. <i>P-y</i> curves for case 2 at depths: (a) 0 m; (b) 5 m; (c) 10 m; and (d) 20 m	130
Figure 4.6. PGV distribution for the SRSS of two lateral ground motion components.....	131
Figure 4.7. PSDMs for column maximum drift ratio at column of bent 2 for: (a) Case 1; and (b) Case 2	132

Figure 4.8. PSDMs for maximum relative deck end-back wall displacement at left abutment for: (a) Case 1; and (b) Case 2.....	133
Figure 4.9. Repair cost disaggregated for each PG for: (a) Case 1; and (b) Case 2	134
Figure 4.10. RCR loss models for each case.	135
Figure 4.11. Repair time (CWD) loss model (with probabilistic moments) for both cases	135
Figure 4.12. Repair cost ratio hazard curve.....	136
Figure 4.13. Repair time hazard curve.	136
Figure 5.1. Samoa Channel Bridge: (a) photo of the bridge (http://www.strongmotioncenter.org); (b) global elevation view of the bridge ; and (c) map view (Wang <i>et al.</i> 2018)....	151
Figure 5.2. Samoa Bridge FE model created in MSBridge (bottom-right window shows the side view of the bridge model).....	152
Figure 5.3. Pier S-8 configuration: (a) before retrofit; and (b) after retrofit (Wang <i>et al.</i> 2016)	153
Figure 5.4. Fiber discretization of bridge column cross-sections: (a) Pier S-8 after retrofit; (b) Pier S-8 before retrofit; (c) Pier S-14 after retrofit; and (d) Pier S-14 before retrofit...	154
Figure 5.5. Bridge column modeling: (a) core concrete; (b) reinforcing steel; (c) moment-curvature response for Pier S-8; and (d) moment-curvature response for Pier S-14.....	155
Figure 5.6. Local coordinates system for foundation matrix, where x, y, z are the longitudinal, transverse, and vertical directions (Elgamal <i>et al.</i> 2016)	156
Figure 5.7. Lateral foundation matrix force-displacement relationships for Pier S-2	156
Figure 5.8. Lateral foundation matrix force-displacement relationships for Pier S-3	157
Figure 5.9. Lateral foundation matrix force-displacement relationships for Pier S-4	157
Figure 5.10. Lateral foundation matrix force-displacement relationships for Pier S-5	158
Figure 5.11. Lateral foundation matrix force-displacement relationships for Pier S-6	158

Figure 5.12. Lateral foundation matrix force-displacement relationships for Pier S-7	159
Figure 5.13. Lateral foundation matrix force-displacement relationships for Pier S-8	159
Figure 5.14. Lateral foundation matrix force-displacement relationships for Pier S-9	160
Figure 5.15. Lateral foundation matrix force-displacement relationships for Pier S-10	160
Figure 5.16. Lateral foundation matrix force-displacement relationships for Pier S-11	161
Figure 5.17. Lateral foundation matrix force-displacement relationships for Pier S-12	161
Figure 5.18. Lateral foundation matrix force-displacement relationships for Pier S-13	162
Figure 5.19. Lateral foundation matrix force-displacement relationships for Piers S-14 and S-15	162
Figure 5.20. Lateral foundation matrix force-displacement relationships for Piers S-16 to S-20	163
Figure 5.21. Mode shapes for Samoa Bridge (grey lines represent undeformed mesh): (a) first transverse mode; (b) first longitudinal mode; and (c) second transverse mode	164
Figure 5.22. PGV, PGA and SA distributions for the SRSS (square root of the sum of the squares) of the two horizontal components of ground input motions.	165
Figure 5.23. Pier S-8 and Pier S-14 column top displacement and input motion time histories for the Ferndale 2010 motion for: (a) longitudinal direction; and (b) transverse direction	166
Figure 5.24. Column base moment-curvature response of Pier S-8 for: (a) the Ferndale 2010 motion (low shaking event); and (b) the Chi-Chi (tcu068) motion (strong shaking event)	167
Figure 5.25. Column base moment-curvature response of Pier S-14 for: (a) the Ferndale 2010 motion (low shaking event); and (b) the Chi-Chi (tcu068) motion (strong shaking	

event)	168
Figure 5.26. Foundation response time history and force-displacement relationship for: (a) the Ferndale 2010 motion (low shaking event); and (b) the Chi-Chi (tcu068) motion (strong shaking event)	169
Figure 5.27. Repair cost contribution for each PG vs. PGV: (a) after retrofit; and (b) before retrofit	170
Figure 5.28. Repair cost contribution for column PGs vs. PGV: (a) after retrofit; and (b) before retrofit	171
Figure 5.29. Loss models: (a) repair cost ratio; (b) repair time	172
Figure 5.30. Hazard curves for: (a) repair cost ratio; and (b) repair time	173
Figure 6.1. Uniform hazard spectra for: (a) Rock site, and (b) Soil site	189
Figure 6.2. Longitudinal time histories for 50% in 50 years (motion 1-11)	190
Figure 6.3. Longitudinal time histories for 50% in 50 years (motion 12-22)	191
Figure 6.4. Transverse time histories for 50% in 50 years (motion 1-11)	192
Figure 6.5. Transverse time histories for 50% in 50 years (motion 12-22)	193
Figure 6.6. Longitudinal time histories for 10% in 50 years (motion 1-9)	194
Figure 6.7. Longitudinal time histories for 10% in 50 years (motion 10-19)	195
Figure 6.8. Transverse time histories for 10% in 50 years (motion 1-9)	196
Figure 6.9. Transverse time histories for 10% in 50 years (motion 10-19)	197
Figure 6.10. Longitudinal time histories for 2% in 50 years	198
Figure 6.11. Transverse time histories for 2% in 50 years	199
Figure 6.12. Summary of maximum seismic demand for all three hazard levels for: (a) after retrofit, and (b) before retrofit	200

Figure 7.1. Bridge geometric configuration (dimensions shown in ft): (a) elevation view; (b) deck section.....	216
Figure 7.2. Bridge FE model created in MSBridge (dimensions shown in ft): (a) plan view; (b) elevation view; (c) close-up of 3D view; (d) side view of a bent (typical)	217
Figure 7.3. Schematic of spring abutment model	218
Figure 7.4. Modeling of column and pile: (a) column cross-section; (b) fiber discretization; (c) concrete model; (d) reinforcing steel bilinear inelastic model; (e) monotonic moment-curvature	219
Figure 7.5. Slope stability model (dimensions shown in ft): (a) geometry and layering for the slope under study; and (b) typical failure surface for the analyzed slope.	220
Figure 7.6. p - y curves for: (a) the crust; (b) middle of the liquefied layer; and (c) middle of the dense sand layer	221
Figure 7.7. Displacement demand displacement for a representative motion.....	222
Figure 7.8. Bridge response: (a) displacement profile for the left abutment pile; and (b) deformed mesh.....	223
Figure 7.9. Moment-curvature response at column base	224
Figure 7.10. Schematic illustration of PBEE framework with the simplified procedure	224
Figure 7.11. Input ground motions in M-R space.....	225
Figure 7.12. Unrestrained displacement with $k_y = 0.163$ g using Bray and Travararou (2007) .	226
Figure 7.13. Restrained demand displacement vs. PGA	227
Figure 7.14. Repair cost vs. PGA by applying displacements	228
Figure 7.15. Loss models: a) mean repair cost ratio vs. PGA, b) mean repair time vs. PGA	229
Figure 7.16. Hazard curves: (a) mean annual frequency vs. repair time hazard curve; (b) mean	

annual frequency vs. repair cost ratio hazard curve	230
Figure 7.17. Carbon footprint of repair (CFR) vs. PGA	231
Figure 8.1. Shear strength effect on the estimation of the demand displacement	240
Figure 8.2. Residual strengths predicted by Kramer and Wang (2015): (a) different vertical stresses, and (b) with probabilistic moments	241
Figure 8.3. Estimated displacement for different shear strength for: (a) unrestrained, and (b) restrained.....	242
Figure 8.4. Abutment layout for: (a) existing bridge; (b) Retrofit A; (c) Retrofit B	243
Figure 8.5. Estimated displacement for different retrofit configuration for: (a) unrestrained, and (b) restrained	244
Figure 8.6. Estimated displacement using Martin and Qiu (1994) against PGV for: (a) unrestrained, and (b) restrained.....	245
Figure 8.7. Estimated displacement using Martin and Qiu (1994) against PGA for: (a) unrestrained, and (b) restrained.....	246
Figure 8.8. Repair cost disaggregated by PG vs. PGA for: (a) upper bound shear strength; (b) lower bound shear strength.....	247
Figure 8.9. Mean repair cost ratio vs. PGA for shear strength estimation	248
Figure 8.10. Mean repair cost ratio vs. PGA for different retrofit configurations.....	249
Figure 8.11. Mean repair cost ratio vs. PGA for different empirical equations	250
Figure A.1. Global coordinate system employed in MSBridge	275
Figure A.2. Longitudinal displacement response time history for column top	275
Figure A.3. Bridge natural periods and natural frequencies.....	275
Figure A.4. Mode shapes for the bridge model: (a) first mode; (b) second mode; (c) third mode;	

(d) fourth mode; and (e) fifth mode	276
Figure A.5. Longitudinal displacement response time history at elevation of -3 ft for column 2 of bent 6 (Elastic Abutment).....	277
Figure A.6. Longitudinal displacement response time history at elevation of -3 ft for column 2 of bent 6 (Roller Abutment).....	277
Figure A.7. Longitudinal displacement response time history at elevation of -3 ft for column 2 of bent 6 (zero-stiffness Elastic Abutment)	278
Figure A.8. Longitudinal displacement response time history at elevation of -3 ft for column 2 of bent 6 (SDC 2010-Sand).....	278
Figure B.1. Longitudinal PGA histograms of the first 14 input motions.....	281
Figure B.2. Acceleration time histories of the input motion components for Rock site (non-pulse-like motions)	282
Figure B.3. Acceleration time histories of the input motion components for Rock site (pulse-like motions)	283
Figure B.4. Pseudo-spectral acceleration for rock site (non-pulse-like motions).....	284
Figure B.5. Pseudo-spectral acceleration for rock site (pulse-like motions).....	285
Figure C.1. Typical bent of Salinas Bridge (dimensions in ft).....	309
Figure C.2. Idealized bilinear moment-curvature relationship employed for the columns (plastic moment = 6,100 kip-ft; yield curvature = 2.92×10^{-5} rad/in).....	310
Figure C.3. Idealized bilinear moment-curvature relationship employed for the pile shafts (plastic moment = 19,400 kip-ft; yield curvature = 8.23×10^{-5} rad/in).....	310
Figure C.4. Shear force vs. transverse displacement for pushover analysis	311
Figure C.5. Single bent model for Case 1 (with rigid base at mudline).....	311

Figure C.6. Single bent model for Case 2	312
Figure C.7. Single bent model for Case 3 (with rigid base at mudline).....	312
Figure C.8. Moment-curvature response at column top for Motion #1 ROCKS1N1 (Red part shows the end of shaking) for Case 3	313
Figure C.9. Moment-curvature response at column top for Motion #2 ROCKS1N2 (Red part shows the end of shaking) for Case 3	313
Figure C.10. Single bent model for Case 4	314
Figure C.11. Moment-curvature response at column top for Motion #1 ROCKS1N1 (Red part shows the end of shaking) for Case 4.....	314
Figure C.12. Moment-curvature response at column top for Motion #2 ROCKS1N2 (Red part shows the end of shaking) for Case 4.....	315
Figure C.13. Single bent model for Case 5	315
Figure C.14. Pushover load vs. transverse displacement for the transverse ESA	316
Figure C.15. Axial force vs. transverse displacement for the transverse ESA.....	316
Figure C.16. Moment-curvature response at column top for Motion #1 ROCKS1N1 (Red part shows the end of shaking) for Case 5.....	317
Figure C.17. Moment-curvature response at column top for Motion #2 ROCKS1N2 (Red part shows the end of shaking) for Case 5.....	317
Figure C.18. Multi-bent model for Case 6	318
Figure C.19. First transverse mode of the multi-bent model (period = 2.0 seconds): (a) plan view; (b) 3D view	318
Figure C.20. Multi-bent model with end-bents: (a) plan view; (b) 3D view; (c) bent close-up..	319
Figure C.21. First transverse mode of the multi-bent model (period = 1.94 seconds)	320

Figure C.22. Moment-curvature response at column top for Column 1 of Bent 6 for Motion #1 ROCKS1N1 (Red part shows the end of shaking) for Case 7	320
Figure C.23. Moment-curvature response at column top for Column 1 of Bent 6 for Motion #2 ROCKS1N2 (Red part shows the end of shaking) for Case 7	321
Figure C.24. Idealized bilinear force-displacement relationship employed for the abutment in the transverse direction	321
Figure C.25. Column shear force vs. displacement response in pushover analysis	322
Figure C.26. First transverse mode of Salinas River Bridge (period = 1.91 seconds): (a) plan view; (b) 3D view	322
Figure C.27. Moment-curvature response at column top for Column 1 of Bent 6 for Motion #1 ROCKS1N1 (Red part shows the end of shaking) for Case 8	323
Figure C.28. Abutment (left or right) transverse resisting force-displacement response for Motion #1 ROCKS1N1 (Red part shows the end of shaking) for Case 8	323
Figure C.29. Moment-curvature response at column top for Column 1 of Bent 6 for Motion #2 ROCKS1N2 (Red part shows the end of shaking) for Case 8	324
Figure C.30. Abutment (left or right) transverse resisting force-displacement response for Motion #2 ROCKS1N2 (Red part shows the end of shaking) for Case 8	324
Figure D.1. Bi-linear moment-curvature relationship: (a) column; (b) pile shaft	328
Figure D.2. Idealized soil p - y curve at a depth of 0.5 ft (Caltrans 2005).....	329
Figure D.3. Idealized soil p - y curve at a depth of 16.5 ft (Caltrans 2005).....	329
Figure D.4. Idealized soil p - y curve at a depth of 17.5 ft (Caltrans 2005).....	329
Figure D.5. Idealized soil p - y curve at a depth of 106.5 ft (Caltrans 2005).....	330
Figure D.6. Idealized soil t - z curves (Caltrans 2005)	330

Figure D.7. Idealized soil Q - z curves (Caltrans 2005).....	330
Figure E.1. Column moment-curvature relationship in the longitudinal direction for: (a) Pier S-8 and Pier S-9; (b) other piers	335
Figure E.2. Column moment-curvature relationship in the transverse direction for: (a) Pier S-8 and Pier S-9; (b) other piers	336
Figure E.3. Foundation matrix definition	337
Figure E.4. Acceleration response spectrum employed in the ESA	337
Figure H.1. PEER PBEE methodology (Porter 2003)	352
Figure H.2. Schematic procedure of the LLRCAT methodology for a single bridge component Mackie <i>et al.</i> (2010)	353
Figure H.3. EDP vs. IM in log-log space	353
Figure H.4. Damage states window	354
Figure H.5. Repair quantities window	354
Figure H.6. Unit costs window	355
Figure H.7. Production rates window	356
Figure H.8. Emission factors window.....	357
Figure H.9. Contribution to expected repair cost (\$) from each performance group	358
Figure H.10. Total repair cost ratio (%) as a function of intensity	358
Figure H.11. Contribution to expected repair cost (\$) from each repair quantity	359
Figure H.12. Contribution to repair cost standard deviation (\$) from each repair quantity.....	359
Figure H.13. Total repair time (CWD) as a function of intensity.....	360
Figure H.14. Contribution to expected repair time (CWD) from each repair quantity.....	360
Figure H.15. Contribution to expected carbon footprint (Mg CO ₂ equivalent) from each repair	

quantity	361
Figure H.16. Contribution to expected carbon footprint (Mg CO ₂ equivalent) from each repair	
quantity	361
Figure I.1. Vertical-pile-supported wharf: (a) schematic of wharf transverse section; (b) wharf pile	
plan; (c) prestressed pile details; and (d) pile-to-deck connections from Yang <i>et al.</i>	
(2012)	369
Figure I.2. Numerical wharf model with soil profile from Yang <i>et al.</i> (2012).....	370
Figure I.3. Fragility curves for the pile-to-deck connection.....	370
Figure I.4. Demand model of the wharf under LA motions in terms of PGA (Yang <i>et al.</i> 2012)	
.....	371
Figure I.5. Probabilities of occurrence for each damage state for the wharf with cranes under the	
LA ground motion suite.....	371
Figure I.6. Expected repair cost vs. PGA for one pile	372
Figure J.1. Schematic abutment configuration and soil properties (not to scale).....	382
Figure J.2. Abutment configuration and soil properties.....	383
Figure J.3. Abutment elevation view.	383
Figure J.4. A crust trilinear force-deflection behavior (Caltrans 2017).....	384
Figure J.5. Two possible design cases to calculate the crust ultimate passive force (Caltrans 2017).	
.....	384
Figure J.6. Adjustment factors used in calculation of Δ_{max} : (a) depth factor, and (b) width factor	
(Caltrans 2017).....	385
Figure J.7. Crust trilinear p - y curve	386
Figure J.8. Modification of p_{ult} near liquefaction boundary (Caltrans 2017).....	386

List of Tables

Table 2.1. Natural periods and frequencies for Salinas Bridge	39
Table 2.2. Comparison of MSBridge and wFrame results for ESA of Salinas Bridge	39
Table 2.3. Longitudinal ESA parameters for Salinas Bridge	39
Table 2.4. Longitudinal ESA result for Salinas Bridge	39
Table 2.5. Transverse ESA parameters for Bent 4.....	40
Table 2.6. Transverse ESA result for Salinas Bridge	40
Table 2.7. Salinas bridge deck maximum displacement	41
Table 2.8. Salinas bridge deck maximum acceleration.....	42
Table 2.9. Column heights for Samoa Bridge	43
Table 2.10. Natural periods and frequencies for Samoa Bridge.....	43
Table 2.11. Longitudinal ESA parameters for Samoa Bridge	43
Table 2.12. Longitudinal ESA result for Samoa Bridge	44
Table 2.13. Transverse ESA parameters for Pier S-8	44
Table 2.14. Transverse ESA result for Pier S-8.....	44
Table 2.15. Samoa bridge deck maximum displacement	45
Table 2.16. Samoa bridge deck maximum acceleration.....	46
Table 2.17. Natural periods and frequencies for Samoa Bridge with stiff foundation matrix	46
Table 2.18. Natural periods and frequencies for Samoa Bridge with rigid pier base	47
Table 2.19. Longitudinal ESA parameters for Samoa Bridge with stiff foundation matrix	47
Table 2.20. Longitudinal ESA result for Samoa Bridge with stiff foundation matrix.....	47
Table 2.21. Transverse ESA parameters for Pier S-8	47
Table 2.22. Transverse ESA result for Samoa Bridge with stiff foundation matrix.....	47

Table 2.23. Deck maximum displacement for Samoa Bridge with stiff foundation matrix	48
Table 2.24. Deck maximum acceleration for Samoa Bridge with stiff foundation matrix	49
Table 2.25. Column heights for Eureka Bridge	50
Table 2.26. Natural periods and frequencies for Eureka Bridge	50
Table 2.27. Longitudinal ESA parameters for Eureka Bridge	50
Table 2.28. Longitudinal ESA result for Eureka Bridge	51
Table 2.29. Transverse ESA parameters for Pier E-6	51
Table 2.30. Transverse ESA result for Eureka Bridge	51
Table 2.31. Eureka bridge deck maximum displacement	52
Table 2.32. Eureka bridge deck maximum acceleration	53
Table 3.1. Geometric and material properties of a bearing pad (Lu <i>et al.</i> 2011)	108
Table 3.2. SDC 2010-Sand abutment model properties	108
Table 3.3. Periods of the studied bridge for different abutment models	109
Table 4.1. Performance groups and associated engineering demand parameters after Mackie <i>et al.</i> (2007)	125
Table 4.2. Bridge deck material and section properties	126
Table 4.3. Bridge pier columns material and section properties	126
Table 4.4. Constitutive model parameters for concrete material used in fiber beam-column element	126
Table 4.5. Soil types and properties	127
Table 5.1. Constitutive model parameters for concrete material used in fiber beam-column element	149
Table 5.2. Bridge deck material and section properties for Samoa Bridge (Wang 2015)	149

Table 5.3. Bridge pier columns material and section properties for Samoa Bridge (Wang 2015)	149
Table 5.4. Samoa Bridge constant foundation matrix coefficients for all bents (Wang 2015) ...	150
Table 6.1. Uniform hazard spectra, 5% damping, 50% in 50 years (Somerville and Collins 2002)	182
Table 6.2. Uniform hazard spectra, 5% damping, 10% in 50 years (Somerville and Collins 2002)	183
Table 6.3. Uniform hazard spectra, 5% damping, 2% in 50 years (Somerville and Collins 2002)	184
Table 6.4. Deaggregation of hazard spectra, 5% damping, rock (Somerville and Collins 2002)	185
Table 6.5. Deaggregation of hazard spectra, 5% damping, soil (Somerville and Collins 2002).	185
Table 6.6. Time histories representing the 50% in 50 years hazard level (Somerville and Collins 2002).....	186
Table 6.7. Time histories representing the 10% in 50 years hazard level (Somerville and Collins 2002).....	187
Table 6.8. Time histories representing the 2% in 50 years hazard level (Somerville and Collins 2002).....	188
Table 7.1. Soil properties (Almutairi <i>et al.</i> 2016).....	213
Table 7.2. Bridge deck material and section properties	213
Table 7.3. Bridge bentcap properties	213
Table 7.4. Constitutive model parameters for concrete material of fiber beam-column element	214
Table 7.5. Geometric and material properties of a bearing pad (Lu <i>et al.</i> 2011).....	214

Table 7.6. Performance groups and associated engineering demand parameters and damage states	215
Table 8.1. Summary of comparison for shear strength estimation study	239
Table A.1. MSBridge Feature-verification cases.....	274
Table B.1. Input motions employed in the nonlinear THA.....	280
Table B.2. Intensity measures of the 14 motions.....	280
Table C.1. Comparison of MSBridge and wFrame results for the transverse ESA	299
Table C.2. Comparison of transverse ESA displacement demand and THA maximum displacement (ESA displacement demand for an individual motion is based on the response spectrum of that motion) for Case 1	299
Table C.3. Maximum column shear forces and bending moments (transverse) for Case 1	300
Table C.4. Comparison of transverse ESA displacement demand and THA maximum displacement (ESA displacement demand for an individual motion is based on the response spectrum of that motion) for Case 2.....	300
Table C.5. Maximum column shear forces and bending moments (transverse) for Case 2.....	301
Table C.6. Comparison of transverse ESA displacement demand and THA maximum displacement (ESA displacement demand for an individual motion is based on the response spectrum of that motion) for Case 3.....	301
Table C.7. Maximum column shear forces and bending moments (transverse) for Case 3.....	302
Table C.8. Comparison of transverse ESA displacement demand and THA maximum displacement (ESA displacement demand for an individual motion is based on the response spectrum of that motion) for Case 4.....	302
Table C.9. Maximum column shear forces and bending moments (transverse) for Case 4.....	303

Table C.10. Comparison of transverse ESA displacement demand and THA maximum displacement (ESA displacement demand for an individual motion is based on the response spectrum of that motion) for Case 5	303
Table C.11. Maximum column shear forces and bending moments (transverse) for Case 5	304
Table C.12. Comparison of transverse ESA displacement demand and THA maximum displacement (ESA displacement demand for an individual motion is based on the response spectrum of that motion) for Case 7	304
Table C.13. Comparison of Cases 5 and 7 for THA maximum displacement	305
Table C.14. Maximum column shear forces and bending moments (transverse) for Cases 5 and 7	305
Table C.15. Comparison of transverse ESA displacement demand and THA maximum displacement (ESA displacement demand for an individual motion is based on the response spectrum of that motion) for Case 7	306
Table C.16. Comparison of Cases 5 and 8 for THA maximum displacement	307
Table C.17. Maximum column shear forces and bending moments (transverse) for Cases 5 and 8	307
Table C.18. Comparison of the average ESA displacement demand and THA maximum displacement for all the studied models	308
Table D.1. Salinas Bridge deck material and section properties	327
Table D.2. Salinas Bridge bentcap properties	327
Table E.1. Samoa Bridge foundation matrix coefficients (Wang 2015).....	333
Table E.2. Samoa Bridge constant foundation matrix coefficients for all bents (Wang 2015)...	333
Table E.3. Bridge deck material and section properties for Samoa Bridge (Wang 2015)	334

Table F.1. Bent foundation matrix coefficients for Eureka Bridge (Wang 2015).....	339
Table F.2. Material and section properties of the bridge deck for Eureka Bridge (Wang 2015)	339
Table H.1. PBEE performance groups.....	351
Table I.1. Damage states for wharf piles from Lehman <i>et al.</i> (2009).....	366
Table I.2. Fragility curve parameters from Yang <i>et al.</i> (2012)	366
Table I.3. Repair items: pile damage states after Mackie <i>et al.</i> (2007).....	367
Table I.4. Repair cost estimates after Mackie <i>et al.</i> (2007).....	368
Table J.1. Values of site factors, F_{pga}	381
Table J.2. Residual strengths by location	381
Table J.3. Adjustments for p-multiplier at the boundary of the liquefied layer	381

Acknowledgements

I would like to thank Professor Ahmed Elgamal for his support, guidance, and encouragement throughout the Ph.D. program. His efforts are much appreciated.

In addition, my gratitude to my friends in the research group for their support and advice: Muhammed Zayed, Ismaail Ghaawod, Kyungtae Kim, Athul Prabhakaran, John Li, Zhijian Qiu, and Lan Luo. I will always be grateful for your friendship.

Special thanks to: (i) Dr. Jinchu Lu for his great contribution to the computational aspects and the user-interface (MSBridge). In addition, my gratitude to him for helpful suggestions and technical guidance; (ii) Dr. Ahmed Ebeido for his friendship and technical guidance in liquefaction studies; (iii) Prof. Kevin R. Mackie of the University of Central Florida for time he dedicated to help and provide valuable suggestions and insights; (iv) Prof. Geoffrey Martin for all the information and advice; and (v) Finally, I would like to thank the members of my committee for their help, guidance, and support throughout this work

This work was supported in part by the Pacific Earthquake Engineering Research Center (PEER). Contributions, guidance, and feedback from PEER researchers working within the PEER Transportation Research Program are gratefully acknowledged. In addition, I am grateful for the valuable technical contributions provided by Caltrans engineers, particularly Dr. Charles Sikorsky, Dr. Toorak Zokaie, Mr. Yeo (Tony) Yoon, Dr. Mark Mahan, Dr. Anoosh Shamsabadi, and Mr. Steve Mitchell.

This thesis contains a mix of material published in a technical report, conference papers, and new content being prepared for publication. A summary of this work is given below.

Chapter 2, in part, has been published as it appears in the following technical report publication (The dissertation author was the primary investigator and author of this paper):

Almutairi, A.S., Lu, J., Wang, N., Elgamal, A. (2016). "Analysis of multi-span bridges Using OpenSees." Research Report, SSRP-16/01, Department of Structural Engineering, University of California, San Diego (UCSD).

Chapter 4, in part, is a reprint of material as it appears in the following conference publication (The dissertation author was the primary investigator and author of this paper):

Almutairi, A.S., Lu, J., Elgamal, A., and Mackie, K.R. (2017). "Performance-based earthquake assessment of multi-span bridge systems including soil-pile-structure interaction." Proceedings of the 3rd International Conference on Performance-based Design in Earthquake Geotechnical Engineering (PBD-III), Vancouver, BC, Canada, July 16-19.

Chapter 4, in part, is a reprint of material as it appears in the following conference publication (The dissertation author was the primary investigator and author of this paper):

Lu, J., Almutairi, A.S., Elgamal, A., and Mackie, K.R. (2018). "A computational framework for systematic bridge performance-based earthquake engineering applications." Proceedings of the 11th U.S. National Conference on Earthquake Engineering (Integrating Science, Engineering & Policy), Los Angeles, California, June 25-29.

Chapter 5, in full, is currently being prepared for submission for publication of the material as it may appear in the following journal publication (The dissertation author was the primary investigator and author of this paper):

Almutairi, A.S., Lu, J., Wang, N. and Elgamal, A., "Performance-based earthquake assessment for calibrated model of Samoa Channel Bridge".

Chapter 6, in full, is currently being prepared for submission for publication of the material as it may appear in the following journal publication (The dissertation author was the primary investigator and author of this paper):

Almutairi, A.S., Lu, J., Wang, N. and Elgamal, A., “Probabilistic Seismic Response of Samoa Channel Bridge including ground-foundation interaction”.

Chapter 7, in full, is currently being prepared for submission for publication of the material as it may appear in the following journal publication (The dissertation author was the primary investigator and author of this paper):

Almutairi, A.S., Lu, J., Wang, N. and Elgamal, A., “Framework for Assessment of Bridge-Ground Response due to Liquefaction-Induced Lateral Spreading”.

Chapter 8, in full, is currently being prepared for submission for publication of the material as it may appear in the following journal publication (The dissertation author was the primary investigator and author of this paper):

Almutairi, A.S., Lu, J., Wang, N. and Elgamal, A., “Sensitivity of Seismic Demands of Bridge-Ground System Subjected to Liquefaction-Induced Lateral Spreading”.

Vita

- 01/2011 Bachelor of Engineering in Civil Engineering
Kuwait University, Kuwait City, Kuwait.
- 05/2014 Master of Science in Civil Engineering
Purdue University, West Lafayette, USA.
- 09/2019 Doctor of Philosophy in Structural Engineering
University of California San Diego, La Jolla, USA.

Publications

- Almutairi, A.S.**, Lu, J, Wang, N. and Elgamal, A. (in preparation). “Performance-based earthquake assessment for calibrated model of Samoa Channel Bridge.”
- Almutairi, A.S.**, Lu, J, Wang, N. and Elgamal, A. (in preparation). “Probabilistic Seismic Response of Samoa Channel Bridge including ground-foundation interaction.”
- Almutairi, A.S.**, Ebeido, A, Lu, J. and Elgamal, A. (in preparation). “Framework for Assessment of Bridge-Ground Response due to Liquefaction-Induced Lateral Spreading.”
- Almutairi, A.S.**, Ebeido, A., Lu, J. and Elgamal, A. (in preparation). “Sensitivity of Seismic Demands of Bridge-Ground System Subjected to Liquefaction-Induced Lateral Spreading.”
- Qiu, Z., Lu, J, Elgamal, A., Su, L., Wang, N. and **Almutairi, A.S.** (accepted). “OpenSees Three-Dimensional Computational Modeling of Ground-Structure Systems and Liquefaction Scenarios” *Journal of Computer Modeling in Engineering & Sciences*.
- Lu, J., **Almutairi, A.S.**, Elgamal, A., and Mackie, K.R. (2018). “A computational framework for systematic bridge performance-based earthquake engineering applications.” *Proceedings of the 11th U.S. National Conference on Earthquake Engineering (Integrating Science, Engineering & Policy)*, Los Angeles, California, June 25-29.

Almutairi, A.S., Lu, J., Elgamal, A., and Mackie, K.R. (2017). “Performance-based earthquake assessment of multi-span bridge systems including soil-pile-structure interaction.” Proceedings of the 3rd International Conference on Performance-based Design in Earthquake Geotechnical Engineering (PBD-III), Vancouver, BC, Canada, July 16-19.

Ebeido, A., Qiu, Z., Lu, J., **Almutairi, A.S.**, Elgamal, A. and Martin, G.R. (2017). “Simplified and finite element analysis for lateral spreading effects on bridge foundations.” Research Report, SSRP-17/05, Department of Structural Engineering, University of California, San Diego (UCSD).

Almutairi, A.S., Lu, J., Wang, N., Elgamal, A. (2016). “Analysis of multi-span bridges Using OpenSees.” Research Report, SSRP-16/01, Department of Structural Engineering, University of California, San Diego (UCSD).

Abstract of the Dissertation

Seismic Response and Performance-Based Assessment of Multi-Span Bridge-Ground Systems

by

Abdullah S E S E Almutairi

Doctor of Philosophy in Structural Engineering

University of California San Diego, 2019

Professor Ahmed Elgamal, Chair

The conducted study is directed towards enhancements in performance assessment of highway bridges under a wide range of earthquake input shaking scenarios. Seismic response of the superstructure is highly influenced by the global bridge-ground characteristics as an integral system. Therefore, nonlinear representation of the bridge deck, columns, abutments, and

foundation response are to be integrated within a unified framework. On this basis, a performance-based earthquake engineering (PBEE) framework was extended and utilized to estimate the post-earthquake loss. To facilitate systematic execution of this analysis framework, a graphical user-interface was further developed and employed.

For calibration purposes, a Finite Element (FE) model of an existing large heavily instrumented bridge system at Eureka, California (Samoa Channel Bridge) was developed. Calibration was undertaken based on the recorded earthquake response. Numerical simulations of the bridge model under seismic loading conditions were conducted. Simulation results show that the recorded data provide valuable insights to understand the seismic bridge response and to reliably estimate the damage.

Using a practice-oriented pushover procedure, the response of a bridge subjected to liquefaction-induced lateral spreading was investigated. The analysis framework and representative results are presented, where the abutment lateral slope displacement is resisted by the entire bridge configuration. Permanent ground deformation induces longitudinal displacement on the abutment and consequently the entire bridge system. As such, the response of the bridge and its pile foundations were investigated and correlated with the imposed lateral spreading displacement.

Overall, the novel contributions and findings are summarized as follows: (1) A bridge-ground seismic response computational analysis tool was further developed for routine practical applications; (2) In this tool, a PBEE framework was extended to handle multi-span bridge-ground systems within an integrated simulation environment; (3) Calibrated by recorded earthquake response, a framework was implemented for a representative large instrumented bridge-ground system in California to illustrate the involved response mechanisms and PBEE outcomes; (4) For

response under lateral spreading considerations, a global bridge-ground systematic analysis framework was proposed and developed; (5) Patterned after an existing bridge in California, the framework was implemented with parametric studies addressing the procedure assumptions and potential retrofit bridge configurations.

Chapter 1. Introduction and Literature Review

In this chapter, motivation and scope of this research are presented. A brief overview of highway bridge seismic response studies is provided. In addition, existing literature on numerical simulations of bridge-foundation-ground systems is reviewed. Finally, organization of this dissertation is presented.

1.1. Motivation

From the earthquake engineering point of view, highway bridges are an integral part of critical lifelines, and as such have been receiving much research attention. Smooth operation of the highway systems after a major earthquake facilitates critical rescue and recovery efforts. Disruption of function can also result in substantial negative wide-scale economic consequences.

The increased failure potential of highway bridges and their susceptibility to damage during extreme events necessitate researchers to increase their understanding of the seismic response of bridges to mitigate post-earthquake consequences. For that purpose, more complex numerical tools have been developed and utilized to simulate the bridge response mechanisms.

The effect of soil-structure-interaction (SSI) may play a vital role in shaping the dynamic behavior of bridge components during a seismic event and consequently, the anticipated damage. In particular, the damage caused by ground failures such as liquefaction and lateral displacement has been observed to be a major concern. Recent earthquakes highlight the significance of lateral spreading effects on bridge-ground-foundation systems. Large soil deformation due to liquefaction induced lateral spreading may result in severe damage to bridge abutments and foundations, or even collapse. In order to quantify the damage of bridges at different hazard levels, probabilistic approaches have been proposed and utilized to account for uncertainties in seismic loading and structural modeling.

1.2. Performance of Bridge Systems in Past Earthquakes

Performance-based design has been receiving a great deal of attention, and many design codes are initiating the application of its concepts. The disruption and failure of bridges will result in direct and indirect economic suffering and delay in the post-earthquake recovery efforts. In the United States, 60 percent of bridges were constructed before 1970 without fully considering seismic resistance (Itani *et al.* 2004). For example, the 1964 Alaska earthquake, also known as the Great Alaskan Earthquake, caused a significant amount of damage and caused about 139 deaths. This powerful earthquake produced liquefaction in the region that caused the collapse of more than 20 highway bridges (Kachadoorian 1968; Ross *et al.* 1969; Youd 1993). In 1971, more than 60 bridges were damaged on the Golden State Freeway in California during the 6.6 Mw San Fernando earthquake (O'Rourke *et al.* 1992).

The Northridge earthquake happened 25 years ago in 1994 centered in the north-central San Fernando Valley region of Los Angeles, California. It shook the ground for about 15 seconds with a peak moment magnitude (M_w) of 6.7 and an incredibly high ground acceleration of as much as 1.8g measured in the urban Los Angeles area. The death toll was 57, with more than 8,000 injured. In addition, earthquake-caused property damage was estimated to be more than \$20 billion, making it one of the costliest natural disasters in U.S. history (Mahin 1997; Basoz *et al.* 1999). Bridges among other structures were severely damaged or collapsed. As a result, design code changes were made after the event to avoid a similar loss to bridges (Figure 1.1).

Furthermore, damage to bridges caused by ground failures such as liquefaction and lateral displacement was observed during recent earthquakes, including the 2010 Maule event (Arduino *et al.* 2010; Ledezma *et al.* 2012; Verdugo *et al.* 2011) and the 2011 Christchurch event (Cubrinovski *et al.* 2011, 2014; Whotherspoon *et al.* 2011). From these investigations, the

observed response was often noted to be highly influenced by the global bridge-ground overall characteristics as an integral system.

1.3. Influence of Soil-Structure Interaction on Bridge Seismic Response

It was widely believed among structural engineers that SSI is beneficial to the structural behavior under seismic loading. NEHRP-94 (NEHRP 1994) seismic code states that: “*These [seismic] forces therefore can be evaluated conservatively without the adjustments recommended in Sec. 2.5 [i.e., for SSI effects]*” which supports the past belief of the beneficial effect of SSI on the structural behavior. However, a study by Mylonakis and Gazetas (2000) shows that SSI can be detrimental. Nevertheless, the study by Jeremić *et al.* (2004) shows that the role of SSI can be both beneficial and detrimental depending on the characteristics of the earthquake motion. To reach this conclusion, Jeremić *et al.* (2004) used three scaling factors to match selected period points on the hazard spectra that correspond to damage states of the structural model (i.e., elastic, cracked and yielded) for each of the previously mentioned case.

In general, the response of a bridge structure is often highly influenced by SSI and seismic wave propagation during an earthquake (Stewart *et al.* 1998; Datta 2010). Failure or movement of the foundation is the main cause of bridge’s severe damage or complete collapse. Modeling the bridge-ground overall characteristics as an integral system is finding its way in some studies as a step forward toward more realistic analysis (Chen and Penzien 1977; Dendrou *et al.* 1985; Sweet 1993; Makris *et al.* 1994; McCallen and Romstadt 1994; Kappos *et al.* 2002; Jeremić *et al.* 2004; Elgamal *et al.* 2008; Mackie *et al.* 2012; Almutairi *et al.* 2017; Wang *et al.* 2018).

Jeremić *et al.* (2004) studied the seismic behavior of an elevated highway bridge (the I-880 viaduct) using 3D modeling of a structure-ground system. However, this study was more concerned with the role of soil-foundation-structure interaction (SFSI). For that purpose, the

analyses were carried out using two separate models of the system. The first model assumed a rigid connection between the bridge column and the foundation. The second model was analyzed using equivalent springs derived from 3D finite element analysis of the pile foundation in a layered soil system (Jeremić *et al.* 2004).

Similarly, Mackie *et al.* (2012) performed nonlinear time history analyses (THA) of a bridge-foundation-ground system of a single-column bent founded on four sites of varying stiffness and strength profiles ranging from rigid rock to weak upper soil strata. The analyses were coupled with PBEE framework to quantify the damage consequences of each component of the bridge. Based on the simulation results, Mackie *et al.* (2012) found that including SSI has a detrimental effect on the bridge performance, where the weaker upper soil strata case resulted in the largest post-earthquake repair estimates.

The role of SSI was also studied by Almutairi *et al.* (2017) for a multi-span bridge system derived from Mackie *et al.* (2012). For that purpose and in order to simplify the simulations, SSI was handled by soil p - y curves. Two models were created to run nonlinear THA along with PBEE and to investigate the seismic response and the damage consequences. Similar to the previous study, the detrimental effect of SSI was observed (Almutairi *et al.* 2017).

1.4. Numerical Evaluation of Soil-Structure Interaction

The numerical evaluation of SSI can be divided into two main approaches: (1) *comprehensive model approach*, and (2) *equivalent substructure approach*. Wang (2015) presents a thorough description of both approaches.

1.4.1. Comprehensive Model Approach

The first approach (i.e., *comprehensive model approach*) handles SSI using 3D linear or nonlinear soil constitutive models. This approach is assumed to be more accurate since the

structure, the foundation, and the soil are all analyzed as one integral system. However, this approach is computationally expensive that requires high-speed CPU and large memory. This approach was used by several researchers (Casciati and Borja 2004; Elgamal *et al.* 2008; Zhang *et al.* 2008; Bao *et al.* 2012).

1.4.2. Equivalent Substructure Approach

The second approach (i.e., *equivalent substructure approach*) breaks down SSI into three independent steps (Mylonakis *et al.* 1997): (1) evaluation of the foundation kinematic response, (2) determination of the spring/dashpot properties based on the inertia mechanism, and (3) dynamic analysis of the structure supported on a compliant base. This approach can be classified into two main categories: (1) soil springs approach or (2) foundation matrix approach.

1.4.2.1. Soil Springs Approach

Using the soil springs approach (API 1993, Figure 1.2), the interaction between soil and foundation is modeled using a series of nonlinear force-deflection relationships (i.e., p - y , t - z , and Q - z curves) (Lam and Martin 1986). API (1993) provides criteria in calculating spring resistance forces for different soil types. This approach of handling SSI was used by several researchers (Boulanger *et al.* 2004; Jeremić *et al.* 2004; Shin *et al.* 2008; Li 2014; Li and Conte 2016; Almutairi *et al.* 2017).

1.4.2.2. Foundation Matrix Approach

In this approach, the foundation is represented by a coupled 6×6 pile-head stiffness matrix associated with all six degrees of freedom at the pile head (Lam and Martin 1986; Shamsabadi and Law 2010, Figure 1.3). In calculating stiffness matrices using the computer program PILAY, Novak (1991) defined each stiffness term (k_{ij}) by applying a force (or moment) that was needed to generate a unit displacement (or rotation) in the specified direction.

Nevertheless, Lam and Martin (1986) developed a simpler method to calculate each stiffness matrix term using charts that are functions of soil reaction and pile flexural rigidity (EI). This approach was used by several researchers to simplify the handling of SSI when applying the ground motions on highway bridge systems (Ingham *et al.* 1999; Zhang and Makris 2002; Almutairi *et al.* 2019).

1.5. Damage Caused by Liquefaction

Soil liquefaction and its consequences have been found to be a major concern that may result in significant damage or collapse (Youd 1993; Tokimatsu *et al.* 1995; Hamada *et al.* 1996; Berrill *et al.* 2001; Elgamal *et al.* 2008; Shin *et al.* 2008; Kwon *et al.* 2009; Aygün *et al.* 2009, 2011; Ledezma and Bray 2010; Wotherspoon *et al.* 2011; Ledezma *et al.* 2012; Padgett *et al.* 2013; Cubrinovski *et al.* 2014; Turner *et al.* 2016; Khosravifar *et al.* 2018). Specifically, Elgamal *et al.* (2008) created a 3D nonlinear computational model of Humboldt Bay Bridge to investigate the effect of lateral spreading on bridge components and the contribution to the simulated damage condition. Kwon *et al.* (2009) created fragility curves for the Meloland Road Overcrossing Bridge and studied the damage at the bottom of the central pier.

Earthquake-induced lateral deformation at bridge abutments underlain by liquefied soil may be reduced by restraining forces that come from the pile foundation and bridge superstructure. Armstrong *et al.* (2013, 2014) performed three centrifuge tests involving three non-piled embankments and three piled embankments. Based on the experimental results, the restraining forces from the pile configurations reduced the embankment displacement by 20-80% (Armstrong *et al.* 2013, 2014).

From the practice-oriented point of view, a simplified approach has been proposed in which soil springs are used to impose a level of expected lateral ground deformation at abutments

(Caltrans 2017). This approach and similar techniques were employed by several researchers (Finn and Fujita 2002; Boulanger *et al.* 2006, 2007; Ashford *et al.* 2009, 2011; Armstrong *et al.* 2013, 2014). In particular, Boulanger *et al.* (2006, 2007) derived procedures for the seismic design of pile foundation for liquefaction effects from a combination of dynamic centrifuge model test and nonlinear dynamic finite element studies.

1.6. Performance-Based Earthquake Assessment of Bridge Systems

After an earthquake, there are two main elements necessary for quantifying and minimizing economic loss, the cost associated with damage, and the consequences due to the loss of functionality. Uncertainties in modeling of an actual structure are unavoidable in terms of seismic hazard and the expected loss. Therefore, the probabilistic approach is preferred in order to quantify the damage and loss.

In order to account for uncertainties in seismic loading and structural modeling, the seismic performance of structures must be characterized in a probabilistic manner. Accounting for these uncertainties prompted the development of a well-established methodology originally proposed by Cornell and Krawinkler (2000). A Performance-Based Earthquake Engineering (PBEE) framework was developed by the Pacific Earthquake Engineering Research (PEER) Center. The main objective of this methodology is to enable the quantitative assessment of risk in terms of probability imposed on a civil structure by possible future earthquakes, which involves seismology, geotechnical and structural engineering, and construction or repair cost estimate.

By using the total probability theorem, the desired probability distributions are computed by dividing the task into several intermediate probabilistic models with different sources of randomness: (1) hazard model that uses the input ground motions to determine the intensity measures (IMs), (2) demand model that uses the response after the FE run to determine the

engineering demand parameters (EDPs), and (3) damage model that connects the EDPs to damage measure (DM) and then to repair quantities (Qs).

Earlier, significant research efforts have been devoted to the development of the PEER PBEE methodology (Cornell and Krawinkler 2000; Krawinkler 2002; Porter 2003; Krawinkler and Miranda 2004; Moehle and Deierlein 2004, Mosalam and Günay 2014). Applications of PBEE in probabilistic performance evaluation of various testbed structures can be found in many studies (Goulet *et al.* 2006; Kunnath 2006; and Mitrani-Reiser *et al.* 2006).

During major earthquakes, the seismic response of bridges is influenced by SSI effects (Kappos *et al.* 2002; Shin *et al.* 2008; Ledezma and Bray 2008; Bradley *et al.* 2010). In addition, unrealistic modeling of the foundations will not only affect the seismic response, but also the repair cost and repair time estimates (Mackie *et al.* 2012). Therefore, in order to fully address the post-earthquake repair cost and downtime using PBEE framework, considering the response of the entire bridge-foundation-ground system is essential.

PBEE assessment can be used to compare the effectiveness of different bridge design options and evaluate the performance of existing bridges for different hazard levels (Mackie *et al.* 2010). Therefore, it requires the complete structural response from the FE run before performing the probabilistic analysis to estimate the repair costs and times required to restore a structure to its original function. The framework will provide stakeholders with a valuable tool that contributes to economic-based and environment-based decision making.

1.7. Objectives and Scope

As a whole, this dissertation provides a range of studies to enhance the understanding of nonlinear analysis of multi-span bridge systems including the impact of SSI, and to reliably

estimate the loss under a wide range of earthquake scenarios. Main objectives of this research are summarized as follows:

1. Extend the PBEE framework to account for multi-span bridge systems within an integrated simulation environment.
2. Add carbon footprint of repair as a performance metric by using the economic input-output life cycle assessment (EIO-LCA) method (CMU 2013; Mackie *et al.* 2015).
3. Develop a FE model for an existing heavily instrumented large bridge, calibrate it based on recorded earthquake response.
4. Conduct PBEE analysis on the calibrated bridge model.
5. Investigate the seismic response of the calibrated bridge model using a set of site-specific time histories developed under three hazard levels (Somerville and Collins 2002).
6. Investigate the response of an existing representative bridge system subjected to liquefaction-induced lateral spreading using a proposed simplified (Caltrans 2017, MTD 20-15) method.

1.8. Outline

This dissertation consists of 9 chapters, organized as follow:

- *Chapter 1: Introduction and Literature Review.* Presents a brief overview of the motivation behind the research program and a summary of previous work. This chapter discussed an overview of the methodologies and approaches implemented in this study.
- *Chapter 2: Simplified Equivalent Static Analysis and Nonlinear Time History Analysis of Multi-Span Bridges.* Describes the research work done to establish FE models that can be used to study the seismic response of bridges in California. For that purpose, models for

Salinas River Bridge, Samoa Channel Bridge, and Eureka Channel Bridge were developed. In addition, nonlinear THA and Equivalent Static Analysis (ESA) were conducted.

- *Chapter 3: Effect of Abutment Modeling on the Bridge Seismic Response and Loss Assessment.* Investigate the impact of abutment models on the seismic bridge response. For that purpose, three abutment models were considered and compared.
- *Chapter 4: Implementation of Performance-Based Earthquake Assessment of Multi-Span Bridge-Ground Systems.* Focuses on the significance of including SSI to reliably estimate the post-earthquake consequences in terms of repair cost and repair time. For that purpose, FE simulations were performed using two ground profiles. The first model assumes bridge columns to be rigidly connected to the foundation, excluding SSI. The second model incorporates SSI using the soil p - y curves approach.
- *Chapter 5: Performance-Based Earthquake Assessment of Samoa Channel Bridge-Foundation System.* This chapter investigates the performance of a large retrofitted bridge using a calibrated model based on the actual response within a comparative scope between the case after retrofit and before retrofit.
- *Chapter 6: Seismic Response of Samoa Channel Bridge-Foundation System Subjected to Site-Specific Motions.* Compares the seismic demand model of Samoa Channel Bridge-Foundation system of the three hazard levels, namely 50% in 50 years, 10% in 50 years, and 2% in 50 years.
- *Chapter 7: Framework for Assessment of Bridge-Ground Response due to Liquefaction-Induced Lateral Spreading.* Describes a detailed procedure to estimate the lateral displacement induced by seismic loading using the Simplified Method Approach. In addition, the PBEE framework is utilized to estimate the post-earthquake loss.

- *Chapter 8: Sensitivity of Seismic Demands of Bridge-Ground System Subjected to Liquefaction-Induced Lateral Spreading.* Focuses on the sensitivity of the Equivalent Static Simplified Procedure by varying the shear strength of the liquefiable layer and using an alternative equation to estimate the design displacement. In addition, the effect of different retrofit plans on the abutment was also addressed.
- *Chapter 9: Conclusions and Future Work.* Summarizes the main findings and provides recommendations for future work.

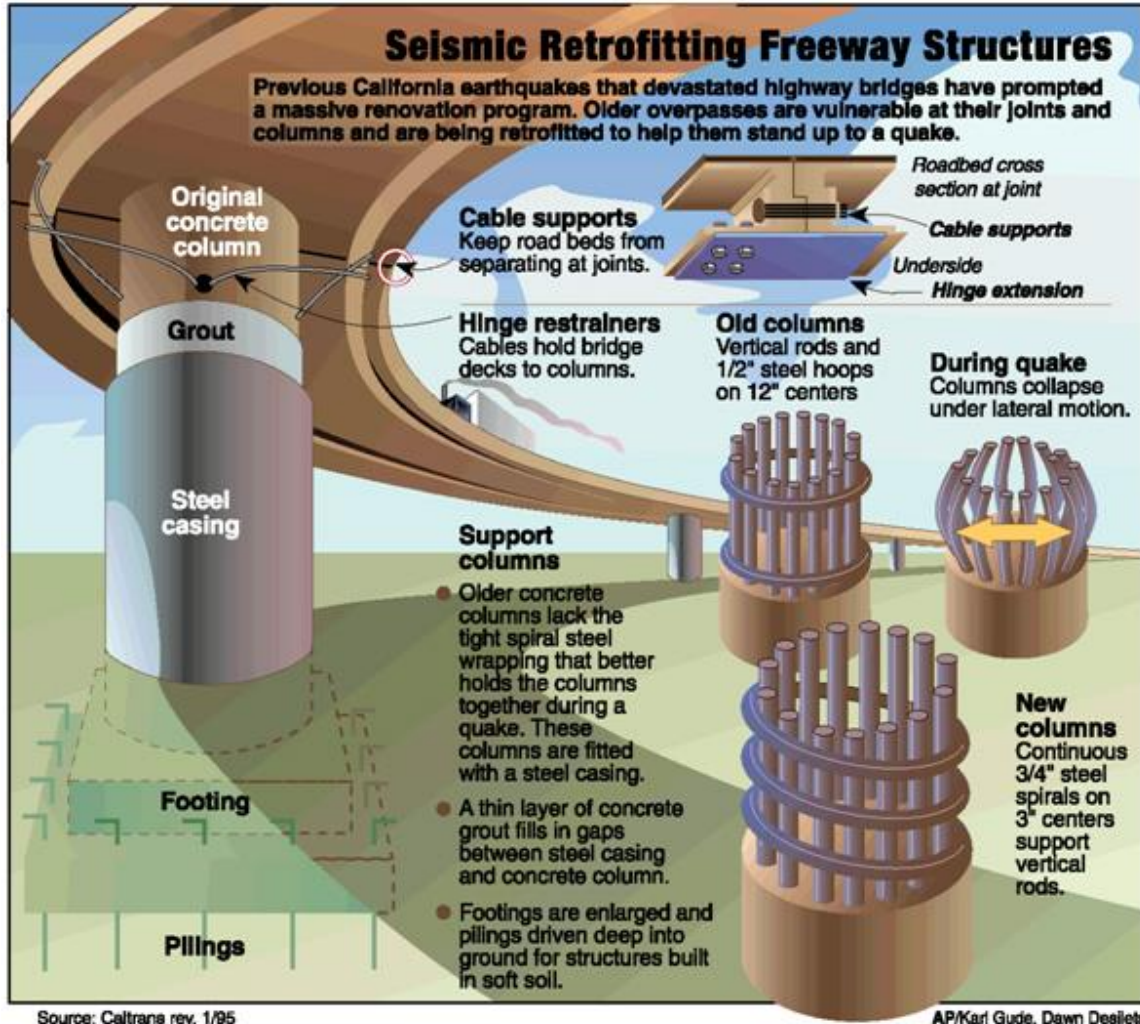


Figure 1.1. Caltrans seismic retrofit program

(<http://www.dot.ca.gov/hq/paffairs/about/retrofit.htm>)

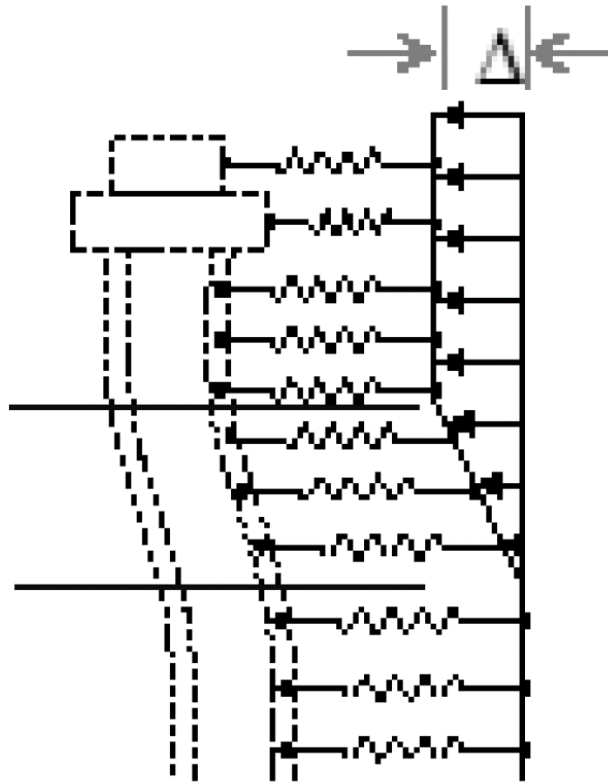


Figure 1.2. Soil springs in the equivalent pile analysis (MTD 20-15, Caltrans 2017)

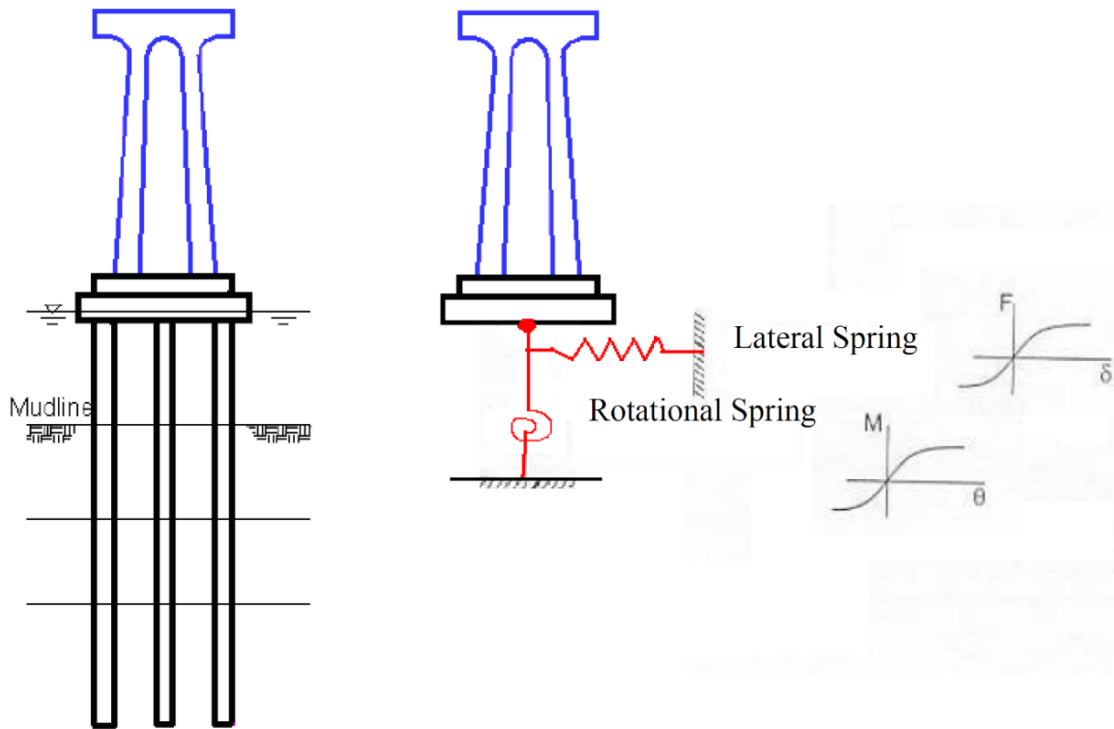


Figure 1.3. Equivalent base spring for pile group foundation (Shamsabadi and Law 2010)

Chapter 2. Simplified Equivalent Static Analysis and Nonlinear Time History Analysis of Multi-Span Bridges

2.1. Abstract

In this chapter, Equivalent Static Analysis (ESA), a well-established simplified procedure, was employed. Representative nonlinear Time History Analysis (THA) was undertaken as well. Conducted earlier in the research effort, this chapter addresses primarily the development of multi-span FE bridge models and the overall THA framework to be employed throughout this research effort. On this basis, seismic response parametric studies of three multi-span bridge-ground systems were performed using OpenSees. The investigated models were derived from three bridge configurations in California (the Salinas River Bridge, the Samoa Channel Bridge, and the Eureka Channel Bridge). THA was conducted for 14 input motions provided by Caltrans. The THA procedures and results are presented in this chapter. Results of the ESA procedure are presented as well. The main purpose of this study is to shed light on additional insights that can be gained from THA. To facilitate the conducted analyses, the user-interface MSBridge, in which Finite Element (FE) computations are performed using OpenSees, was further developed and employed.

In the Salinas River Bridge model, the columns are modeled using the force-based beam-column element (based on the plastic hinge integration method `BeamWithHinges`) with an idealized bi-linear moment-curvature relationship. The column foundation response is represented by p - y , t - z , and Q - z springs. Furthermore, in the Samoa Channel Bridge and the Eureka Channel Bridge models, the pier columns are modeled using the nonlinear fiber section and the force-based beam-column element with the distributed plasticity integration method (`forceBeamColumn`). The pier foundation response is modeled using the Foundation Matrix approach. In all cases, an elastic abutment model is employed for simplicity.

In this preliminary study, comparison of the ESA and THA average results shows that the difference in displacement demand is about 12% for the Salinas River Bridge (for both longitudinal and transverse directions). For the Samoa Channel Bridge and the Eureka Channel Bridge models, the differences are 5.8% and 27.5%, respectively, in the longitudinal direction. In addition, the differences between the ESA and THA results in the transverse direction are 15.8% and 4.5%, respectively, for the above two bridges. In future studies, spectrum matched input ground motions time histories would provide a more appropriate basis for conducting such comparisons.

2.2. Introduction

2.2.1. Background

Three multi-span bridges were modeled using FE to investigate the seismic response. For that purpose, OpenSees (ver.2.5.0), an open-source software for simulating the seismic response of structural and geotechnical systems (Mazzoni *et al.* 2009, McKenna *et al.* 2010) was utilized to perform the nonlinear THA. The investigated models were derived from three bridge configurations in California, namely, the Salinas River Bridge, the Samoa Channel Bridge and the Eureka Channel Bridge.

To facilitate the conducted OpenSees analyses, the user-interface MSBridge (Elgamal *et al.* 2014; Lu *et al.* 2015) was further developed and employed. MSBridge is a PC-based graphical pre- and post-processor (user-interface) for conducting nonlinear FE studies of multi-span bridge systems. The analysis options available in MSBridge include: i) Pushover analysis, ii) Mode shape analysis, iii) Single and multiple three-dimensional (3D) seismic THA, iv) ESA (Caltrans 2013), and v) Pushover analysis of soil movements (imposed displacement profile). Further information about MSBridge, along with the verifications of newly added capabilities, can be found in Appendix A.

Nonlinear Time History Analysis was conducted for 14 input motions (ranging from 0.32g-0.71g for peak acceleration) provided by Caltrans. Further details regarding these motions are provided in Appendix B. The THA procedures and results are presented in this chapter. Results of the corresponding ESA procedure are presented and compared to the THA average displacement demand outcome.

2.2.2. Chapter Scope and Layout

In the initial stage of this study, an effort was made to illustrate and verify the MSBridge salient features and capabilities. Details of the MSBridge feature-verification effort are presented and discussed in Appendix A. In the conducted verification analyses, a number of idealized bridge configurations were employed. Each of these configurations allowed for a simple and systematic assessment of the particular response feature being verified.

A preliminary study was conducted first to compare ESA and THA results. The focus was placed on the response in the transverse direction. The THA effort employed a set of 14 input ground motions provided by Caltrans (Further details regarding these motions are provided in Appendix B). A series of models of increasing complexity were studied in an attempt to separate influence of column nonlinear response, foundation p - y curves, and the added resistance provided at the bridge-end bents and abutments. A single bent model was studied first, followed by models of the entire bridge (to include the abutment end-effects). On this basis, it was noted that: i) Linear models of the bridge bent resulted in essentially identical response (ESA and THA); ii) Nonlinearity of the columns and base soil springs (p - y and t - z) caused a difference of about 25%; and iii) When the abutment effects were included, the difference actually decreased to somewhere in the neighborhood of 10%. Details of this preliminary study are included in Appendix C.

Section 2.3 presents the analysis procedures and results for the Salinas River Bridge idealization (with model properties included in Appendix D). In addition, the analysis procedures and results for the Samoa Channel Bridge and the Eureka Channel Bridge idealizations are presented in Section 2.4 and Section 2.5.

In the conducted nonlinear analyses for the Samoa Channel Bridge and the Eureka Channel Bridge, the pier columns were modeled using nonlinear Fiber section and the force-based beam-column element (`forceBeamcolumn`) with the distributed plasticity integration method. Details of the modeling techniques for the Samoa Channel Bridge and the Eureka Channel Bridge are described in Appendix E and Appendix F, respectively. Furthermore, Appendix G lists the OpenSees Tcl code snippets of the column nonlinear Fiber sections for the Samoa Channel Bridge and the Eureka Channel Bridge (as an example for modeling columns of arbitrary cross-section and reinforcement steel layout, as defined by Wang (2015) and employed in the user-interface).

2.3. Salinas River Bridge

The January flooding of 1997 along the Salinas River resulted in major damage to the North Bound Salinas River Bridge which was built in 1938 (Caltrans 2005). A new Salinas River Bridge (hereinafter referred to as “Salinas Bridge”, Figure 2.1 shows the general plan) was designed as the replacement structure (Caltrans 2005).

2.3.1. Bridge Description and Geometric Configuration

Salinas Bridge is a reinforced concrete box-girder bridge with 11 spans. According to Caltrans (2005), the following characteristics are provided:

- Each interior span is 140 ft long, and the substructure consists of two-column bents.
- Soil profile of the riverbed consists of very loose sand for the top 20 ft followed by 30 ft of loose sand and 150 ft of dense sand thereafter.

- Groundwater was encountered near the surface of the streambed, and there is a moderate to high potential for liquefaction.
- The site is located approximately 4 miles from the King City-Reliz Fault with a maximum credible earthquake of moment magnitude 7.
- Peak bedrock acceleration is estimated at 0.5g.

Figure 2.2 shows a sectional view of the bridge deck along with the pile shaft reinforcement details. The four-cell box girder is 42.5 ft wide by 5.75 ft deep; and the deck and soffit slabs are 8 in and 6 in thick, respectively.

2.3.2. OpenSees Bridge FE Model and Mode Shapes

Earlier, Salinas Bridge was studied by Caltrans (2005) using wFrame, a two-dimensional (2D) program for pushover analysis of bridge bents and frames (Mahan 2005). The analysis procedure and results were reported in Caltrans (2005). The FE model employed in this study (Figure 2.3) was created in MSBridge based on the wFrame model described in the above-mentioned Caltrans report (for purposes of comparison). Thus, uniform column height (48 ft) and span length (140 ft) were employed in this 3D model (Figure 2.3). Details of the employed modeling techniques and associated model properties are included in Appendix D. Comparison of MSBridge and wFrame pushover analysis for the Salinas Bridge model is presented in Section 2.3.3 and summarized in Table 2.2.

The force-based beam-column element (`beamWithHinges`) based on the plastic hinge integration method (Scott and Fenves 2006; Scott and Ryan 2013) with an idealized bi-linear moment-curvature relationship was used to model the columns and the pile shafts (Caltrans 2005). The deck and the bentcap were considered to be linear elastic.

An elastic abutment model, where the transverse abutment resistance was taken as a fraction of the longitudinal resistance provided by Caltrans (2005) was assumed for simplicity (Aviram *et al.* 2008a, 2008b). According to the Caltrans (2005) model, a pin connection was implemented at the base of the abutment.

Furthermore, the column foundation response was modeled by the approach of p - y , t - z , and Q - z soil curves (Caltrans 2005). In this p - y curves foundation representation, lateral soil resistance is provided as the p - y curves interact with the pile shafts (Caltrans 2005). Similarly, vertical soil resistance is provided by t - z and Q - z curves (Caltrans 2005). As such, the values of these curves (p - y , t - z , and Q - z) were converted to proper horizontal and vertical soil springs (Appendix D). Table 2.1 shows the natural periods and frequencies for the first five modes of Salinas Bridge.

2.3.3. Equivalent Static Analysis (ESA)

Caltrans (2005) presents the results of an ESA of the Salinas Bridge using wFrame (Mahan 2005). A comparison with this study was conducted first using MSBridge with the ARS (Figure 2.5) employed by Caltrans (2005). More details about conducting ESA in MSBridge can be found in the user manual (Elgamal *et al.* 2014).

In the longitudinal ESA, the entire bridge system (Figure 2.3) was engaged. The bridge system was pushed in the longitudinal direction until the plastic moment was reached (Figure D.1). The pushover load was applied at the bridge center (i.e., the span between Bents 6 and 7 (Figure 2.3)).

In the transverse ESA, an individual bent (Bent 4, as a typical representative) was employed. The bent was pushed along bridge transverse direction (Figure 2.3) until the plastic moment was reached (Figure D.1). The pushover load was applied at the bentcap center (i.e., the bentcap center between the 2 columns (Figure 2.3)).

Note that in this comparison study, rigid bentcaps were assumed in MSBridge for longitudinal ESA in order to compare with wFrame (since wFrame is a 2D program while a full 3D model was employed in MSBridge). However, the actual bentcap properties (Table D.2) were used in the transverse ESA for both MSBridge and wFrame.

The results are listed in Table 2.2. In general, good agreement (Table 2.2) was noted in the MSBridge and wFrame results in the longitudinal and transverse ESA Salinas Bridge study. The relative differences in initial stiffness between MSBridge and wFrame were 1%, and 2.6% in the longitudinal and transverse directions, respectively.

For the purpose of the current study, ESA was conducted in the longitudinal and transverse directions. Figure 2.6 shows the employed acceleration response spectrum (ARS) for the ESA (derived by Caltrans from the provided corresponding set of input seismic motions).

2.3.3.1. ESA in the Longitudinal Direction

Table 2.3 lists the parameters related to the longitudinal ESA. The pushover load at initial yielding (i.e., the plastic moment was reached) was about 24% of the tributary dead load (Table 2.3). Table 2.4 shows the longitudinal ESA result for Salinas Bridge. The displacement demand is 12.5 in for the longitudinal ESA (Table 2.4).

2.3.3.2. ESA in the Transverse Direction

Table 2.5 (also shown in Table 2.2) lists the parameters related to the transverse ESA (Bent 4, typical). The pushover load at initial yielding (i.e., the plastic moment was reached) was about 20% of the tributary dead load (Table 2.5). Table 2.6 shows the transverse ESA result for Salinas Bridge. The displacement demand is 16.8 in for the transverse ESA (Table 2.6).

2.3.4. Nonlinear Time History Analysis

Nonlinear THA was conducted for the 14 input motions provided by Caltrans (Appendix B). Uniform base excitation was studied using each of these input ground motions. In future studies, a more representative investigation can be conducted with input ground motion varying along the depth of the foundation shafts (and possibly along the lateral extent of the bridge configuration).

Rayleigh damping was used with a 5% damping ratio (defined at the periods of 1.6 and 2.1 seconds) in the nonlinear THA. For the time integration scheme, the Newmark average acceleration method ($\gamma = 0.5$ and $\beta = 0.25$) was employed.

Variable time-stepping scheme (`VariableTransient`) was used in the conducted Nonlinear THA. The starting value for each step was 0.005 second (the time step of the input motions), and the minimum time step was 5×10^{-5} second (upon splitting of time step when needed).

2.3.4.1. Maximum Displacement and Acceleration

Table 2.7 lists Salinas Bridge deck maximum displacement for 28 simulations from the nonlinear THA (the 14 motions were employed as both bridge longitudinal and transverse input). Among the simulations with the longitudinal component only (Simulations 1-14), Simulation 9 (motion ROCKS1P2) gave the least maximum displacement (8.2 in) while Simulation 4 (motion ROCKS1N4) gave the largest maximum displacement (14.0 in). The maximum displacement values of Table 2.7 are also presented in a graphical format against Peak Ground Acceleration (PGA) in Figure 2.7 and Figure 2.8.

The Salinas Bridge columns generally deformed more in the transverse direction, compared to the longitudinal direction, when subjected to the same input excitation (Table 2.7).

This general trend was also noted in the ESA displacement demand results (Table 2.4 and Table 2.6).

Table 2.8 lists Salinas Bridge deck maximum acceleration for the 28 simulations. Among the simulations with the longitudinal component only (Simulations 1-14), Simulations 2 (motion ROCKS1N2) and 9 (motion ROCKS1P2) gave the least maximum acceleration (0.3g) while Simulations 4 (motion ROCKS1N4) and 11 (motion ROCKS1P4) gave the largest maximum acceleration (0.45g). The maximum acceleration values of Table 2.8 are also presented in a graphical format against PGA in Figure 2.9 and Figure 2.10.

2.3.4.2. Response Time Histories

In this section, response time histories for Column 1 of Bent 7 (i.e., the middle bent, shown in Figure 2.3) for 2 representative simulations in the longitudinal directions (Simulations 1 and 4) are presented.

1) Simulation 1 (Longitudinal Input ROCKS1N1)

For Simulation 1, the deck maximum displacement was 12.6 in (Table 2.7). Figure 2.11 displays the column longitudinal response time histories. The input motion ROCKS1N1 is shown in Figure 2.11d for reference.

Figure 2.12 displays the moment-curvature response at the column top. A maximum bending moment of 6,100 kip-ft was reached as expected upon yielding (Figure 2.12). A level of yielding may be seen in the column response (Figure 2.11c). The deformed mesh when the deck maximum displacement was reached (i.e., 12.6 in as shown in Table 2.7) is shown in Figure 2.13.

2) Simulation 4 (Longitudinal Input ROCKS1N4)

The deck maximum displacement was 14.0 in for Simulation 4 (Table 2.7). The column longitudinal response time histories are displayed in Figure 2.14. In addition, Figure 2.15 shows

the moment-curvature response at the column top. A maximum bending moment of 6,100 kip-ft was also reached as expected upon yielding. The deformed mesh when the deck maximum displacement was reached (i.e., 14.0 in as shown in Table 2.7) is shown in Figure 2.16.

2.4. Samoa Channel Bridge

This section presents the seismic response of Samoa Channel Bridge. For that purpose, FE was utilized to create the numerical model. Considering the significance of the SSI, Foundation Matrix was used to account for the foundation flexibility at the column base level. As such, the results are presented within a comparative scope between ESA and nonlinear THA.

2.4.1. Bridge Description and Geometric Configuration

The 20-span Samoa Channel Bridge (hereinafter referred to as “Samoa Bridge”, Figure 2.17) near Eureka in northern California is a 2506 ft (764 m) long and 34 ft (10.4 m) wide structure connecting Samoa Peninsula and Indian Island (Figure 2.18). The bridge was designed in 1968, constructed in 1971 and underwent a seismic retrofit in 2002 (Clatrans 1968; Caltrans 2002) (Shamsabadi and Taciroglu 2013). The bridge superstructure, which consists of cast-in-place reinforced concrete deck and four pre-cast pre-stressed concrete I-girders, is supported by 19 single hexagonal concrete pier bents on pile group foundations. For convenience, the piers (including abutments) are numbered #1 through #21 from Indian Island side to Samoa Peninsula side. The typical span length is 120 ft (36.6 m) long except the main channel, which is 225 ft (68.6 m) long extending from centerline of pier 8 to the centerline of pier 9.

Samoa Bridge is heavily instrumented as shown in Figure 2.18 in order to record any significant earthquake excitation. There are 33 accelerometers in total on the Samoa Bridge System, including 24 accelerometers on the bridge structure, 6 accelerometers on the pile foundations, and 3 accelerometers at a nearby free-field site. Sensors on the structure are oriented

in the longitudinal and transverse direction of the bridge and sensors at the free field are oriented in the north-south, east-west and vertical directions.

The abutments and piers were founded originally on pile-group foundations consisting of driven pre-cast pre-stressed concrete piles. Referenced to the mean sea level (MSL), the elevation of the mud line varies from -51.8 ft (-15.8 m) below Pier S-8 to +3 ft (+0.9 m) at Pier S-20. Eleven pile groups (from S-3 to S-13) have a pile cap located above the mudline with a maximum value of +54.9 ft (+16.72 m) (elevation of cap base) at Pier S-8 (Figure 2.19a). Elevation view of Samoa Bridge is shown in Figure 2.19.

For simplicity, two column cross-sections along with the reinforcement details were considered in this study. Figure 2.20a and Figure 2.20b show the column reinforcement details at Pier S-8 and S-9, and the column reinforcement details at Piers other than Pier S-8 and S-9, respectively. The columns are precast pre-stressed concrete I-girders along with cast-in-place concrete slabs are supported on concrete seat-type abutments and the hammerhead cap beams of column type piers. The column/pier heights of this vertical curved bridge range from 20.3 ft (6.19 m; for Pier S-3) to 42.3 ft (12.9 m; for Pier S-14) as shown in Table 2.9 with no deck offset and no column top rigid link.

2.4.2. OpenSees Bridge FE Model and Mode Shapes

Using MSBridge, the FE model of Samoa bridge was developed (Figure 2.21). In the conducted OpenSees analyses, the pier columns were modeled using the nonlinear Fiber section (Appendix G) and the forceBeamColumn (with the distributed plasticity integration method) element. The deck was considered linearly elastic and the bentcap was ignored (the pier column top was considered to extend to the deck CG). Elastic abutment model was employed (for

simplicity). The Foundation Matrix technique was used to handle the SSI at the pier column base. The employed modeling techniques and associated model properties are presented in Appendix E.

Linear lateral springs were attached to the base of bridge structure (bottom of the pier column) to account for stiffness of the underlying pile foundations and the soil-foundation-structure interaction. Determination of linear foundation stiffness was achieved through the extended OpenSees- Sparse Nonlinear Optimization (SNOPT) framework (Gill *et al.* 2002; Wang 2015). Spring values were calibrated by minimizing the sum of squared errors by comparing the computed and recorded seismic response at the location of sensors (bridge deck and pile cap response) for the selected observation period. The evaluated base spring values obtained from the optimization problem are defined as the matrix of foundation stiffness coefficients (k_x and k_y , Table E.1 in Appendix E), which were obtained by conducting pushover analysis on individual bent FE model (Wang 2015).

The Mode shape analysis was performed. The natural periods of the first five modes are listed in Table 2.10, and the corresponding mode shapes are shown in Figure 2.22.

2.4.3. Equivalent Static Analysis (ESA)

Similar to the previous studied bridge, ESA was conducted for Samoa Bridge in the longitudinal and transverse directions. For that purpose, the ARS curve shown in Figure 2.23 was employed.

2.4.3.1. ESA in the Longitudinal Direction

The entire bridge system (Figure 2.21) was employed in the longitudinal ESA. The bridge system was pushed along the bridge deck (longitudinal) direction until initial yielding occurred (when the curvature reached 5×10^{-5} rad/in based on the moment-curvature shown in Appendix E). The pushover load was applied at the bridge center (i.e., near Bent 11, see Figure 2.21).

Table 2.11 lists the parameters related to the longitudinal ESA. The pushover load at initial yielding was about 40% of the tributary dead load (Table 2.11). Table 2.12 shows the longitudinal ESA result for Samoa Bridge. The displacement demand was 6.9 in for the longitudinal ESA (Table 2.12).

2.4.3.2. ESA in the Transverse Direction

Transverse ESA was conducted for Pier S-8 (Pier S-8 was chosen in order to compare ESA and THA results in the next section, since maximum displacement in the THA occurs in Pier S-8). The pier was pushed along the bridge transverse direction (Figure 2.21) until initial yielding occurred (when the curvature reached 3×10^{-5} rad/in based on the moment-curvature shown in Appendix E). The pushover load was applied at the pier top (Figure 2.21).

Table 2.13 lists the parameters related to the transverse ESA (for Pier S-9). Table 2.14 shows the transverse ESA result for Samoa Bridge (for Pier S-9). The displacement demand for Pier S-9 was 14.4 inches for the transverse ESA (Table 2.14).

2.4.4. Nonlinear Time History Analysis

Nonlinear THA was conducted for the 14 input motions provided by Caltrans (Appendix B). The input motions were applied directly at the pier base and both abutments.

Rayleigh damping was used with a 5% damping ratio (defined at the periods of 0.91 and 1.14 second) in the nonlinear THA. For the time integration scheme, the Newmark average acceleration method ($\gamma = 0.5$ and $\beta = 0.25$) was employed.

Variable time-stepping scheme (VariableTransient) was used in the analysis. The starting value for each step was 0.005 second (same as the time step of the input motions) and the minimum time step was 5×10^{-5} second (upon splitting of time step when needed).

2.4.4.1. Maximum Displacement and Acceleration

Table 2.15 lists Samoa Bridge deck maximum displacement for the 28 simulations from the nonlinear THA. Among the simulations with longitudinal component only (Simulations 1-14), Simulations 6 (motion ROCKS1N6) and 13 (motion ROCKS1P6) gave the least maximum displacement (5.9 in) while Simulations 4 (motion ROCKS1N4) and 11 (motion ROCKS1P4) gave the largest maximum displacement (9.1 in). The maximum displacements of Table 2.15 are also presented in a graphical format against PGA in Figure 2.24 and Figure 2.25.

The Samoa Bridge piers also generally deformed more in the transverse direction, compared to the longitudinal direction, when subjected to the same input excitation (Table 2.15). This might be due to the more flexible transverse pier response, compared to that in the longitudinal direction (Table 2.11 and Table 2.13).

Table 2.16 displays Samoa Bridge deck maximum acceleration for the 28 simulations. Among the simulations with the longitudinal component only (Simulations 1-14), Simulations 6 (motion ROCKS1N6) and 13 (motion ROCKS1P6) gave the least maximum acceleration (0.56g) while Simulation 1 (ROCKS1N1) gave the largest maximum acceleration (0.82g). The maximum accelerations of Table 2.16 are also presented in a graphical format against PGA in Figure 2.26 and Figure 2.27.

2.4.4.2. Response Time Histories

In this section, response time histories for Pier S-8 (see Figure 2.21) from 2 representative simulations (Simulations 1 and 4) are presented (Longitudinal seismic excitation).

1) Simulation 1 (motion ROCKS1N1)

For Simulation 1, the deck maximum displacement was 6.6 in (Table 2.15). The pier top longitudinal response time histories at Pier S-8 are displayed in Figure 2.28 where the displacement

time history refers to the displacement at the pier top. The input motion ROCKS1N1 is also shown in Figure 2.28d for reference.

Figure 2.29 displays the moment-curvature response at the pier top for selected piers. A maximum bending moment of 12,000 kip-ft was reached for Pier S-8 (Figure 2.29). The deformed mesh when the deck maximum displacement was reached (i.e., 6.6 in as shown in Table 2.15) is shown in Figure 2.30.

2) Simulation 4 (motion ROCKS1N4)

For Simulation 4, the deck maximum displacement is 9.1 in (Table 2.15). The pier top longitudinal response time histories at Pier S-8 are displayed in Figure 2.31. The input motion ROCKS1N4 is also shown in Figure 2.31d for reference.

Figure 2.32 displays the moment-curvature response at the pier top for selected piers. A maximum bending moment of 14,500 kip-ft was reached for Pier S-8 (Figure 2.29). (Figure 2.29). The deformed mesh when the deck maximum displacement was reached for Motion 4 ROCKS1N4 (i.e., 9.1 in as shown in Table 2.15) is shown in Figure 2.33.

2.4.5. Analysis of Samoa Bridge with Stiff Foundation Matrix

There are scenarios where foundations are built on stiff and competent soils. The resulting foundation matrix is typically a stiff one with large coefficients. In this section, the analysis of Samoa Bridge was conducted with a much stiffer foundation matrix (Figure 2.34), compared the foundation matrix employed in previous sections (Figure 2.34). The results of Mode shape analysis, ESA, and Nonlinear THA are presented and discussed in this section.

2.4.5.1. Mode Shape Analysis

Similar to the previous section, this section shows the response from mode shape analysis. The natural periods of the first five modes are listed in Table 2.17, and the corresponding mode shapes are shown in Figure 2.35.

For comparison purposes, Mode shape analysis was also conducted for Samoa Bridge with rigid pier bases. The natural periods and frequencies are shown in Table 2.18. It is seen that both Table 2.17 and Table 2.18 are almost identical, which indicates that the stiff foundation matrix employed in this section (Figure 2.34) is essentially equivalent to the rigid base.

2.4.5.2. Equivalent Static Analysis (ESA)

ESA was conducted in the bridge longitudinal and transverse directions. For the procedure to conduct ESA in MSBridge, please refer to the MSBridge user manual (Elgamal *et al.* 2014) with Figure 2.23 showing the employed ARS curve.

The entire bridge system (Figure 2.21) was employed in the longitudinal ESA. The bridge system was pushed along the bridge deck (longitudinal) direction until initial yielding occurred (when the curvature reached 5×10^{-5} rad/in based on the moment-curvature shown in Appendix). The pushover load was applied at the bridge center (i.e., near Bent 11, see Figure 2.21).

Table 2.19 lists the parameters related to the longitudinal ESA. The pushover load at initial yielding was about 48% of the tributary dead load (Table 2.19). Table 2.20 shows the longitudinal ESA result. The displacement demand is 3.0 in for the longitudinal ESA (Table 2.20).

Transverse ESA was also conducted for Pier S-8. The pier was pushed along the bridge transverse direction (Figure 2.21) until initial yielding occurred (at a curvature of 3×10^{-5} rad/in based on the moment-curvature shown in Appendix E). The pushover load was applied at the pier top (Figure 2.21). Table 2.21 lists the parameters related to the transverse ESA. Table 2.22 shows

the transverse ESA result for Samoa Bridge. The displacement demand for Pier S-8 is 4.0 inches for the transverse ESA (Table 2.22).

2.4.5.3. Nonlinear Time History Analysis

Nonlinear THA was conducted for the 14 input motions provided by Caltrans. The input motions were applied directly at the pier base as well as at both abutments.

Rayleigh damping was used with a 5% damping ratio (defined at the periods of 0.36 and 0.32 second) in the nonlinear THA. For the time integration scheme, the Newmark average acceleration method ($\gamma = 0.5$ and $\beta = 0.25$) was employed.

Variable time-stepping scheme (`VariableTransient`) was used in the analysis. The starting value for each step was 0.005 second (same as the time step of the input motions) and the minimum time step was 5×10^{-5} second (upon splitting of time step when needed).

Similar to the previous section, Table 2.23 lists the deck maximum displacement for the 28 simulations from the nonlinear THA. Among the simulations with the longitudinal component only (Simulations 1-14), Simulation 11 (motion ROCKS1P4) gave the least maximum displacement (2.16 in) while Simulation 7 (motion ROCKS1N7) gave the largest maximum displacement (2.67 in). The maximum displacements of Table 2.23 are also presented in a graphical format against PGA in Figure 2.36 and Figure 2.37.

Table 2.24 displays the deck maximum acceleration for the 28 simulations. Among the simulations with the longitudinal component only (Simulations 1-14), Simulation 3 (motion ROCKS1N3) gave the least maximum acceleration (0.674g) while Simulation 1 (motion ROCKS1N1) gave the largest maximum acceleration (0.868g). The maximum accelerations of Table 2.24 are also presented in a graphical format against PGA in Figure 2.38 and Figure 2.39.

Similarly, response time histories for Pier S-8 (see Figure 2.21) from 2 representative simulations (Simulations 1 and 8) are presented (Longitudinal seismic excitation).

1) Simulation 1 (motion ROCKS1N1)

For Simulation 1, the deck maximum displacement is 2.6 in (Table 2.23). The pier top longitudinal response time histories at Pier S-8 are displayed in Figure 2.40 where the displacement time history refers to the displacement at the pier top. The input motion ROCKS1N1 is shown in Figure 2.40d for reference.

Figure 2.41 displays the moment-curvature response at the pier top. A maximum bending moment of 19,500 kip-ft was reached (Figure 2.41). The deformed mesh when the deck maximum displacement was reached (i.e., 2.6 in as shown in Table 2.23) is shown in Figure 2.42.

2) Simulation 8 (motion ROCKS1P1)

For Simulation 8, the deck maximum displacement is 2.59 in (Table 2.23). The pier top longitudinal response time histories at Pier S-8 are displayed in Figure 2.43. The input motion ROCKS1P1 is shown in Figure 2.43d for reference.

Figure 2.44 displays the moment-curvature response at the pier top. A maximum bending moment of 19,200 kip-ft was reached (Figure 2.44). The deformed mesh when the deck maximum displacement was reached (i.e., 2.59 in as shown in Table 2.23) is shown in Figure 2.45.

2.5. Eureka Channel Bridge

The 15-span Eureka Channel Bridge (hereinafter referred to as “Eureka Bridge”, Figure 2.46) near Eureka in northern California is a 1,815.75 ft (553.44 m) long and 34 ft (10.36 m) wide structure, supported by 14 single hexagonal concrete pier bents on pile group foundations (Figure 2.47). From Abutment 1 at south-bound, the alignment of the span has a 1,014.3 ft (309.157 m) length on a 1,800 ft (548.64 m) radius curve and an 802.4 ft (244.573 m) straight segment at

Abutment 16 to north-bound. The bridge piers are labeled from the Eureka area to Samoa area as Pier E-1 (abutment), Pier E-2, Pier E-3 and so on. Length of span is in a range of 81 ft (24.69 m) to 190 ft (57.91 m) with main channel between pier 7 and pier 8.

Eureka Bridge is heavily instrumented as shown in Figure 2.47 in order to record any significant earthquake excitation. There are 27 accelerometers in total on the Eureka Bridge System, including 18 accelerometers on the bridge structure, 6 accelerometers on the pile foundations, and 3 accelerometers at a nearby free-field site. Sensors on the structure are oriented in the longitudinal and transverse direction of the bridge and sensors at the free field are oriented in the north-south, east-west and vertical directions.

2.5.1. Geometric Configuration

Figure 2.48 shows the elevation view of Eureka Bridge. Moreover, Figure 2.19b shows the column reinforcement details at Pier E-7. Precast pre-stressed concrete I-girders along with cast-in-place concrete slabs (16.5 cm of thickness) are supported on concrete seat-type abutments and the hammerhead cap beams of column type piers. The height of the columns/piers ranges from 7.8 ft (2.39 m; for Pier E-15) to 40.2 ft (12.25 m; for Pier E-6) as depicted in Figure 2.47. The offset between the column top and the deck was not represented in this study and no column top rigid link. Table 2.25 shows the column heights for each pier.

2.5.2. OpenSees Finite Element Modeling

Figure 2.49 shows the Eureka Bridge model created in MSBridge. The employed modeling techniques and associated model properties are presented in Appendix F. Pier columns were modeled using the nonlinear Fiber section and the forceBeamColumn (with the distributed plasticity integration method) element was employed as shown in Appendix G. For simplicity, the deck was considered linearly elastic and the bentcap was ignored (the pier column top was

considered to extend to the deck center of gravity [CG]). Elastic abutment model was employed (for simplicity). The pier column base was not fixed. Instead, the Foundation Matrix technique was used to handle the SSI at the pier column base level.

2.5.3. Mode Shape Analysis

Similar to the previous bridges, this section shows the response from Mode shape analysis. The natural periods of the first five modes are listed in Table 2.26, and the corresponding mode shapes are shown in Figure 2.50.

2.5.4. Equivalent Static Analysis (ESA)

ESA was conducted for Eureka Bridge in the bridge longitudinal and transverse directions. For the procedure to conduct ESA in MSBridge, please refer to the MSBridge user manual (Elgamal *et al.* 2014). Figure 2.51 shows the ARS curve employed in the ESA.

2.5.4.1. ESA in the Longitudinal Direction

The entire bridge system (Figure 2.49) was employed in the longitudinal ESA. The bridge system was pushed along the bridge deck (longitudinal) direction until initial yielding occurred (when the curvature reached 5×10^{-5} rad/in based on the moment-curvature shown in Appendix F). The pushover load was applied at the bridge center.

Table 2.27 lists the parameters related to the longitudinal ESA. The pushover load at initial yielding was about 42% of the tributary dead load (Table 2.27). Table 2.28 shows the longitudinal ESA result for Eureka Bridge. The displacement demand is 6.1 in for the longitudinal ESA (Table 2.28).

2.5.4.2. ESA in the Transverse Direction

Transverse ESA was conducted for Pier E-6 (Pier E-6 was chosen in order to compare ESA and THA results later on since maximum displacement in the THA occurs in Pier E-6). The pier

was pushed along the bridge transverse direction (Figure 2.49) until initial yielding occurred (when the curvature reached 3×10^{-5} rad/in based on the moment-curvature shown in Appendix F). The pushover load was applied at the pier top (Figure 2.49).

Table 2.29 lists the parameters related to the transverse ESA. Table 2.30 shows the transverse ESA result for Eureka Bridge. The displacement demands for Pier E-6 is 13.1 inches for the transverse ESA (Table 2.30).

2.5.5. Nonlinear Time History Analysis

Nonlinear THA was conducted for the 14 input motions provided by Caltrans (see Appendix B for the characteristics of the 14 motions). The input motions were applied directly at the column base as well as at both abutments.

Rayleigh damping was used with a 5% damping ratio (defined at the periods of 1.24 and 0.94 second) in the nonlinear THA. For the time integration scheme, the Newmark average acceleration method ($\gamma = 0.5$ and $\beta = 0.25$) was employed.

Variable time-stepping scheme (`VariableTransient`) was used in the analysis. The starting value for each step was 0.005 second (same as the time step of the input motions) and the minimum time step was 5×10^{-5} second (upon splitting of time step when needed).

2.5.5.1. Maximum Displacement and Acceleration

Table 2.31 lists Eureka Bridge deck maximum displacement for the 28 simulations from the nonlinear THA. Among the simulations with the longitudinal component only (Simulations 1-14), Simulation 14 (motion ROCKS1P7) gave the least maximum displacement (4.0 in) while Simulation 9 (motion ROCKS1P2) gave the largest maximum displacement (5.5 in). Note that the deck maximum displacement is recorded in the local coordinate system (Appendix A). Thus, the longitudinal maximum displacement refers to the displacement along the tangential direction of

the bridge at a given superstructure location. In addition, the maximum displacements of Table 2.31 are presented in a graphical format against PGA in Figure 2.52 and Figure 2.53.

Table 2.32 list Eureka Bridge deck maximum acceleration for the 28 simulations. Among the simulations with the longitudinal component only (Simulations 1-14), Simulation 4 (motion ROCKS1N4) gave the least maximum acceleration (0.73g) while Simulation 9 (motion ROCKS1P2) gave the largest maximum acceleration (1.05g). Note that the deck maximum acceleration also is recorded in the local coordinate system (Appendix A). Thus, the longitudinal maximum acceleration refers to the acceleration along the tangential direction of the bridge at a given superstructure location. The maximum accelerations of Table 2.32 are also presented in a graphical format against PGA in Figure 2.54 and Figure 2.55.

2.6. Summary

Three bridges (the Salinas River Bridge, the Samoa Channel Bridge and the Eureka Channel Bridge) were studied using OpenSees. In this context, the seismic response is being investigated from a system-level perspective. The deck, columns, abutments, and foundation response mechanisms are integrated within a unified framework. Systematic evaluation of the global system response is conducted under a wide range of expected earthquake input shaking scenarios. The analysis procedures and results for the three studied bridges were presented in this report.

For the Salinas River Bridge, an idealized bi-linear moment-curvature relationship was used to model the columns. The force-based beam-column element based on the plastic hinge integration method (`BeamWithHinges`) in OpenSees was employed to model the columns while the deck and bentcap were considered linearly elastic. The column foundation response was modeled by soil springs calculated based on p - y , t - z , and Q - z curves. An elastic abutment model

was employed. In addition, an effort was also made to compare OpenSees and wFrame pushover analysis results for the Salinas River Bridge model.

For the Samoa Channel Bridge and the Eureka Channel Bridge, the pier foundation response was model by Foundation Matrix. The pier columns were modeled using the nonlinear Fiber section. The force-based beam-column element with the distributed plasticity integration method (`forceBeamColumn`) in OpenSees was employed to model the pier column while the deck was considered linearly elastic. Elastic abutment model was also employed.

To facilitate the conducted analyses in OpenSees, the user-interface MSBridge was further developed and employed. Nonlinear THA was conducted for 14 input motions provided by Caltrans. ESA was performed in OpenSees as well using MSBridge. Furthermore, an effort was made to illustrate and verify the MSBridge salient features and capabilities.

2.7. Conclusions

Based on this preliminary representative investigation, a number of conclusions were drawn as presented below. For future studies, it is emphasized that a more representative comparison would be based on employment of a spectrum-matched set of input motion time histories.

1. Good agreement was noted in the OpenSees and wFrame results in the longitudinal and transverse ESA Salinas River Bridge study. The relative differences in initial stiffness between OpenSees and wFrame were 1%, and 2.6% in the longitudinal and transverse directions, respectively.

2. For the Salinas River Bridge, the differences between the ESA displacement demand and the average THA maximum displacement was about 12% (for both longitudinal and transverse directions).

3. For the Samoa Channel Bridge and the Eureka Channel Bridge models, the differences between the ESA displacement demand and the average THA maximum displacement were 5.8% and 27.5%, respectively, in the longitudinal direction. The differences between the ESA and THA results in the transverse direction were 15.8% and 4.5%, respectively, for the above 2 bridges.

4. In the longitudinal direction, for the Salinas River Bridge, about 36% of the shaking events resulted in column displacement demand that exceeded that of the ESA. This demand reached a maximum of 12% in excess of that from the corresponding ESA. For the Samoa Channel Bridge and the Eureka Channel Bridge, 64% and 0%, respectively, of the shaking events resulted in column displacement demand that exceeded that of the ESA. This demand reached a maximum of 32% in excess of that from the corresponding ESA (for the Samoa Channel Bridge).

5. In the transverse direction, for the Salinas River Bridge, about 14% of the shaking events resulted in column displacement demand that exceeded that of the ESA. This demand reached a maximum of 25% in excess of that from the corresponding ESA. For the Samoa Channel Bridge and the Eureka Channel Bridge, 14% and 43%, respectively, of the shaking events resulted in column displacement demand that exceeded that of the ESA. This demand reached a maximum of 20% and 47%, respectively, in excess of that from the corresponding ESA.

2.8. Acknowledgements

Chapter 2, in part, has been published as it appears in the following technical report publication (The dissertation author was the primary investigator and author of this paper):

Almutairi, A.S., Lu, J., Wang, N., Elgamal, A. (2016). "Analysis of multi-span bridges Using OpenSees." Research Report, SSRP-16/01, Department of Structural Engineering, University of California, San Diego (UCSD).

Table 2.1. Natural periods and frequencies for Salinas Bridge

Mode	Natural period (sec)	Natural Frequency (Hz)
1*	1.89	0.53
2	1.72	0.58
3**	1.62	0.62
4	1.47	0.68
5	1.08	0.92

* Fundamental mode in the transverse direction

** Fundamental mode in the longitudinal direction

Table 2.2. Comparison of MSBridge and wFrame results for ESA of Salinas Bridge

Program	Longitudinal ESA			Transverse ESA		
	MSBride	wFrame	Difference	MSBridge	wFrame	Difference
Yield Displacement (in)	5.2	4.87	6.8%	9.4	9.76	3.4%
Pushover Load (kip)	4222	3961.5	6.6%	376	382.4	1.7%
Initial Stiffness (kip/in)	805	813.5	1.0%	40	39	2.6%
Period (seconds)	1.63	1.62	0.6%	2.21	2.24	1.3%
Displacement Demand (in)	14.8	15.37	3.7%	18.8	18.6	1.1%

Table 2.3. Longitudinal ESA parameters for Salinas Bridge

Parameter	Value
Tributary dead load (kip)	20,850.8
Tributary mass (kip-sec ² /in)	54.0
Pushover load at initial yielding (kip)	5004.19
Yield displacement (in)	6.5
Initial stiffness (kip/in)	768.0
Period (sec)	1.7

Table 2.4. Longitudinal ESA result for Salinas Bridge

Parameter	Longitudinal Direction
Displacement Demand (in)	12.5

Table 2.5. Transverse ESA parameters for Bent 4

Parameter	Value
Tributary dead load (kip)	1912.4
Tributary mass (kip-sec ² /in)	4.9
Pushover load at initial yielding (kip)	376
Yield displacement (in)	9.4
Initial stiffness (kip/in)	40
Period (sec)	2.21

Table 2.6. Transverse ESA result for Salinas Bridge

Pier # (see Figure 2.3a)	Displacement Demand in Transverse Direction (in)
Bent 4 (typical bent)	16.8

Table 2.7. Salinas bridge deck maximum displacement

Simulation	Longitudinal Input	Transverse Input	Longitudinal Displacement (in)	Transverse Displacement (in)
1	ROCKS1N1 (0.7g)	-	12.6	0
2	ROCKS1N2 (0.38g)	-	8.3	0
3	ROCKS1N3 (0.32g)	-	9.4	0
4	ROCKS1N4 (0.34g)	-	14.0	0
5	ROCKS1N5 (0.53g)	-	10.5	0
6	ROCKS1N6 (0.42g)	-	9.8	0
7	ROCKS1N7 (0.36g)	-	11.8	0
8	ROCKS1P1 (0.71g)	-	13.1	0
9	ROCKS1P2 (0.44g)	-	8.2	0
10	ROCKS1P3 (0.48g)	-	11.0	0
11	ROCKS1P4 (0.32g)	-	13.8	0
12	ROCKS1P5 (0.67g)	-	9.4	0
13	ROCKS1P6 (0.41g)	-	9.7	0
14	ROCKS1P7 (0.4g)	-	12.7	0
Average			11.0	
15	-	ROCKS1N1 (0.7g)	0	14.0
16	-	ROCKS1N2 (0.38g)	0	13.8
17	-	ROCKS1N3 (0.32g)	0	10.4
18	-	ROCKS1N4 (0.34g)	0	15.8
19	-	ROCKS1N5 (0.53g)	0	16.8
20	-	ROCKS1N6 (0.42g)	0	14.0
21	-	ROCKS1N7 (0.36g)	0	14.1
22	-	ROCKS1P1 (0.71g)	0	15.4
23	-	ROCKS1P2 (0.44g)	0	14.2
24	-	ROCKS1P3 (0.48g)	0	17.0
25	-	ROCKS1P4 (0.32g)	0	14.6
26	-	ROCKS1P5 (0.67g)	0	21.0
27	-	ROCKS1P6 (0.41g)	0	14.0
28	-	ROCKS1P7 (0.4g)	0	12.7
Average				14.8

Notes:

- ESA longitudinal displacement demand is 12.5 in, corresponding to a difference of 11.8% (compared to the average THA maximum displacement of 11 in)
- ESA transverse displacement demand is 16.8 in, corresponding to a difference of 11.7% (compared to the average THA maximum displacement of 14.8 in)

Table 2.8. Salinas bridge deck maximum acceleration

Simulation	Longitudinal Input	Transverse Input	Longitudinal Acceleration (g)	Transverse Acceleration (g)
1	ROCKS1N1 (0.7g)	-	0.42	0
2	ROCKS1N2 (0.38g)	-	0.30	0
3	ROCKS1N3 (0.32g)	-	0.33	0
4	ROCKS1N4 (0.34g)	-	0.45	0
5	ROCKS1N5 (0.53g)	-	0.37	0
6	ROCKS1N6 (0.42g)	-	0.34	0
7	ROCKS1N7 (0.36g)	-	0.41	0
8	ROCKS1P1 (0.71g)	-	0.43	0
9	ROCKS1P2 (0.44g)	-	0.30	0
10	ROCKS1P3 (0.48g)	-	0.38	0
11	ROCKS1P4 (0.32g)	-	0.45	0
12	ROCKS1P5 (0.67g)	-	0.34	0
13	ROCKS1P6 (0.41g)	-	0.34	0
14	ROCKS1P7 (0.4g)	-	0.42	0
15	-	ROCKS1N1 (0.7g)	0	0.35
16	-	ROCKS1N2 (0.38g)	0	0.31
17	-	ROCKS1N3 (0.32g)	0	0.34
18	-	ROCKS1N4 (0.34g)	0	0.36
19	-	ROCKS1N5 (0.53g)	0	0.38
20	-	ROCKS1N6 (0.42g)	0	0.36
21	-	ROCKS1N7 (0.36g)	0	0.42
22	-	ROCKS1P1 (0.71g)	0	0.37
23	-	ROCKS1P2 (0.44g)	0	0.31
24	-	ROCKS1P3 (0.48g)	0	0.38
25	-	ROCKS1P4 (0.32g)	0	0.36
26	-	ROCKS1P5 (0.67g)	0	0.41
27	-	ROCKS1P6 (0.41g)	0	0.36
28	-	ROCKS1P7 (0.4g)	0	0.37

Table 2.9. Column heights for Samoa Bridge

Pier # (see Figure 2.18a)	Column Heights (ft)
Pier S-2	36.49
Pier S-3	32.04
Pier S-4	34.86
Pier S-5	39.34
Pier S-6	43.03
Pier S-7	45.41
Pier S-8	46.49
Pier S-9	48.23
Pier S-10	49.01
Pier S-11	47.98
Pier S-12	46.15
Pier S-13	44.28
Pier S-14	53.87
Pier S-15	51.47
Pier S-16	49.07
Pier S-17	46.16
Pier S-18	43.76
Pier S-19	38.87
Pier S-20	36.47

Table 2.10. Natural periods and frequencies for Samoa Bridge

Mode	Natural period (sec)	Natural Frequency (Hz)
1	1.14	0.88
2	0.96	1.04
3	0.91	1.10
4	0.73	1.36
5	0.68	1.48

Table 2.11. Longitudinal ESA parameters for Samoa Bridge

Parameter	Value
Tributary dead load (kip)	21,618.6
Tributary mass (kip-sec ² /in)	56.0
Pushover load at initial yielding (kip)	8,561.0
Yield displacement (in)	3.8
Initial stiffness (kip/in)	2,274.15
Period (sec)	1.0

Table 2.12. Longitudinal ESA result for Samoa Bridge

Parameter	Longitudinal Direction
Displacement Demand (in)	6.9

Table 2.13. Transverse ESA parameters for Pier S-8

Parameter	Value
Tributary dead load (kip)	1590.8
Tributary mass (kip-sec ² /in)	4.1
Pushover load at initial yielding (kip)	585.4
Yield displacement (in)	12.57
Initial stiffness (kip/in)	46.56
Period (sec)	1.87

Table 2.14. Transverse ESA result for Pier S-8

Pier # (see Figure 2.18a)	Displacement Demand in Transverse Direction (in)
Pier S-8	14.1

Table 2.15. Samoa bridge deck maximum displacement

Simulation	Longitudinal Input	Transverse Input	Longitudinal Displacement (in)	Transverse Displacement (in)
1	ROCKS1N1 (0.7g)	-	6.6	0
2	ROCKS1N2 (0.38g)	-	6.9	0
3	ROCKS1N3 (0.32g)	-	7.2	0
4	ROCKS1N4 (0.34g)	-	9.1	0
5	ROCKS1N5 (0.53g)	-	7.5	0
6	ROCKS1N6 (0.42g)	-	5.9	0
7	ROCKS1N7 (0.36g)	-	7.1	0
8	ROCKS1P1 (0.71g)	-	7.0	0
9	ROCKS1P2 (0.44g)	-	7.0	0
10	ROCKS1P3 (0.48g)	-	8.1	0
11	ROCKS1P4 (0.32g)	-	9.1	0
12	ROCKS1P5 (0.67g)	-	7.9	0
13	ROCKS1P6 (0.41g)	-	5.9	0
14	ROCKS1P7 (0.4g)	-	6.9	0
Average			7.3	
15	-	ROCKS1N1 (0.7g)	0	12.1
16	-	ROCKS1N2 (0.38g)	0	9.8
17	-	ROCKS1N3 (0.32g)	0	16.9
18	-	ROCKS1N4 (0.34g)	0	13.1
19	-	ROCKS1N5 (0.53g)	0	9.1
20	-	ROCKS1N6 (0.42g)	0	11.1
21	-	ROCKS1N7 (0.36g)	0	13.4
22	-	ROCKS1P1 (0.71g)	0	12.2
23	-	ROCKS1P2 (0.44g)	0	9.7
24	-	ROCKS1P3 (0.48g)	0	9.2
25	-	ROCKS1P4 (0.32g)	0	13.6
26	-	ROCKS1P5 (0.67g)	0	8.5
27	-	ROCKS1P6 (0.41g)	0	11.2
28	-	ROCKS1P7 (0.4g)	0	16.2
Average				11.9

Notes:

- ESA longitudinal displacement demand is 6.9 in, corresponding to a difference of 5.8% (compared to the average THA maximum displacement of 7.3 in)
- ESA transverse displacement demand is 14.1 in, corresponding to a difference of 15.8% (compared to the average THA maximum displacement of 11.9 in)

Table 2.16. Samoa bridge deck maximum acceleration

Simulation	Longitudinal Input	Transverse Input	Longitudinal Acceleration (g)	Transverse Acceleration (g)
1	ROCKS1N1 (0.7g)	-	0.82	0
2	ROCKS1N2 (0.38g)	-	0.65	0
3	ROCKS1N3 (0.32g)	-	0.65	0
4	ROCKS1N4 (0.34g)	-	0.76	0
5	ROCKS1N5 (0.53g)	-	0.73	0
6	ROCKS1N6 (0.42g)	-	0.56	0
7	ROCKS1N7 (0.36g)	-	0.70	0
8	ROCKS1P1 (0.71g)	-	0.81	0
9	ROCKS1P2 (0.44g)	-	0.65	0
10	ROCKS1P3 (0.48g)	-	0.75	0
11	ROCKS1P4 (0.32g)	-	0.77	0
12	ROCKS1P5 (0.67g)	-	0.76	0
13	ROCKS1P6 (0.41g)	-	0.56	0
14	ROCKS1P7 (0.4g)	-	0.64	0
15	-	ROCKS1N1 (0.7g)	0	1.40
16	-	ROCKS1N2 (0.38g)	0	1.30
17	-	ROCKS1N3 (0.32g)	0	1.20
18	-	ROCKS1N4 (0.34g)	0	1.18
19	-	ROCKS1N5 (0.53g)	0	1.16
20	-	ROCKS1N6 (0.42g)	0	1.25
21	-	ROCKS1N7 (0.36g)	0	1.14
22	-	ROCKS1P1 (0.71g)	0	1.44
23	-	ROCKS1P2 (0.44g)	0	1.30
24	-	ROCKS1P3 (0.48g)	0	1.17
25	-	ROCKS1P4 (0.32g)	0	1.16
26	-	ROCKS1P5 (0.67g)	0	1.17
27	-	ROCKS1P6 (0.41g)	0	1.26
28	-	ROCKS1P7 (0.4g)	0	1.19

Table 2.17. Natural periods and frequencies for Samoa Bridge with stiff foundation matrix

Mode	Natural Period (sec)	Natural Frequency (Hz)
1	0.36	2.77
2	0.32	3.15
3	0.31	3.22
4	0.309	3.24
5	0.308	3.25

Table 2.18. Natural periods and frequencies for Samoa Bridge with rigid pier base

Mode	Natural Period (sec)	Natural Frequency (Hz)
1	0.36	2.78
2	0.32	3.16
3	0.309	3.23
4	0.3073	3.254
5	0.3072	3.255

Table 2.19. Longitudinal ESA parameters for Samoa Bridge with stiff foundation matrix

Parameter	Value
Tributary dead load (kip)	21,374.8
Tributary mass (kip-sec ² /in)	55.3
Pushover load at initial yielding (kip)	10,259.9
Yield displacement (in)	1.43
Initial stiffness (kip/in)	7,192.58
Period (sec)	0.55

Table 2.20. Longitudinal ESA result for Samoa Bridge with stiff foundation matrix

Parameter	Longitudinal Direction
Displacement Demand (in)	3.0

Table 2.21. Transverse ESA parameters for Pier S-8

Parameter	Value
Tributary dead load (kip)	1579
Tributary mass (kip-sec ² /in)	4.1
Pushover load at initial yielding (kip)	840.8
Yield displacement (in)	2.41
Initial stiffness (kip/in)	349.5
Period (sec)	0.68

Table 2.22. Transverse ESA result for Samoa Bridge with stiff foundation matrix

Pier # (see Figure 2.18a)	Displacement Demand in Transverse Direction (in)
Pier S-8	4.0

Table 2.23. Deck maximum displacement for Samoa Bridge with stiff foundation matrix

Simulation	Longitudinal Input	Transverse Input	Longitudinal Displacement (in)	Transverse Displacement (in)
1	ROCKS1N1 (0.7g)	-	2.60	0
2	ROCKS1N2 (0.38g)	-	2.45	0
3	ROCKS1N3 (0.32g)	-	2.24	0
4	ROCKS1N4 (0.34g)	-	2.18	0
5	ROCKS1N5 (0.53g)	-	2.24	0
6	ROCKS1N6 (0.42g)	-	2.45	0
7	ROCKS1N7 (0.36g)	-	2.67	0
8	ROCKS1P1 (0.71g)	-	2.59	0
9	ROCKS1P2 (0.44g)	-	2.43	0
10	ROCKS1P3 (0.48g)	-	2.44	0
11	ROCKS1P4 (0.32g)	-	2.16	0
12	ROCKS1P5 (0.67g)	-	2.18	0
13	ROCKS1P6 (0.41g)	-	2.42	0
14	ROCKS1P7 (0.4g)	-	2.41	0
Average			2.4	
15	-	ROCKS1N1 (0.7g)	0	4.40
16	-	ROCKS1N2 (0.38g)	0	2.32
17	-	ROCKS1N3 (0.32g)	0	2.49
18	-	ROCKS1N4 (0.34g)	0	2.33
19	-	ROCKS1N5 (0.53g)	0	2.43
20	-	ROCKS1N6 (0.42g)	0	2.77
21	-	ROCKS1N7 (0.36g)	0	2.85
22	-	ROCKS1P1 (0.71g)	0	4.46
23	-	ROCKS1P2 (0.44g)	0	2.39
24	-	ROCKS1P3 (0.48g)	0	2.62
25	-	ROCKS1P4 (0.32g)	0	2.34
26	-	ROCKS1P5 (0.67g)	0	4.38
27	-	ROCKS1P6 (0.41g)	0	2.78
28	-	ROCKS1P7 (0.4g)	0	2.70
Average				2.9

Notes:

- ESA longitudinal displacement demand is 3.0 in, corresponding to a difference of 20.3% (compared to the average THA maximum displacement of 2.4 in)
- ESA transverse displacement demand is 4.0 in, corresponding to a difference of 26.3% (compared to the average THA maximum displacement of 2.9 in)

Table 2.24. Deck maximum acceleration for Samoa Bridge with stiff foundation matrix

Simulation	Longitudinal Input	Transverse Input	Longitudinal Acceleration (g)	Transverse Acceleration (g)
1	ROCKS1N1 (0.7g)	-	0.868	0
2	ROCKS1N2 (0.38g)	-	0.751	0
3	ROCKS1N3 (0.32g)	-	0.674	0
4	ROCKS1N4 (0.34g)	-	0.680	0
5	ROCKS1N5 (0.53g)	-	0.685	0
6	ROCKS1N6 (0.42g)	-	0.795	0
7	ROCKS1N7 (0.36g)	-	0.781	0
8	ROCKS1P1 (0.71g)	-	0.865	0
9	ROCKS1P2 (0.44g)	-	0.748	0
10	ROCKS1P3 (0.48g)	-	0.717	0
11	ROCKS1P4 (0.32g)	-	0.677	0
12	ROCKS1P5 (0.67g)	-	0.726	0
13	ROCKS1P6 (0.41g)	-	0.792	0
14	ROCKS1P7 (0.4g)	-	0.717	0
15	-	ROCKS1N1 (0.7g)	0.125	3.59
16	-	ROCKS1N2 (0.38g)	0.042	1.34
17	-	ROCKS1N3 (0.32g)	0.022	1.01
18	-	ROCKS1N4 (0.34g)	0.047	1.57
19	-	ROCKS1N5 (0.53g)	0.052	1.74
20	-	ROCKS1N6 (0.42g)	0.046	2.14
21	-	ROCKS1N7 (0.36g)	0.038	1.58
22	-	ROCKS1P1 (0.71g)	0.125	3.62
23	-	ROCKS1P2 (0.44g)	0.051	1.34
24	-	ROCKS1P3 (0.48g)	0.054	1.74
25	-	ROCKS1P4 (0.32g)	0.048	1.59
26	-	ROCKS1P5 (0.67g)	0.121	3.41
27	-	ROCKS1P6 (0.41g)	0.048	2.16
28	-	ROCKS1P7 (0.4g)	0.028	0.96

Table 2.25. Column heights for Eureka Bridge

Pier # (see Figure 2.47a)	Column Height (ft)
Pier E-2	32.40
Pier E-3	37.57
Pier E-4	42.41
Pier E-5	45.89
Pier E-6	53.00
Pier E-7	42.24
Pier E-8	40.59
Pier E-9	39.28
Pier E-10	35.08
Pier E-11	39.50
Pier E-12	32.95
Pier E-13	26.36
Pier E-14	21.81
Pier E-15	19.54

Table 2.26. Natural periods and frequencies for Eureka Bridge

Mode	Natural Period (sec)	Natural Frequency (Hz)
1	1.24	0.80
2	1.18	0.85
3	1.02	0.98
4	0.89	1.12
5	0.85	1.18

Table 2.27. Longitudinal ESA parameters for Eureka Bridge

Parameter	Value
Tributary dead load (kip)	14,586.9
Tributary mass (kip-sec ² /in)	37.8
Pushover load at initial yielding (kip)	6,126.5
Yield displacement (in)	3.4
Initial stiffness (kip/in)	1807.1
Period (sec)	0.9

Table 2.28. Longitudinal ESA result for Eureka Bridge

Parameter	Longitudinal Direction
Displacement Demand (in)	6.1

Table 2.29. Transverse ESA parameters for Pier E-6

Parameter	Value
Tributary dead load (kip)	1,080.64
Tributary mass (kip-sec ² /in)	2.8
Pushover load at initial yielding (kip)	459
Yield displacement (in)	12.5
Initial stiffness (kip/in)	36.7
Period (sec)	1.74

Table 2.30. Transverse ESA result for Eureka Bridge

Pier # (see Figure 2.47a)	Displacement Demand in Transverse Direction (in)
Pier E-6	13.1

Table 2.31. Eureka bridge deck maximum displacement

Simulation	Longitudinal Input	Transverse Input	Longitudinal Displacement (in)	Transverse Displacement (in)
1	ROCKS1N1 (0.7g)	-	4.4	3.3
2	ROCKS1N2 (0.38g)	-	5.2	3.1
3	ROCKS1N3 (0.32g)	-	4.2	3.7
4	ROCKS1N4 (0.34g)	-	4.1	4.5
5	ROCKS1N5 (0.53g)	-	5.0	3.4
6	ROCKS1N6 (0.42g)	-	4.1	3.9
7	ROCKS1N7 (0.36g)	-	3.5	3.3
8	ROCKS1P1 (0.71g)	-	4.5	3.3
9	ROCKS1P2 (0.44g)	-	5.5	3.1
10	ROCKS1P3 (0.48g)	-	4.6	3.4
11	ROCKS1P4 (0.32g)	-	4.2	4.5
12	ROCKS1P5 (0.67g)	-	4.2	3.3
13	ROCKS1P6 (0.41g)	-	4.1	3.9
14	ROCKS1P7 (0.4g)	-	4.0	3.6
Average			4.4	
15	-	ROCKS1N1 (0.7g)	6.0	15.5
16	-	ROCKS1N2 (0.38g)	4.6	12.6
17	-	ROCKS1N3 (0.32g)	7.1	19.2
18	-	ROCKS1N4 (0.34g)	5.7	16.9
19	-	ROCKS1N5 (0.53g)	3.5	8.7
20	-	ROCKS1N6 (0.42g)	4.5	12.1
21	-	ROCKS1N7 (0.36g)	4.8	12.1
22	-	ROCKS1P1 (0.71g)	6.0	15.4
23	-	ROCKS1P2 (0.44g)	4.6	12.5
24	-	ROCKS1P3 (0.48g)	3.6	9.2
25	-	ROCKS1P4 (0.32g)	5.7	17.0
26	-	ROCKS1P5 (0.67g)	4.1	9.4
27	-	ROCKS1P6 (0.41g)	4.6	12.0
28	-	ROCKS1P7 (0.4g)	7.1	19.0
Average				13.7

Notes:

- ESA longitudinal displacement demand is 6.1 in, corresponding to a difference of 27.5% (compared to the average THA maximum displacement of 4.4 in)
- ESA transverse displacement demand is 13.1 in, corresponding to a difference of 4.5% (compared to the average THA maximum displacement of 13.7 in)

Table 2.32. Eureka bridge deck maximum acceleration

Simulation	Longitudinal Input	Transverse Input	Longitudinal Acceleration (g)	Transverse Acceleration (g)
1	ROCKS1N1 (0.7g)	-	0.80	0.59
2	ROCKS1N2 (0.38g)	-	1.01	0.47
3	ROCKS1N3 (0.32g)	-	0.76	0.59
4	ROCKS1N4 (0.34g)	-	0.73	0.64
5	ROCKS1N5 (0.53g)	-	0.95	0.62
6	ROCKS1N6 (0.42g)	-	0.78	0.67
7	ROCKS1N7 (0.36g)	-	0.66	0.59
8	ROCKS1P1 (0.71g)	-	0.81	0.59
9	ROCKS1P2 (0.44g)	-	1.05	0.46
10	ROCKS1P3 (0.48g)	-	0.89	0.62
11	ROCKS1P4 (0.32g)	-	0.74	0.64
12	ROCKS1P5 (0.67g)	-	0.79	0.53
13	ROCKS1P6 (0.41g)	-	0.78	0.67
14	ROCKS1P7 (0.4g)	-	0.76	0.56
15	-	ROCKS1N1 (0.7g)	0.52	1.10
16	-	ROCKS1N2 (0.38g)	0.57	1.10
17	-	ROCKS1N3 (0.32g)	0.67	1.23
18	-	ROCKS1N4 (0.34g)	0.65	1.20
19	-	ROCKS1N5 (0.53g)	0.52	1.28
20	-	ROCKS1N6 (0.42g)	0.60	1.30
21	-	ROCKS1N7 (0.36g)	0.56	1.14
22	-	ROCKS1P1 (0.71g)	0.51	1.07
23	-	ROCKS1P2 (0.44g)	0.55	1.07
24	-	ROCKS1P3 (0.48g)	0.51	1.26
25	-	ROCKS1P4 (0.32g)	0.65	1.22
26	-	ROCKS1P5 (0.67g)	0.55	1.31
27	-	ROCKS1P6 (0.41g)	0.61	1.31
28	-	ROCKS1P7 (0.4g)	0.66	1.17

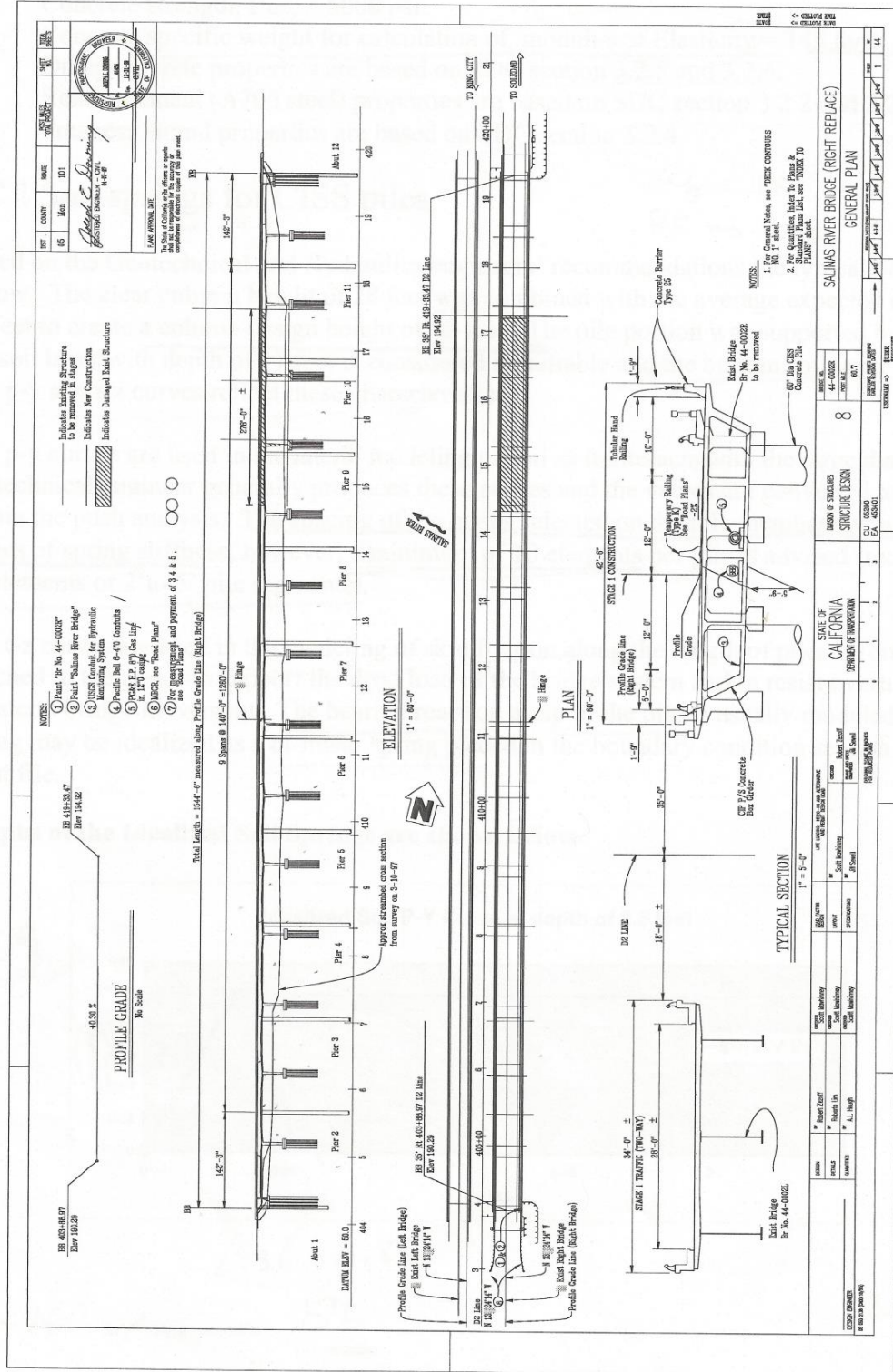
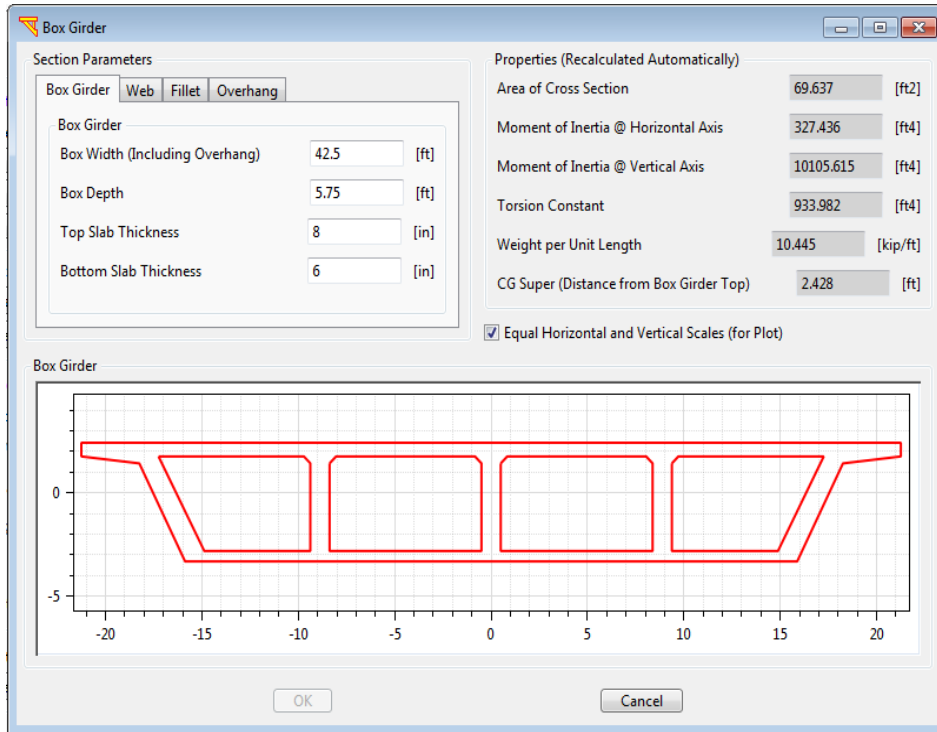
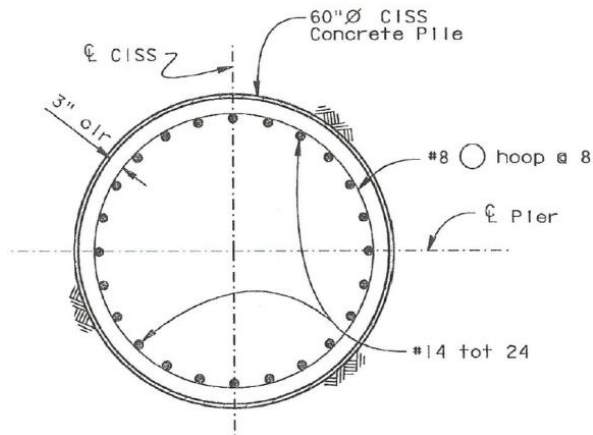


Figure 2.1. General layout of Salinas Bridge (Caltrans 2005)



a)



b)

Figure 2.2. Sectional details of Salinas Bridge: (a) deck; (b) Type I shaft cross-section

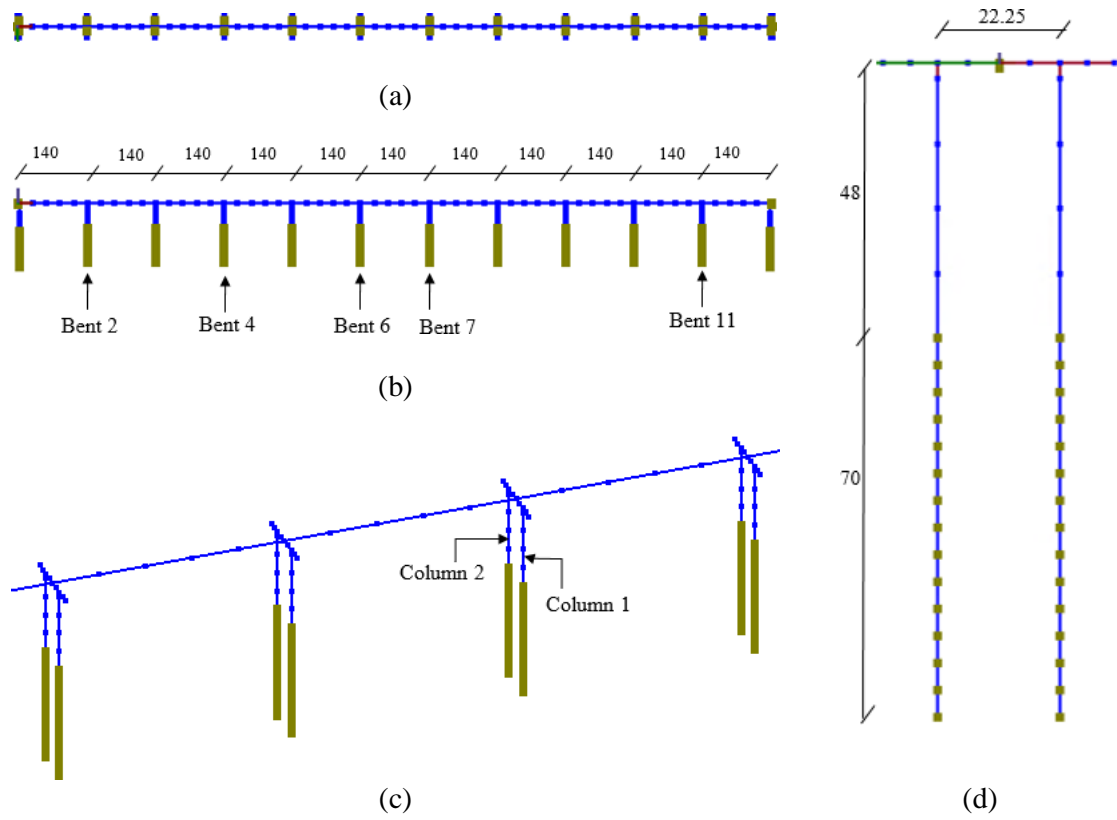
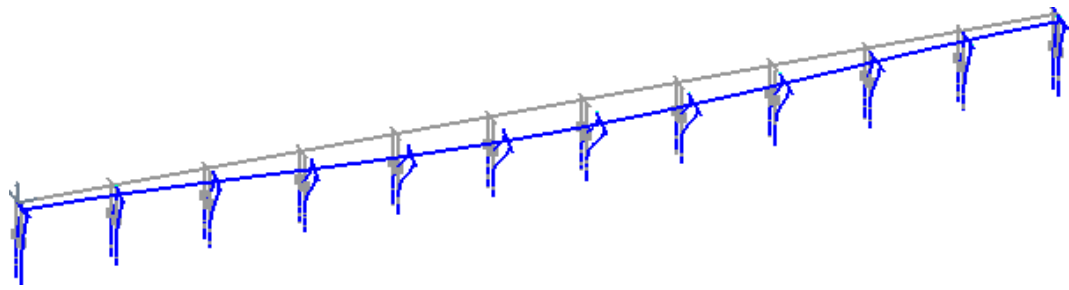
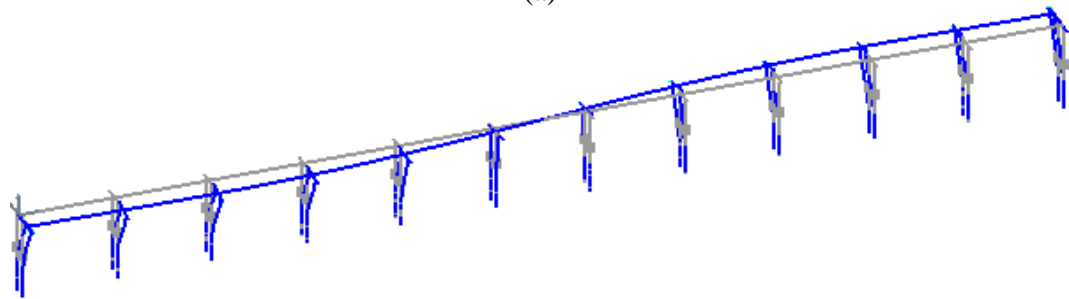


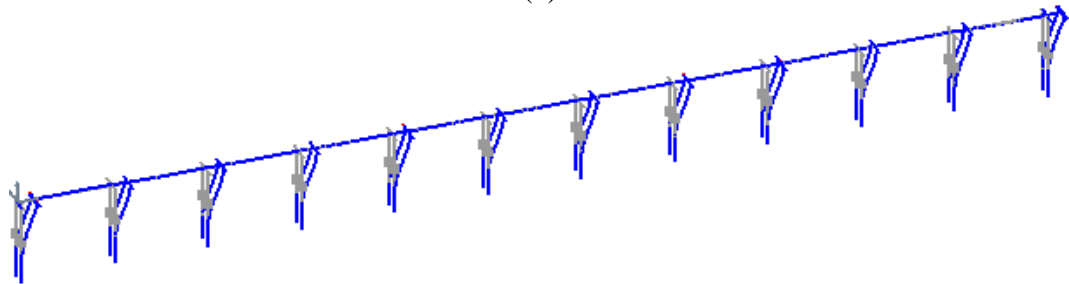
Figure 2.3. Salinas Bridge FE model created in MSBridge (dimensions in ft): (a) plan view; (b) elevation view; (c) close-up of 3D view; (d) side view of a bent (typical)



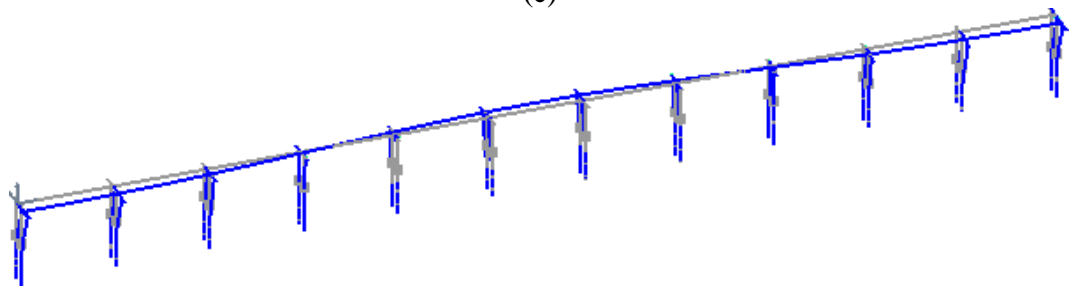
(a)



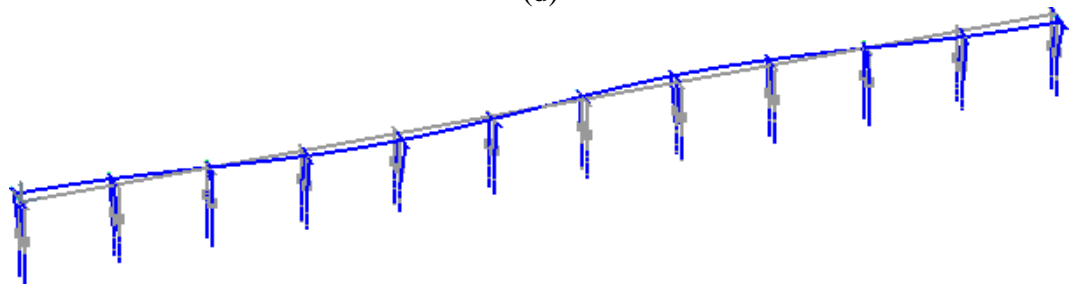
(b)



(c)



(d)



(e)

Figure 2.4. Salinas Bridge mode shapes: (a) first mode; (b) second mode; (c) third mode; (d) fourth mode; and (e) fifth mode

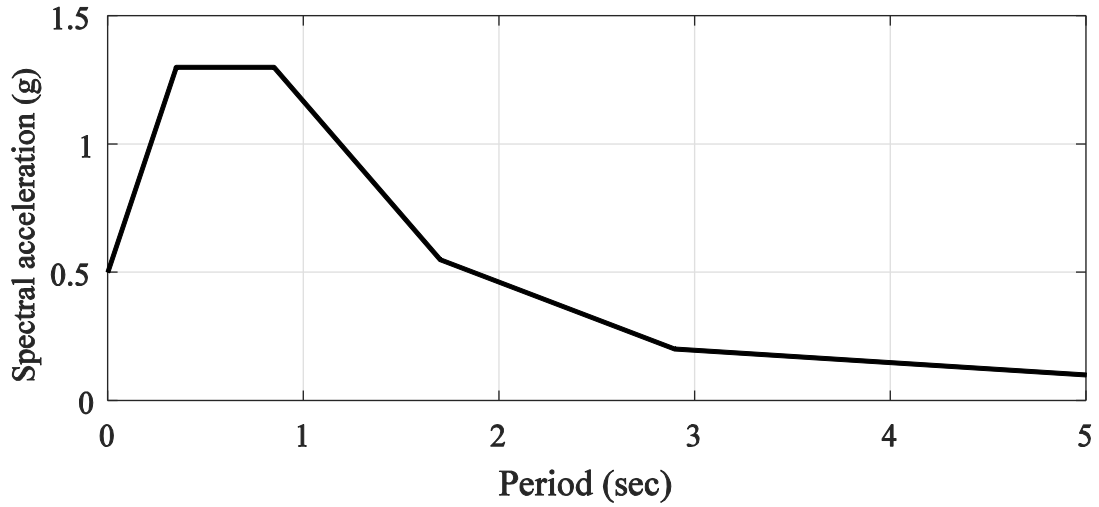


Figure 2.5. Acceleration response spectrum (ARS) curve employed in Caltrans (2005)

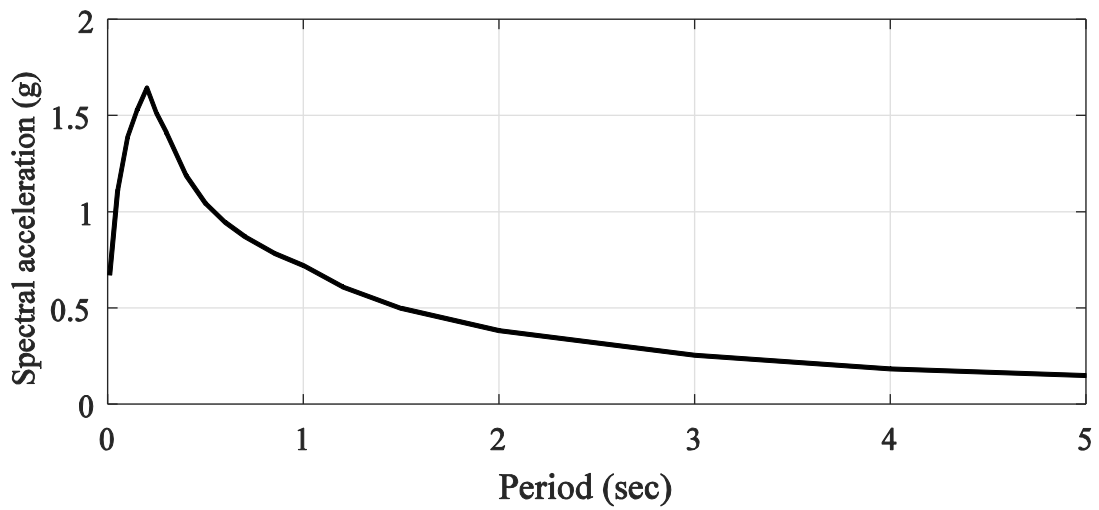


Figure 2.6. ARS curve employed in the ESA

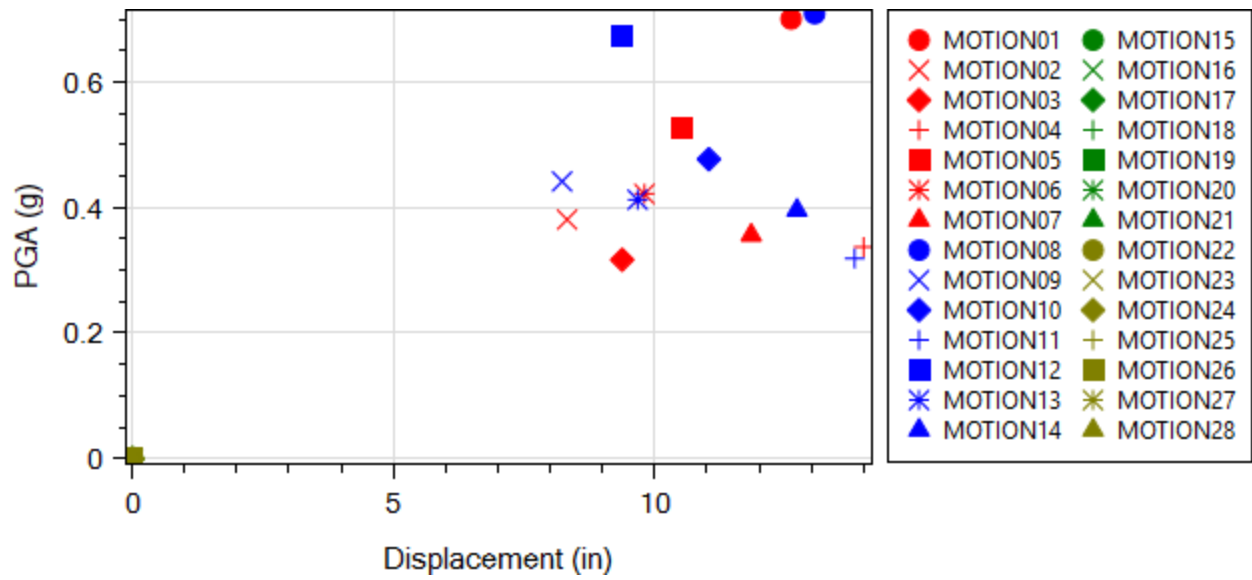


Figure 2.7. Bridge deck maximum longitudinal displacement

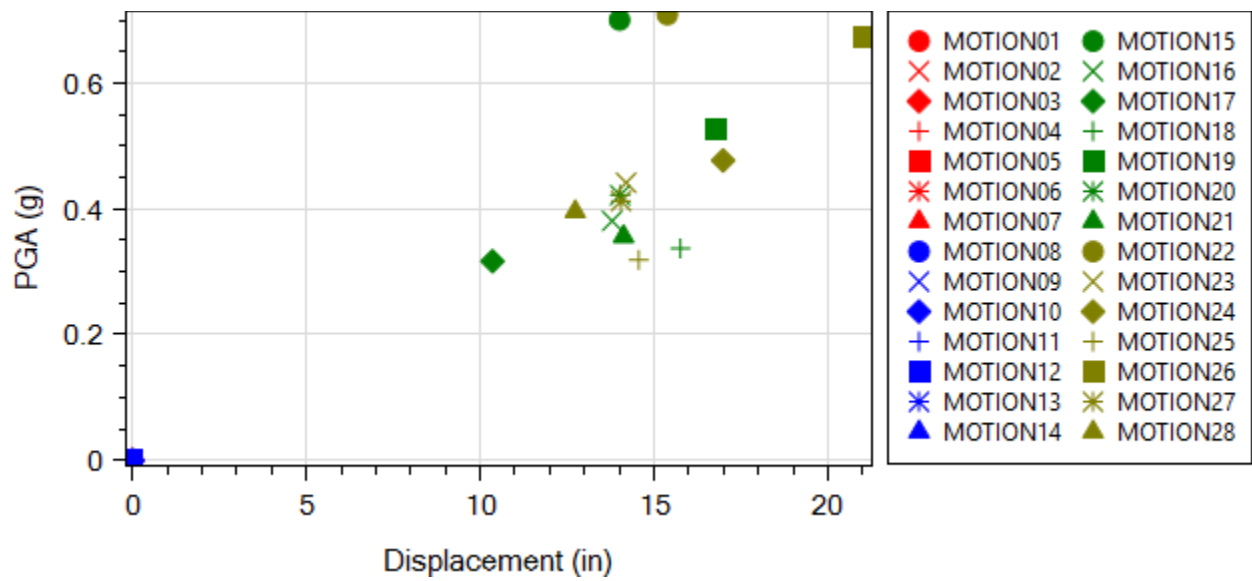


Figure 2.8. Bridge deck maximum transverse displacement

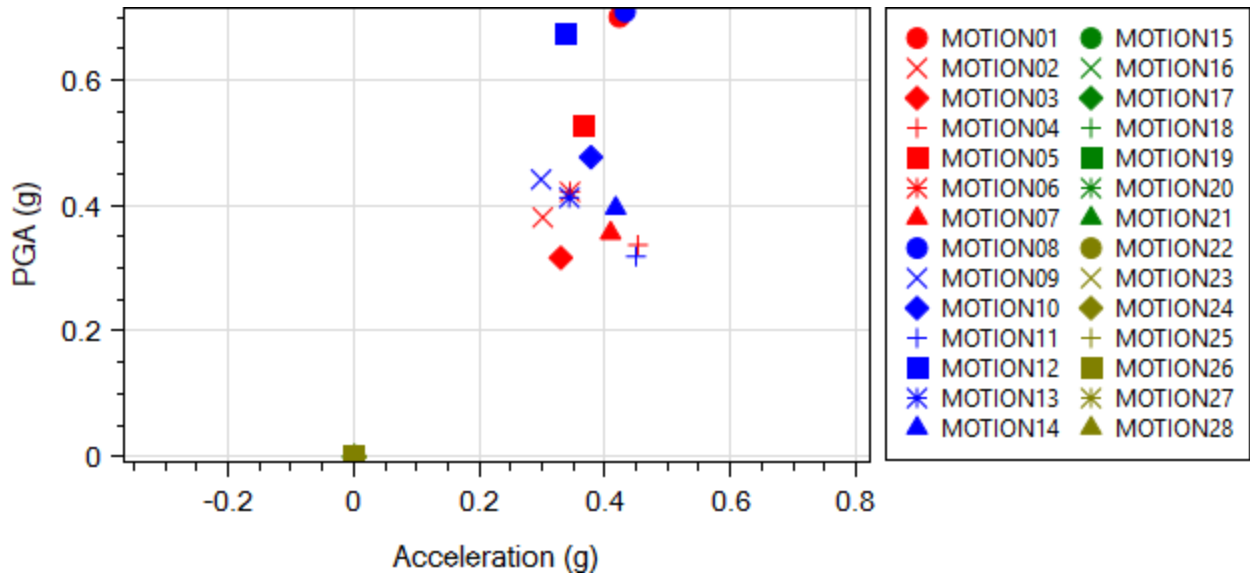


Figure 2.9. Bridge deck maximum longitudinal acceleration

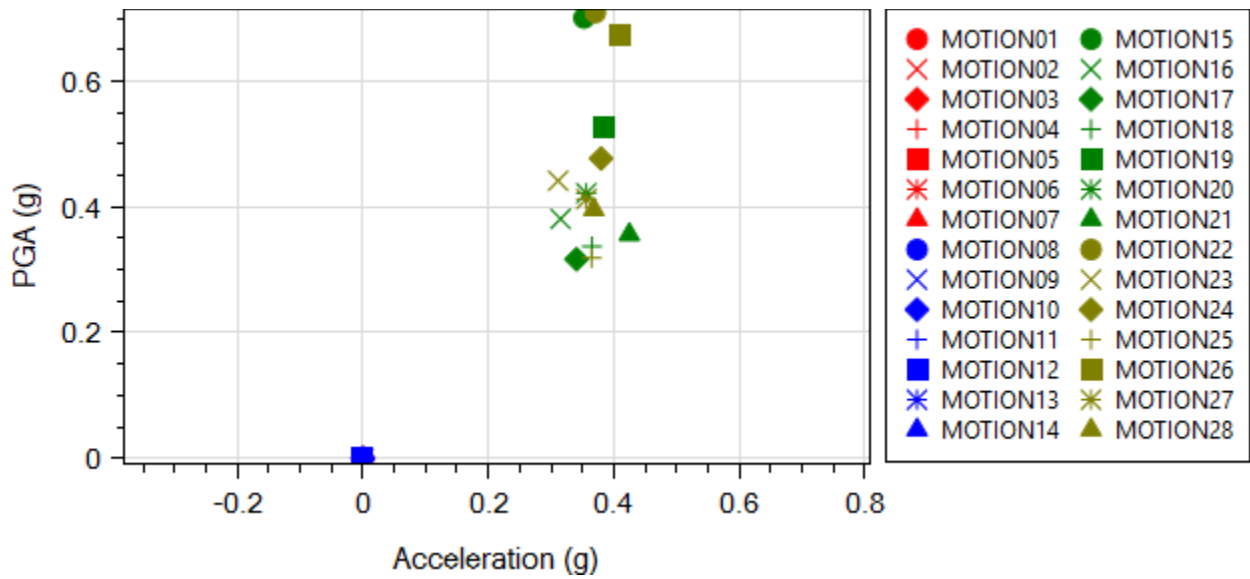


Figure 2.10. Bridge deck maximum transverse acceleration

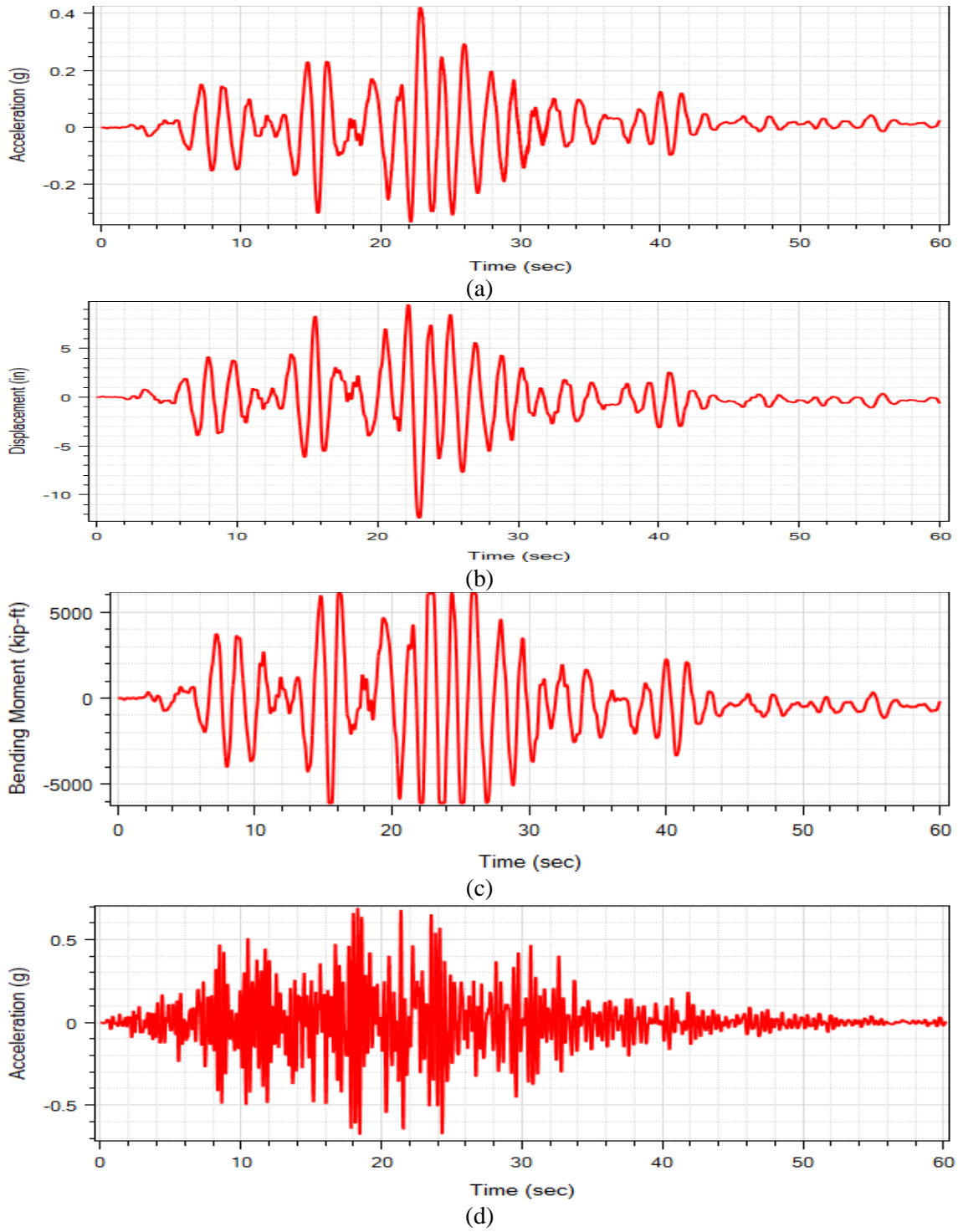


Figure 2.11. Column top longitudinal response time histories of Column 1 of Bent 7 for Simulation 1 (ROCKS1N1): (a) acceleration; (b) displacement; (c) bending moment; (d) and base excitation

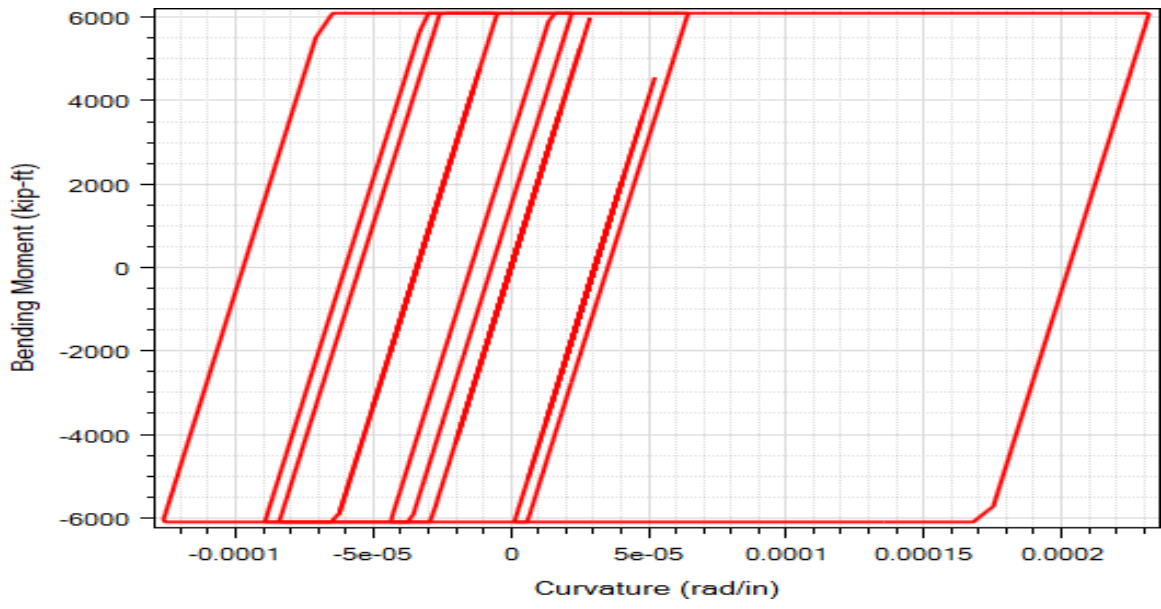
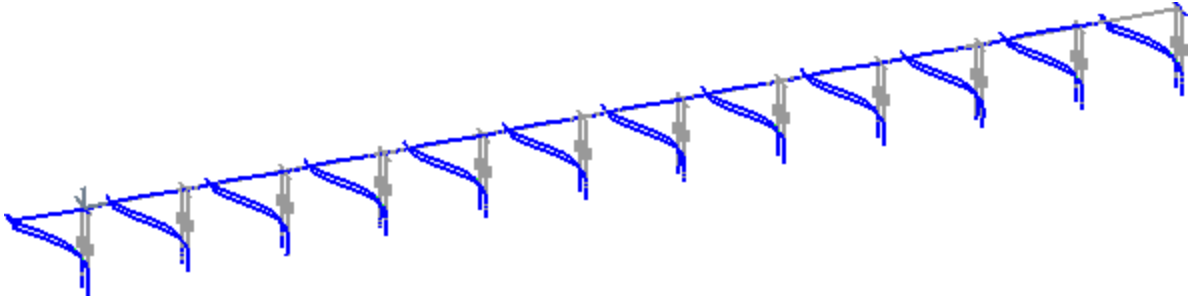
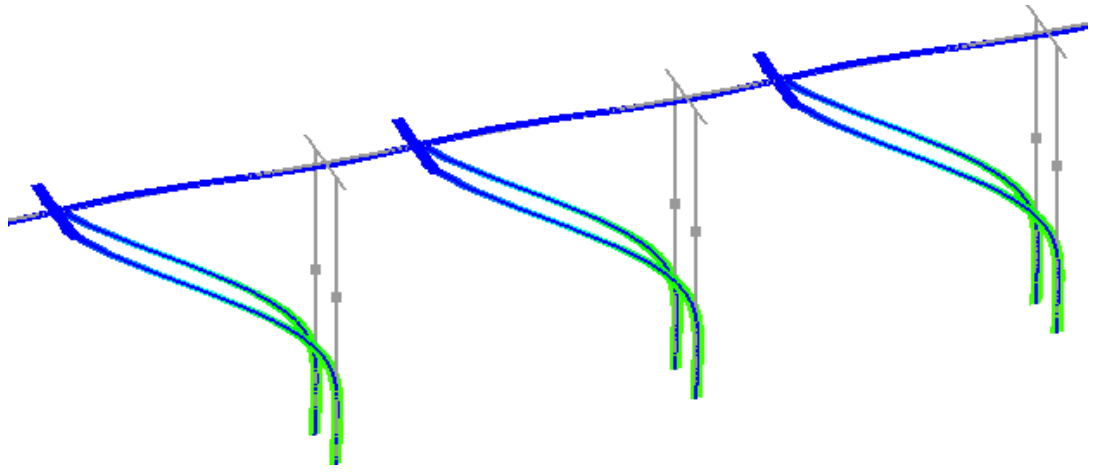


Figure 2.12. Column top longitudinal moment-curvature response of Column 1 of Bent 7 for Simulation 1



(a)



(b)

Figure 2.13. Deformed mesh (factor of 100) for Simulation 1 at the maximum displacement step (grey lines represent undeformed mesh): (a) entire bridge; (b) close-up of Bents 6, 7, and 8 (from left to right)

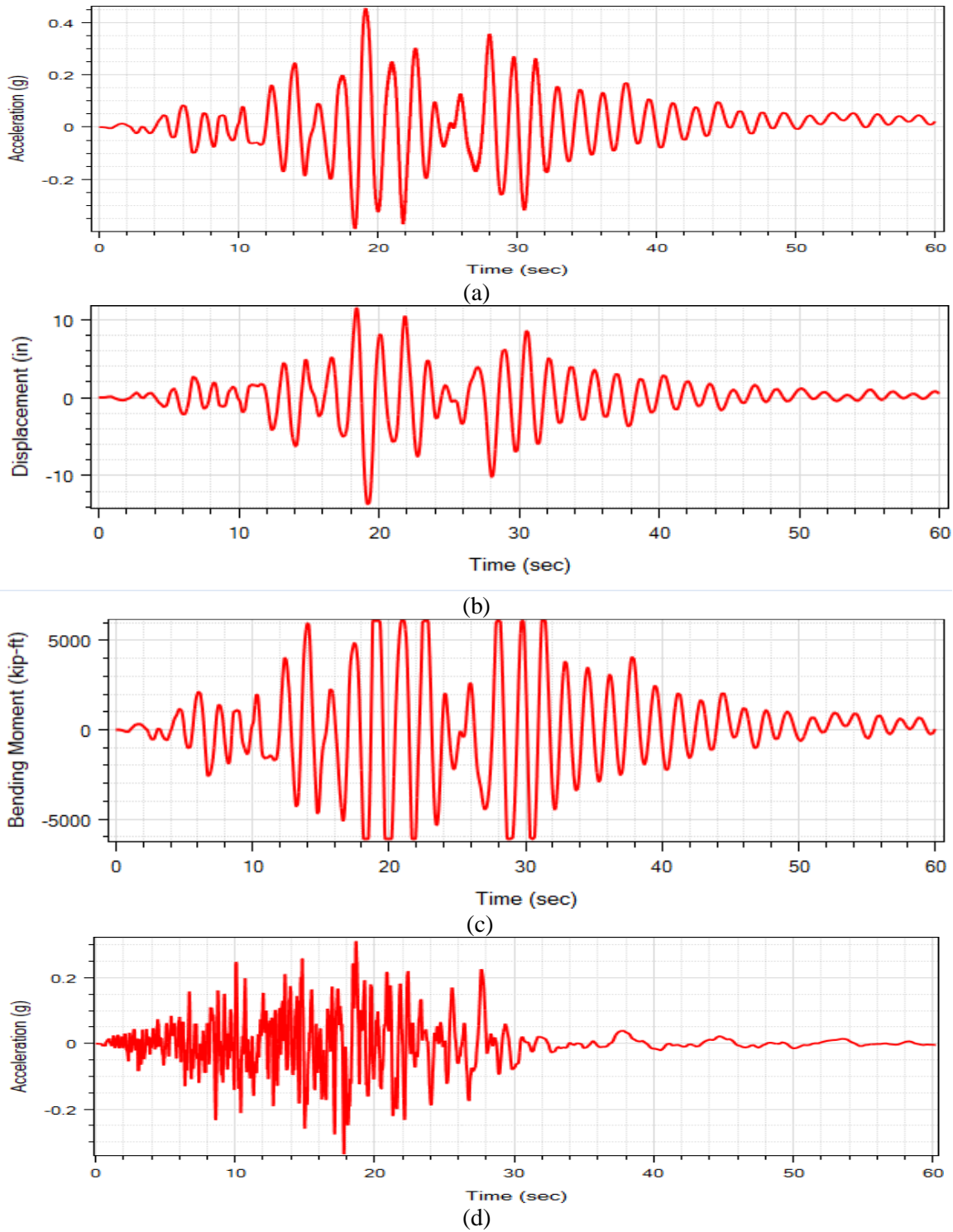


Figure 2.14. Column top longitudinal response time histories of Column 1 of Bent 7 for Simulation 4 (ROCKS1N4): (a) acceleration; (b) displacement; (c) bending moment; and (d) base excitation

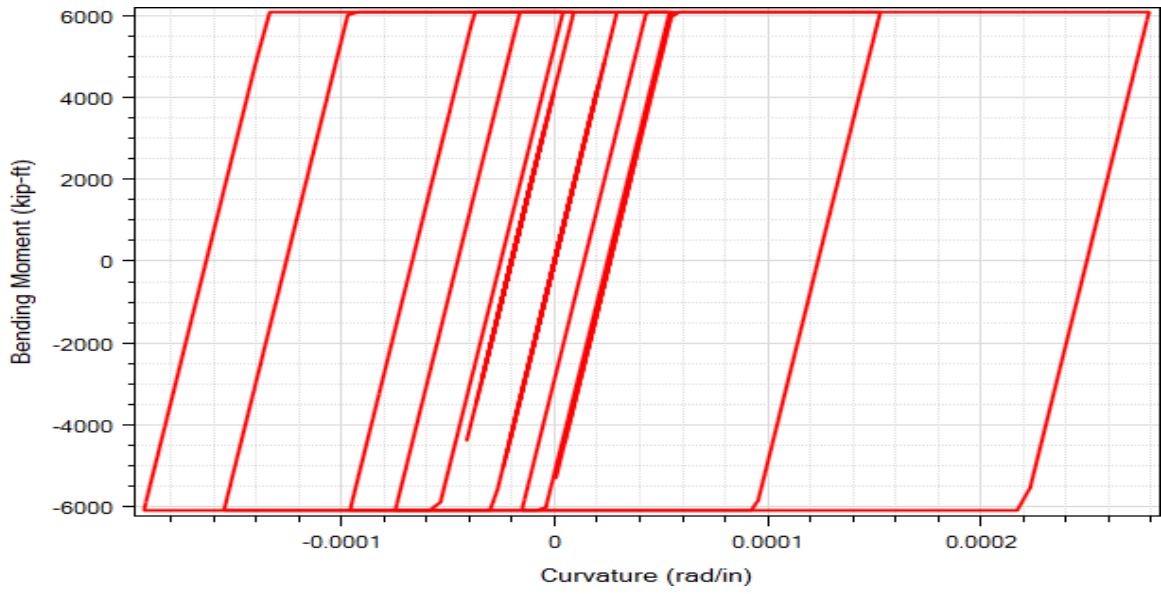
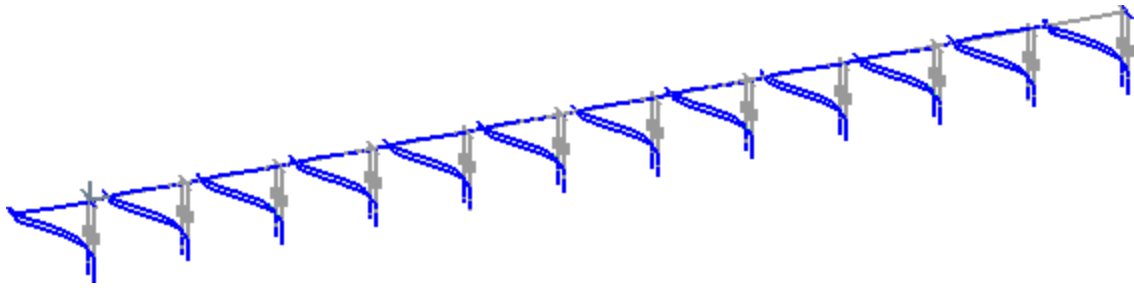
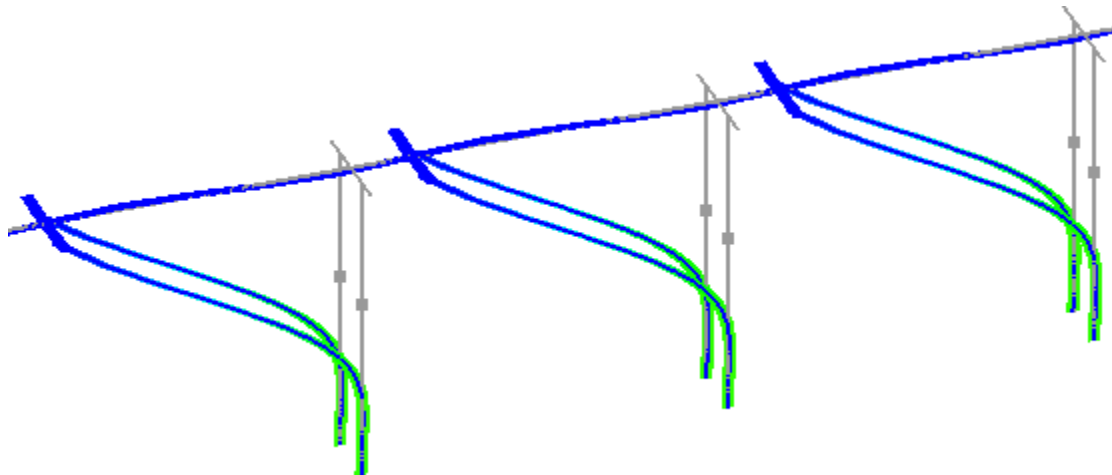


Figure 2.15. Column top longitudinal moment-curvature response of Column 1 of Bent 7 for Simulation 4

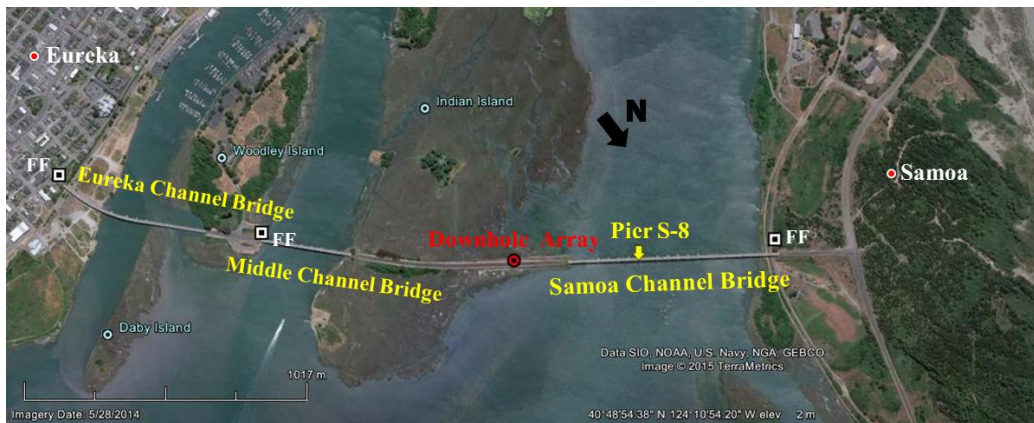


(a)



(b)

Figure 2.16. Deformed mesh (factor of 100) for Simulation 4 at the step of the maximum displacement (14 in @ 19.2 seconds) (grey lines represent undeformed mesh): (a) entire bridge; (b) close-up of Bents 6, 7, and 8 (from left to right)

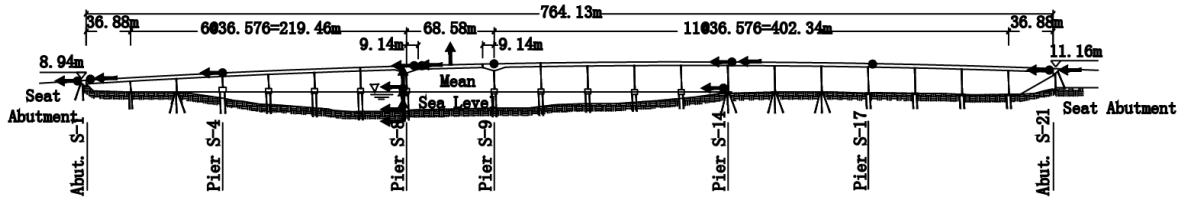


(a)

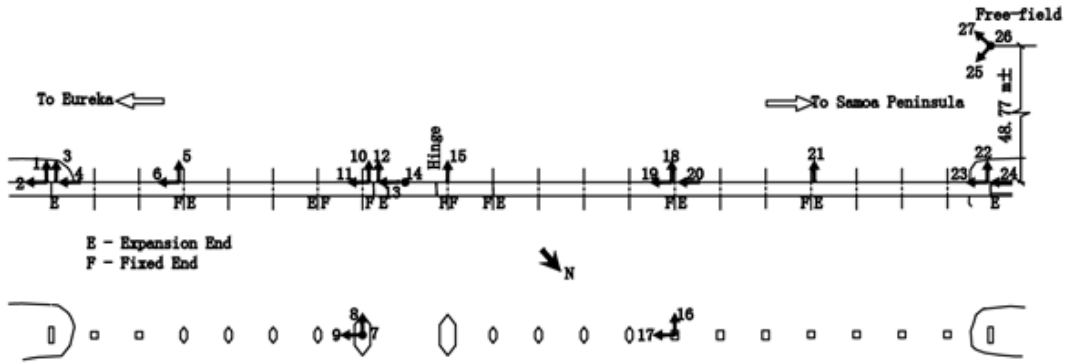


(b)

Figure 2.17. Bridge configuration: (a) Samoa Channel Bridge, Eureka geotechnical array, Middle Channel Bridge and Eureka Channel Bridge (Map Data @ 2015 Google) and (b) photo of the Samoa Channel Bridge (<http://www.strongmotioncenter.org>)



(a)



(b)

Figure 2.18. Layout of instrumentation at Samoa Bridge (<http://www.strongmotioncenter.org>): (a) elevation view; (b) plan view

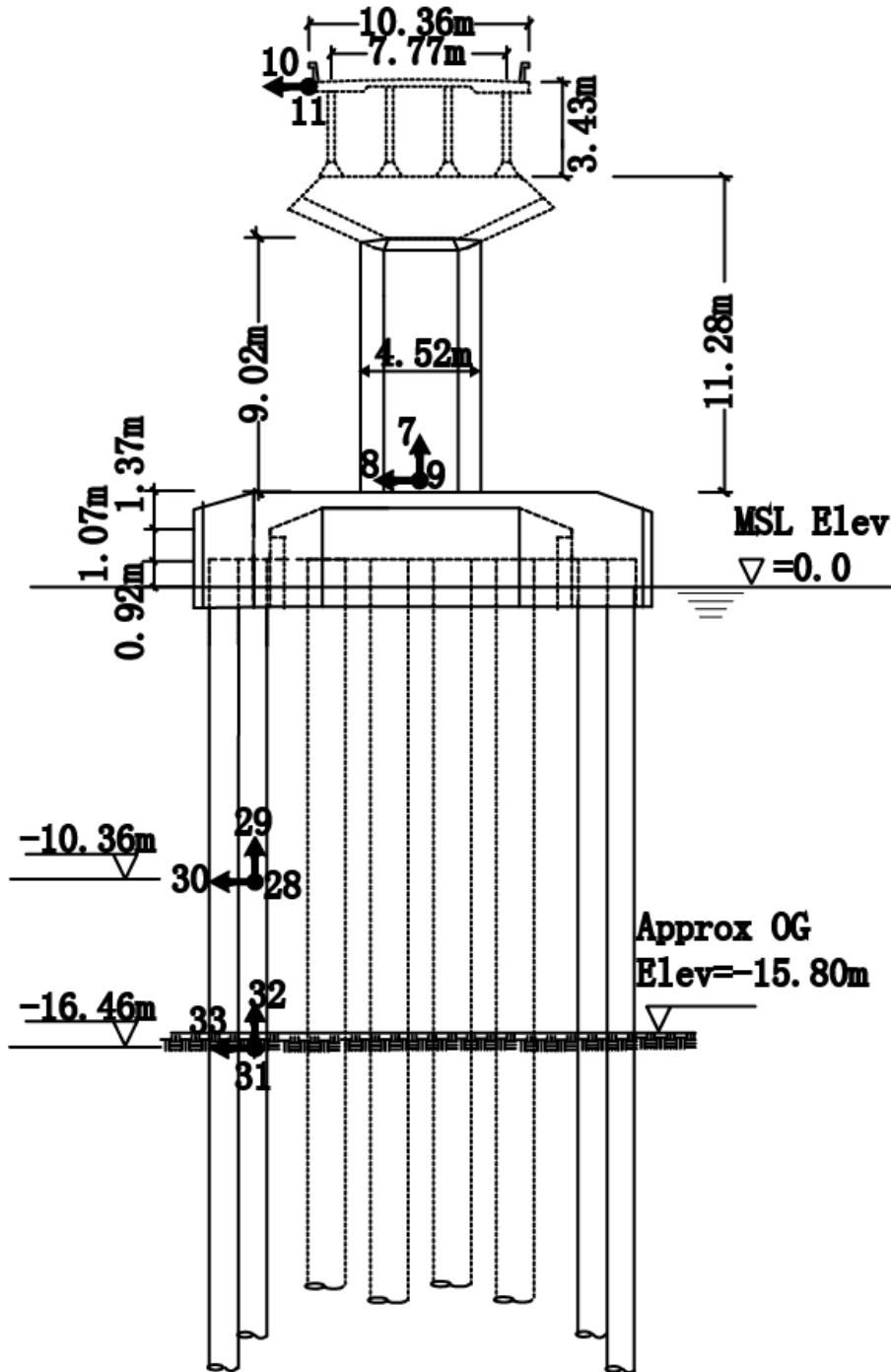
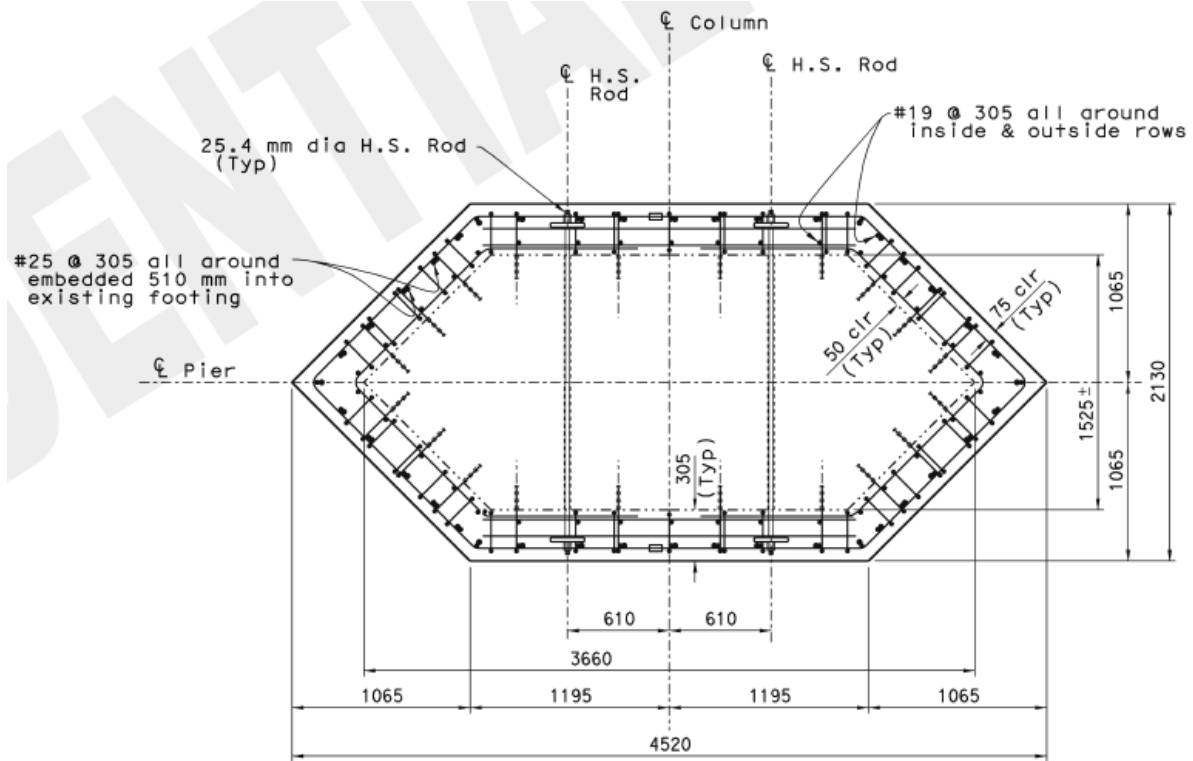
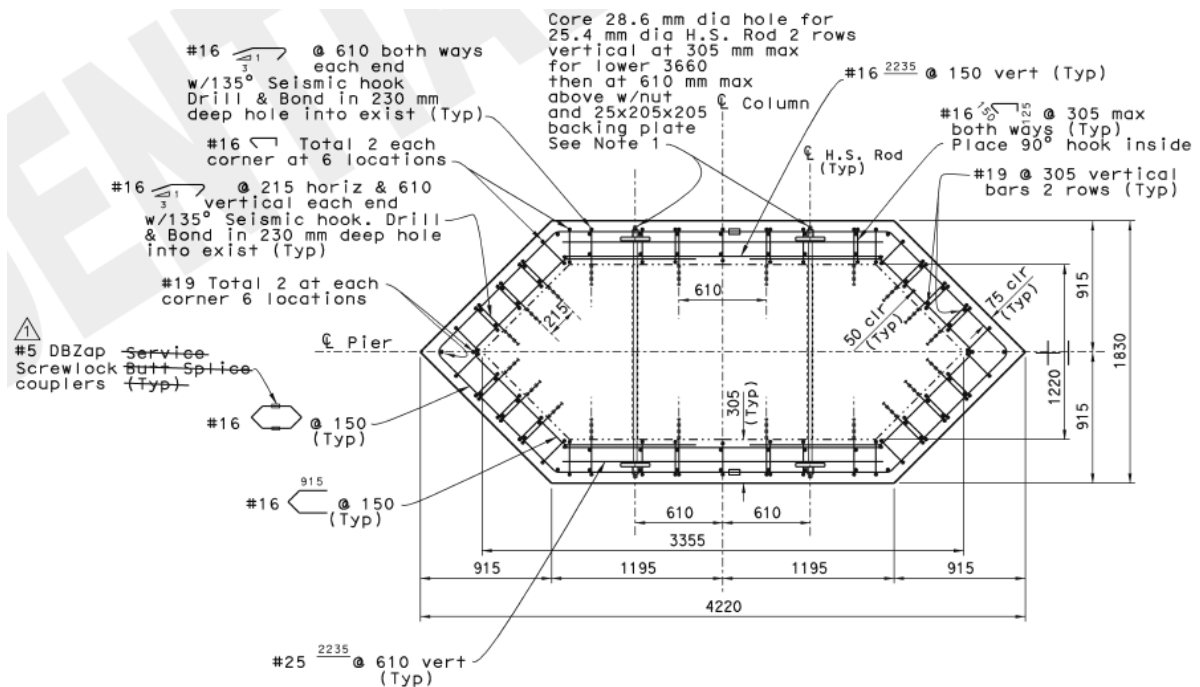


Figure 2.19. Elevation and bridge deck of Pier S-8 of Samoa Bridge



(a)



(b)

Figure 2.20. Samoa Bridge: (a) column detail of Piers S-8 and S-9; and (b) column detail of other piers except Piers S-8 and S-9

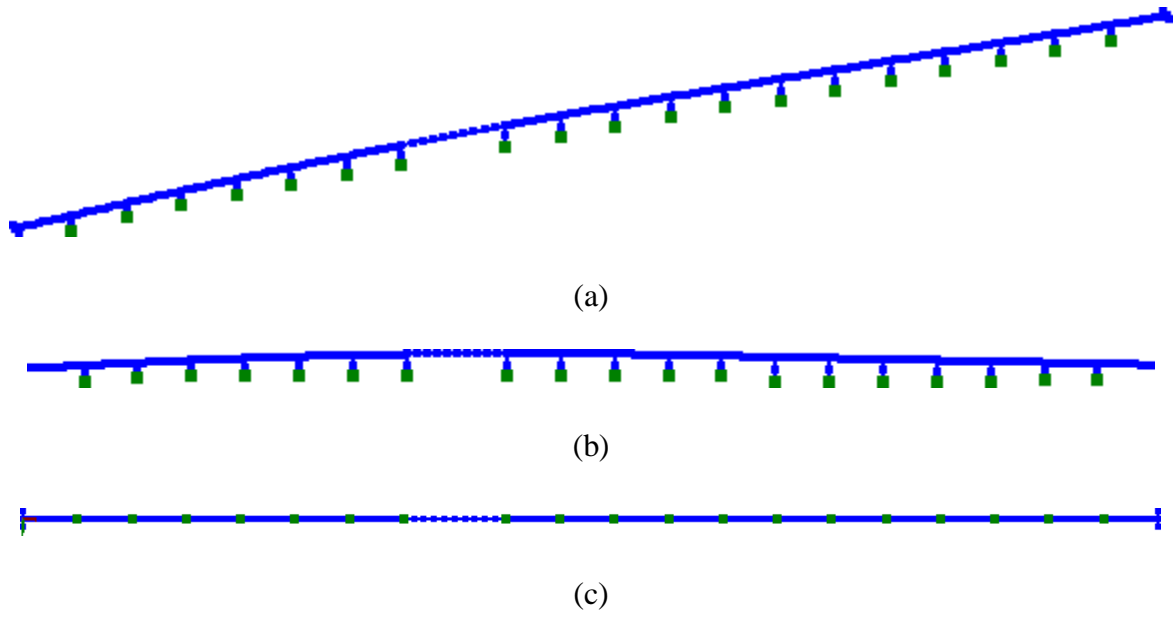
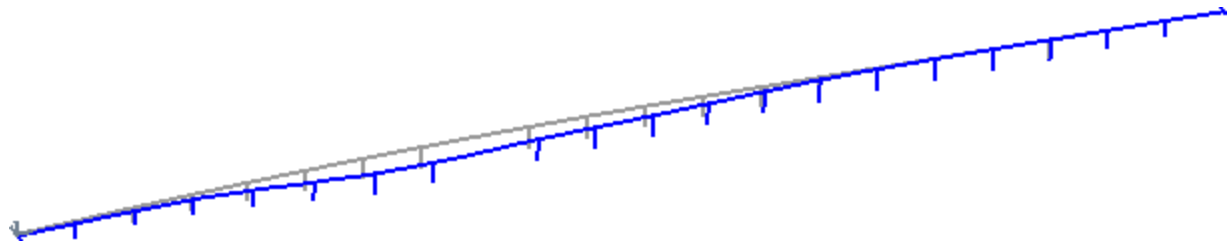
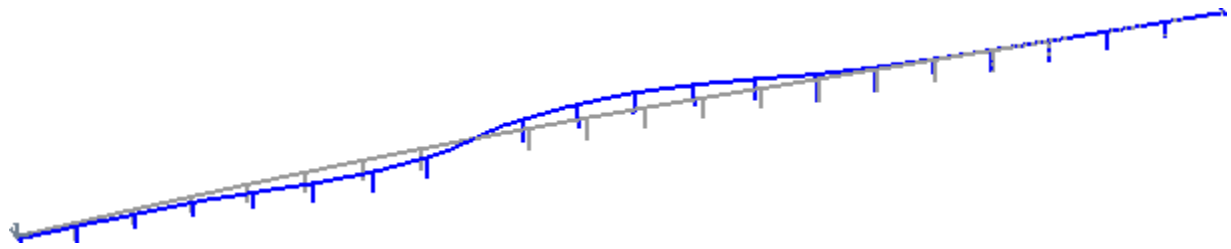


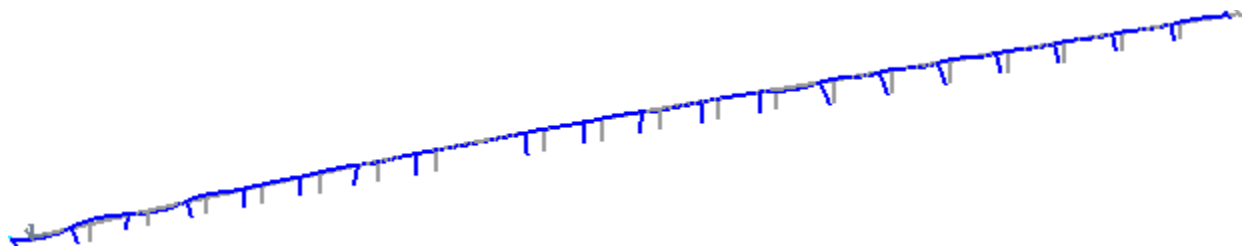
Figure 2.21. Samoa Bridge FE mesh created in MSBridge: (a) 3D view; (b) elevation view; (c) plan view



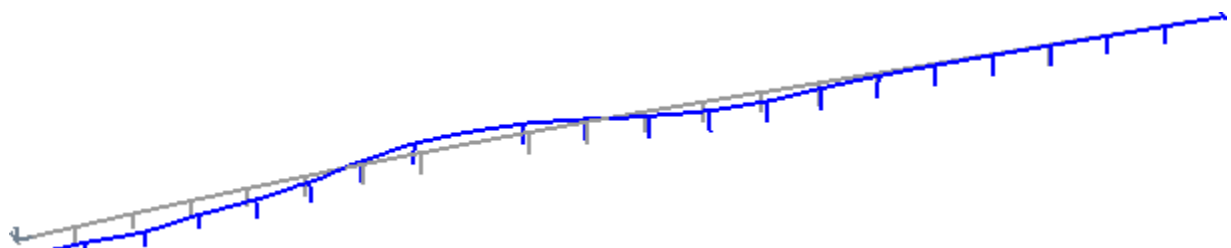
(a)



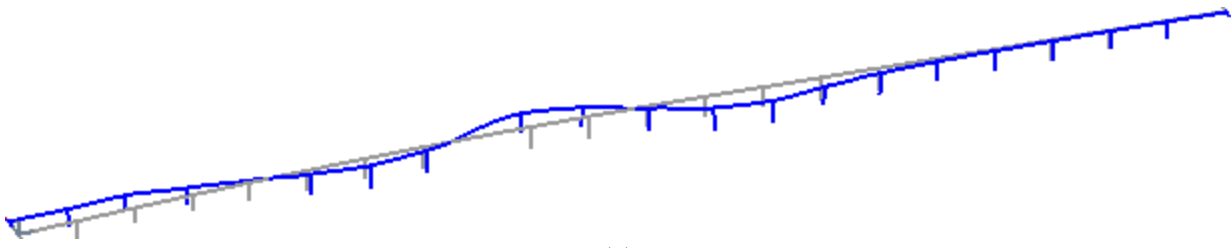
(b)



(c)



(d)



(e)

Figure 2.22. Mode shapes for Samoa Bridge: (a) first mode; (b) second mode; (c) third mode; (d) fourth mode; and (e) fifth mode

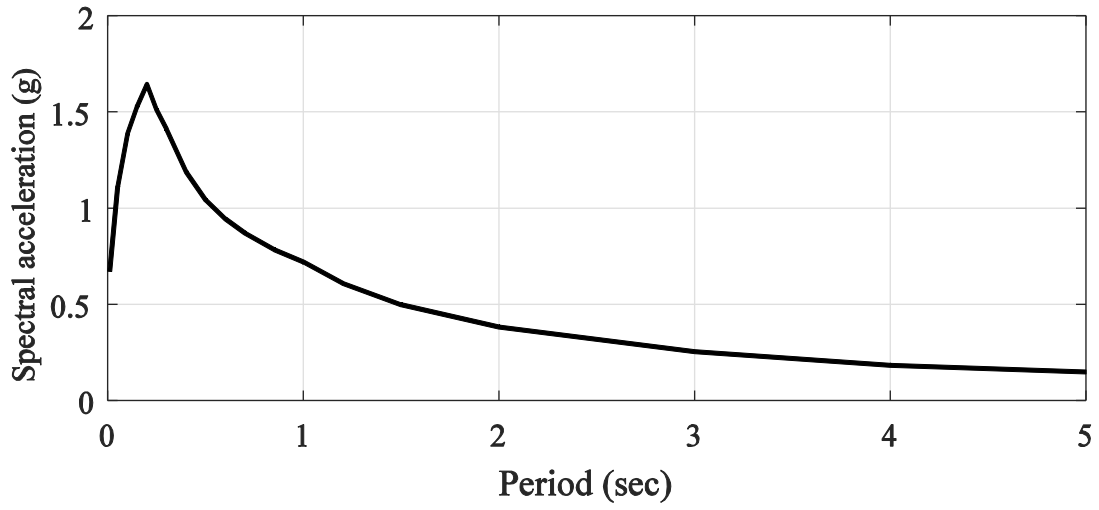


Figure 2.23. ARS curve employed in the ESA

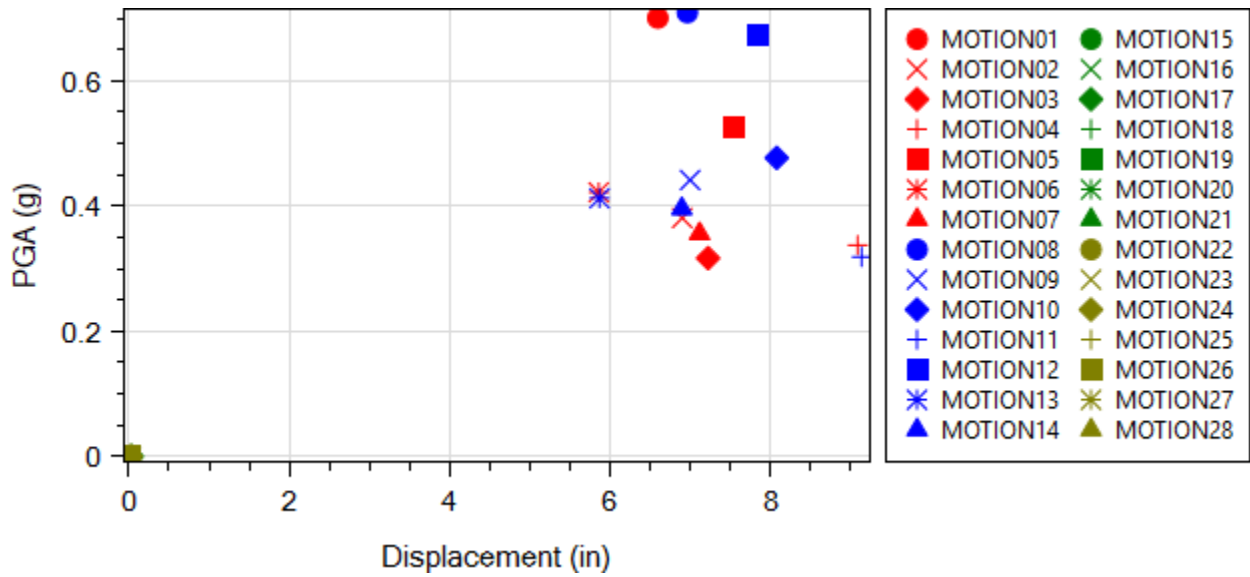


Figure 2.24. Bridge deck maximum longitudinal displacement

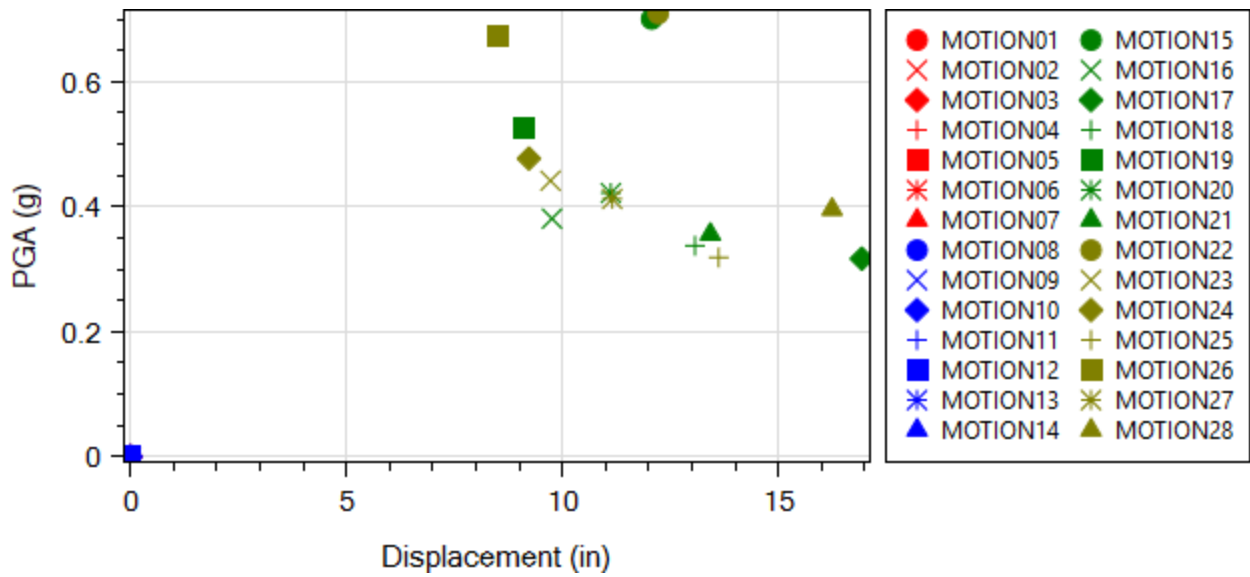


Figure 2.25. Bridge deck maximum transverse displacement

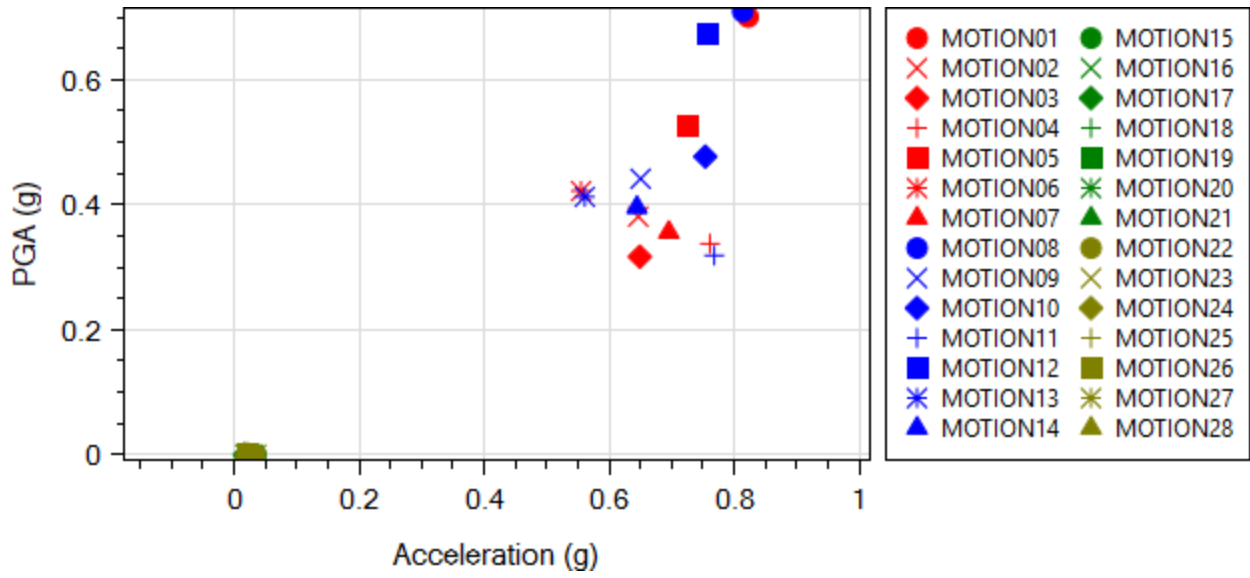


Figure 2.26. Bridge deck maximum longitudinal acceleration

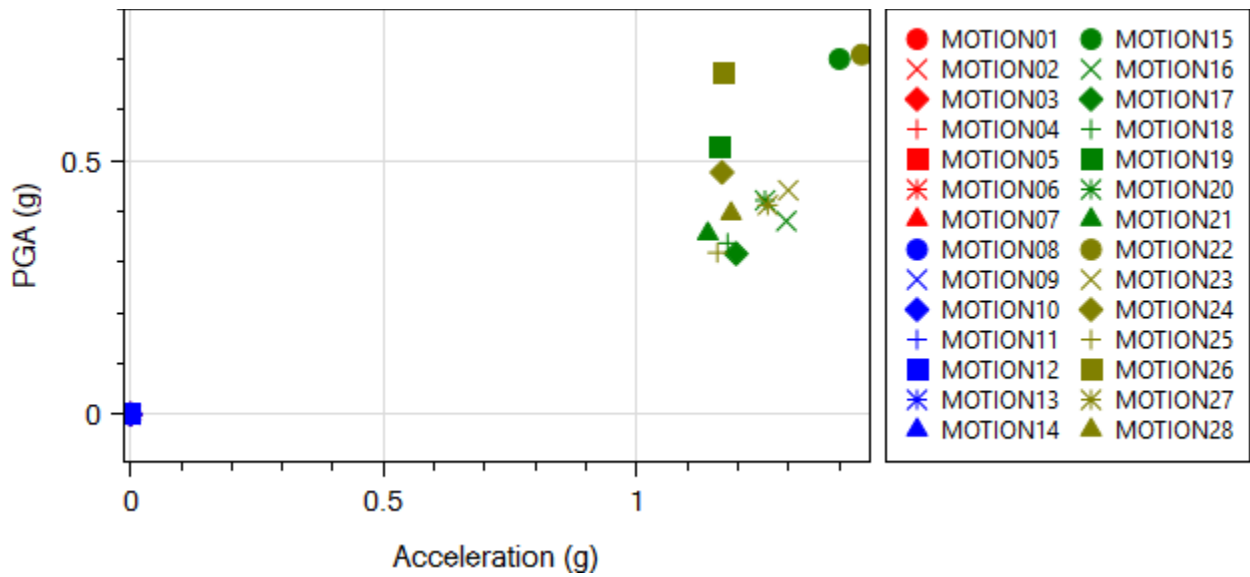


Figure 2.27. Bridge deck maximum transverse acceleration

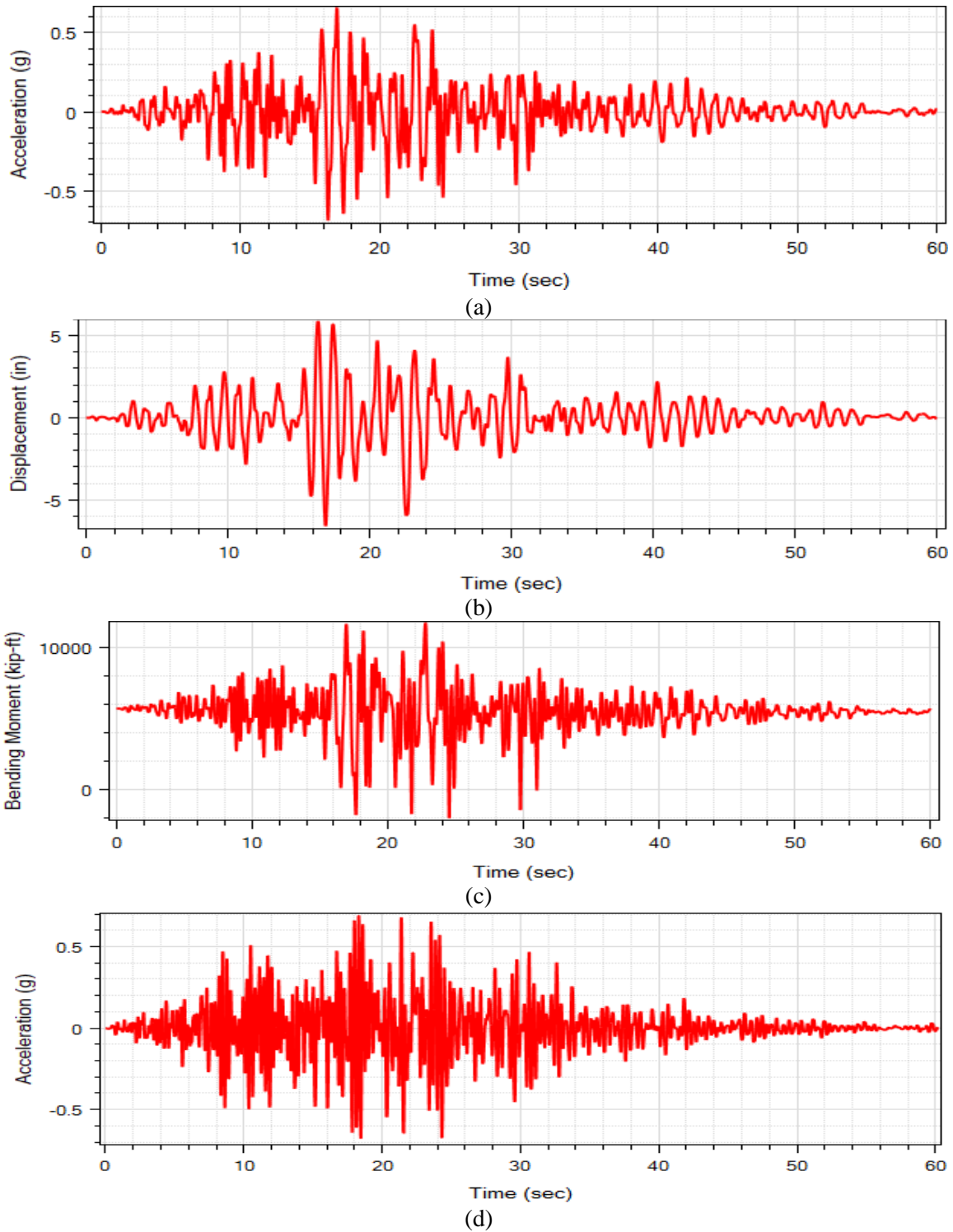
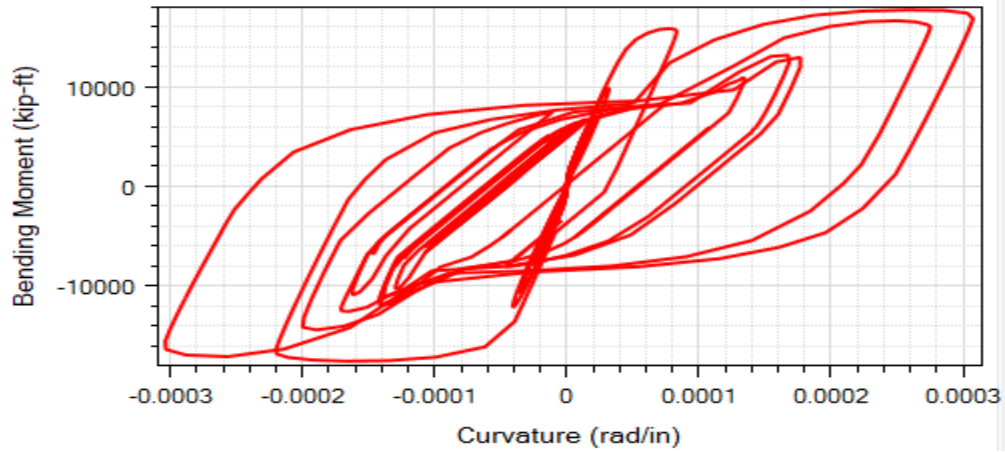
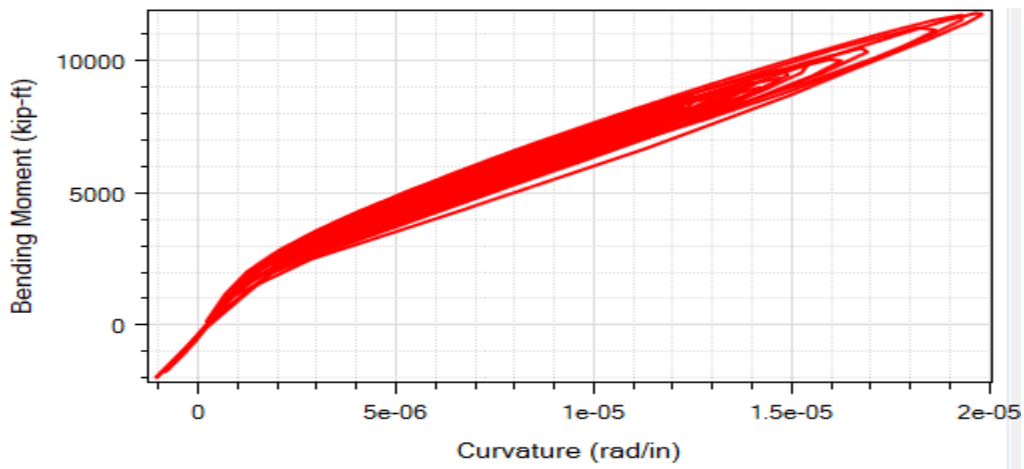


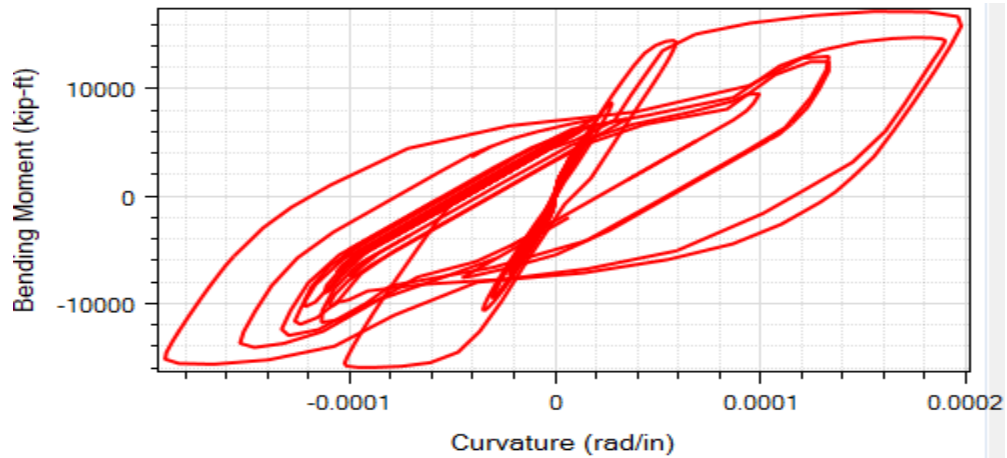
Figure 2.28. Pier S-8 column top longitudinal response time histories for Simulation 1 (ROCKS1N1): (a) acceleration; (b) displacement; (c) bending moment; and (d) base excitation



(a)

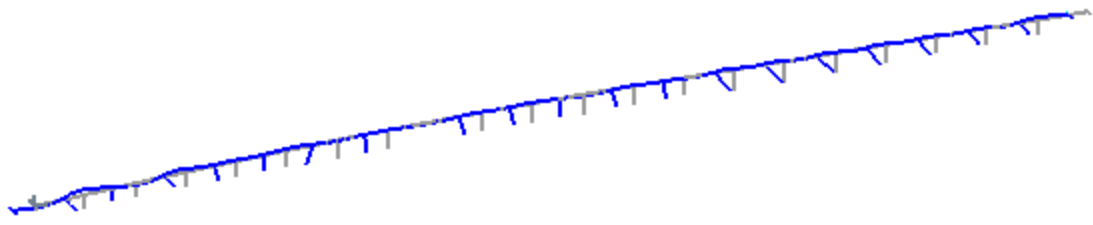


(b)

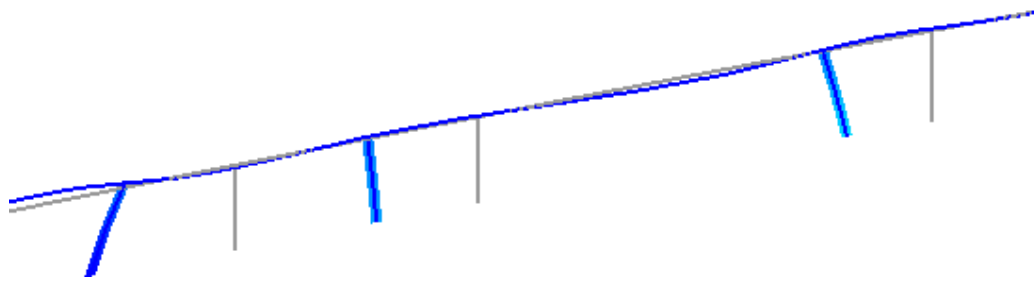


(c)

Figure 2.29. Column top longitudinal moment-curvature response for Simulation 1: (a) Pier S-4; (b) Pier S-8; (c) Pier S-19



(a)



(b)

Figure 2.30. Deformed mesh (factor of 100) for Simulation 1 at the maximum displacement step (grey lines represent undeformed mesh): (a) entire bridge; (b) close-up of Bents 6, 7, and 8 (from left to right)

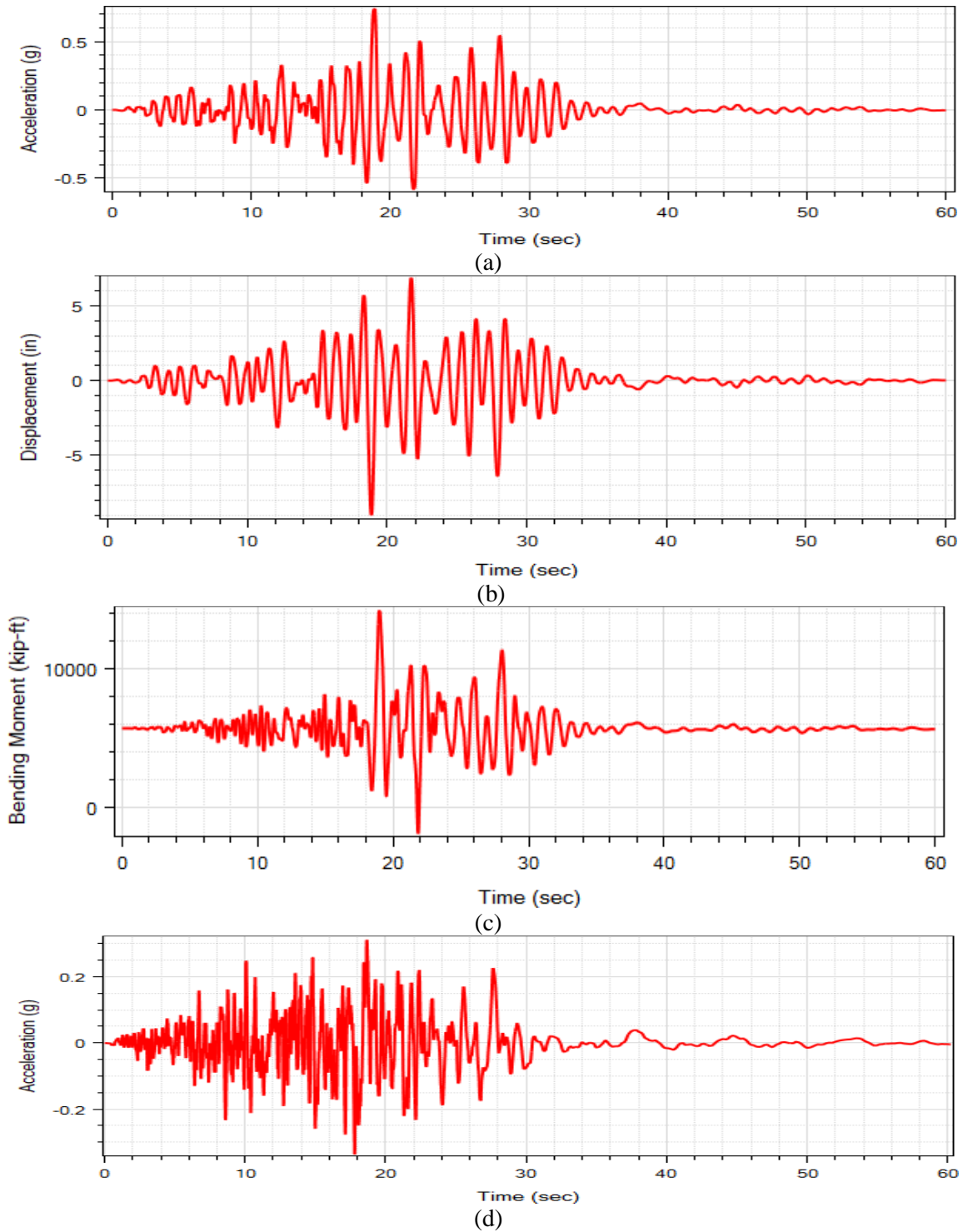


Figure 2.31. Pier S-8 column top longitudinal response time histories for Simulation 4 (ROCKS1N4): (a) acceleration; (b) displacement; (c) bending moment; and (d) base excitation

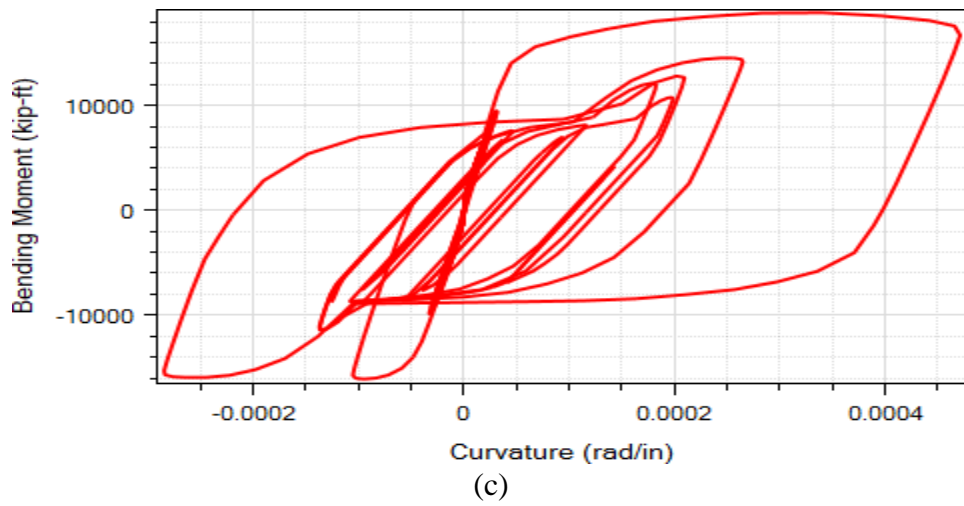
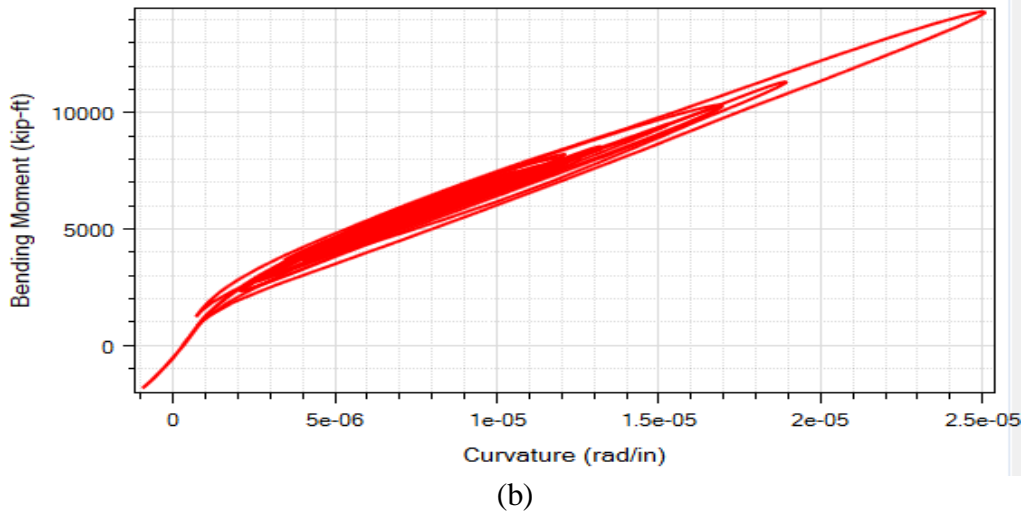
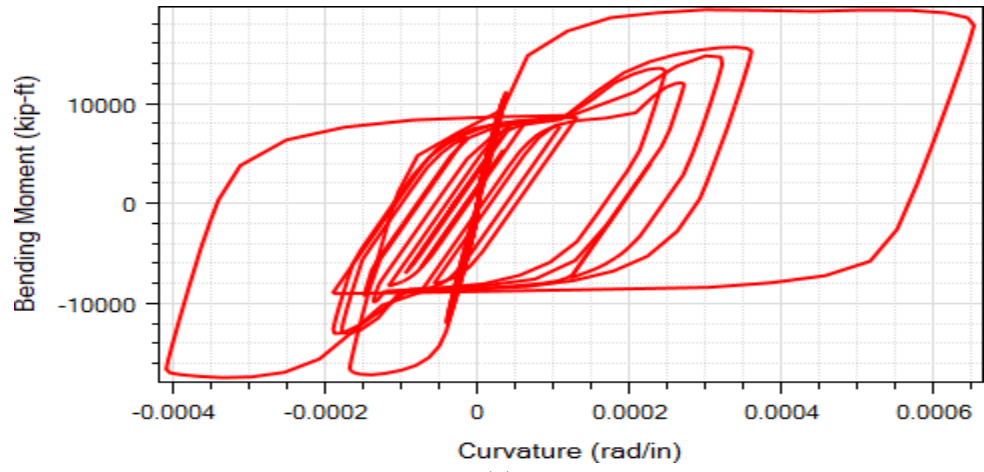


Figure 2.32. Column top longitudinal moment-curvature response for Simulation 4: (a) Pier S-4; (b) Pier S-8; (c) Pier S-19

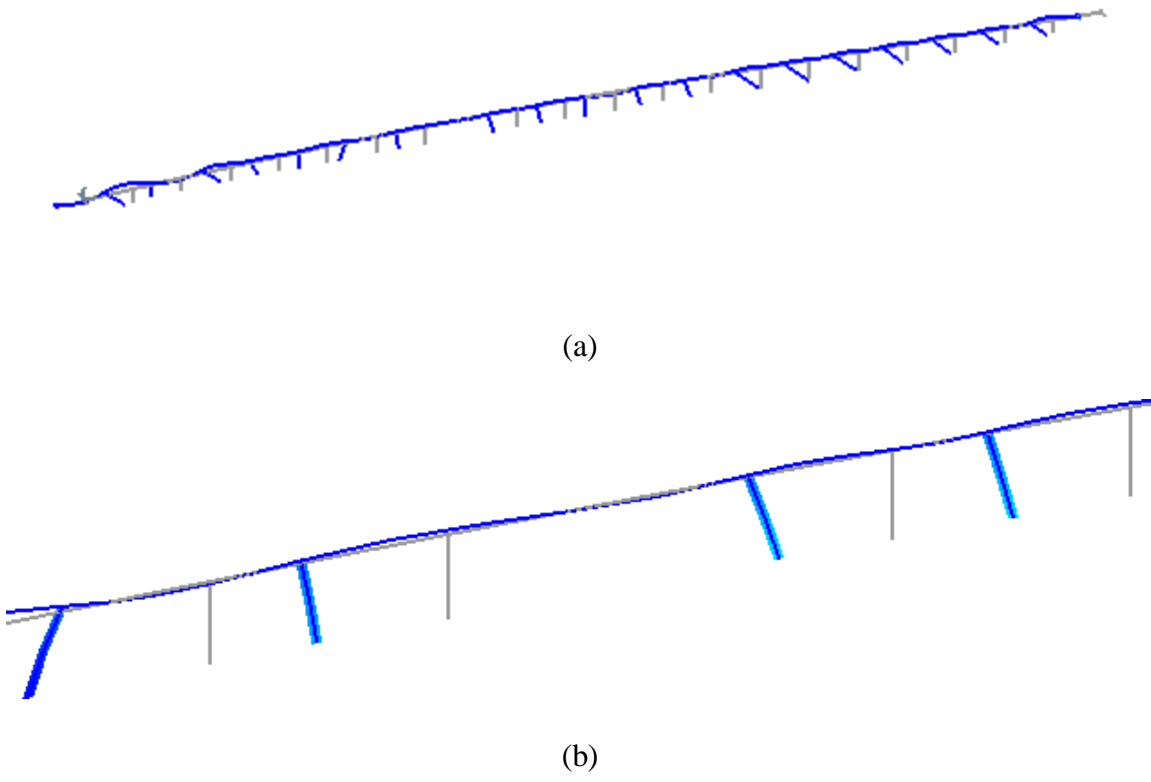
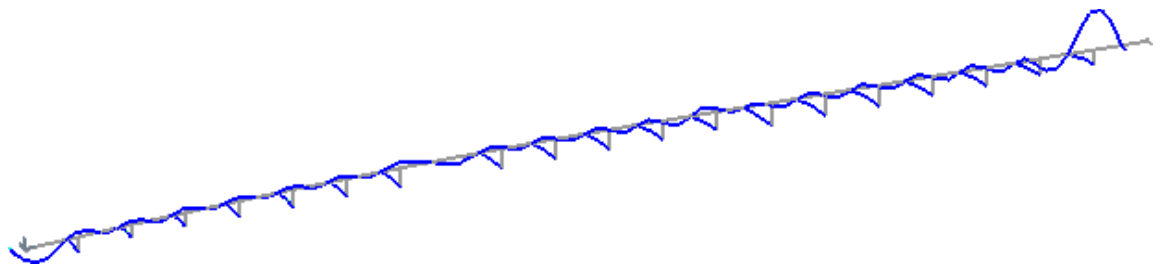


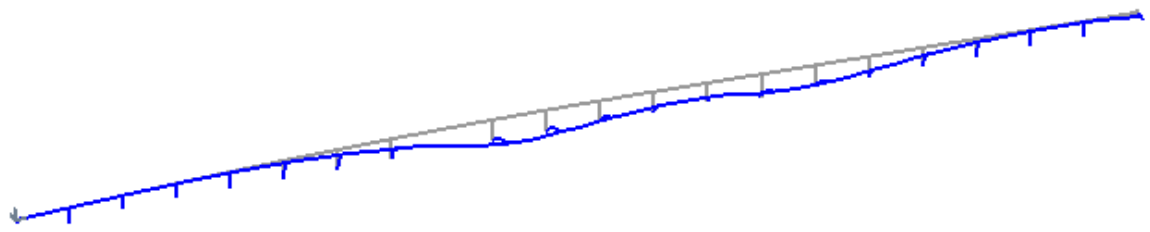
Figure 2.33. Deformed mesh (factor of 100) for Simulation 4 at the maximum displacement step (grey lines represent undeformed mesh): (a) entire bridge; (b) close-up of Bents 6, 7, and 8 (from left to right)

K =	SDx	SDy	SDz	SRx	Sry	SRz	
	150000	0	0	0	0	0	SDx
	0	150000	0	0	0	0	SDy
	0	0	650000	0	0	0	SDz
	0	0	0	3.00E+09	0	0	SRx
	0	0	0	0	3.00E+09	0	Sry
	0	0	0	0	0	7.00E+08	SRz

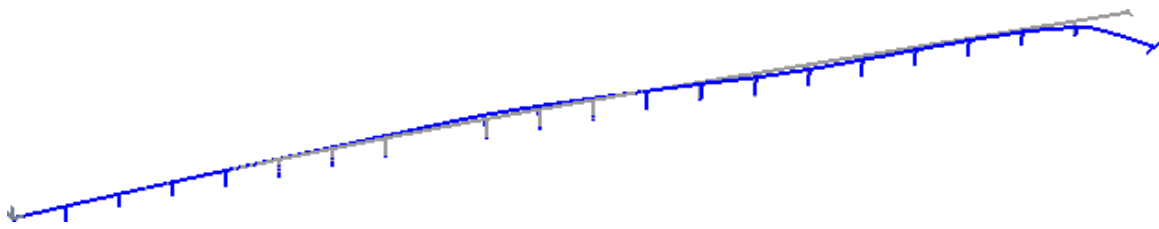
Figure 2.34. Stiff foundation matrix employed (Caltrans, personal communications)



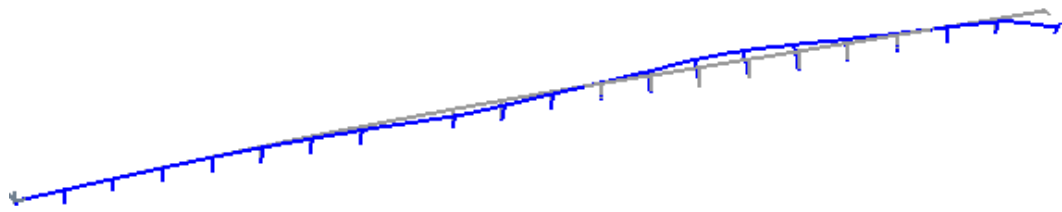
(a)



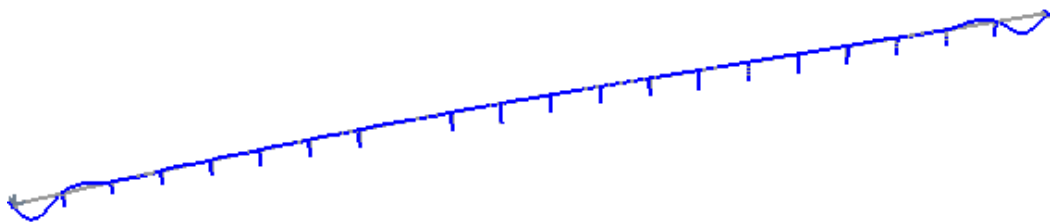
(b)



(c)



(d)



(e)

Figure 2.35. Mode shapes for Samoa Bridge with stiff foundation matrix: (a) first mode; (b) second mode; (c) third mode; (d) fourth mode; and (e) fifth mode

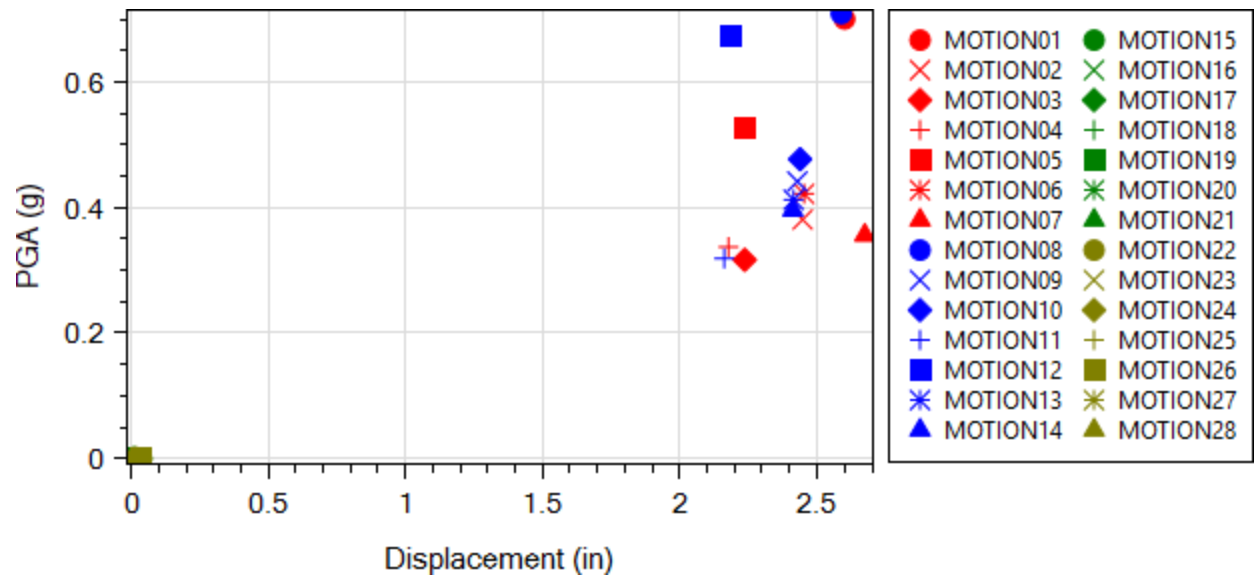


Figure 2.36. Bridge deck maximum longitudinal displacement

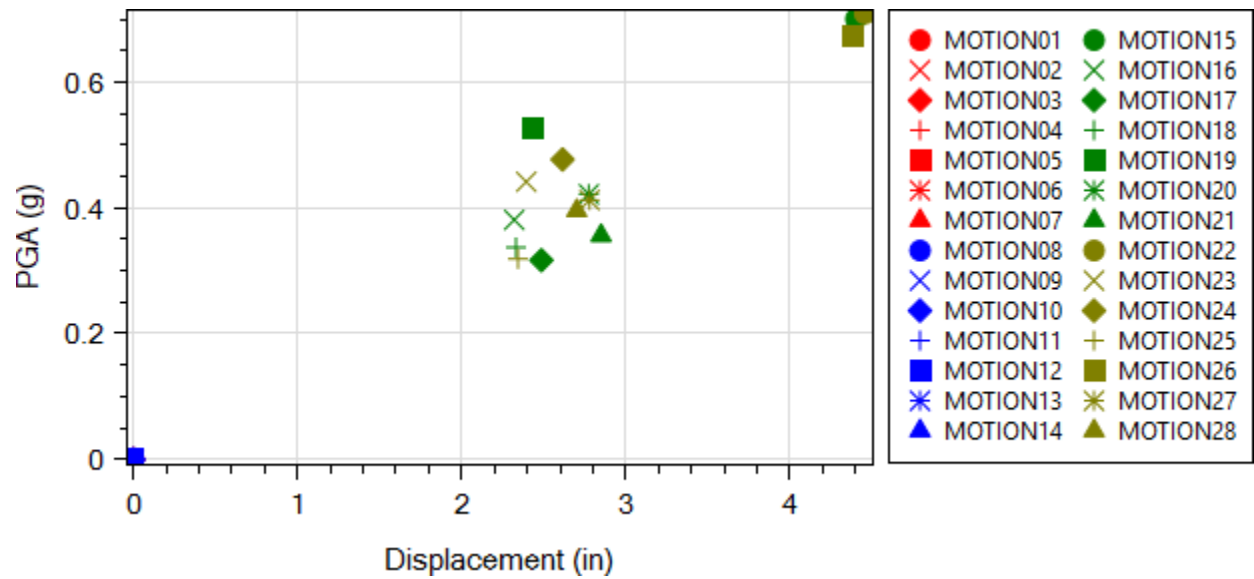


Figure 2.37. Bridge deck maximum transverse displacement

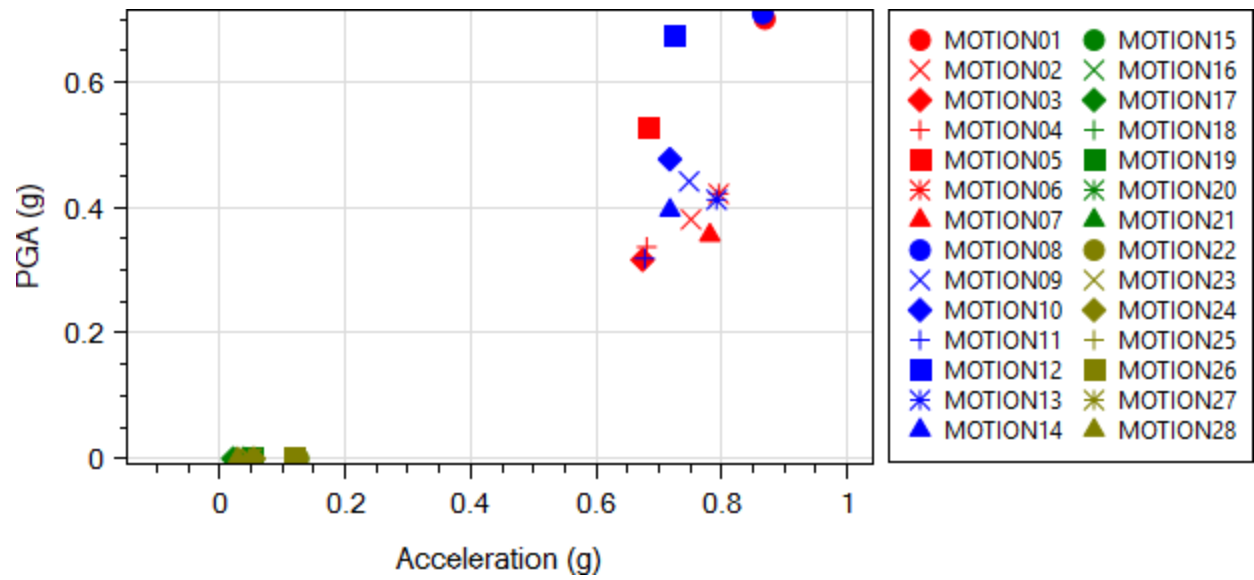


Figure 2.38. Bridge deck maximum longitudinal acceleration

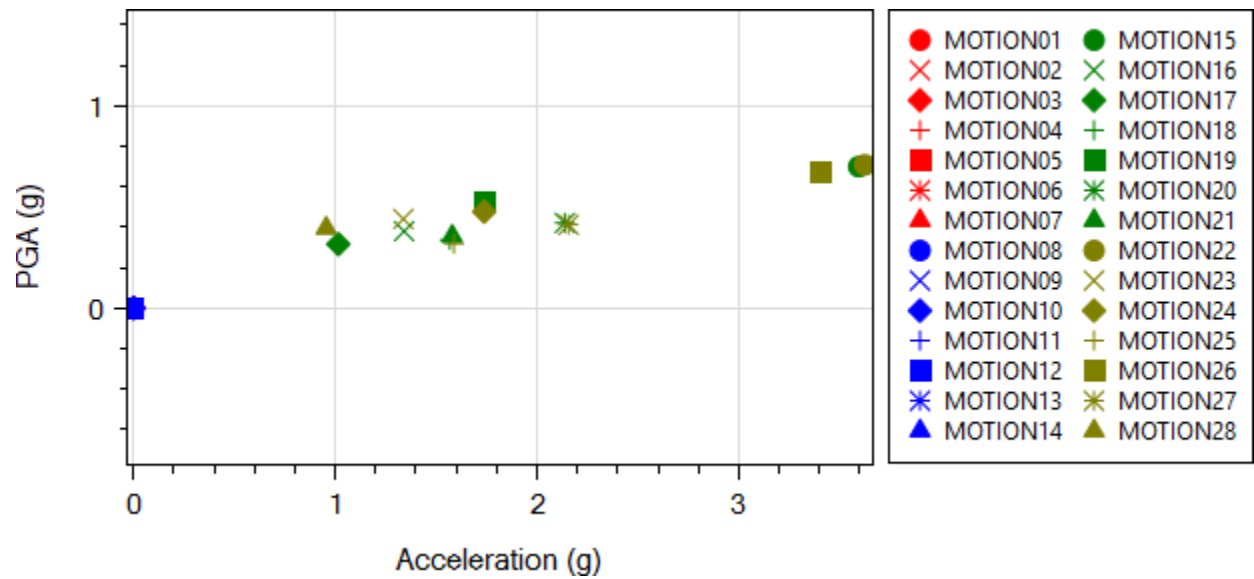


Figure 2.39. Bridge deck maximum transverse acceleration

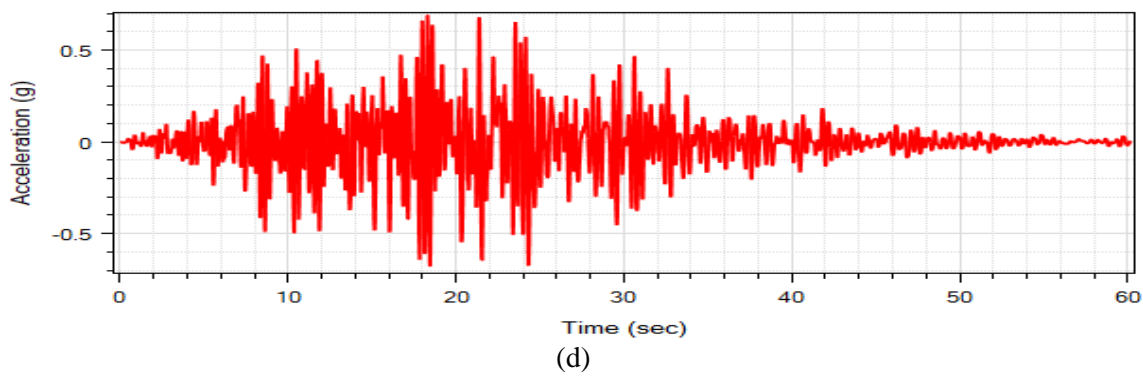
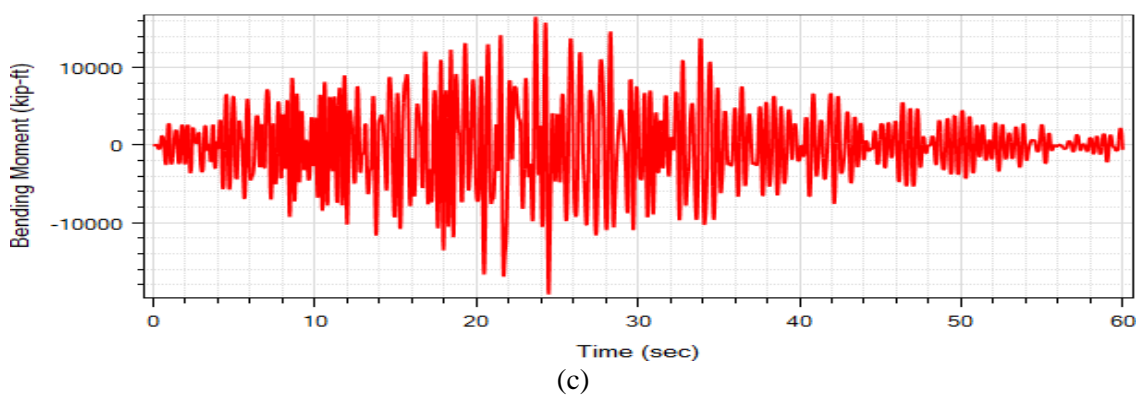
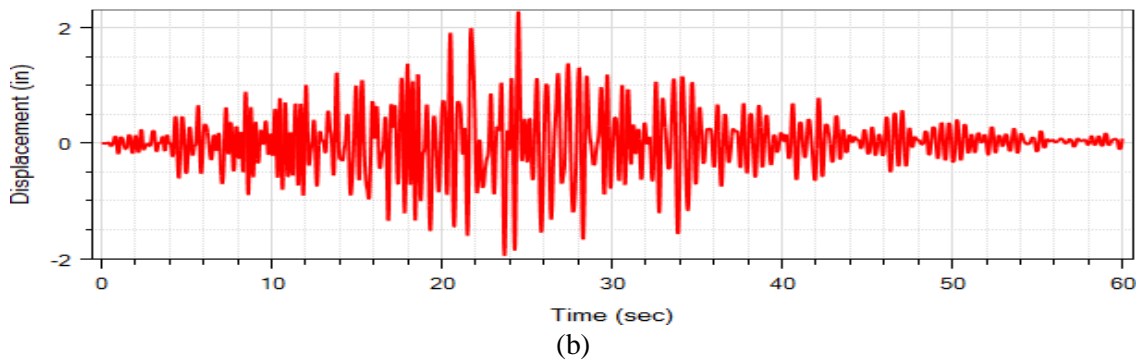
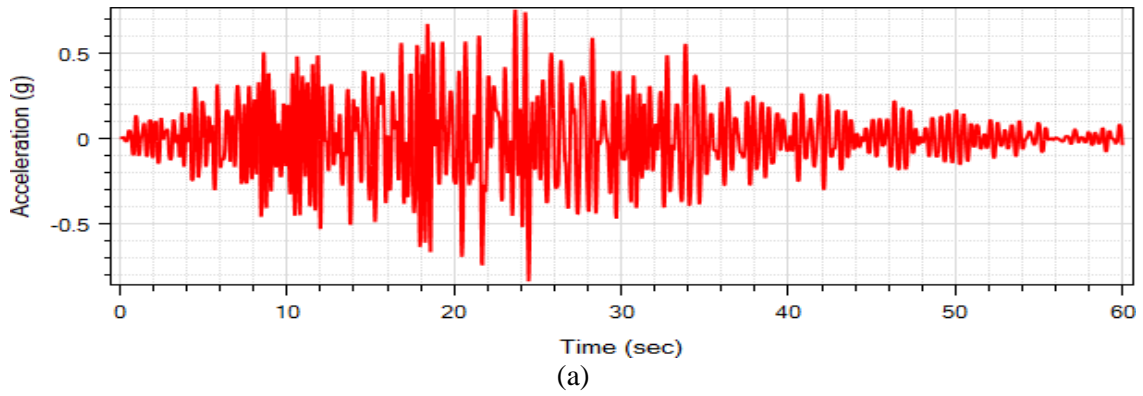


Figure 2.40. Pier S-8 column top longitudinal response time histories for Simulation 1 (ROCKS1N1): (a) acceleration; (b) displacement; (c) bending moment; and (d) base excitation

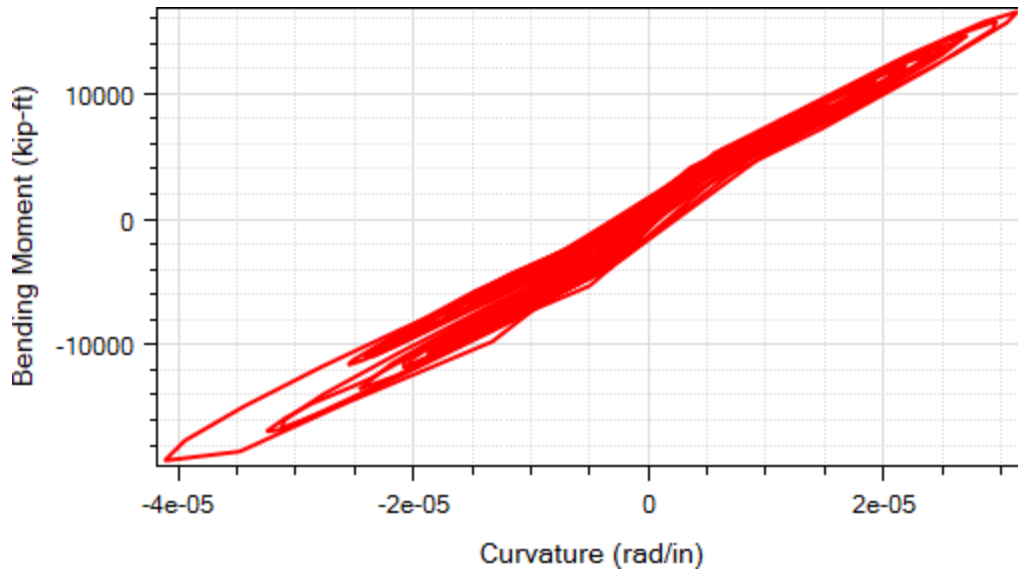


Figure 2.41. Pier S-8 column top longitudinal moment-curvature response for Simulation 1

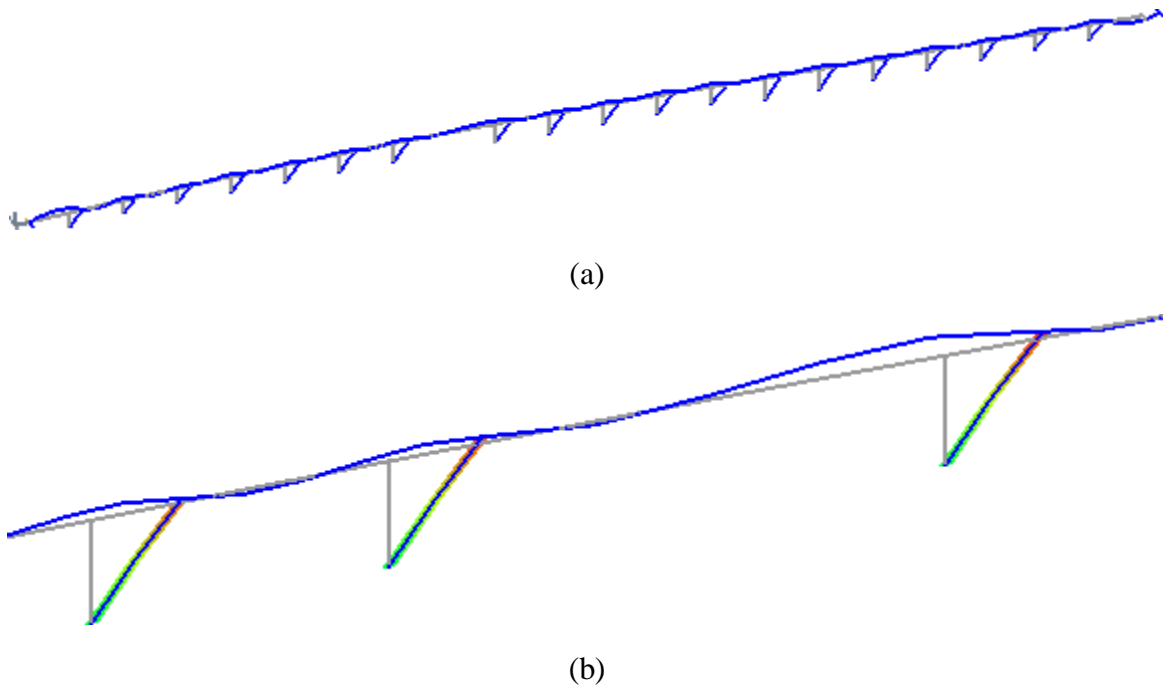
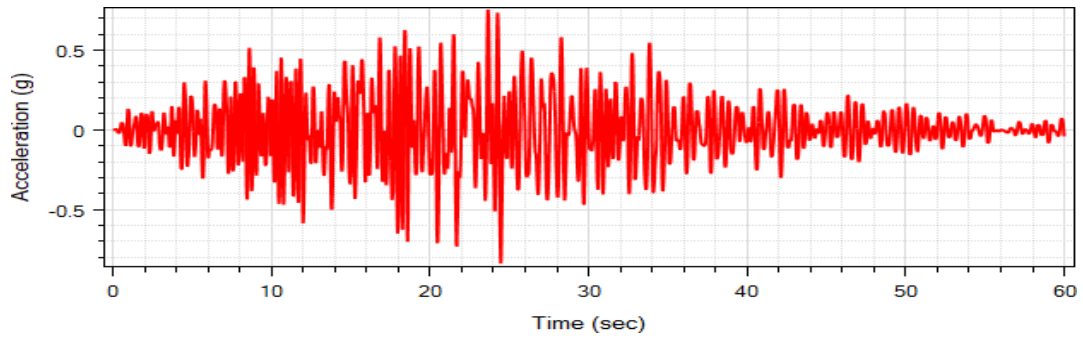
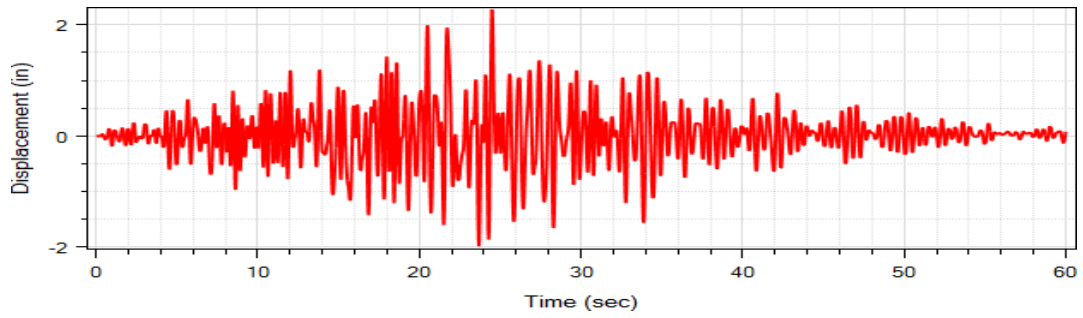


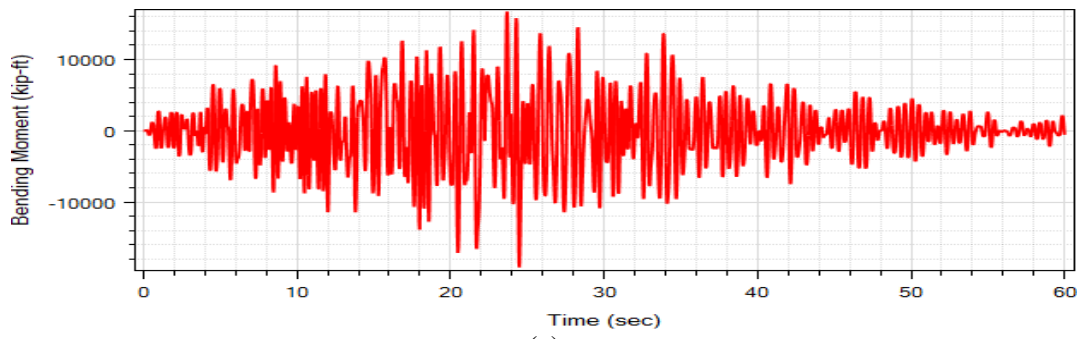
Figure 2.42. Deformed mesh (factor of 200) for Simulation 1 at the maximum displacement step (grey lines represent undeformed mesh): (a) entire bridge; (b) close-up of Bents 6, 7, and 8 (from left to right)



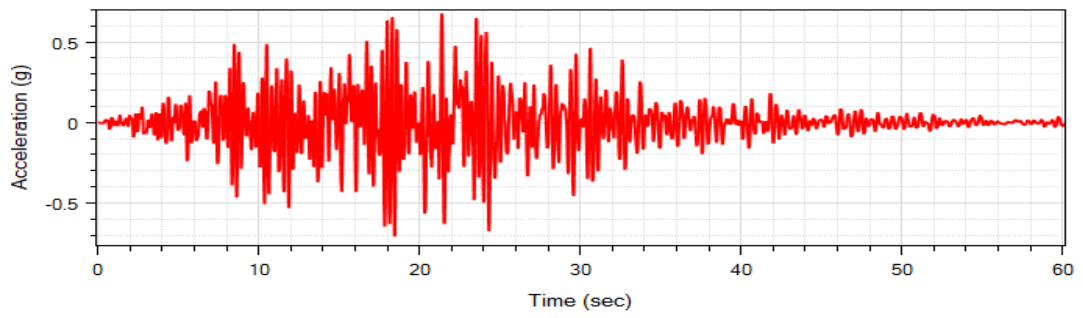
(a)



(b)



(c)



(d)

Figure 2.43. Pier S-8 column top longitudinal response time histories for Simulation 8 (ROCKS1P1): (a) acceleration; (b) displacement; (c) bending moment; and (d) base excitation

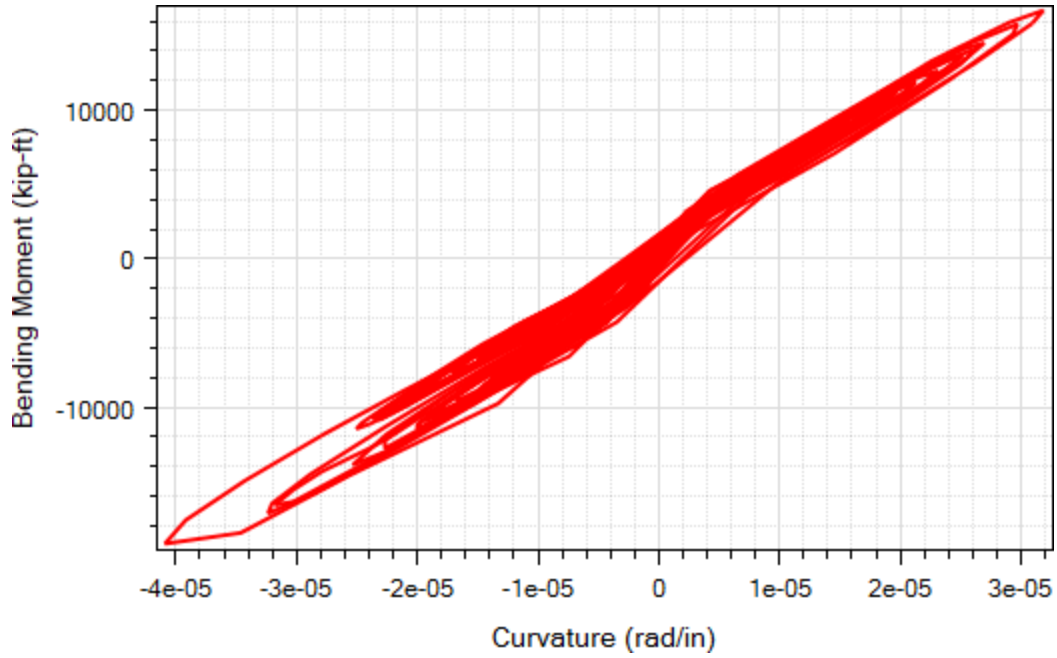


Figure 2.44. Pier S-8 column top longitudinal moment-curvature response for Simulation 8

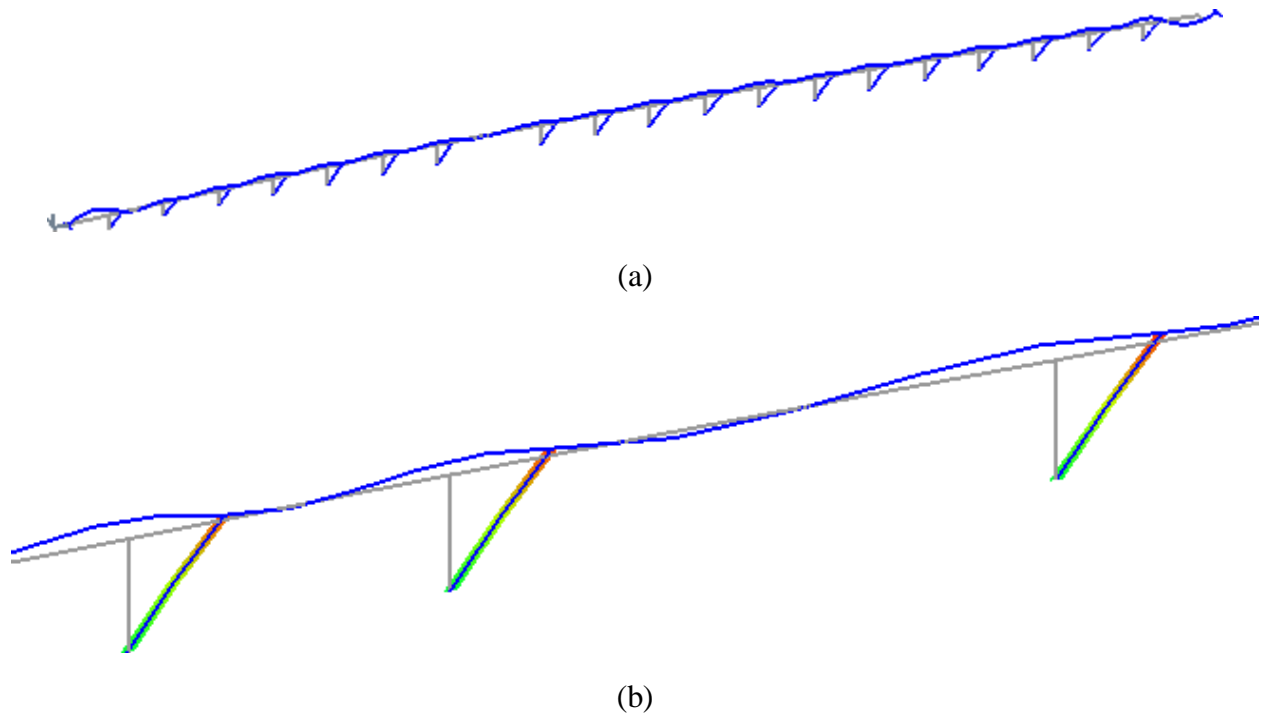


Figure 2.45. Deformed mesh (factor of 200) for Simulation 8 at the maximum displacement step (grey lines represent undeformed mesh): (a) entire bridge; (b) close-up of Bents 6, 7, and 8 (from left to right)



(a)



(b)

Figure 2.46. Bridge configuration: (a) Samoa Bridge, Eureka Geotechnical Array, Middle Channel Bridge and Eureka Bridge (Map Data @ 2015 Google) and (b) photo of the Eureka Bridge (<http://www.strongmotioncenter.org>)

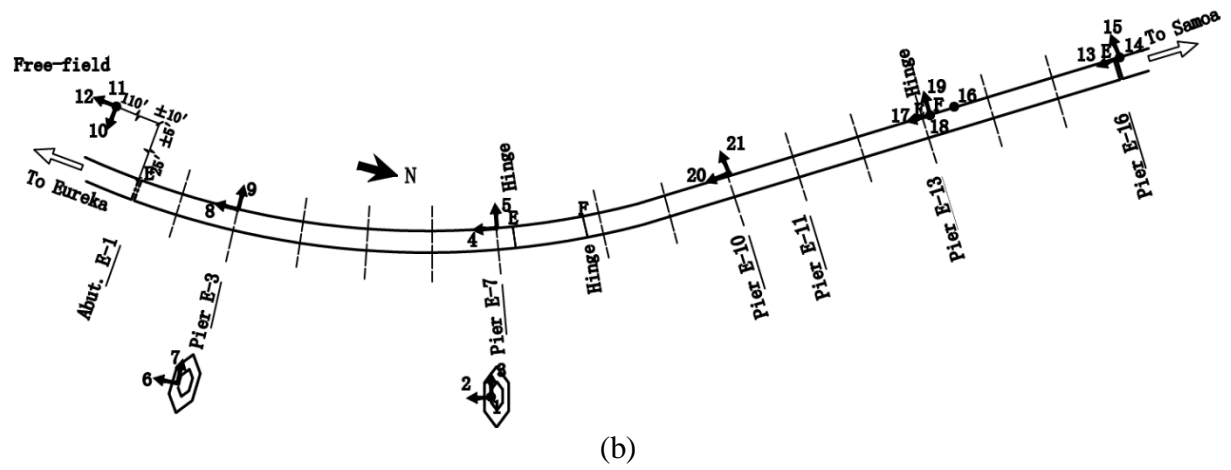
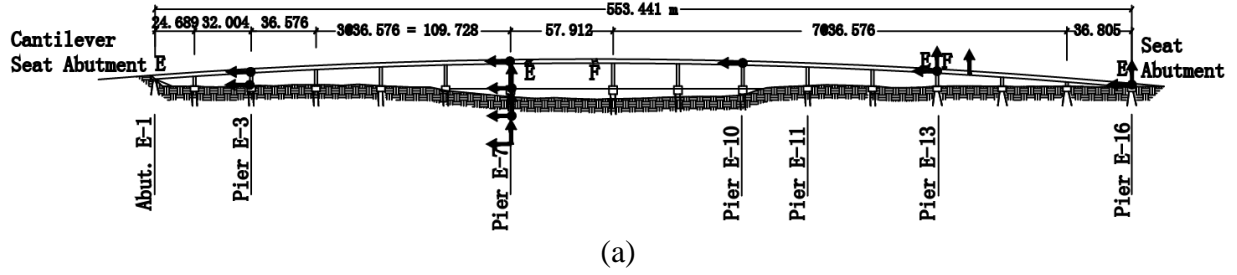


Figure 2.47. Layout of instrumentation at Eureka Bridge (<http://www.strongmotioncenter.org>):
 (a) elevation view; (b) plan view

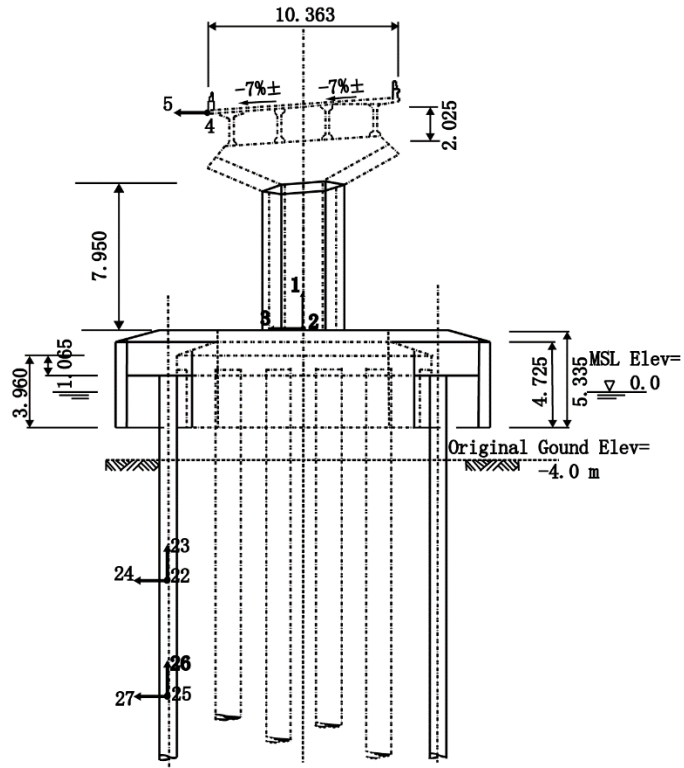


Figure 2.48. Elevation and bridge deck for Pier E-6

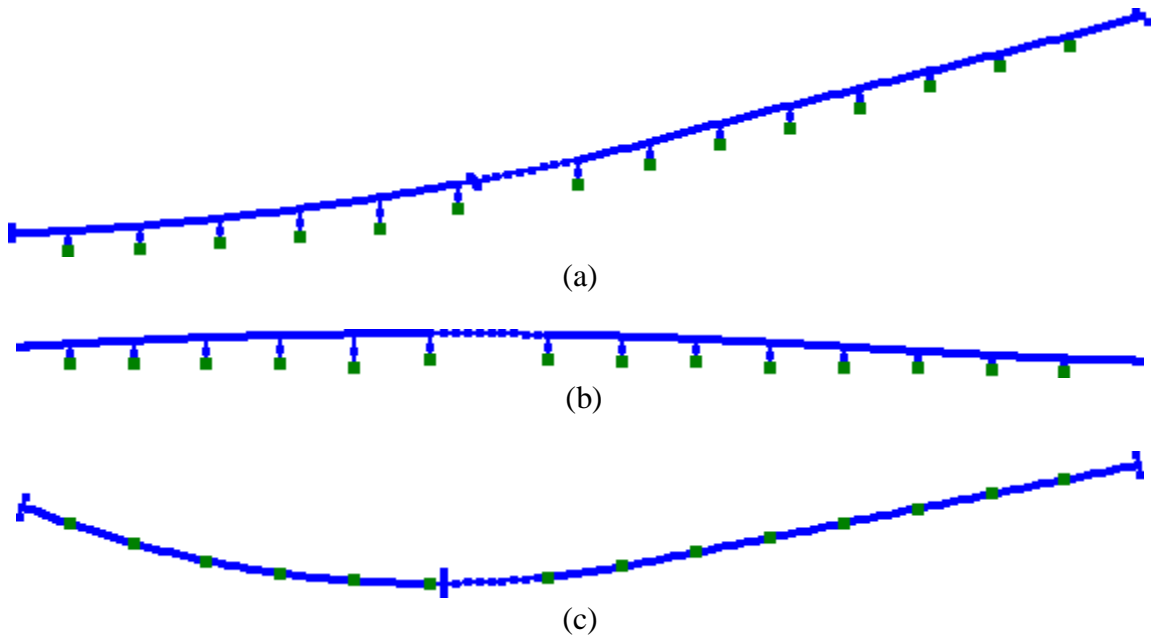
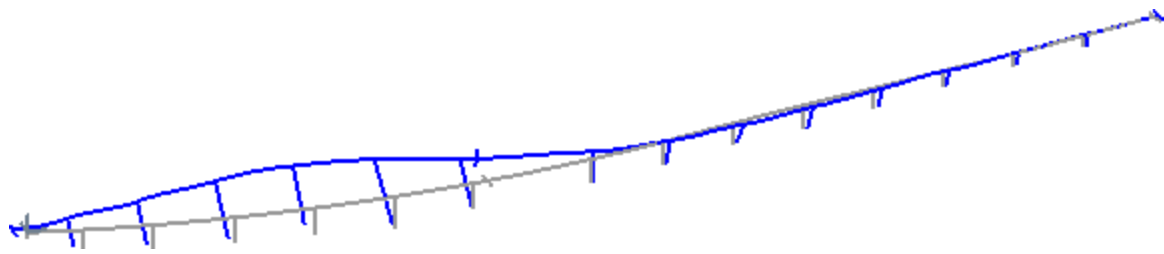
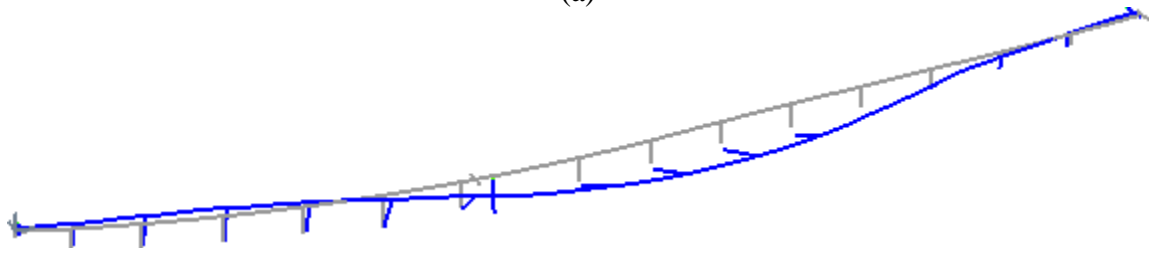


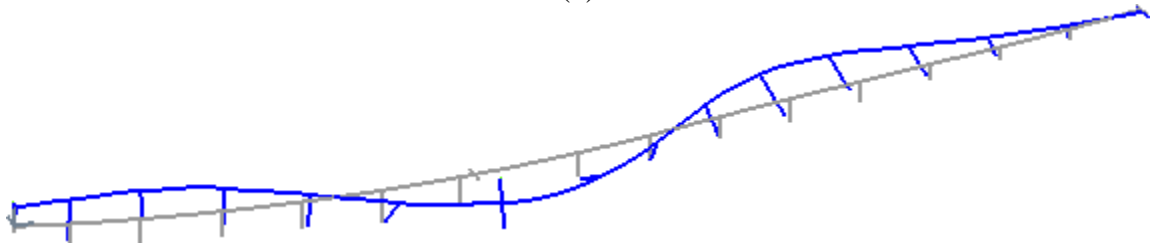
Figure 2.49. Eureka Bridge FE mesh created in MSBridge: (a) 3D view; (b) elevation view; (c) plan view



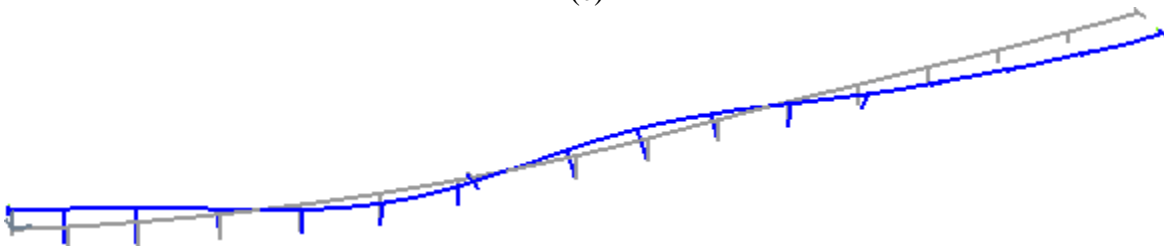
(a)



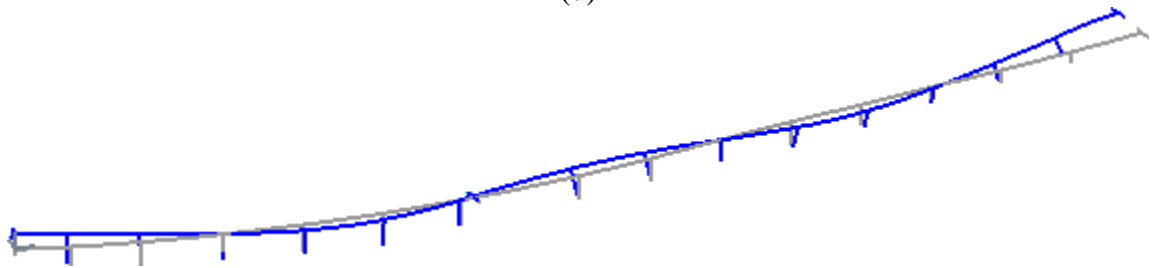
(b)



(c)



(d)



(e)

Figure 2.50. Mode shapes for Eureka Bridge: (a) first mode; (b) second mode; (c) third mode; (d) fourth mode; and (e) fifth mode

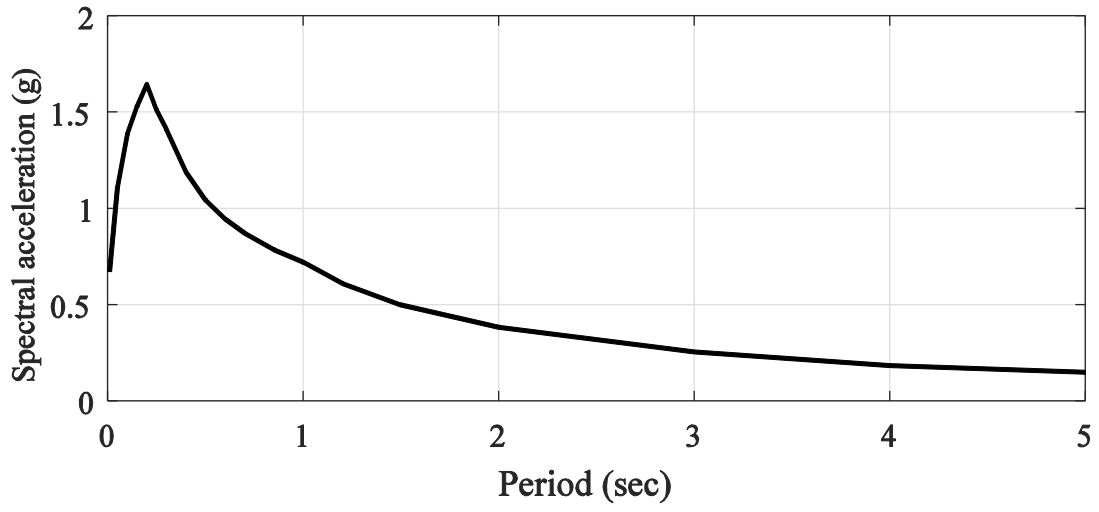


Figure 2.51. ARS curve employed in the ESA

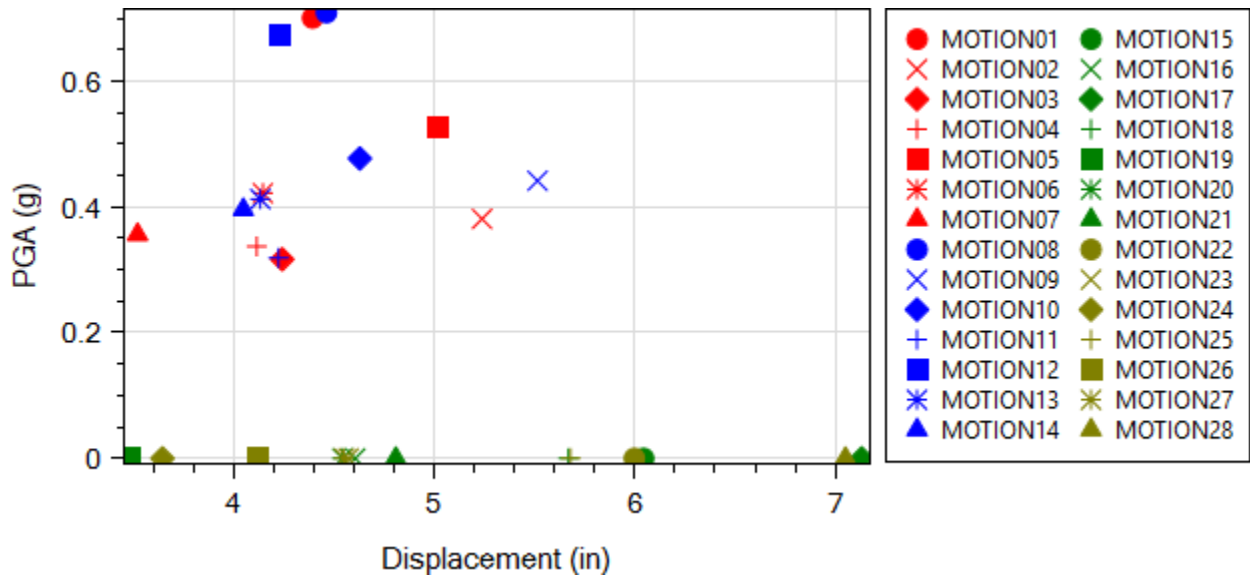


Figure 2.52. Bridge deck maximum longitudinal displacement

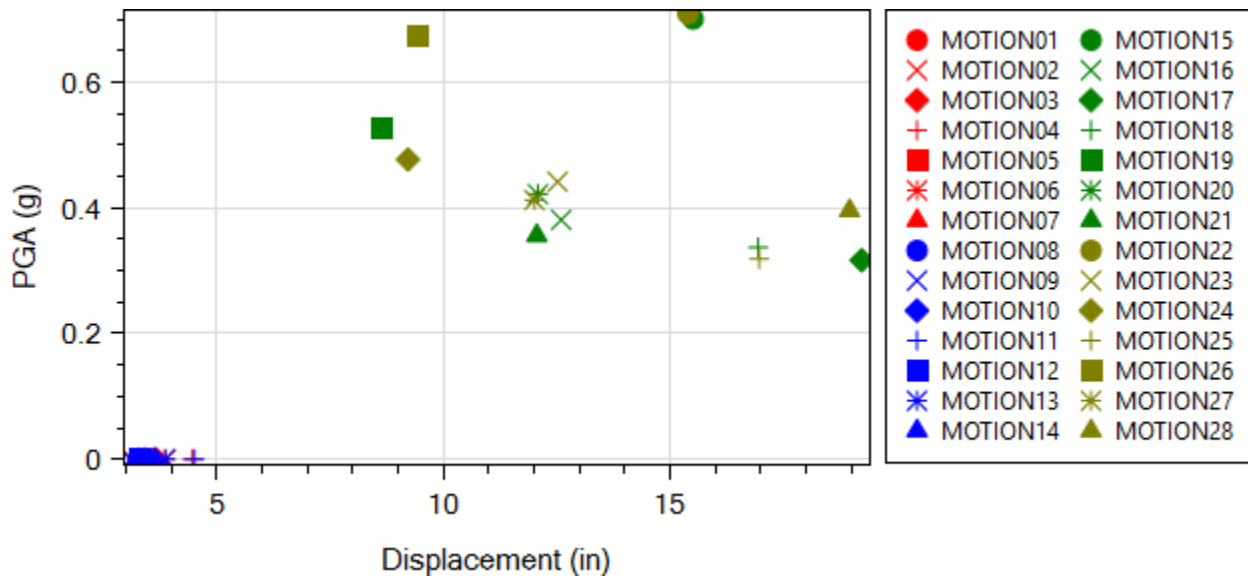


Figure 2.53. Bridge deck maximum transverse displacement

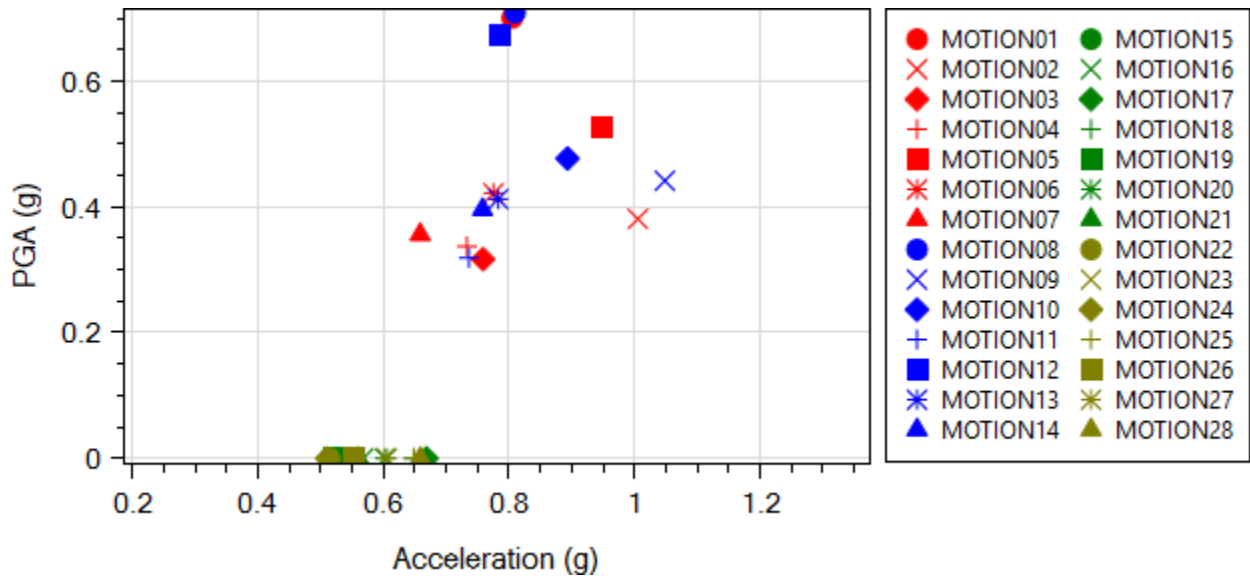


Figure 2.54. Bridge deck maximum longitudinal acceleration

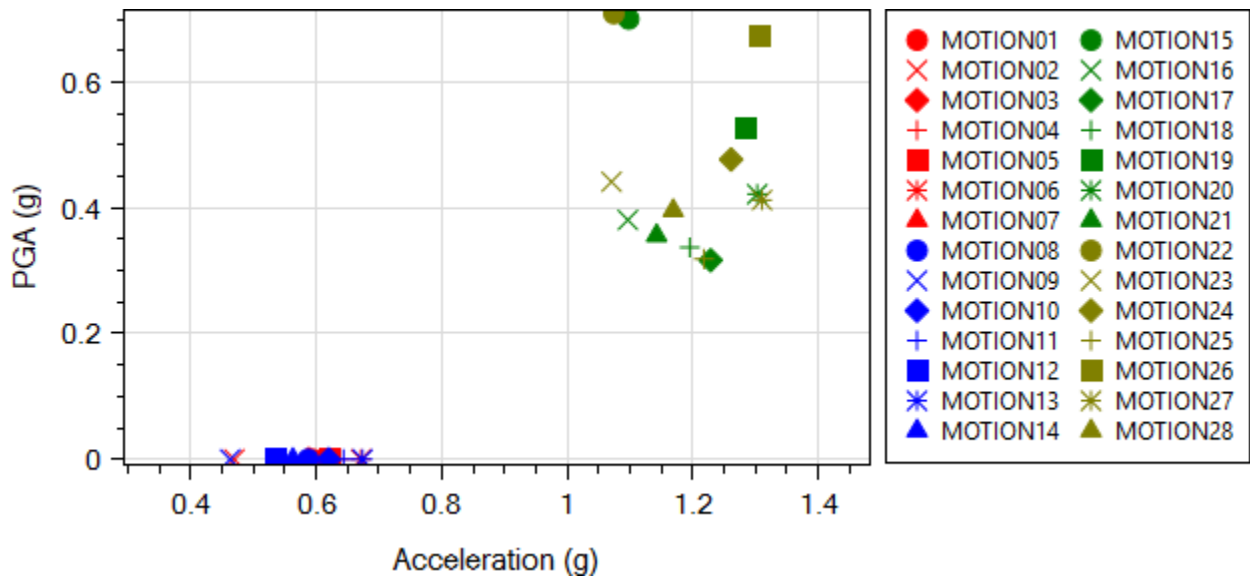


Figure 2.55. Bridge deck maximum transverse acceleration

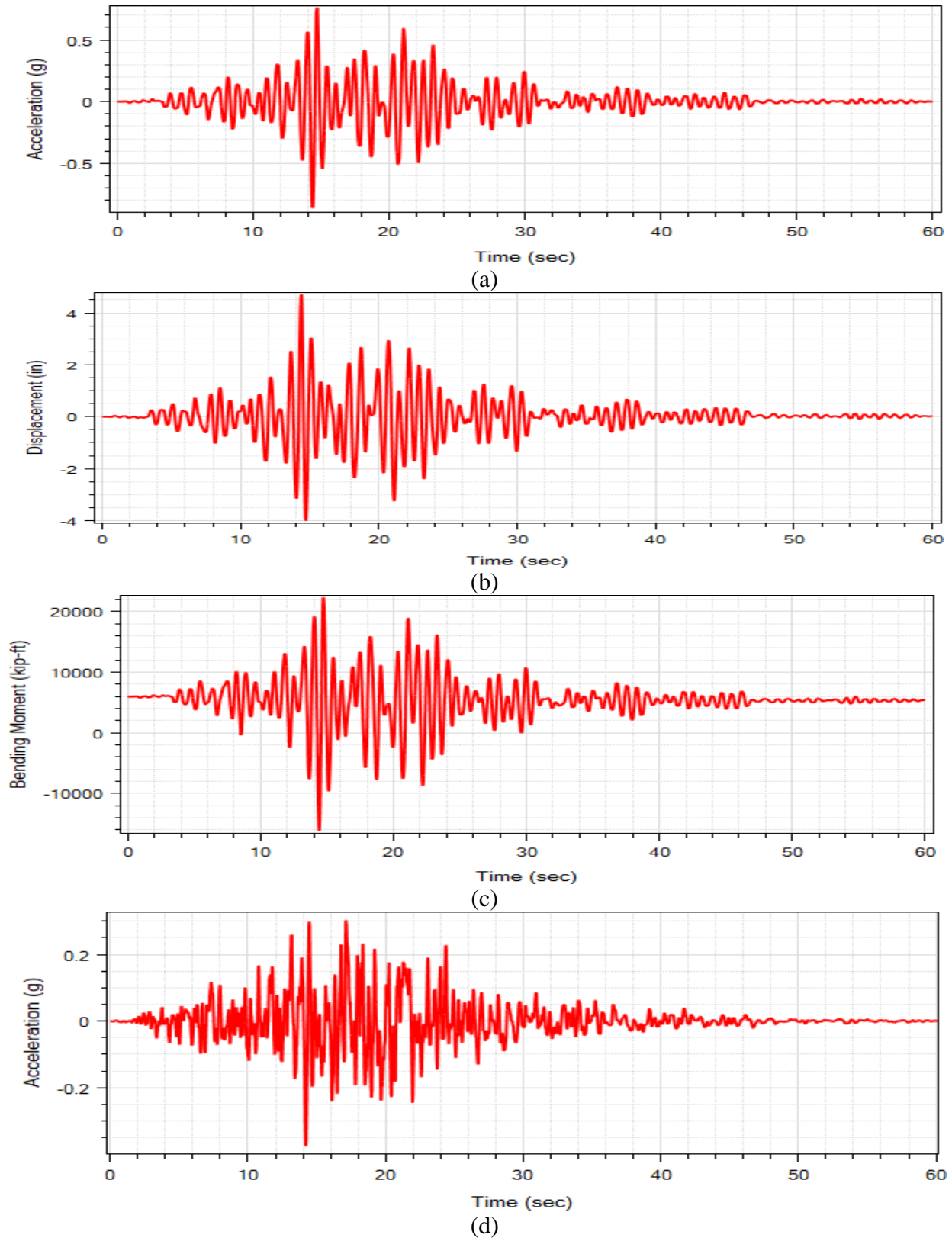
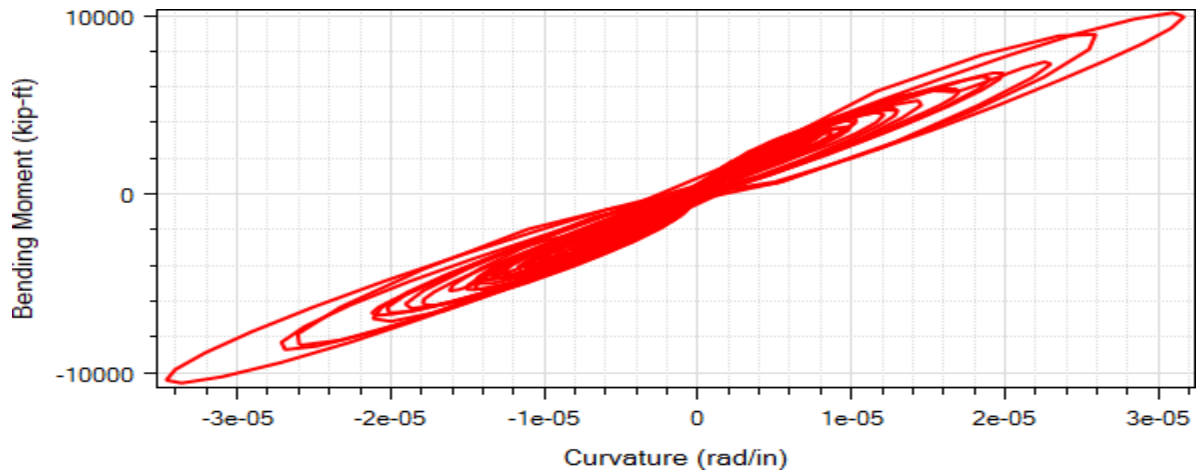
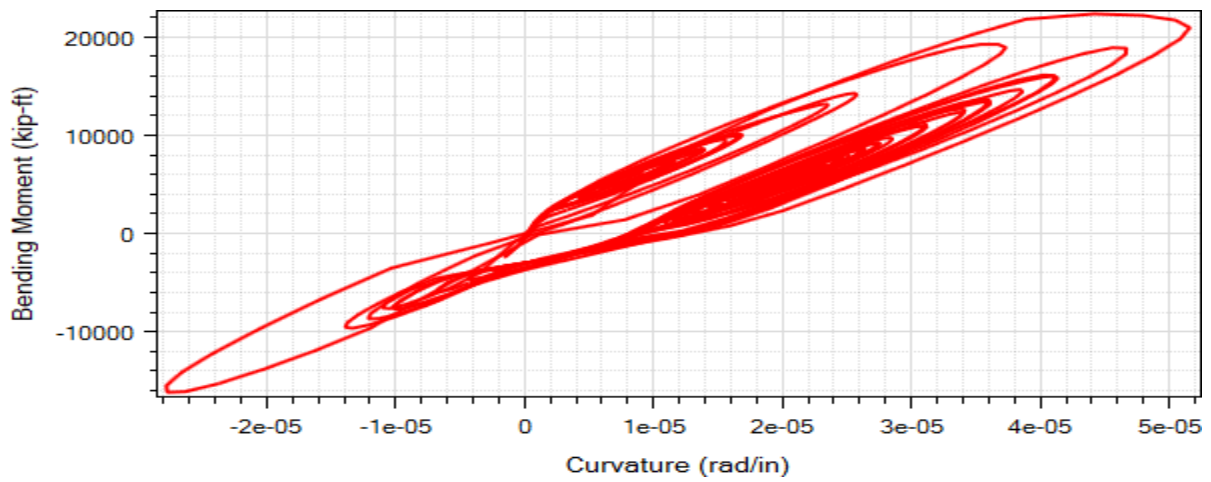


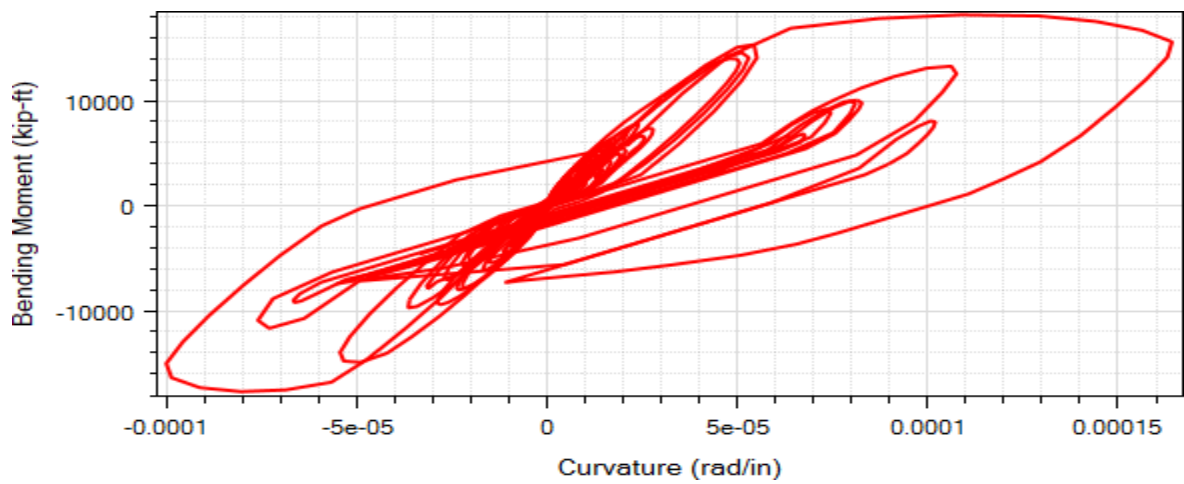
Figure 2.56. Pier E-7 Column top longitudinal response time histories for Simulation 2: a) acceleration; b) displacement; c) bending moment; d) base excitation ROCKS1N2



(a)



(b)



(c)

Figure 2.57. Column top longitudinal moment-curvature response for Simulation 2 (motion ROCKS1N2): (a) Pier E-6; (b) Pier E-7; (c) Pier E-13

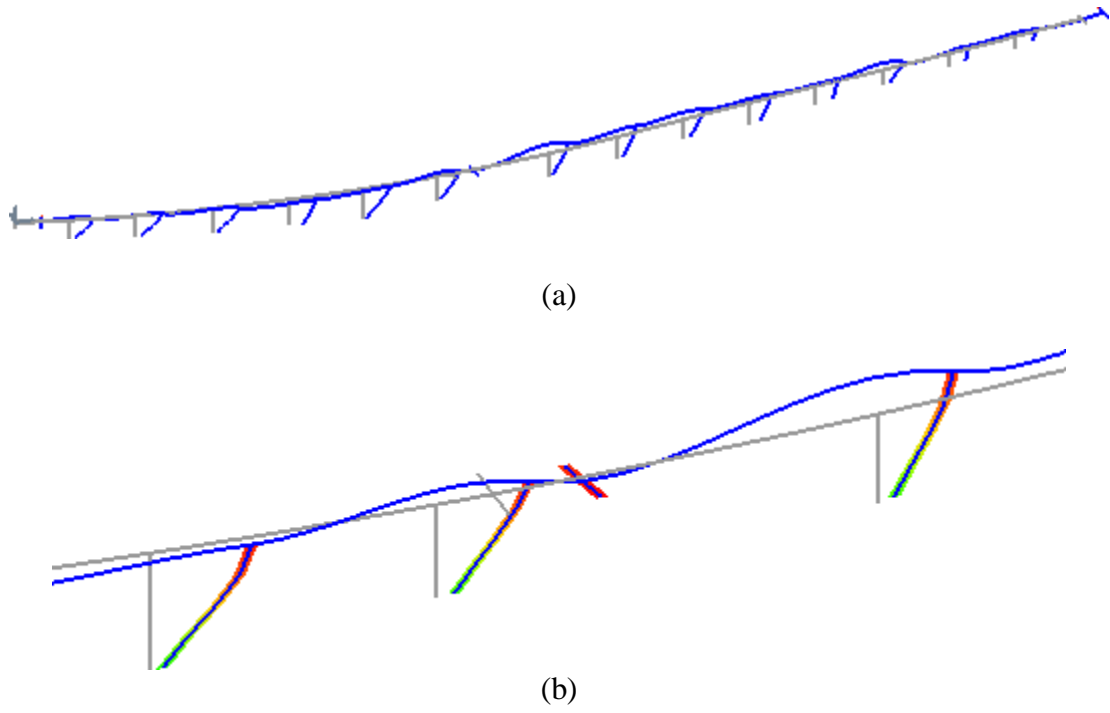
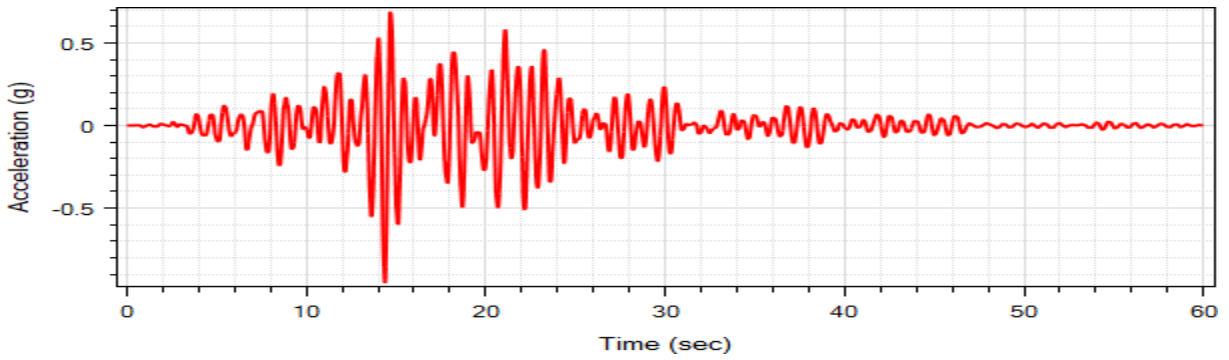
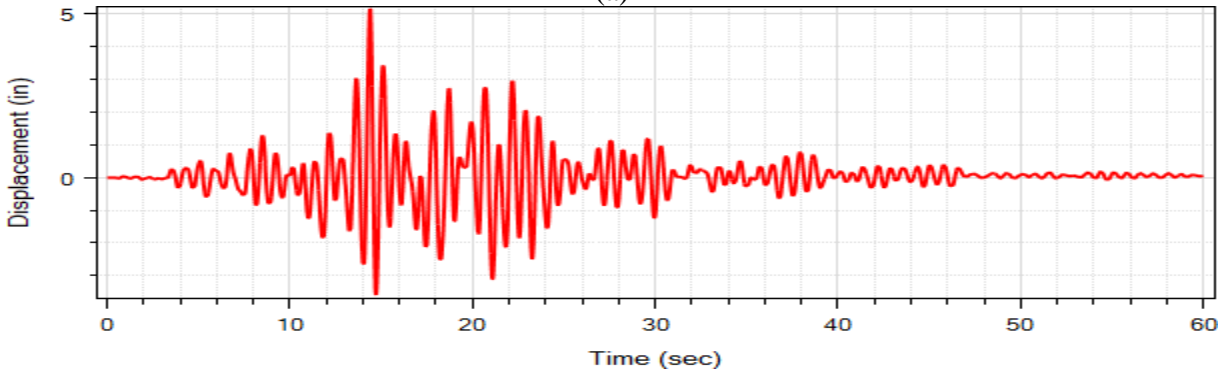


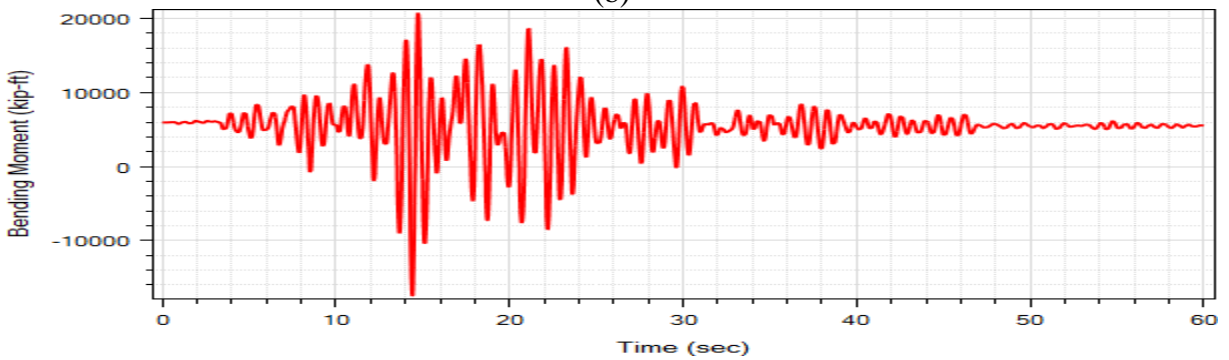
Figure 2.58. Deformed mesh (factor of 100) for Simulation 1 (motion ROCKS1P2) at the maximum displacement step (grey lines represent undeformed mesh): (a) entire bridge; (b) close-up of Piers 6, 7, and 8 (from left to right)



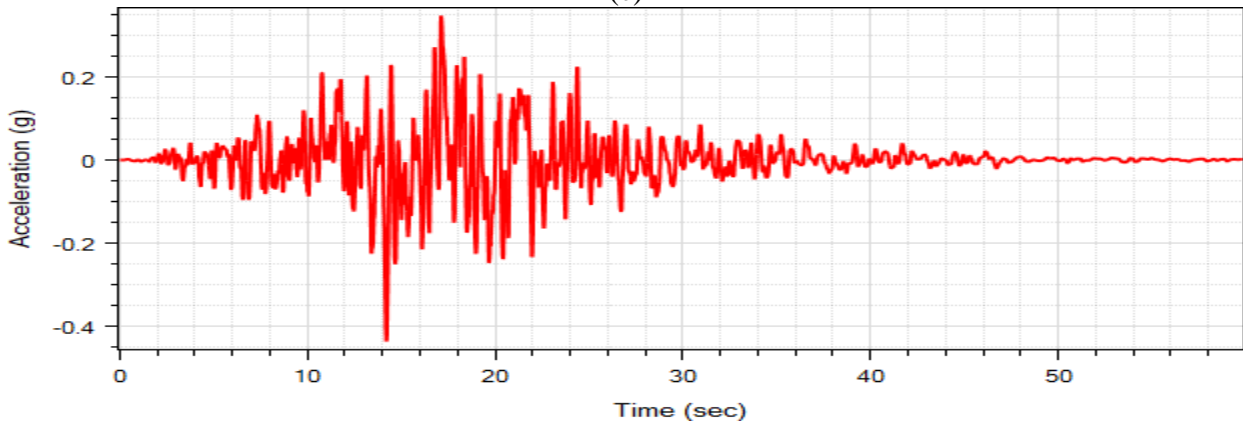
(a)



(b)

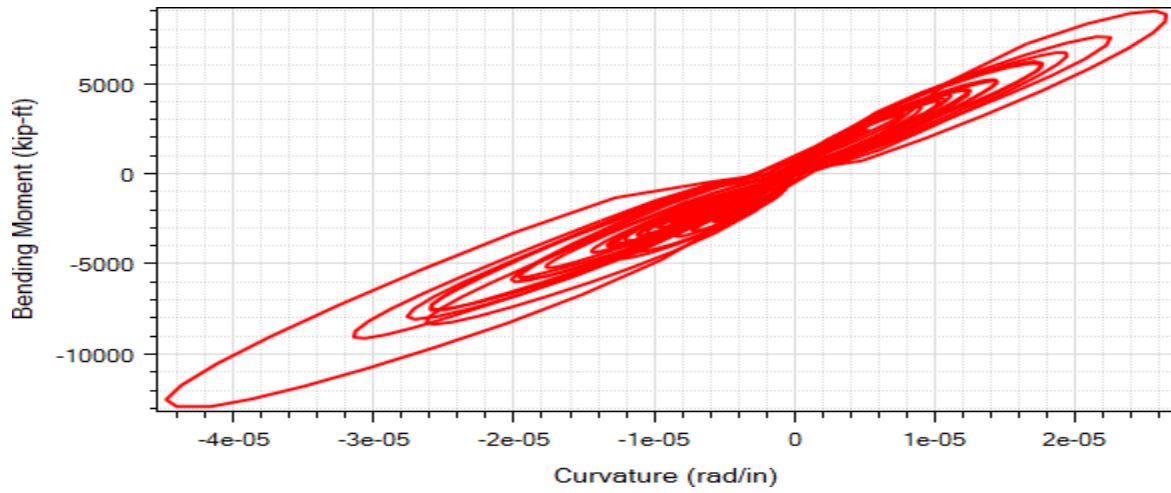


(c)

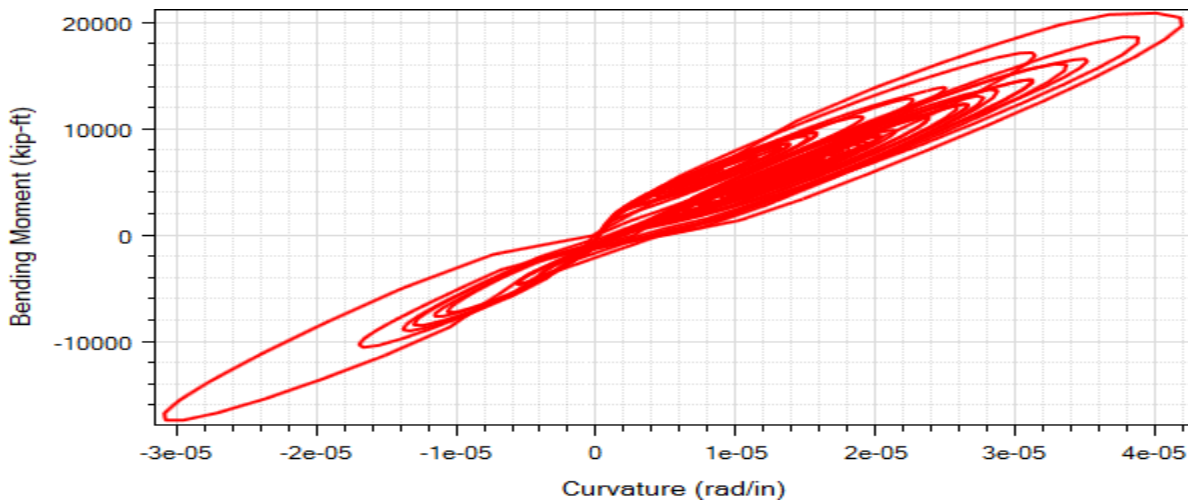


(d)

Figure 2.59. Pier E-7 column top longitudinal response time histories for Simulation 9: (a) acceleration; (b) displacement; (c) bending moment; (d) base excitation ROCKS1P2



(a)



(b)

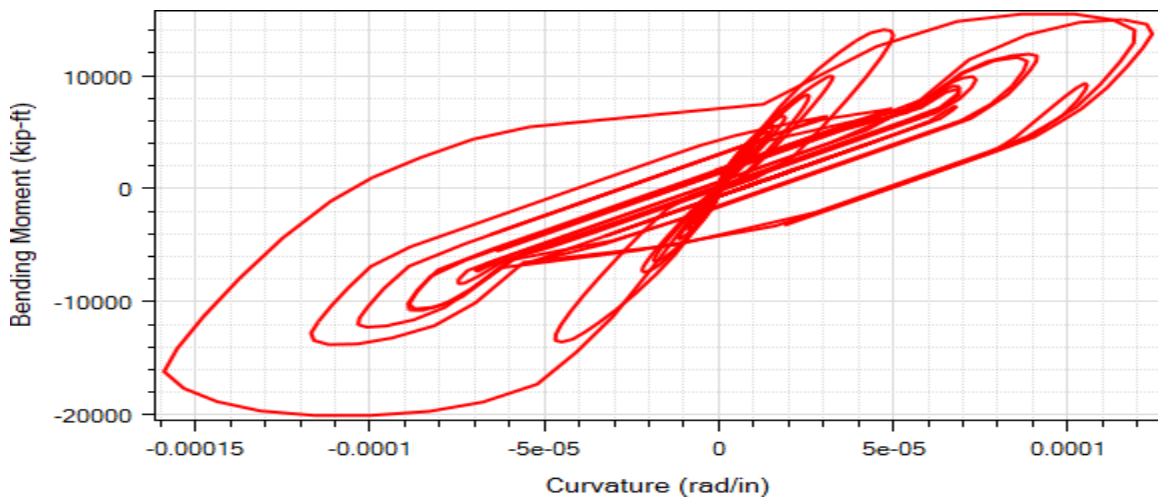


Figure 2.60. Column top longitudinal moment-curvature response for Simulation 9 (motion ROCKS1P2): (a) Pier E-6; (b) Pier E-7; (c) Pier E-13

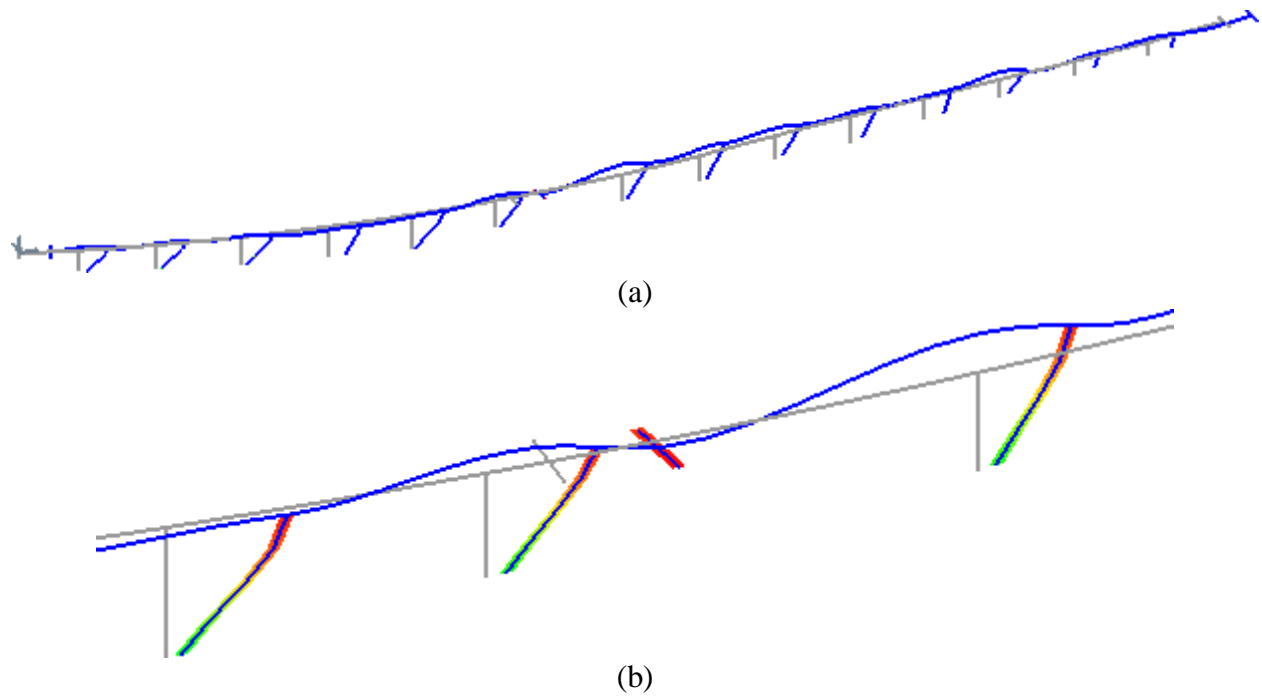


Figure 2.61. Deformed mesh (factor of 100) for Simulation 9 (motion ROCKS1P2) at the maximum displacement step (grey lines represent undeformed mesh): (a) entire bridge; (b) close-up of Piers 6, 7, and 8 (from left to right)

Chapter 3. Effect of Abutment Modeling on the Bridge Seismic Response

3.1. Abstract

The bridge seismic response can be significantly influenced by the behavior of the abutment, especially for Ordinary Standard Bridges (OSBs) with short spans and relatively stiff superstructures. This chapter investigates the sensitivity of a typical OSB bridge seismic response with respect to three abutment models. Abutment models considered in this study are: (i) the Roller Abutment model, (ii) the SDC (Seismic Design Criteria) 2010-Sand Abutment model, and (iii) the High-Speed Rail Hyperbolic Force-Displacement (HSR-HFD) Abutment model. Roller Abutment is included in this study to represent minimal abutment resistance. SDC 2010-Sand Abutment Model represents the response by a bi-linear relationship. Hyperbolic Force-Displacement (HFD) Abutment is a relationship that is employed to represent abutment resistance to bridge displacement using a hyperbolic curve. OpenSees was utilized to create the Finite Element (FE) model and perform the analyses for a typical Reinforced Concrete (RC) two-span bridge structure. Mode shape, pushover, and nonlinear dynamic time history analyses were conducted for the studied bridge using the three abutment models. Comparisons of the analysis results show differences in the pushover response mechanisms as well as the longitudinal relative deck-back wall displacement demand. As such, significance of abutment response is highlighted.

3.2. Introduction

Impact of abutment modeling has been studied by a number of researchers (Werner 1994; Zhang and Makris 2002; Aviram *et al.* 2008). As such, several abutment models were developed to consider major components of the abutment in order to realistically investigate the bridge seismic response. During past earthquakes, it has been noted that abutment behavior was among

the main factors that dominate the response of the bridge, especially for bridges with short spans and relatively stiff superstructure that were commonly constructed in California (Kotsoglu and Pantazopoulou 2006).

In the FE simulation environment, the abutment model approach should represent all major resistance mechanisms and components to realistically investigate the seismic response of the bridge system (Aviram *et al.* 2008). Among the major components are the gap, the bearing pads, abutment back wall, and soil backfill material behind the back wall.

Damage to the abutment has been noted to be among the major parameters that contribute to the overall expected loss (Mackie *et al.* 2008; Almutairi *et al.* 2017). Therefore, the effect of abutment modeling on the bridge seismic response and on the demand models was investigated in this study.

The main objective of this chapter is to investigate the seismic response of a bridge model using three different abutment models, denoted as Roller Abutment, SDC 2010-Sand Abutment, and HSR-HFD Abutment. As such, the three abutment models were implemented in MSBridge. Focus was placed on the longitudinal response.

3.3. Bridge-Foundation model

The structure is a single column bent, box girder, reinforced concrete bridge. This class of structures is classified as OSB that is typical in California. OSBs are those with lengths of less than 300 ft, standard abutment and bent cap details, and standard foundations on soil that do not require extensive site work (Caltrans 2006). The bridge dimensions considered in this chapter are 150 ft spans, 22 ft clear column heights, 4 ft circular column diameter, 39 ft wide two-cell box girder. The properties were derived from the Type 1 class of bridge designs presented in Ketchum

et al. (2004). The complete bridge mesh with the bridge supported on rigid base for simplicity is shown in Figure 3.1.

3.4. Abutment Models

Three abutment models were used to evaluate the dynamic characteristics and response of bridge model, Roller abutment; Seismic Design Criteria (SDC) 2010-Sand Abutment and High-Speed Rail Hyperbolic Force-Displacement (HSR-HFD). Roller abutment model represents the lower-bound resistance of the bridge in the longitudinal direction. The other two abutment models account for the soil-structure interaction and embankment flexibility.

3.4.1. Roller Abutment

The Roller Abutment Model (Figure 3.2) consists of rollers in the transverse and longitudinal directions, and a simple boundary condition module that applies single-point constraints against displacement in the vertical direction (i.e., bridge and abutment are rigidly connected in the vertical direction). These vertical restraints also provide a boundary that prevents rotation of the deck about its axis (torsion). This model can be used to provide a lower-bound estimate of the longitudinal resistance of the bridge that may be displayed through a pushover analysis.

3.4.2. SDC 2010-Sand Abutment

SDC 2010-Sand Abutment Model was developed based on the Spring Abutment Model by Mackie and Stojadinovic (2006). This model includes a sophisticated longitudinal, transverse, and vertical nonlinear abutment response. Table 3.1 shows the geometric and material properties of the bearing pads. In addition, Table 3.2 shows the modeling details of the employed abutment model.

In the longitudinal direction, the response is based on the elastomeric bearing pads to provide resistance prior to gap closure. After gap closure, the bridge resistance is provided the

back wall and the backfill pressure. A schematic of the longitudinal response of the SDC 2010-Sand abutment model is shown in Figure 3.3. In addition, the abutment stiffness (K_{abut}) and back wall strength (P_{bw}) were obtained for the longitudinal direction from Section 7.8 of SDC 2010 (Caltrans 2010, Figure 3.4). Figure 3.5 shows SDC 2010-Sand abutment model longitudinal response.

3.4.3. HSR-HFD Abutment

HSR-HFD (HSR stands for High-Speed Rail) relationship was employed to represent abutment resistance to bridge displacement in the longitudinal direction using a hyperbolic relationship. For HSR, a much stiffer and stronger material was used (Shamsabadi 2019) In this HFD model, resistance appears after a user-specified gap is closed, and the bridge thereafter gradually mobilizes the abutment's passive earth pressure strength. The force-displacement relationship of the HFD abutment along with the equations used to calculate the main parameters is shown in Figure 3.6. In addition, Figure 3.7 shows HSR-HFD abutment model longitudinal response.

3.5. Abutment Model Comparison

Mode shape, pushover, and nonlinear time history analyses were performed using the three abutment models. For that purpose, OpenSees was utilized to perform the analyses. To investigate the impact of each abutment model, the results are presented in a comparative scope for the three abutment models. A set of 100 ground motions were employed for the dynamic analysis and were selected to be representative of seismicity in typical regions in California. More details about the ground motion data set can be found in Chapter 4 (Mackie and Stojadinovic 2005).

3.5.1. Mode Shape Analysis

Table 3.3 summarizes the first five modes of the bridge model using the three abutment models. The comparison shows that the mode shapes were affected by the abutment model and as such resulted in different periods. In addition, Figure 3.8 shows representative mode shapes for the studied bridge model.

3.5.2. Pushover Analysis

The pushover response curves of the abutment response (longitudinal relative deck-end/abutment displacement) using two different abutment models are shown in Figure 3.9. Overall, HSR-HFD abutment model produces a pushover curve with the highest capacity (Shamsabadi 2019).

3.5.3. Nonlinear Time History Analysis

Nonlinear THA was performed for the employed ground motions. The demand models of the longitudinal maximum relative deck-back wall displacement for the three abutment models are shown in Figure 3.10. Based on the simulation results, Roller Abutment model resulted in higher displacement demand than the other two abutment models. Inclusion of the back wall pressure in the other two abutment models reduced the demand displacement, especially for the HSR-HFD abutment model that provides higher back wall pressure (Shamsabadi 2019).

3.6. Conclusions

The seismic response of an entire bridge system has been found to be significantly influenced by the abutment behavior, especially, in the case of short spans and relatively stiff superstructure under strong intensity dynamic excitation. In order to realistically capture the bridge dynamic behavior, an abutment model that includes the major components of the abutment system such as gap, bearing pads, back wall, and foundation should be used. Based on the simulation

results, the Roller abutment model represents the lower-bound resistance to the bridge. As such, it resulted in higher demand deck-back wall relative displacement. Conversely, using SDC 2010-Sand or HSR-HFD models that include all the major components can realistically capture the dynamic characteristics of the abutment. After gap closure, the HSR-HFD abutment model provided higher back wall pressure than the SDC 2010-Sand abutment model. Therefore, the simulation results showed less demand deck-back wall displacement for the HSR-HFD model compared to SDC 2010-Sand model.

Table 3.1. Geometric and material properties of a bearing pad (Lu *et al.* 2011)

Parameter	Value
Number of bearings	3
Bearing height (in)	2
Longitudinal gap (in)	0.5
Shear Modulus G (ksi)	0.15
Young's Modulus E (ksi)	5
Yield Displacement	150% shear strain
Lateral Stiffness	$\frac{GA}{h}$ (where A is the cross-section area and h is the height)

Table 3.2. SDC 2010-Sand abutment model properties

Parameter	Value
Soil mass density (pcf)	109.9
Skew angle (degree)	0
Soil shear wave velocity (ft/s)	492.1
Embankment slope	2
Longitudinal gap (in)	1

Table 3.3. Periods of the studied bridge for different abutment models

Roller Abutment		SDC 2010-Sand Abutment		HSR-HFD Abutment	
Period (s)	Mode	Period (s)	Mode	Period (s)	Mode
0.786	Transverse translation	0.644	Longitudinal translation	0.642	Longitudinal translation
0.705	Longitudinal translation	0.470	Transverse translation	0.468	Vertical superstructure deformation (S-shape)
0.473	Vertical superstructure deformation (S-shape)	0.469	Vertical superstructure deformation (S-shape)	0.409	Transverse translation
0.422	Global torsion	0.365	Vertical superstructure deformation (W-shape)	0.365	Vertical superstructure deformation (W-shape)
0.356	Vertical superstructure deformation (W-shape)	0.222	Global torsion	0.149	Global torsion

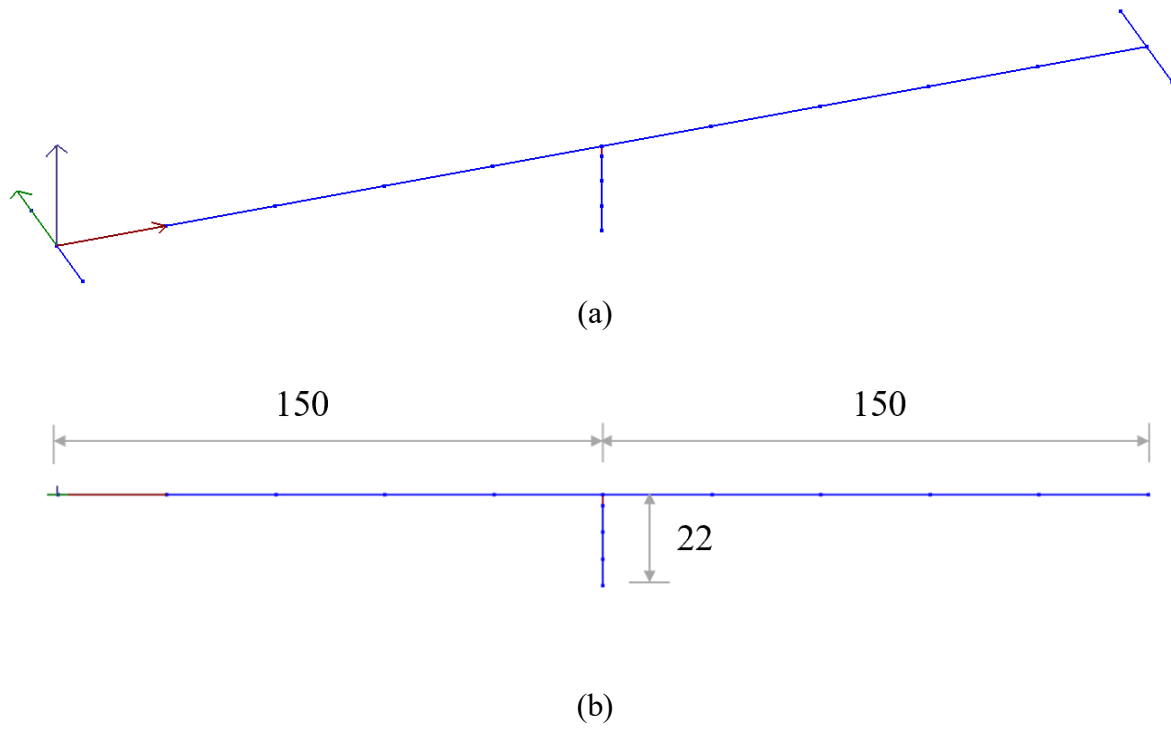


Figure 3.1. Finite element mesh: (a) 3D view, (b) elevation view (dimensions are in ft)

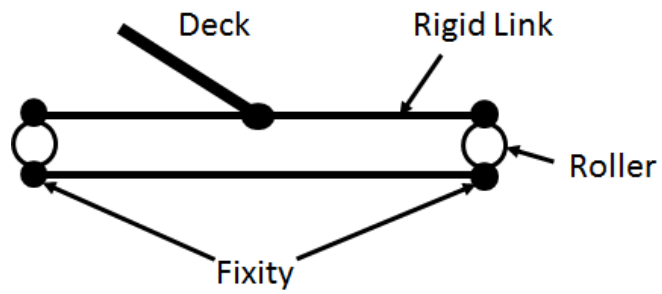


Figure 3.2. General scheme of the Roller Abutment Model

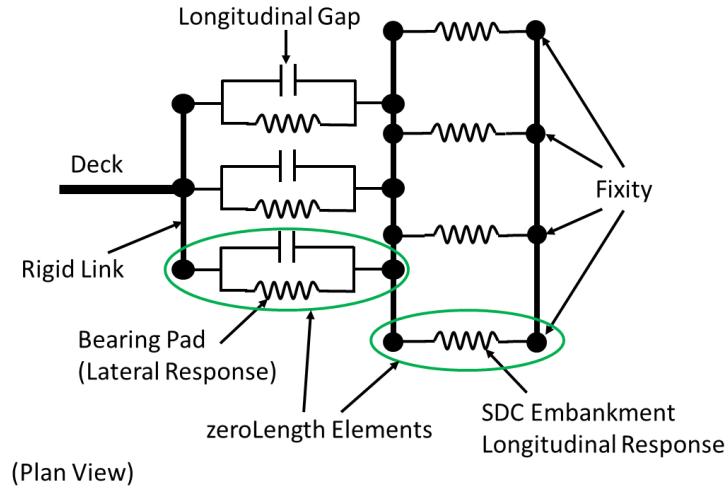


Figure 3.3. General scheme of the longitudinal response of the Abutment Model

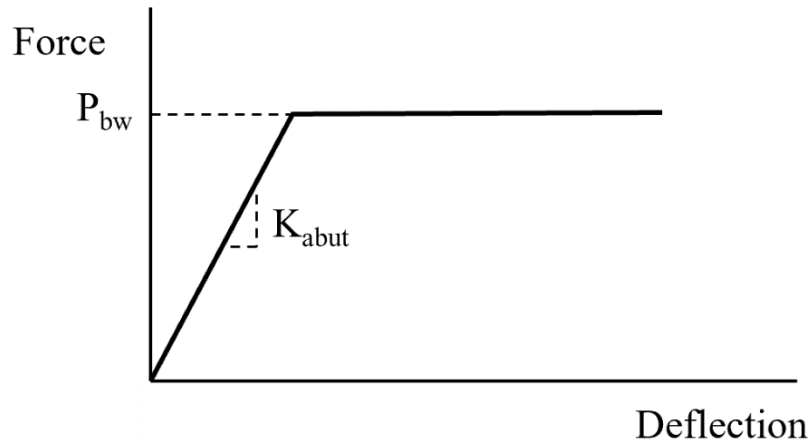


Figure 3.4. Definition of the SDC 2010-Sand Abutment Model (after Caltrans 2010)

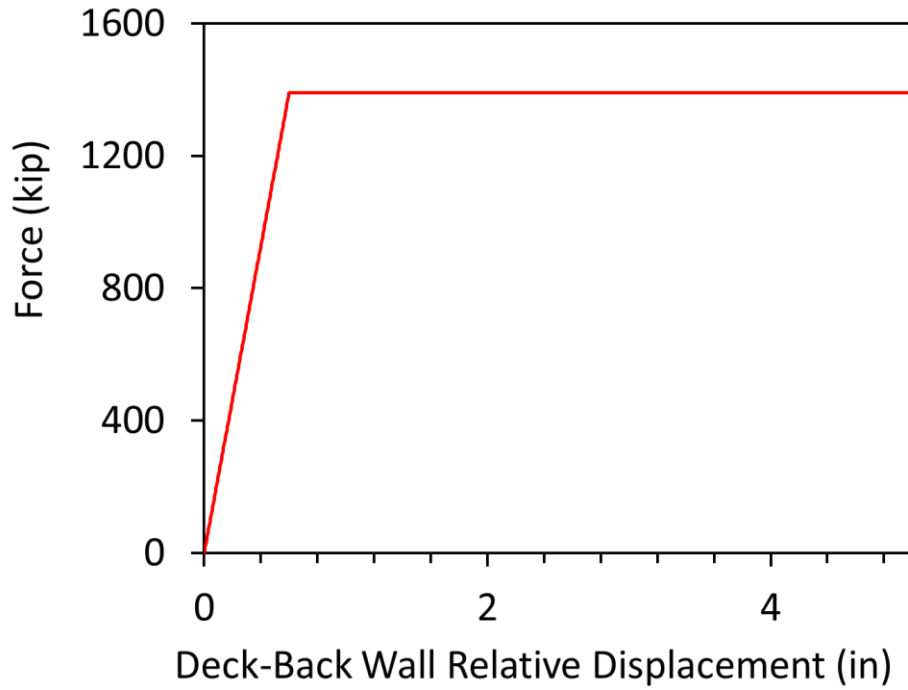


Figure 3.5. SDC 2010-Sand abutment longitudinal response

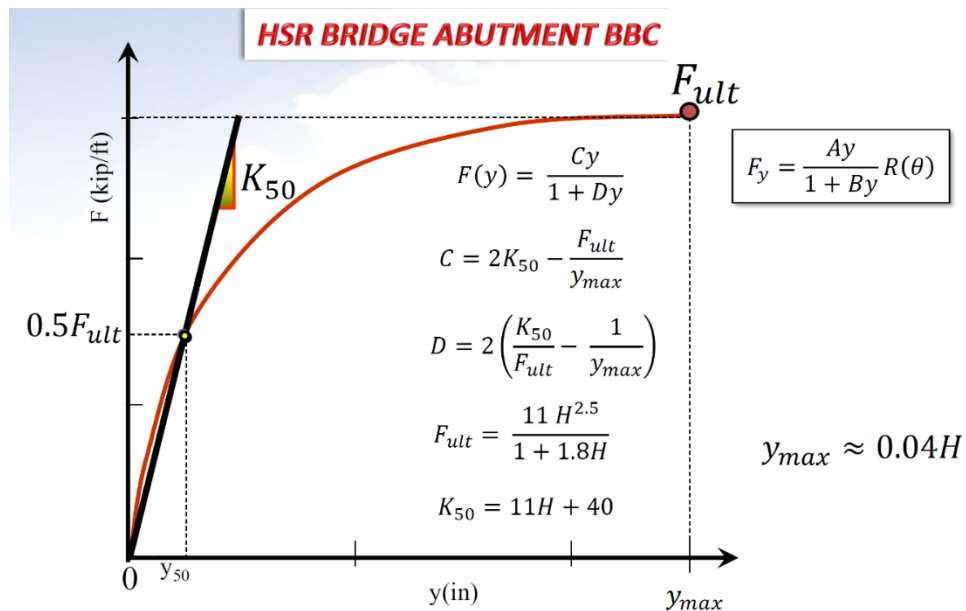


Figure 3.6. Definition of the HSR-HFD Abutment Model (Shamsabadi *et al.* 2007, 2010; Shamsabadi 2019)

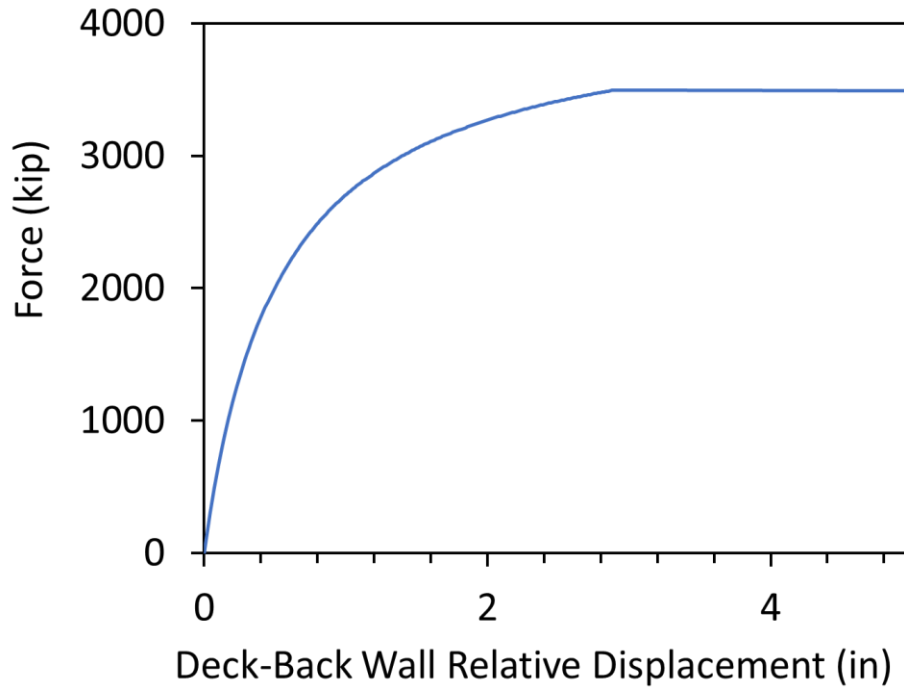
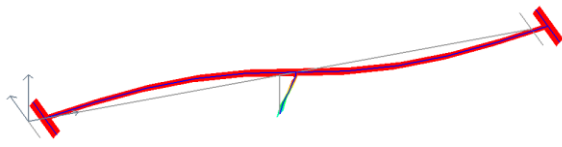
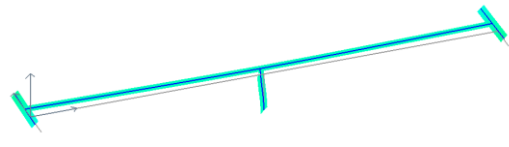


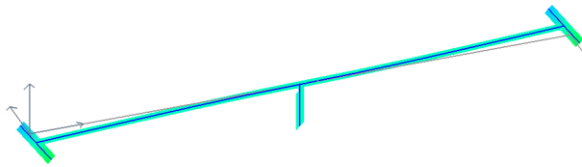
Figure 3.7. HSR-HFD abutment longitudinal response



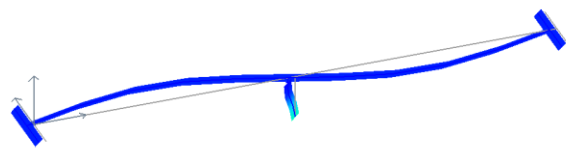
(a) Longitudinal translation



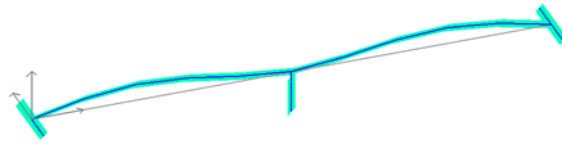
(b) Transverse translation



(c) Global torsion



(d) Vertical superstructure (S-shape)



(e) Vertical superstructure (W-shape)

Figure 3.8. First five mode shapes of the studied bridge model

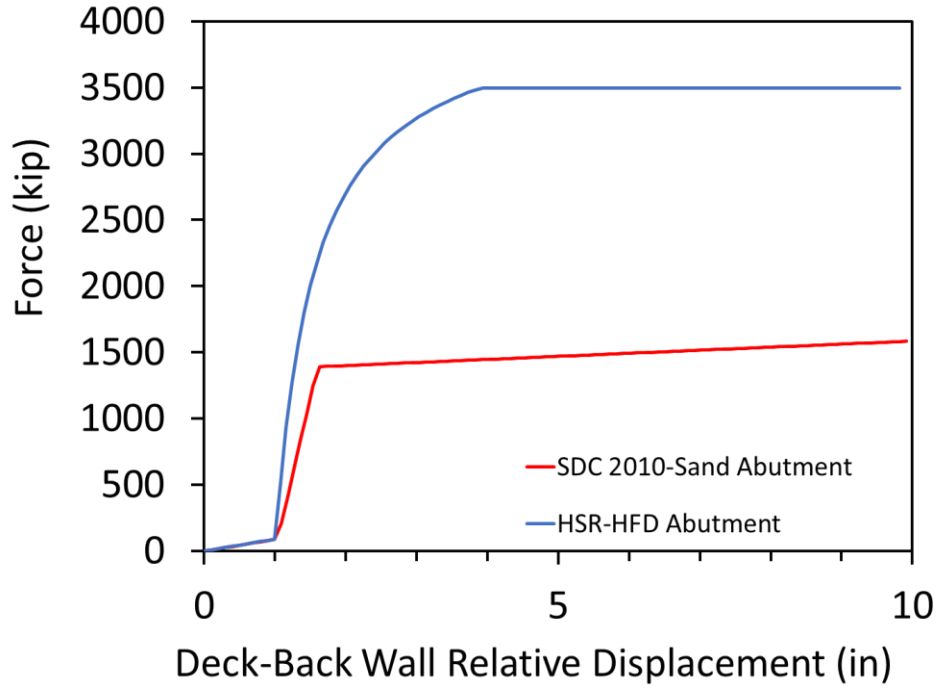


Figure 3.9. Longitudinal abutment response from the pushover analysis

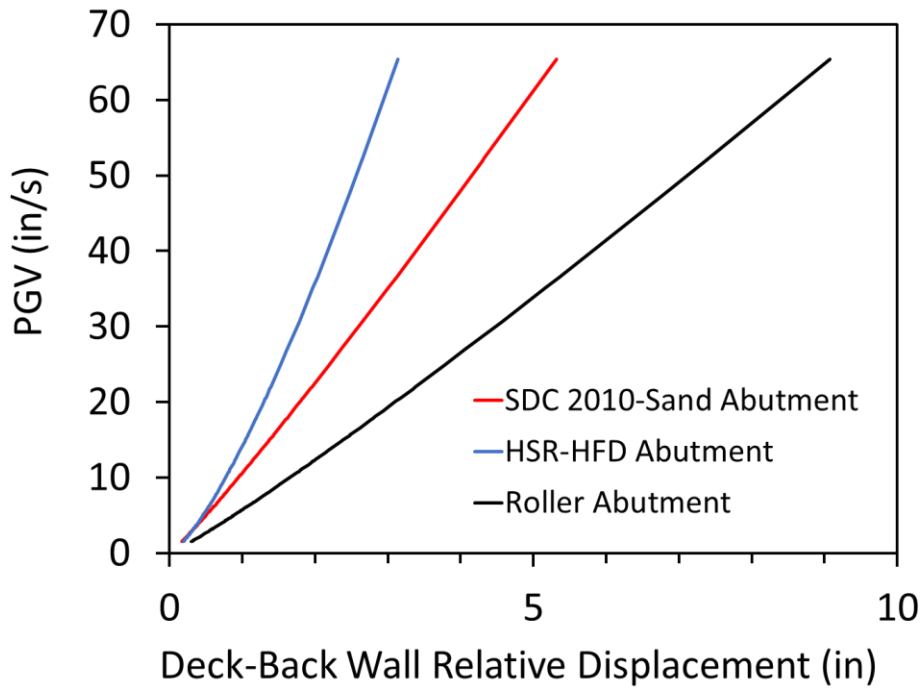


Figure 3.10. Demand model of longitudinal relative deck-back wall displacement

Chapter 4. Implementation of the Performance-Based Earthquake Engineering Framework for Multi-Span Bridge-Ground Systems

4.1. Abstract

In this chapter, the performance-based earthquake engineering (PBEE) framework is presented. Efforts to extend the framework to account for multi-span bridge configurations within an integrated simulation environment are shown. To facilitate this undertaking, the soil p - y curves approach was employed to represent the soil below grade. This approach can provide less complex, and more applicable way to run the Finite Element (FE) simulations compared to the 3D soil mesh approach. On this basis, the framework was utilized to estimate post-earthquake repair cost and repair time of a multi-span bridge configuration. Intensity-dependent repair cost and repair time were disaggregated by performance groups (PGs) to evaluate the contribution of each bridge component to the overall system at different hazard levels. A reinforced concrete highway bridge was considered, with multi-column bents founded on two different sites of varying stiffness and strength profiles. The deck, columns, abutments, and foundation response mechanisms were integrated within a unified framework. Systematic evaluation of the global system response was conducted under a wide range of earthquake input shaking scenarios. Based on the simulation results, the performance evaluation of the bridge model without considering SSI underestimated the loss outcomes in terms of repair cost and repair time. In addition, the damage states and repair quantities related to the foundation and abutments were among the most significant parameters.

4.2. Introduction

Seismic Response of highway bridges have been receiving much attention (Elgamal *et al.* 2008; FHWA 2011; Mackie *et al.* 2012). After an earthquake, there are two main elements necessary for quantifying and minimizing economic loss, the cost associated with damage of the bridge and the consequences due to the loss of functionality (Mackie *et al.* 2010).

A probabilistic approach is preferred in seismic assessment to account for uncertainties in seismic loading and structural modeling. For that purpose, a well-established methodology is utilized. The employed PBEE framework was originally proposed by Cornell and Krawinkler (2000), and this methodology has been promoted and developed by PEER Center.

Previous performance evaluations of bridge systems were performed solely for the superstructure without fully considering the bridge-ground system as an integral entity (Solberg *et al.* 2008). However, after major earthquakes, the seismic response of bridges is significantly influenced by many factors including the soil-structure interaction effects (Kappos *et al.* 2002; Shin *et al.* 2008; Ledezma and Bray 2008; Bradley *et al.* 2010). Therefore, and to fully address the post-earthquake repair cost and downtime, considering the response of the bridge-foundation-ground is essential.

The PBEE framework can be used to compare the effectiveness of different bridge design options and evaluate the performance of existing bridges for different hazard levels. Therefore, it requires the complete structural response from the FE simulations before performing the probabilistic assessment to estimate the repair costs and times required to restore the structure to its original function.

The focus of this chapter is the probabilistic seismic performance and loss assessment of a three-span bridge structure supported on pile foundations founded on two sites of varying stiffness

and strength profiles. Two ground profiles were considered, rigid rock case and cohesive soil strata with gradually increasing shear moduli and undrained shear strengths. The objectives are to perform an analysis of the bridge using an integrated bridge-foundation-ground model and apply the performance-based assessment framework for both bridge-ground cases. To further show the significance of SSI, the presented results are shown within a comparative scope in terms of structural response, resulting damage, and expected loss (repair costs and repair times).

4.3. Computational Framework

4.3.1. Performance-Based Earthquake Engineering Framework

By using the total probability theorem, the desired probability distributions are calculated by dividing the task into four probabilistic models, each with its uncertainties and outcomes: (i) Hazard model that uses the input ground motions to determine the Intensity Measures (IMs), (ii) Demand model that uses the FE simulations results to determine the Engineering Demand Parameters (EDPs), (iii) Damage model that connects the EDPs to pre-defined Damage States (DSs), and (iv) Loss model that quantifies the DSs into repair Quantities (Qs) and then correlates Qs to loss outcomes in terms of repair cost and repair time. This methodology is based on linearization of the damage model and called local linearization repair cost and time methodology (LLRCAT), more details about this methodology can be found in (Mackie *et al.* 2008).

To facilitate the disaggregation when applying the total probability theorem, Mackie *et al.* (2010) divided the bridge into a collection of structural components known as performance groups (PGs). Each PG is characterized by the DSs that are triggered when critical values of the EDPs are reached. Consequently, the higher DS corresponds to more severe consequences. For example, the DS1 in the column is the cracking, while the DS4 is a complete failure.

The estimated Repair costs (RC) are obtained by multiplying each Q to the corresponding Unit Cost (UC). Similarly, the estimated Repair times (RT) are obtained using the corresponding Production Rate (PR). Finally, the expected RC is estimated from the assembly of loss in each discrete DSs from all PGs. Table 4.1 shows the PGs (and associated EDPs and DSs) used in this study. In addition, more details about the framework are presented in Appendix H.

4.3.2. Finite Element Computational Framework

The Open System for Earthquake Engineering Simulation (OpenSees, McKenna *et al.* 2010, <http://opensees.berkeley.edu>) framework was used to conduct the nonlinear bridge-ground system analysis subjected to seismic excitation. OpenSees was developed by PEER Center, and it is widely used for simulation of structural and geotechnical systems including SSI applications (Yang and Elgamal 2002; Elgamal *et al.* 2008; Su *et al.* 2017).

4.3.3. User-Interface for Nonlinear Bridge-Foundation Analysis

Recently, under Caltrans' support, an effort was made to develop a tool (Elgamal *et al.* 2014) for efficiently conducting nonlinear THA studies for a wide range of multi-span bridge configurations (using Opensees). In this tool (MSBridge, Figure 4.1), bridge structure, abutments, and foundation response mechanisms were integrated within a unified framework. In the user-interface, the PEER PBEE was implemented to perform the probabilistic seismic performance assessment and loss estimation using the LLRCAT methodology presented in Section 4.3.1.

4.4. Simulation Models

The studied bridge configuration is straight, single column bents, box girder, reinforced concrete structure with three spans (Figure 4.2). Dimensions of the bridge considered in this chapter are 45.7 m spans, 6.71 m clear column heights, 1.22 m circular column diameter, and 11.9 m wide two-cell box girder (Ketchum *et al.* 2004).

Figure 4.3 shows the constitutive models for the concrete and reinforcing steel used in the analysis with the material properties shown in Table 4.2 and Table 4.3. In addition, seat-type abutment was used in this bridge configuration.

4.5. Ground Profiles

Two ground properties were considered in this study, the rigid column base and the shallow soft ground stratum. However, the same superstructure geometry and materials were used for both cases.

4.5.1. Bridge-Ground Case Study 1: Fixed-Base/Rigid Soil

This scenario was introduced to represent the traditional performance evaluation of the bridge considering the structural-only analysis. This case (herein, defined as Case 1) assumes fixed boundaries at the base of the column.

4.5.2. Bridge-Ground Case Study 2: Benchmark Soil Profile

Using the same bridge configuration, Case 2 that includes the effect of SSI was considered in this study. Thus, the damage states of the bents and abutment foundations were included in the overall loss estimation. The soil profile includes cohesive soil strata with gradually increasing shear moduli and undrained shear strengths, this profile is known as a benchmark soil profile (Caltrans 2003). The properties of the layers are shown in Figure 4.4 and Table 4.5 with the groundwater table at 2.4 m.

The p - y curves approach was employed to define the strength of the soil below grade. This approach can provide less complex, and more applicable way to run the FE simulations compared to the soil mesh approach that was used by Mackie *et al.* (2012). The p - y curves were obtained from LPILE using the soil properties shown in Table 4.5. Using this approach, the FE and PBEE analyses were performed. Figure 3 shows the p - y curves at selected depths.

4.6. Ground Motions for PBEE Analysis

An ensemble of 100 ground motions was obtained from the PEER NGA database (<http://peer.berkeley.edu/nga/>). Each motion is composed of 3 perpendicular acceleration time history components (2 lateral and one vertical). These motions were selected through earlier efforts (Gupta and Krawinkler 2000; Mackie *et al.* 2005) to be representative of seismicity in typical regions of California. The motions are divided into 5 bins of 20 motions each with characteristics: i) moment magnitude (M_w) 6.5-7.2 and closest distance (R) 15-30 km, ii) M_w 6.5-7.2 and R 30-60 km, iii) M_w 5.8-6.5 and R 15-30 km, iv) M_w 5.8-6.5 and R 30-60 km, and v) M_w 5.8-7.2 and R 0-15 km.

MSBridge allows for the specification of numerous Intensity measures, so as to display the outcomes against any of these measures. Herein each earthquake motion will be represented by its PGV as the intensity measure (IM). Figure 4.6 shows the distribution of horizontal PGV SRSS values.

4.7. Time History Results

Nonlinear time history analysis (THA) was conducted for the 100 input motions using MSBridge. Uniform base excitation was applied using each of these input ground motions. Rayleigh damping was used with a 5% damping ratio (defined at the periods of 1.43 and 0.33 second) in the nonlinear THA. For the time integration scheme, the Newmark average acceleration method ($\gamma = 0.5$ and $\beta = 0.25$) was employed. Variable time-stepping scheme (VariableTransient) was used in the conducted Nonlinear THA. The starting value for each step was 0.02 second (the time step of the input motions).

The time history results were used to create the probabilistic seismic demand models (PSDMs). As such, the EDP values for each PG were used to trigger the DSs and the associated

repair quantities. Figure 4.7 shows the PSDM for the maximum column drift ratio (PG1) for both cases. The results showed a decrease in column demand for Case 2 compared to Case 1 since the weaker soil case (Case 2) allows the column base to move, which would result in a reduction of the drift ratio. However, the increase in abutment PSDM (maximum relative deck-end/abutment displacement, PG3) offsets the reduction in the column demand model as can be depicted in Figure 4.8.

4.8. PBEE Results

Figure 4.9 shows the repair cost disaggregated for each PG. It can be gleaned from Figure 4.9 that Case 1 begins to accumulate cost at higher IM than Case 2 since higher demands are expected for Case 2. In addition, Figure 4.10 shows the mean repair cost ratio (RCR), the ratio between cost of repair and cost of replacement (not including the demolition), against PGV as the IM. From both cases, the consequence of shaking and repair do not begin to accumulate until a PGV of approximately 20 cm/s for Case 1 and 40 cm/s for Case 2.

Similarly, Figure 4.11 shows the repair time in crew working day (CWD) against PGV. The jumps in the repair times for both cases are due to the triggering of different DSs that require more repair efforts. In addition, it is worth noting that Case 1 reaches a plateau around 50 cm/s, while Case 2 around 40 cm/s.

To obtain Hazard Curves for a particular seismicity scenario (based on geographic location), three probabilities of exceedance (2%, 5%, and 10% in 50 years) are needed. The hazard selected (PGV=160, 80, and 10 cm/s) is consistent with infrequent events of larger magnitude such as the central US.

On this basis, Figure 4.12 shows the mean annual frequency (MAF) of exceedance vs. RCR. Similarly, Figure 4.13 shows the MAF of exceedance vs. Repair Time (RT). The hazard

curves provide a clear illustration of the increased cost and time hazards associated with decreasing the strength and stiffness of the soil profile.

4.9. PBEE Application for Other Types of Civil Infrastructure

The PBEE framework has been developed and proposed with a potential for a wide range of applications. As a representative, Appendix I presents an undertaken effort to apply this framework to a wharf system. As such, the damage states and corresponding probabilities of exceedance were defined.

4.10. Summary and Conclusions

Performance-based evaluations of bridge systems need to consider bridge-foundation-ground to get a more reliable estimation of bridge performance. MSBridge was utilized in this chapter to combine the finite element analysis and the PBEE framework in a graphical user environment that has enabled such studies to be more easily implemented. The repair costs and repair times for a three-span ordinary standard bridge founded on two different soil scenarios, rigid rock, and weak upper soil strata were studied and compared. Furthermore, the seismic hazard curves for a particular seismicity scenario (geographic location) were calculated.

The presented results in this chapter show that the repair quantities do not start to accumulate until the first damage states are triggered (40 cm/s for Case 1 and 20 cm/s for Case 2). In general, Case 2 results in higher post-earthquake repair at lower intensities.

Overall, the abutment repairs are among the most significant parameters that contribute to the expected costs and times. In addition, including the SSI can reduce the column demands. However, this reduction offsets by the increase in the other demands, especially for the abutment (the most contributing PG to the total expected repair cost).

4.11. Acknowledgements

Chapter 4, in part, is a reprint of material as it appears in the following conference publication (The dissertation author was the primary investigator and author of this paper):

Almutairi, A.S., Lu, J., Elgamal, A., and Mackie, K.R. (2017). "Performance-based earthquake assessment of multi-span bridge systems including soil-pile-structure interaction." Proceedings of the 3rd International Conference on Performance-based Design in Earthquake Geotechnical Engineering (PBD-III), Vancouver, BC, Canada, July 16-19.

Chapter 4, in part, is a reprint of material as it appears in the following conference publication (The dissertation author was the primary investigator and author of this paper):

Lu, J., Almutairi, A.S., Elgamal, A., and Mackie, K.R. (2018). "A computational framework for systematic bridge performance-based earthquake engineering applications." Proceedings of the 11th U.S. National Conference on Earthquake Engineering (Integrating Science, Engineering & Policy), Los Angeles, California, June 25-29

Table 4.1. Performance groups and associated engineering demand parameters after Mackie *et al.* (2007)

PG	EDP	DS	Description	Repair item
PG1	Maximum column tangential drift ratio	DS0	Concrete cracking	N/A
		DS1	Onset of spalling	Epoxy inject cracks, patching
		DS2	Buckling of bars	Epoxy inject cracks, concrete
		DS3	Failure	Temporary support, column replacement, excavation and backfill
PG2	Residual column tangential drift ratio	DS0	Tolerable	N/A
		DS1	Enlarge pier and jacket	Temporary support, column jacket, steel bar, excavation and backfill
		DS2	Failure	Temporary support, column replacement, excavation and backfill
PG3 & PG4	Max. longitudinal relative deck-end/abutment displacement for left & right abutments	DS0	Joint cleaning	N/A
		DS1	Repair joint seal	Joint seal assembly, patching
		DS2	Back wall repair	Concrete, joint seal assembly, patching, excavation and backfill
		DS3	Back wall failure	Approach slab, concrete and steel, joint seal assembly, excavation and backfill
PG5 & PG6	Max. bearing displacement for left and right abutments	DS0	Yielding	N/A
		DS1	Failure	Temporary support, all bearings replaced
PG7 & PG8	Approach residual vertical displacement for left & right abutments	DS0	Pavement	N/A
		DS1	Regrade	Asphalt concrete
PG9 & PG10	Residual pile cap displacement for left & right abutments	DS2	Rebuild	Asphalt concrete, mud jacking
		DS0	Add pile threshold	N/A
PG11	Residual pile cap displacement for columns	DS1	Enlarge foundation	Concrete, steel, dowels, pipe piles, excavation and backfill
		DS0	Add pile threshold	N/A
		DS1	Enlarge foundation	Concrete, steel, dowels, pipe piles, excavation and backfill

Table 4.2. Bridge deck material and section properties

Parameter	Value
Young's modulus (kPa)	2.53×10^7
Shear modulus (kPa)	1.05×10^7
Unit weight (kPa)	25.11
Area of cross-section (m ²)	5.05
Moment of inertia @ horizontal axis (m ⁴)	6.78
Moment of inertia @ vertical axis (m ⁴)	41.89
Torsion constant (m ⁴)	0.98

Table 4.3. Bridge pier columns material and section properties

Parameter	Value
Young's modulus (kPa)	2.53×10^7
Shear modulus (kPa)	1.05×10^7
Unit weight (kPa)	25.11
Area of cross-section (m ²)	5.66
Moment of inertia @ horizontal axis (m ⁴)	5.11
Moment of inertia @ vertical axis (m ⁴)	1.11
Torsion constant (m ⁴)	3.53

Table 4.4. Constitutive model parameters for concrete material used in fiber beam-column element

Parameter	Confined concrete	Unconfined concrete
Concrete compressive strength at 28 days, f'_c (kPa)	-3.47×10^4	3.40×10^4
Concrete strain at maximum strength, ϵ_{c0}	-0.0025	-0.002
Concrete crushing strength, f'_{cu} (kPa)	-3.07×10^4	0
Concrete strain at crushing strength, ϵ_{cu}	-0.006	-0.005

Table 4.5. Soil types and properties

Layer depth (m)	Soil type	ρ (kg/m ³)	S_u (kPa)
0-5	Soft clay	1500	41.5
5-10			74.5
10-15			108
15-20	Stiff clay	2000	142

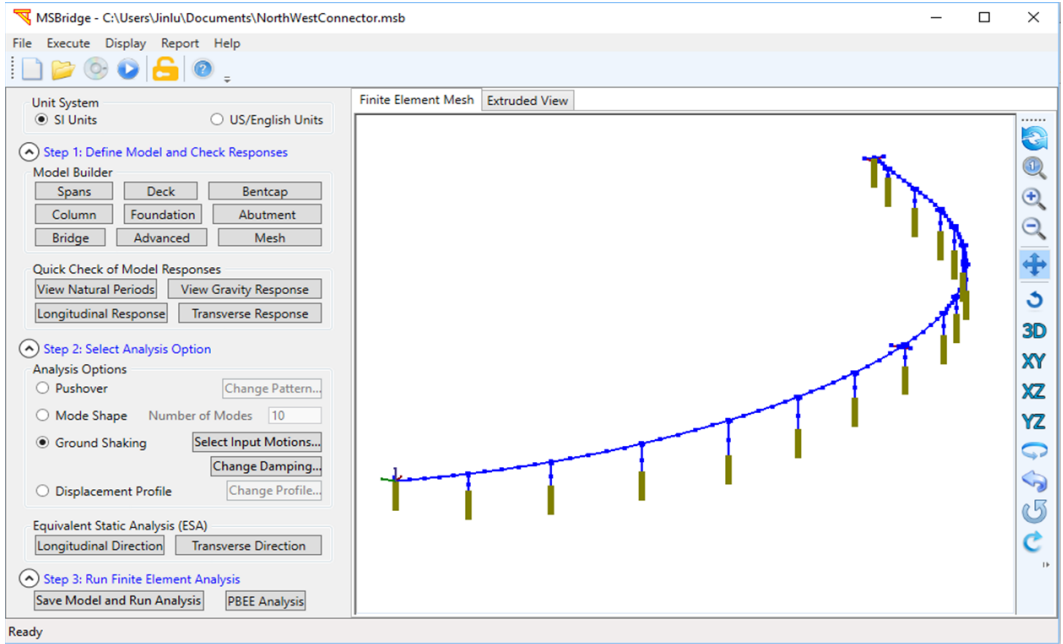


Figure 4.1. MSBridge user-interface

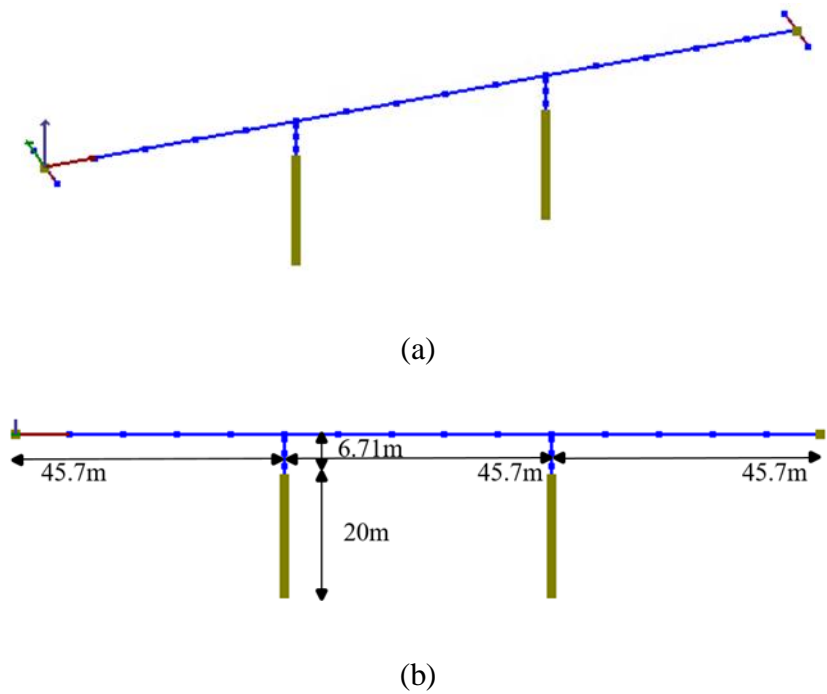


Figure 4.2. Finite element mesh: (a) 3D view, (b) elevation view

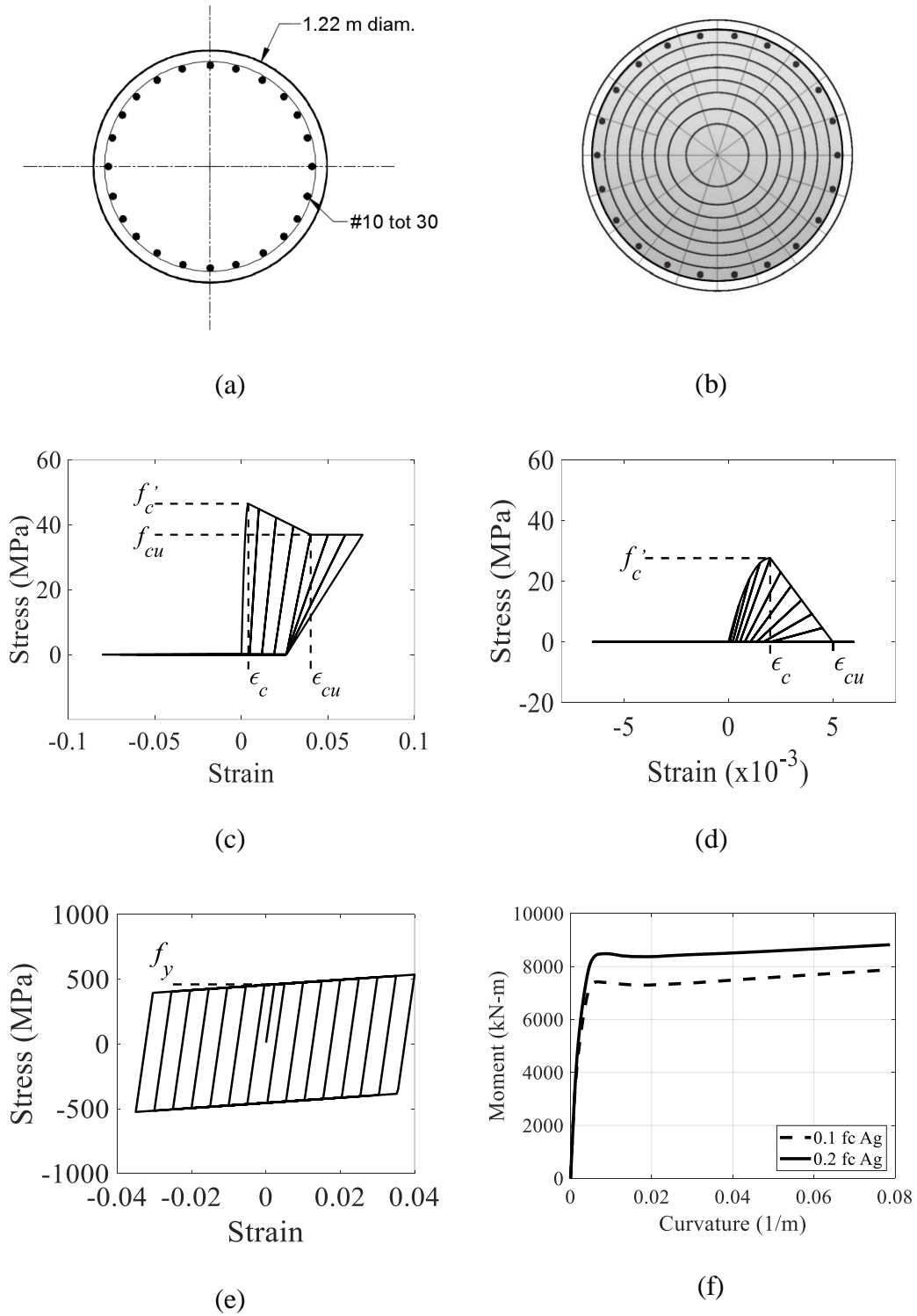


Figure 4.3. Modeling of column and pile: (a) column cross-section; (b) fiber discretization; (c) core concrete; (d) cover concrete; (e) reinforcing steel; and (f) moment-curvature response

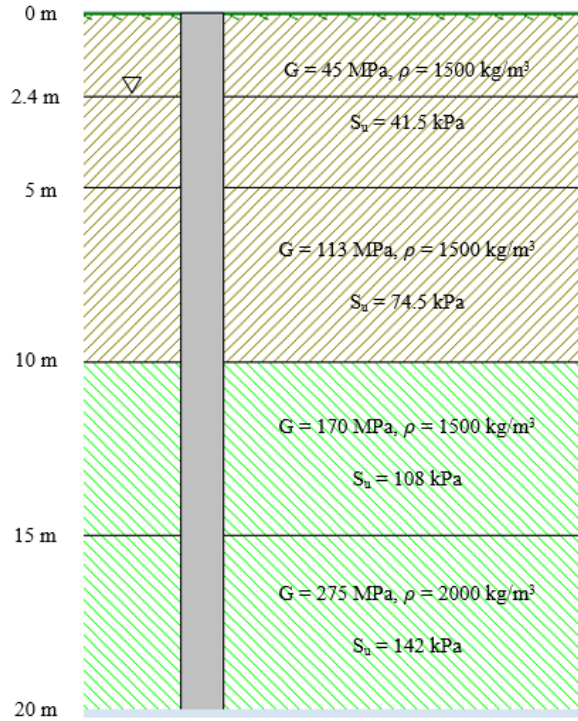


Figure 4.4. Soil layer properties for case 2 (benchmark)

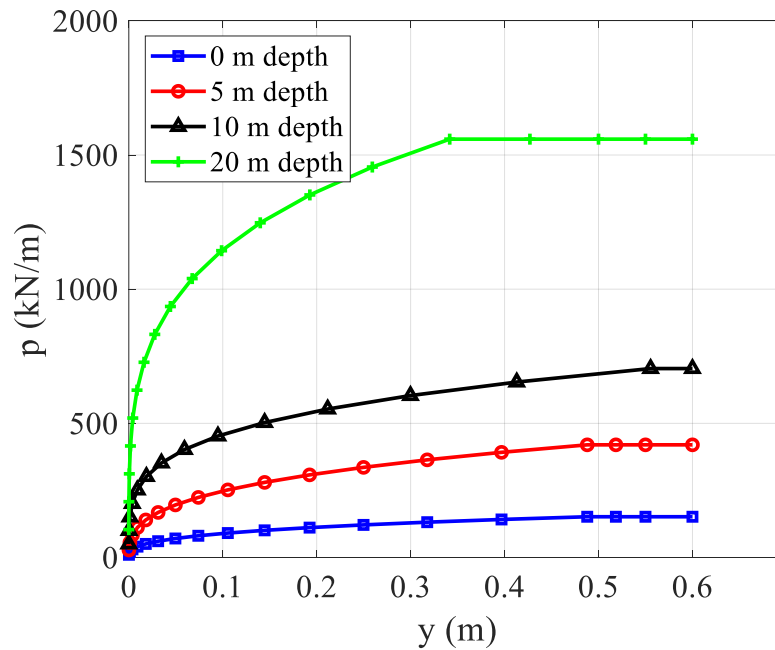
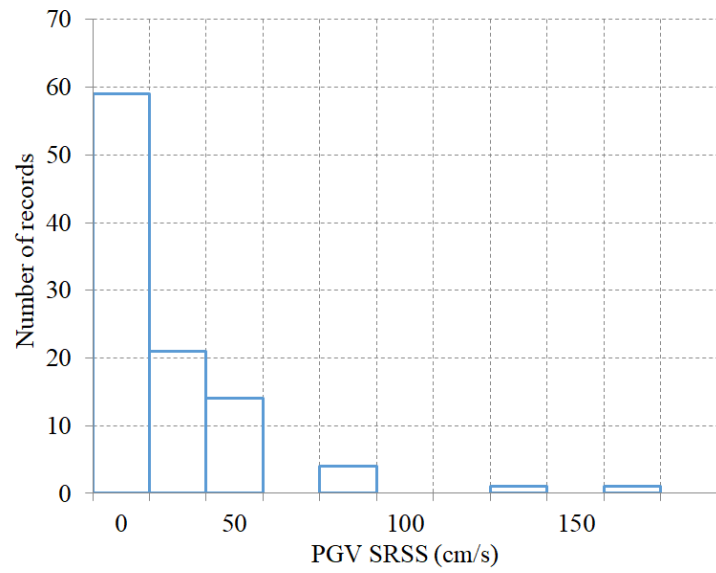
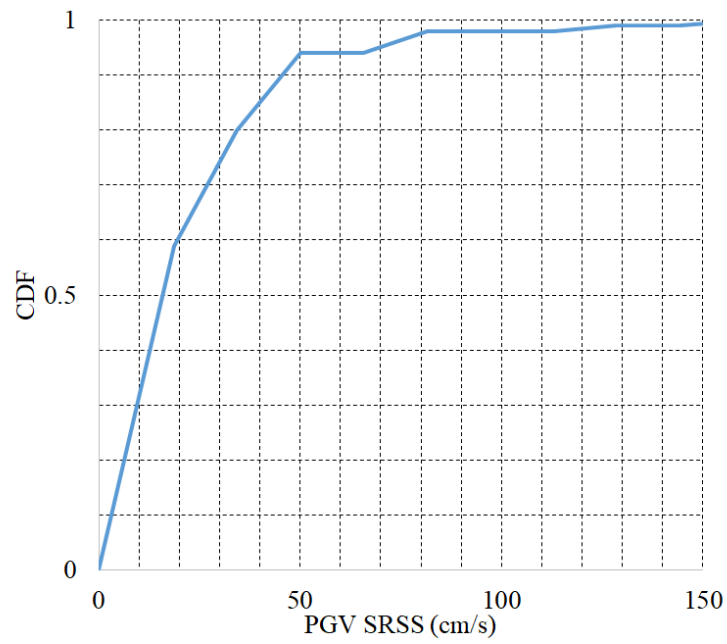


Figure 4.5. P - y curves for case 2 at depths: (a) 0 m; (b) 5 m; (c) 10 m; and (d) 20 m

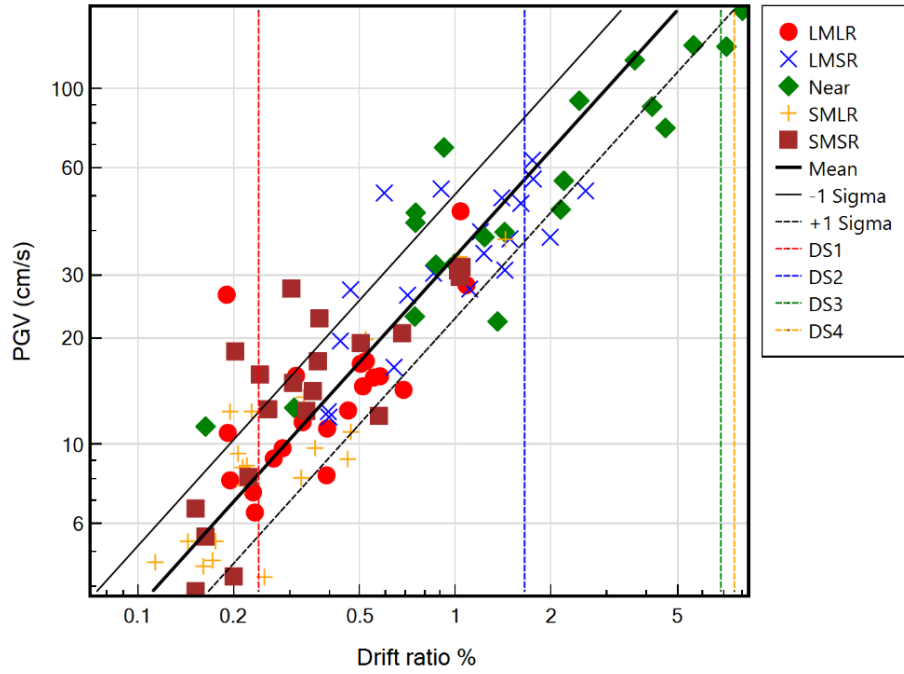


(a)

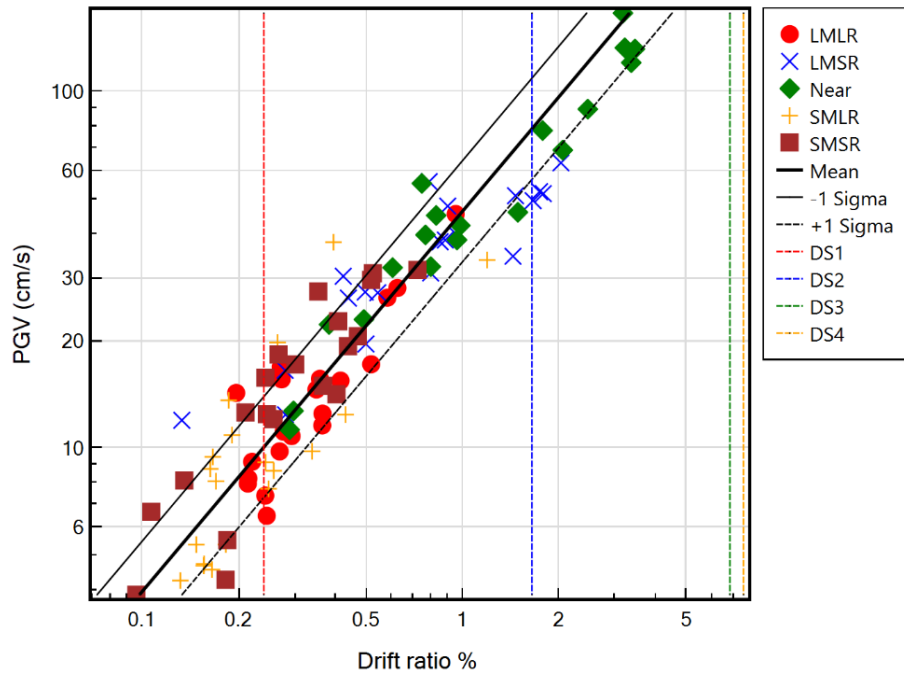


(b)

Figure 4.6. PGV distribution for the SRSS of two lateral ground motion components

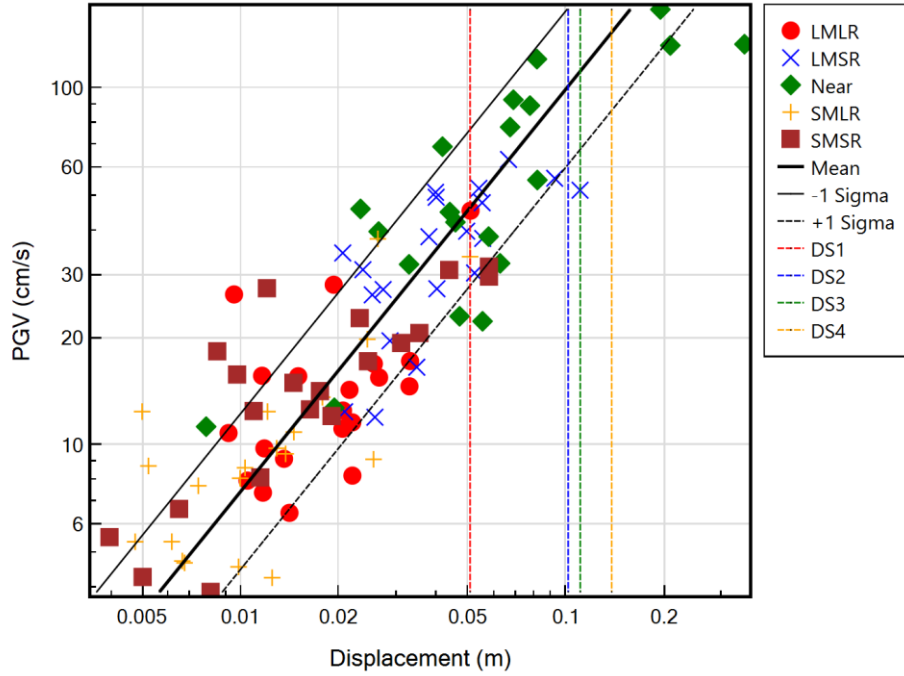


(a)

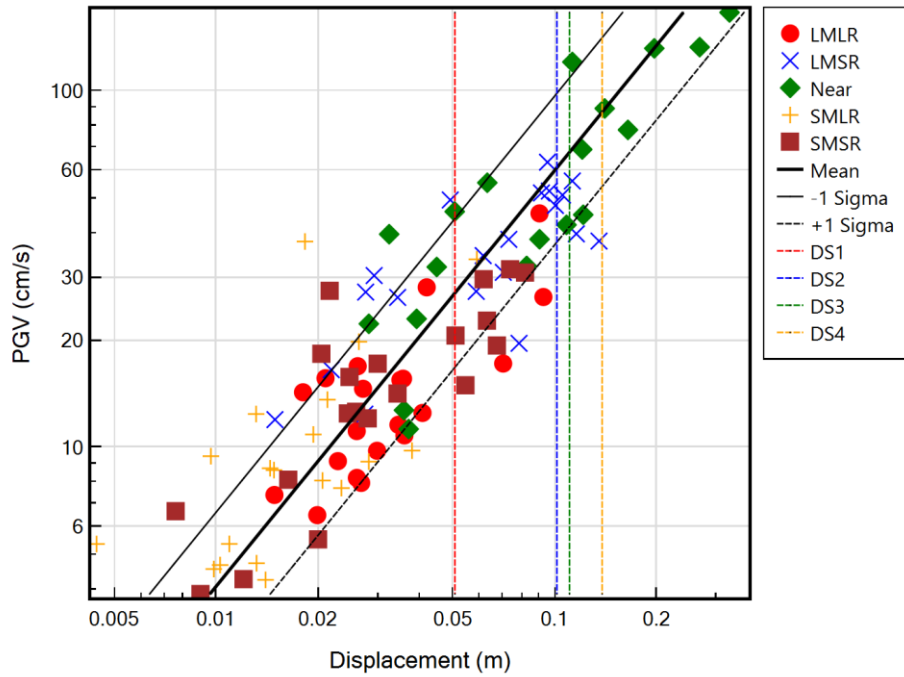


(b)

Figure 4.7. PSDMs for column maximum drift ratio at column of bent 2 for: (a) Case 1; and (b) Case 2



(a)



(b)

Figure 4.8. PSDMs for maximum relative deck end-back wall displacement at left abutment for: (a) Case 1; and (b) Case 2

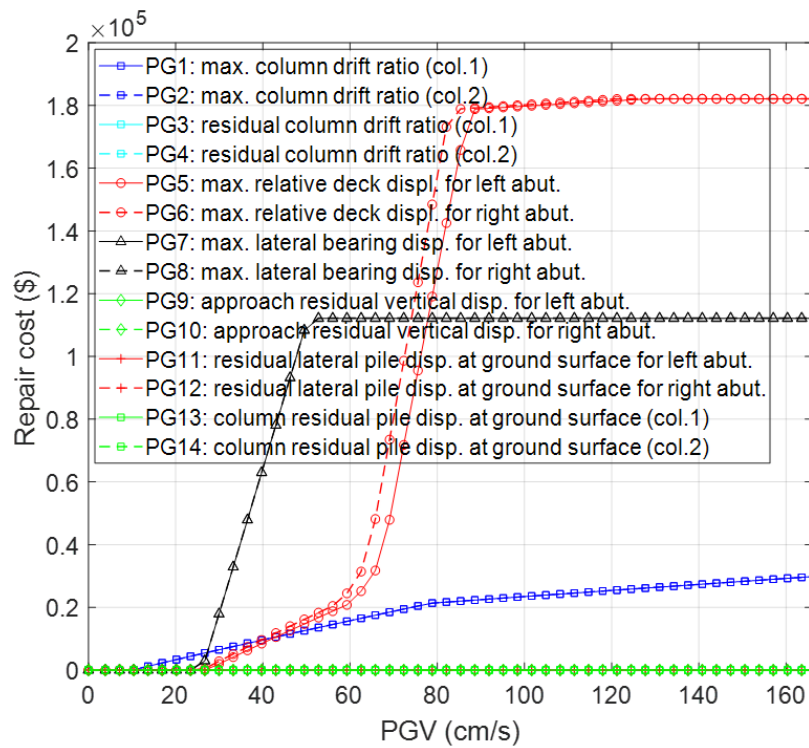
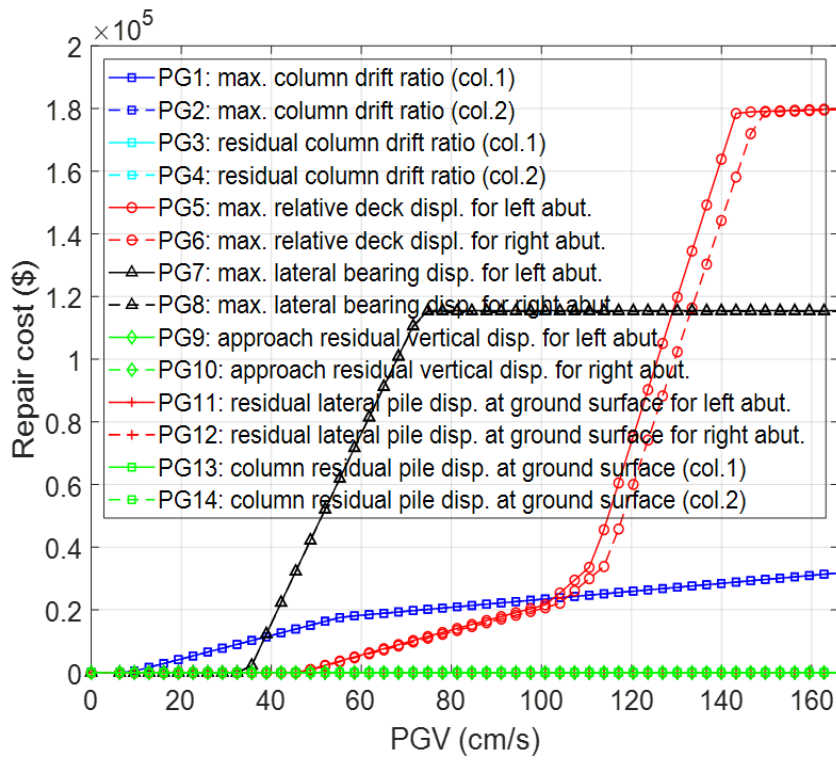


Figure 4.9. Repair cost disaggregated for each PG for: (a) Case 1; and (b) Case 2

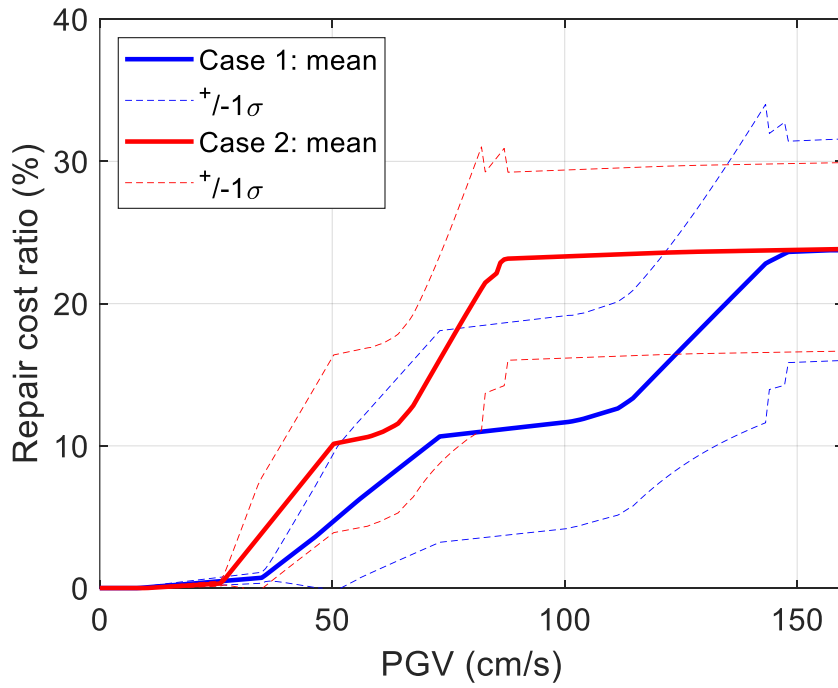


Figure 4.10. RCR loss models for each case.

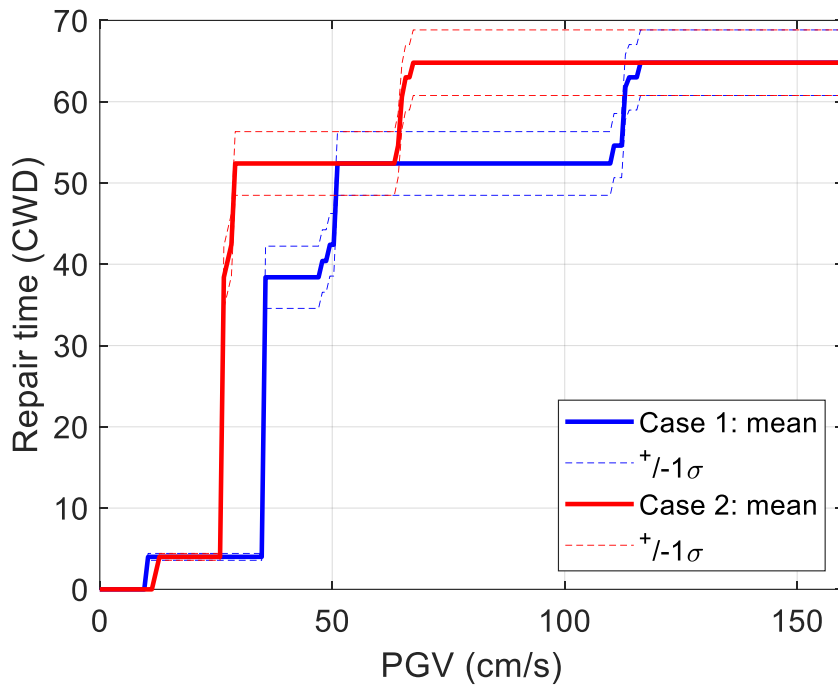


Figure 4.11. Repair time (CWD) loss model (with probabilistic moments) for both cases

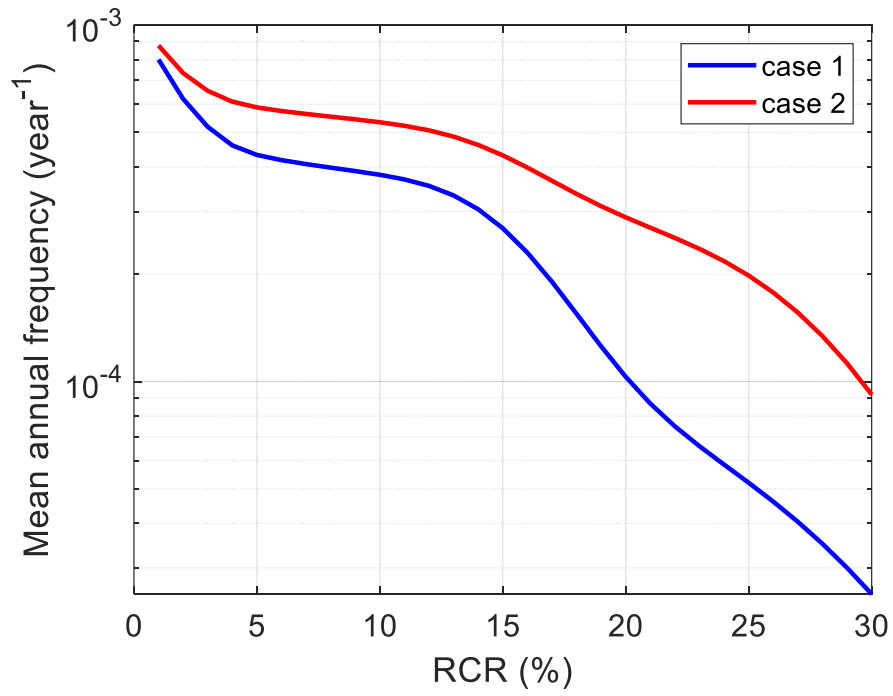


Figure 4.12. Repair cost ratio hazard curve.

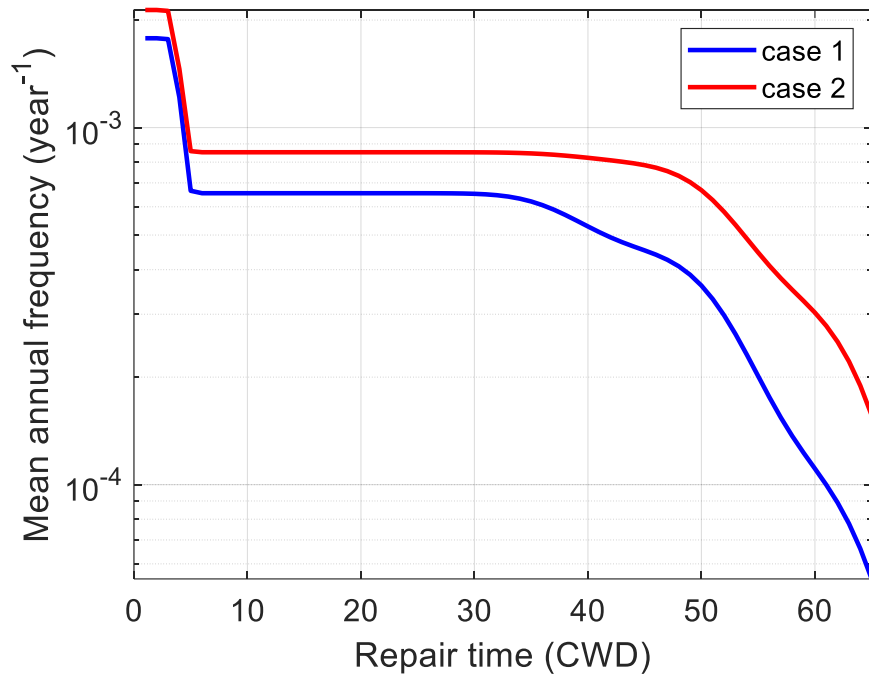


Figure 4.13. Repair time hazard curve.

Chapter 5. Performance-Based Earthquake Assessment of Samoa Channel Bridge-Foundation System

5.1. Abstract

In this chapter, a PBEE framework was utilized to perform probabilistic seismic performance assessment of the Samoa Channel Bridge, a large, retrofitted bridge-ground system in California. In view of the significance of soil-structure interaction (SSI), response of the coupled bridge-foundation-ground system was addressed. For that purpose, a Finite Element (FE) model of the global bridge-ground system was developed. Nonlinear representation of the bridge columns, abutments, and foundation response mechanisms was integrated within a unified framework. To facilitate this endeavor, a graphical user-interface was further developed and utilized. The entire bridge model was calibrated based on the actual response recorded by seismic sensors. The PBEE outcomes were presented within a comparative scope than contrast the case before the retrofit with the case after the retrofit. Based on the simulation results, the damage states and repair quantities related to the abutments were found to be among the most significant parameters that contribute to the loss estimation. Overall, the significance of the seismic retrofit program on the bridge resilience can be assessed based on the results of the loss and hazard models.

5.2. Introduction

Bridge response during earthquakes has received significant attention in recent decades (McCallen and Romstadt 1994; Conte *et al.* 2002; Jeremic *et al.* 2004; Mackie and Stojadinovic 2006; Elgamal *et al.* 2008; Zhang *et al.* 2008; Kwon *et al.* 2009; FHWA 2011; Mackie *et al.* 2010, 2012; Wang *et al.* 2013; Soltanieh *et al.* 2019). The increased failure potential of highway bridges and their susceptibility to damage during extreme events necessitate a further understanding of the seismic response of bridges in order to mitigate post-earthquake consequences. For that purpose,

advanced numerical tools have been developed and used to simulate and calibrate bridge response mechanisms (e.g., McKenna *et al.* 2010).

During an earthquake, the seismic response of a bridge is influenced by SSI (Kappos *et al.* 2002; Shin *et al.* 2008; Ledezma and Bray 2008; Bradley *et al.* 2010). In addition, unrealistic modeling of the foundations will not only affect the seismic response, but also the repair cost and repair time estimates (Mackie *et al.* 2012). Therefore, considering the bridge-foundation-ground interaction is essential for fully addressing the post-earthquake repair cost and downtime.

PBEE assessment can be used to compare the effectiveness of different bridge design options and evaluate the performance of existing bridges for different hazard levels (Mackie *et al.* 2010). Therefore, the complete structural response from FE analysis is required before probabilistic analysis can be performed to estimate the post-earthquake loss. The PBEE framework can provide the stakeholders with a valuable tool that contributes to economic-based and environment-based decision making (Mackie *et al.* 2008, 2012, 2015).

In this chapter, the extensively instrumented Samoa Channel Bridge (Figure 5.1) was modeled to evaluate the salient ground-foundation-structure response mechanisms. For that purpose, FE modeling was employed to represent the bridge structural elements and configuration (Calibrated based on the recorded seismic response as described in Wang *et al.* 2018). The model of the entire bridge was developed, with foundation-matrix springs at each column base (at the pile cap locations). A study by Wang *et al.* (2018) showed a reduction in the foundation stiffness as the response amplitude increases. Therefore, nonlinear force-displacement relationships for the foundation matrix elements were used to account for that reduction. In addition, column flexural rigidity (EI) values that match the actual response were employed (Wang *et al.* 2018).

The focus of this paper is the probabilistic seismic performance and loss assessment of Samoa Channel Bridge supported on pile-group foundations consisting of driven pre-cast prestressed concrete piles (before and after retrofit). The main objective is to perform an analysis of the bridge using a calibrated integrated bridge-foundation-ground model within the performance-based assessment framework. Outcomes are presented in terms of structural response, resulting damage, and expected repair costs and times, and compared to show the significance of the retrofit program.

5.3. Computational Framework

5.3.1. Performance-Based Earthquake Engineering Framework

The PBEE framework used in this study was proposed by Mackie *et al.* (2008). Table 4.1 shows the PGs (and associated EDPs and DSs) used in this study. More details about the PBEE framework can be found in Chapter 4 and Appendix H.

5.3.2. Finite Element Computational Framework

The Open System for Earthquake Engineering Simulation (OpenSees, McKenna *et al.* 2010, <http://opensees.berkeley.edu>) framework was used to conduct the nonlinear bridge-ground system analysis subjected to seismic excitation. OpenSees was developed by PEER Center, and is widely used for simulation of structural and geotechnical systems including SSI applications (Yang and Elgamal 2002; Elgamal *et al.* 2008; Su *et al.* 2017).

5.3.3. User-Interface for Nonlinear Bridge-Foundation Analysis

Recently, under Caltrans' support, an effort was made to develop a tool (Elgamal *et al.* 2014) for efficiently conducting nonlinear THA studies for a wide range of multi-span bridge configurations (using Opensees). In this tool (MSBridge, Figure 5.2), bridge structures, abutments, and foundation response mechanisms were integrated within a unified framework. MSBridge

(Elgamal *et al.* 2014) also allows for addressing possible variability in the bridge deck, bentcap, column, foundation, or soil configuration/ properties (on a bent-by-bent basis). In addition, MSBridge permits the simulation of key scenarios of significance for bridge upgrades, widening, extensions, and retrofits. In the user-interface, the PEER PBEE was implemented to quantify the loss in terms of repair cost and repair time.

5.4. Finite Element Model

The 20-span Samoa Channel Bridge (hereinafter referred to as “Samoa Bridge”, Figure 5.1) near Eureka in northern California is a 2,506 ft (764 m) long and 34 ft (10.4 m) wide structure connecting Samoa Peninsula and Indian Island (Figure 5.1). The bridge superstructure (Wang *et al.* 2016; Almutairi *et al.* 2016), which consists of cast-in-place reinforced concrete deck and four pre-cast prestressed concrete I-girders, is supported by 19 single hexagonal concrete pier bents on pile group foundations. For convenience, the piers (including abutments) are numbered #1 through #21 from Indian Island side (left side in Figure 5.1) to Samoa Peninsula side (right side in Figure 5.1). The typical span length is 120 ft (36.6 m) long except for the main channel between Piers S-8 and S-9, which is 225 ft (68.6 m) long. Soil profile for the bridge consists of silty clay fill underlain by dense medium-compact gray sand (Figure 5.1). Very dense coarse gravelly sand can be found below a depth of 20 m. In general, the soil layers vary in thickness and are not continuous horizontally.

The bridge is heavily instrumented as shown in Figure 5.1 in order to record any significant earthquake excitation. There are 33 accelerometers in total on the Samoa Bridge, including 24 accelerometers on the bridge structure, six accelerometers on the pile foundations, and three accelerometers at a nearby free-field site. Sensors on the structure are oriented in the longitudinal

and transverse direction of the bridge, and sensors at the free field are oriented in the north-south and east-west directions.

Abutments and piers were founded originally on pile-group foundations consisting of driven pre-cast pre-stressed concrete piles. Referenced to the mean sea level (MSL), the elevation of the mud line varies from -51.8 ft (-15.8 m) below Pier S-8 to +3 ft (+0.9 m) at Pier S-20. Eleven pile groups (from Piers S-3 to S-13) have pile caps located above the mudline with a maximum value of +54.9 ft (+16.72 m) (elevation of cap base) at Pier S-8 (Figure 5.3a). More details about the pile properties can be found in Wang *et al.* (2018).

Elevation view of the bridge is shown in Figure 5.1b. For simplicity, two column cross-sections along with the reinforcement details are considered in this study. Figure 5.4 shows the column reinforcement details at Piers S-8 and S-14 (before and after retrofit), and the column reinforcement details at the piers other than Piers S-8 and S-14 (before and after retrofit), respectively. The columns are precast prestressed concrete I-girders along with cast-in-place concrete slabs are supported on concrete seat-type abutments and the hammerhead cap beams of column type piers. The column/pier heights of this vertical curved bridge range from 20.3 ft (6.19 m; for Pier S-3) to 42.3 ft (12.9 m; for Pier S-14).

The bridge was retrofitted, and the retrofit work included: i) strengthening of the foundations by installing additional cast-in-steel shell (CISS) piles, ii) adding or enlarging the pile caps to cover the new piles, and iii) encasing the bridge columns in reinforced concrete column jackets to improve ductility. More details about the retrofit work can be found in Wang (2015). The significance of the retrofit efforts is of paramount importance. As such, the loss models are presented for the scenarios of before and after retrofit.

5.4.1. Bridge Model

Figure 5.2 shows the FE mesh of the Samoa Bridge model. To facilitate the conducted analyses, a recently developed user-interface MSBridge was employed. In the conducted OpenSees analyses, the pier columns were modeled using the nonlinear fiber section and the forceBeamColumn (with the distributed plasticity integration method) element was employed. The deck was considered linearly elastic and the pier column top was considered to extend to the deck center of gravity. Seat-type abutment model was employed.

Based on calibration by the observed response (Wang *et al.* 2018), the following properties were identified. Nominal concrete compressive strength for the columns is specified as 28 MPa (5 ksi). Properties of the core concrete are derived using Mander's confinement model (Mander *et al.* 1988) while the unconfined properties are based on the Kent–Park (Kent and Park 1971) model. Relevant parameters for the concrete model are listed in Table 5.1. Figure 5.5 illustrates the stress-strain parameters used in the analysis. Longitudinal reinforcing steel used in all the piers is modeled as a bilinear material with an assumed yield strength of 303 MPa (44 ksi), an effective elastic stiffness of 200 GPa, and 0.8% post-yield stiffness (strain hardening ratio $b = 0.008$) (Figure 5.5).

Table 5.2 shows the employed linear elastic material and section properties of the I-girder. The weight of the bridge deck per unit length is 8.687 kip/ft (126.82 kN/m). In addition, Table 5.3 shows the pier column properties.

The moment-curvature response of the column Fiber sections for Piers S-8 and S-14 are shown in Figure 5.5. In this Figure, an axial compressive load of 8,896 kN (2,000 kips) was applied for the moment-curvature analysis in both the longitudinal and the transverse directions for Pier

S-8. In addition, an axial compressive load of 5,782 kN (1,300 kips) was applied for the moment-curvature analysis in both the longitudinal and the transverse directions for Pier S-14.

5.4.2. Foundation Matrix

Foundations of the bridge are represented by the Foundation Matrix model, a technique developed by Lam and Martin (1986). In this method, the stiffness of a single pile is represented by a 6 x 6 matrix associated with all six degrees of freedom at the pile head (Figure 5.6). However, the overall pile-soil stiffness should reflect the soil characteristics and the structural properties of the pile. A study by Wang *et al.* (2018) has shown that the lateral stiffness values in the foundation matrix are varying as a function of the response amplitude. Therefore, a nonlinear force-displacement relationship was used to calibrate the model at the pile cap locations. Figure 5.13 shows the hyperbolic force-displacement relationship of the Foundation Matrix model for Piers S-8 and S-14.

Table 5.4 shows the foundation matrix coefficients for all bents (Wang 2015). The local coordinate system employed for the foundation matrix is parallel to the global coordinate system. However, the characterization of the stiffness characteristics of an individual pile involves an evaluation for both axial and lateral loading conditions. The overall pile-soil stiffness should reflect the soil characteristics and the structural properties of the pile as well.

Nonlinear lateral springs were attached to the base of the bridge structure (bottom of the pier column) to account for the stiffness of the underlying pile foundations and the soil-foundation-structure interaction. As such, the springs were defined as hyperbolic curves to account for the variation in the foundation stiffness as a function of response amplitude. A robust OpenSees user-interface was utilized to evaluate the large pile-ground system stiffness under static lateral load (OpenSeesPL, <http://soilquake.net/openseespl/>). For simplicity, equal values were specified for

lateral stiffness of the relatively similar S-14, S-15 foundations, as well as for the S-16 to S-20 foundations. In addition, S-9 lateral stiffness was assumed to be 1.3 that of S-8 (based on the difference in pile group free-span height). After obtaining the lateral force-displacement curves, they were scaled to match the recorded lateral stiffness of Ferndale 2010 and Trinidad 2007 input motions. Figure 5.7 - Figure 5.20 show the foundation matrix nonlinear force-displacement relationship for each Pier as previously described.

5.4.3. Mode Shape Analysis

Mode shape analysis was performed for Samoa bridge. Figure 5.21 shows the first transverse mode, the first longitudinal mode, and the second transverse mode.

5.5. Ground Motions

A set of 151 ground motions that were selected to be representative of seismicity in typical regions in California was employed in the FE and PBEE analyses (Mackie and Stojadinovic 2005; Somerville and Collins 2002). Among the motions, five bins of 20 motions are used to divide the motions based on characteristics: (i) moment magnitude (M_w) 6.5-7.2 and closest distance R 15-30 km (denoted LMSR bin), (ii) M_w 6.5-7.2 and R 30-60 km (LMLR), M_w 5.8-6.5 and R 15-30 km (SMSR), (iv) M_w 5.8-6.5 and R 30-60 km (SMLR), and (v) M_w 5.8-7.2 and R 0-15 km (denoted Near bin).

Furthermore, three more bins of 51 ground motions prepared by Somerville and Collins (2002) that represent three hazard levels of the Samoa site were utilized in the analysis and categorized in three sets. For each set of recordings, a scaling factor was employed to match the time history to the uniform hazard spectrum at a period of 1.23 sec (Somerville and Collins 2002). This scaling factor was then applied to all three components of the recording. This scaling procedure preserves the relative scaling between the three components of the recording.

Consequently, the transverse component is larger than the longitudinal component at longer periods for many of the recordings. In addition, Figure 5.22 shows the distribution of horizontal Peak Ground Velocity (PGV), Peak Ground Acceleration (PGA) and Spectral Acceleration (Sa) for each of the employed ground motion.

5.6. Representative Time History Results

Nonlinear time history analysis (THA) was conducted for the 151 input motions using MSBridge. Rayleigh damping was used with a 5% damping ratio (defined at the periods of 1.43 and 0.33 second) in the nonlinear THA. For the time integration scheme, the Newmark average acceleration method ($\gamma = 0.5$ and $\beta = 0.25$) was employed. Variable time-stepping scheme (VariableTransient) was used in the conducted Nonlinear THA. The starting value for each step was 0.02 second (the time step of the input motions).

Response time histories for Piers S-8 and S-14 from two representative input motions are presented. These two input motions are selected to represent the response under a moderate and strong shaking event. It can be gleaned from the mode shapes (Figure 5.21) that the first transverse mode shape is dominating the response at Pier S-8. Conversely, Pier S-14 response is dominated by the second transverse mode shape (that has a lower frequency). The column top displacement response of Piers S-8 and S-14 shown in Figure 5.23b can illustrate this conclusion. On the other hand, the longitudinal response time histories (Figure 5.23a) are controlled by the longitudinal mode shape.

Furthermore, Figure 5.24 and Figure 5.25 show the moment-curvature relationships for both Piers in both directions. From the simulation results, it can be seen that for the low shaking event, the response remains mostly linear. Conversely, the response relationships are highly

nonlinear for the strong shaking event. The same conclusion can be drawn from the Foundation Matrix response shown in Figure 5.26.

5.7. PBEE Results

5.7.1. Loss Models

By applying the ground motion records to the bridge, corresponding repair cost and repair downtime were computed. These values were then correlated with an intensity measure that represents each particular motion employed. MSBridge allows for the specification of numerous intensity measures, to display the outcomes against any of these measures. Herein each earthquake motion will be represented by its PGV as the intensity measure.

Figure 5.27 shows the mean repair cost contribution for each PG against PGV. It can be observed that each PG contributes differently to the repair cost. The presented results show that the case after retrofit delays the triggering of the first damage state. As such, the repair costs do not begin to accumulate until a PGV of approximately 50 cm/s. On the other hand, the case before retrofit shows earlier accumulation at a PGV of approximately 30 cm/s. Furthermore, Figure 5.28 shows the repair cost contribution for the columns PG to better illustrate the impact of the retrofit on the overall cost estimate. In general, the PGs related to the abutment are the largest cost driver PGs (PG3 & PG4 for the bearing and PG5 & PG6 for the abutment back wall).

The comparison can be presented in terms of the repair cost ratio (RCR), the ratio between cost of repair and cost of replacement (not including the demolition). The costs are increasing rapidly in the range of PGV between 50 and 100 cm/s where abutment repair quantities are triggered. It can also be gleaned from the results that the damage quantities related to the column are not dominating at specific IM range, rather they have been spread throughout the IM range.

Similarly, Figure 5.29b shows the repair time in crew working day (CWD) against PGV. The jumps in the repair times are due to triggering of further repair efforts.

5.7.2. Hazard Models

To obtain hazard curves for a particular seismicity scenario (based on geographic location), three probabilities of exceedance (2%, 5%, and 10% in 50 years) are needed. For the case study, the resulting PGV estimates are 170, 110, 80 cm/s, respectively, which are consistent with the location of Samoa Channel Bridge (<https://earthquake.usgs.gov/hazards/interactive/>).

On this basis, Figure 5.30 shows the mean annual frequency (MAF) of exceedance vs. RCR. In addition, Figure 5.30 provides a clear illustration of the increased cost hazard curve associated with the case before the retrofit. Similar conclusions can be drawn from the comparison of the Repair time hazard curves.

5.8. Summary and Conclusions

A PBEE framework was utilized to perform probabilistic seismic performance assessment of an actual bridge-ground system in California (Samoa Channel Bridge). For that purpose, a FE model of the global bridge-ground system was developed using an OpenSees user-interface (MSBridge). Based on the recorded data set, the model was calibrated and verified. SSI was conveniently handled by using a foundation matrix approach. Site-specific ground motions were used to conduct FE simulation. PBEE outcomes were presented within a comparative scope for the cases before and after retrofit. Conclusions were drawn from the simulation results and PBEE outcomes that can be summarized as follow:

1. Beneficial outcomes can result from the adoption of an analysis model that is calibrated and verified by recorded data set.
2. The use of site-specific earthquake ground motions provides a solid basis for understanding

the entire structure-foundation-ground system response and for probabilistically estimating the post-earthquake loss.

3. The response of the bridge piers and foundation matrix remain relatively linear elastic for low shaking earthquake (Ferndale 2010). Conversely, the response shows higher nonlinearity when subjected to strong shaking event (Chi-Chi, tcu068).
4. The seismic retrofit has a significant effect on the bridge resilience by reducing the estimated loss in terms of RCR from 35% to 20% at 2% in 50 years hazard level.
5. Based on the simulation results, abutment DSs (and corresponding repair quantities) are among the main parameters that contribute to the overall loss estimate.

5.9. Acknowledgements

Chapter 5, in full, is currently being prepared for submission for publication of the material as it may appear in the following journal publication (The dissertation author was the primary investigator and author of this paper):

Almutairi, A.S., Lu, J., Wang, N. and Elgamal, A., "Performance-based earthquake assessment for calibrated model of Samoa Channel Bridge".

Table 5.1. Constitutive model parameters for concrete material used in fiber beam-column element

Parameter	Confined concrete	Unconfined concrete
Concrete compressive strength at 28 days, f'_c (kPa)	-3.47×10^4	3.40×10^4
Concrete strain at maximum strength, ϵ_{c0}	-0.0025	-0.002
Concrete crushing strength, f'_{cu} (kPa)	-3.07×10^4	0
Concrete strain at crushing strength, ϵ_{cu}	-0.006	-0.005

Table 5.2. Bridge deck material and section properties for Samoa Bridge (Wang 2015)

Parameter	Between S-8 and S-9	All other locations
Young's modulus (kPa)		2.53×10^7
Shear modulus (kPa)		1.05×10^7
Unit weight (kPa)		25.11
Area of cross-section (m ²)	5.05	3.76
Moment of inertia @ horizontal axis (m ⁴)	6.78	1.68
Moment of inertia @ vertical axis (m ⁴)	41.89	31.72
Torsion constant (m ⁴)	0.98	0.34

Table 5.3. Bridge pier columns material and section properties for Samoa Bridge (Wang 2015)

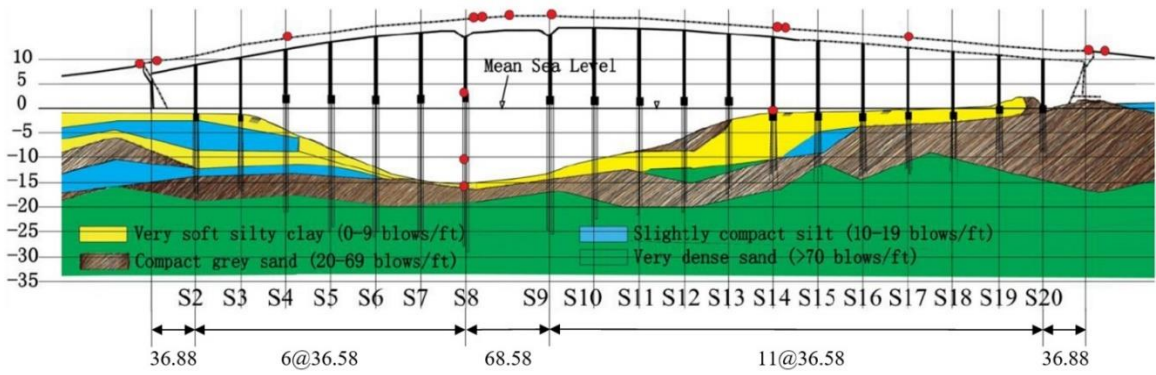
Parameter	Piers S-8 and S-9	All other piers
Young's modulus (kPa)		2.53×10^7
Shear modulus (kPa)		1.05×10^7
Unit weight (kPa)		25.11
Area of cross-section (m ²)	7.01	5.66
Moment of inertia @ horizontal axis (m ⁴)	7.06	5.11
Moment of inertia @ vertical axis (m ⁴)	1.88	1.11
Torsion constant (m ⁴)	5.77	3.53

Table 5.4. Samoa Bridge constant foundation matrix coefficients for all bents (Wang 2015)

Parameter	Value
k_z (kN/m)	5.25×10^6
$k_{rx} = k_{ry}$ (kN/m)	3.50×10^9
k_t (kN-m/rad)	8.75×10^3
$k_{y-rx} = -k_{x-ry}$ (kN)	4.44×10^4



(a)



(b)



(c)

Figure 5.1. Samoa Channel Bridge: (a) photo of the bridge (<http://www.strongmotioncenter.org>); (b) global elevation view of the bridge ; and (c) map view (Wang *et al.* 2018)

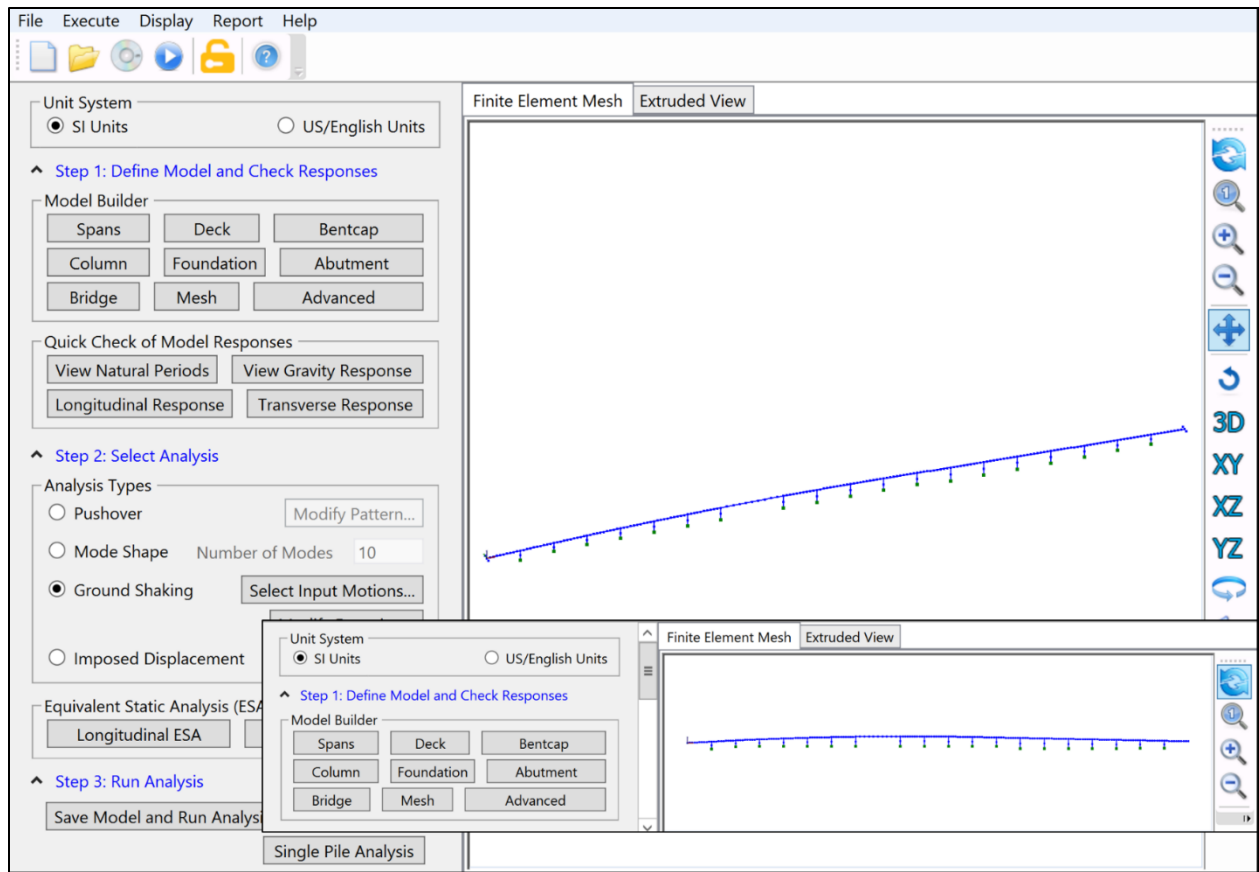


Figure 5.2. Samoa Bridge FE model created in MSBridge (bottom-right window shows the side view of the bridge model)

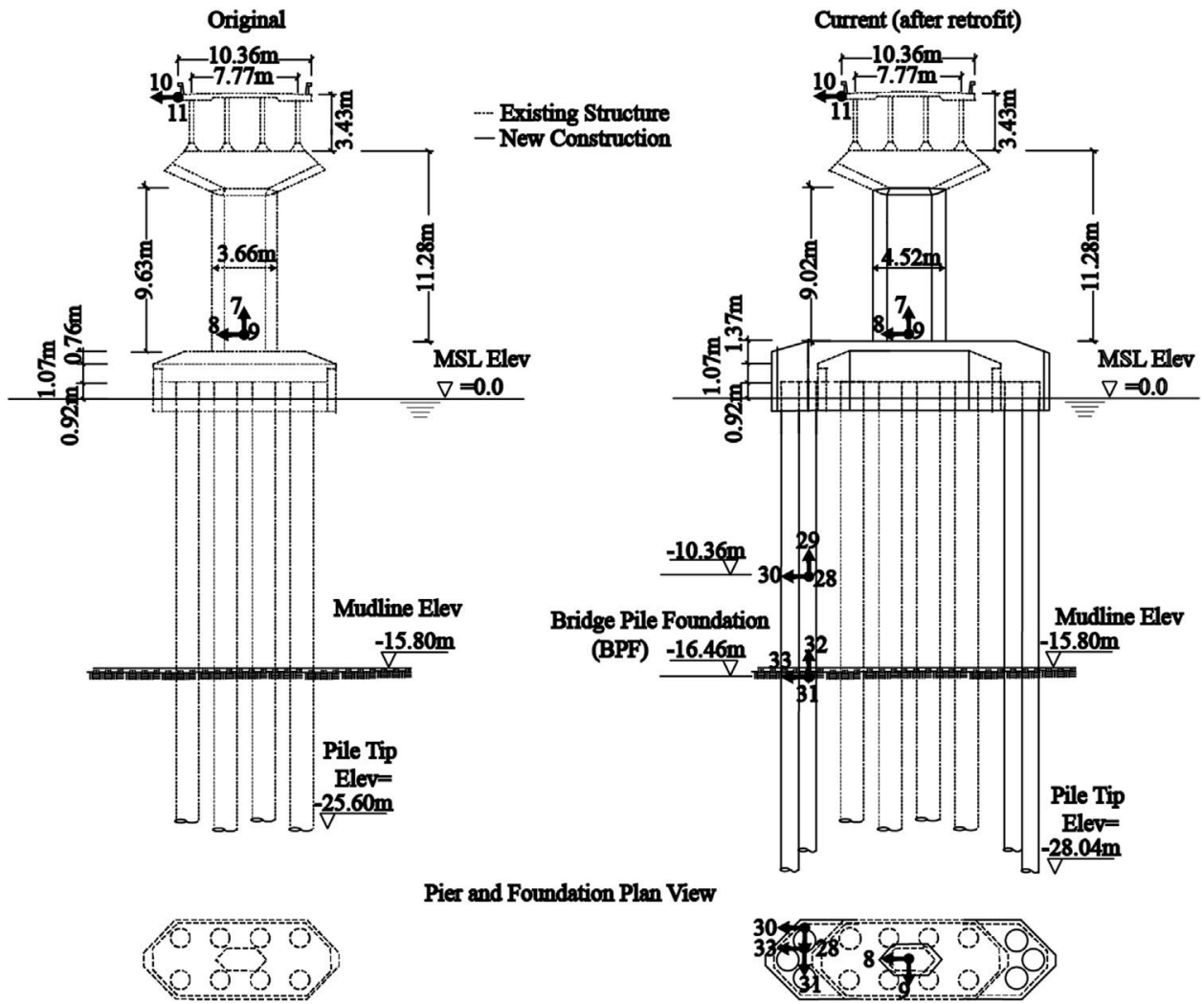


Figure 5.3. Pier S-8 configuration: (a) before retrofit; and (b) after retrofit (Wang *et al.* 2016)

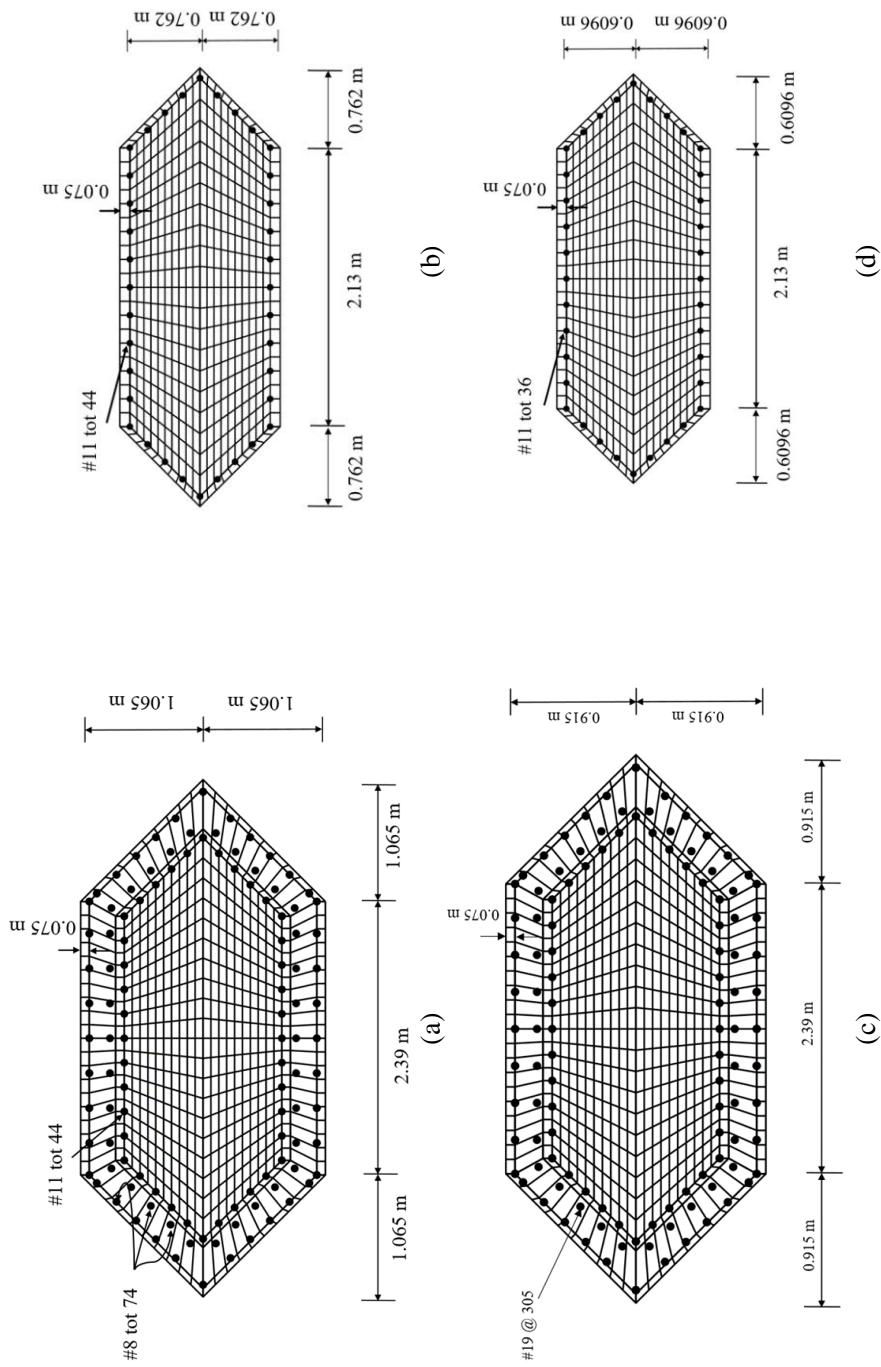


Figure 5.4. Fiber discretization of bridge column cross-sections: (a) Pier S-8 after retrofit; (b) Pier S-8 before retrofit; (c) Pier S-14 after retrofit; and (d) Pier S-14 before retrofit

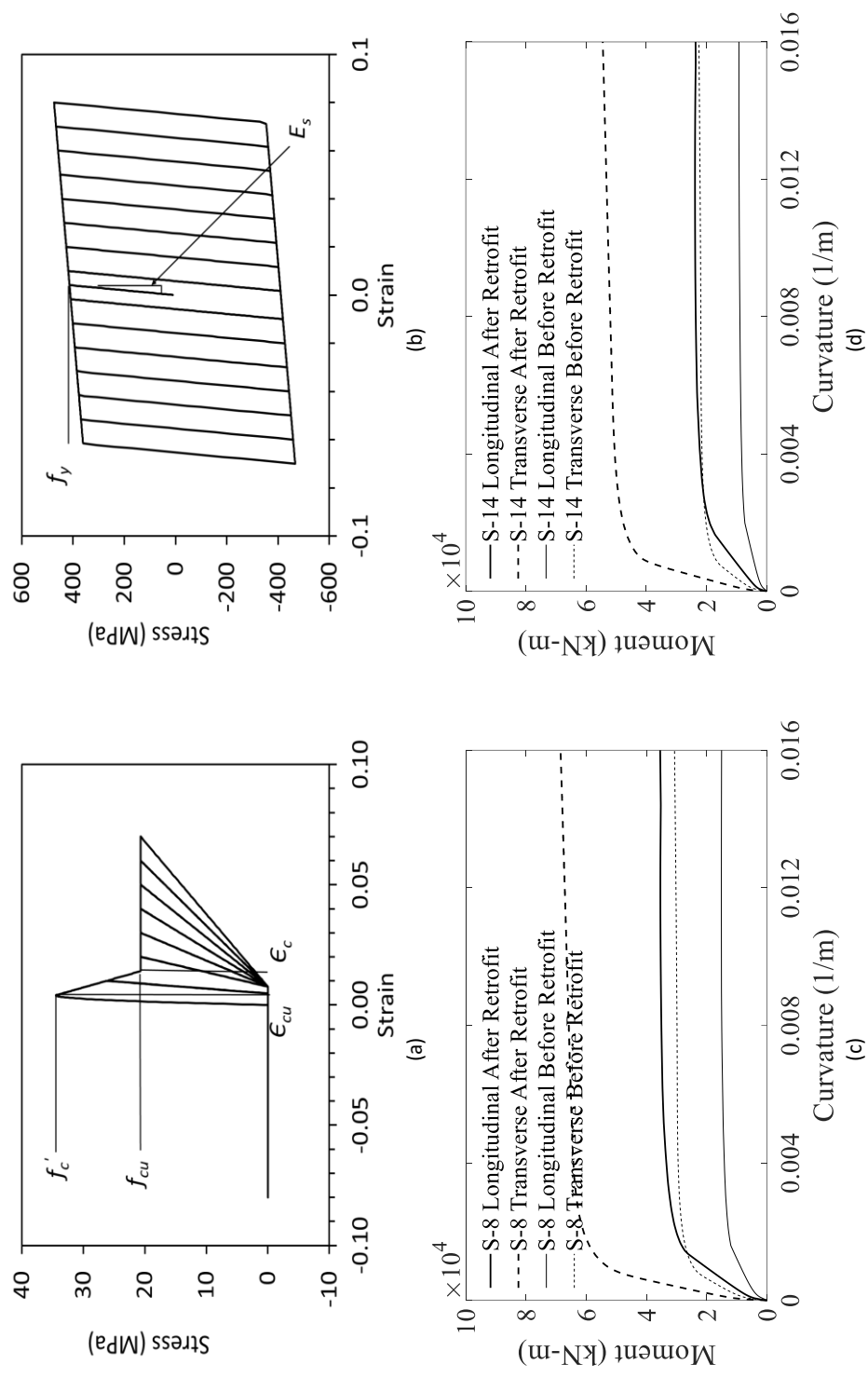


Figure 5.5. Bridge column modeling: (a) core concrete; (b) reinforcing steel; (c) moment-curvature response for Pier S-8; and (d) moment-curvature response for Pier S-14

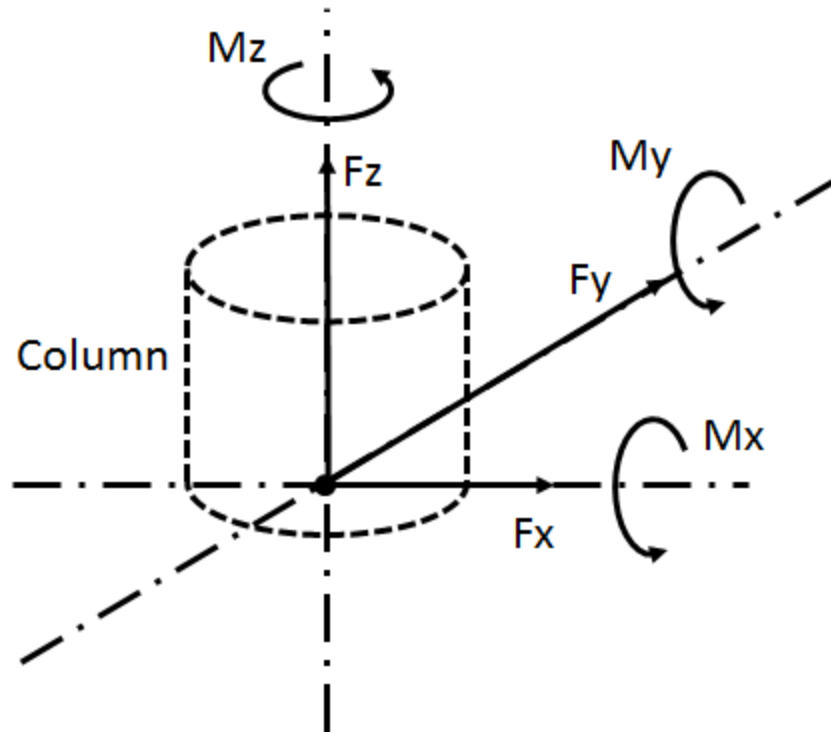


Figure 5.6. Local coordinates system for foundation matrix, where x, y, z are the longitudinal, transverse, and vertical directions (Elgamal *et al.* 2016)

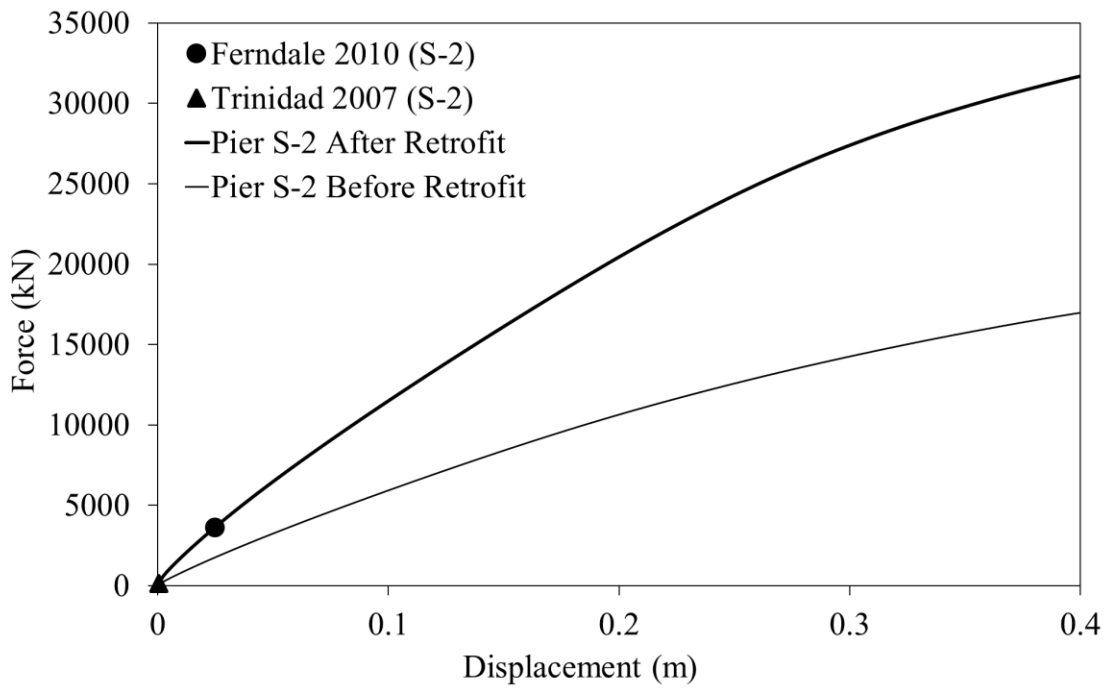


Figure 5.7. Lateral foundation matrix force-displacement relationships for Pier S-2

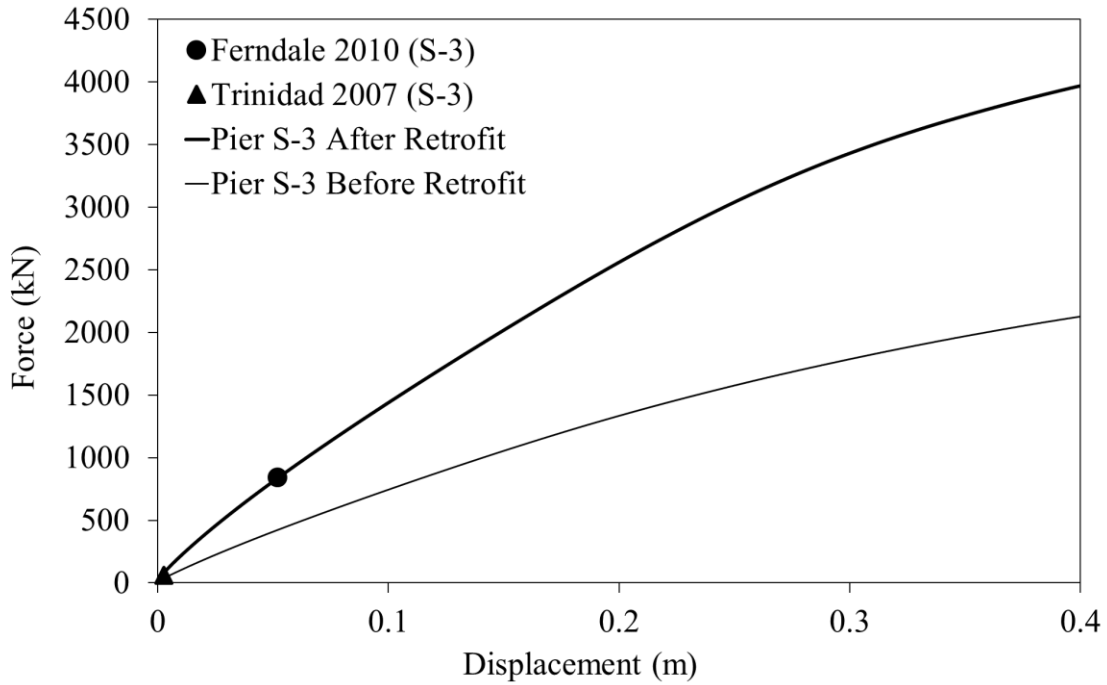


Figure 5.8. Lateral foundation matrix force-displacement relationships for Pier S-3

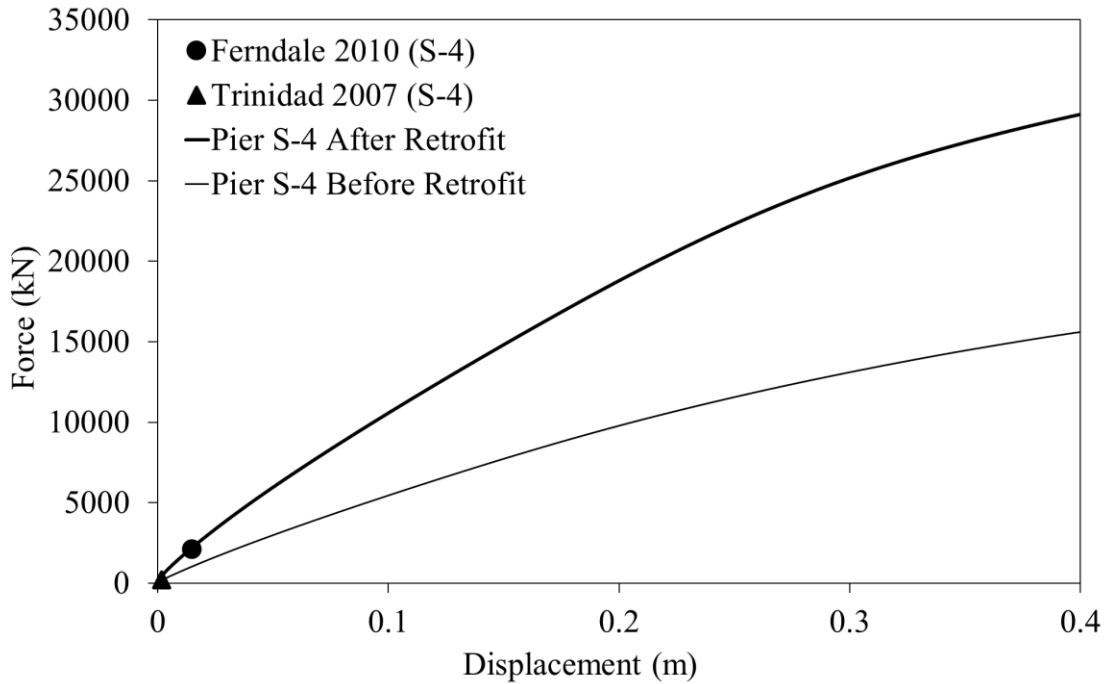


Figure 5.9. Lateral foundation matrix force-displacement relationships for Pier S-4

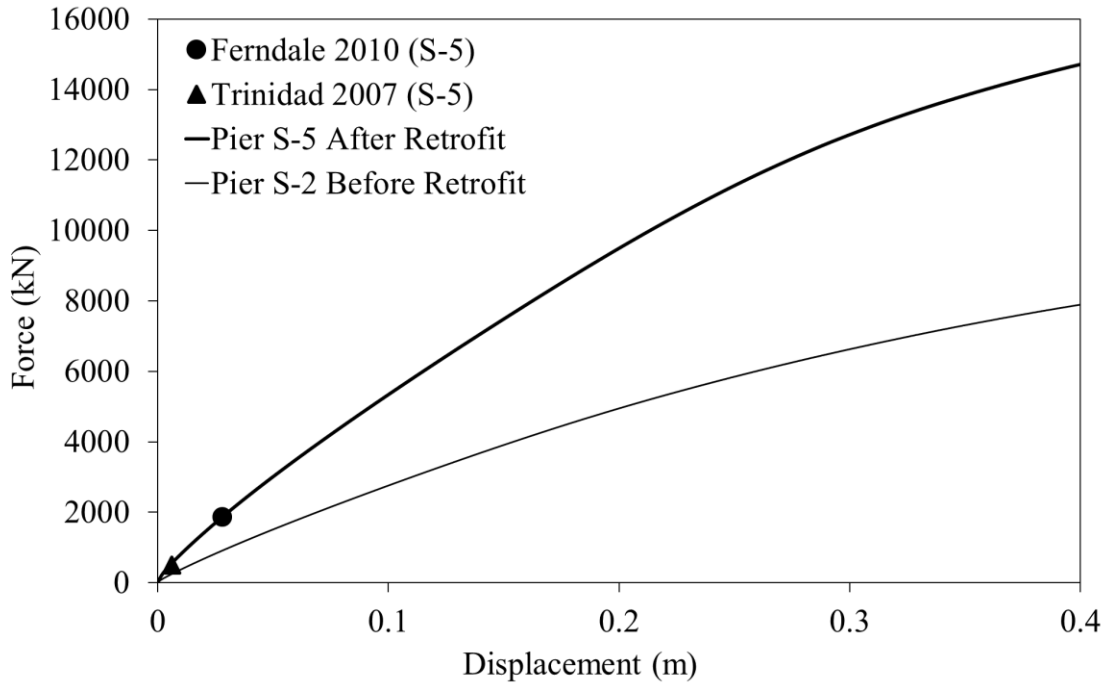


Figure 5.10. Lateral foundation matrix force-displacement relationships for Pier S-5

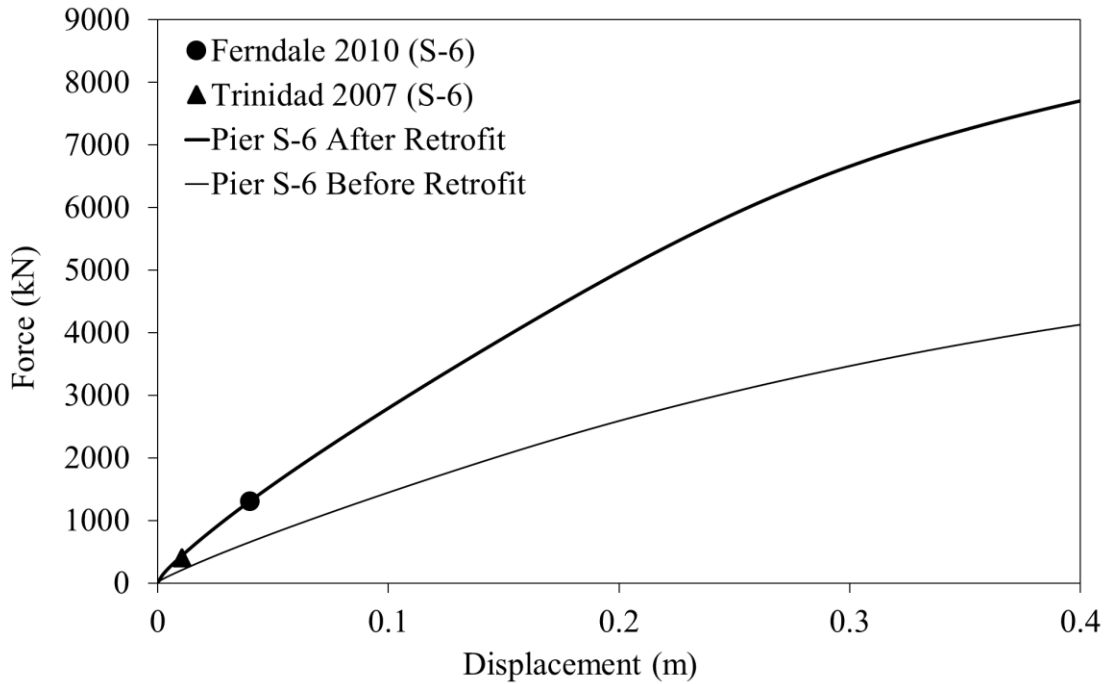


Figure 5.11. Lateral foundation matrix force-displacement relationships for Pier S-6

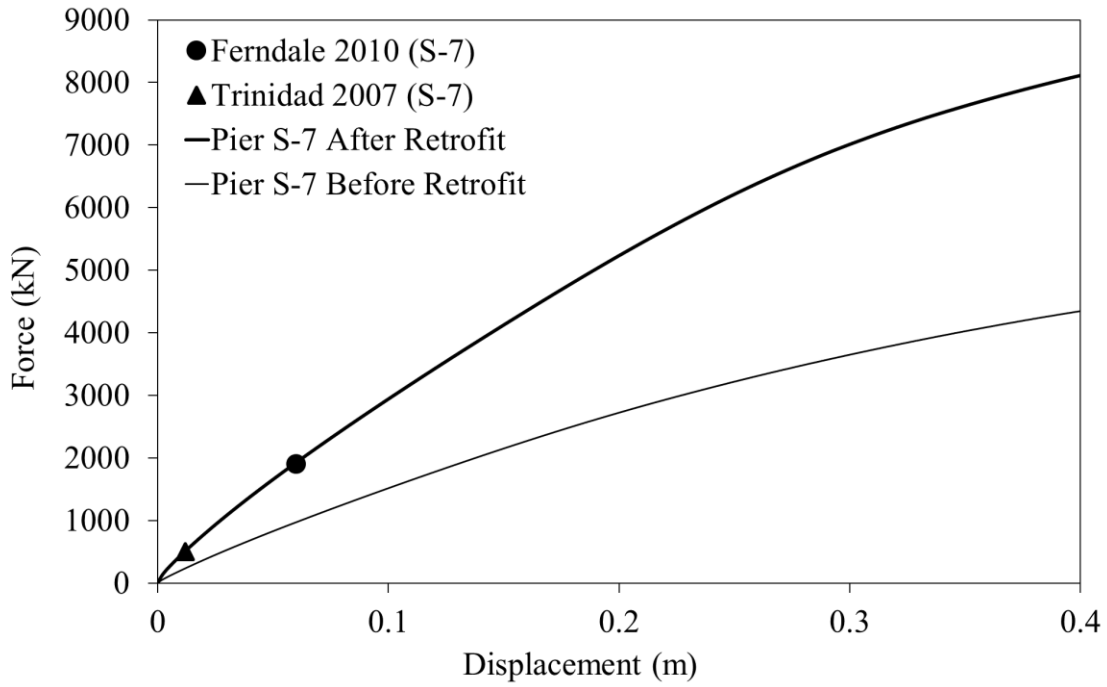


Figure 5.12. Lateral foundation matrix force-displacement relationships for Pier S-7

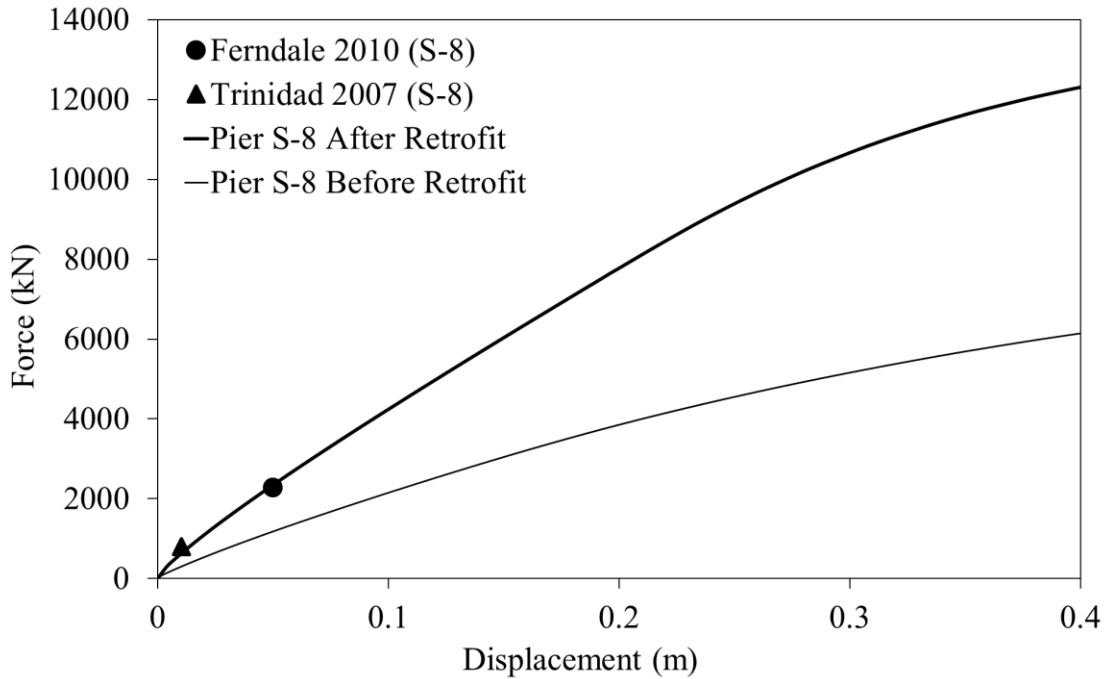


Figure 5.13. Lateral foundation matrix force-displacement relationships for Pier S-8

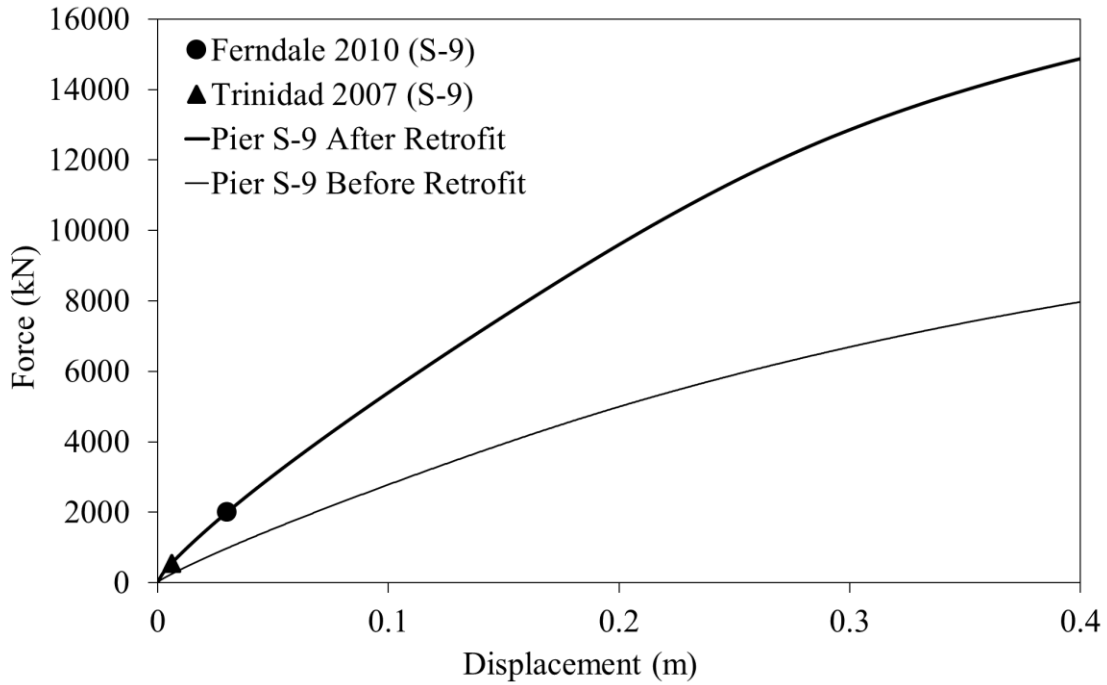


Figure 5.14. Lateral foundation matrix force-displacement relationships for Pier S-9

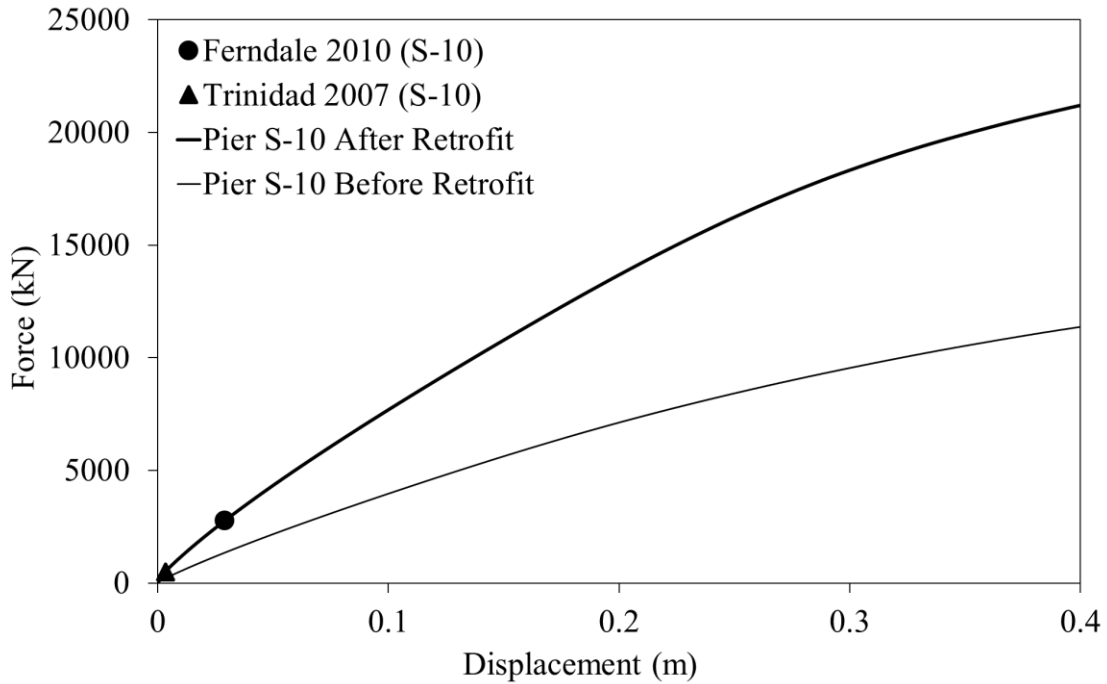


Figure 5.15. Lateral foundation matrix force-displacement relationships for Pier S-10

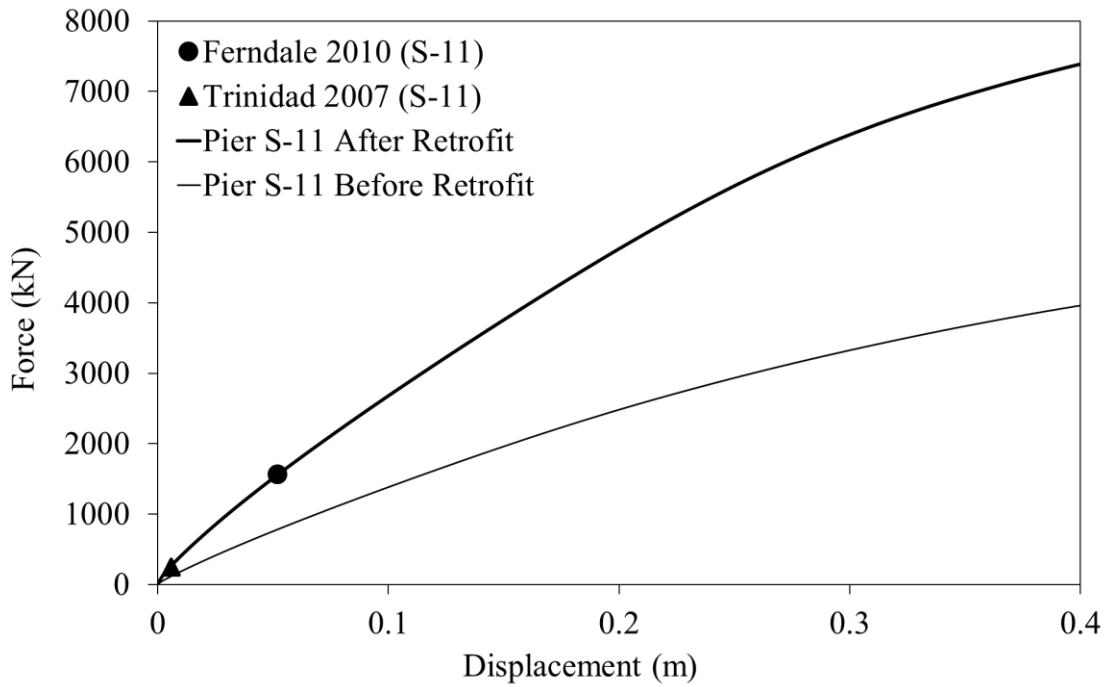


Figure 5.16. Lateral foundation matrix force-displacement relationships for Pier S-11

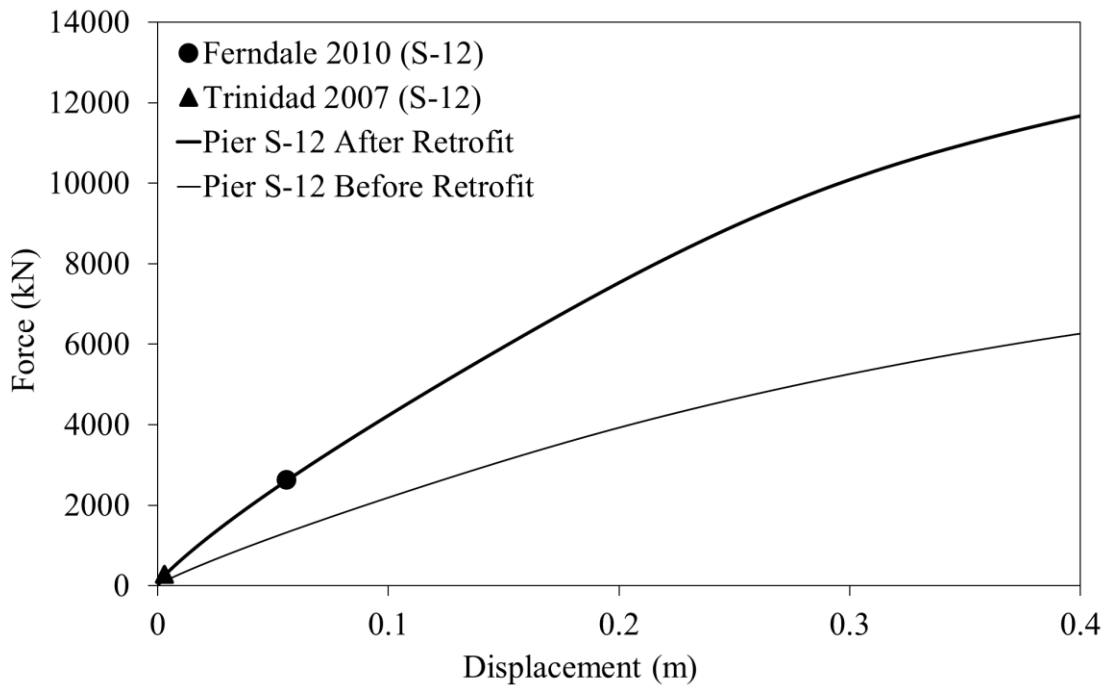


Figure 5.17. Lateral foundation matrix force-displacement relationships for Pier S-12

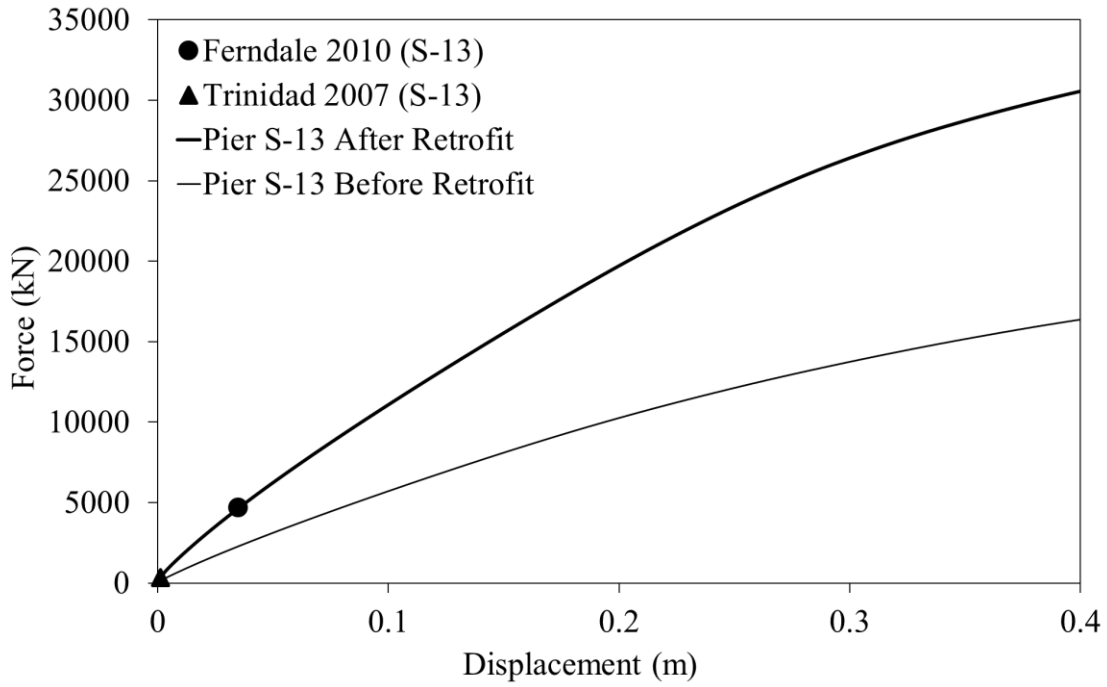


Figure 5.18. Lateral foundation matrix force-displacement relationships for Pier S-13

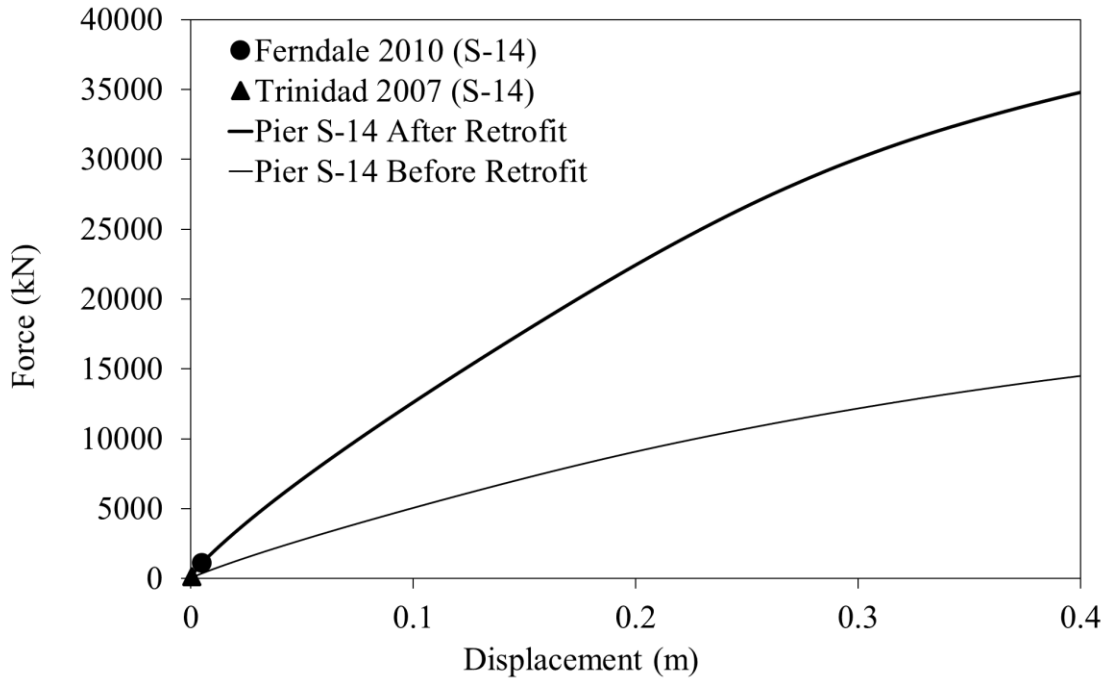


Figure 5.19. Lateral foundation matrix force-displacement relationships for Piers S-14 and S-15

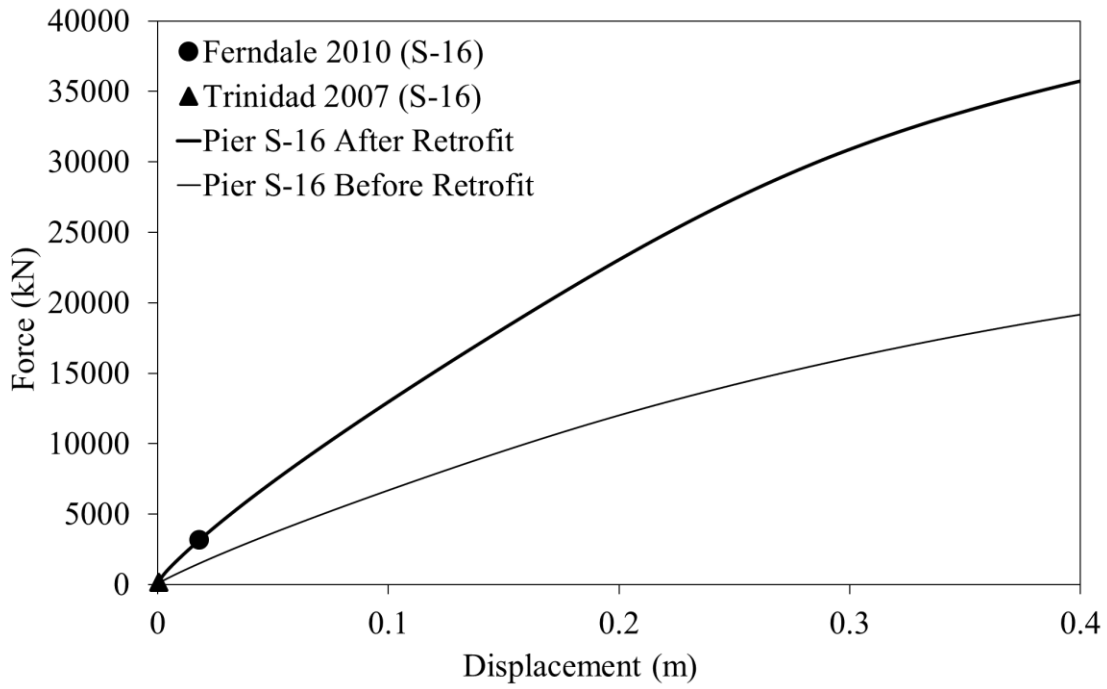
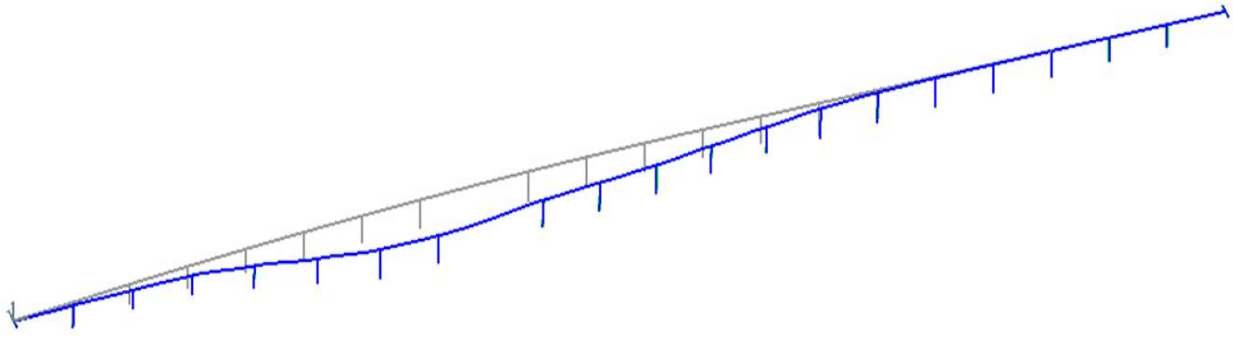
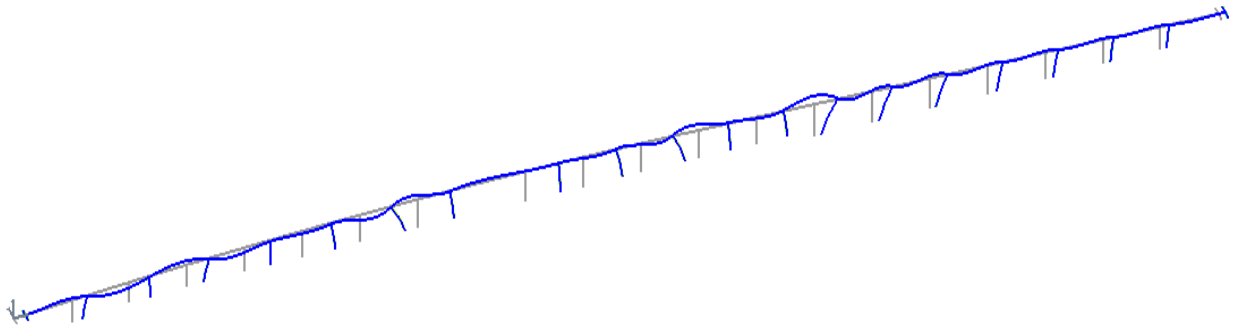


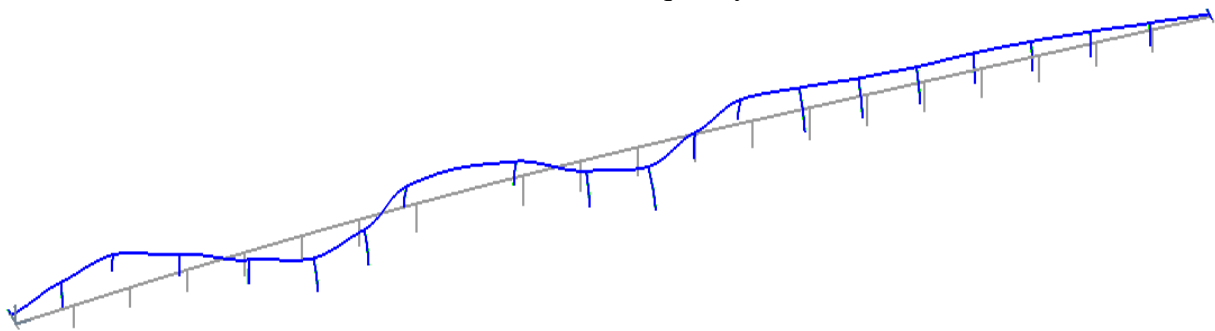
Figure 5.20. Lateral foundation matrix force-displacement relationships for Piers S-16 to S-20



(a) Period = 1.1 sec; frequency = 0.9 Hz

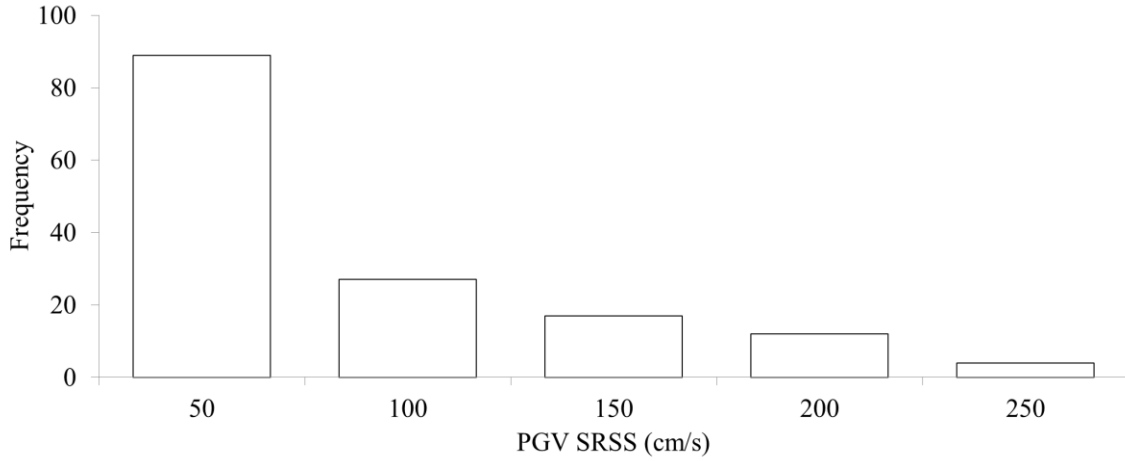


(b) Period = 0.7 sec; frequency = 1.3 Hz

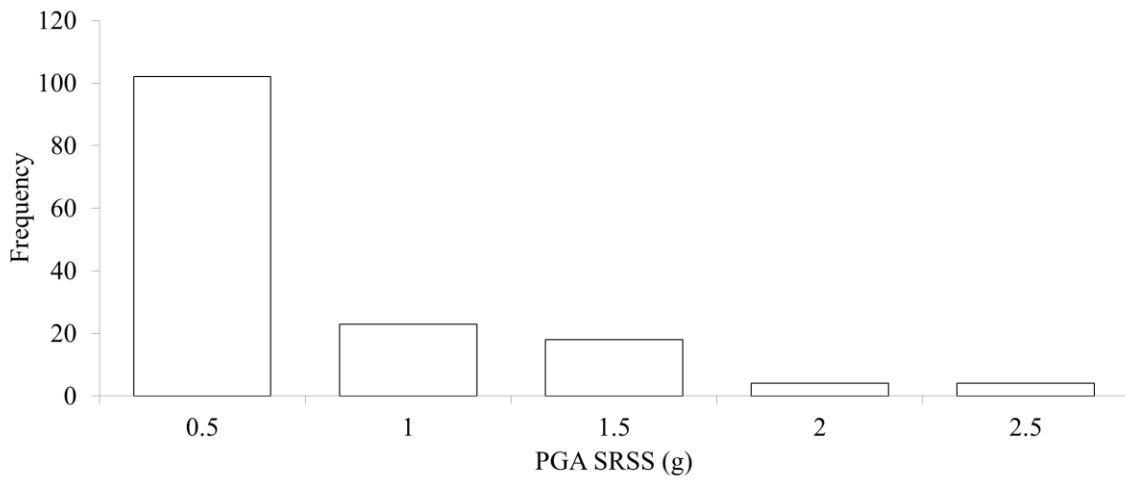


(c) Period = 0.5 sec; frequency = 1.8 Hz

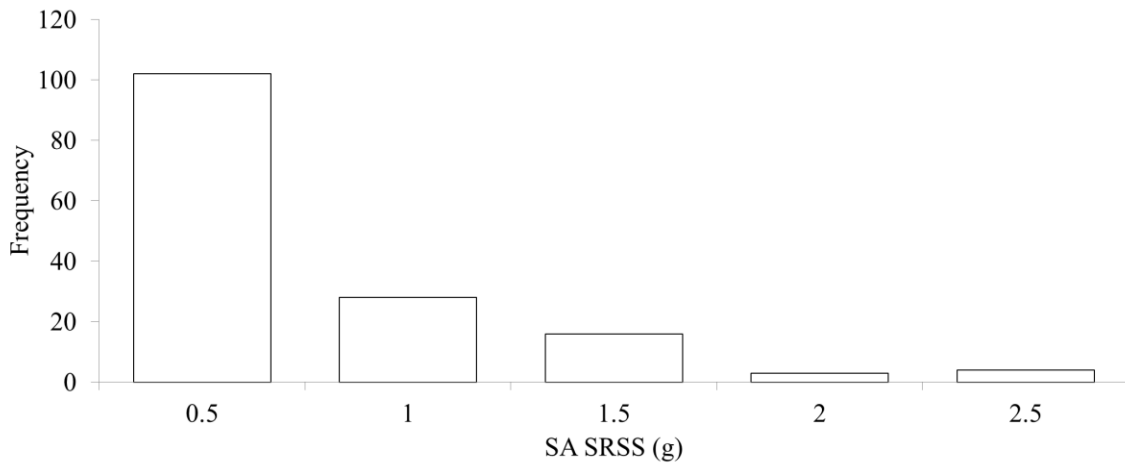
Figure 5.21. Mode shapes for Samoa Bridge (grey lines represent undeformed mesh): (a) first transverse mode; (b) first longitudinal mode; and (c) second transverse mode



(a)



(b)



(c)

Figure 5.22. PGV, PGA and SA distributions for the SRSS (square root of the sum of the squares) of the two horizontal components of ground input motions.

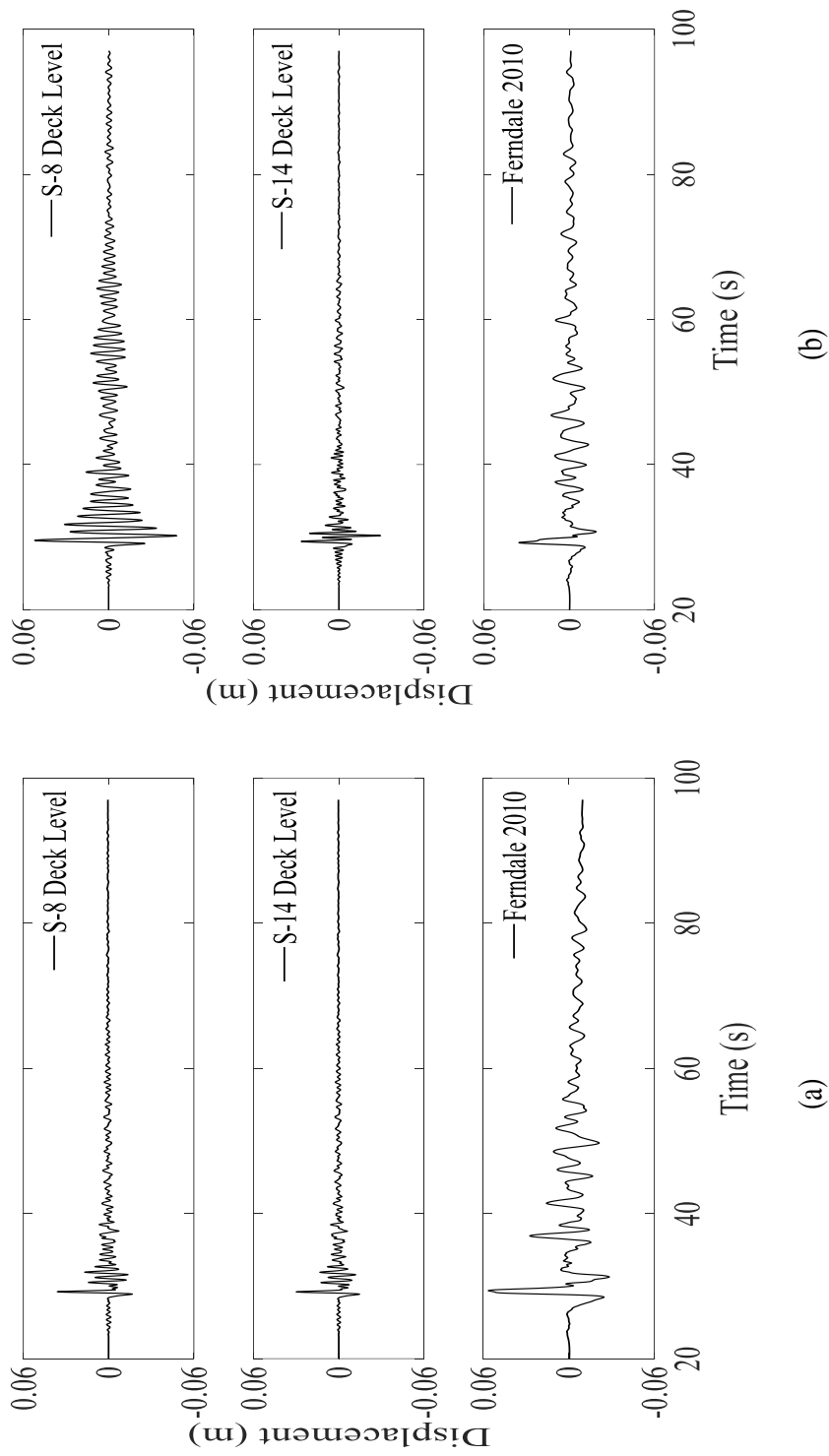


Figure 5.23. Pier S-8 and Pier S-14 column top displacement and input motion time histories for the Ferndale 2010 motion for: (a) longitudinal direction; and (b) transverse direction

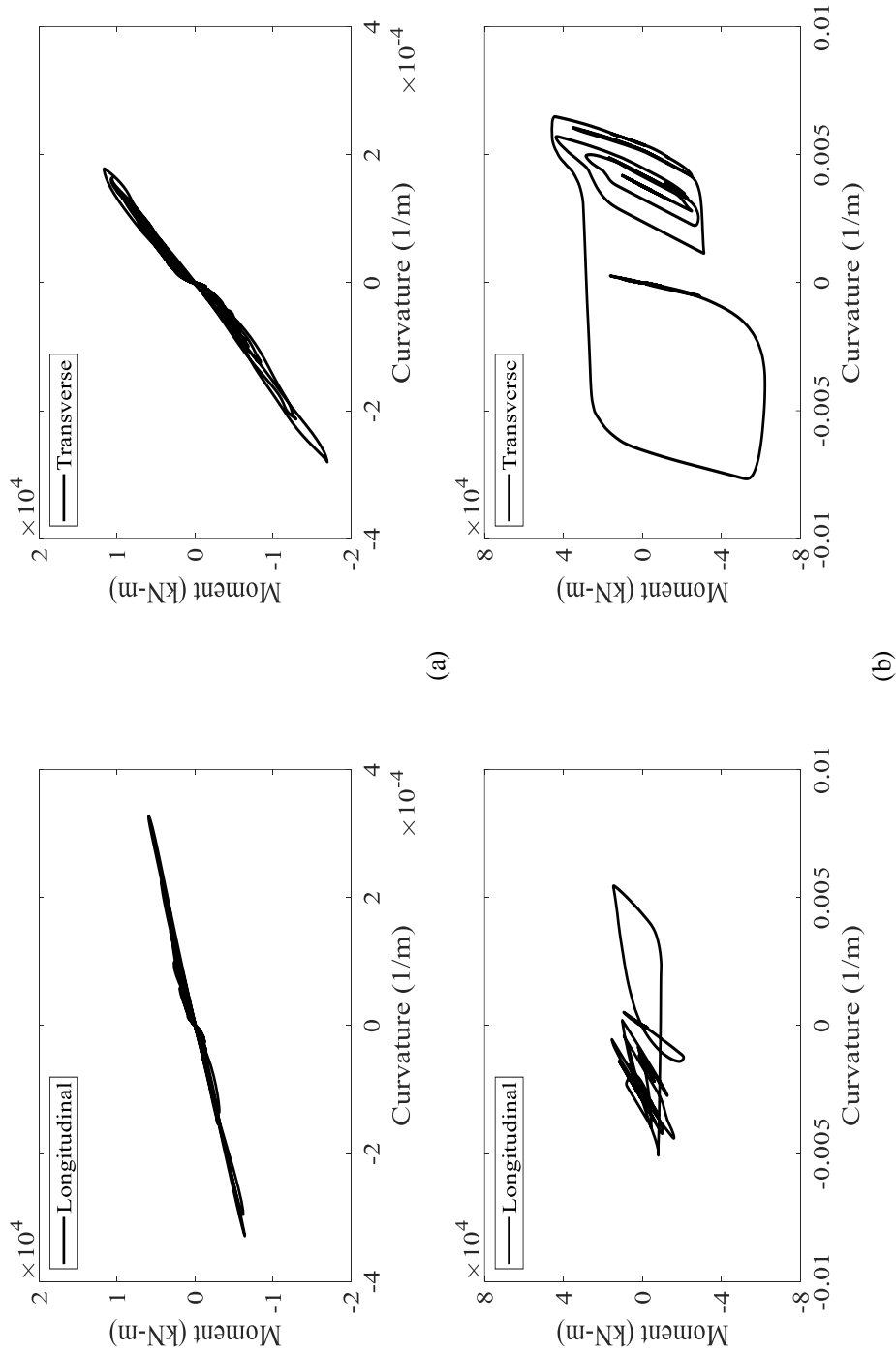


Figure 5.24. Column base moment-curvature response of Pier S-8 for: (a) the Ferndale 2010 motion (low shaking event); and (b) the Chi-Chi (tcu068) motion (strong shaking event)

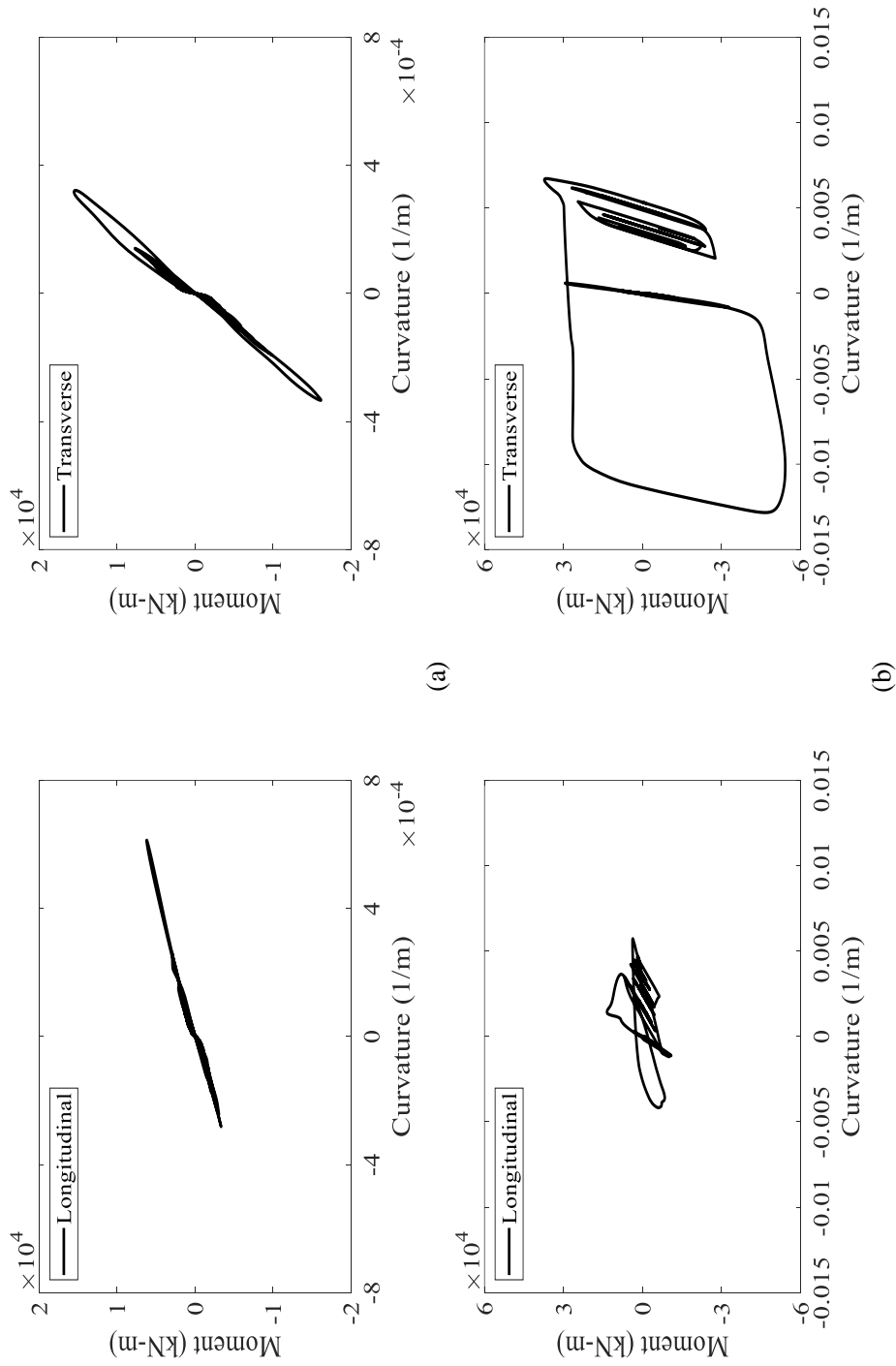


Figure 5.25. Column base moment-curvature response of Pier S-14 for: (a) the Ferndale 2010 motion (low shaking event); and (b) the Chi-Chi (tcu068) motion (strong shaking event)

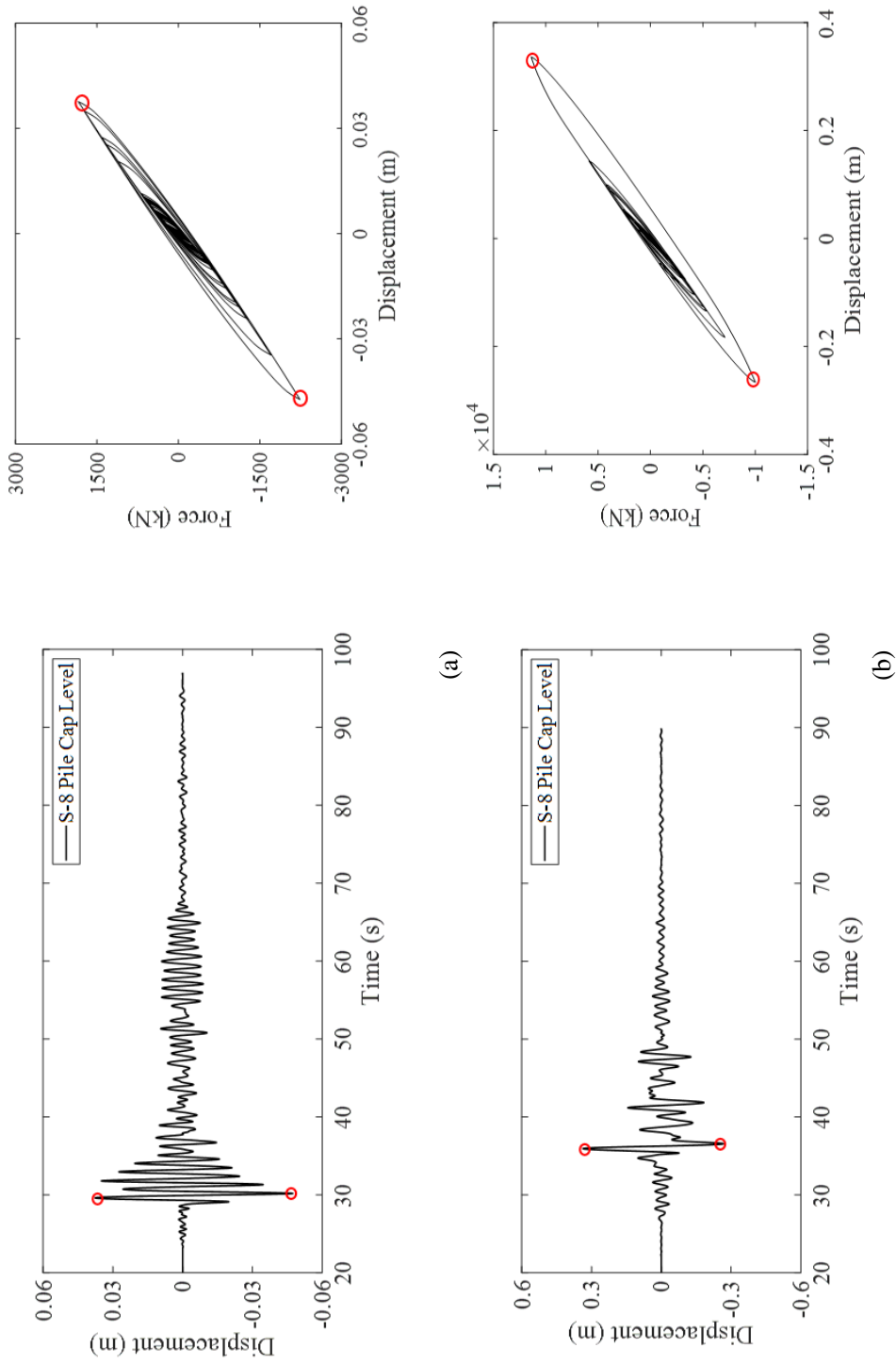
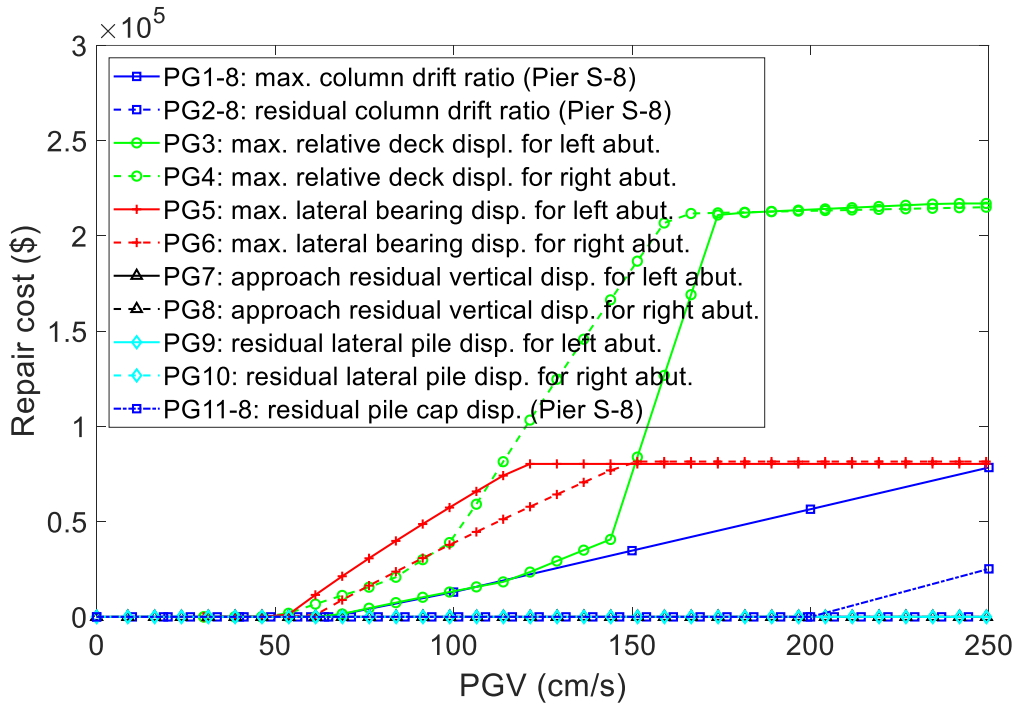
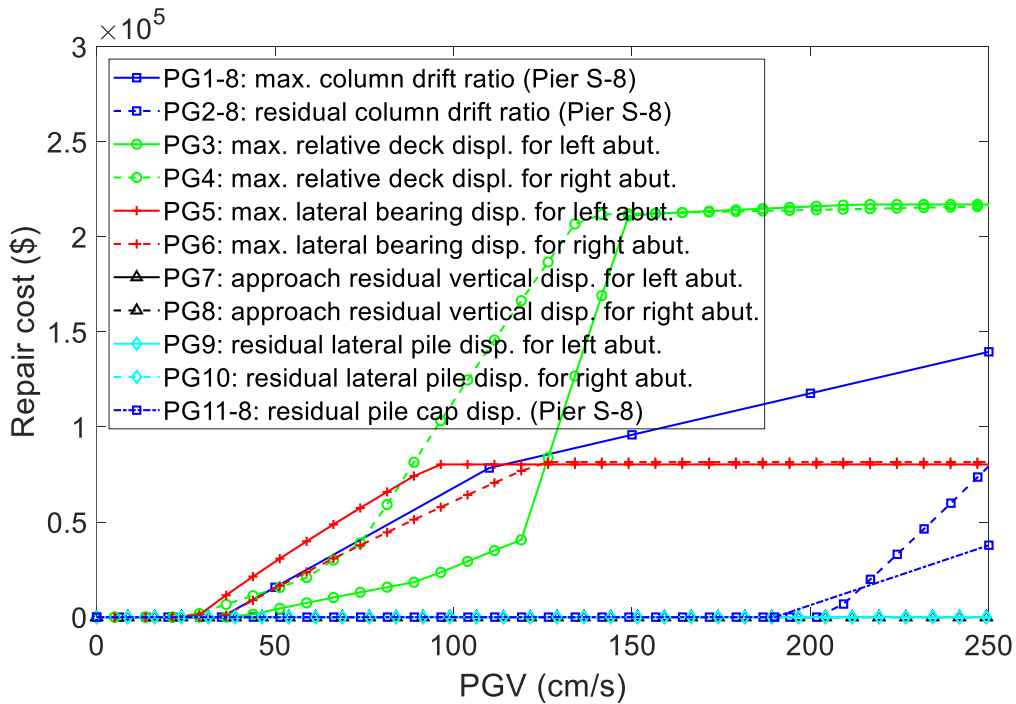


Figure 5.26. Foundation response time history and force-displacement relationship for: (a) the Ferndale 2010 motion (low shaking event); and (b) the Chi-Chi (tcu068) motion (strong shaking event)

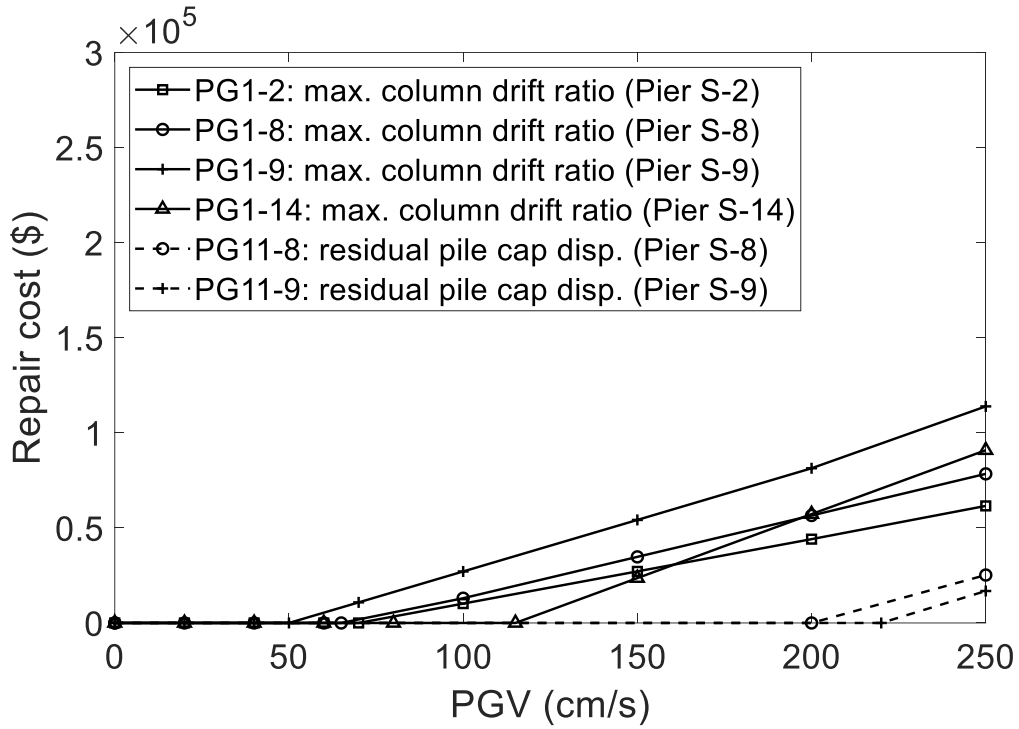


(a)

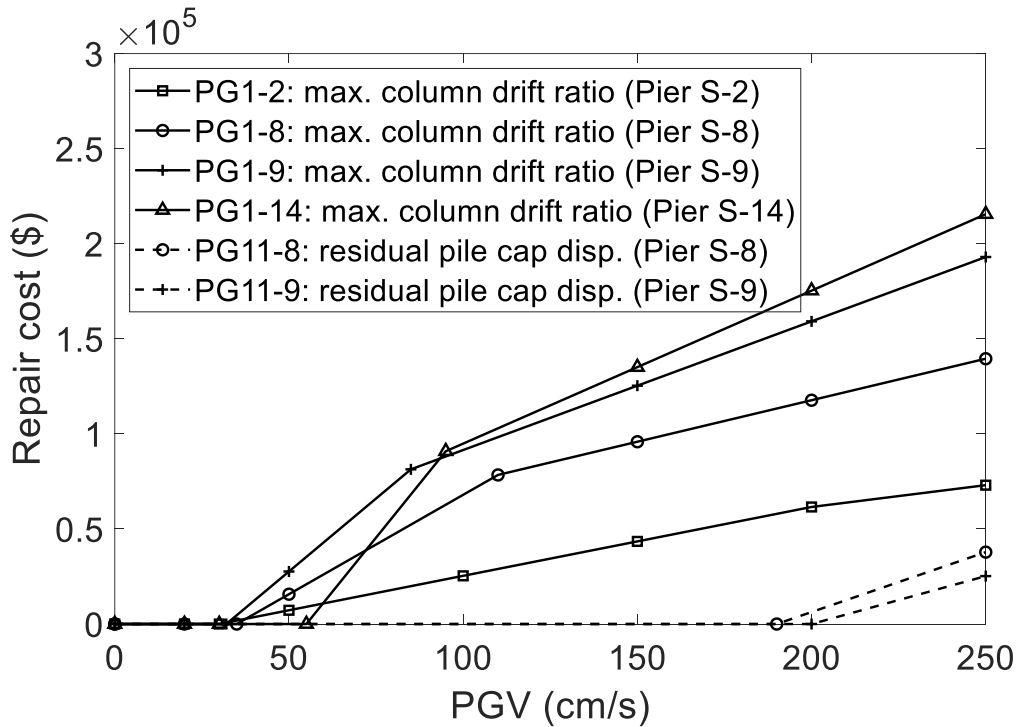


(b)

Figure 5.27. Repair cost contribution for each PG vs. PGV: (a) after retrofit; and (b) before retrofit

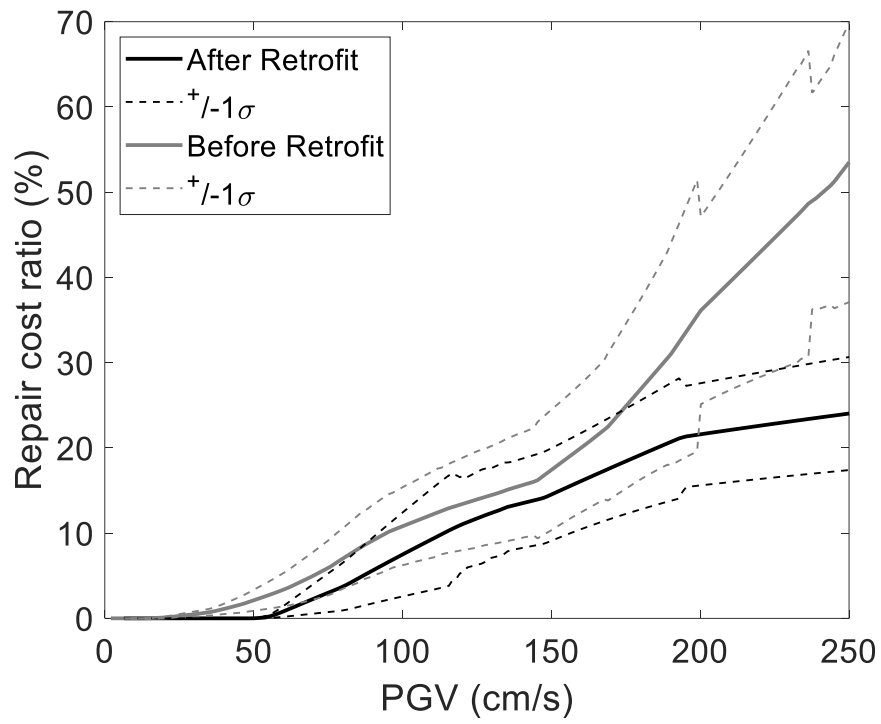


(a)

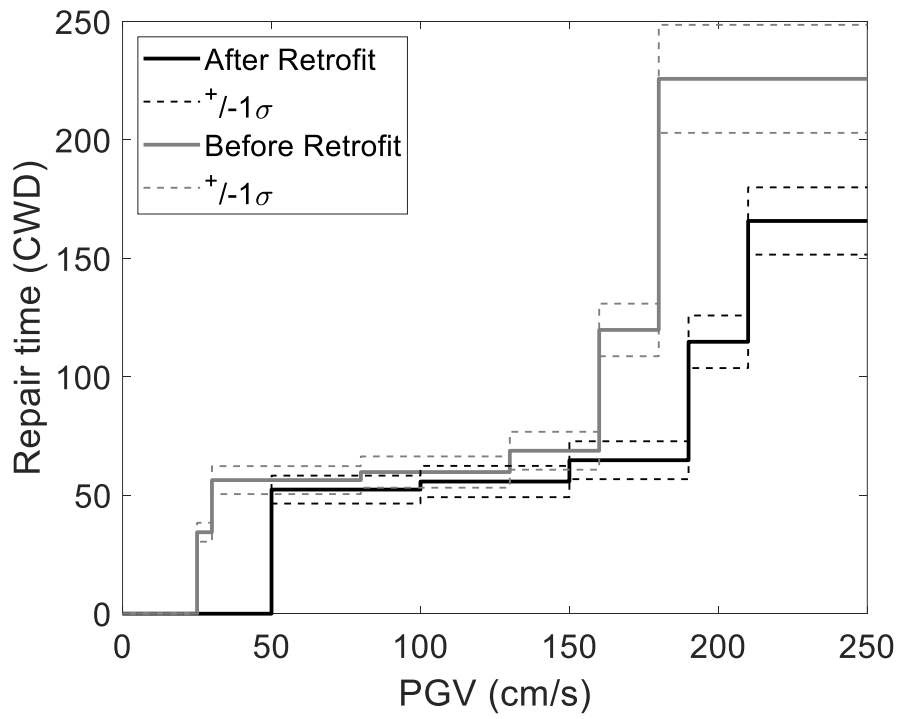


(b)

Figure 5.28. Repair cost contribution for column PGs vs. PGV: (a) after retrofit; and (b) before retrofit

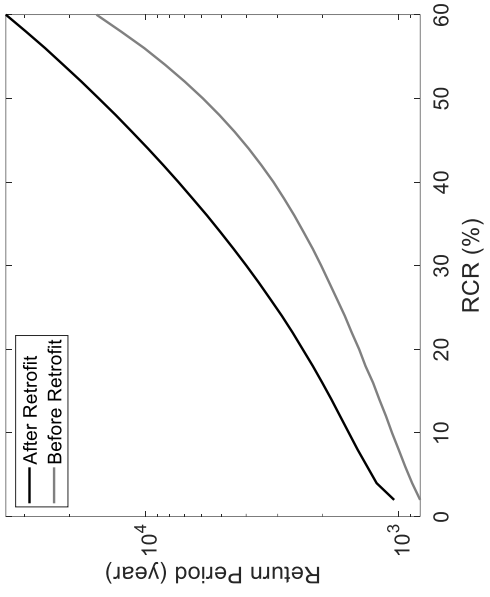


(a)

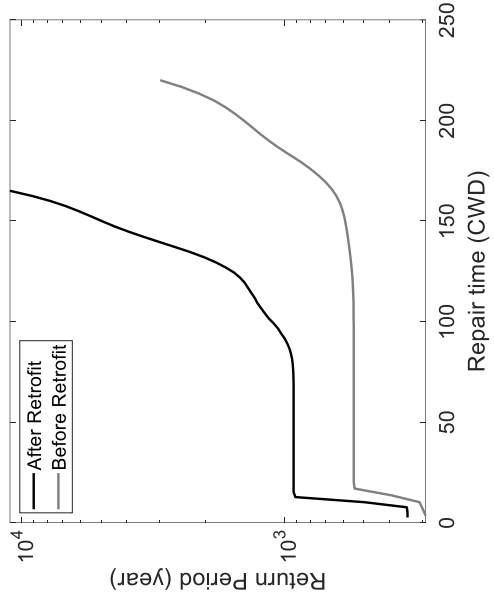


(b)

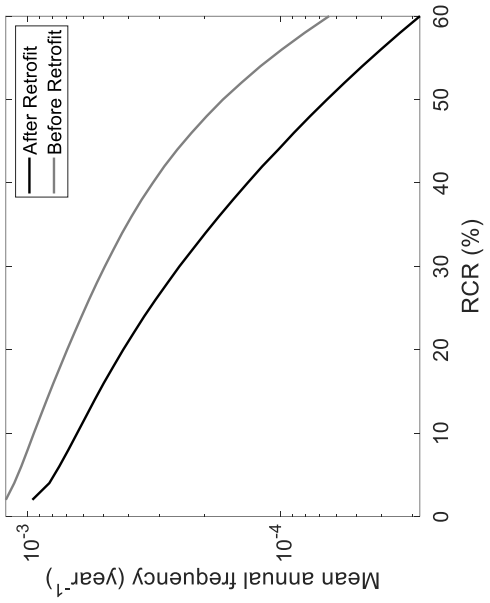
Figure 5.29. Loss models: (a) repair cost ratio; (b) repair time



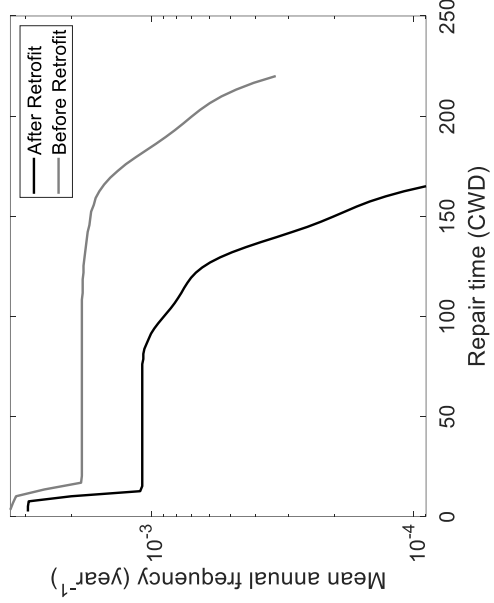
(a)



(b)



(a)



(b)

Figure 5.30. Hazard curves for: (a) repair cost ratio; and (b) repair time

Chapter 6. Seismic Response of Samoa Channel Bridge-Foundation System Subjected to Site-Specific Motions

6.1. Abstract

In this chapter, seismic response was investigated for the Samoa Channel Bridge, a large bridge-foundation-ground system (before and after retrofit) subjected to site-specific input motions that match three hazard levels (Somerville and Collins 2002). For that purpose, a calibrated Finite Element (FE) model was developed for Samoa Channel Bridge system. Three seismic hazard levels were obtained for the geographic location of the bridge, namely 50%, 10% and 2% probability of exceedance in 50 years. As such, ground motions were selected and scaled based on the seismic hazard deaggregation at the site. Seismic demands in terms of maximum column drift ratio as a representative engineering demand parameter (EDP) were obtained via nonlinear structural seismic response simulations. Mean EDP values for each bent which capture the global and local demand and consequent damage to the bridge were presented in a comparative scope for the three hazard levels. In addition, the presented results were contrasted with the case before retrofit for the three hazard levels to show the significance of the undertaken retrofit. Overall, the EDP values increased when a higher hazard level was applied. The levels of column deformation were in the range of about 0.5-2.5%. Conversely, before retrofit case showed higher demands in the range of about 1.0 - 3.5%.

6.2. Introduction

Performance of highway bridges subjected to earthquake motions that match specific hazard levels have been studied by a number of researchers (Kunnath *et al.* 2006; Zhang *et al.* 2008; and Li and Conte 2016). In particular, two earthquake motions were studied by Zhang *et al.* (2008) to represent two hazard levels (i.e., 50% in 50 years and 2% in 50 years) for Humboldt Bay

Bridge. The consequences were presented and discussed for each hazard level. Similarly, in the study by Li and Conte (2016), two earthquake motions were selected and scaled to represent two hazard levels (maximum considered earthquake [MCE] and operating basis earthquake [OBE]).

Three hazard levels were considered in this study: (i) 50% in 50 years, the motion that matches this hazard level represents an occasional event with a reasonable probability of exceedance (i.e., 50 % in 50 years) during the life of the structure. (ii) 10% in 50 years, that represents a rare event with a low probability of exceedance (i.e., 10 % in 50 years) during the life of the structure. (iii) 2% in 50 years, that represents a very rare or maximum credible event with a very low probability of exceedance (i.e., 2% in 50 years) during the life of the structure.

In this chapter, Samoa Channel Bridge was considered for analyzing the salient ground-foundation-structure response mechanisms. For that purpose, Finite Element (FE) modeling was employed to represent the bridge structural elements and configuration. This model was calibrated based on actual recorded data (Chapter 5). The model of the entire bridge was developed, with foundation-matrix springs at each column base (at the pile cap locations).

6.3. Bridge Model

The 20-span Samoa Channel Bridge (hereinafter referred to as “Samoa Bridge”, Figure 5.1) near Eureka in northern California is a 2,506 ft (764 m) long and 34 ft (10.4 m) wide structure connecting Samoa Peninsula and Indian Island (Figure 5.1). The bridge superstructure, which consists of cast-in-place reinforced concrete deck and four pre-cast prestressed concrete I-girders, is supported by 19 single hexagonal concrete pier bents on pile group foundations. More details about the bridge description and modeling can be found in Chapter 5.

6.4. Specification of Ground Motion Input

An ensemble of 51 selected ground motions was employed in the analysis illustrated in this chapter. Each motion is composed of 3 perpendicular acceleration time history components (2 lateral and one vertical). These motions were obtained through earlier efforts by Somerville and Collins (2002) and were selected to be representative of the region of Samoa Channel Bridge. The motions are divided into three bins: i) 50% in 50 years, ii) 10% in 50 years, and iii) 2% in 50 years. Full details about the ground motions data set can be found in Somerville and Collins (2002). Figure 6.1 shows the site hazard spectra for the three considered hazard levels and for two site conditions.

6.4.1. Uniform Hazard Spectra

Uniform hazard spectra for the site are shown in Table 6.1 - Table 6.3. Rock spectra and soil spectra were considered in Somerville and Collins (2002). Soil spectra were generated from the rock site spectra by multiplying the rock spectra by the ratio of soil to rock spectra based on Abrahamson and Silva (1997) ground motion model.

6.4.2. Hazard Deaggregation (Somerville and Collins 2002)

The deaggregation of the hazard at a period of 1.23 seconds is given in Table 6.4 and Table 6.5 for rock site conditions and soil site conditions, respectively. For the 50% in 50 years hazard level, the largest contributions come from magnitude 7 earthquakes within the Gorda Plate, which underlies the site at a depth of 20 km. For the 10% in 50 years hazard level, the largest contributions come from magnitude 7.5 shallow thrust earthquakes on the Little Salmon fault. For the 2% in 50 years hazard level, the largest contributions come from magnitude 8 of a large subduction earthquake on the Gorda – North America plate interface and rupture of the Little Salmon fault, modeled as an imbricate fault connected to the plate interface at depth.

6.4.3. Process for Selecting Ground Motions (Somerville and Collins 2002)

The selected motions satisfy to the extent possible the magnitude and distance combinations from the deaggregation listed in Table 6.4 and Table 6.5. All motions are from earthquakes in subduction zone environments. In most cases, the selected motions are from earthquakes having appropriate magnitudes, distances and faulting style (thrust). Table 6.6 - Table 6.8 shows the earthquake motions that were classified using broad rock and soil categories.

6.4.4. Time Histories for 50% in 50 years (Somerville and Collins 2002)

The time histories used to represent 50% in 50 years ground motions are shown in Figure 6.2 - Figure 6.5. It is worth noting that only the longitudinal and transverse components are presented in this study since the results of the seismic demands are the square root sum of squares sum (SRSS) of the maximum tangential drift ratio. A number of earthquakes that satisfy the deaggregation of hazard spectra shown in Table 6.4 and Table 6.5 were used. Earthquakes in the Cape Mendocino region are described by Oppenheimer *et al.* (1993) and Hagerty and Schwartz (1996). The two 1992 aftershocks occurred within the subducting Gorda Plate, which is the type of event that controls the seismic hazard at the site at this return period. Both aftershocks had strike-slip focal mechanisms. Somerville and Collins (2002) used moderate scale factors, mostly in the range of 0.5 to 3.0, to scale these recordings to the spectra at 1.23 seconds period. Table 6.6 shows the time histories representing 50% in 50 years hazard level along with the scale factors.

6.4.5. Time Histories for 10% in 50 years (Somerville and Collins 2002)

Similarly, the time histories used to represent 10% in 50 years ground motions are shown in Figure 6.6- Figure 6.9. These time histories are from diverse earthquakes. Two are from the 1992 Cape Mendocino earthquake, which may have occurred on the interface between the Gorda and North American plates (Oppenheimer *et al.* 1993). Two are from the 1978 Tabas, Iran

earthquake (Hartzell and Mendoza 1991). Fifteen are from the 1999 Chi-Chi, Taiwan earthquake (Ma *et al.* 2001; Thio *et al.* 2001). Scale factors in the range of 1.0 to 4.2 were used to match the spectra at 1.23 seconds period for 10% in 50 years. Table 6.7 shows the time histories representing 10% in 50 years hazard level along with the scale factors.

6.4.6. Time Histories for 2% in 50 years (Somerville and Collins 2002)

Similarly, the time histories used to represent 2% in 50 years ground motions are shown in Figure 6.10 and Figure 6.11. These time histories are from large interplate subduction earthquakes: the 1985 Valparaiso, Chile and Michoacan, Mexico earthquakes (Somerville *et al.* 1990). Large scale factors in the range of 1.9 to 11.5 were used to match the spectra at 1.23 seconds period for 50% in 50 years. Table 6.8 shows the time histories representing 20% in 50 years hazard level along with the scale factors.

6.4.7. Scaling of the Ground motions (Somerville and Collins 2002)

For each set of recordings, scaling factors were found to match the strike parallel (longitudinal) time history to the strike parallel (longitudinal) uniform hazard spectrum at a period of 1.23 sec. These scaling factors were then applied to all three components of the recording. This scaling procedure preserves the relative scaling between the three components of the recording. Consequently, the transverse component is larger than the longitudinal component at longer periods for many of the recordings.

6.5. Nonlinear Time History Analysis

All simulations were carried out using Newmark's implicit algorithm with $\gamma = 0.5$ and $\beta = 0.25$, which assumes average acceleration between two successive time steps. Rayleigh damping was used with a 5% damping ratio (defined at the periods of 1 and 0.167 second) in the nonlinear THA. Variable time-stepping scheme (VariableTransient) was used in the conducted nonlinear

THA. The starting value for each step Δt was taken equal to or less than the interval of the earthquake input to ensure reliable results.

6.5.1. Simulation of Seismic Demand (Engineering Demand Parameters)

The developed simulation model for Samoa Bridge was subjected to 51 input motions that represent the three hazard levels. The outcomes of this phase generate the values of EDP of interest for use in the performance assessment of the bridge.

6.5.2. Primary EDP Used in Evaluation

Numerous EDPs at the structural level and foundation system can be recorded for each simulation as explained in previous chapters. However, the choice of an EDP for this study was influenced by variabilities it can produce to distinguish between the demands of each hazard level. Therefore, the primary EDP is the peak tangential drift of the individual columns. The EDP is a measure of the larger relative lateral deformation from the column top to the base of the column. Similar to Chapter 5, the results of the case after retrofit and the case before retrofit are presented and compared.

6.5.3. Variation of Bridge Column Drift Ratio

Figure 6.12 shows the variation of the mean column drift ratio for each bent using the three hazard levels defined in Somerville and Collins (2002). The corresponding level of deformation shown in Figure 6.12 in the range of about 0.5-2.5% for the case after the retrofit, with the lower values for shorter columns (i.e., S17 – S20, Figure 5.1). In addition, the case before retrofit shows higher demands in the range of about 1-3.5%.

6.6. Conclusions

This chapter presents a study of a calibrated bridge-foundation system, Samoa Channel Bridge, response in terms of the column drift ratio EDP. Site-specific motions, namely, 50%, 10%

and 2% probability of exceedance in 50 years, were selected, at which subsequent structural seismic response simulations were performed. The deaggregation of the seismic hazard was performed by Somerville and Collins (2002) to find out the magnitude and distance combinations at each of three selected seismic hazard levels. A total of 51 ground motion records were selected to satisfy to the extent possible the magnitude and distance combinations revealed by the deaggregation analysis. These records were scaled to match the IM value at the corresponding seismic hazard level.

A nonlinear finite element (FE) model was developed for the bridge foundation-ground system to investigate the bridge seismic demands. SSI was handled using Foundation Matrix approach calibrated using the actual bridge response of this heavily instrumented bridge after the retrofit program. The most significant findings can be summarized below:

- (i) The use of a developed set of site-specific time histories can provide an effective mechanism for understanding the entire structure-foundation-ground system and reliably investigating the seismic demands.
- (ii) The response of the bridge piers remains linear to earthquakes with a probability of exceedance of 50% in 50 years and as such minor damage is expected. Conversely, the results show higher demands to earthquakes at 2% in 50 years seismic hazard level.
- (iii) Based on the simulation results, the column drift ratios were found to be in the range of about 0.5-2.5% for the case after the retrofit. On the other hand, larger demands were found for the case before retrofit with values that are in the range of about 1.0 - 3.5%.

6.7. Acknowledgements

Chapter 6, in full, is currently being prepared for submission for publication of the material as it may appear in the following journal publication (The dissertation author was the primary investigator and author of this paper):

Almutairi, A.S., Lu, J., Wang, N. and Elgamal, A., “Probabilistic Seismic Response of Samoa Channel Bridge including ground-foundation interaction”.

Table 6.1. Uniform hazard spectra, 5% damping, 50% in 50 years (Somerville and Collins 2002)

Samoa Channel Bridge – 50% in 50 Years		
Period	Rock	Soil
0.01	0.39	0.324
0.1	0.75	0.546
0.2	0.87	0.712
0.3	0.82	0.801
0.5	0.62	0.762
1	0.327	0.5
1.23	0.25	0.42
1.5	0.211	0.37
2	0.149	0.264
3	0.089	0.16

Table 6.2. Uniform hazard spectra, 5% damping, 10% in 50 years (Somerville and Collins 2002)

Samoa Channel Bridge – 10% in 50 Years		
Period	Rock	Soil
0.01	0.77	0.515
0.1	1.42	0.795
0.2	1.73	1.126
0.3	1.68	1.366
0.5	1.3	1.427
1	0.704	1.074
1.23	0.52	0.9
1.5	0.432	0.785
2	0.333	0.61
3	0.193	0.362

Table 6.3. Uniform hazard spectra, 5% damping, 2% in 50 years (Somerville and Collins 2002)

Samoa Channel Bridge – 2% in 50 Years		
Period	Rock	Soil
0.01	1.25	0.89
0.1	2.35	1.421
0.2	2.8	1.949
0.3	2.75	2.359
0.5	2.3	2.609
1	1.273	1.943
1.23	0.925	1.59
1.5	0.756	1.359
2	0.554	1.006
3	0.341	0.632

Table 6.4. Deaggregation of hazard spectra, 5% damping, rock (Somerville and Collins 2002)

Hazard Level	S_a at 1.23 sec	M mode	R (km)
50% in 50 years	0.25	7	20
10% in 50 years	0.52	7.5	5
2% in 50 years	0.925	8	15

Table 6.5. Deaggregation of hazard spectra, 5% damping, soil (Somerville and Collins 2002)

Hazard Level	S_a at 1.23 sec	M mode	R (km)
50% in 50 years	0.42	7	20
10% in 50 years	0.9	7.5	5
2% in 50 years	1.59	8	15

Table 6.6. Time histories representing the 50% in 50 years hazard level (Somerville and Collins 2002)

Earthquake	Magnitude	Station	Distance (km)	Site	Scaling Factor
Honeydew, 1991	6.1	Cape Mendocino	20	rock	2.4531
		Petrolia	17	soil	3.8325
Cape Mendocino, 1992	6.8	Bunker Hill	8.8	rock	0.7403
		Butler Valley	37	rock	1.2458
		Centerville	16	soil	1.3733
		Eureka College	21	soil	1.3054
		Eureka School	24	soil	1.8152
		Ferndale	14	soil	0.658
		Fortuna	13	soil	1.9781
		Loleta	17	soil	1.5969
		Rio Dell	13	soil	4.9913
Cape Mendocino aftershock, 1992	6.6	Bunker Hill	27	rock	1.4670
		Centerville	27	soil	2.3654
		Eureka College	46	soil	2.3149
		Eureka School	48	soil	3.0937
		Ferndale	34	soil	2.3805
		Fortuna	43	soil	3.0577
		Loleta	41	soil	2.2928
Cape Mendocino aftershock, 1992	6.6	Bunker Hill	27	rock	0.8592
		Centerville	28	soil	3.6598
		Ferndale	34	soil	0.8964
		Fortuna	43	soil	2.3033

Table 6.7. Time histories representing the 10% in 50 years hazard level (Somerville and Collins 2002)

Earthquake	Magnitude	Station	Distance (km)	Site	Scaling Factor
Tabas, 1978	7.4	Dayhook	14	rock	2.5058
		Tabas	1.1	rock	1.1124
Cape Mendocino, 1992	6.8	Cape Mendocino	6.9	rock	1.0262
		Petrolia	8.1	soil	2.1611
Chi-Chi, 1999	7.6	TCU052	1.4	soil	0.7781
		TCU065	5	soil	1.1207
		TCU067	2.4	soil	1.7928
		TCU068	0.2	soil	1.2273
		TCU071	2.9	soil	1.6726
		TCU072	5.9	soil	1.8885
		TCU074	12.2	soil	1.7245
		TCU075	5.6	soil	4.2283
		TCU076	5.1	soil	1.4660
		TCU078	6.9	soil	2.3375
		TCU079	9.3	soil	2.0677
		TCU089	7	rock	1.7126
		TCU101	4.9	soil	2.6824
		TCU102	3.8	soil	1.5644
TCU129	3.9	soil	3.1964		

Table 6.8. Time histories representing the 2% in 50 years hazard level (Somerville and Collins 2002)

Earthquake	Magnitude	Station	Distance (km)	Site	Scaling Factor
Valparaiso, 1985	8.0	Llollea	34	rock	1.9800
		Pichilemu	24	rock	7.1923
		Valparaiso - Ventanas	28	rock	11.1475
		Valparaiso - del Mar	28	soil	4.4245
		Vina	30	soil	3.8483
		Zapaller	30	rock	11.5101
Michoacan, 1985	8.0	Caleta de Campos	12	rock	5.4386
		La Union	22	rock	7.1285
		La Villita	18	rock	8.9710
		Zihuatenejo	21	rock	6.4156

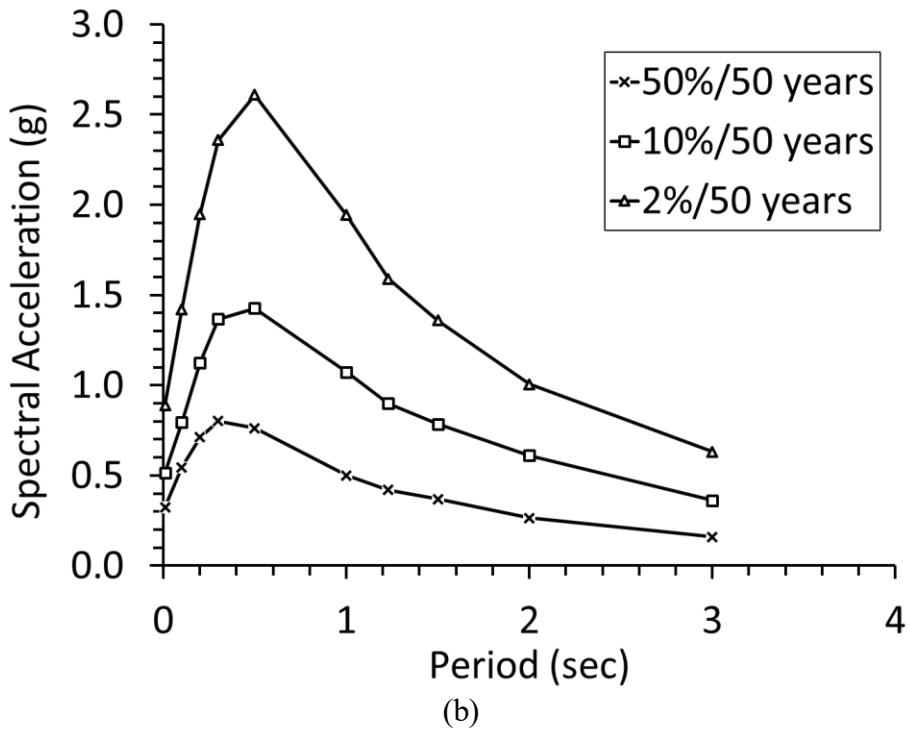
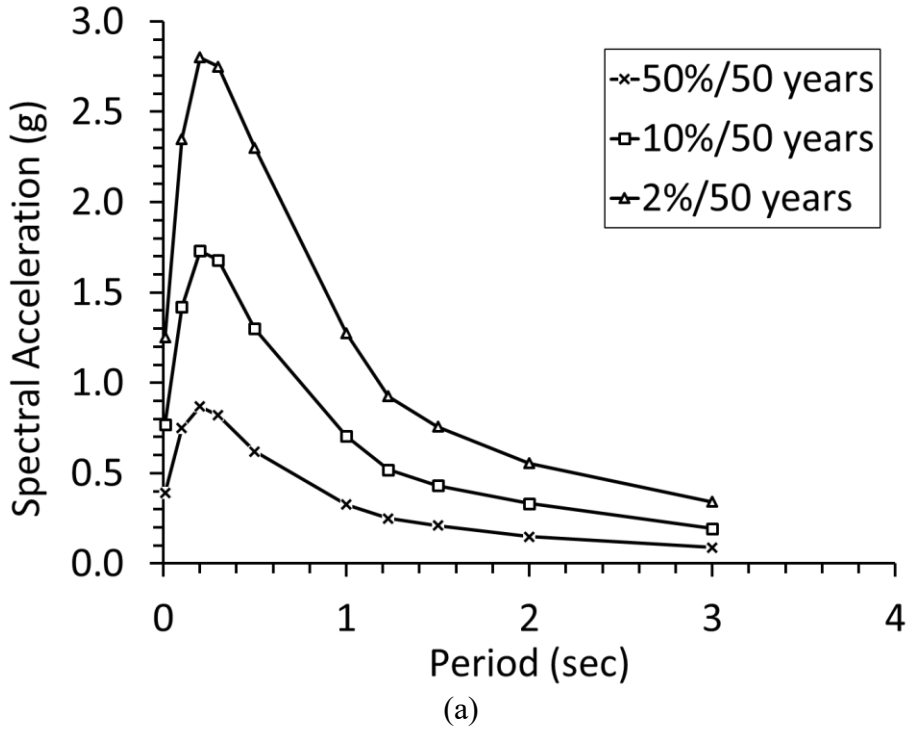


Figure 6.1. Uniform hazard spectra for: (a) Rock site, and (b) Soil site

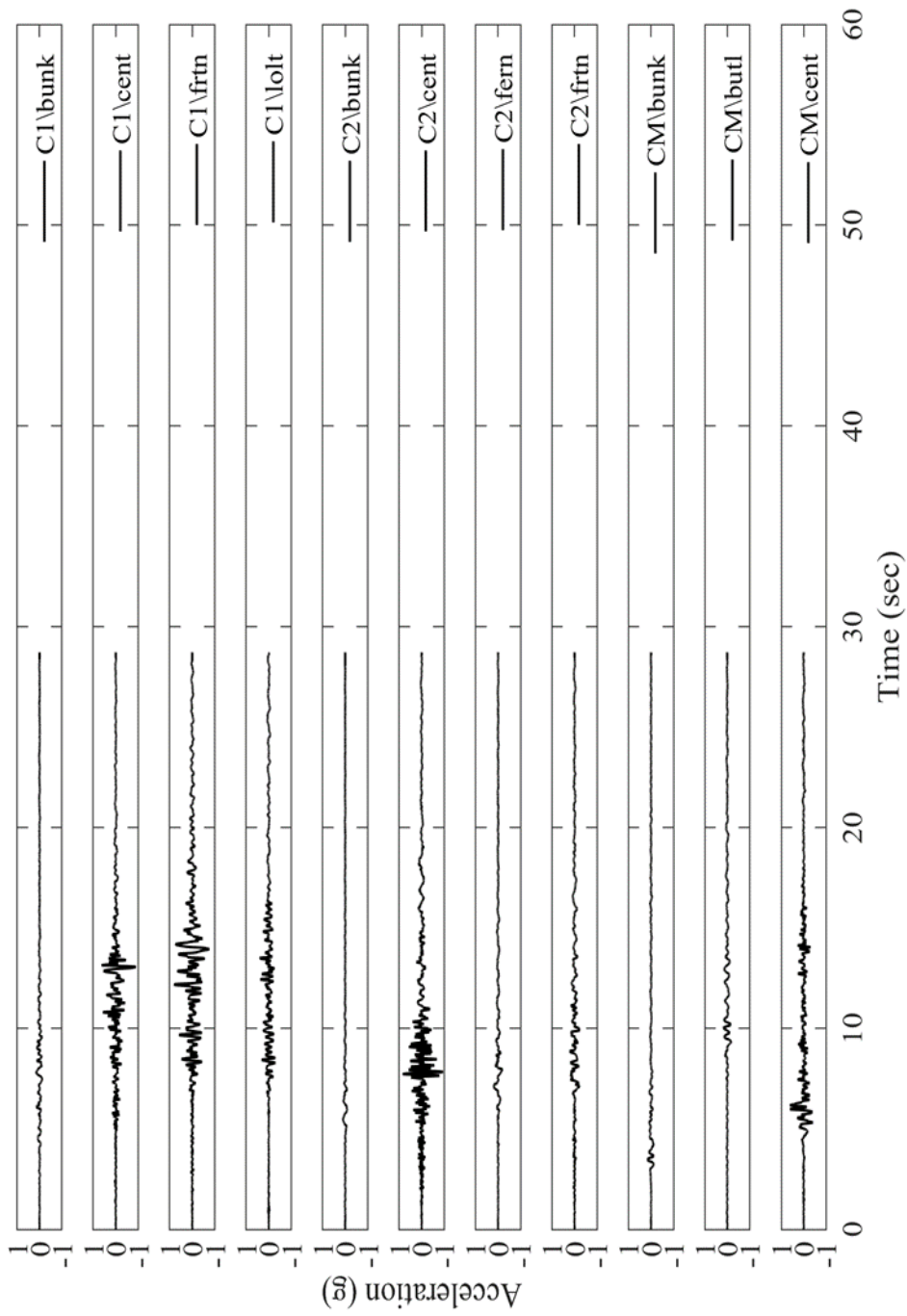


Figure 6.2. Longitudinal time histories for 50% in 50 years (motion I-11)

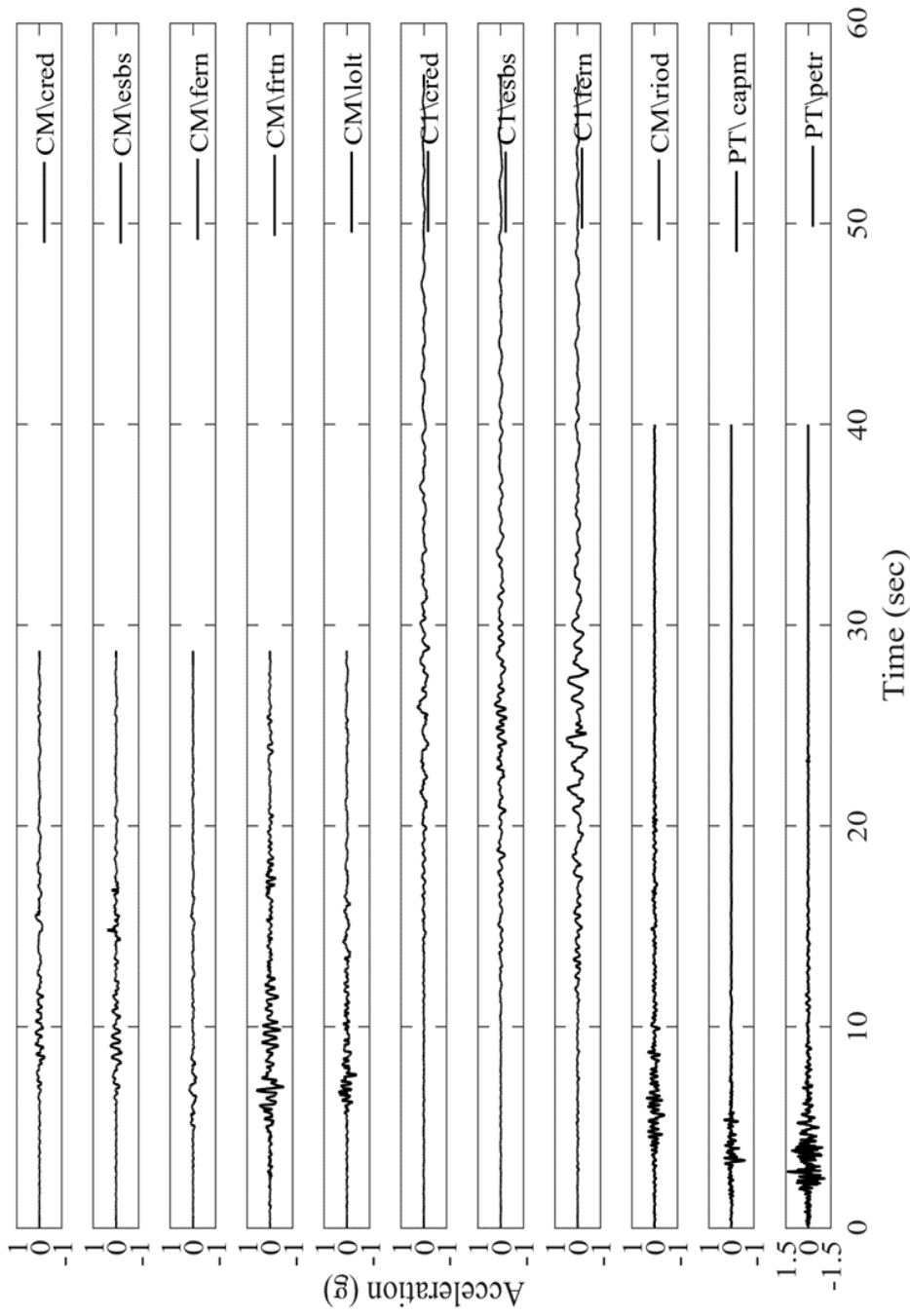


Figure 6.3. Longitudinal time histories for 50% in 50 years (motion 12-22)

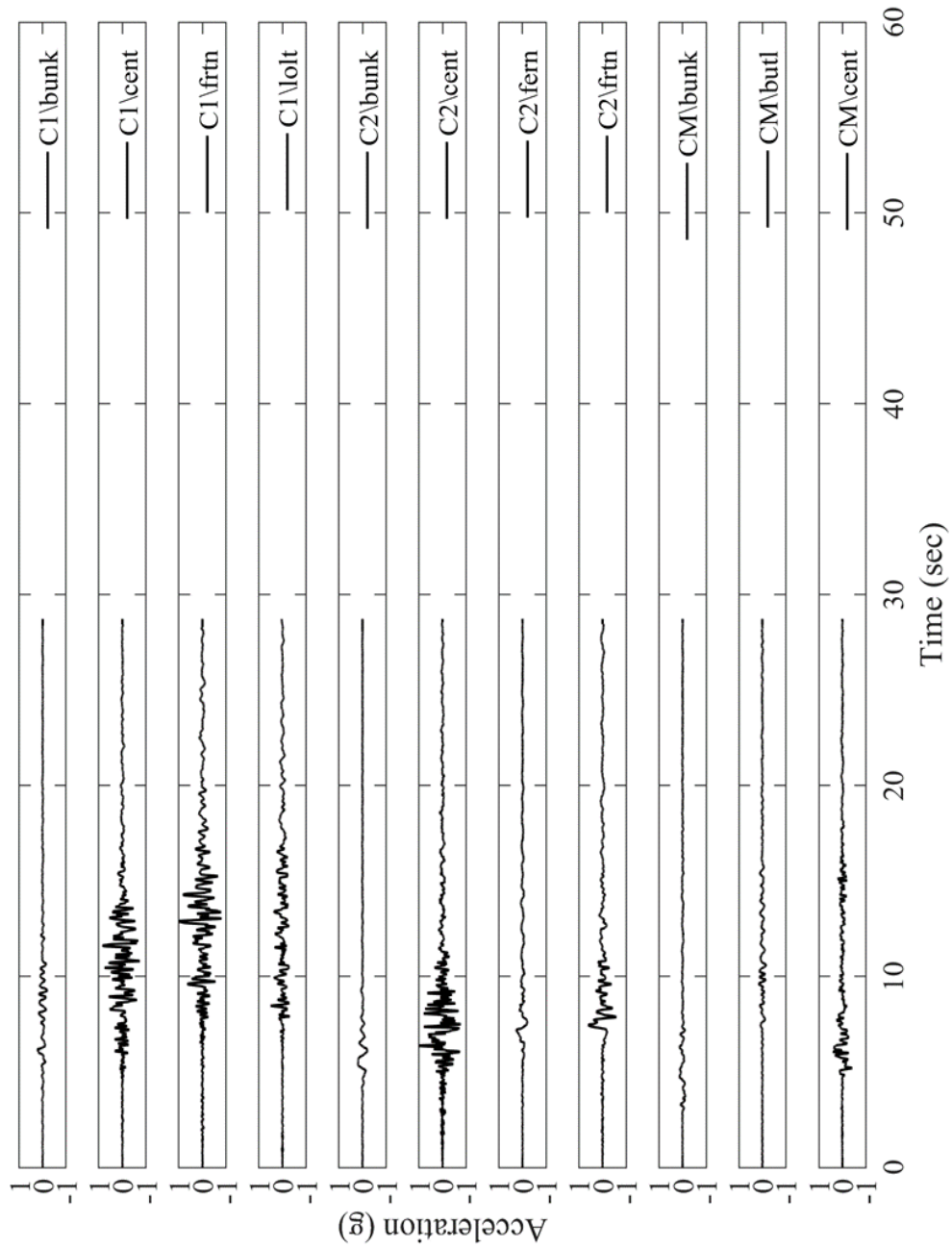


Figure 6.4. Transverse time histories for 50% in 50 years (motion 1-11)

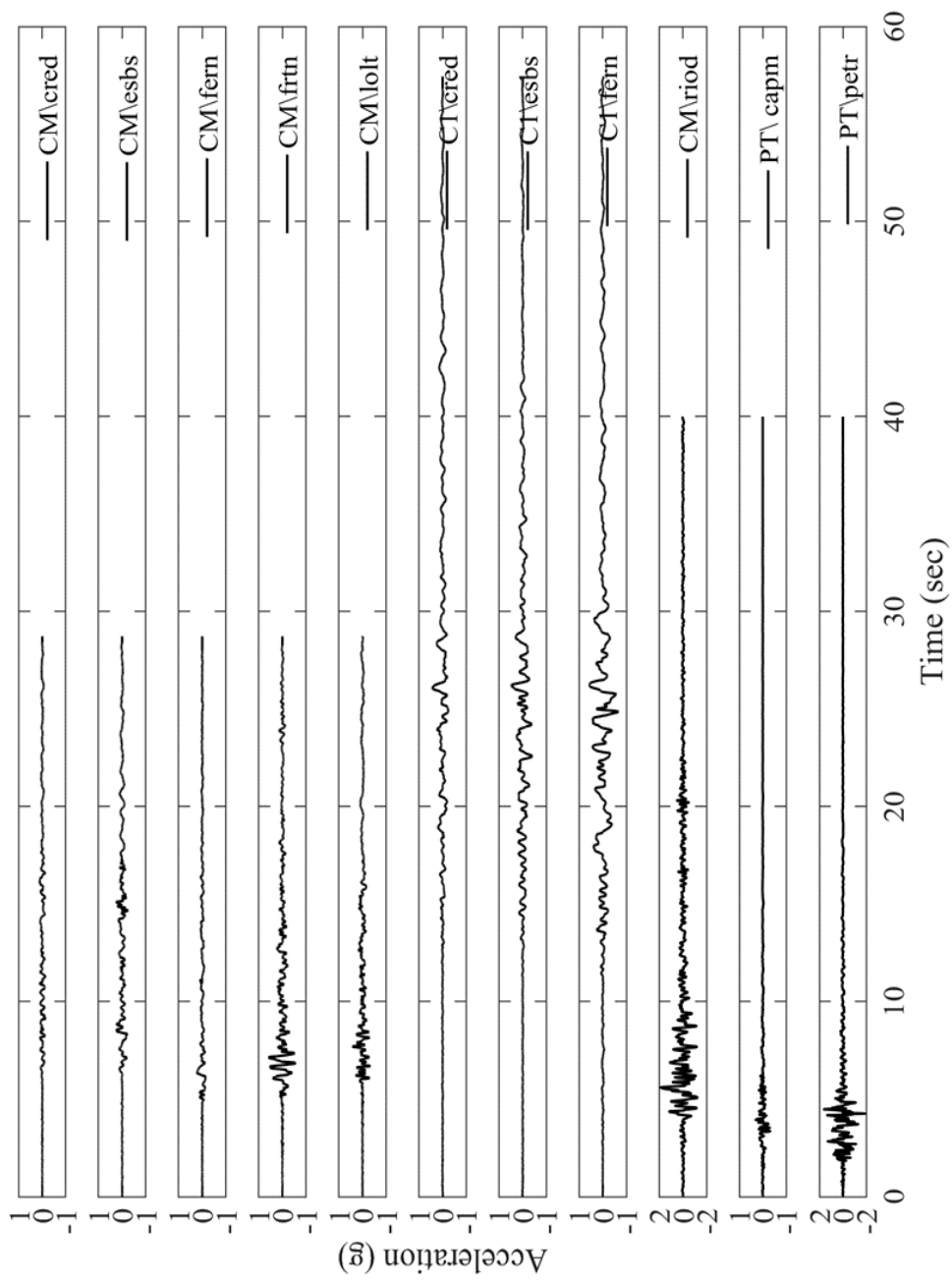


Figure 6.5. Transverse time histories for 50% in 50 years (motion 12-22)

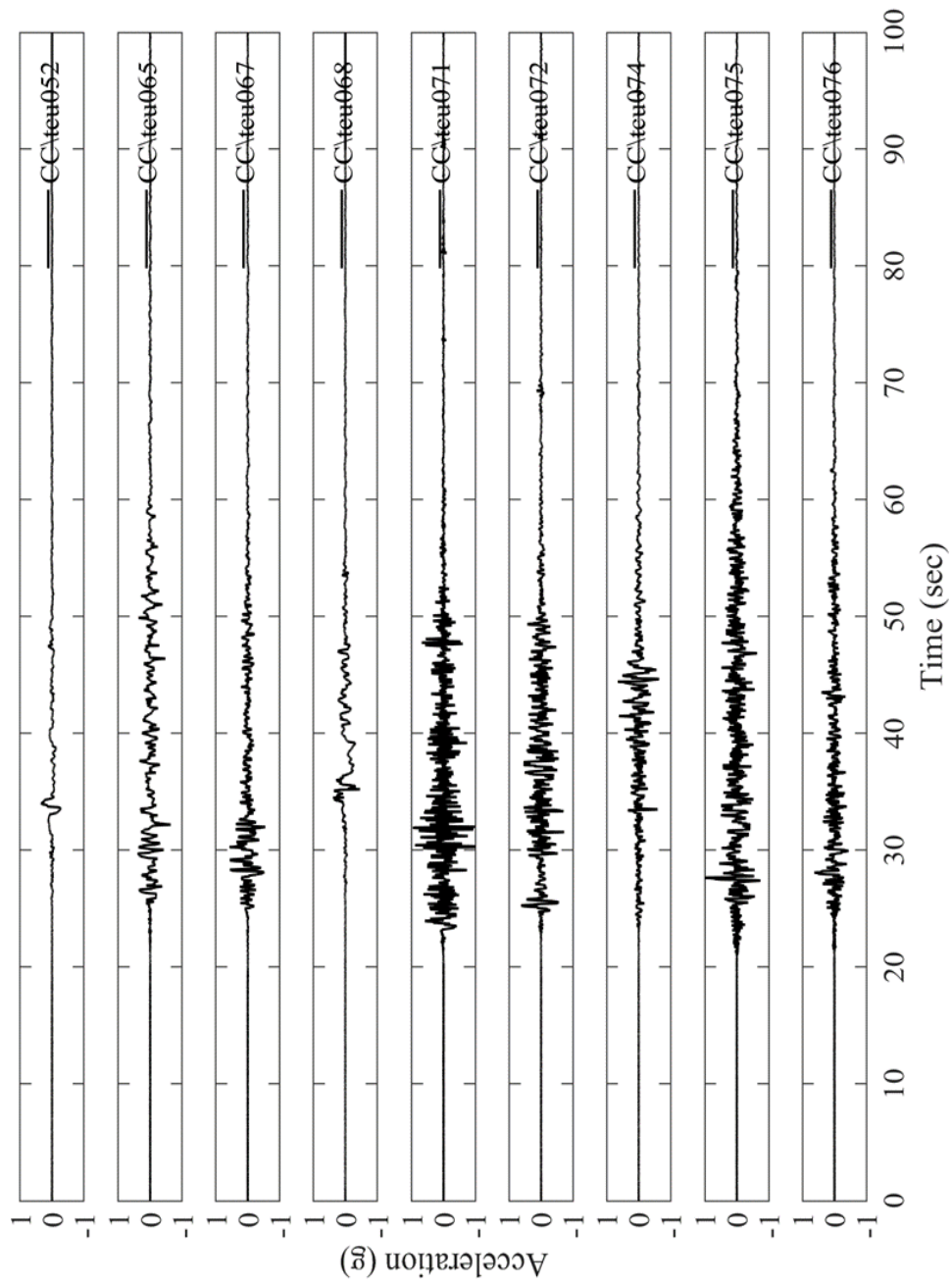


Figure 6.6. Longitudinal time histories for 10% in 50 years (motion 1-9)

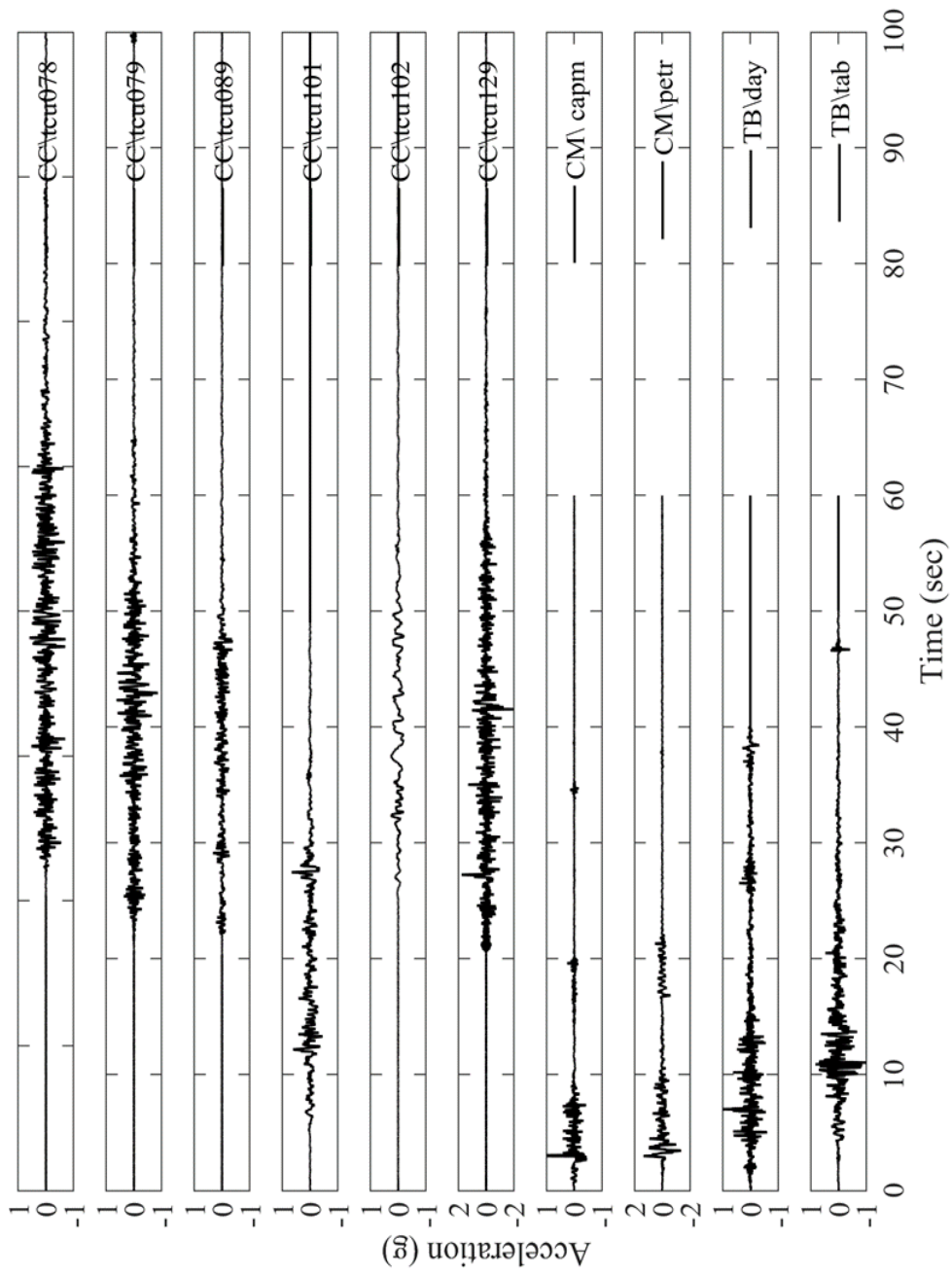


Figure 6.7. Longitudinal time histories for 10% in 50 years (motion 10-19)

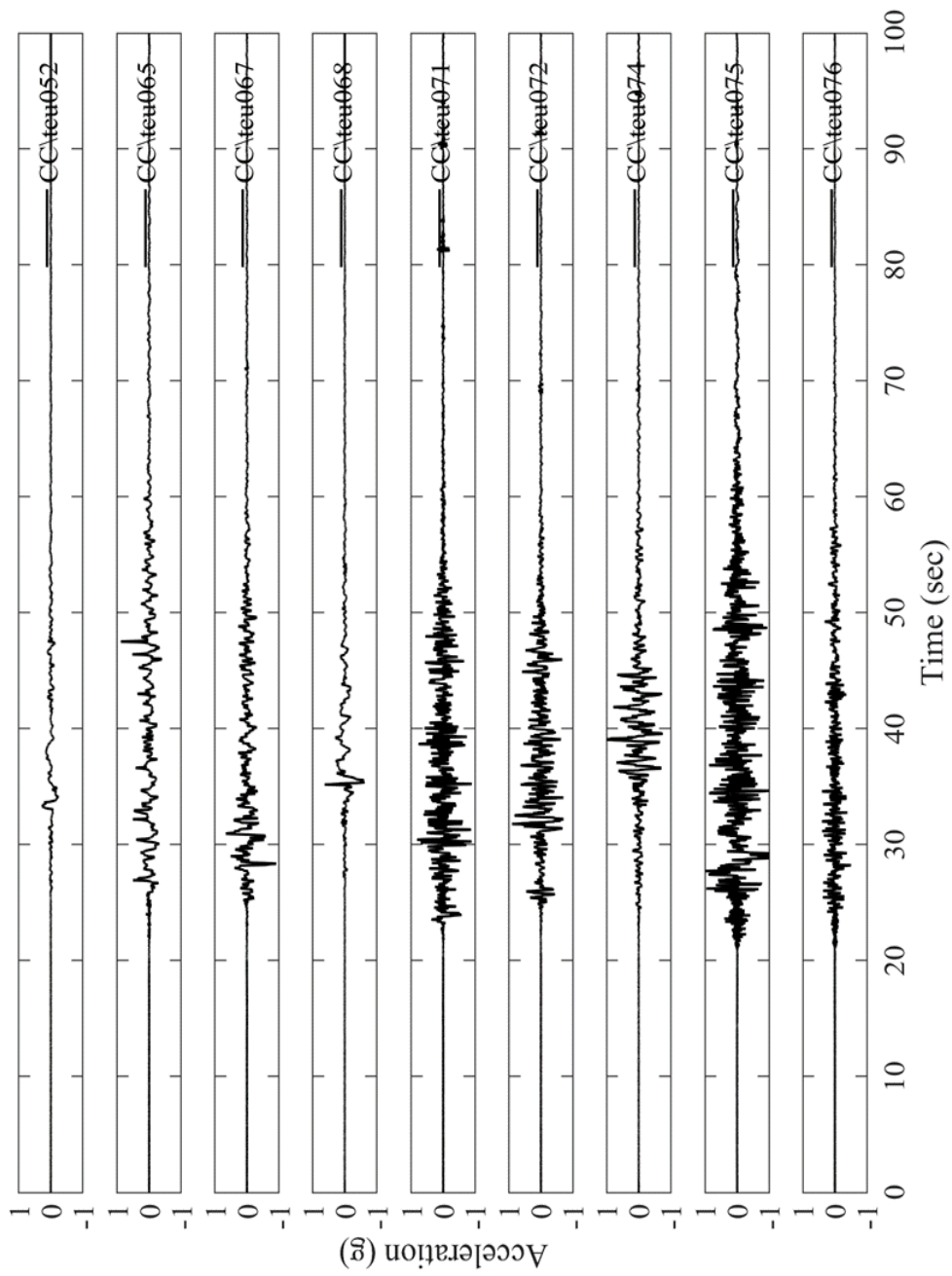


Figure 6.8. Transverse time histories for 10% in 50 years (motion 1-9)

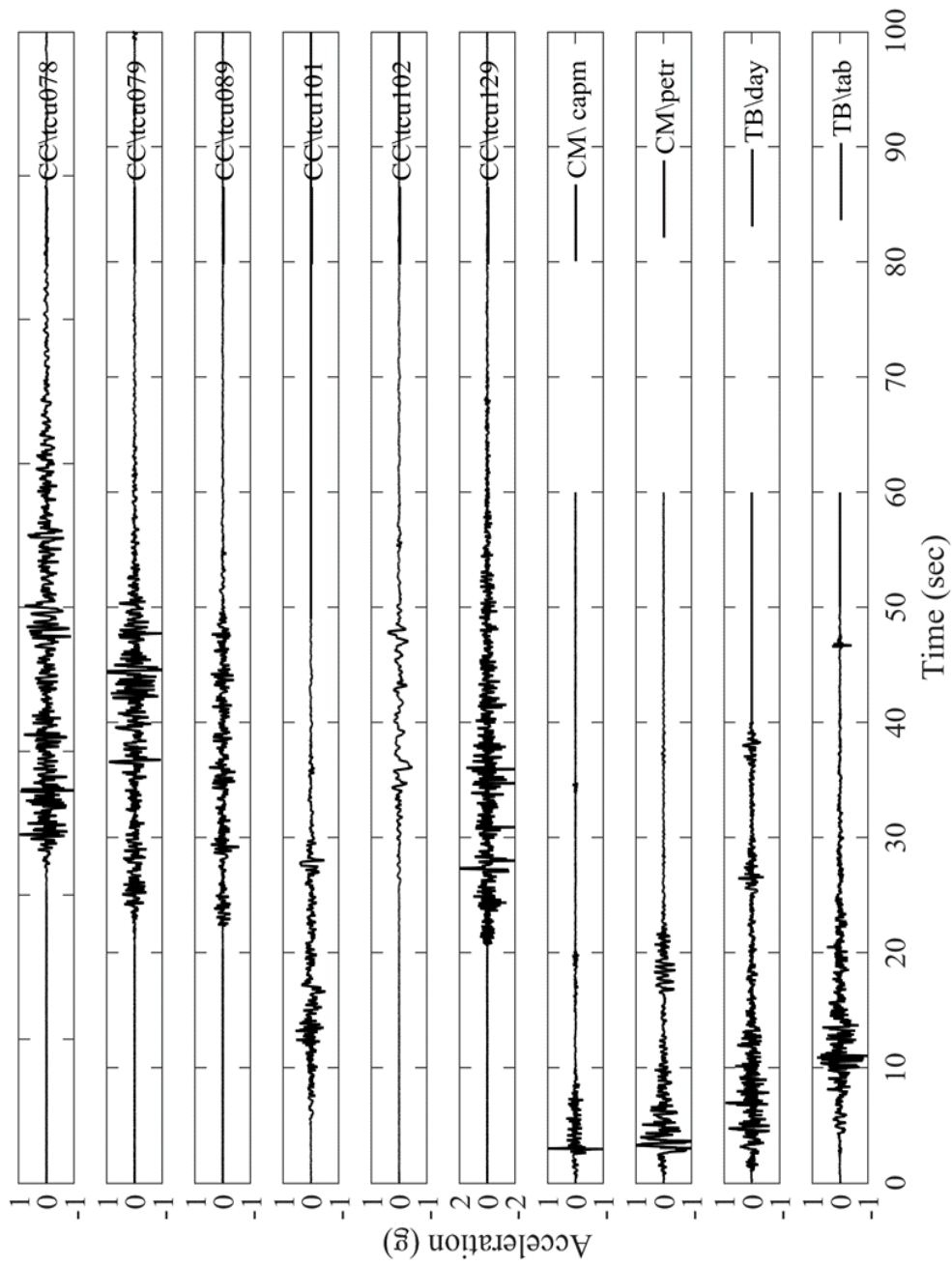


Figure 6.9. Transverse time histories for 10% in 50 years (motion 10-19)

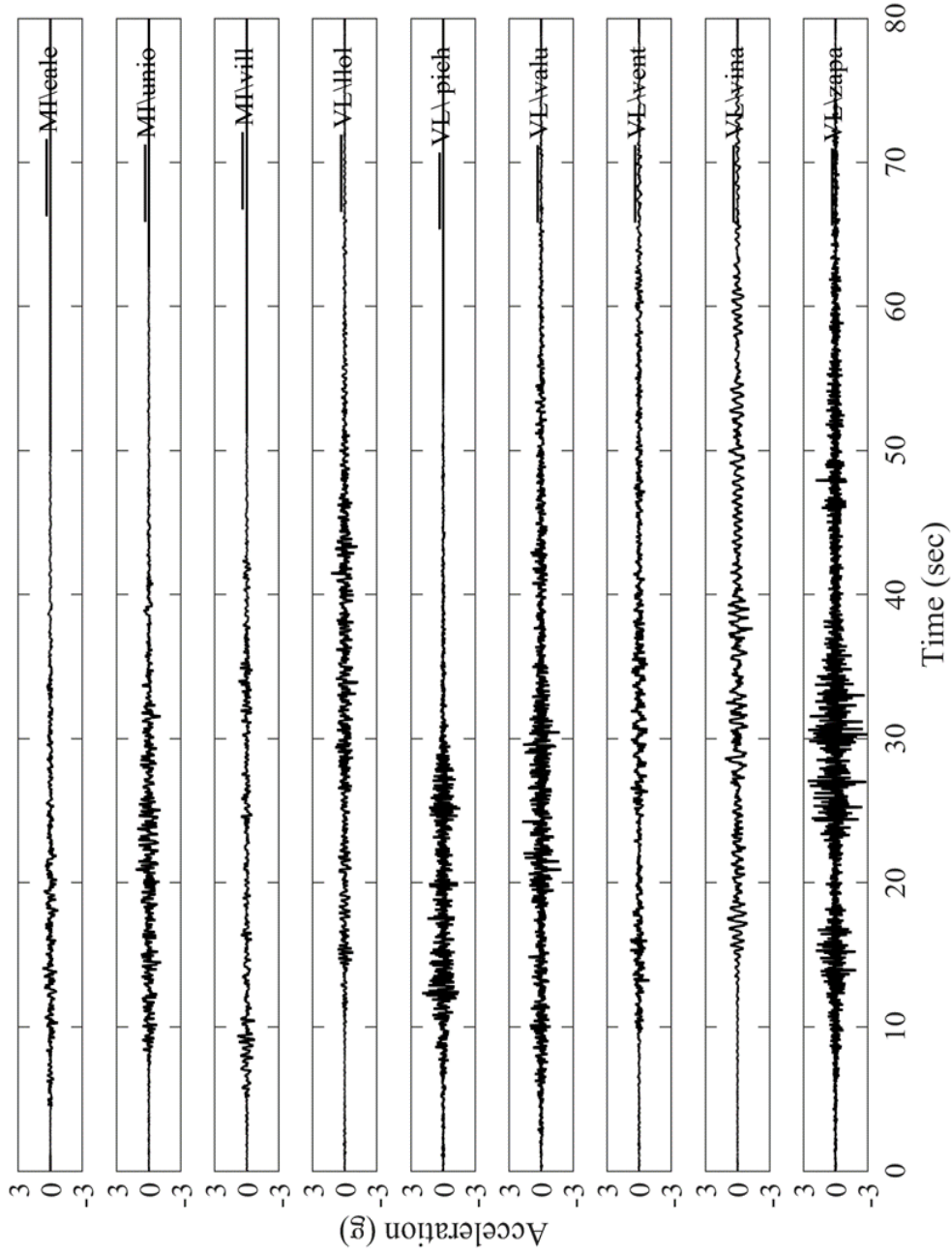


Figure 6.10. Longitudinal time histories for 2% in 50 years

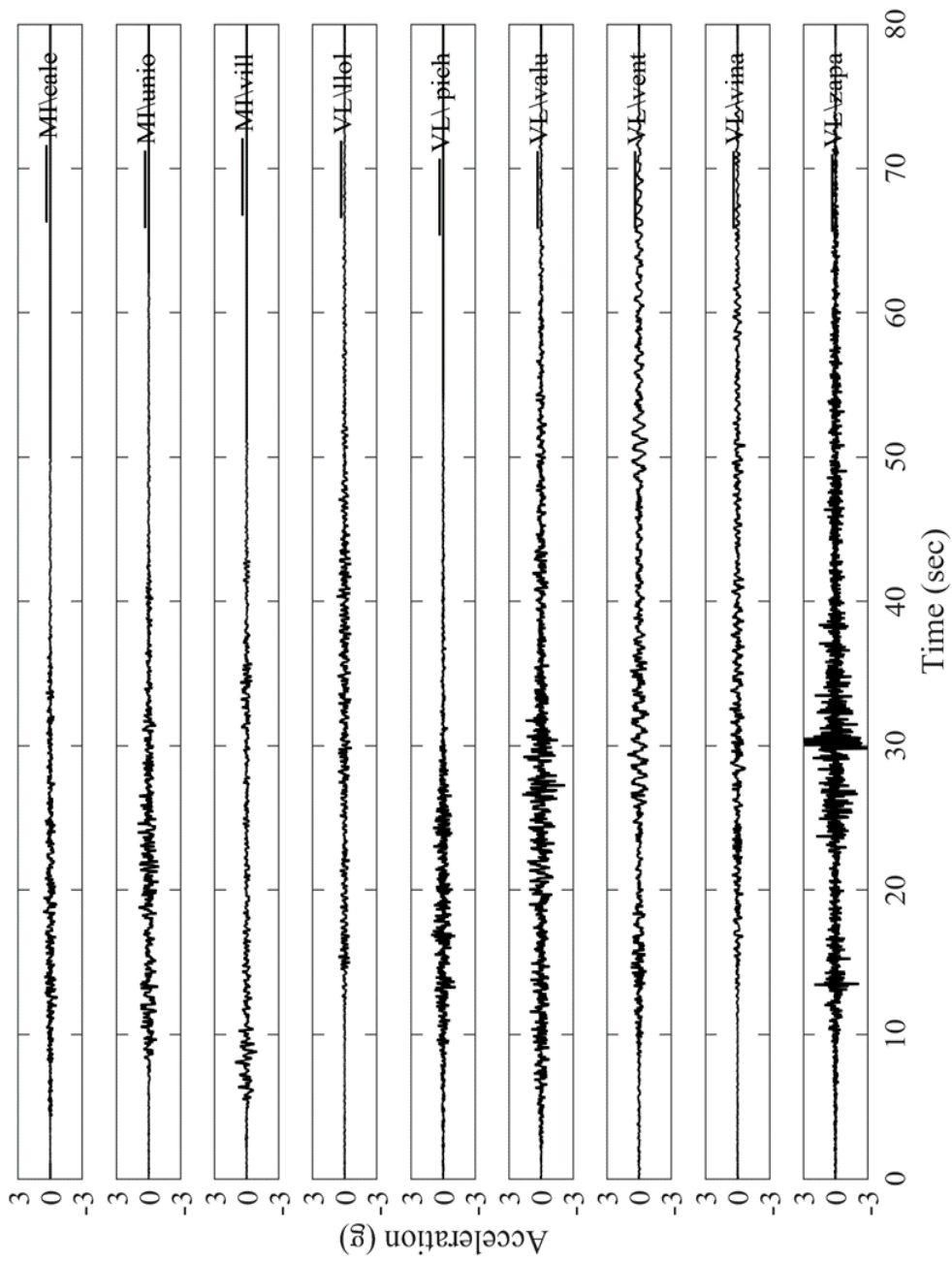
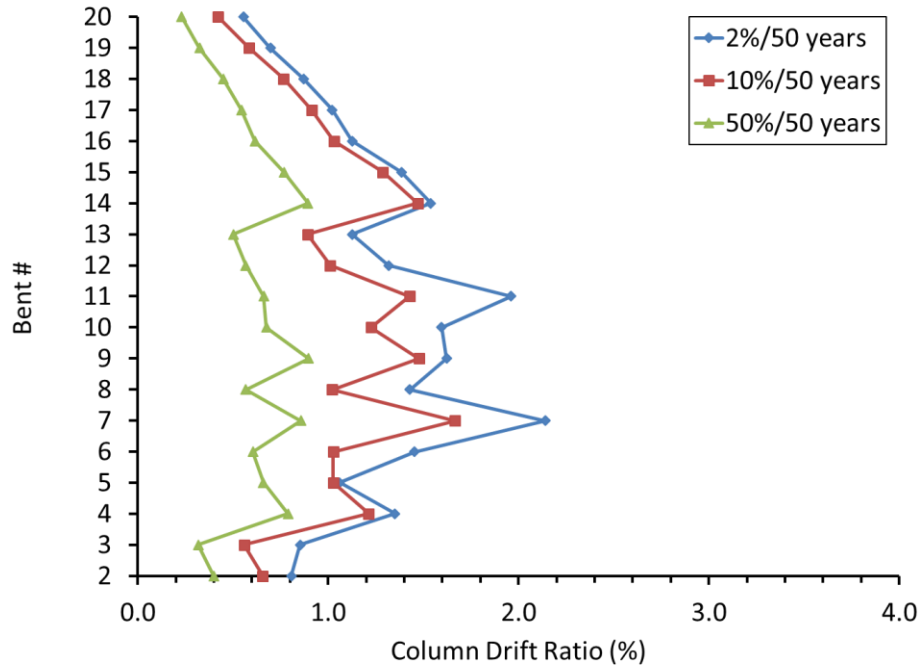
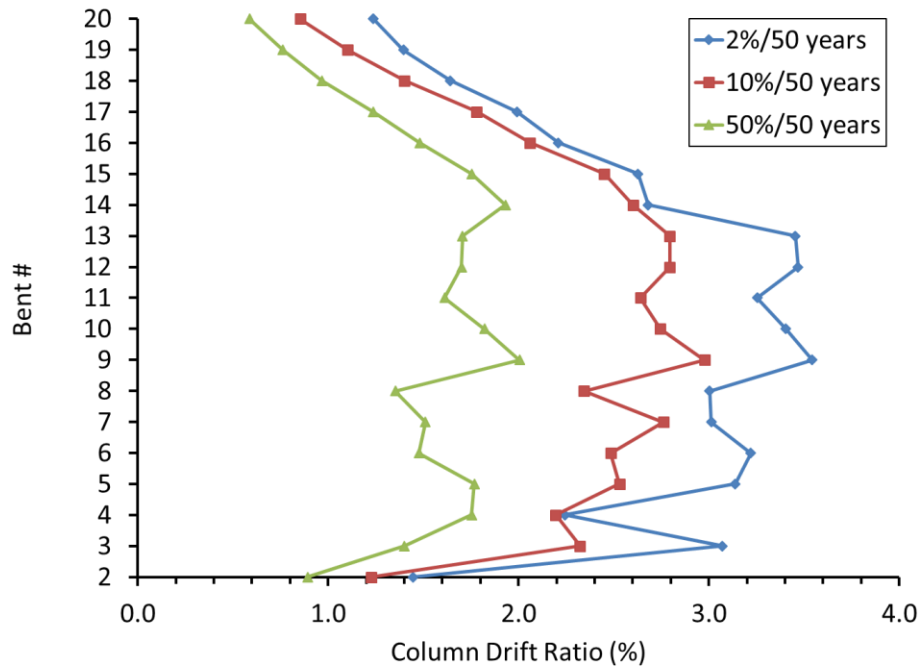


Figure 6.11. Transverse time histories for 2% in 50 years



(a)



(b)

Figure 6.12. Summary of maximum seismic demand for all three hazard levels for: (a) after retrofit, and (b) before retrofit

Chapter 7. Framework for Assessment of Bridge-Ground Response Due to Liquefaction-Induced Lateral Spreading

7.1. Abstract

In this chapter, a global bridge-ground systematic analysis framework developed for response under lateral spreading consideration is presented. Patterned after an existing bridge in California, Salinas River Bridge, this global analysis framework was implemented. As such, the response of the bridge subjected to liquefaction-induced lateral spreading was investigated using a practice-oriented pushover procedure. The analysis framework and representative results are presented, where the abutment lateral slope displacements were resisted by the entire bridge configuration. Significance of Soil-Structure Interaction (SSI) for this coupled bridge-foundation-ground system was addressed. For that purpose, Finite Element (FE) modeling was employed to represent the bridge seismic response, and SSI was conveniently handled by the soil springs approach. In this regard, modeling of the bridge superstructure as a global system is of paramount importance. In addition, a Performance-Based Earthquake Engineering (PBEE) formulation was employed to assess the consequences of the imposed ground deformation. Furthermore, sustainability was addressed using carbon footprint as the performance metric. To facilitate execution of this overall analysis framework, a graphical user-interface was developed and utilized. Based on the simulation results, it is shown that the permanent ground deformation induces longitudinal displacement on the abutment and consequently, the entire bridge system would be affected. As such, the response of the bridge and its pile foundations were investigated and correlated with the demand lateral spreading displacement. On this basis, the repair quantities related to the foundation and abutments were noted to be among the most significant parameters.

7.2. Introduction

As critical lifelines in a transportation network, bridge response during earthquakes has been receiving significant attention (McCallen and Romstadt 1994; Conte *et al.* 2002; Jeremic *et al.* 2004; Mackie and Stojadinovic 2006; Elgamal *et al.* 2008; Zhang *et al.* 2008; Kwon *et al.* 2009; FHWA 2011; Mackie *et al.* 2010, 2012; Wang *et al.* 2013; Soltanieh *et al.* 2019). In particular, soil liquefaction and its consequences have been noted to be a major concern that may result in significant damage or even collapse. This damage was observed and reported after recent events, including 2010 Maule (Arduino *et al.* 2010; Ledezma *et al.* 2012; Verdugo *et al.* 2012), 2010 El Mayor-Cucapah (Turner *et al.* 2016) and 2011 Christchurch (Cubrinovski *et al.* 2011, 2014; Wotherspoon *et al.* 2011). From these investigations, the observed response demonstrated the importance of considering the bridge and its components as an integral system.

Earthquake-induced lateral deformation at bridge abutments underlain by liquefied soil may be reduced by the restraining forces that come from the pile foundation and bridge superstructure. Armstrong *et al.* (2013, 2014) performed three centrifuge tests involving non-piled and piled embankments. These tests showed that the restraining forces exerted by the piles reduced the embankment displacement by 20-80%.

From the practice-oriented point of view, a simplified approach has been proposed in which soil springs were used to impose the expected lateral ground deformation at the abutments on the bridge (Caltrans 2017). This approach and similar techniques were developed and employed by a number of researchers (Finn and Fujita 2002; Boulanger *et al.* 2006, 2007; Ashford *et al.* 2009, 2011; Armstrong *et al.* 2013, 2014). Specifically, Boulanger *et al.* (2006, 2007) derived procedures for the seismic design of pile foundation for liquefaction effects from a combination of dynamic

centrifuge model test and nonlinear dynamic finite element studies. More recent efforts were reported by Turner *et al.* (2016).

In this study, a framework for analysis is developed, in which a representative bridge model (Caltrans 2005, 2016) was employed. As such, the entire bridge configuration reacted to and resisted the imposed abutment lateral slope displacements. In this regard, this approach implements the vision in Caltrans Memo to Designers (MTD) 20-15 (Caltrans 2017), expressing the significance of using a global bridge model.

To facilitate the conducted analyses, the user-interface MSBridge (Elgamal *et al.* 2014) was further developed and employed. MSBridge is a PC-based graphical pre- and post-processor (user-interface) for conducting nonlinear FE simulations for multi-span bridge systems. FE computations in MSBridge are performed using OpenSees (McKenna *et al.* 2010, <http://opensees.berkeley.edu>).

In the following sections, the employed lateral spreading practice-oriented procedure and the FE modeling details of the bridge ground foundation system are presented. The deck, columns, abutments, and foundation response mechanisms were integrated within a unified framework. The conventional soil-spring approach was used to account for SSI (Caltrans 2017). As such, lateral stiffness of the underlying pile foundation and the resulting soil-foundation-structure interaction were modeled using soil p - y curves.

Using this analysis framework, a PBEE approach (Cornell and Krawinkler 2000; Krawinkler 2002) was adapted to generate probabilistic estimates of repair cost, repair time, and carbon footprint of repair. The results are presented in terms of structural response and resulting loss.

7.3. Bridge-Foundation Model

The employed configuration (Figure 7.1a) is that of an 11-span reinforced concrete box-girder bridge (Caltrans 2005; Caltrans 2016). Each interior span is 140 ft long and each exterior span is 142.25 ft. The substructure consists of multiple two-column bents. Figure 7.1b and Figure 7.1c show a sectional view of the bridge deck along with the pile shaft reinforcement details. The four-cell box girder is 42.5 ft wide by 5.75 ft deep; and the deck and soffit slabs are 8 in and 6 in thick, respectively. Figure 7.2 shows the FE model where each column is 48 ft in height and 60 inches in diameter. The pile shaft has the cross-section and reinforcement of the column above grade (i.e., Type-I Caltrans pile shaft).

A spring SDC 2010-Sand abutment model (Aviram *et al.* 2008) was used to simulate the seat-type abutment (Figure 7.3). The longitudinal response is based on the system response of the elastomeric bearing pads (total of 5 bearings), gap (4 in), abutment back-wall, and soil backfill material. Prior to gap closure, the superstructure forces are transmitted through the elastomeric bearing pads (Table 7.5) to the stem wall, and subsequently to the piles and backfill. After gap closure, the superstructure pushes directly on the abutment back wall as such mobilizes the full passive backfill pressure.

The material and section properties of the box-girder are listed in Table 7.2. Weight of the bridge deck per unit length is 10.445 kip/ft ($= 69.64 \text{ ft}^2 \times 0.15 \text{ kcf}$). Material and section properties of the bentcap are listed in Table 7.3. Weight of the bridge bentcap per unit length is 5.175 kip/ft ($= 34.5 \text{ ft}^2 \times 0.15 \text{ kcf}$).

The bridge columns were modeled using force-based beam-column elements with nonlinear fiber material (Table 7.4). Discretization of the column cross-section, concrete and steel

stress-strain relationship, and the moment-curvature response are shown in Figure 7.4. As such, the bridge model was developed using user-interface MSBridge.

7.4. The Caltrans Simplified Method (Lateral spreading)

The simplified method (Caltrans 2017) is a one-dimensional analysis used to estimate the deformation demands (and capacities) of bridge foundations and abutments resulting from liquefaction induced spreading ground (i.e., horizontal ground displacement). Therefore, only the longitudinal component was considered in this study. Two procedures were combined to calculate the demand displacement and forces acting on the pile foundation. The first procedure is the slope stability analysis to evaluate the soil lateral movement, and the second procedure is to impose this ground displacement on the pile foundation via p - y curves.

Table 7.1 shows the soil profile and properties. The slope configuration is 2:1, as displayed in Figure 7.5. Using the soil profile properties (Table 7.1), slope stability analysis led to a lateral yield acceleration of 0.163 g for a free unrestrained slope. More details about the method and a worked example for the studied bridge configuration can be found in Appendix J.

7.4.1. Implementation of the Simplified Method to the Bridge Abutment Foundation

The demand displacements were determined using Bray and Travararou (2007) (equation J.2). In the analysis, liquefiable soil was modeled as soft clay having a residual undrained shear strength calculated using an equation by Kramer and Wang (2015) (equation J.1). The slope stability analysis was performed with and without the pile-supported bridge abutment (restrained and unrestrained).

The imposed demand displacement was applied to an abutment pile to evaluate the response in a global model of the bridge. Full-bridge is supporting the slope by taking the restraining force in the center of the liquefiable layer and the axial force at the deck level to present

the engagement of the superstructure. According to the simplified procedure (Caltrans 2017), application of the permanent lateral ground displacement follows the pattern (Figure J.1) by which the soil above the liquefied layer moves as a rigid block and the displacement decreases linearly in the liquefied layer. The effective width in the calculation according to MTD 20-15 is 68 ft.

Figure 7.6 shows the p - y curves used for interaction between the ground and the embedded foundation system for the crust, the middle of the liquefied layer, and the non-liquefied layer (dense sand layer). The liquefied layer was modeled as soft clay with the undrained shear strength equal to the residual strength of the liquefied soil. The p - y models used in this analysis are i) Soft Clay (Matlock 1970) for the liquefied layer and soft clay layer, and ii) Sand (Reese *et al.* 1974) for the fill and dense sand layer. The top dry layer (crust) was modeled using user-specified p - y curves to represent the ultimate crust load on the pile, and the relative soil displacement required to achieve that load (Appendix J).

7.4.2. Pile-pinning Effect

Liquefaction-induced displacements can cause severe damage to an engineered structure. Therefore, a number of ground improvement techniques have been developed and enhanced to bring the ground deformations to an acceptable level. However, mitigation cost can be reduced if the foundation piles are designed to “pin” the layers above and below the liquefied layer which would stabilize the slope. This technique is known as the “pile-pinning” effect where the piles are locked into both non-liquefiable soil layers above and below the liquefiable soil layer.

7.5. Representative Bridge Response Due to Lateral Ground Displacement

The response to an individual ground motion record was investigated to provide insight into the trends observed in the subsequent PBEE analysis results. For that purpose, the calculations for estimating the restrained displacement from the Tarzana Cedar Hill (TAR) record

during the Northridge earthquake ($M_w = 6.69$, $R=15.6$ km, $PGA = 1.78g$) that resulted in the highest displacement demand are presented (Figure 7.7). From the slope stability analysis, the only affected pile is that of the abutment pile (Figure 7.1). Therefore, the displacement demand was applied to the abutment pile according to the global displacement profile shown in Figure J.1. In this study, applying the displacement demands to one side of the bridge (left side) was considered to account for the worst-case scenario. It can be immediately gleaned from Figure 7.7 that the unrestrained displacement demand was reduced from 51 inches to 22 inches because of the presence of the pile. In addition, Figure 7.8 shows the deformed shape of the bridge where all its components are engaged in resisting the soil displacement and the displacement response profile. In addition, since the bridge columns are restrained at their bases, the maximum bending moment occurs at the base of each column (at the mudline). Figure 7.9 shows the moment-curvature response.

7.6. Performance-Based Earthquake Engineering Framework

A PBEE framework was utilized to estimate the post-earthquake loss of the bridge-ground system subjected to liquefaction-induced lateral spreading using the proposed procedures. Table 7.6 shows the PGs (and associated DSs) used in this study. More details about the PBEE framework can be found in Chapter 4 and Appendix H. To further illustrate the combination of the Simplified Method and PBEE framework, Figure 7.7 shows a schematic illustration of PBEE framework with the simplified procedure.

Sustainability is increasingly becoming a major concern in highway bridge construction and repair. Systematic inclusion of environmental impact as a metric in a performance-based earthquake engineering framework is essential in the decision-making strategy. As such, the framework is presented along with the necessary underlying computations and outcomes related

to carbon footprint of repair (CFR). Carbon emissions were computed via the economic input-output (EIO) life cycle assessment (LCA) approach (CMU, 2013) that calculates supply chain emissions of the bridge repair work. The EIO-LCA model is based on the cost of the materials and EIO-multipliers. The EIO-LCA model uses EIO-multipliers to convert the dollars spent into emissions generated. More details about the inclusion of CFR can be found in Appendix H (Mackie *et al.* 2015; Vijayakumar *et al.* 2016).

7.7. Lateral Displacements for PBEE Analysis

An ensemble of 160 ground motions was employed in the PBEE analyses, with all motions obtained from the PEER NGA database (<http://peer.berkeley.edu/nga/>). This PBEE motion ensemble (Medina and Krawinkler 2003) consists of 160 3D input ground motions, sorted into 4 bins. Each motion is composed of 3 perpendicular acceleration time history components (2 lateral and one vertical). However, since the Simplified Method is a 1D analysis approach, only the longitudinal component was considered in this study. These motions were selected through earlier efforts (Medina and Krawinkler 2003; Mackie and Stojadinovic 2005) to be representative of seismicity in typical regions of California. The motions are divided into 4 bins of 40 motions each. The bins are divided based on each motion's characteristics: i) moment magnitude (Mw) 6.5-7.2 and closest distance (R) 15-30 km, ii) Mw 6.5-7.2 and R 30-60 km, iii) Mw 5.8-6.5 and R 15-30 km, iv) Mw 5.8-6.5 and R 30-60 km, and v) Mw 5.8-7.2 and R 0-15 km. The provided ground motions are based on earlier PEER research (Mackie and Stojadinovic 2005). These motions are developed by Mackie *et al.* (2008) to account for site classification (NEHRP C and NEHRP D). Figure 7.11 shows the input ground motions in M-R space.

The slope stability analysis was performed with and without the pile-supported bridge abutment (restrained and unrestrained).

Figure 7.12 shows the unrestrained displacement estimates before accounting for the existence of the bridge by Bray and Travararou (2007) equation. In order to account for bridge restraining effect, the MSBridge model of the bridge is used to convert the above unrestrained displacement to demand displacement (Figure 7.13).

7.8. PBEE Results

Using MSBridge, demand displacements shown in Figure 7.13 were applied to the left abutment piles while engaging resistance from the entire bridge structure. As such, the corresponding repair cost and repair downtime were computed. These values are then correlated with an Intensity measure that represents each motion employed. MSBridge allows for the specification of numerous Intensity measures, so as to display the outcomes against any of these measures. Herein each earthquake motion will be represented by its PGA as the intensity measure since the Bray and Travararou (2007) equation used to estimate the demand displacement is PGA dependent.

PBEE analysis was performed to obtain intensity-dependent repair cost and time estimates. LLRCAT proposed by Mackie *et al.* (2008) was utilized. Table 7.6 shows the breakdown of the PGs and associated DSs.

7.8.1. Repair Cost and Time

Figure 7.14 shows the repair costs disaggregated by PG against PGA to specifically describe which PG contributes most to the overall loss in terms of the repair cost. For PGA less than 0.5 g, the demand displacements values were small not to trigger any DSs. Therefore, zero loss was expected for the range between 0 – 0.5 g. In addition, the PGs related to the left abutment (PG3 and PG5 for the left abutment and left bearings, respectively) were among the first PGs that showed damage since the demand displacements were applied to the left abutment piles. After the

gap closure, the columns and right abutment PGs started to show some damage. Unlike the case where base excitations were applied, the results showed the left and the right abutment damage were not triggered the same at IM level because of the presence of the gap. Furthermore, rapid increase in to the estimated repair costs can be seen at approximately 1.5 g because of triggering of the abutment foundation PGs which indicated damage to the foundations.

Furthermore, application of the displacement demands implies that the maximum drift ratios (PG1) and the residual drift ratios have the same values. However, the contributions from PG1 and PG2 were found to be different since the repair quantities and associated damage involved in each PG are not the same. In addition, one representative column was shown in Figure 7.14 because of a similar response from all the columns as can be implied from Figure 7.8. Nevertheless, the total repair cost (in terms of repair cost ratio) includes the repair costs from all the columns (Figure 7.15a).

In addition, Figure 7.15a and Figure 7.15b show the loss models (along with probabilistic models) of RCR and the RT against PGA. It can be seen from Figure 7.15a that the dispersion was higher for the range greater than 1.5 g because of triggering of the abutment foundation damage. Similarly, Figure 7.15b shows a jump around 1.2 g (for the abutment foundation damage) after which no more repair efforts were triggered, and a plateau was reached.

The normalized repair costs are obtained by using RCR, the ratio between cost of repair and cost of replacement (not including the demolition). The unit price of repair cost used in this study is based on \$190 per square foot of the bridge deck. Based on the January 2015 Caltrans comparative bridge costs (Division of Engineering Services - Cost Estimates Branch, 2014), the construction cost for the studied bridge was estimated to be \$12.4 million.

7.8.2. Hazard Curves

To obtain Hazard Curves for a particular seismicity scenario (based on geographic location), three probabilities of exceedance (2%, 10%, and 50% in 50 years) are needed. The USGS offers a website that does interactive hazard disaggregation for the United States (<https://earthquake.usgs.gov/hazards/interactive/>) and for the bridge site, the resulting PGA estimates were 1.49 g, 0.89 g, 0.51 g, respectively.

On this basis, Figure 7.16a shows the mean annual frequency (MAF) of exceedance vs. RCR and RT. In addition, the results were shown in terms of the return period (the reciprocal of the MAF).

7.8.3. Carbon Footprint of Repair Results

The EIO-LCA computes the carbon emissions through a conversion factor based on the monetary value of the quantities called EIO-multiplier in kgCO₂/\$ (CMU 2008). These multipliers are obtained from the EIO-LCA tool for the U.S. 2002 benchmark producer price model (CMU 2008). As mentioned earlier, EIO-multipliers account for emission within the context of “cradle-to-gate.”. As such, Figure 7.17 shows the carbon footprint vs. PGA. The presented results show that the carbon emission from each PG does not necessarily contribute to the same level as it does to the repair cost; rather it depends on the emission factors. In general, the results indicate that the abutment PGs (PG3, PG5, and PG7) generate the majority of the repair cost and carbon.

7.9. Conclusions

The seismic response of a multi-span bridge-ground system subjected to liquefaction-induced permanent displacement was studied and discussed. For that purpose, a global bridge-ground systematic analysis was proposed and developed in light of the simplified method (proposed in MTD 20-15) assumptions. As such, the response of the bridge and its pile foundations

were investigated and correlated with the imposed lateral spreading displacement. Overall, the main conclusions can be summarized as follow:

- (i) Modeling of the bridge superstructure as a global system is of paramount importance to realistically estimate the demand displacement including the bridge resistance.
- (ii) The damage states and repair quantities related to the foundations and abutments are among the main parameters that contribute to the overall loss estimate.
- (iii) Based on the presented results, the repair costs start to accumulate at around PGA of 0.5 g, then increase as more damage states are triggered.
- (iv) The expected damage (and repair) from the left abutment are triggered at an earlier intensity measure level than the right abutment because of the gap presence.
- (v) Carbon emissions related to the abutment foundation PG generate a majority of expected emission because of the repair efforts involved in that damage state.
- (vi) Since the method EIO model links the repair cost to the carbon emission, then the parameters associated with the highest repair cost are also expected to be critical in the environmental impact.

7.10. Acknowledgements

Chapter 7, in full, is currently being prepared for submission for publication of the material as it may appear in the following journal publication (The dissertation author was the primary investigator and author of this paper):

Almutairi, A.S., Lu, J., Wang, N. and Elgamal, A., "Framework for Assessment of Bridge-Ground Response due to Liquefaction-Induced Lateral Spreading".

Table 7.1. Soil properties (Almutairi *et al.* 2016)

Depth (ft)	Soil Type	Unit Weight (lb/ft ³)	Friction Angle (degrees)	(N ₁) ₆₀
0 - 58	Fill	114	36	-
58 - 75	Loose Sand	130	33	30
75 - 128	Dense Sand	127	38	14

Table 7.2. Bridge deck material and section properties

Parameter	Value
Young's modulus (ksi)	4,031
Shear modulus (ksi)	1,668
Unit weight (kcf)	0.15
Area of cross-section (ft ²)	69.64
Moment of inertia @ horizontal axis (ft ⁴)	327.44
Moment of inertia @ vertical axis (ft ⁴)	10105.6
Torsion constant (ft ⁴)	934

Table 7.3. Bridge bentcap properties

Parameter	Value
Young's modulus (ksi)	4,031
Shear modulus (ksi)	1,668
Unit weight (kcf)	0.15
Area of cross-section (ft ²)	34.5
Moment of inertia @ horizontal axis (ft ⁴)	95.1
Moment of inertia @ vertical axis (ft ⁴)	103.5
Torsion constant (ft ⁴)	166.79

Table 7.4. Constitutive model parameters for concrete material of fiber beam-column element

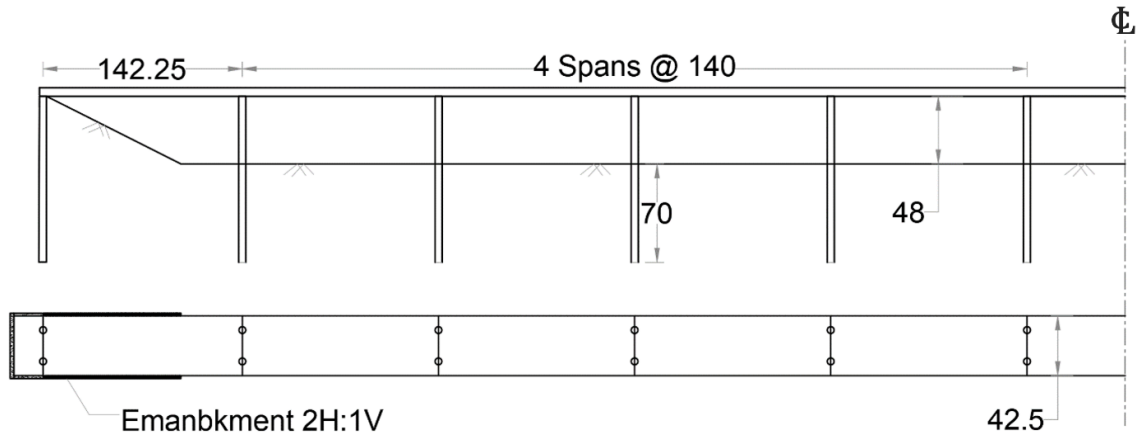
Parameter	Value
Concrete compressive strength at 28 days, f'_c (ksi)	-5.03
Concrete strain at maximum strength, ϵ_{c0}	-0.0025
Concrete crushing strength, f'_{cu} (ksi)	-4.45
Concrete strain at crushing strength, ϵ_{cu}	-0.006

Table 7.5. Geometric and material properties of a bearing pad (Lu *et al.* 2011)

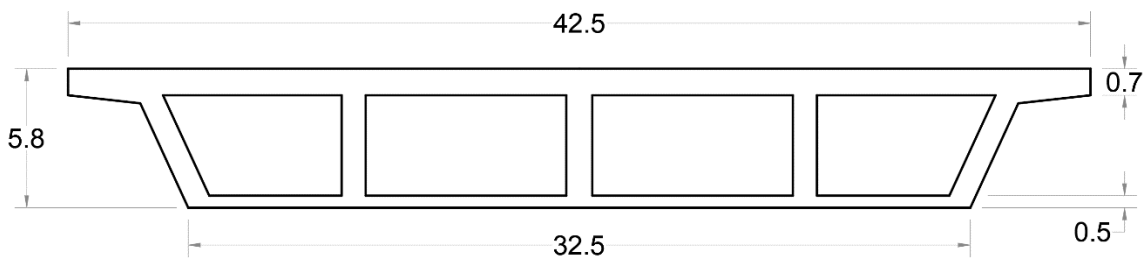
Parameter	Value
Shear Modulus G	0.15 ksi
Young's Modulus E	5 ksi
Yield Displacement	150% shear strain
Lateral Stiffness	$\frac{GA}{h}$ (where A is the cross-section area and h is the height)
Vertical Stiffness	$\frac{EA}{h}$
Vertical Tearing Stress	2.25 ksi
Number of bearings	5
Bearing height (in)	2
Longitudinal gap (in)	4

Table 7.6. Performance groups and associated engineering demand parameters and damage states

PG	Response measure	DS1	DS2	DS3	DS4
PG1	Maximum column drift ratio	Concrete cracking (0.24%)	Concrete cover spalling (1.68%)	Longitudinal reinforcing bar buckling (6.1%)	Failure (7.5%)
PG2	Residual column drift ratio	Threshold (0.5%)	Thicken pier (1.25%)	Re-center column (2%)	Failure (7.5%)
PG3 & PG4	Maximum relative longitudinal deck-end/abutment displacement for left & right abutments	Joint cleaning (0.16 ft)	Joint seal assembly replacement (0.33 ft)	Back wall (retaining wall) spalling (0.36 ft)	Back wall (retaining wall) failure (0.46 ft)
PG5 & PG6	Maximum lateral bearing displacement for left & right abutments	Yield (0.25 ft)	Failure (0.49 ft)	-	-
PG7 & PG8	Residual lateral pile displacement at ground surface for left & right abutments	Add pile threshold (0.62 ft)	Enlarge foundation (1.05 ft)	-	-
PG9	Column residual pile displacement at ground surface	Add pile threshold (0.82 ft)	Enlarge foundation (1.38 ft)	-	-



(a)



(b)

Figure 7.1. Bridge geometric configuration (dimensions shown in ft): (a) elevation view; (b) deck section

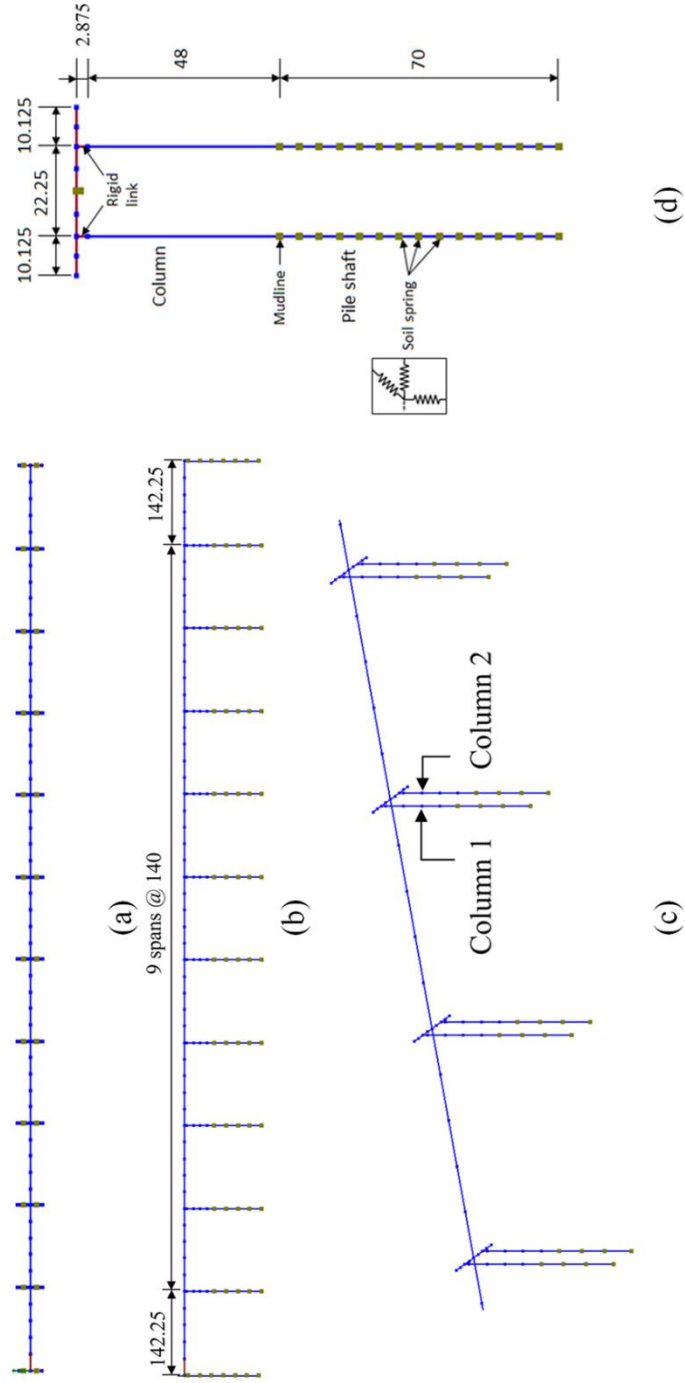


Figure 7.2. Bridge FE model created in MSBridge (dimensions shown in ft): (a) plan view; (b) elevation view; (c) close-up of 3D view; (d) side view of a bent (typical)

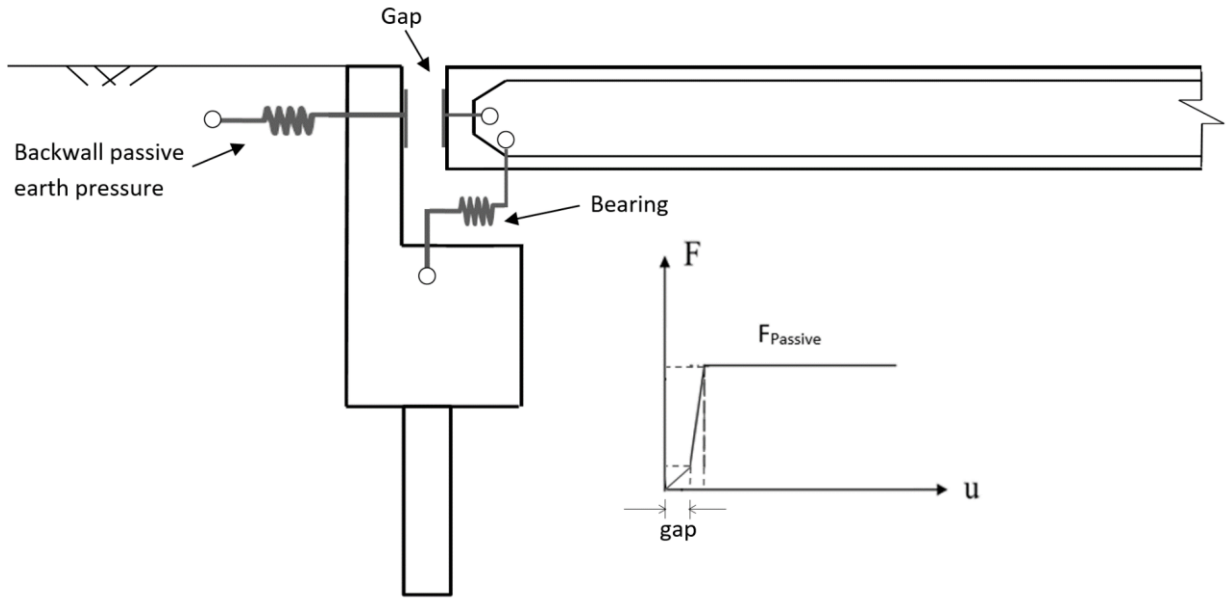


Figure 7.3. Schematic of spring abutment model

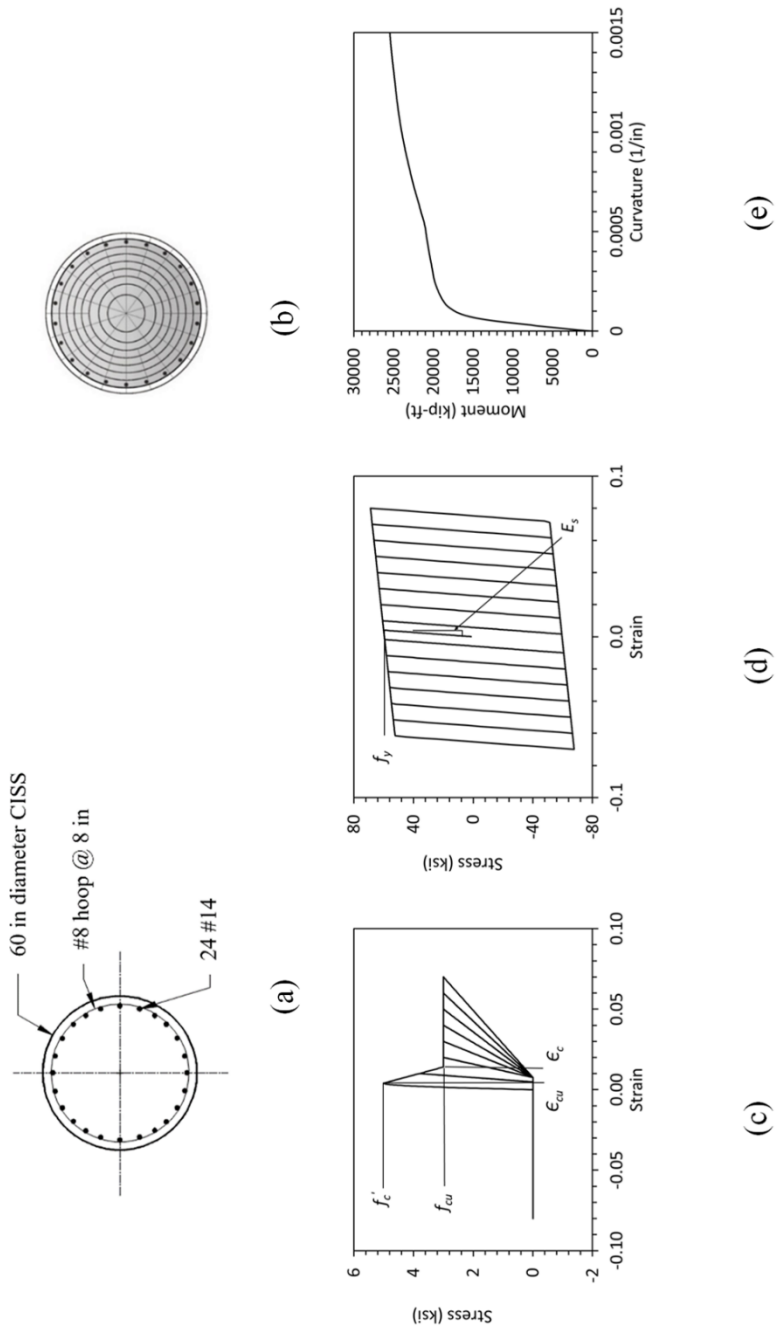
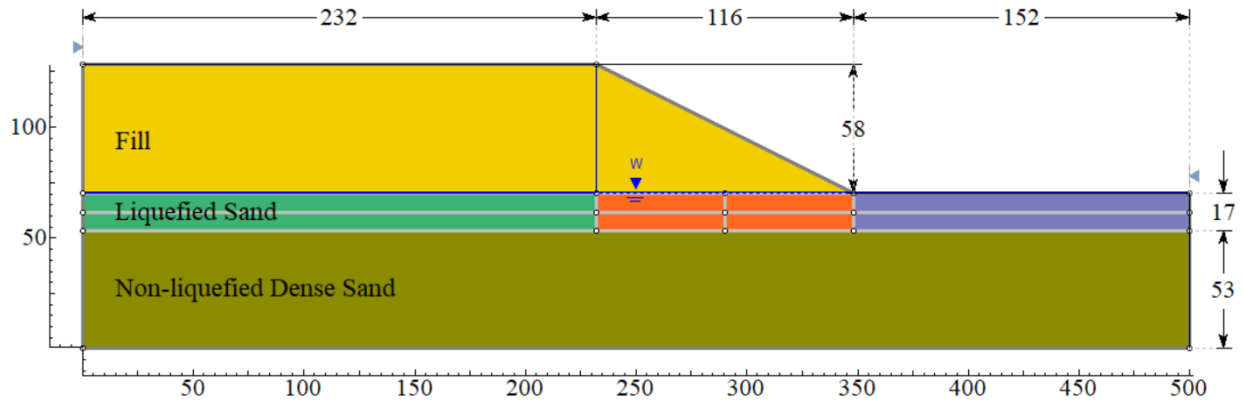
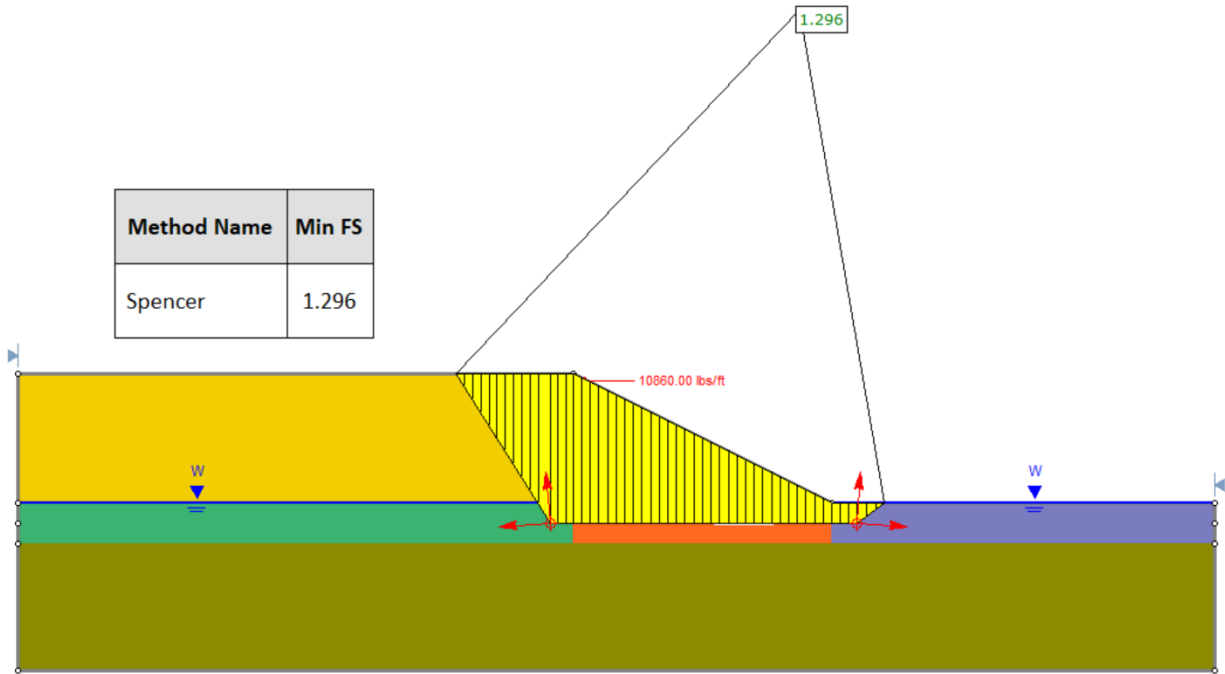


Figure 7.4. Modeling of column and pile: (a) column cross-section; (b) fiber discretization; (c) concrete model; (d) reinforcing steel bilinear inelastic model; (e) monotonic moment-curvature

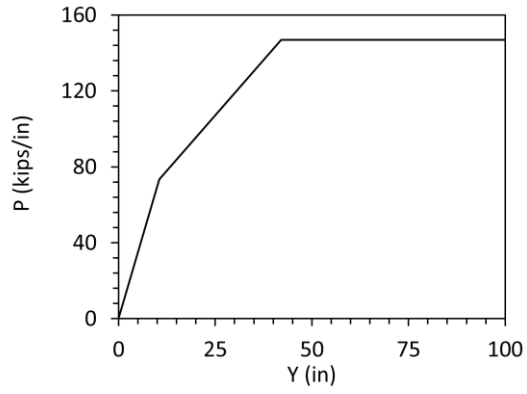


(a)

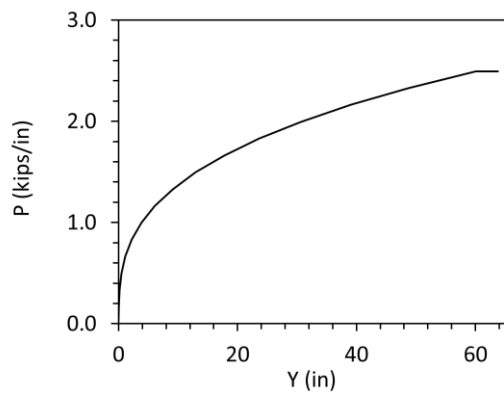


(b)

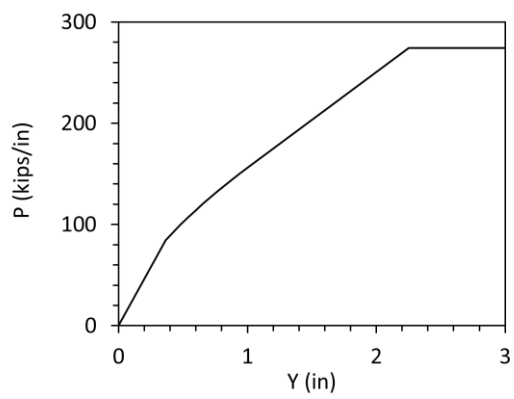
Figure 7.5. Slope stability model (dimensions shown in ft): (a) geometry and layering for the slope under study; and (b) typical failure surface for the analyzed slope.



(a)



(b)



(c)

Figure 7.6. p - y curves for: (a) the crust; (b) middle of the liquefied layer; and (c) middle of the dense sand layer

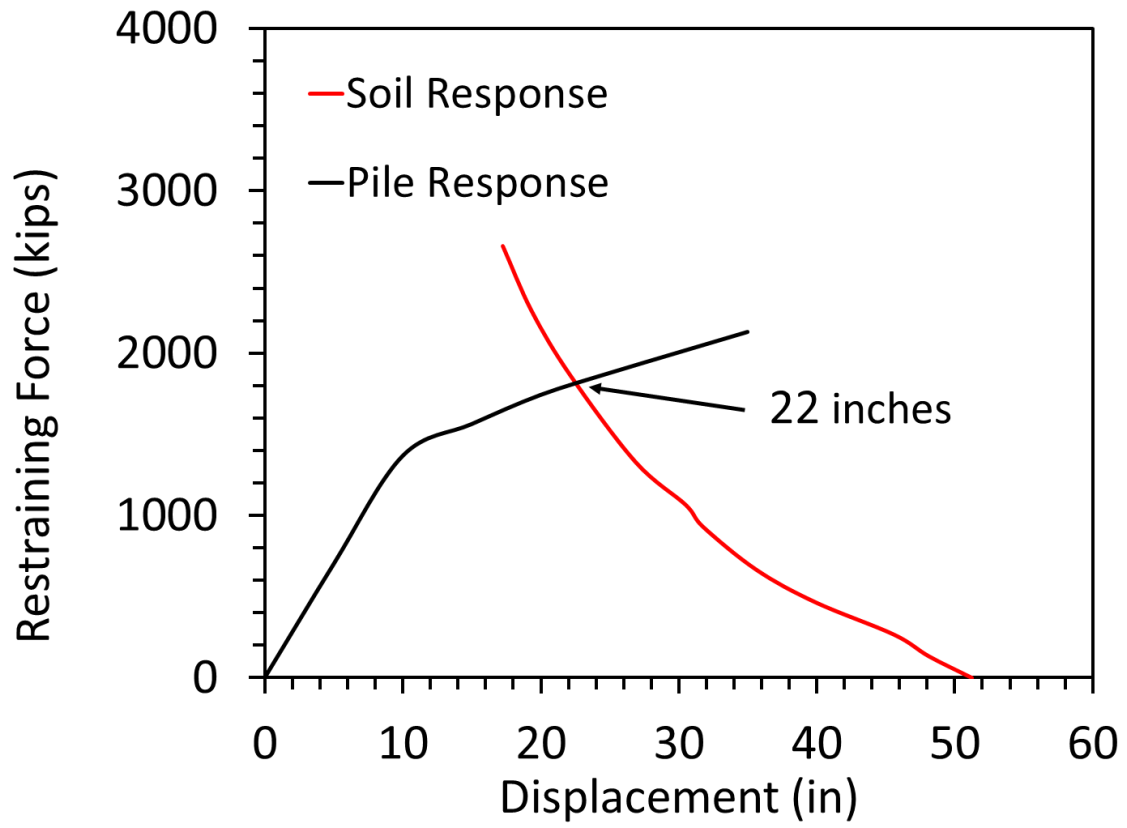


Figure 7.7. Displacement demand displacement for a representative motion

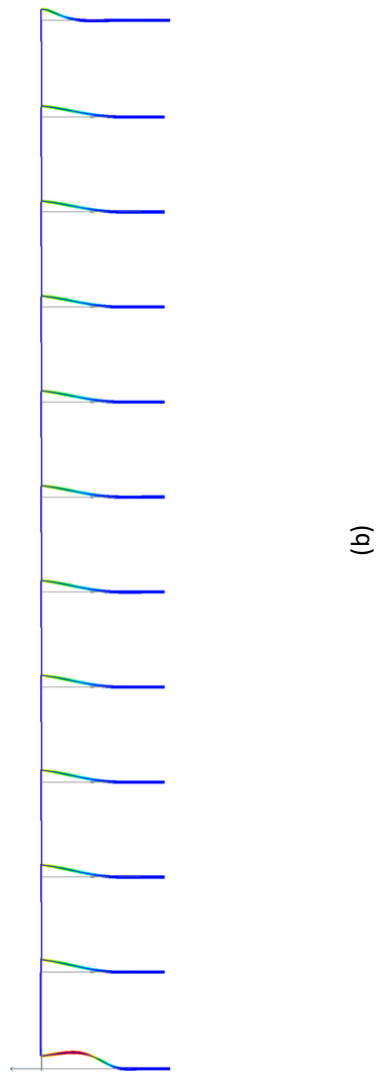
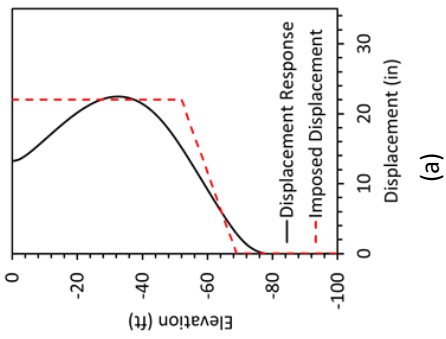


Figure 7.8. Bridge response: (a) displacement profile for the left abutment pile; and (b) deformed mesh

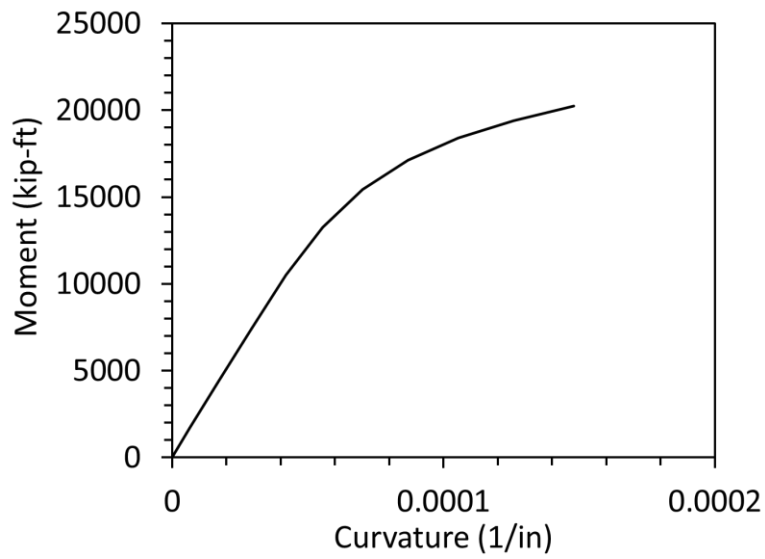


Figure 7.9. Moment-curvature response at column base

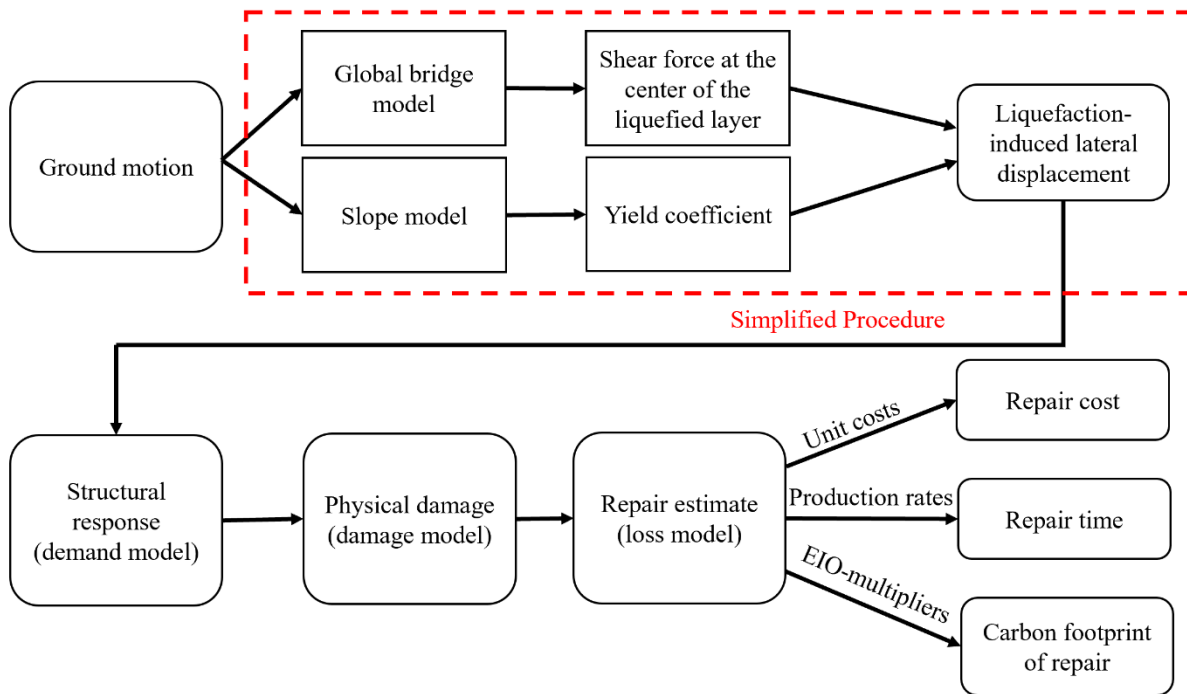


Figure 7.10. Schematic illustration of PBEE framework with the simplified procedure

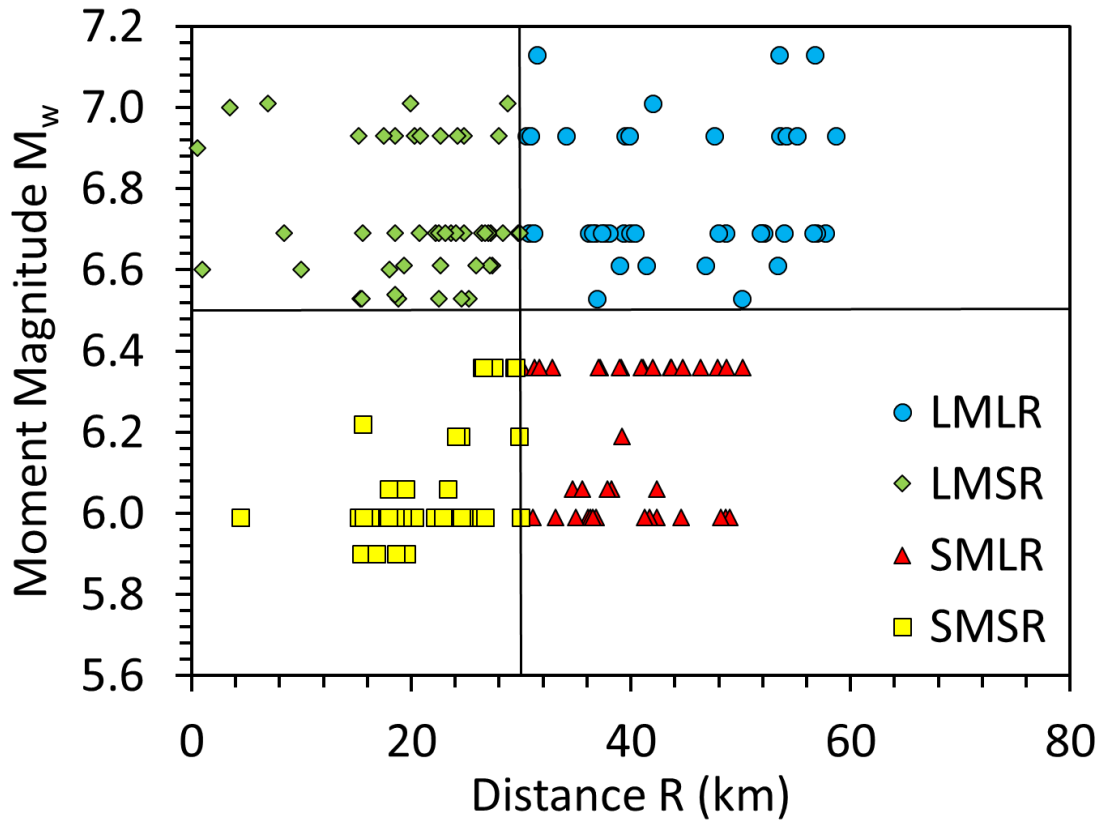


Figure 7.11. Input ground motions in M-R space

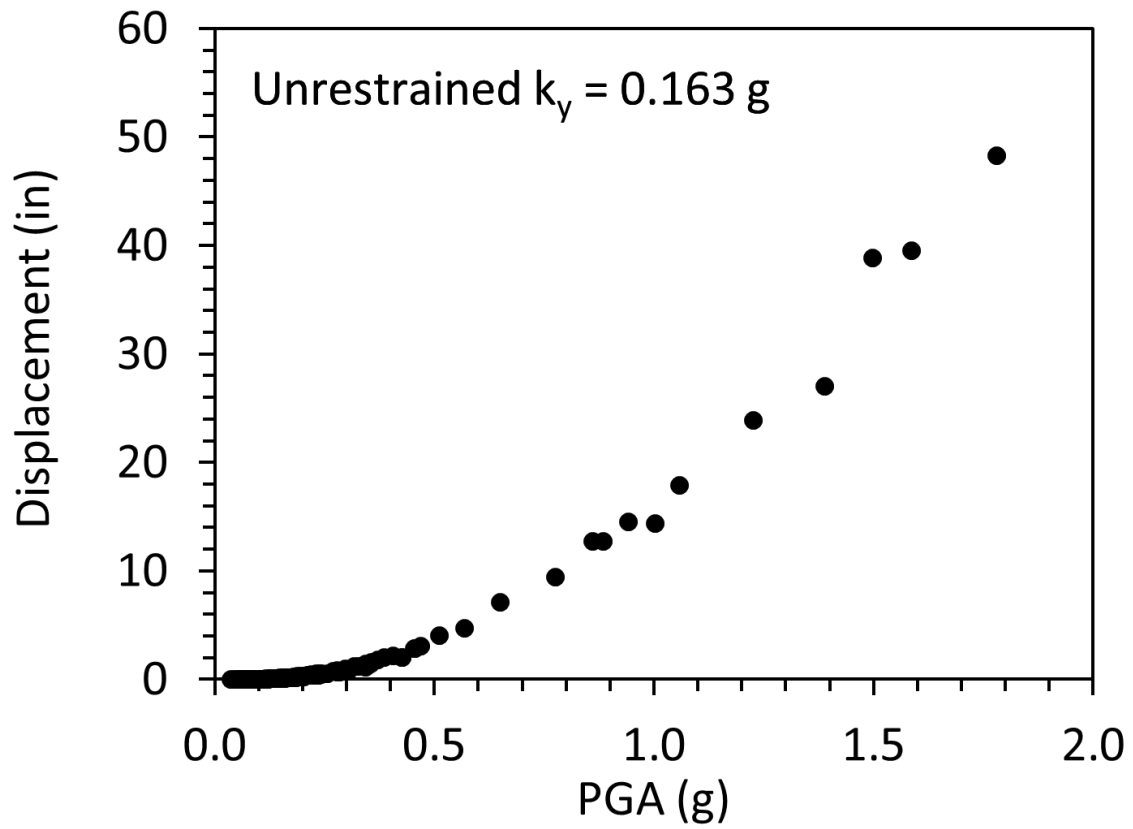


Figure 7.12. Unrestrained displacement with $k_y = 0.163$ g using Bray and Travararou (2007)

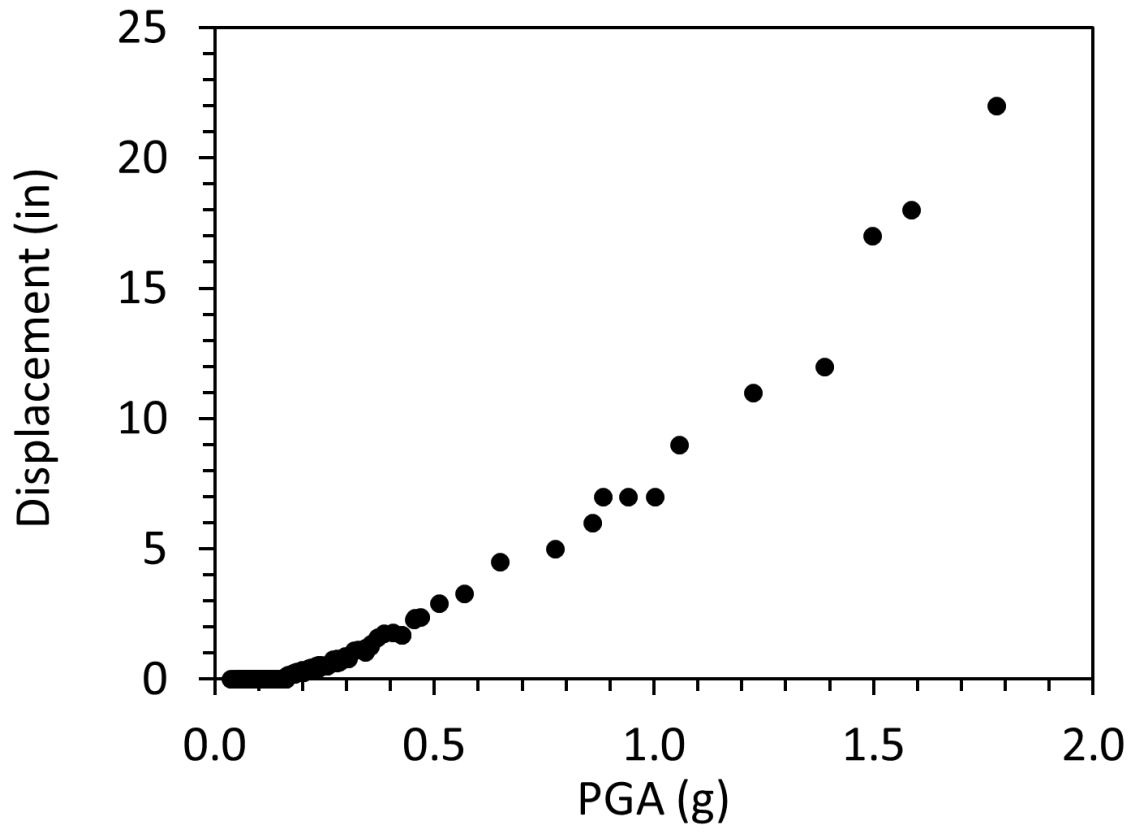


Figure 7.13. Restrained demand displacement vs. PGA

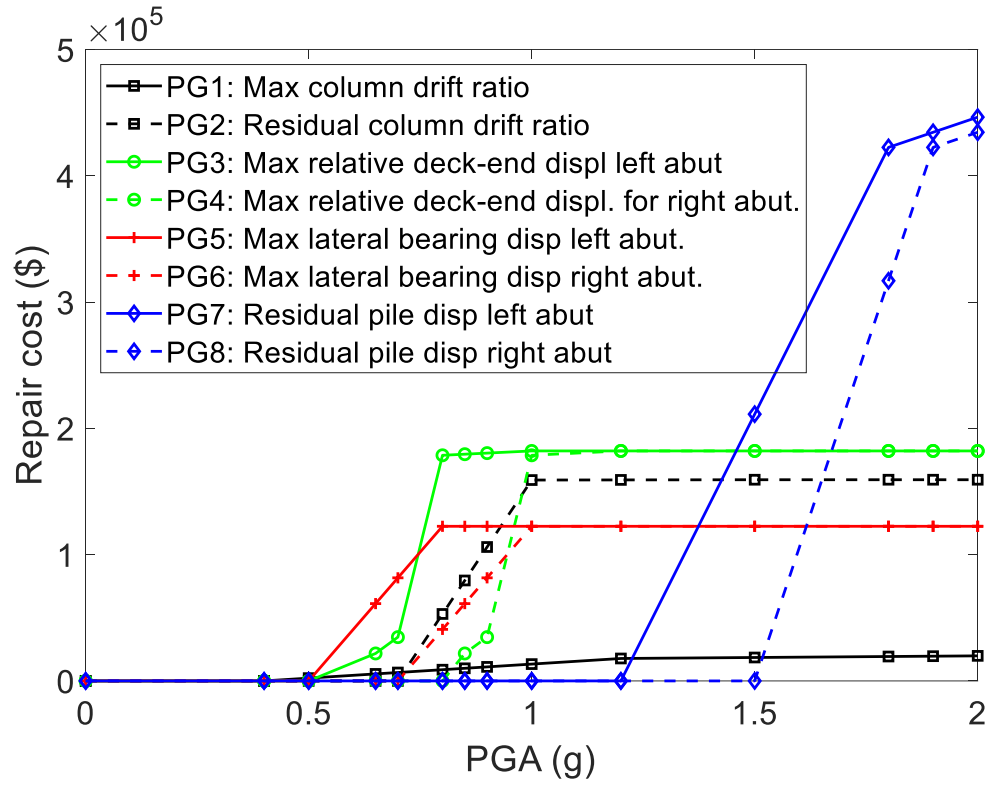
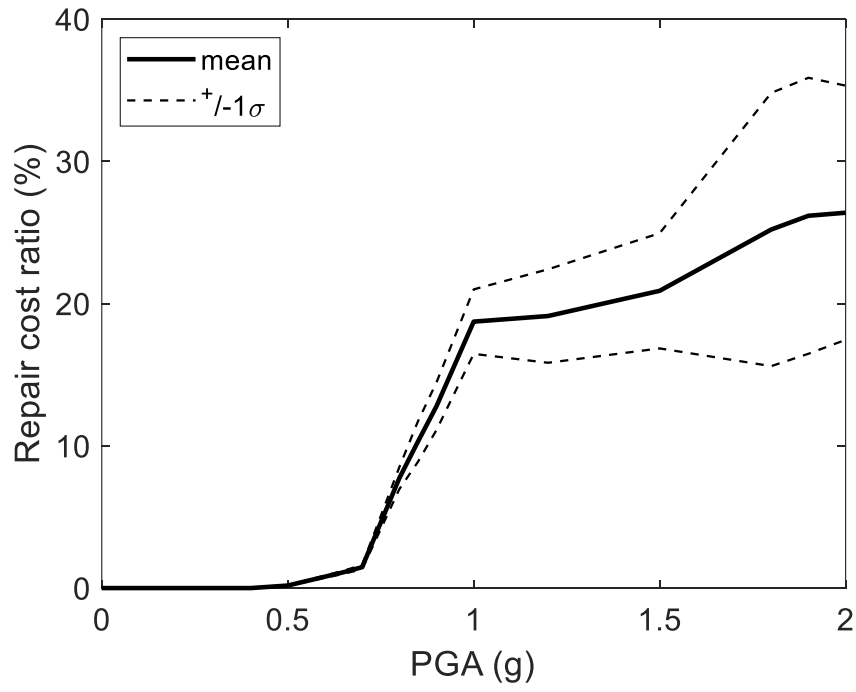
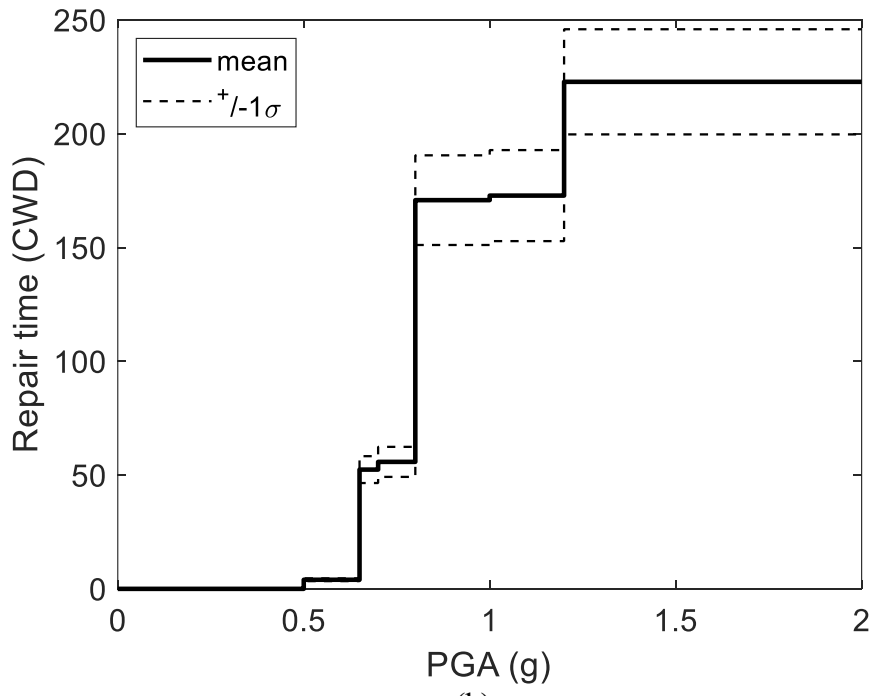


Figure 7.14. Repair cost vs. PGA by applying displacements

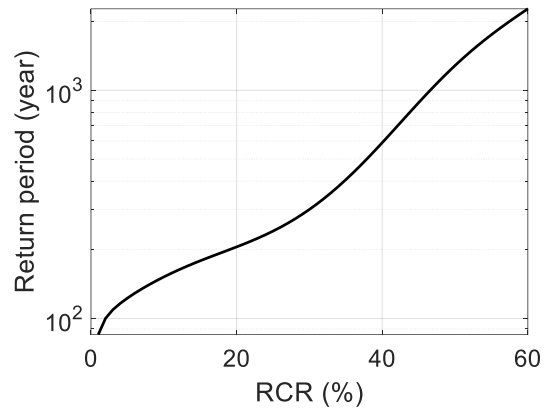
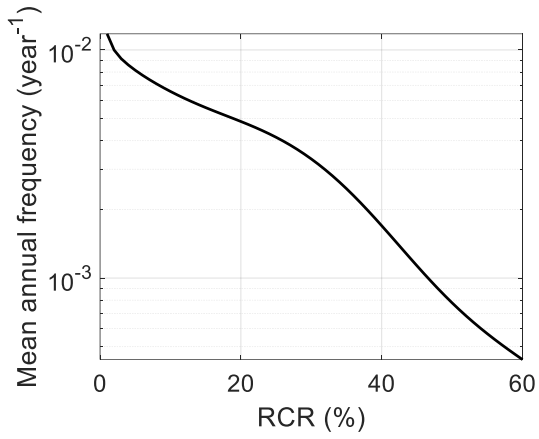


(a)

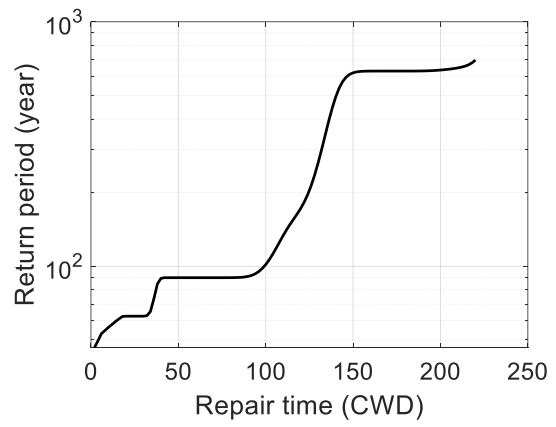
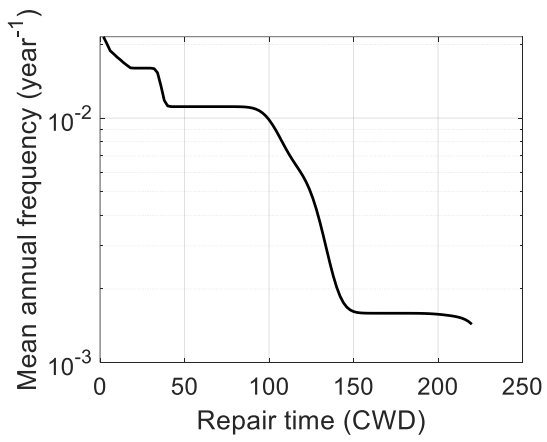


(b)

Figure 7.15. Loss models: a) mean repair cost ratio vs. PGA, b) mean repair time vs. PGA



(a)



(b)

Figure 7.16. Hazard curves: (a) mean annual frequency vs. repair time hazard curve; (b) mean annual frequency vs. repair cost ratio hazard curve

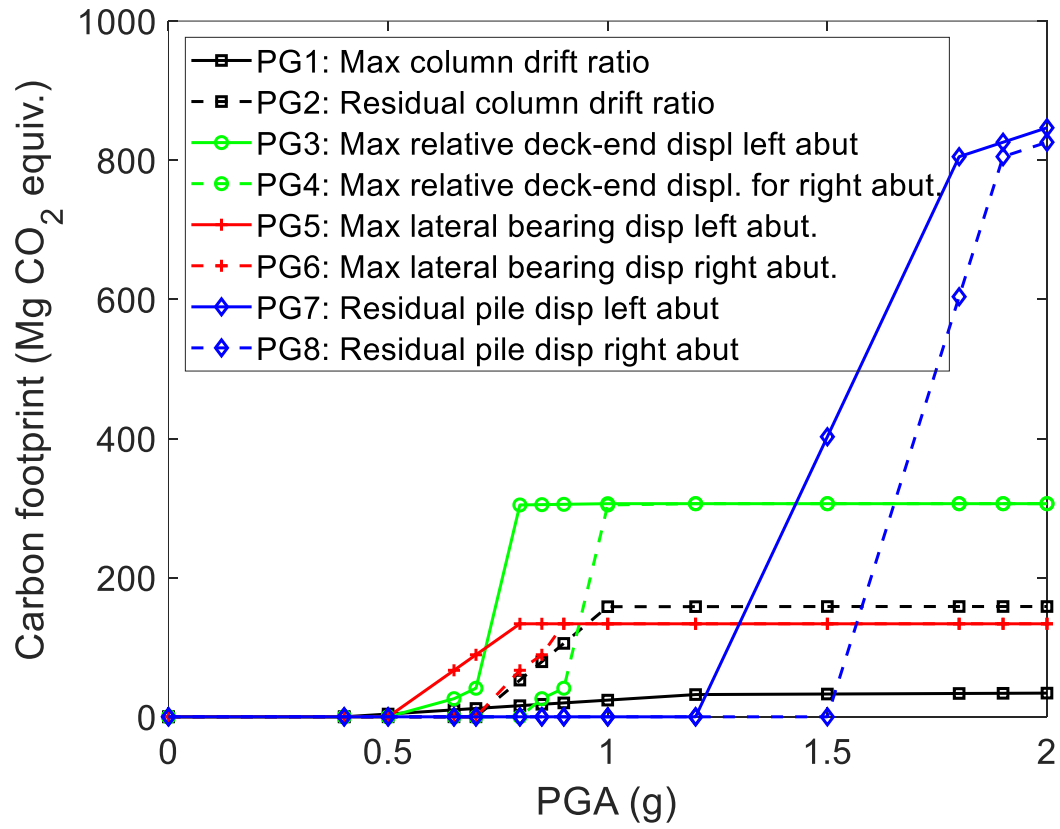


Figure 7.17. Carbon footprint of repair (CFR) vs. PGA

Chapter 8. Sensitivity of Seismic Demands for Bridge-Ground Systems Subjected to Liquefaction-Induced Lateral Spreading

8.1. Abstract

In this chapter, a practice-oriented pushover procedure was used to investigate the response of a global bridge-ground system subjected to liquefaction-induced lateral spreading. In particular, a number of parametric studies were performed to address the procedure assumptions and potential retrofit program. In light of the simplified method (proposed in MTD 20-15), the empirical equations used to estimate the demand displacement and the shear strength of the liquefied layer were considered. This study is directed towards performing a sensitivity analysis related to the assessment of liquefaction-induced lateral spreading effects on bridge foundation systems. Equivalent Static Simplified Procedure consists of two response studies: i) the slope response, and ii) the pile response. Within this analysis framework, SSI was conveniently handled by the soil p - y curves approach. In addition, the expected damage and loss were investigated using a Performance-based earthquake engineering (PBEE) framework. To facilitate this endeavor, a graphical user-interface was further developed and utilized. Based on the simulation results, the slope response was found to be highly sensitive to changes in the shear strength. Conversely, the pile response is less sensitive because of the “pile-pinning” effect. Overall, the presented results highlight the significance of the Equivalent Static Simplified Procedure parameters on the demand displacement estimation and corresponding damage to the bridge.

8.2. Introduction

In the United States, 60 percent of bridges were constructed before 1970 without fully considering seismic resistance (Itani *et al.* 2004). In particular, permanent ground displacement can cause severe damage, or even collapse to the bridge. Recent studies have shown the

significance of lateral spreading effects on bridge-ground-foundation systems (Youd 1993; Tokimatsu *et al.* 1995; Hamada *et al.* 1996; Berrill *et al.* 2001; Elgamal *et al.* 2008; Shin *et al.* 2008; Kwon *et al.* 2009; Aygün *et al.* 2009, 2011; Ledezma and Bray 2010; Wotherspoon *et al.* 2011; Ledezma *et al.* 2012; Padgett *et al.* 2013; Cubrinovski *et al.* 2014; Turner *et al.* 2016; Khosravifar *et al.* 2018).

From the practice-oriented point of view, a simplified approach has been proposed in which soil springs are used to impose the level of expected lateral ground deformation at the abutment (Caltrans 2017). This approach and similar techniques were developed and employed by a number of researchers (Finn and Fujita 2002; Boulanger *et al.* 2006, 2007; Ashford *et al.* 2009, 2011; Armstrong *et al.* 2013, 2014). In particular, Boulanger *et al.* (2006) studied the effect of two parameters on the estimation of the demand displacement: (1) the embankment width, and (2) the pile fixity in the abutment. The results showed that the design displacement was affected by varying the above-mentioned parameters.

In this study, a representative bridge model (Caltrans 2016; Caltrans 2005) was employed to exercise the analysis framework. As such, the entire bridge configuration reacted to and resisted the imposed abutment slope lateral displacements. The soil p - y curves approach was used to account for SSI according to the Simplified Method (Caltrans 2016).

In this chapter, the Simplified Procedure and the FE modeling details of the bridge ground foundation system are presented. This study is directed towards performing a sensitivity analysis related to the assessment of liquefaction-induced lateral spreading effects on bridge foundation systems. The conducted study outcomes are presented within the scope of a comparative scope to highlight the significance of the procedure assumptions and potential retrofit bridge configurations. An empirical equation proposed by Bray and Travararou (2007) was used to

estimate the demand displacement in the Simplified Method (MTD 20-15, Caltrans 2017). In addition, the empirical equation proposed by Martin and Qiu (1994) was considered and contrasted with that of Bray and Travasarou (2007). Overall, the main investigations address: i) estimation of the residual strength of liquefied soil using Kramer and Wang (2105), ii) considering potential retrofit bridge configurations; and iii) estimation of the demand displacement using alternative empirical equations.

8.3. Bridge-Foundation Model

The employed bridge configuration is a reinforced concrete box-girder bridge with 11 spans (Caltrans 2005; Caltrans 2016). Each interior span is 140 ft long and each exterior span is 142.25 ft. The substructure consists of multiple two-column bents. More details about the bridge model can be found in Chapter 7.

8.4. The Caltrans Simplified Method (Lateral spreading)

The simplified method (Caltrans 2017) combines two procedures to calculate the design displacement and forces acting on the pile foundation. More details about the method and a worked example for the studied bridge configuration can be found in Appendix J.

8.4.1. Implementation of the Simplified Method to the Bridge Abutment Foundation

The demand displacement is determined using Bray and Travasarou (2007). In the analysis, liquefiable soil was modeled as soft clay having a residual undrained shear strength calculated using an equation by Kramer and Wang (2015). Details about implementing the procedure and main outcomes of applying the demand displacements on the global bridge-ground system were presented in Chapter 7.

8.4.2. Effect of Liquefied Layer Shear Strength

The residual strength for the liquefied loose sand layer was determined using Kramer and Wang (2015) equation (equation J.1). In order to study the effect of residual strength on the overall estimates of the demand displacement, the upper bound and the lower bound of residual strength values were considered (equation J.3). Table 8.1 summarizes the comparison results of the shear strength estimation parametric study. The representative ground motion presented in Chapter 7 was also considered in this parametric study (Figure 8.1). It can be immediately gleaned from Figure 8.1 that the soil response was found to be very sensitive to the change in the residual shear strength since it was calculated using the slope model without the presence of the pile. Conversely, the pile response was found to be less sensitive to the variation in the residual shear strength, since the p - y curve resistance for the liquefied layer was originally very weak and because of the “pile-pinning” effect.

Figure 8.1 shows that the demand displacement can swing in the range of 12 inches to 34 inches with a median of 22 inches. Furthermore, Figure 8.2 shows the residual shear strength (S_r) as a function of the blow count ($(N_1)_{60}$) for a number of vertical effective stress scenarios and the variations of the estimated shear strength.

By applying the 160 motions employed in Chapter 7, the estimated demand displacements can be shown in Figure 8.3 for the median with the upper and lower bounds. Figure 8.3 shows that less demand displacement was estimated for the stronger layer and vice versa. In addition, the dispersion from the median was found to increase as the intensity measure increases using Bray and Travararou (2007) (equation J.2).

8.4.3. Effect of Potential Retrofit Configurations

The abutment pile was the only affected pile by the sliding soil. Therefore, three potential retrofit configurations were studied in this chapter to highlight the effectiveness of retrofitting the abutment piles on mitigating the lateral spreading displacements. Figure 8.4 shows the potential retrofit configurations along with the unrestrained yield acceleration.

In addition, Figure 8.5 shows the estimated demand displacements for the 160 ground motions under the unrestrained and restrained conditions. In this case, the variation of the restrained demand displacement (Figure 8.5b) was larger than the variation in the unrestrained demand displacements (Figure 8.5a).

8.4.4. Effect of the Empirical Equations to Estimate the Demand Displacement

In light of the Simplified Method found in MTD 20-15 (Caltrans 2017), the Bray and Travararou (2007) equation (equation J.2) was employed to estimate the demand displacements. An effort was made to study the effect of using an alternative empirical equation to estimate demand displacement. As such, the empirical equation proposed by Martin and Qiu (1994) (equation J.4) was used. Figure 8.6 and Figure 8.7 show the unrestrained and restrained displacements against PGV and PGA, respectively. In general, Martin and Qiu (1994) relationship resulted in lower lateral spreading displacements.

8.5. PBEE Results

Similar to the procedure implementation presented in Chapter 7, each of the demand displacements was applied to the left abutment piles while engaging the bridge resistance. These values were then correlated with an intensity measure that represents each of the employed motion. MSBridge allows for the specification of numerous Intensity measures, so as to display the

outcomes against any of these measures. Herein each earthquake motion will be represented by its PGA as the intensity measure.

For the shear strength parametric study, Figure 8.8 shows the repair costs disaggregated by each PG. The results can be further informative by directly comparing the outcomes with Figure 7.14 that represents the median case. Based on the presented results, the case of weaker liquefied layer (Median - σ) triggered damage at lower intensity measure values. Similar to the results shown in Figure 7.14, the abutment foundations PGs were the major contributors to the overall loss in terms of the repair cost. Conversely, the case of stronger liquefied layer triggered damage at higher intensity measure values. Furthermore, it worth noting that a plateau was not reached for the abutment foundation PGs which indicates that the DS2 was not triggered.

In addition, the loss models in terms of repair cost ratio (RCR) are shown in Figure 8.9. The results showed that reducing the shear strength of the liquefied layer by one standard deviation resulted significant difference over a wide range of intensity measure values.

For the potential retrofit configurations parametric study, Figure 8.10 shows the loss models in terms of RCR. The results show relatively little change. More favorable would result from placing the retrofit piles within the original deck width zone. Thus, an additional analysis of this scenario is warranted.

For alternative displacement equations parametric study, a similar conclusion was drawn from the comparison of the loss from applying demand displacements estimated using two different empirical equations. In general, differences were found. In particular, in the range between 1g-1.5g, less damage was expected when using Martin and Qiu (1994) equation.

8.6. Summary and Conclusions

The seismic response of a global multi-span bridge-ground system subjected to liquefaction-induced permanent displacement is studied and discussed in light of the simplified method (proposed in MTD 20-15) assumptions. In addition, sensitivity studies on the effect of the major procedure assumptions are conducted. The main conclusions and finding are summarized below:

- (i) the estimated demand displacements were very sensitive to the shear strength of the liquefied layer. In particular, the soil response was significantly influenced.
- (ii) On the other hand, that effect was limited to the pile response since the p - y curves were already weak.
- (iii) Based on the PBEE outcomes, reducing the shear strength resulted significant difference over a wide range of intensity measure values.
- (iv) For potential retrofit configurations consideration, the results showed relatively little change.
- (v) Use of Martin and Qiu (1994) empirical equation over Bray and Travararou (2007) empirical equation resulted in less demand displacement and consequently, less loss estimation.

8.7. Acknowledgements

Chapter 8, in full, is currently being prepared for submission for publication of the material as it may appear in the following journal publication (The dissertation author was the primary investigator and author of this paper):

Almutairi, A.S., Lu, J., Wang, N. and Elgamal, A., "Sensitivity of Seismic Demands of Bridge-Ground System Subjected to Liquefaction-Induced Lateral Spreading".

Table 8.1. Summary of comparison for shear strength estimation study

Embankment zone	σ'_v (psf)	S_r (psf)		
		Median - σ	Median	Median + σ
Bottom	658	155	251	406
Midslope	2026	288	444	683
top	3394	386	589	898
k_y (g)		0.087	0.163	0.266
Unrestrained displacement (in)		101	51	25
Restrained displacement (in)		34	22	12

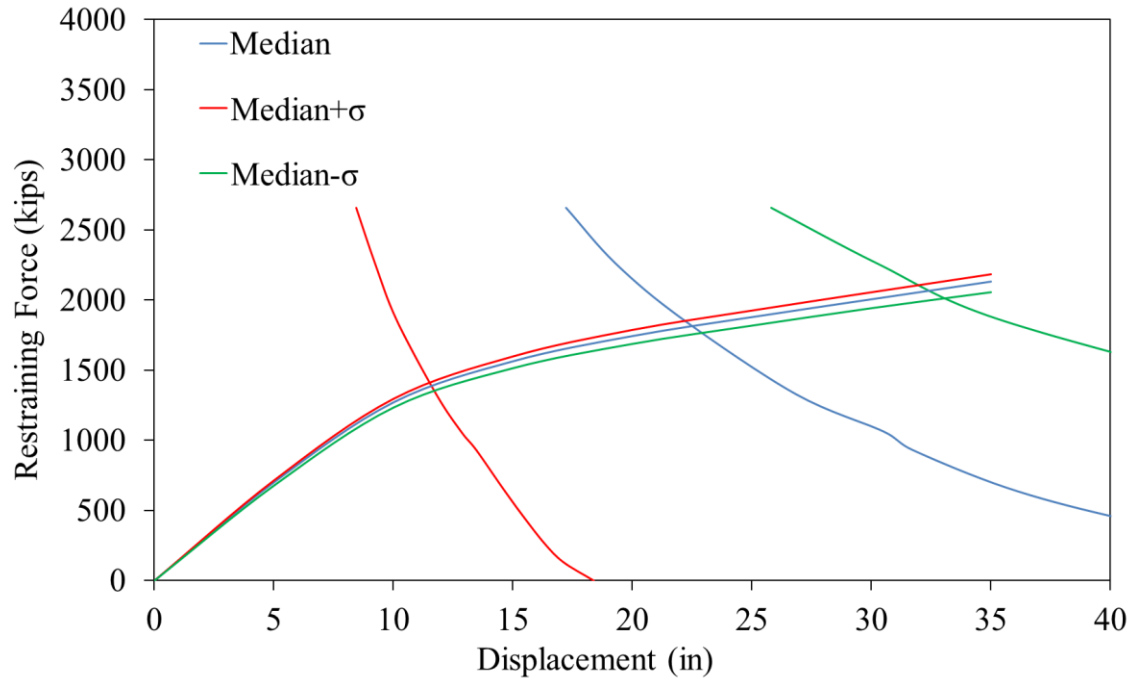
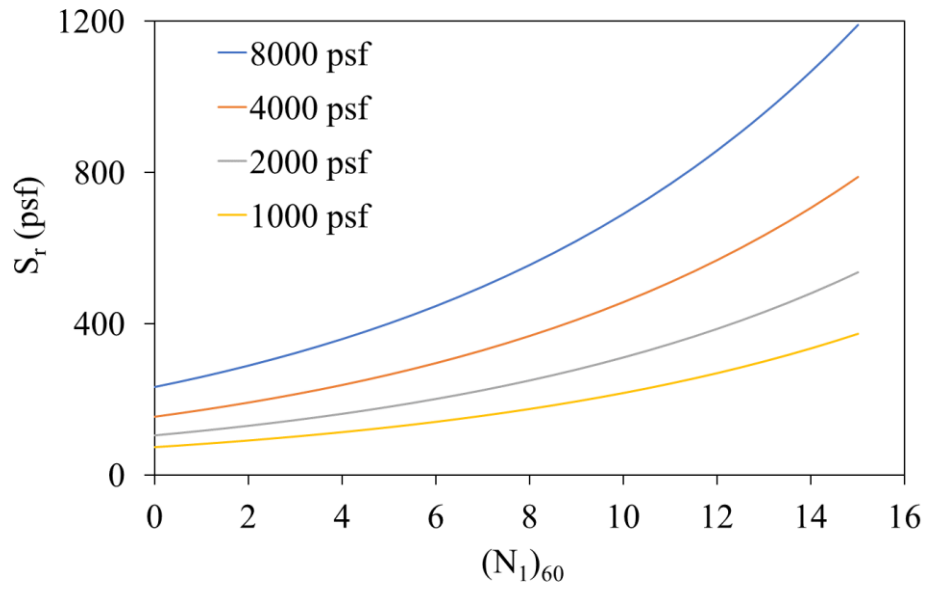
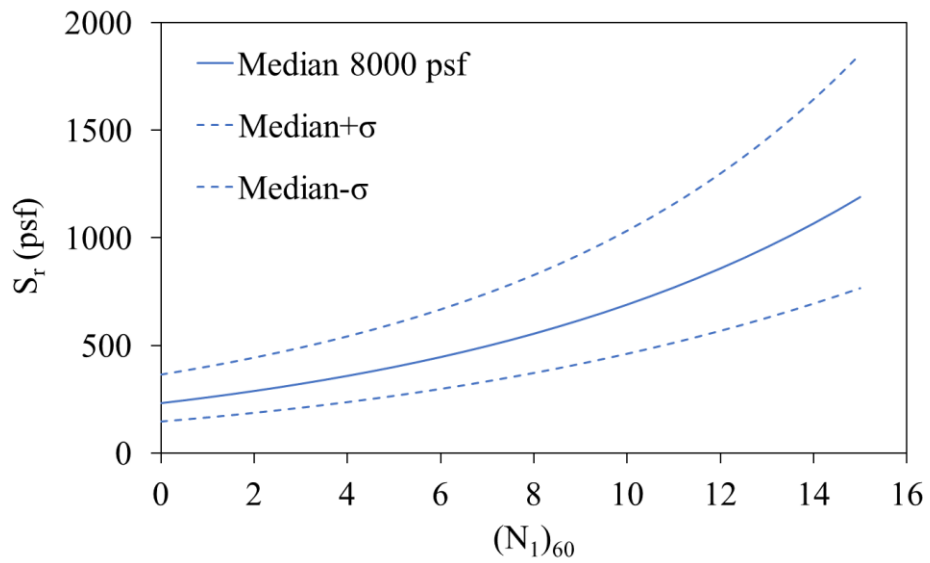


Figure 8.1. Shear strength effect on the estimation of the demand displacement

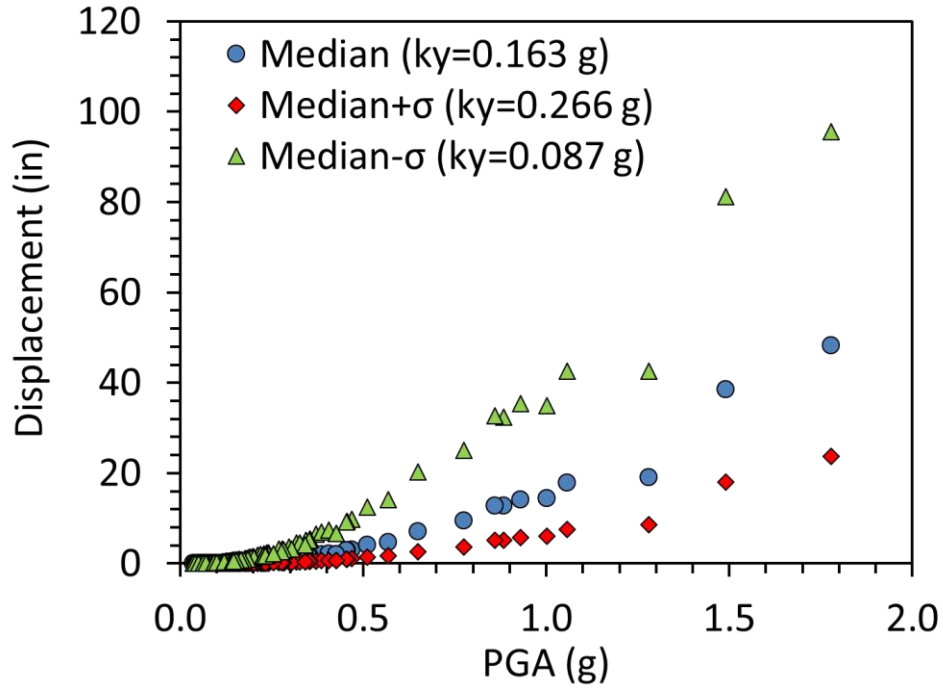


(a)

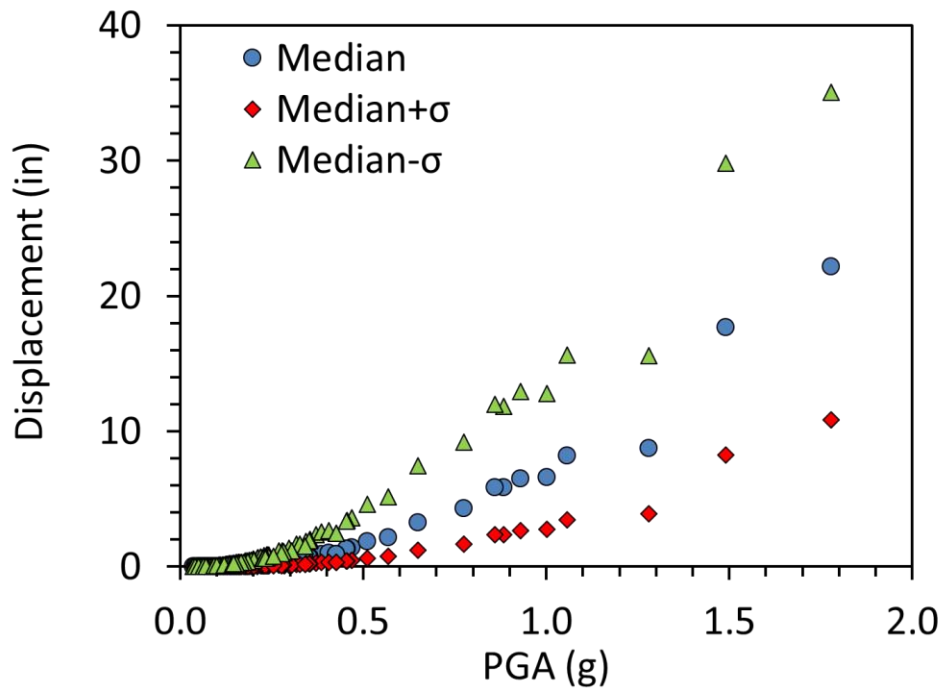


(b)

Figure 8.2. Residual strengths predicted by Kramer and Wang (2015): (a) different vertical stresses, and (b) with probabilistic moments

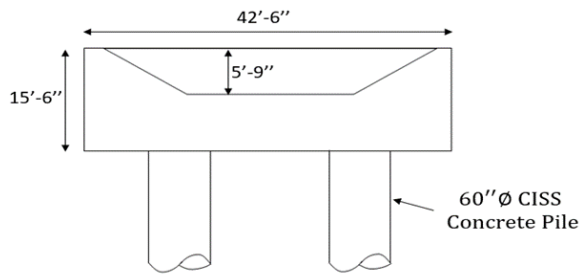


(a)

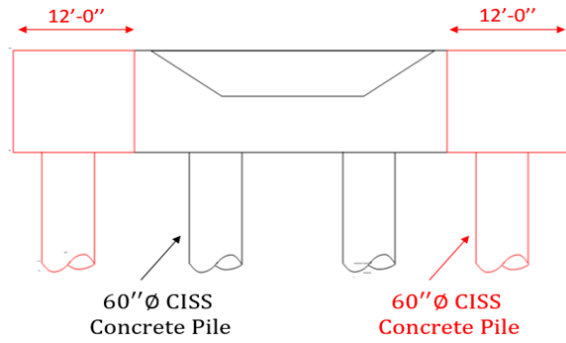


(b)

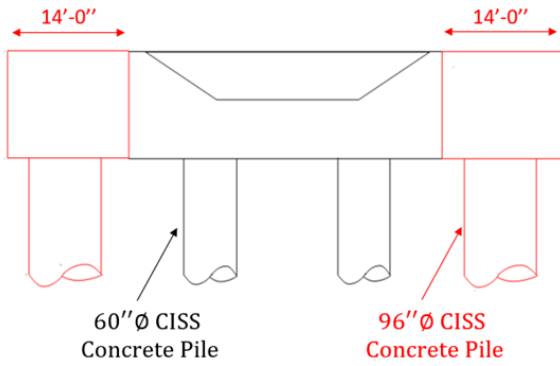
Figure 8.3. Estimated displacement for different shear strength for: (a) unrestrained, and (b) restrained



(a)



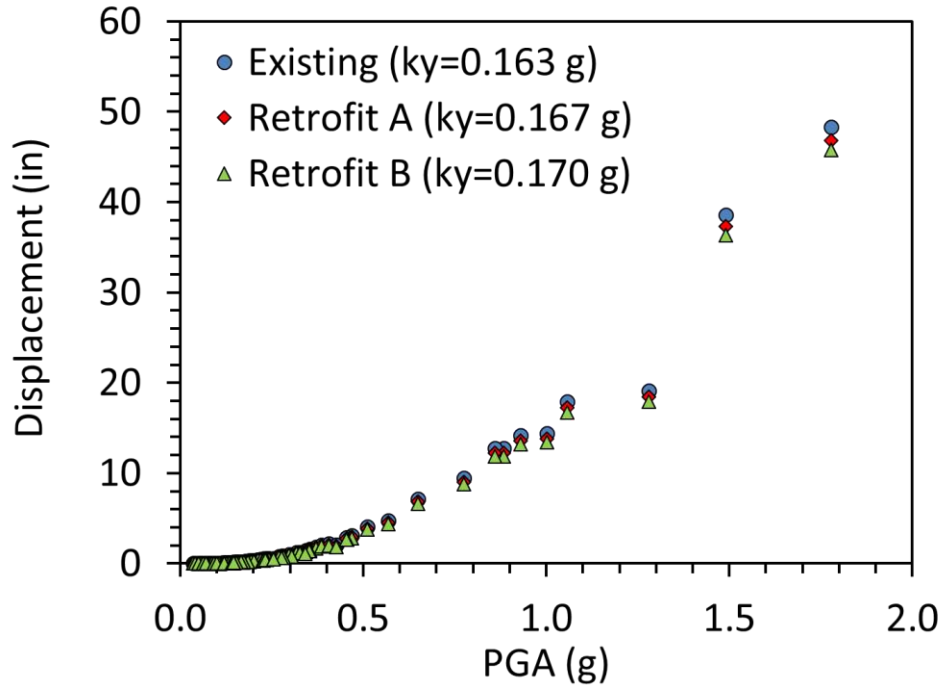
(b)



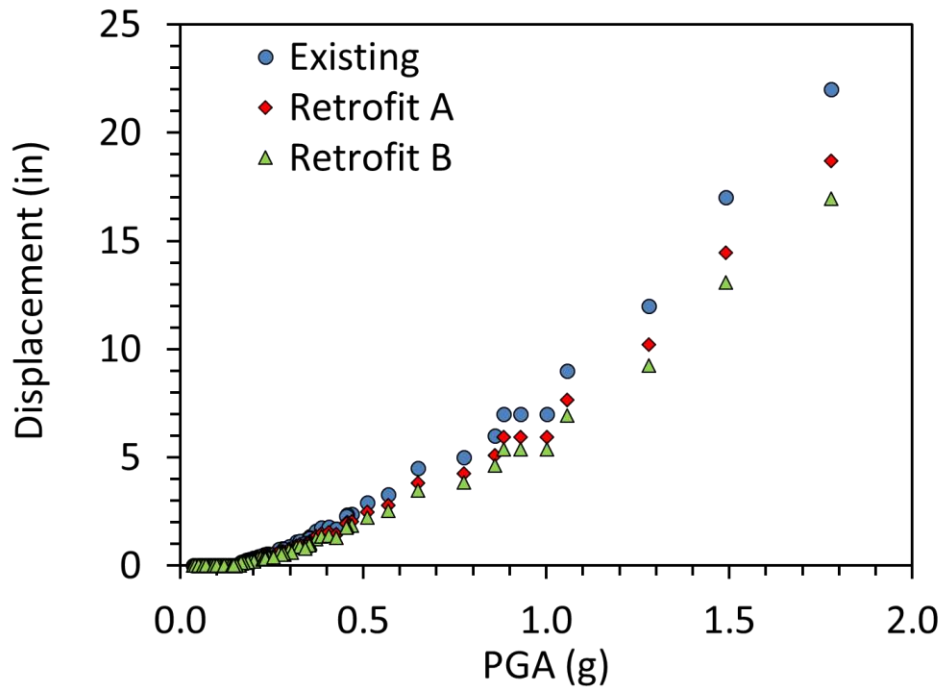
(c)

Case	k_y (g)	F_{deck} (lbs/ft)
Existing Bridge	0.163	8,000
Retrofit A	0.167	9,000
Retrofit B	0.170	9,400

Figure 8.4. Abutment layout for: (a) existing bridge; (b) Retrofit A; (c) Retrofit B

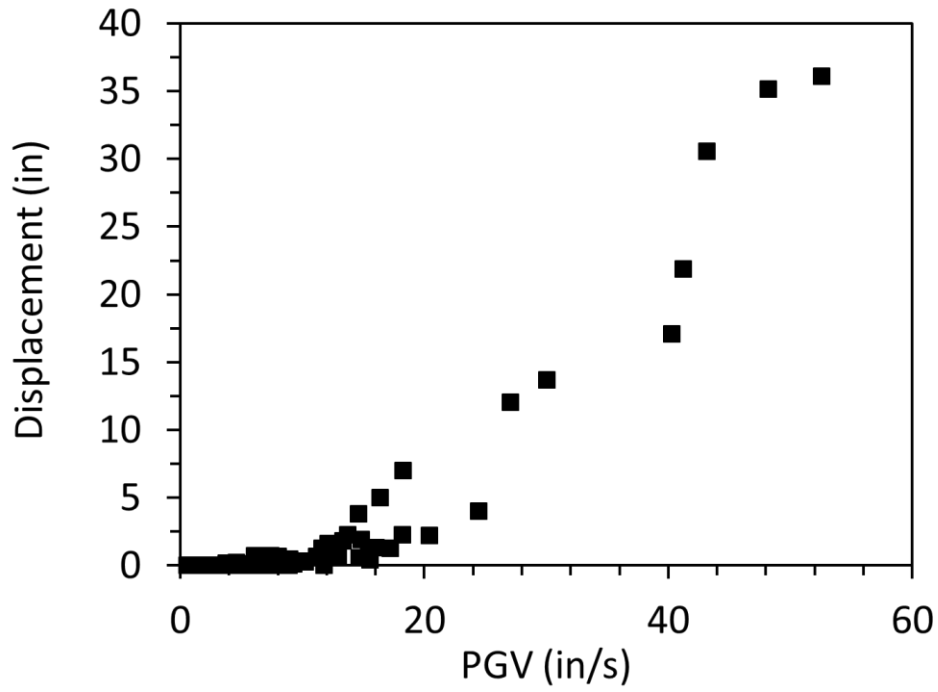


(a)

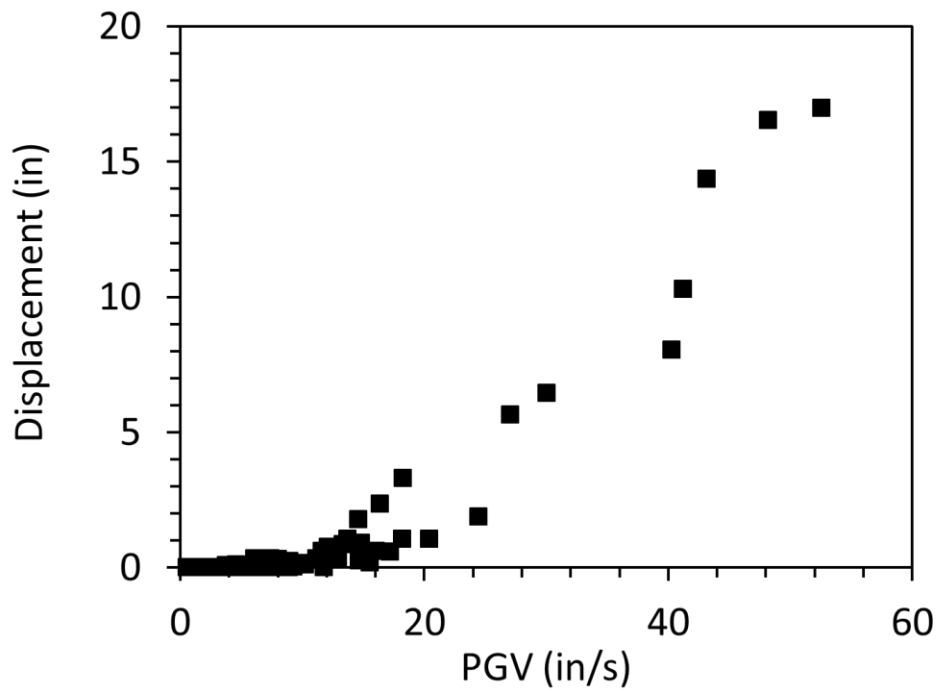


(b)

Figure 8.5. Estimated displacement for different retrofit configuration for: (a) unrestrained, and (b) restrained

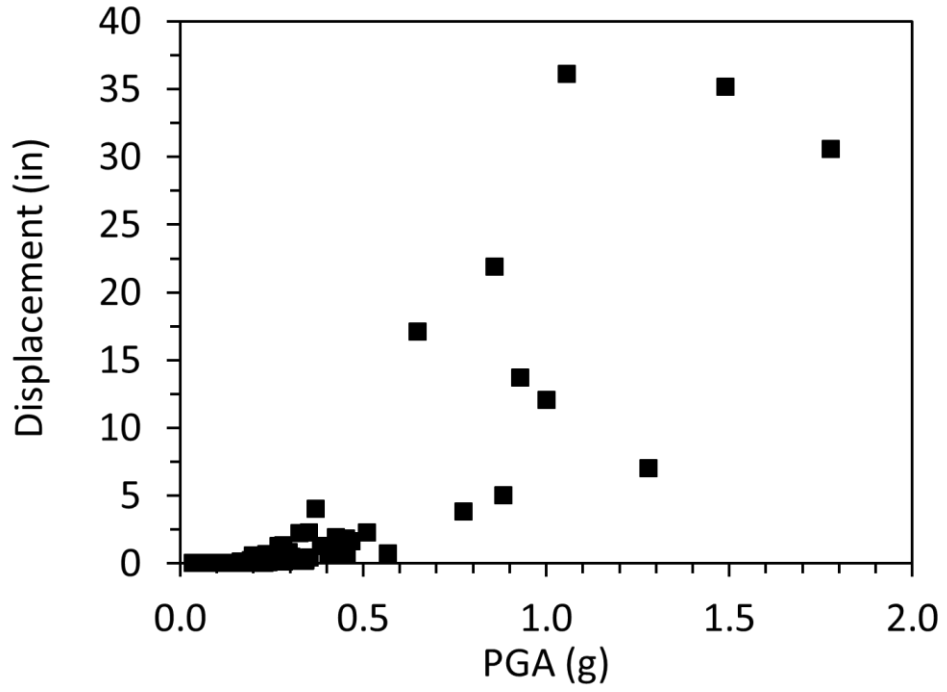


(a)

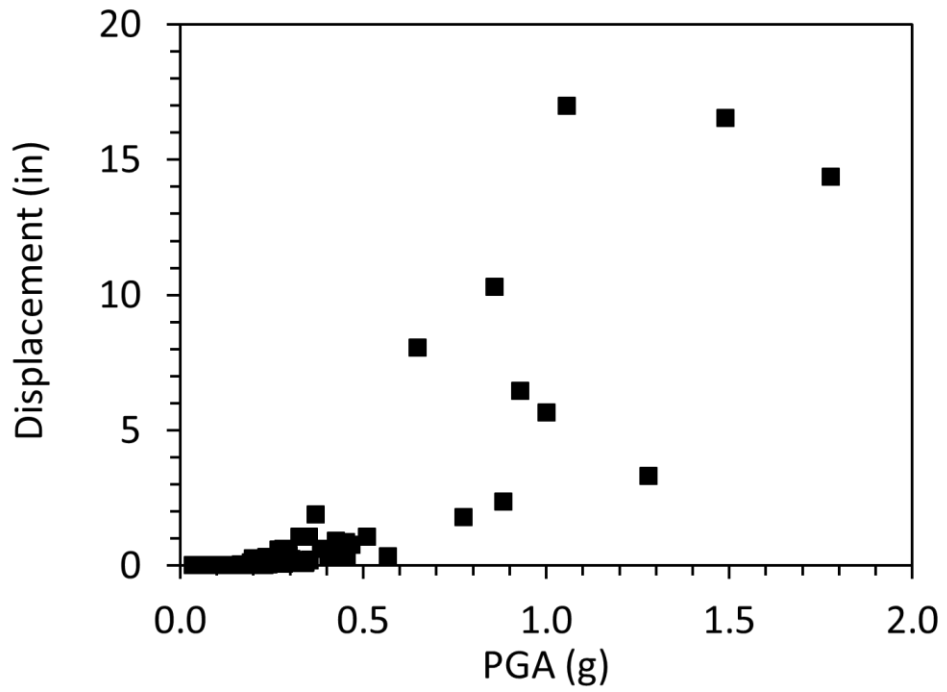


(b)

Figure 8.6. Estimated displacement using Martin and Qiu (1994) against PGV for: (a) unrestrained, and (b) restrained



(a)



(b)

Figure 8.7. Estimated displacement using Martin and Qiu (1994) against PGA for: (a) unrestrained, and (b) restrained

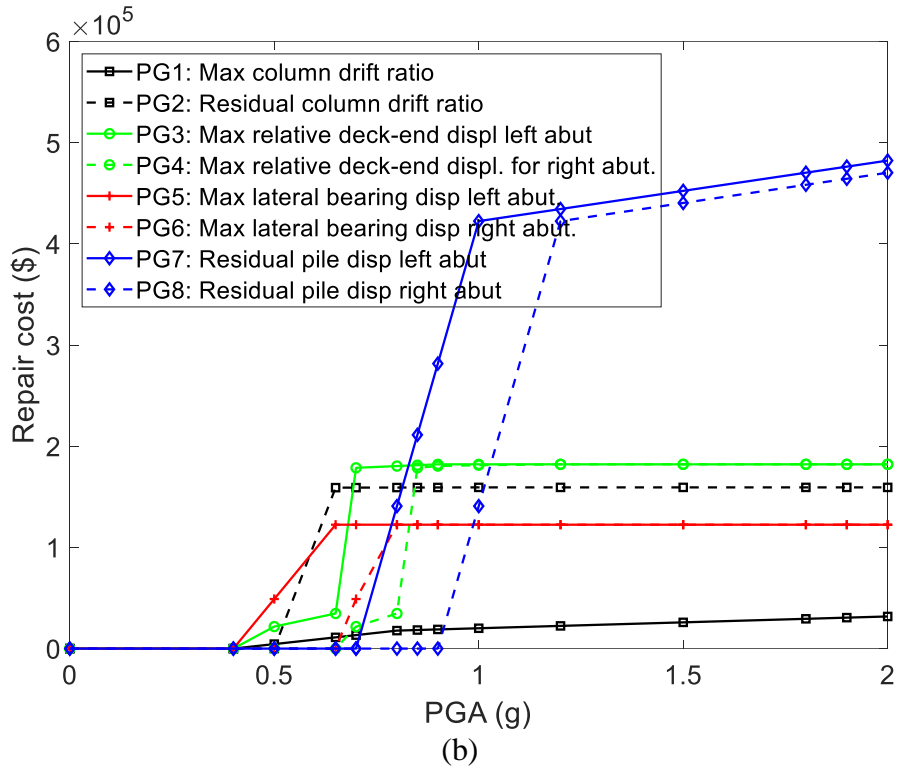
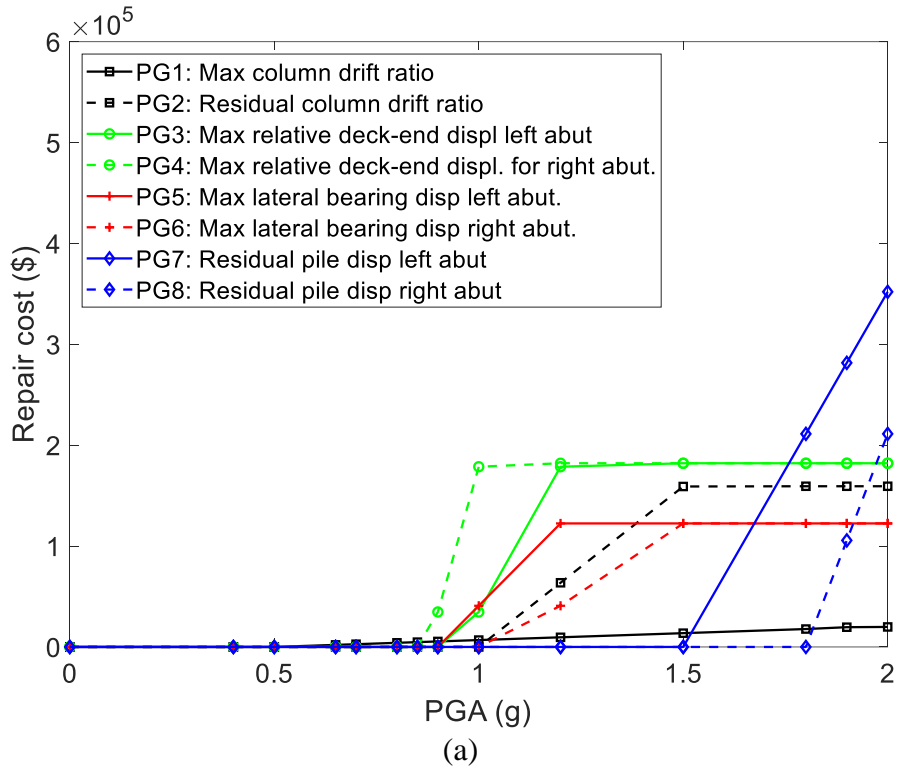


Figure 8.8. Repair cost disaggregated by PG vs. PGA for: (a) upper bound shear strength; (b) lower bound shear strength

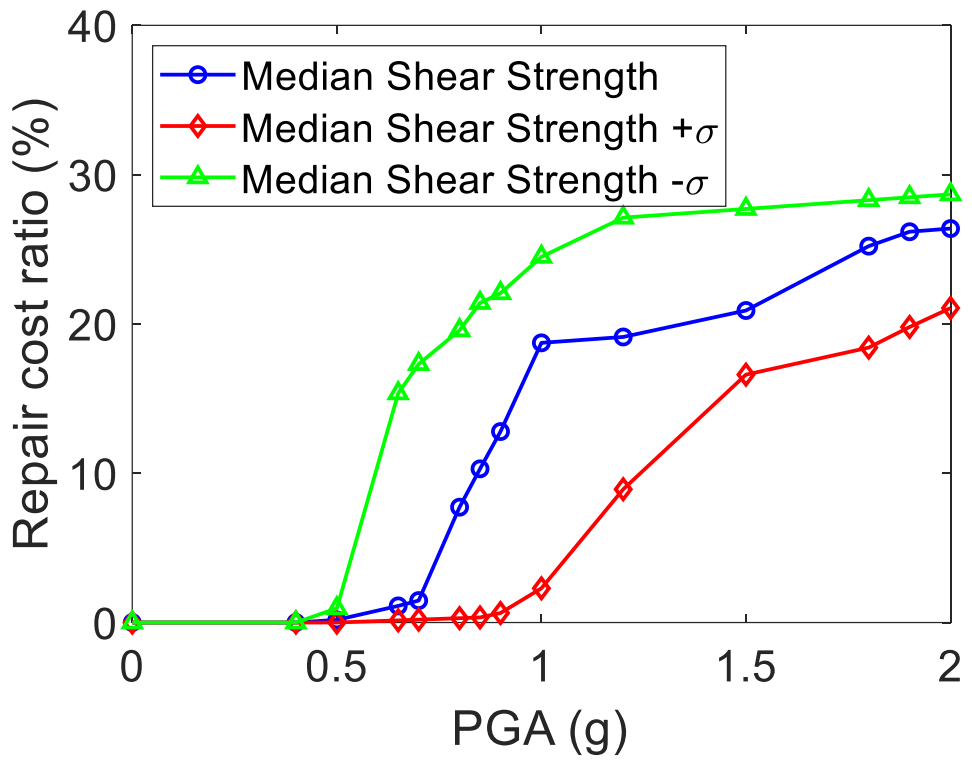


Figure 8.9. Mean repair cost ratio vs. PGA for shear strength estimation

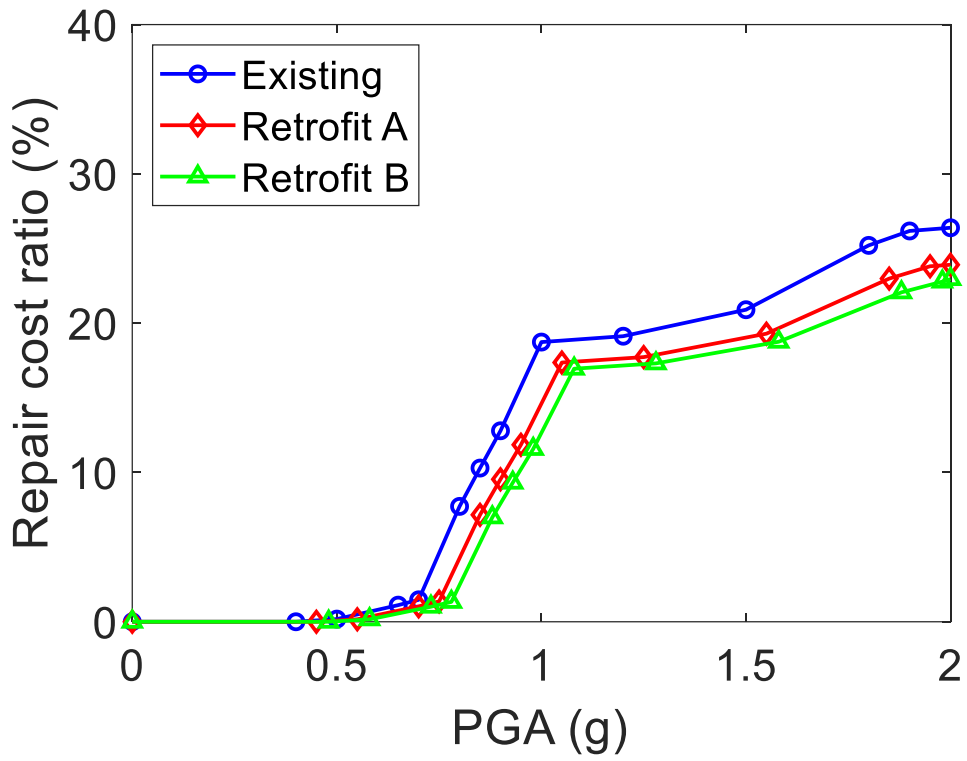


Figure 8.10. Mean repair cost ratio vs. PGA for different retrofit configurations

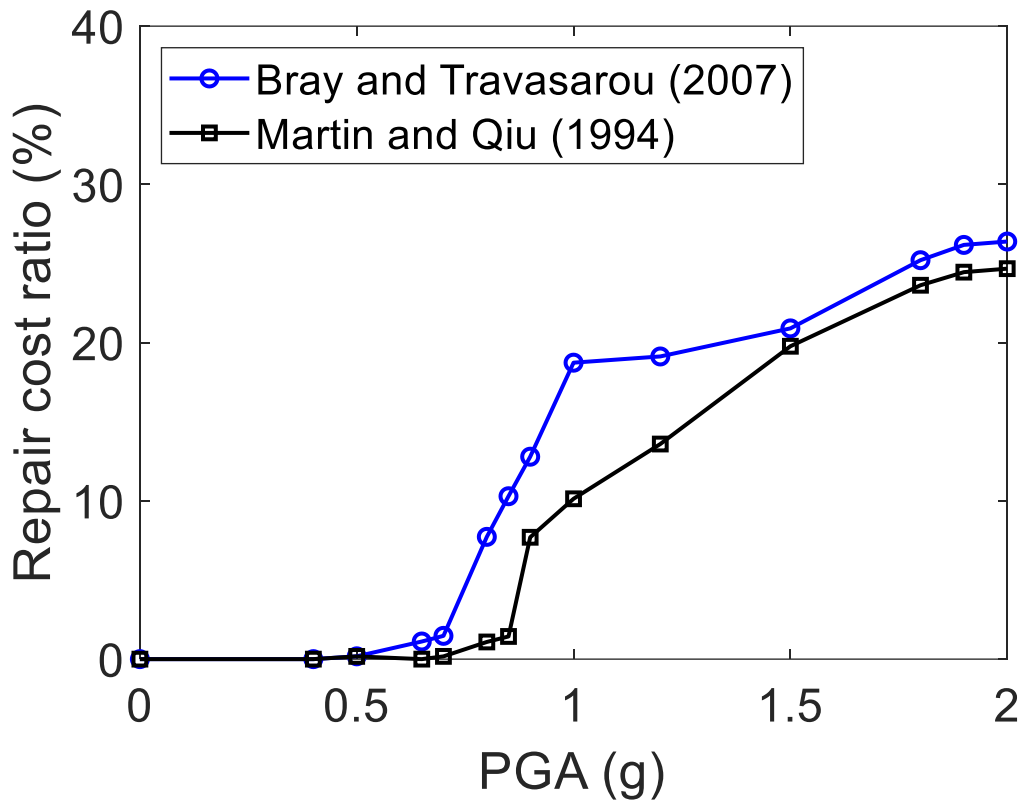


Figure 8.11. Mean repair cost ratio vs. PGA for different empirical equations

Chapter 9. Conclusions and Future Work

9.1. Summary

Finite Element (FE) modeling provides an effective mechanism for understanding the entire structure-foundation-ground system response. OpenSees (ver. 2.5.0), an open-source software for simulating the seismic response of structural and geotechnical systems (Mazzoni *et al.* 2009, McKenna *et al.* 2010) is utilized to conduct nonlinear FE studies of multi-span bridge systems. To facilitate the conducted OpenSees analyses, the user-interface MSBridge (Elgamal *et al.* 2014; Lu *et al.* 2015) was further developed and employed.

Seismic response studies of multi-span bridges were performed using OpenSees. The models investigated were derived from three bridge configurations, namely, the Salinas River Bridge, the Samoa Channel Bridge, and the Eureka Channel Bridge. Nonlinear Time History Analysis (THA) was conducted for 14 input motions provided by Caltrans (ranging from 0.32g-0.71g in peak acceleration). The THA procedures and results are presented for the studied bridge configurations. To provide insights, results of the conventional Equivalent Static Analysis (ESA) procedure are presented and compared to the THA average displacement demand outcome.

Recently, performance-based design in civil engineering has been receiving a great deal of attention, and many design codes are initiating the application of its concepts. As a result, the PEER Performance-Based Earthquake Engineering (PBEE) framework was employed to estimate the probabilistic seismic system response. This framework is implemented in MSBridge to provide a unique tool that enables nonlinear FE studies as well as performance-based assessment within an integrated simulation environment. This tool systematically provides valuable insights on the demand, damage, and loss models of multi-span bridge-ground systems.

Seismic response was addressed by the global modeling of the bridge-ground system as an integral entity. Therefore, nonlinear representation of the bridge deck, columns, abutments, and foundation response were integrated within a unified framework.

A FE model of an existing large heavily instrumented bridge system at Eureka California (Samoa Channel Bridge) was developed. Focus was placed on calibrating the bridge model based on recorded earthquake response. Numerical simulations of the bridge under seismic loading conditions were conducted. PBEE was utilized to estimate the post-earthquake loss in terms of repair cost and repair time.

Furthermore, the assessment of liquefaction induced lateral spreading effects on global bridge foundation systems was studied in light of the simplified MTD 20-15 procedure (Caltrans 2017). The method uses slope stability analysis (step 1) to evaluate the soil lateral movement and imposes this ground displacement on the affected piles via p - y curves (step 2) to evaluate the response. The combination of the two steps produces the demand displacement and forces acting on the pile foundation. Sensitivity studies on the effect of the equations used to estimate the demand displacement and the shear strength of the liquefied layer were conducted. The presented results display a significant influence on the final estimated displacement demands.

As a whole, this dissertation provides a range of studies to enhance the understanding of nonlinear analysis of multi-span bridge systems including the impact of Soil-Structure Interaction (SSI), and to reliably estimate the loss under a wide range of earthquake scenarios.

9.2. Conclusions

9.2.1. Seismic Response of Highway Bridges

The seismic response of overall bridge-ground systems is studied. Numerical simulations of the bridge model under seismic loading conditions were conducted. To facilitate systematic

execution of this analysis, a graphical-user-interface (OpenSees-MSBridge) was further developed and utilized. Among the main conclusions are:

1. Beneficial outcomes can result from the adoption of an analysis model that is calibrated and verified by the recorded data set.
2. The use of site-specific earthquake ground motions provides a solid basis for understanding the entire structure-foundation-ground system response and for probabilistically estimating the post-earthquake loss.
3. A finite element model developed for the bridge-foundation-ground system as an integral entity provides detailed insights and captures the main interaction mechanisms between the primary bridge components.
4. Such interactions would be difficult to simulate without fully considering SSI as in current practice.
5. SSI may play a vital role in shaping the dynamic response characteristics of the bridge-ground system. In this regard, soil may isolate or amplify the shaking felt by the superstructure.
6. Particularly for short bridges, seismic response has been found to be significantly influenced by the abutment behavior. Therefore, a model that includes the major components of the abutment system such as gap, bearing pads, back wall, and foundation resistance should be used.

9.2.2. Performance-Based Assessment

The PEER PBEE framework was employed to estimate the seismic probabilistic assessment of a bridge-ground system. This framework is implemented in MSBridge to provide

valuable insights on the demand, damage and loss models in terms of repair cost, repair time and carbon footprint of repair. The main conclusions are summarized as follows:

1. SSI may cause a reduction in estimated column loss (by reducing the drift ratio). However, that reduction may be offset by the increased abutment and foundation deformations.
2. In the conducted studies, applying motions with a probability of exceedance of 50% in 50 years results in minor expected damage. Conversely, the bridge-ground systems are vulnerable to earthquakes at the 2% in 50 years seismic hazard level with higher expected damage.
3. In the conducted studies of relatively more recent constructed/retrofitted bridges, the foundation and abutment repairs are among the most significant parameters that contribute to the repair costs and the repair times. Therefore, special attention should be given to these quantities especially when considering the coupled soil-structure system response.

9.2.3. Practice-Oriented Lateral Spreading Analysis Approach

The seismic response of a global multi-span bridge-ground system subjected to liquefaction-induced permanent displacement was studied and discussed in light of the simplified method (proposed in MTD 20-15, Caltrans 2017) assumptions. In addition, sensitivity studies on the effect of the major procedure assumptions were conducted. The main conclusions and findings are summarized below:

1. Modeling of the bridge superstructure as a global system is of paramount importance to realistically estimate the demand displacement.
2. The estimated displacement is highly sensitive to the residual strength of the liquefied layer and the displacement empirical equations.

9.3. Future Work

To extend the work presented in this dissertation, additional research is needed to further investigate the seismic response of bridges and to estimate the loss. The following is a list of topics that are likely to advance the field:

1. For ESA and THA comparison, a more representative investigation can be conducted with input ground motion varying along the depth of the foundation shafts.
2. In light of the significance of the model calibration, newly constructed/retrofitted bridges should have sensors installed to record the bridge actual response under a wide range of shaking events. As such, the gap between the actual response and that from the simulation environment can be reduced.
3. Based on conducted investigations, abutment and foundations are the main contributing components to the repair cost estimation. Therefore, additional research focused on these bridge components is required to increase the understanding of their behavior.
4. For lateral spreading demand, the use of different equations to estimate the displacement should be considered. In addition, conducting sliding block displacement analysis with site-specific earthquake motions is suggested.

References

- Abrahamson, N.A. and W.J. Silva (1997). "Empirical response spectral attenuation relations for shallow crustal earthquakes." *Seismological Research Letters*, 68, 94-127.
- Almutairi, A., Lu, J., Wang, N., & Elgamal, A. (2016). "Analysis of Multi-span Bridges Using OpenSees." (No. CA15-2582). California. Dept. of Transportation. Division of Engineering Services.
- Almutairi, A.S., Lu, J., Elgamal, A., and Mackie, K.R. (2017). "Performance-based earthquake assessment of multi-span bridge systems including soil-pile-structure interaction." *Proceedings of the 3rd International Conference on Performance-based Design in Earthquake Geotechnical Engineering (PBD-III)*, Vancouver, BC, Canada, July 16-19.
- American Petroleum Institute (1993). "Recommended Practice for Planning Designing and Constructing fixed Offshore Platforms.", API-RP2A - WSD, American Petroleum Institute, Washington D.C.
- Arduino, P., Ashford, S., Assimaki, D., Bray, J., Eldridge, T., Frost, D., Hashash, Y., Hutchinson, T., Johnson, L., Kelson, K. and Kayen, R. (2010). "*Geo-engineering reconnaissance of the 2010 Maule, Chile earthquake.*" GEER Association Report No. GEER-022, 1.
- Armstrong, R. J., Boulanger, R. W., & Beaty, M. H. (2013). "Liquefaction effects on piled bridge abutments: Centrifuge tests and numerical analyses." *Journal of Geotechnical and Geoenvironmental Engineering*, 139(3), 433-443.
- Armstrong, R. J., Boulanger, R. W., & Beaty, M. H. (2014). "Equivalent static analysis of piled bridge abutments affected by earthquake-induced liquefaction." *Journal of Geotechnical and Geoenvironmental Engineering*, 140(8), 04014046.
- Arulmoli K, Johnson GS, Yin P, et al. Geotechnical considerations and soil-structure interaction: proposed ASCE standards for seismic design of piers and wharves." Sacramento, CA: *Geotechnical Earthquake Engineering and Soil Dynamics IV*; 2008. p. 1–10.
- Ashford, S. A., Boulanger, R. W., Brandenberg, S. J., & Shantz, T. (2009). "Overview of Recommended Analysis Procedures for Pile Foundations in Laterally Spreading Ground." In *TCLEE 2009: Lifeline Earthquake Engineering in a Multihazard Environment* (pp. 1-8).
- Ashford, S. A., Boulanger, R. W., & Brandenberg, S. J. (2011). "Recommended Design Practice for Pile Foundations in Laterally Spreading Ground." PEER Report 2011/04. University of California at Berkeley.
- Aygün, B., Dueñas-Osorio, L., Padgett, J.E. and DesRoches, R. (2009). "Seismic Vulnerability of Bridges Susceptible to Spatially Distributed Soil Liquefaction Hazards." In *Structures Congress 2009: Don't Mess with Structural Engineers: Expanding Our Role*, 1-10.

- Aygün, B., Dueñas-Osorio, L., Padgett, J.E. and DesRoches, R. (2011). “Efficient longitudinal seismic fragility assessment of a multispan continuous steel bridge on liquefiable soils.” *Journal of Bridge Engineering*, 16(1), 93-107.
- Aviram, A., Mackie, K. R., & Stojadinovic, B. (2008a). “Effect of abutment modeling on the seismic response of bridge structures.” *Earthquake engineering and engineering vibration*, 7(4), 395-402.
- Aviram, A., Mackie, K. R., & Stojadinović, B. (2008b). “Guidelines for nonlinear analysis of bridge structures in California.” Pacific Earthquake Engineering Research Center.
- Bao, Y., Ye, G., Ye, B., and Zhang, F. (2012), “Seismic evaluation of soil–foundation–superstructure system considering geometry and material nonlinearities of both soils and structures.” *Soils and Foundations*, 52(2), 257-278.
- Basoz, N. I., Kiremidjian, A. S., King, S. A., & Law, K. H. (1999). “Statistical analysis of bridge damage data from the 1994 Northridge, CA, earthquake.” *Earthquake Spectra*, 15(1), 25-54.
- Berrill, J. B., Christensen, S. A., Keenan, R. P., Okada, W., & Pettinga, J. R. (2001). “Case study of lateral spreading forces on a piled foundation.” *Geotechnique*, 51(6), 501-517.
- Boulanger, R. W., Chang, D., Gulerce, U., Brandenburg, S. J., & Kutter, B. L. (2006). “Evaluating pile pinning effects on abutments over liquefied ground. In Seismic performance and simulation of pile foundations in liquefied and laterally spreading ground.” (pp. 306-318).
- Boulanger, R. W., Chang, D., Brandenburg, S. J., Armstrong, R. J., & Kutter, B. L. (2007). “Seismic design of pile foundations for liquefaction effects.” In *Earthquake Geotechnical Engineering* (pp. 277-302). Springer, Dordrecht.
- Brackmann, E. M. (2009). *Performance tools for piles and pile-to-wharf connections* (Doctoral dissertation, University of Washington).
- Bradley, B. A., Cubrinovski, M., Dhakal, R. P., & MacRae, G. A. (2010). “Probabilistic seismic performance and loss assessment of a bridge–foundation–soil system.” *Soil Dynamics and Earthquake Engineering*, 30(5), 395-411.
- Bray, J. D., & Travasarou, T. (2007). “Simplified procedure for estimating earthquake-induced deviatoric slope displacements.” *Journal of geotechnical and geoenvironmental engineering*, 133(4), 381-392.
- Caltrans (1968). “As-Built Plans, Samoa Channel Bridge.” California Department of Transportation, Sacramento, CA, personal communication.
- Caltrans (2002). “As-Built Plans, Earthquake Retrofit Project for Samoa Channel Bridge.” California Department of Transportation, Sacramento, CA, personal communication.

- Caltrans (2005). “SDC Example A: Pushover Design Example (Version 1.2), Salinas River Bridge (Right Replace), Br. No. 44-002R”, California Department of Transportation, Sacramento, California.
- Caltrans (2010). Seismic design Criteria (SDC) Version 1.6, California Department of Transportation, Sacramento, CA 95816.
- Caltrans (2013). Seismic design Criteria (SDC) Version 1.7, California Department of Transportation, Sacramento, CA 95816.
- Caltrans (2017). Bridge Memo to Designer (MTD) 20-15: “Lateral Spreading Analysis for New and Existing Bridges.” California Department of Transportation, Sacramento, CA 95816.
- Casciati, S., & Borja, R. I. (2004). “Dynamic FE analysis of South Memnon Colossus including 3D soil–foundation–structure interaction.” *Computers & structures*, 82(20-21), 1719-1736.
- Chen, M. C., & Penzien, J. (1977). “*Nonlinear soil-structure interaction of skew highway bridges.*” (No. UCB/EERC-77/24). Earthquake Engineering Research Center, University of California.
- CMU (2013). “Economic Input-Output Life Cycle Assessment (EIO-LCA) US 2002 (428 sectors) Producer model”, Carnegie Mellon University Green Design Institute, <http://www.eiolca.net/>.
- Conte, J. P., Elgamal, A., Yang, Z., Zhang, Y., Acero, G., & Seible, F. (2002, June). “Nonlinear seismic analysis of a bridge ground system.” In Proceedings of the 15th ASCE Engineering Mechanics Conference, New York, NY.
- Cornell, C. A., & Krawinkler, H. (2000). “Progress and challenges in seismic performance assessment”, PEER Center News 3. *University of California, Berkeley*.
- Cubrinovski, M., Bradley, B., Wotherspoon, L., Green, R., Bray, J., Wood, C., Pender, M., Allen, J., Bradshaw, A., Rix, G. and Taylor, M. (2011). Geotechnical aspects of the 22 February 2011 Christchurch earthquake.
- Cubrinovski, M., Winkley, A., Haskell, J., Palermo, A., Wotherspoon, L., Robinson, K., Bradley, B., Brabhakaran, P. and Hughes, M. (2014). “Spreading-induced damage to short-span bridges in Christchurch, New Zealand.” *Earthquake Spectra*, 30(1), 57-83.
- Datta, T. K. (2010), *Seismic analysis of structures*, John Wiley & Sons.
- Dendrou, B., Werner, S., & Toridis, T. (1985). “Three-dimensional response of a concrete bridge system to traveling seismic waves.” *Computers & Structures*, 20(1-3), 593-603.
- Division of Engineering Services—Cost Estimates Branch. Comparative bridge costs, 2014. Technical Report, California Department of Transportation.
- Doran, B., Shen, J., & Akbas, B. (2015). “Seismic evaluation of existing wharf structures subjected to earthquake excitation: case study.” *Earthquake Spectra*, 31(2), 1177-1194.

- Elgamal, A., Yan, L., Yang, Z., & Conte, J. P. (2008). "Three-dimensional seismic response of Humboldt Bay bridge-foundation-ground system." *Journal of structural engineering*, 134(7), 1165-1176.
- Elgamal, A., & Lu, J. (2009). "A framework for 3D finite element analysis of lateral pile system response." In *Contemporary Topics in In Situ Testing, Analysis, and Reliability of Foundations* (pp. 616-623).
- Elgamal, A., Lu, J., & Mackie, K. (2014). "MSBridge: OpenSees pushover and earthquake Analysis of multi-span bridges-user manual." Project SSRP-14/04 Department of Structural Engineering, University of California, San Diego.
- FHWA (2011). "LRFD Seismic Analysis and Design of Transportation Geotechnical Features and Structural Foundations." Publication No. FHWA-NHI-11-032, US Department of Transportation, Federal Highway Administration, Washington DC.
- Finn, W. D. L., & Fujita, N. (2002). "Piles in liquefiable soils: seismic analysis and design issues." *Soil Dynamics and Earthquake Engineering*, 22(9-12), 731-742.
- Goulet, C., Haselton, C., Mitrani-Reiser, J., Stewart, J. P., Taciroglu, E., & Deierlein, G. (2006, April). Evaluation of the seismic performance of a code-conforming reinforced-concrete frame building-Part I: Ground motion selection and structural collapse simulation. In *8th National Conference on Earthquake Engineering (100th Anniversary Earthquake Conference)* (pp. 18-22).
- Gupta, A., & Krawinkler, H. (2000). "Behavior of ductile SMRFs at various seismic hazard levels." *Journal of Structural Engineering*, 126(1), 98-107.
- Hagerty, M.T. and S.Y. Schwartz (1996). "The 1992 Cape Mendocino earthquake: broadband determination of source parameters." *J. Geophys. Res.*, **101**, 16,043–16,058.
- Hamada, M., Isoyama, R. and Wakamatsu, K. (1996). "Liquefaction-induced ground displacement and its related damage to lifeline facilities." *Soils and foundations*, 36(Special), 81-97.
- Hartzell, S.H. and C. Mendoza (1991). Application of an iterative least-squares waveform inversion of strong-motion and teleseismic records to the 1978 Tabas, Iran earthquake. *Bull. Seism. Soc. Am.*, **81**, 3-5-331.
- Ingham, T. J., Rodriguez, S., Donikian, R., & Chan, J. (1999). "Seismic analysis of bridges with pile foundations." *Computers & structures*, 72(1-3), 49-62.
- Itani, A. M., Bruneau, M., Carden, L., & Buckle, I. G. (2004). "Seismic behavior of steel girder bridge superstructures." *Journal of Bridge Engineering*, 9(3), 243-249.
- Jellin, A. R. (2008). *Improved seismic connections for pile-wharf construction* (Doctoral dissertation, University of Washington).

- Jeremić, B., Kunnath, S., & Xiong, F. (2004). "Influence of soil–foundation–structure interaction on seismic response of the I-880 viaduct." *Engineering Structures*, 26(3), 391-402.
- Kachadoorian, R. (1968). "*Effects of the earthquake of March 27, 1964, on the Alaska Highway System.*" US Government Printing Office.
- Kappos, A. J., Manolis, G. D., & Moschonas, I. F. (2002). "Seismic assessment and design of R/C bridges with irregular configuration, including SSI effects." *Engineering Structures*, 24(10), 1337-1348.
- Kent, D. C., & Park, R. (1971). "Flexural members with confined concrete." *Journal of the Structural Division*.
- Ketchum, M., Chang, V., & Shantz, T. (2004). "Influence of design ground motion level on highway bridge costs." *Report No. Lifelines 6D01*.
- Khosravifar, A., Elgamal, A., Lu, J. and Li, J. (2018). "A 3D model for earthquake-induced liquefaction triggering and post-liquefaction response." *Soil Dynamics and Earthquake Engineering*, 110, 43-52.
- Kotsoglu, A., & Pantazopoulou, S. (2006, September). Modeling of embankment flexibility and soil-structure interaction in integral bridges. In *Proceedings of First European Conference on Earthquake Engineering and Seismology* (pp. 3-8).
- Kramer, S. L., & Wang, C. H. (2015). "Empirical model for estimation of the residual strength of liquefied soil." *Journal of Geotechnical and Geoenvironmental Engineering*, 141(9), 04015038.
- Krawinkler, H. (2002, August). "A general approach to seismic performance assessment." In *Proceedings* (Vol. 3, pp. 173-80).
- Krawinkler, H., & Miranda, E. (2004). "Performance-based earthquake engineering." *Earthquake engineering: from engineering seismology to performance-based engineering*, 9, 1-9.
- Kunnath, S. K. (2006). *Application of the PEER PBEE Methodology to the I-880 Viaduct: I-880 Testbed Committee*. Pacific Earthquake Engineering Research (PEER) Center, College of Engineering, University of California.
- Kwon, O.S., Sextos, A. and Elnashai, A. (2009). "Seismic fragility of a bridge on liquefaction susceptible soil." In 10th international conference on seismic safety and reliability, 13-17.
- Lam, I. P., & Martin, G. R. (1986). Seismic design for highway bridge foundations. In *Lifeline Earthquake Engineering: Performance, Design and Construction* (pp. 7-21). ASCE.
- Ledezma, C. A., & Bray, J. D. (2008). *Performance-based earthquake engineering design evaluation procedure for bridge foundations undergoing liquefaction-induced lateral ground displacement*. Pacific Earthquake Engineering Research Center.

- Ledezma, C., & Bray, J. D. (2010). "Probabilistic performance-based procedure to evaluate pile foundations at sites with liquefaction-induced lateral displacement." *Journal of geotechnical and geoenvironmental engineering*, 136(3), 464-476.
- Ledezma, C., Hutchinson, T., Ashford, S.A., Moss, R., Arduino, P., Bray, J.D., Olson, S., Hashash, Y.M., Verdugo, R., Frost, D. and Kayen, R. (2012). "Effects of ground failure on bridges, roads, and railroads." *Earthquake Spectra*, 28(S1), S119-S143.
- Lehman, D. E., Brackmann, E., Jellin, A., & Roeder, C. W. (2009). "Seismic performance of pile-wharf connections." In *TCLÉE 2009: Lifeline Earthquake Engineering in a Multihazard Environment* (pp. 1-13).
- Li, Y., & Conte, J. P. (2016). "Effects of seismic isolation on the seismic response of a California high-speed rail prototype bridge with soil-structure and track-structure interactions." *Earthquake Engineering & Structural Dynamics*, 45(15), 2415-2434.
- Lu J., Yang Z., Elgamal A. (2006). "OpenSeesPL three-dimensional lateral pile-ground interaction version 1.00 user's manual." Report No. SSRP-06/03, Department of Structural Engineering, University of California, San Diego CA.
- Lu, J., Mackie, K. R., Elgamal, A., & Almutairi, A. (2011). "BridgePBEE: OpenSees 3D pushover and earthquake analysis of single-column 2-span bridges, User manual, beta 1.0."
- Lu, J., Elgamal, A., and Mackie, K. (2015). "Parametric Study of Ordinary Standard Bridges using OpenSees and CSiBridge." Structural Systems Research Project SSRP-14/03, University of California at San Diego, La Jolla.
- Ma, K.-F., J. Mori, S.-J. Lee, and B. Yu (2001). Spatial and temporal distribution of slip for the 1999 Chi-Chi, Taiwan earthquake. *Bull. Seism. Soc. Am.*, **91**, 1069-1087.
- Mackie, K.R., and Stojadinovic, B. (2005). "Fragility basis for California highway overpass bridge seismic decision making." PEER Report No. 2005/02, Pacific Earthquake Engineering Research Center, University of California, Berkeley.
- Mackie, K. R., & Stojadinović, B. (2006). "Post-earthquake functionality of highway overpass bridges." *Earthquake engineering & structural dynamics*, 35(1), 77-93.
- Mackie, K.R., Wong, J.M., and Stojadinovic, B. (2008). Integrated Probabilistic Performance-Based Evaluation of Benchmark Reinforced Concrete Bridges. *Technical Report PEER 2007/09*. Pacific Earthquake Engineering Research Center, University of California, Berkeley California.
- Mackie, K. R., Wong, J. M., & Stojadinović, B. (2010). "Post-earthquake bridge repair cost and repair time estimation methodology." *Earthquake Engineering & Structural Dynamics*, 39(3), 281-301.

- Mackie, K. R., Lu, J., & Elgamal, A. (2012). "Performance-based earthquake assessment of bridge systems including ground-foundation interaction." *Soil Dynamics and Earthquake Engineering*, 42, 184-196.
- Mackie, K. R., Kucukvar, M., Tatari, O., & Elgamal, A. (2015). "Sustainability metrics for performance-based seismic bridge response." *Journal of Structural Engineering*, 142(8), C4015001.
- Mahan, M. (2005). wFrame - Pushover Analysis of Bridge Bents and Frames, California Department of Transportation, Sacramento, California.
- Mahin, S. A. (1997). "Lessons from damage to steel buildings during the Northridge earthquake." *Engineering structures*, 20(4-6), 261-270.
- Makris, N., Badoni, D., Delis, E., & Gazetas, G. (1994). Prediction of observed bridge response with soil-pile-structure interaction. *Journal of Structural Engineering*, 120(10), 2992-3011.
- Mander, J. B., Priestley, M. J., & Park, R. (1988). "Theoretical stress-strain model for confined concrete." *Journal of structural engineering*, 114(8), 1804-1826.
- Martin, G. R., & Qiu, P. (1994). Effects of liquefaction on vulnerability assessment. *NCEER Highway Project on Seismic Vulnerability of New and Existing Highway Construction, Year One Research Tasks—Technical Research Papers, National Center for Earthquake Engineering Research, Buffalo, NY.*
- Matlock, H. (1970). "Correlations for design of laterally loaded piles in soft clay." *Offshore technology in civil engineering's hall of fame papers from the early years*, 77-94.
- Mazzoni, S., McKenna, F., Scott, M. H., & Fenves, G. L. (2009). "Open system for earthquake engineering simulation user command-language manual—OpenSees version 2.0." *Pacific Earthquake Engineering Research Center, Univ. of California, Berkeley, CA.*
- McCallen, D. B., & Romstad, K. M. (1994). "Dynamic analyses of a skewed short-span, box-girder overpass." *Earthquake spectra*, 10(4), 729-756.
- McKenna, F., Scott, M., and Fenves, G. (2010). "Nonlinear finite-element analysis software architecture using object composition." *Journal of Computing in Civil Engineering*, 24(1), 95-107
- Medina, R. A., & Krawinkler, H. (2003). *Seismic demands for nondeteriorating frame structures and their dependence on ground motions* (pp. 1381-1381). Pacific Earthquake Engineering Research Center.
- Mitrani-Reiser, J., Haselton, C., Goulet, C., Porter, K., Beck, J., & Deierlein, G. (2006, April). Evaluation of the seismic performance of a code-conforming reinforced-concrete frame building-Part II: Loss estimation. In *8th National Conference on Earthquake Engineering (100th Anniversary Earthquake Conference)* (pp. 18-22).

- Moehle, J., & Deierlein, G. G. (2004, August). A framework methodology for performance-based earthquake engineering. In *13th world conference on earthquake engineering* (Vol. 679).
- Mosalam, K. M., & Günay, S. (2014). "Seismic performance evaluation of high voltage disconnect switches using real-time hybrid simulation: I. System development and validation." *Earthquake Engineering & Structural Dynamics*, 43(8), 1205-1222.
- Mylonakis, G., Nikolaou, A., & Gazetas, G. (1997). "Soil–pile–bridge seismic interaction: kinematic and inertial effects. Part I: soft soil." *Earthquake Engineering & Structural Dynamics*, 26(3), 337-359.
- Mylonakis, G., & Gazetas, G. (2000). "Seismic soil-structure interaction: beneficial or detrimental?." *Journal of Earthquake Engineering*, 4(3), 277-301.
- Na, U. J., Chaudhuri, S. R., and Shinozuka, M. (2008) "Probabilistic assessment for seismic performance of port structures," *Soil Dynamics and Earthquake Engineering* 28, 147–158.
- Novak, M. (1991), "Piles under Dynamic Loads," *Proceedings of Second International Conference on Recent Advances In Geotechnical Earthquake Engineering and Soil Dynamics*, St. Louis, Missouri, 2433-2456.
- NCHRP-12-49. (1998). "Comprehensive specification for the seismic design of bridges."
- Oppenheimer, D., G. Beroza, G. Carver, L. Dengler, J. Eaton, L. Gee, F. Gonzalez, A. Jayko, W.H. Li, M. Lisowski, M. Magee, G. Marshal, M. Murray, R. McPherson, B. Romanowicz, K. Satake, R. Simpson, P. Somerville, R. Stein, and D. Valentine (1993). The Cape Mendocino, California, earthquakes of April 1992: subduction at the triple junction. *Science*, 261, 433-438.
- O'Rourke, T. D. (1992). "Large ground deformations and their effects on lifeline facilities: 1906 San Francisco earthquake." In *Case studies liquefaction and lifeline performance during past earthquakes: United states case studies* (pp. 1-130). US National Center for Earthquake Engineering Research (NCEER).
- Padgett, J. E., Ghosh, J., & Dueñas-Osorio, L. (2013). "Effects of liquefiable soil and bridge modelling parameters on the seismic reliability of critical structural components." *Structure and Infrastructure Engineering*, 9(1), 59-77.
- Porter, K. A. (2003, July). An overview of PEER's performance-based earthquake engineering methodology. In *Proceedings of ninth international conference on applications of statistics and probability in civil engineering*.
- Porter, K., Kennedy, R., & Bachman, R. (2007). "Creating fragility functions for performance-based earthquake engineering." *Earthquake Spectra*, 23(2), 471-489.
- Reese, L. C., Cox, W. R. and Koop, F. D. (1974). "Analysis of laterally loaded piles in sand," Proc., 6th Offshore Technology Conf., Houston, Texas, (Paper No. 2080), 473-483.

- Reese, L. C.; Cox, W. R.; and Koop, F. D., 1975. "Field Testing and Analysis of Laterally Loaded Piles in Stiff Clay," Proceedings, 7th Offshore Technology Conference, pp. 671-690.
- Reese, L. C., Wang, S. T., Isenhower, W. M., Arrelaga, J.A., and Hendrix, J. A. (2005). "LPILE Plus Version 5.0," Ensoft, Inc. Austin, TX.
- Roeder, C. W., Graff, R., Soderstrom, J., & Yoo, J. H. (2005). "Seismic performance of pile-wharf connections." *Journal of Structural Engineering*, 131(3), 428-437.
- Rollins, K.M., Gerber, T.M., Dusty Lane, J. and Ashford, S.A. (2005). "Lateral resistance of a full-scale pile group in liquefied sand." *Journal of Geotechnical and Geoenvironmental Engineering*, 131(1), 115-125.
- Ross, G. A., Seed, H. B., & Migliaccio, R. R. (1969). "Bridge foundation behavior in Alaska earthquake." *Journal of the Soil Mechanics and Foundations Division*, 95(4), 1007-1036.
- Scott, M. and G. Fenves. (2006). "Plastic Hinge Integration Methods for Force-Based Beam-Column Element.," *Journal of Structural Engineering*, 132(2), 244-252.
- Scott, M. and K. Ryan. (2013). "Moment-Rotation Behavior of Force-Based Plastic Hinge Elements.," *Earthquake Spectra*, 29(2), 597-607.
- Shafieezadeh, A., DesRoches, R., Rix, G. J., & Werner, S. D. (2012). "Seismic performance of pile-supported wharf structures considering soil-structure interaction in liquefied soil." *Earthquake Spectra*, 28(2), 729-757.
- Shamsabadi, A., Rollins, K.M, and Kapuskar, M. (2007). "Nonlinear Soil-Abutment-Bridge Structure Interaction for Seismic Performance-Based Design.," *Journal of Geotechnical and Geoenvironmental Engineering*, 133(6), 707-720, June.
- Shamsabadi, A., & Law, H. K. (2010). Current Seismic Soil-Foundation-Structure Interaction State of the Art and Practice on California Toll Bridge Program.
- Shamsabadi, A., Khalili-Tehrani, P., Stewart, J.P., and Taciroglu, E. (2010). "Validated Simulation Models for Lateral Response of Bridge Abutments with Typical Backfills." *J. Bridge Eng.*, 15(3), 302-311, May.
- Shamsabadi, A. and Taciroglu, E. (2013). "A Frequency-Time Domain Handshake Method For Seismic SoilFoundation-Structure Interaction Analysis of Long-Span Bridges", Seventh National Seismic Conference on Bridge and Highways, Oakland, California.
- Shamsabadi, A. (2019). personal communication
- Shin, H., Arduino, P., Kramer, S.L. and Mackie, K. (2008). "Seismic response of a typical highway bridge in liquefiable soil." In *Geotechnical Earthquake Engineering and Soil Dynamics IV*, 1-11.

- Solberg, K. M., Dhakal, R. P., Mander, J. B., & Bradley, B. A. (2008). "Computational and rapid expected annual loss estimation methodologies for structures." *Earthquake engineering & structural dynamics*, 37(1), 81-101.
- Soltanieh, S., Memarpour, M. M., & Kilanehei, F. (2019). "Performance assessment of bridge-soil-foundation system with irregular configuration considering ground motion directionality effects." *Soil Dynamics and Earthquake Engineering*, 118, 19-34.
- Somerville, P.G., M.K. Sen and B.P. Cohee (1990). "Simulation of strong ground motions recorded during the 1985 Michoacan, Mexico and Valparaiso, Chile earthquakes." *Bull. Seism. Soc. Am.*, 81, 1-27.
- Somerville, P., & Collins, N. (2002). "Ground motion time histories for the Humboldt Bay Bridge." *Pasadena, CA, URS Corporation*.
- Stewart, J. P., Seed, R. B., & Fenves, G. L. (1998). *Empirical evaluation of inertial soil-structure interaction effects*. Univ. of California, Berkeley, CA: Pacific Earthquake Engineering Research Center.
- Su, L., Lu, J., Elgamal, A., & Arulmoli, A. K. (2017). "Seismic performance of a pile-supported wharf: Three-dimensional finite element simulation." *Soil Dynamics and Earthquake Engineering*, 95, 167-179.
- Sweet, J. (1993). A technique for nonlinear soil–structure interaction. *Rep. No. CAI093, 100*.
- Thio, H.K., P. Somerville, T. Sato, and T. Ishii (2001). Rupture model of the 1999 Chi-Chi, Taiwan earthquake derived from the inversion of teleseismic, strong motion, and GPS data. Unpublished manuscript.
- Tokimatsu, K., & Asaka, Y. (1998). "Effects of liquefaction-induced ground displacements on pile performance in the 1995 Hyogoken-Nambu earthquake." *Soils and Foundations*, 38(Special), 163-177.
- Heidary-Torkamani, H., Bargi, K., Amirabadi, R., & McClough, N. J. (2014). "Fragility estimation and sensitivity analysis of an idealized pile-supported wharf with batter piles." *soil dynamics and earthquake engineering*, 61, 92-106.
- Turner, B. J., Brandenberg, S. J., & Stewart, J. P. (2016). "Case study of parallel bridges affected by liquefaction and lateral spreading." *Journal of Geotechnical and Geoenvironmental Engineering*, 142(7), 05016001.
- Verdugo, R., Sitar, N., Frost, J.D., Bray, J.D., Candia, G., Eldridge, T., Hashash, Y., Olson, S.M. and Urzua, A. (2012) "Seismic performance of earth structures during the February 2010 Maule, Chile, earthquake: dams, levees, tailings dams, and retaining walls." *Earthquake Spectra*, 28(S1), S75-S96.
- Vijayakumar, M., Cheng, J. J., Küçükvar, M., Elgamal, A., Mackie, K. R., & Tatari, O. Carbon Footprint: "Liquefaction Effects on a Private Residence." In *Geo-Chicago 2016* (pp. 633-642).

- Wang, Z., Dueñas-Osorio, L., & Padgett, J. E. (2013). "Seismic response of a bridge–soil–foundation system under the combined effect of vertical and horizontal ground motions." *Earthquake Engineering & Structural Dynamics*, 42(4), 545-564.
- Wang, N. (2015), "Three-Dimensional Modeling of Ground-Pile Systems and Bridge Foundations", PhD Thesis, Department of Structural Engineering, University of California, San Diego, La Jolla, CA.
- Wang, N., Elgamal, A., & Shantz, T. (2016). "Recorded seismic response of the Samoa Channel Bridge-foundation system and adjacent downhole array." *Soil Dynamics and Earthquake Engineering*, 92, 358-376.
- Wang, N., Elgamal, A., & Lu, J. (2018). "Assessment of the Samoa Channel Bridge-foundation seismic response." *Soil Dynamics and Earthquake Engineering*, 108, 150-159.
- Werner, S. D. (1994). "Study of Caltrans" seismic evaluation procedures for short bridges. In *Proc., 3rd Annual Seism. Research Workshop*.
- Wotherspoon, L., Bradshaw, A., Green, R., Wood, C., Palermo, A., Cubrinovski, M., & Bradley, B. (2011). "Performance of bridges during the 2010 Darfield and 2011 Christchurch earthquakes." *Seismological Research Letters*, 82(6), 950-964.
- Yang, C. S. W., DesRoches, R., & Rix, G. J. (2012). Numerical fragility analysis of vertical-pile-supported wharves in the western United States. *Journal of Earthquake Engineering*, 16(4), 579-594.
- Yang Z., and Elgamal A. (2002). "Influence of permeability on liquefaction-induced shear deformation." *Journal of Engineering Mechanics*, 128(7), 720-729.
- Youd, T. L. (1993). Liquefaction-induced damage to bridges. *Transportation Research Record*, 1411, 35-41.
- Youd, T. L., Idriss, I. M., Andrus, R. D., Arango, I., Castro, G., Christian, J. T., Dobry, R., Finn, W., Harder, D. L. Jr., Hynes, M. E., Ishihara, K., Koester, J. P., Liao, S. S. C., Marcuson, W. F. III, Martin, G. R., Mitchell, J. K. Moriwaki, Y. Power, M. S., Robertson, P. K., Seed, R. B., and Stokoe, K. H. II. (2001). "Liquefaction Resistance of Soils: Summary Report from the 1996 NCEER and 1998 NCEER/NSF Workshops on Evaluation of Liquefaction Resistance of Soils," *ASCE/SEI Journal of Geotechnical Geoenvironmental Engineering*, 127(10).
- Zeghal, M. and Elgamal, A.-W. (1994). "Analysis of site liquefaction using earthquake records" *Journal of Geotechnical Engineering* 120(6), 996-1017.
- Zhang, Y., Conte, J.P., Yang, Z., Elgamal, A., Bielak, J. and Acero, G. (2008). "Two-dimensional nonlinear earthquake response analysis of a bridge-foundation-ground system." *Earthquake Spectra*, 24(2), 343-386.
- Zhang, J., & Makris, N. (2002). "Kinematic response functions and dynamic stiffnesses of bridge embankments." *Earthquake Engineering & Structural Dynamics*, 31(11), 1933-1966.

Appendix A. MSBridge: Multi-span Bridge Analysis

A.1. General Overview

MSBridge is a PC-based graphical pre- and post-processor (user-interface) for conducting nonlinear Finite Element (FE) studies for multi-span multi-column bridge systems. The user-interface development was funded by California Department of Transportation (Caltrans). Main features of MSBridge include:

- i) Automatic mesh generation of multi-span (straight or curved) bridge systems
- ii) Options of foundation soil springs and foundation matrix
- iii) Options of deck hinges, isolation bearings, and steel jackets
- iv) A number of advanced abutment models (Elgamal *et al.* 2014; Aviram 2008a, 2008b)
- v) Management of ground motion suites
- vi) Simultaneous execution of nonlinear time history analyses for multiple motions
- vii) Visualization and animation of response time histories

FE computations in MSBridge are conducted using OpenSees (currently ver. 2.5.0 is employed). OpenSees is an open-source software framework (McKenna *et al.* 2010, Mazzoni *et al.* 2009) for simulating the seismic response of structural and geotechnical systems. OpenSees has been developed as the computational platform for research in performance-based earthquake engineering at the Pacific Earthquake Engineering Research (PEER) Center. More information about OpenSees can be found in <http://opensees.berkeley.edu/>.

The analysis options available in MSBridge include:

- i) Pushover analysis
- ii) Mode shape analysis
- iii) Single and multiple 3D base input acceleration analysis
- iv) Equivalent Static Analysis (ESA)
- v) Pushover analysis of soil movements (imposed displacement profile)

MSBridge supports analysis in both the US/English and SI unit systems. The default unit system is US/English units. This unit option can be interchanged during model creation, and MSBridge will convert all input data to the desired unit system. Some commonly used quantities can be converted as follows:

1 kPa	=	0.14503789 psi
1 psi	=	6.89475 kPa
1 m	=	39.37 in
1 in	=	0.0254 m

The global coordinate system employed in MSBridge is shown in Figure A.1. The origin is located at the left deck-end of the bridge. The bridge deck direction in a straight bridge is referred to as “longitudinal direction (X)”, while the horizontal direction perpendicular to the longitudinal direction is referred to as “transverse direction (Y)”. At any time, “Z” denotes the vertical direction.

In MSBridge, the maximum response quantities (e.g., displacement, acceleration) are reported in the local coordinate system. In a straight bridge, the local coordinate system is parallel to the global one. For a curved bridge, the local coordinate system is defined in such a way that the longitudinal axis (x) is tangent to the bridge curve at a given superstructure location while the

transverse axis (y) is another horizontal direction that is perpendicular to the longitudinal axis (x). The vertical axis (z) in a local coordinate system is still parallel to the global one.

MSBridge was written in Microsoft .NET Framework (Windows Presentation Foundation or WPF). OpenTK (OpenGL) library (website: <http://www.opentk.com/>) was used for visualization of the FE mesh and the OxyPlot package (<http://oxyplot.codeplex.com/>) was employed for x-y plotting. For more information about MSBridge, please refer to the MSBridge user manual (Elgamal *et al.* 2014).

A.2. Verification of MSBridge Response Mechanism

The main purpose of this verification effort is to illustrate and verify the salient new features and capabilities of MSBridge using appropriate idealized bridge configurations. Each of these configurations allowed for a simple and systematic assessment of the particular response feature being verified. Table A.1 summarizes the cases and conclusions.

A.2.1. Pushover Analysis

The pushover options consist of Monotonic Pushover, Cyclic Pushover, and U-Push (pushover by a user-defined loading pattern). However, in this verification study, only the monotonic pushover is presented and discussed.

Pushover analysis was done with an equivalent bridge model of rigid deck, no abutment effects and the height of the same column of 50 ft to check the linear response. Linear column (elastic modulus (E) = 4,000 ksi, section inertia (I) = 30.68 ft⁴ and height (L) = 50 ft) results are shown below in the longitudinal direction. For the Force-Based Method, a force increment was applied per step, where the pushover load linearly increases per step in a monotonic pushover mode. The pushover load is applied at the bridge deck center or at the bent as chosen by the user.

Figure A.2 shows the column top displacement time history. The column lateral stiffness for fixed-fixed connection (K) = $12EI/L^3$ for each column where: $E = 4,000$ ksi, and $I = 30.68$ ft⁴, where $I = \frac{\pi}{64}D^4$ and D is the diameter.

$$K = \frac{12 EI}{L^3} = \frac{12 \times 4000 \text{ ksi} \times 30.68 \text{ ft}^4 \times 12^4 \text{ in}^4/\text{ft}^4}{(50 \text{ ft} \times 12 \text{ in}/\text{ft})^3} = 141 \text{ K/in}$$

The total bridge stiffness = $141 \frac{K}{in} \times 10 \text{ bents} = 1410 \text{ K/in}$

Therefore, the results from MSBridge are compatible with the analytical solution. Moreover, the same conclusion will result if the Displacement-Based Analysis was performed.

A.2.2. Mode Shapes Analysis

Figure A.3 shows the natural periods and frequencies of the first five modes after performing the Mode Shapes Analysis, and the corresponding mode shapes are shown in Figure A.4. The bridge natural frequency of vibration was calculated analytically and compared with the value obtained from the MSBridge.

Figure A.4c shows the longitudinal mode shape. The longitudinal mode shape obtained from MSBridge matches the analytical solution as shown in the calculations.

Given: deck cross-sectional area = 69.64 ft^2

$$\text{Deck weight} = 69.64 \text{ ft}^2 \times 145 \text{ pcf} = 10.1 \text{ Kips/ft}$$

Also, column cross-sectional area = 69.64 ft^2

$$\text{Deck weight} = 19.63 \text{ ft}^2 \times 145 \text{ pcf} = 2.85 \text{ Kips/ft}$$

$$\text{Total bridge length} = 2 \times 142.25 \text{ ft} + 9 \times 140 \text{ ft} = 1544.5 \text{ ft}$$

$$\text{Half Column height} = 25 \text{ ft, the total heights} = 25 \text{ ft} * 10 \text{ columns} = 250 \text{ ft}$$

$$\text{The gravity acceleration (g)} = 386 \text{ in/s}^2$$

$$m = \frac{10.1 \frac{k}{ft} \times 1544.5 ft + 2.85 \frac{k}{ft} \times 250 ft}{386 in/s^2} = 42.26 \frac{K \cdot s^2}{in}$$

$$K = 10 \times \frac{12EI}{L^3} = 1410 \frac{k}{in}$$

$$\omega = \sqrt{\frac{K}{m}} = \sqrt{\frac{1410}{42.26}} = 5.77 s^{-1}$$

$$f = \frac{\omega}{2\pi} = \frac{5.77}{2\pi} = 0.91 Hz$$

where K is the column lateral stiffness, m is the mass, ω is the angular frequency in rad/s, and f is the frequency in Hz.

A.2.3. Abutment Model

The aim of this section is to assign each abutment model to the bridge, then to apply the Pushover analysis and check the effects of the abutment model on the bridge response. In addition, to find correlations between the models.

The abutment models implemented in MSBridge consist of seven types, and are defined as Elastic, Roller, SDC 2004, SDC 2010 Sand, SDC 2010 Clay, EPP-Gap and HFD abutment models. The abutment type has a significant influence on the response of the entire bridge system under moderate to strong intensity ground motions. However, the differences between only three types (Elastic, Roller, SDC 2010 Sand) will be studied and presented in this section.

Implementation

Similar to the previous section, an equivalent bridge model was used to run the analysis. It has the same number of spans with equal-height columns, linear columns, and rigid deck to study the effect of the abutment models.

A.2.3.1. Elastic Abutment Model

The Elastic Abutment Model consists of a total of six elastic springs, three of which are translational in the longitudinal, transverse and vertical directions, and three rotational around the longitudinal, transverse and vertical directions. All the series of springs are assigned at each node at the end of the bridge. By default, there will be two series of springs at the ends of the rigid element along the deck width, where the rigid element width is the same as the deck width. However, the user can define multiple distributed springs (equal spacing within deck width).

For the longitudinal direction (translational and rotational), each of the distributed (Elastic) springs carries its tributary amount. In addition, it is worth noting that the results from the elastic abutment model depend on the stiffness values associated with the abutment. For instance, making the stiffness values very minimal as if there no motion resistance and the vertical translational stiffness is infinity; it would make the abutment model as a roller. As a matter of fact, this will be one of the checks for this section and similar results should be maintained for zero stiffness values elastic abutment model with the vertical translational stiffness is infinity and roller abutment model (Figure A.5).

A.2.3.2. Roller Abutment Model

The Roller Abutment Model acts as single-point constraints against displacement in the vertical direction. Therefore, it consists of rollers in the transverse and longitudinal directions only; the vertical restraint also provides a boundary that prevents rotation of the deck about its axis (torsion). Similar to the elastic abutment model; there will be two rollers at the ends of the rigid element along the deck width, where the rigid element width is the same as the deck width. However, the user can define multiple rollers (equal spacing within deck width). Each of the assigned roller resists the motion in the vertical direction only.

In addition, this model can be used to provide a lower-bound estimate of the longitudinal and transverse resistance of the bridge that may be displayed through a pushover analysis. The roller abutment model result is shown in Figure A.6.

Correlations

The elastic abutment model with zero stiffness and the vertical translational stiffness is infinity is used and its results are shown to compare them with the roller one (Figure A.7). The roller abutment model shows similar results to the zero-stiffness elastic abutment model with the vertical translational stiffness is infinity.

A.2.3.3. SDC Abutment Model

Unlike the other abutment models, the SDC model requires defining more than one parameter. The user should define the elastomeric bearing pads, gap, abutment back wall, abutment piles, and soil backfill material. Prior to impact or gap closure, the superstructure forces are transmitted through the elastomeric bearing pads to the stem wall, and subsequently to the piles and backfill, in a series system. After gap closure, the superstructure bears directly on the abutment back wall and mobilizes the full passive backfill pressure.

The SDC abutment models implemented in MSBridge consist of three types, SDC 2004, SDC 2010 Sand and SDC 2010 Clay. By default, there will be two distributed springs at the ends of the rigid element along the deck width, where the rigid element width is the same as the deck width. However, the user can define multiple rollers (equal spacing within deck width). Figure A.8 shows the pushover result for the SDC 2010 Sand abutment model.

Conclusion

The highest Pushover displacement was found with the roller abutment type. On the other hand, the lowest displacement was associated with the SDC 2010 abutment type.

Table A.1. MSBridge Feature-verification cases

Section	Aim	Configuration	Conclusion
A.2.1 Pushover Analysis	To verify the lateral stiffness of linear columns in a multi-span bridge configuration via	Bridge model with equal height columns (50 ft), single column per bent, rigid deck and roller abutment	Deformed shapes and displacement for all columns are identical. Column bending stiffness in fixed-fixed configuration is verified to match the value of $12EI/L^3$ (long. direction), with corresponding mode shapes and resonant frequencies.
A.2.2 Mode Shapes Analysis	Pushover and Mode shape analyses		
A.2.3 Abutment Model	To verify stiffness contribution of different abutment models in multi-span bridge configuration	Same as above	Roller, SDC, and Elastic abutment models function as expected, according to the underlying modeling assumptions.

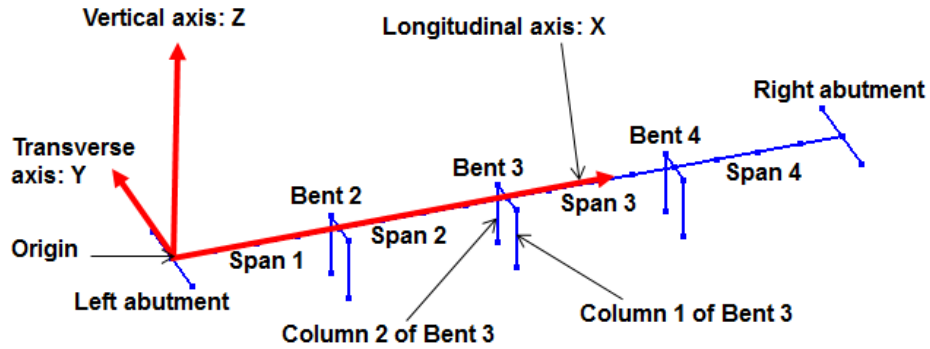


Figure A.1. Global coordinate system employed in MSBridge

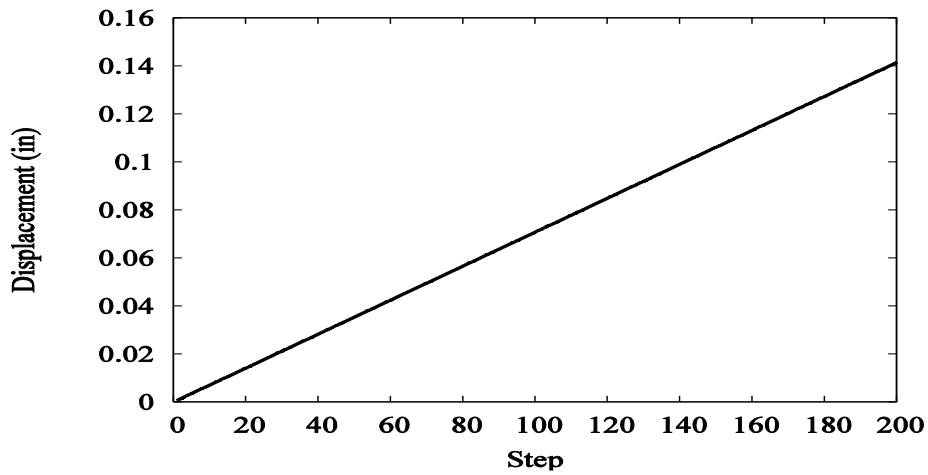
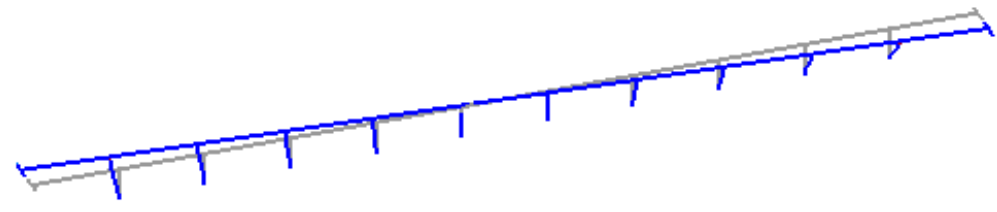


Figure A.2. Longitudinal displacement response time history for column top

Mode	Natural Period (sec)	Natural Frequency (hz)
1	1.21414	0.823625
2	1.09907	0.909858
3	1.09837	0.910443
4	0.0896941	11.149
5	0.0788706	12.679

Figure A.3. Bridge natural periods and natural frequencies



(a)



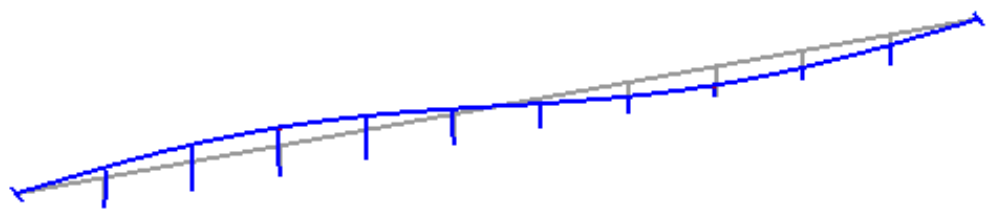
(b)



(c)



(d)



(e)

Figure A.4. Mode shapes for the bridge model: (a) first mode; (b) second mode; (c) third mode; (d) fourth mode; and (e) fifth mode

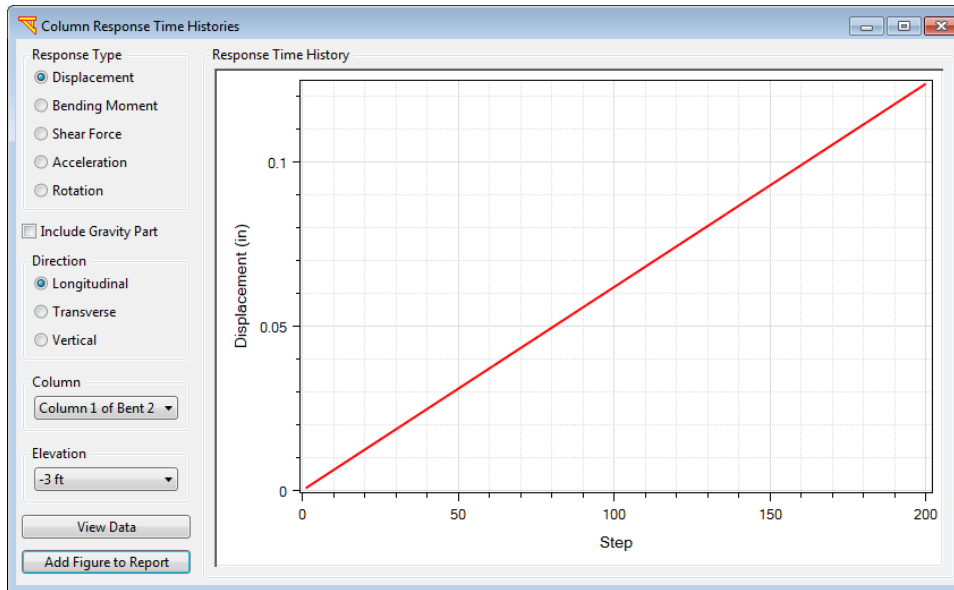


Figure A.5. Longitudinal displacement response time history at elevation of -3 ft for column 2 of bent 6 (Elastic Abutment)

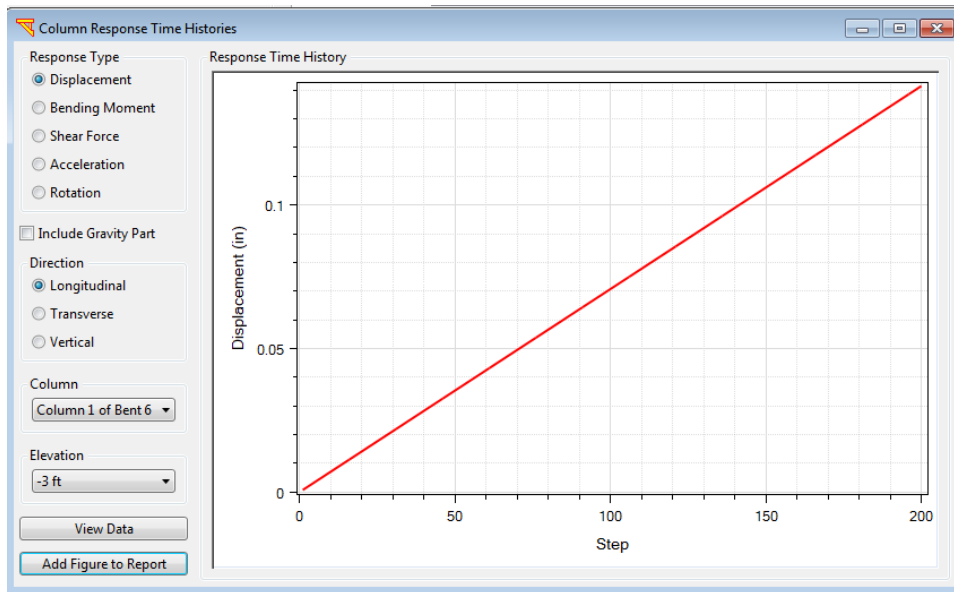


Figure A.6. Longitudinal displacement response time history at elevation of -3 ft for column 2 of bent 6 (Roller Abutment)

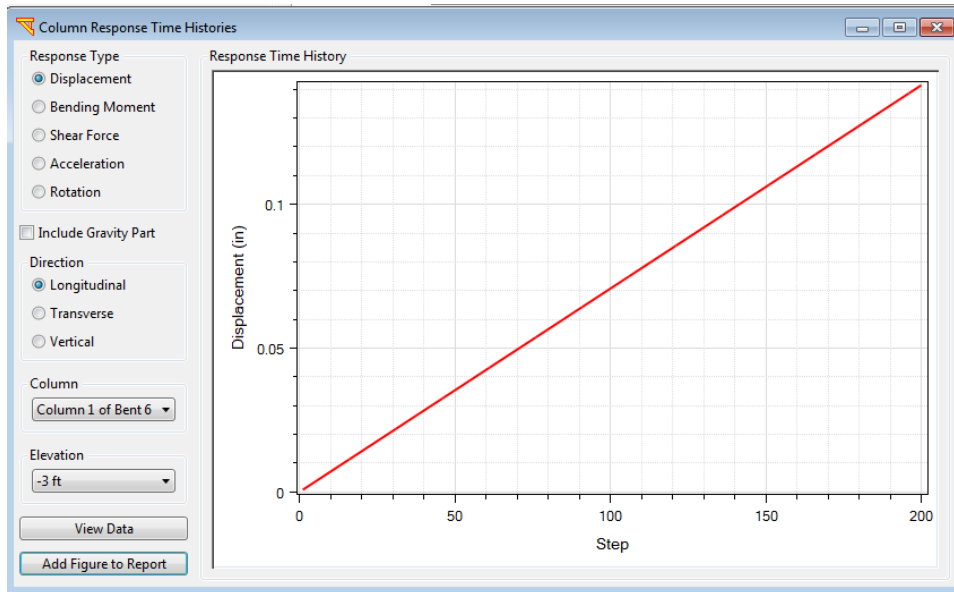


Figure A.7. Longitudinal displacement response time history at elevation of -3 ft for column 2 of bent 6 (zero-stiffness Elastic Abutment)

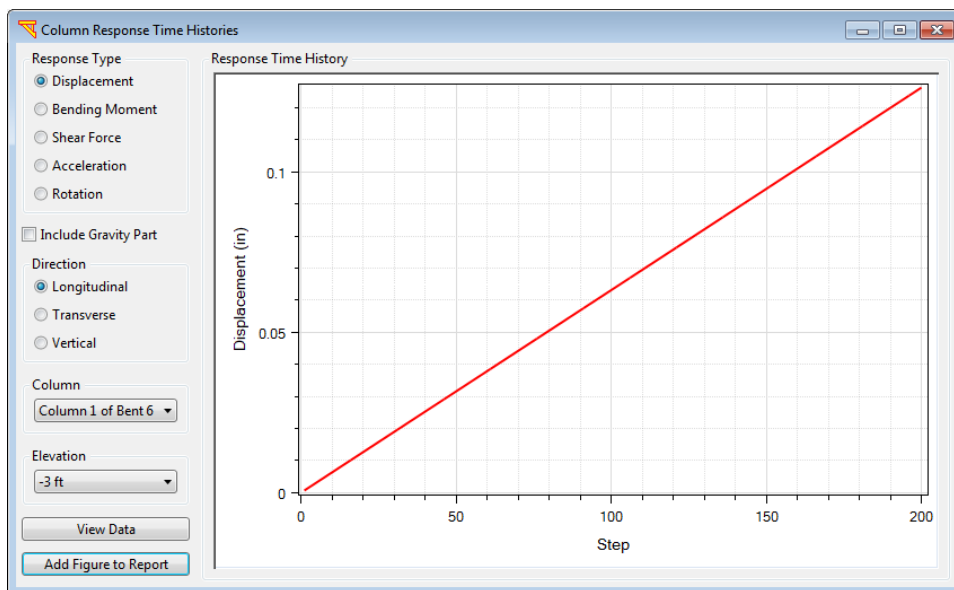


Figure A.8. Longitudinal displacement response time history at elevation of -3 ft for column 2 of bent 6 (SDC 2010-Sand)

Appendix B. Base Input Motions

Table B.1 lists the 14 input motions employed in the study. These motion files were provided by Caltrans. The motion names (Table B.1) have 8 or 9 character with naming convention as follows:

TypeAiBjC , where

Type = ROCK

A = S for Synthetic, N for Natural

i = 1 for base record (1000 year return)

B = P for pulse-like motion, N for non-pulse-like motion

j = Record number for records of same TypeAiB

C = N for normal component, P for Parallel component, nonexistent for one component synthetic

Note that the vertical acceleration input is zero for all motions. Figure B.1 shows the PGA histograms for the 14 input motions. Most motions are within 0.32g – 0.43g whereas 3 motions (i.e., Motions 1, 8, and 12) are between 0.67g – 0.71g.

Table B.2 displays the Intensity Measures of the 14 motions. The acceleration time histories of the input motion components are shown in Figure B.2 and Figure B.3. The Pseudo-Spectral Accelerations of the input motions are displayed in Figure B.4 and Figure B.5.

Table B.1. Input motions employed in the nonlinear THA

Motion No.	Name	Peak Acceleration (g)
Motion 1	ROCKS1N1	0.70
Motion 2	ROCKS1N2	0.38
Motion 3	ROCKS1N3	0.32
Motion 4	ROCKS1N4	0.34
Motion 5	ROCKS1N5	0.53
Motion 6	ROCKS1N6	0.42
Motion 7	ROCKS1N7	0.36
Motion 8	ROCKS1P1	0.71
Motion 9	ROCKS1P2	0.44
Motion 10	ROCKS1P3	0.48
Motion 11	ROCKS1P4	0.32
Motion 12	ROCKS1P5	0.67
Motion 13	ROCKS1P6	0.41
Motion 14	ROCKS1P7	0.40

Table B.2. Intensity measures of the 14 motions

Motion #	PGA (g)	PGV (in/sec)	PGD (in)	D(5-95) (sec)	CAV (in/sec)	Arias Intensity (in/sec)	SD (in)*	PSA (g)*	PSV (in/sec)*
1	0.7	35.231	21.634	86.875	2409.428	844.027	6.369	0.651	40.02
2	0.381	32.859	22.431	86.295	834.813	131.109	7.203	0.736	45.255
3	0.317	29.943	16.469	89.285	794.067	115.058	6.191	0.632	38.897
4	0.337	35.984	43.945	87.145	909.658	146.66	8.242	0.842	51.783
5	0.526	28.869	25.416	83.895	1071.14	195.452	6.887	0.704	43.275
6	0.422	25.616	37.547	83.82	1226.601	219.001	5.642	0.576	35.449
7	0.356	35.106	41.365	88.025	1033.964	170.179	6.74	0.689	42.348
8	0.709	44.435	45.36	86.87	2404.713	835.79	6.606	0.675	41.506
9	0.441	41.297	51.113	85.52	840.053	139.417	7.039	0.719	44.227
10	0.477	45.129	40.75	83.885	1077.207	199.85	7.259	0.742	45.609
11	0.319	40.454	71.431	87.08	922.947	152.089	8.282	0.846	52.04
12	0.672	53.511	60.915	87.95	1442.94	406.681	8.351	0.853	52.473
13	0.412	24.455	37.643	83.83	1228.427	219.589	5.656	0.578	35.538
14	0.396	55.165	53.625	89.09	815.733	125.978	6.228	0.636	39.132

*For period = 1 sec

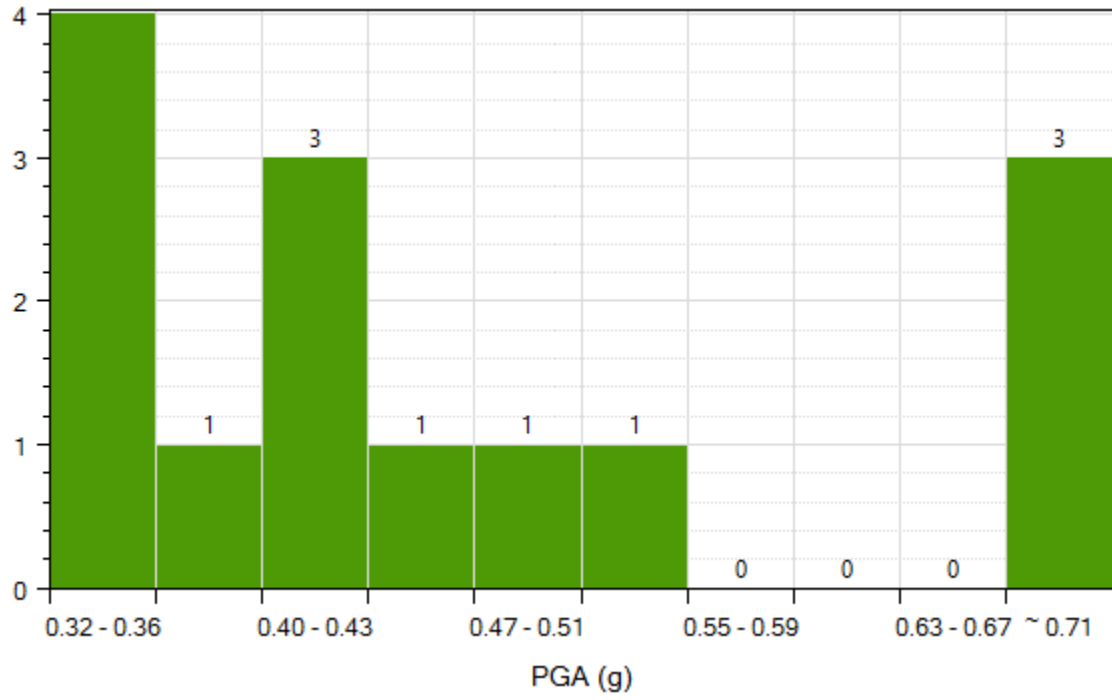


Figure B.1. Longitudinal PGA histograms of the first 14 input motions

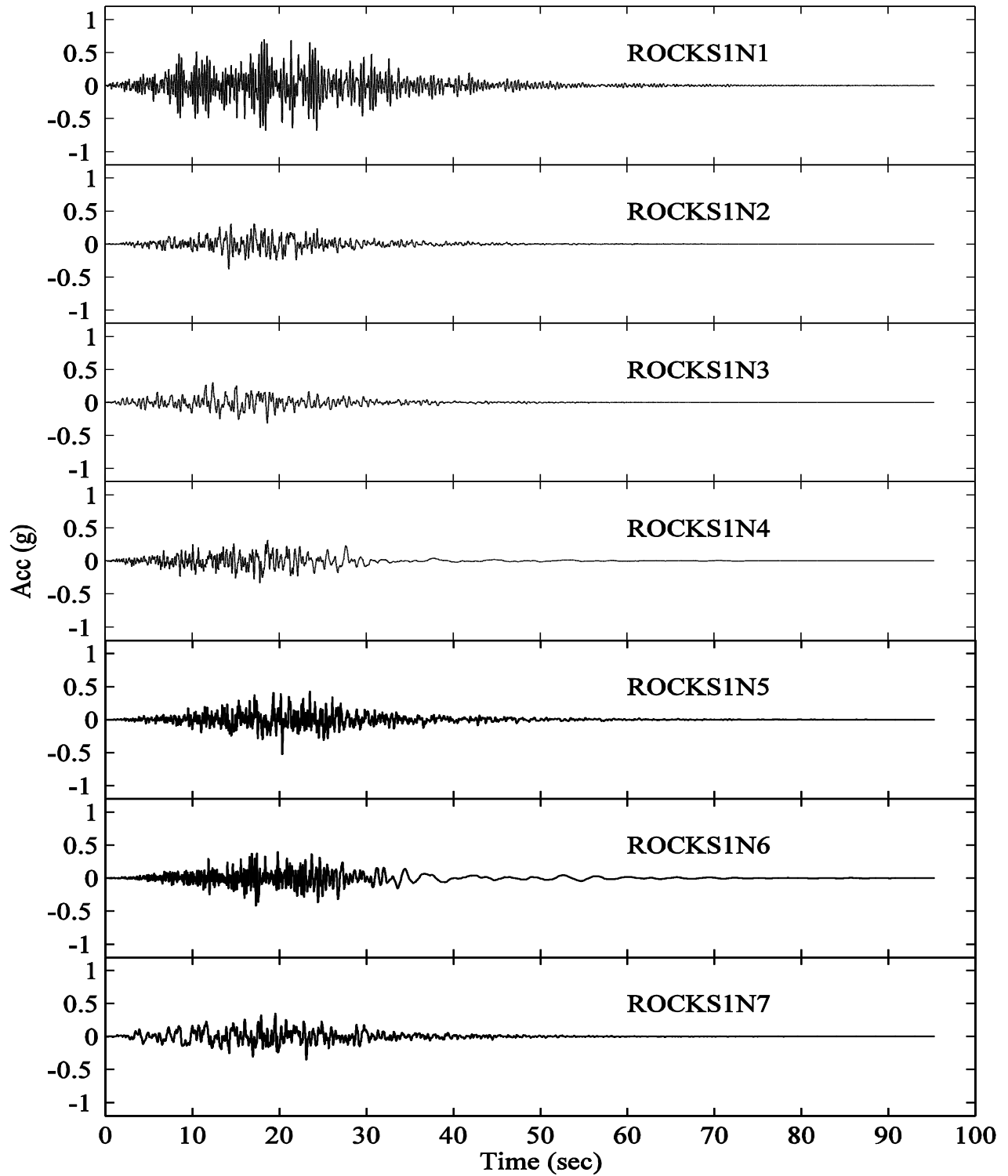


Figure B.2. Acceleration time histories of the input motion components for Rock site (non-pulse-like motions)

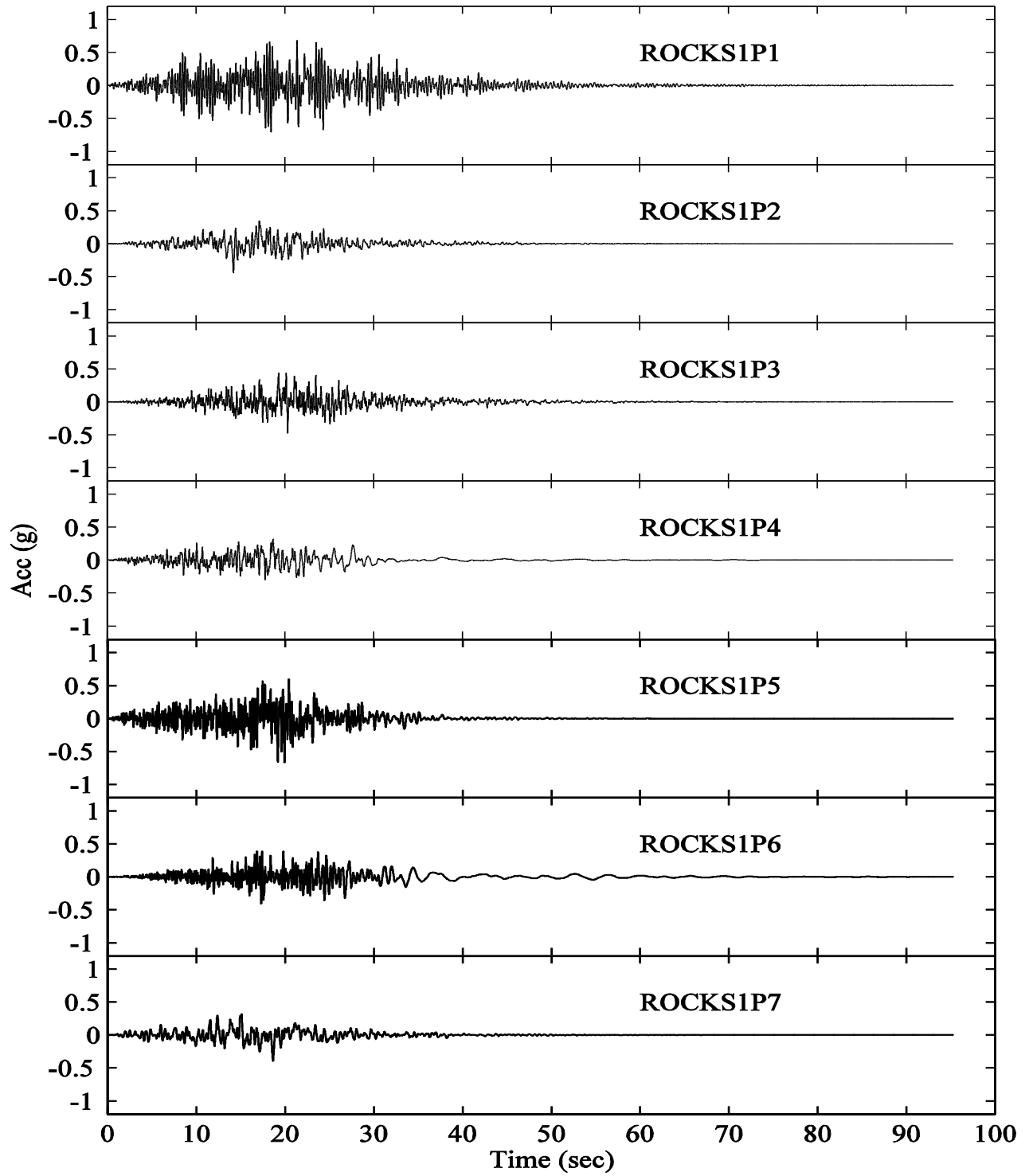


Figure B.3. Acceleration time histories of the input motion components for Rock site (pulse-like motions)

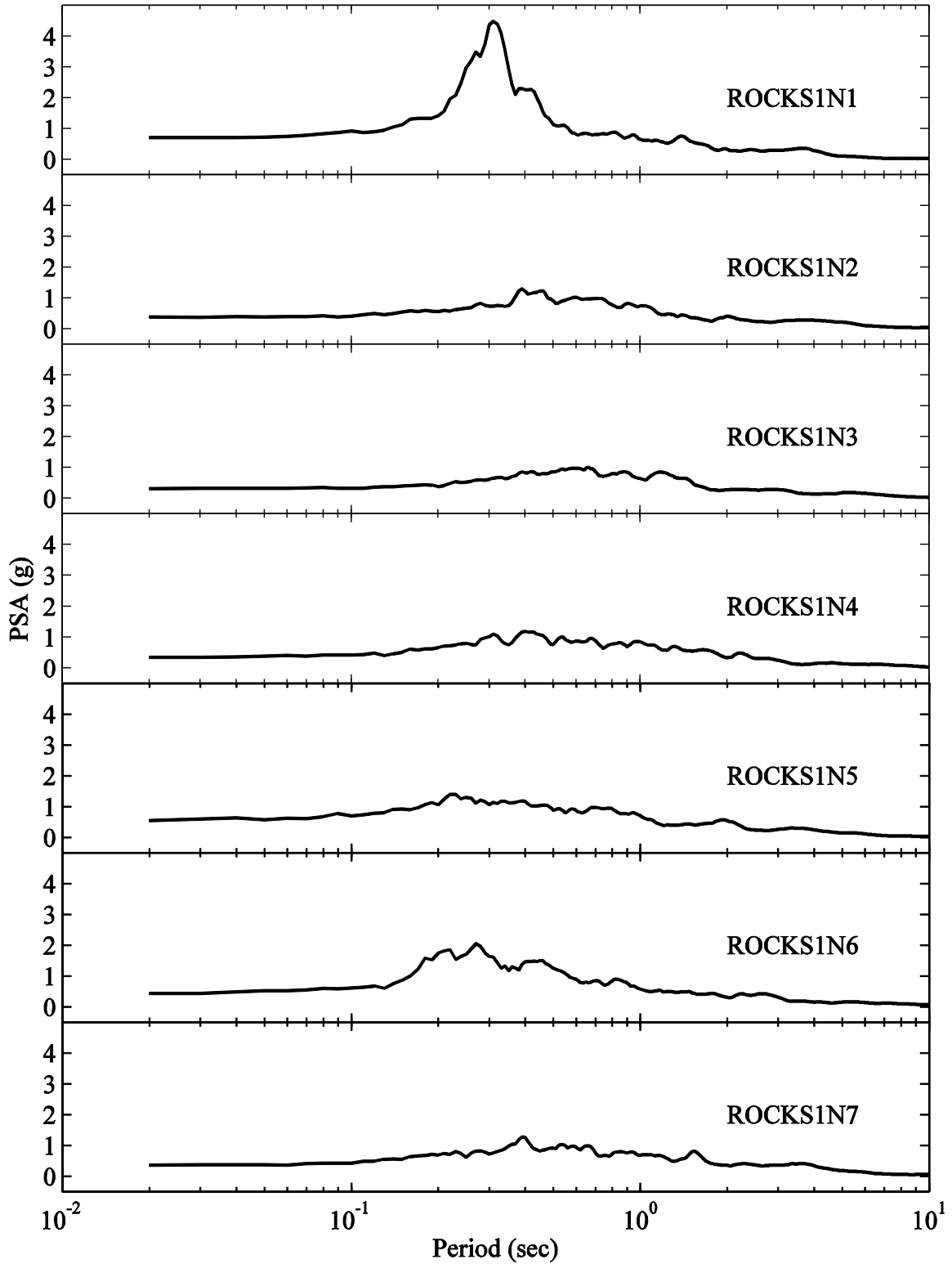


Figure B.4. Pseudo-spectral acceleration for rock site (non-pulse-like motions)

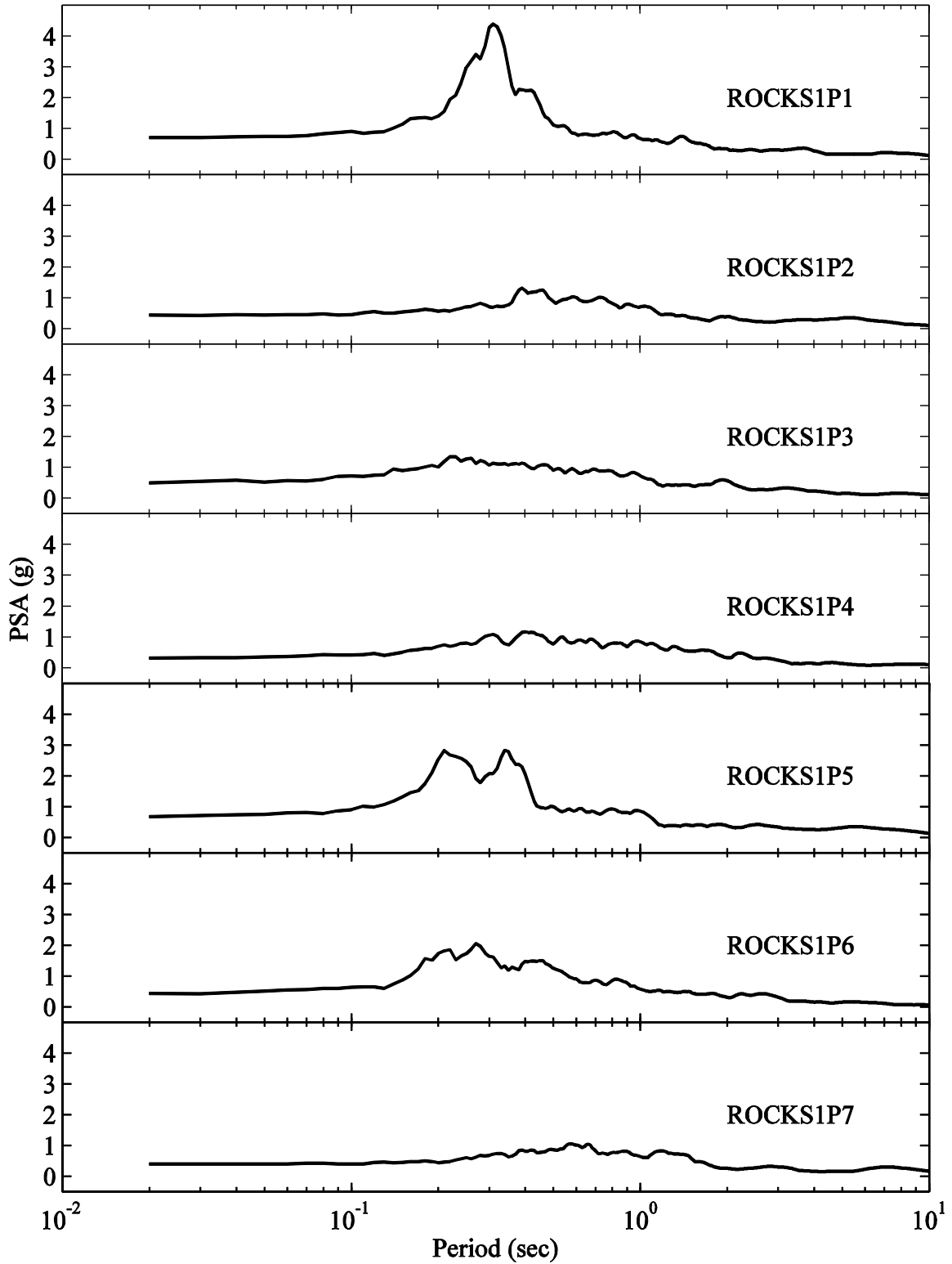


Figure B.5. Pseudo-spectral acceleration for rock site (pulse-like motions)

Appendix C. Comparison of ESA and THA Results in the Transverse Direction

The purpose of this Appendix is to compare ESA and THA results. Focus was placed on the transverse direction response. A series of models of increasing complexity were studied in an attempt to separate influence of column nonlinear response, foundation p - y springs, and the added resistance provided at the bridge end-bents and abutments. A single bent model was studied first, followed by models of the entire bridge (to include the abutment end-effects). On this basis, it was found that:

1. Linear models of the bridge bent resulted in essentially identical responses (ESA and THA).
2. Nonlinearity of the columns and base soil springs (p - y and t - z curves) caused a difference of about 25 %.
3. When the abutment effects were included, the difference actually decreased to somewhere in the neighborhood of 10 %.

C.1. Introduction

C.1.1. Purpose of Study

The purpose is to compare ESA and THA results. Specifically, comparison of ESA displacement demand and THA maximum displacement was conducted for a set of 14 motions provided by Caltrans. Focus was placed on the transverse direction only. Patterned after the Salinas River Bridge (Caltrans 2005), the bent is supported on two columns (with Type 2 foundation, when activated).

To elucidate the mechanisms behind similarity/difference in ESA and THA estimates, the comparison was conducted for a series of models of increasing complexity according to the following:

To explore linear response under a fixed base scenario

1. **Linear** columns with **fixed base** at mudline

To explore influence of including a p - y and t - z spring foundation

2. **Linear** columns with **linear p - y and t - z spring** foundation.

To explore influence of nonlinear columns

3. **Nonlinear** (bilinear) columns with **fixed base** at mudline

4. **Nonlinear** (bilinear) columns with **linear p - y and t - z spring** foundation.

Towards full bridge model with nonlinear foundation springs, bridge-end bents, and abutment lateral resistance

5. **Nonlinear** (bilinear) columns with **nonlinear p - y and t - z spring** foundation.

6. Same as 5, with 10 bents (to check full model vs. single bent behavior)

7. Same as 6, with 2 end bents at the abutments (Salinas River Bridge configuration)

8. Same as 7 with bilinear abutment springs (full Salinas River Bridge model)

As such, it was observed that:

1. As expected, Case 1 (linear with fixed base) shows complete agreement between ESA and THA

2. Also as expected, Case 2 (linear columns with linear p - y and t - z spring foundation) shows good agreement between ESA and THA.

3. Nonlinearity of the columns causes an overall difference of about 23.8%.

4. This difference increased a bit (about 25%) because of nonlinearity of the soil p - y and t - z curves.

5. The difference decreased to 15% when stiffness from the bridge-end bents was included.

6. Further stiffness introduced by the abutments led to a final overall difference of about 10%.

C.1.2. Salient Modeling Considerations

For simplicity, the bridge weight was assumed uniformly distributed on the superstructure (Caltrans 2005; Mahan 2005). Bentcap and columns were assumed massless (along the logic of a SDOF-type idealization). No resistance from the abutments was assumed for all cases (unless otherwise stated). Finally, connection between the bridge deck and the columns was assumed rigid throughout (including at the abutments).

All analyses (including ESA, THA and Mode shape analysis) were conducted in MSBridge user-interface (Elgamal *et al.* 2014) where the Finite Element (FE) framework OpenSees (Mazzoni *et al.* 2009, McKenna *et al.* 2010) was employed for the numerical simulations. For the columns and pile shafts, the `forceBeamColumn` (with the distributed plasticity integration method) element was employed (Only one `forceBeamColumn` was used for each column in this study). Rayleigh damping was considered for the soil spring zero-length elements (In OpenSees, Rayleigh damping is not included for `zeroLength` element by default).

C.1.3. Layout

This study starts with a single-bent model with rigid base and linear columns (Case 1, see Section C.3). Case 1 is very similar to an SDOF (Single-Degree-Of-Freedom) problem. ESA displacement demand and THA maximum displacement for Case 1 are expected to be identical for this case.

Compared to Case 1, Case 2 (see Section C.4) includes a foundation of linear soil springs (instead of rigid base foundation). Cases 3 (see Section C.5) and 4 (see Section C.6) activate the bilinear moment-curvature behavior for the columns, compared to Cases 1 and 2, respectively.

Compared to Case 4, Case 5 activates nonlinear soil springs (instead of linear springs) for the foundation. Case 5 (Section C.7) essentially represents a typical bent of the Salinas River Bridge model. Case 6 (Section C.8) is multi-bent bridge model with 10 identical bents (each bent is the same as Case 5). No abutment is considered in Case 6. Compared to Case 6, Case 7 (Section C.9) adds 2 end bents. Thus Case 7 represents the idealized Salinas River Bridge model without lateral abutment stiffness. Finally, Case 8 (Section C.10) adds the transverse abutment stiffness, compared to Case 7. Case 8 essentially represents the idealized Salinas River Bridge model.

C.2. Typical Bent

Salinas River Bridge is a reinforced concrete box-girder bridge with 11 spans (Caltrans 2005). Each span is 140 ft long (corresponding to a total weight of 1,912.4 kips lumped at bent). The substructure consists of multiple two-column bents. Figure C.1 shows the side view of a typical bent (column height = 48 ft). For the nonlinear column cases, an idealized bilinear moment-curvature relationship was used to model the columns (Figure C.2) and pile shafts (Figure C.3). As such, one cross-section (Figure C.2) defines the column properties and another (Figure C.3) defines pile properties (due to current capabilities of MSBridge). The column foundation response (Figure C.1) was modeled by the approach of soil p - y and t - z curves (Caltrans 2005).

Figure C.4 shows the pushover response (for the bent with soil springs). It can be seen that plastic hinges form at column top when the pushover displacement reaches 9.4 inches. At 17.2 inches, plastic hinges form near the base, and ultimate lateral resistance load is reached. As such, the bent ultimate capacity is 508.4 kips (= 2 x 254.2 kips), which corresponds to a lateral bent acceleration of 0.27g. In the conducted THA numerical simulations, Rayleigh damping of 5% was employed (a value of 5% was specified in the range of first few natural periods of the system).

C.2.1. ESA Comparison for MSBridge and wFrame

Transverse ESA was conducted using MSBridge for the bent (Figure C.1). In the ESA pushover analysis, the bent was pushed at bentcap laterally until initial yielding occurred (at column top in this case).

The ESA outcomes (Table C.1) were compared to the wFrame (Mahan 2005) results reported in Caltrans (2005). In general, good agreement (Table C.1) was noted in the MSBridge and wFrame results. The difference in initial stiffness between MSBridge and wFrame is about 2.6%. Note that in wFrame, three cross-sections were employed for each column (Caltrans 2005). However, in MSBridge, only one cross-section was used for the columns and the other 2 sections which are more flexible (but with a higher plastic moment) were not considered due to the current capabilities of MSBridge. This simplification resulted in a lower yield displacement (9.4 in) in MSBridge, compared to the yield displacement of 9.76 in obtained in wFrame (Table C.1).

C.3. Case 1: Single Bent Model with Rigid Base and Linear Columns

C.3.1. Case 1 Description

Case 1 (Figure C.5) is very similar to an SDOF problem. Mode shape analysis shows the first transverse period is 0.86 seconds, which matches the period calculated by the transverse ESA procedure.

C.3.2. Comparison of ESA and THA Results

For this single-bent bridge model with rigid base and linear columns, Table C.2 shows the ESA displacement demand and the THA maximum displacement are in good agreement (less than 1% difference for most motions while reaching 2.3% for 2 motions). Note that the differences were

calculated based on the actual displacement values while the displacement values shown in Table C.2 were rounded to 2 decimal places (for the sake of simplicity).

Table C.3 shows the maximum column bending moments and shear forces for the 14 motions. The maximum column bending moments range from around 18,000 kip-ft – 21,000 kip-ft. Note that, in this linear analysis, all of these maximum bending moments exceed the plastic moment (6,100 kip-ft) to be employed for the nonlinear columns (to be studied in later sections).

C.4. Case 2: Single Bent Model with Linear Soil Springs and Linear Columns

C.4.1. Case 2 Description

Pile shaft was also assumed linear in this case (Figure C.6). Mode shape analysis shows the first transverse period is 2.0 seconds, which also matches the period calculated by the transverse ESA procedure.

C.4.2. Comparison of ESA and THA Results

Table C.4 displays the comparison of ESA and THA results for Case 2. Essentially, the ESA displacement demand and THA maximum displacement are nearly the same for this linear case (around 1% or less for most motions while reaching about 4% for Motions# 2, 3 and 9). Note that Rayleigh damping was included for the soil spring zero-length elements.

Table C.5 shows the maximum column bending moments and shear forces for the 14 motions. The maximum column bending moments range from around 9,370 kip-ft – 19,900 kip-ft. Note that all of these maximum bending moments also exceed the plastic moment (6,100 kip-ft) to be employed for the nonlinear columns (Figure C.2; to be studied in later sections).

C.5. Case 3: Single Bent Model with Rigid Base and Nonlinear Columns

C.5.1. Case 3 Description

Compared to Case 1, Case 3 (Figure C.7) activates the bilinear moment-curvature behavior for the columns. Mode shape analysis shows the first transverse period is 0.86 seconds, which also matches the period calculated by the transverse ESA procedure.

C.5.2. Comparison of ESA and THA Results

Table C.6 displays the comparison of ESA and THA results for Case 3. An overall (average) difference of about 23.8% was observed while some motions significantly exceed this value (Table C.6). It is indicated that these (large) differences are due to the nonlinearity of the columns.

Table C.7 shows the maximum column bending moments and shear forces for the 14 motions. As can be seen, the maximum column bending moment reached the plastic value of 6,100 kip-ft (also see Figure C.8 and Figure C.9), as defined in the moment-curvature relationship for the columns (Figure C.2). The maximum shear force reached the ultimate value of 254.2 kips for all motions (Figure C.4).

C.6. Case 4: Single Bent Model with Linear Soil Springs and Nonlinear Column

C.6.1. Case 4 Description

Compared to Case 2, Case 4 (Figure C.10) activates the bilinear moment-curvature behavior for the columns. Mode shape analysis shows the first transverse period is 2.0 seconds (same as that of Case 2), which also matches the period calculated by the transverse ESA procedure.

Table C.8 displays the comparison of ESA and THA results for Case 4. The differences between the ESA displacement demand and THA maximum displacement are as large as 30% or more. The average difference for the 14 motions is about 11%. These large differences are due to the column nonlinearity.

Table C.9 shows the maximum column bending moments and shear forces for the 14 motions. As can be seen, the maximum column bending moment reached the plastic value of 6,100 kip-ft (also see Figure C.11 and Figure C.12), as defined in the moment-curvature relationship for the columns (Figure C.2).

C.7. Case 5: Single Bent Model with Nonlinear Soil Springs and Nonlinear Columns

C.7.1. Case 5 Description

Compared to Case 4, Case 5 (Figure C.13) employs nonlinear soil springs (instead of linear soil springs). The bilinear model (Figure C.3) was also employed for the pile shaft. As such, Case 5 essentially represents a typical bent of the Salinas River Bridge model. Mode shape analysis shows the first transverse period is 2.0 seconds (the period calculated by the transverse ESA procedure is 2.21 seconds).

C.7.2. Transverse Pushover Loading

Pushover analysis was conducted by applying a load at the bentcap in 500 steps (in the transverse direction). Figure C.14 shows the pushover load-displacement response of the pushover analysis. The first batch of 2 plastic hinges formed at column top (for the 2 columns) when the pushover displacement reaches 9.4 in (at a load of about 376 kips). The second batch of 2 plastic hinges formed at column base (for the 2 columns) when the pushover displacement reached about

17.2 in (at a load of about 508 kips). After that, the bent cannot resist any additional lateral load (Figure C.14).

Based on Figure C.4, the ESA initial stiffness is 40 kip/in (= 376 kips / 9.4 in). The bending moment-curvature and shear force-displacement response at column top are shown in Figure C.2 and Figure C.4, respectively. During the pushover analysis, the axial force of one column increased when the other one decreased while both were in compression (Figure C.15).

Table C.10 displays the comparison of ESA and THA results for Case 5. An overall (average) difference between the ESA displacement demand and THA maximum displacement is about 25% (while some motions resulted in more than 40%). These (large) differences are mainly due to the nonlinearity of the columns and the soil-spring foundation.

Table C.11 shows the maximum column bending moments and shear forces for the 14 motions. As can be seen, the maximum column bending moment reached the plastic value of 6,100 kip-ft (also see Figure C.16 and Figure C.17), as defined in the moment-curvature relationship for the columns (Figure C.2).

C.8. Case 6: Multi-bent Model with Nonlinear Soil Springs and Nonlinear Columns

Case 6 (Figure C.18) is a multi-bent bridge model with 10 identical bents (each bent is the same as Case 5). No abutment was considered in Case 6. Mode shape analysis (Figure C.19) showed the first transverse period is 2.0 seconds (the period calculated by the transverse ESA procedure is 2.21 seconds). THA numerical simulations were conducted for Case 6. The THA results show the response of Case 6 is the same as that of Case 5.

C.9. Case 7: Multi-bent Model with End-bents

C.9.1. Case 7 Description

Compared to Case 6, Case 7 (Figure C.20) included two end-bents (same as the other bents) at the abutment locations. However, lateral abutment stiffness was not considered in Case 7. Mode shape analysis (Figure C.21) showed the first transverse period is 1.94 seconds (the period calculated by the transverse ESA procedure is 2.21 seconds).

C.9.2. Comparison of ESA and THA Results

Table C.12 displays the comparison of ESA and THA results for Case 7. The differences between the ESA displacement demand and THA maximum displacement are as large as about 44%. An overall difference of 15% between ESA and THA was observed (Table C.12). These (large) differences are mainly due to the nonlinearity of the columns and the soil-spring foundation.

Table C.13 shows the comparison of THA maximum displacement for Cases 5 and 7 where Case 7 shows higher maximum displacement. In addition, Table C.14 shows the maximum column bending moments and shear forces for the 14 motions. As can be seen, the maximum column bending moment reached the plastic value of 6,100 kip-ft (also see Figure C.22 and Figure C.23), as defined in the moment-curvature relationship for the columns (Figure C.2).

C.10. Case 8: Salinas River Bridge Model

C.10.1. Case 8 Description

Compared to Case 7, Case 8 (see Figure C.20) included abutment resistance in the transverse direction. The transverse abutment resistance was taken as a fraction of the longitudinal resistance (Aviram *et al.* 2008a, 2008b). According to Caltrans SDC Example (2005), a bilinear

model of initial stiffness of 128.25 kip/in and yield displacement of 4 in was employed for the longitudinal direction of each abutment for the Salinas River Bridge model. As a result, a bilinear model with a yield force of 222.5 kips at a yield displacement of 4 in was employed (Figure C.24) for the transverse direction of each abutment (Aviram *et al.* 2008a, 2008b; Caltrans 2013; Mahan 2005). Note that Rayleigh damping was not included in the `zeroLength` elements of the abutments. Compared to the response of a typical bent (Figure C.25), it may be seen that:

1. Total stiffness from bridge bents is 480 kip/in (= 40 kip/in x 12 bents), compared to 111.25 kip/in (=55.625 kip/in x 2) from the abutments.
2. Abutments yield first at a displacement of 4 inches.
3. First yield of intermediate bents occurs at 9.4 inches, and full resistance was reached at 17.2 inches.

Abutment total ultimate resistance is $222.5 \times 2 = 445$ kips, compared to total ultimate resistance from the bridge bents of $254.2 \times 24 = 6,100.8$ kips. The quantities above can be used to assess the level of deformation reached in each earthquake shaking event below.

Mode shape analysis (Figure C.26) shows the first transverse period is 1.91 seconds, which is a bit lower than Case 7 due to the increased transverse abutment resistance (the period reported by the transverse ESA for a typical bent is 2.21 seconds).

C.10.2. Comparison of ESA and THA Results

Table C.15 displays the comparison of ESA and THA results for Case 8. An overall (average) difference of about 10% was observed (while some motions resulted in 30% or more). These (large) differences are mainly due to the nonlinearity of the columns and the soil-spring foundation. Table C.16 shows the comparison of THA maximum displacement for Cases 5 and 8 where Case 8 shows higher maximum displacement (in general).

Table C.17 shows the maximum column bending moments and shear forces for the 14 motions. As can be seen, the maximum column bending moment and the ultimate abutment resistance force reached 6,100 kip-ft (also see Figure C.26), and 222.5 kips (also see Figure C.27), respectively, as defined in Figure C.2 and Figure C.24. Figure C.26 and Figure C.27 show the column and abutment response for Column 1 of Bent 6 (center bent) for Motion #1 ROCKS1N1. Figure C.28 and Figure C.29 display the response for Motion #2 ROCKS1N2.

C.11. Summary and Conclusions

C.11.1. Summary

Comparison of ESA displacement demand and THA maximum displacement was conducted in the transverse direction. A series of models of increasing complexity were studied in an attempt to separate influence of column nonlinear response, foundation p - y curves, and the added resistance provided at the bridge abutments. A set of 14 motions (and target ARS) provided by Caltrans was employed. Comparison of the average ESA and THA results (for the 14 motions) for all the studied models is summarized in Table C.18.

C.11.2. Conclusions

The main findings are:

- 1) For the single bent model studied, the difference between ESA displacement demand and THA maximum displacement is about 25% (overall).
- 2) Ultimately, for the full Salinas River Bridge model, an overall difference of about 10% was observed between ESA and THA due to: i) nonlinearity of the bridge columns and p - y / t - z curves; and ii) the added lateral resistance provided by the bridge-end bents and the abutments.

- 3) For linear cases (case of linear columns with rigid base, and case of linear columns with linear soil springs), the ESA displacement demand and the THA maximum displacement are in good agreement (around 1% or less for most shaking events).

Table C.1. Comparison of MSBridge and wFrame results for the transverse ESA

Response	MSBridge	wFrame	Difference
Yield Displacement (in)	9.4	9.76	3.4%
Pushover Load (kips)	376	382.4	1.7%
Initial Stiffness (kip/in)	40	39	2.6%
Period (seconds)	2.21	2.24	1.3%
Displacement Demand (in)	18.8	18.6	1.1%

Table C.2. Comparison of transverse ESA displacement demand and THA maximum displacement (ESA displacement demand for an individual motion is based on the response spectrum of that motion) for Case 1

Motion#	Motion (PGA)	THA Maximum Displacement (in)	ESA Displacement Demand (in)	Difference (“-” sign means ESA is less)
1	ROCKS1N1 (0.70g)	5.46	5.49	0.4%
2	ROCKS1N2 (0.38g)	5.30	5.18	-2.3%
3	ROCKS1N3 (0.32g)	6.22	6.16	-0.9%
4	ROCKS1N4 (0.34g)	5.86	5.84	-0.3%
5	ROCKS1N5 (0.53g)	5.65	5.61	-0.7%
6	ROCKS1N6 (0.42g)	6.18	6.17	-0.2%
7	ROCKS1N7 (0.36g)	5.82	5.79	-0.5%
8	ROCKS1P1 (0.71g)	5.52	5.54	0.4%
9	ROCKS1P2 (0.44g)	5.16	5.04	-2.3%
10	ROCKS1P3 (0.48g)	5.29	5.25	-0.7%
11	ROCKS1P4 (0.32g)	5.75	5.73	-0.3%
12	ROCKS1P5 (0.67g)	5.91	5.88	-0.5%
13	ROCKS1P6 (0.41g)	6.17	6.16	-0.2%
14	ROCKS1P7 (0.40g)	5.91	5.85	-0.9%
Average		5.73	5.69	-0.6%

Note: ESA displacement demand based on target ARS is 5.67 inches, corresponding a difference of 1.0%.

Table C.3. Maximum column shear forces and bending moments (transverse) for Case 1

Motion#	Motion (PGA)	Maximum Bending Moment (kip-ft)	Maximum Shear Force (kips)
1	ROCKS1N1 (0.70g)	18,628.3	753.2
2	ROCKS1N2 (0.38g)	18,080.5	731.4
3	ROCKS1N3 (0.32g)	21,109.6	851.7
4	ROCKS1N4 (0.34g)	19,932.3	805.0
5	ROCKS1N5 (0.53g)	19,242.3	777.6
6	ROCKS1N6 (0.42g)	20,974.3	846.4
7	ROCKS1N7 (0.36g)	19,791.5	799.4
8	ROCKS1P1 (0.71g)	18,822.8	760.9
9	ROCKS1P2 (0.44g)	17,625.2	713.3
10	ROCKS1P3 (0.48g)	18,042.4	729.9
11	ROCKS1P4 (0.32g)	19,562.7	790.3
12	ROCKS1P5 (0.67g)	20,110.1	812.0
13	ROCKS1P6 (0.41g)	20,939.6	845.0
14	ROCKS1P7 (0.40g)	20,080.6	810.9

Table C.4. Comparison of transverse ESA displacement demand and THA maximum displacement (ESA displacement demand for an individual motion is based on the response spectrum of that motion) for Case 2

Motion#	Motion (PGA)	THA Maximum Displacement (in)	ESA Displacement Demand (in)	Difference (“-” sign means ESA is less)
1	ROCKS1N1 (0.70g)	12.9	13.1	1.3%
2	ROCKS1N2 (0.38g)	15.9	15.3	-4.5%
3	ROCKS1N3 (0.32g)	10.9	10.5	-3.8%
4	ROCKS1N4 (0.34g)	13.2	13.1	-0.6%
5	ROCKS1N5 (0.53g)	21.4	21.5	0.2%
6	ROCKS1N6 (0.42g)	12.3	12.4	0.8%
7	ROCKS1N7 (0.36g)	14.0	13.9	-0.9%
8	ROCKS1P1 (0.71g)	13.3	13.4	1.2%
9	ROCKS1P2 (0.44g)	15.7	15.0	-4.5%
10	ROCKS1P3 (0.48g)	22.4	22.5	0.2%
11	ROCKS1P4 (0.32g)	13.2	13.2	-0.1%
12	ROCKS1P5 (0.67g)	14.7	14.9	1.2%
13	ROCKS1P6 (0.41g)	12.3	12.4	0.8%
14	ROCKS1P7 (0.40g)	10.1	10.0	-1.0%
Average		14.5	14.4	-0.6%

Note: ESA displacement demand based on target ARS is 14.8 inches, corresponding a difference of 2.3%.

Table C.5. Maximum column shear forces and bending moments (transverse) for Case 2

Motion#	Motion (PGA)	Maximum Bending Moment (kip-ft)	Maximum Shear Force (kips)
1	ROCKS1N1 (0.70g)	11,777.4	330.5
2	ROCKS1N2 (0.38g)	14,371.0	405.1
3	ROCKS1N3 (0.32g)	10,084.4	281.9
4	ROCKS1N4 (0.34g)	12,010.7	337.2
5	ROCKS1N5 (0.53g)	19,049.3	539.5
6	ROCKS1N6 (0.42g)	11,273.8	316.1
7	ROCKS1N7 (0.36g)	12,756.3	358.7
8	ROCKS1P1 (0.71g)	12,105.0	340.0
9	ROCKS1P2 (0.44g)	14,156.2	398.9
10	ROCKS1P3 (0.48g)	19,908.7	564.2
11	ROCKS1P4 (0.32g)	12,051.1	338.4
12	ROCKS1P5 (0.67g)	13,352.4	375.8
13	ROCKS1P6 (0.41g)	11,300.8	316.8
14	ROCKS1P7 (0.40g)	9,369.5	261.3

Table C.6. Comparison of transverse ESA displacement demand and THA maximum displacement (ESA displacement demand for an individual motion is based on the response spectrum of that motion) for Case 3

Motion#	Motion (PGA)	THA Maximum Displacement (in)	ESA Displacement Demand (in)	Difference (“-” sign means ESA is less)
1	ROCKS1N1 (0.70g)	5.82	5.82	0.0%
2	ROCKS1N2 (0.38g)	5.70	4.76	-19.7%
3	ROCKS1N3 (0.32g)	6.19	5.41	-14.5%
4	ROCKS1N4 (0.34g)	5.42	5.46	0.7%
5	ROCKS1N5 (0.53g)	9.46	5.53	-71.0%
6	ROCKS1N6 (0.42g)	5.16	6.10	15.3%
7	ROCKS1N7 (0.36g)	6.77	5.35	-26.5%
8	ROCKS1P1 (0.71g)	9.88	5.87	-68.3%
9	ROCKS1P2 (0.44g)	7.36	5.02	-46.7%
10	ROCKS1P3 (0.48g)	10.18	5.19	-96.0%
11	ROCKS1P4 (0.32g)	6.11	5.45	-12.0%
12	ROCKS1P5 (0.67g)	5.01	5.86	14.6%
13	ROCKS1P6 (0.41g)	5.14	6.09	15.7%
14	ROCKS1P7 (0.40g)	7.27	5.22	-39.2%
Average		6.82	5.51	-23.8%

Note: ESA displacement demand based on target ARS is 5.40 inches, corresponding a difference of -26.3%.

Table C.7. Maximum column shear forces and bending moments (transverse) for Case 3

Motion#	Motion (PGA)	Maximum Bending Moment (kip-ft)	Maximum Shear Force (kips)
1	ROCKS1N1 (0.70g)	6,100	254.2
2	ROCKS1N2 (0.38g)	6,100	254.2
3	ROCKS1N3 (0.32g)	6,100	254.2
4	ROCKS1N4 (0.34g)	6,100	254.2
5	ROCKS1N5 (0.53g)	6,100	254.2
6	ROCKS1N6 (0.42g)	6,100	254.2
7	ROCKS1N7 (0.36g)	6,100	254.2
8	ROCKS1P1 (0.71g)	6,100	254.2
9	ROCKS1P2 (0.44g)	6,100	254.2
10	ROCKS1P3 (0.48g)	6,100	254.2
11	ROCKS1P4 (0.32g)	6,100	254.2
12	ROCKS1P5 (0.67g)	6,100	254.2
13	ROCKS1P6 (0.41g)	6,100	254.2
14	ROCKS1P7 (0.40g)	6,100	254.2

Table C.8. Comparison of transverse ESA displacement demand and THA maximum displacement (ESA displacement demand for an individual motion is based on the response spectrum of that motion) for Case 4

Motion#	Motion (PGA)	THA Maximum Displacement (in)	ESA Displacement Demand (in)	Difference (“-” sign means ESA is less)
1	ROCKS1N1 (0.70g)	11.0	13.1	15.7%
2	ROCKS1N2 (0.38g)	16.2	15.3	-5.4%
3	ROCKS1N3 (0.32g)	10.7	10.5	-1.7%
4	ROCKS1N4 (0.34g)	13.1	13.1	-0.3%
5	ROCKS1N5 (0.53g)	13.5	21.5	37.3%
6	ROCKS1N6 (0.42g)	10.8	12.4	12.8%
7	ROCKS1N7 (0.36g)	11.5	13.9	17.9%
8	ROCKS1P1 (0.71g)	12.4	13.4	7.5%
9	ROCKS1P2 (0.44g)	15.0	15.1	0.4%
10	ROCKS1P3 (0.48g)	15.4	22.5	31.8%
11	ROCKS1P4 (0.32g)	12.1	13.2	8.4%
12	ROCKS1P5 (0.67g)	17.0	14.9	-14.0%
13	ROCKS1P6 (0.41g)	10.8	12.4	12.9%
14	ROCKS1P7 (0.40g)	9.8	10.0	1.8%
Average		12.8	14.4	11.0%

Note: ESA displacement demand based on target ARS is 14.8 inches, corresponding to a difference of 13.6%.

Table C.9. Maximum column shear forces and bending moments (transverse) for Case 4

Motion#	Motion (PGA)	Maximum Bending Moment (kip-ft)	Maximum Shear Force (kips)
1	ROCKS1N1 (0.70g)	6,100	208.5
2	ROCKS1N2 (0.38g)	6,100	254.1
3	ROCKS1N3 (0.32g)	6,100	205.8
4	ROCKS1N4 (0.34g)	6,100	226.9
5	ROCKS1N5 (0.53g)	6,100	230.5
6	ROCKS1N6 (0.42g)	6,100	207.0
7	ROCKS1N7 (0.36g)	6,100	212.9
8	ROCKS1P1 (0.71g)	6,100	220.3
9	ROCKS1P2 (0.44g)	6,100	243.9
10	ROCKS1P3 (0.48g)	6,100	247.0
11	ROCKS1P4 (0.32g)	6,100	218.2
12	ROCKS1P5 (0.67g)	6,100	254.2
13	ROCKS1P6 (0.41g)	6,100	207.1
14	ROCKS1P7 (0.40g)	6,100	198.1

Table C.10. Comparison of transverse ESA displacement demand and THA maximum displacement (ESA displacement demand for an individual motion is based on the response spectrum of that motion) for Case 5

Motion#	Motion (PGA)	THA Maximum Displacement (in)	ESA Displacement Demand (in)	Difference (“-” sign means ESA is less)
1	ROCKS1N1 (0.70g)	9.9	13.4	26.1%
2	ROCKS1N2 (0.38g)	15.7	14.7	-6.4%
3	ROCKS1N3 (0.32g)	10.5	13.8	23.8%
4	ROCKS1N4 (0.34g)	13.6	23.1	40.9%
5	ROCKS1N5 (0.53g)	13.7	18.5	26.3%
6	ROCKS1N6 (0.42g)	11.0	19.9	45.1%
7	ROCKS1N7 (0.36g)	11.8	19.2	38.3%
8	ROCKS1P1 (0.71g)	11.2	13.7	18.4%
9	ROCKS1P2 (0.44g)	15.0	14.6	-2.7%
10	ROCKS1P3 (0.48g)	15.7	18.3	14.1%
11	ROCKS1P4 (0.32g)	13.0	23.3	44.2%
12	ROCKS1P5 (0.67g)	16.8	15.4	-8.9%
13	ROCKS1P6 (0.41g)	11.0	20.0	45.2%
14	ROCKS1P7 (0.40g)	10.1	10.9	7.5%
Average		12.8	17.1	25.1%

Note: ESA displacement demand based on target ARS is 17.0 inches, corresponding a difference of 24.6%.

Table C.11. Maximum column shear forces and bending moments (transverse) for Case 5

Motion#	Motion (PGA)	Maximum Bending Moment (kip-ft)	Maximum Shear Force (kips)
1	ROCKS1N1 (0.70g)	6,100	193.7
2	ROCKS1N2 (0.38g)	6,100	241.1
3	ROCKS1N3 (0.32g)	6,100	198.4
4	ROCKS1N4 (0.34g)	6,100	224.4
5	ROCKS1N5 (0.53g)	6,100	225.0
6	ROCKS1N6 (0.42g)	6,100	202.5
7	ROCKS1N7 (0.36g)	6,100	209.7
8	ROCKS1P1 (0.71g)	6,100	203.1
9	ROCKS1P2 (0.44g)	6,100	235.1
10	ROCKS1P3 (0.48g)	6,100	241.7
11	ROCKS1P4 (0.32g)	6,100	219.2
12	ROCKS1P5 (0.67g)	6,100	250.8
13	ROCKS1P6 (0.41g)	6,100	202.5
14	ROCKS1P7 (0.40g)	6,100	195.3

Table C.12. Comparison of transverse ESA displacement demand and THA maximum displacement (ESA displacement demand for an individual motion is based on the response spectrum of that motion) for Case 7

Motion#	Motion (PGA)	THA Maximum Displacement (in)	ESA Displacement Demand (in)	Difference (“-” sign means ESA is less)
1	ROCKS1N1 (0.70g)	12.2	13.4	8.7%
2	ROCKS1N2 (0.38g)	16.1	14.7	9.0%
3	ROCKS1N3 (0.32g)	10.7	13.8	22.3%
4	ROCKS1N4 (0.34g)	14.3	23.1	38.0%
5	ROCKS1N5 (0.53g)	17.4	18.5	6.4%
6	ROCKS1N6 (0.42g)	13.1	19.9	34.4%
7	ROCKS1N7 (0.36g)	12.5	19.2	34.6%
8	ROCKS1P1 (0.71g)	14.0	13.7	2.5%
9	ROCKS1P2 (0.44g)	15.7	14.6	8.0%
10	ROCKS1P3 (0.48g)	19.7	18.3	7.2%
11	ROCKS1P4 (0.32g)	13.1	23.3	43.6%
12	ROCKS1P5 (0.67g)	20.6	15.4	33.7%
13	ROCKS1P6 (0.41g)	13.1	20.0	34.6%
14	ROCKS1P7 (0.40g)	10.5	10.9	3.7%
Average		14.5	17.1	15.0%

Note: ESA displacement demand based on target ARS is 17.0 inches, corresponding to a difference of 14.5%.

Table C.13. Comparison of Cases 5 and 7 for THA maximum displacement

Motion#	Motion (PGA)	THA Maximum Displacement (in)		
		Case 5	Case 7	Difference (“-” sign means Case 7 is less)
1	ROCKS1N1 (0.70g)	9.9	12.2	19.0%
2	ROCKS1N2 (0.38g)	15.7	16.1	2.3%
3	ROCKS1N3 (0.32g)	10.5	10.7	1.9%
4	ROCKS1N4 (0.34g)	13.6	14.3	4.8%
5	ROCKS1N5 (0.53g)	13.7	17.4	21.2%
6	ROCKS1N6 (0.42g)	11.0	13.1	16.2%
7	ROCKS1N7 (0.36g)	11.8	12.5	5.6%
8	ROCKS1P1 (0.71g)	11.2	14.0	20.4%
9	ROCKS1P2 (0.44g)	15.0	15.7	4.8%
10	ROCKS1P3 (0.48g)	15.7	19.7	19.9%
11	ROCKS1P4 (0.32g)	13.0	13.1	1.0%
12	ROCKS1P5 (0.67g)	16.8	20.6	18.5%
13	ROCKS1P6 (0.41g)	11.0	13.1	16.2%
14	ROCKS1P7 (0.40g)	10.1	10.5	4.0%
Average		12.8	14.5	11.9%

Table C.14. Maximum column shear forces and bending moments (transverse) for Cases 5 and 7

Motion#	Motion (PGA)	Maximum Bending Moment (kip-ft)	Maximum Shear Force (kips)		
			Case 5	Case 7	Difference (“-” sign means Case 7 is less)
1	ROCKS1N1 (0.70g)	6,100	193.7	213.2	9.1%
2	ROCKS1N2 (0.38g)	6,100	241.1	244.8	1.5%
3	ROCKS1N3 (0.32g)	6,100	198.4	200.2	0.9%
4	ROCKS1N4 (0.34g)	6,100	224.4	229.6	2.3%
5	ROCKS1N5 (0.53g)	6,100	225.0	254.2	11.5%
6	ROCKS1N6 (0.42g)	6,100	202.5	220.1	8.0%
7	ROCKS1N7 (0.36g)	6,100	209.7	215.7	2.8%
8	ROCKS1P1 (0.71g)	6,100	203.1	227.0	10.5%
9	ROCKS1P2 (0.44g)	6,100	235.1	241.8	2.8%
10	ROCKS1P3 (0.48g)	6,100	241.7	254.2	4.9%
11	ROCKS1P4 (0.32g)	6,100	219.2	220.6	0.7%
12	ROCKS1P5 (0.67g)	6,100	250.8	254.2	1.3%
13	ROCKS1P6 (0.41g)	6,100	202.5	220.2	8.0%
14	ROCKS1P7 (0.40g)	6,100	195.3	198.9	1.8%

Table C.15. Comparison of transverse ESA displacement demand and THA maximum displacement (ESA displacement demand for an individual motion is based on the response spectrum of that motion) for Case 7

Motion#	Motion (PGA)	THA Maximum Displacement (in)	ESA Displacement Demand (in)	Difference (“-” sign means ESA is less)
1	ROCKS1N1 (0.70g)	14.7	13.4	-9.7%
2	ROCKS1N2 (0.38g)	14.9	14.7	-1.4%
3	ROCKS1N3 (0.32g)	10.4	13.8	24.3%
4	ROCKS1N4 (0.34g)	16.2	23.1	29.6%
5	ROCKS1N5 (0.53g)	17.1	18.5	7.8%
6	ROCKS1N6 (0.42g)	13.9	19.9	30.1%
7	ROCKS1N7 (0.36g)	14.7	19.2	23.4%
8	ROCKS1P1 (0.71g)	15.7	13.7	-14.9%
9	ROCKS1P2 (0.44g)	15.6	14.6	-6.9%
10	ROCKS1P3 (0.48g)	18.9	18.3	-3.2%
11	ROCKS1P4 (0.32g)	14.9	23.3	35.9%
12	ROCKS1P5 (0.67g)	21.1	15.4	-36.7%
13	ROCKS1P6 (0.41g)	14.0	20.0	30.2%
14	ROCKS1P7 (0.40g)	12.5	10.9	-14.5%
Average		15.3	17.1	10.1%

Note: ESA displacement demand based on target ARS is 17.0 inches, corresponding to a difference of 9.5%.

Table C.16. Comparison of Cases 5 and 8 for THA maximum displacement

Motion#	Motion (PGA)	THA Maximum Displacement (in)		
		Case 5	Case 8	Difference (“-” sign means Case 8 is less)
1	ROCKS1N1 (0.70g)	9.9	14.7	32.6%
2	ROCKS1N2 (0.38g)	15.7	14.9	-5.0%
3	ROCKS1N3 (0.32g)	10.5	10.4	-0.7%
4	ROCKS1N4 (0.34g)	13.6	16.2	16.1%
5	ROCKS1N5 (0.53g)	13.7	17.1	20.1%
6	ROCKS1N6 (0.42g)	11.0	13.9	21.4%
7	ROCKS1N7 (0.36g)	11.8	14.7	19.4%
8	ROCKS1P1 (0.71g)	11.2	15.7	29.0%
9	ROCKS1P2 (0.44g)	15.0	15.6	3.9%
10	ROCKS1P3 (0.48g)	15.7	18.9	16.8%
11	ROCKS1P4 (0.32g)	13.0	14.9	13.0%
12	ROCKS1P5 (0.67g)	16.8	21.1	20.3%
13	ROCKS1P6 (0.41g)	11.0	14.0	21.5%
14	ROCKS1P7 (0.40g)	10.1	12.5	19.2%
Average		12.8	15.3	16.7%

Table C.17. Maximum column shear forces and bending moments (transverse) for Cases 5 and 8

Motion#	Motion (PGA)	Maximum Bending Moment (kip-ft)	Maximum Shear Force (kips)		
			Case 5	Case 8	Difference (“-” sign means Case 8 is less)
1	ROCKS1N1 (0.70g)	6,100	193.7	233.3	17.0%
2	ROCKS1N2 (0.38g)	6,100	241.1	235.4	-2.4%
3	ROCKS1N3 (0.32g)	6,100	198.4	197.8	-0.3%
4	ROCKS1N4 (0.34g)	6,100	224.4	245.6	8.6%
5	ROCKS1N5 (0.53g)	6,100	225.0	253.7	11.3%
6	ROCKS1N6 (0.42g)	6,100	202.5	227.3	10.9%
7	ROCKS1N7 (0.36g)	6,100	209.7	233.3	10.1%
8	ROCKS1P1 (0.71g)	6,100	203.1	241.0	15.7%
9	ROCKS1P2 (0.44g)	6,100	235.1	240.5	2.2%
10	ROCKS1P3 (0.48g)	6,100	241.7	254.2	4.9%
11	ROCKS1P4 (0.32g)	6,100	219.2	234.6	6.6%
12	ROCKS1P5 (0.67g)	6,100	250.8	254.2	1.3%
13	ROCKS1P6 (0.41g)	6,100	202.5	227.4	11.0%
14	ROCKS1P7 (0.40g)	6,100	195.3	215.3	9.3%

Table C.18. Comparison of the average ESA displacement demand and THA maximum displacement for all the studied models

Case#	Case Description	Average of THA Maximum Displacement (in)	Average of ESA Displacement Demand (in)	Difference*
Case 1	Linear columns with fixed base	5.73	5.69	-0.6%
Case 2	Linear columns with linear p - y and t - z spring foundation	14.5	14.4	-0.6%
Case 3	Nonlinear columns with fixed base	6.82	5.51	-23.8%
Case 4	Nonlinear columns with linear p - y and t - z spring foundation	12.8	14.4	11.0%
Case 5	Nonlinear columns with nonlinear p - y and t - z spring foundation	12.8	17.1	25.1%
Case 6	Same as 5, with 10 bents		Same as Case 5	
Case 7	Case as 6, with 2 end-bents at the abutment	14.5	17.1	15.0%
Case 8	Same as 7, with bilinear abutment springs	15.3	17.1	10.1%

Note: * “-” sign means ESA is less

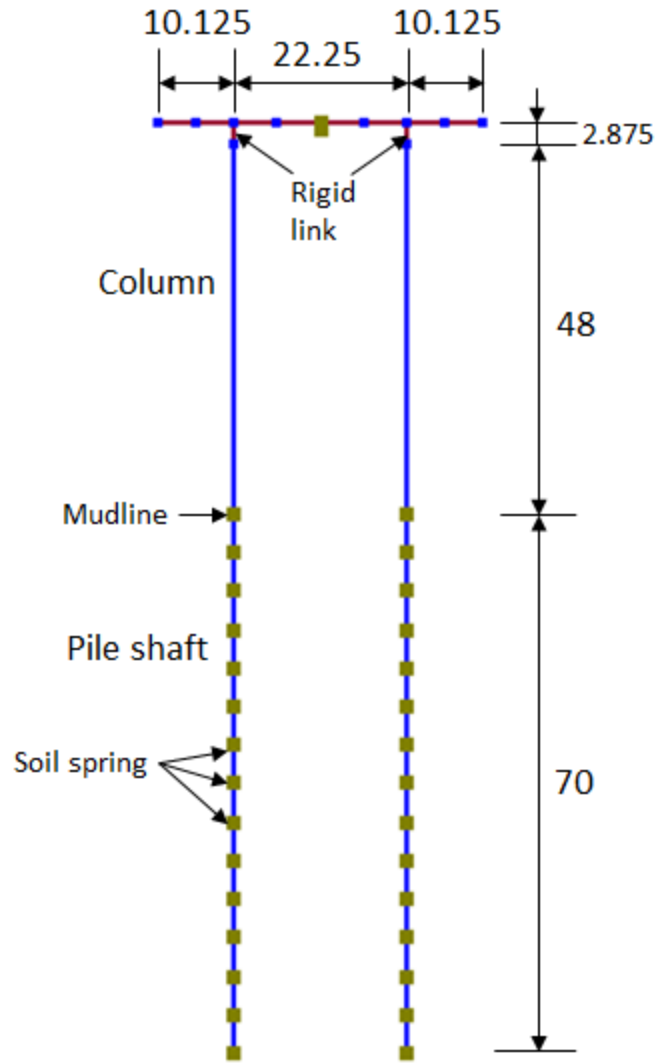


Figure C.1. Typical bent of Salinas Bridge (dimensions in ft)

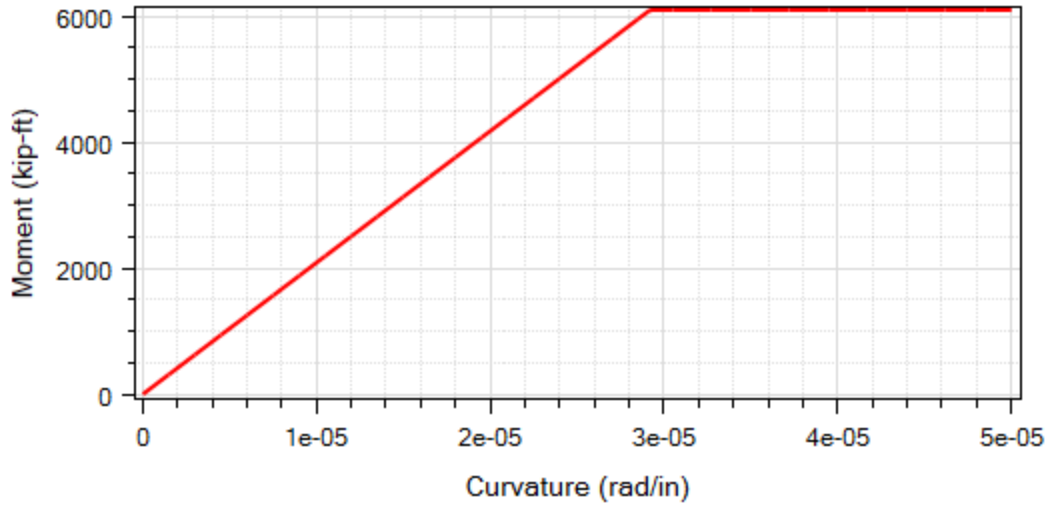


Figure C.2. Idealized bilinear moment-curvature relationship employed for the columns (plastic moment = 6,100 kip-ft; yield curvature = 2.92×10^{-5} rad/in)

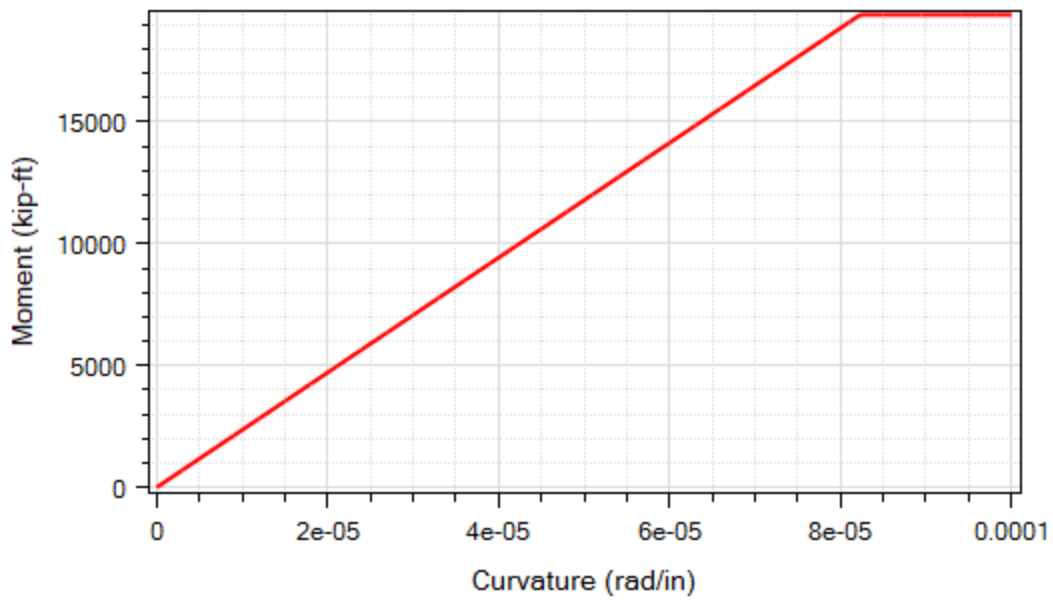


Figure C.3. Idealized bilinear moment-curvature relationship employed for the pile shafts (plastic moment = 19,400 kip-ft; yield curvature = 8.23×10^{-5} rad/in)

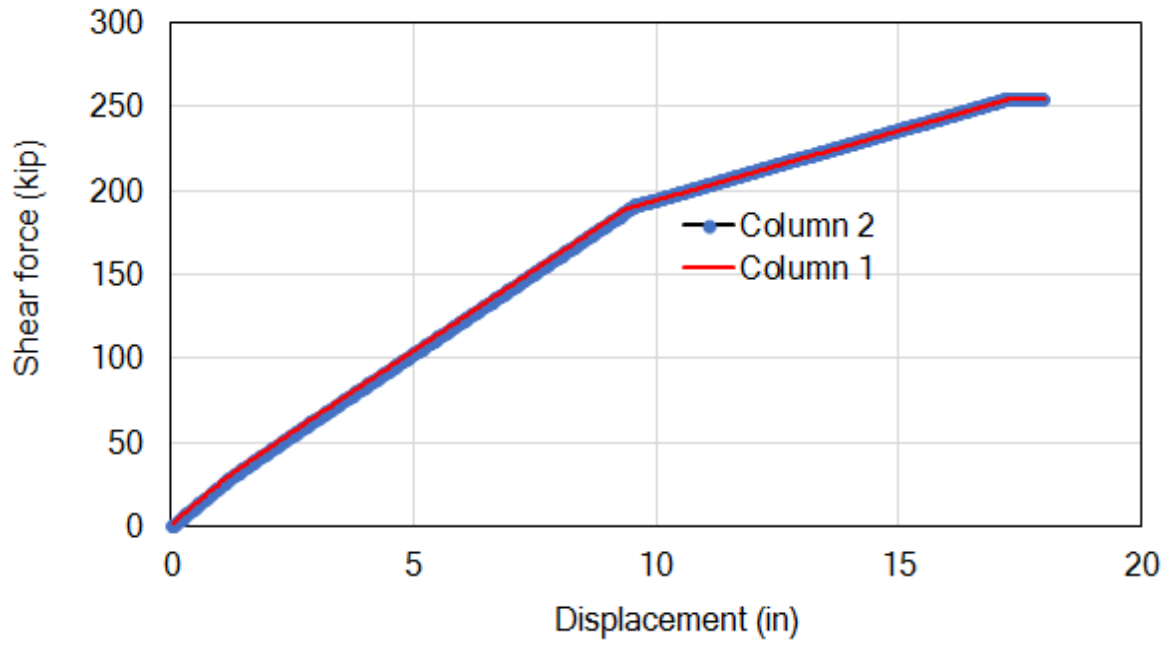


Figure C.4. Shear force vs. transverse displacement for pushover analysis

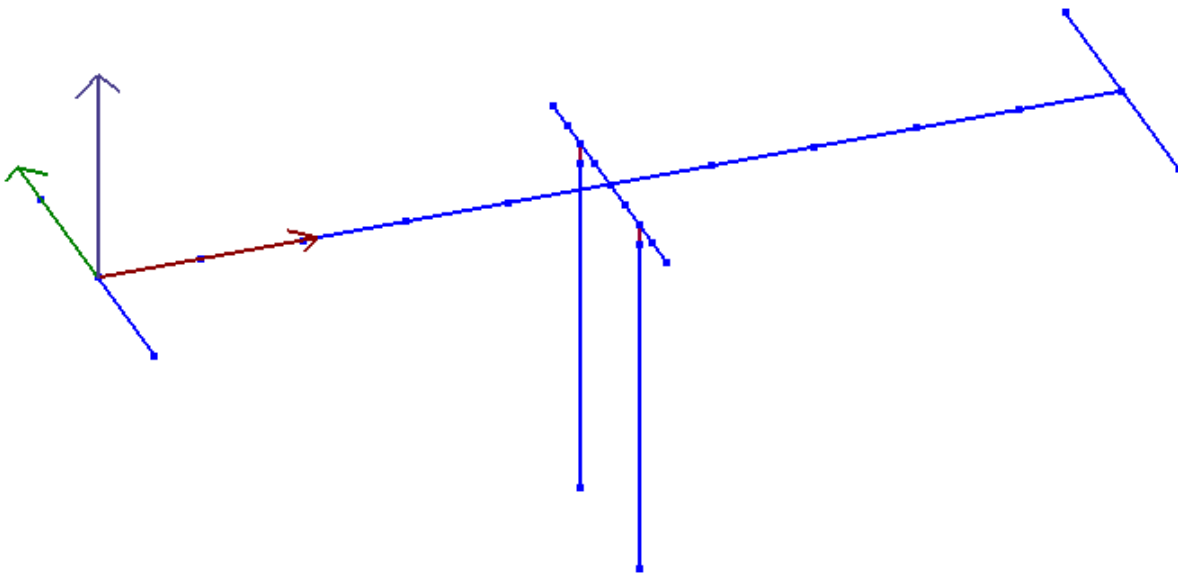


Figure C.5. Single bent model for Case 1 (with rigid base at mudline)

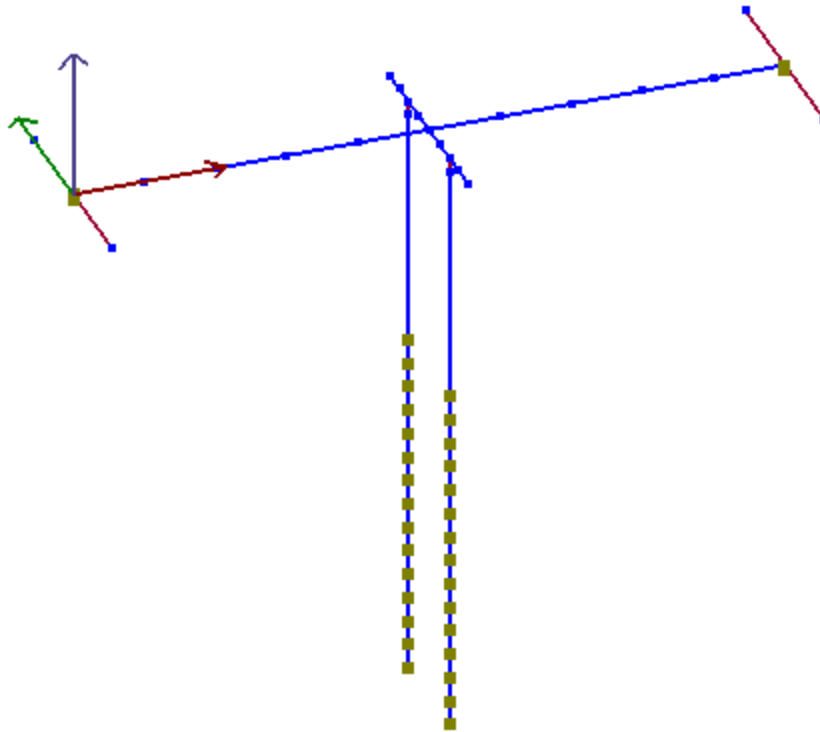


Figure C.6. Single bent model for Case 2

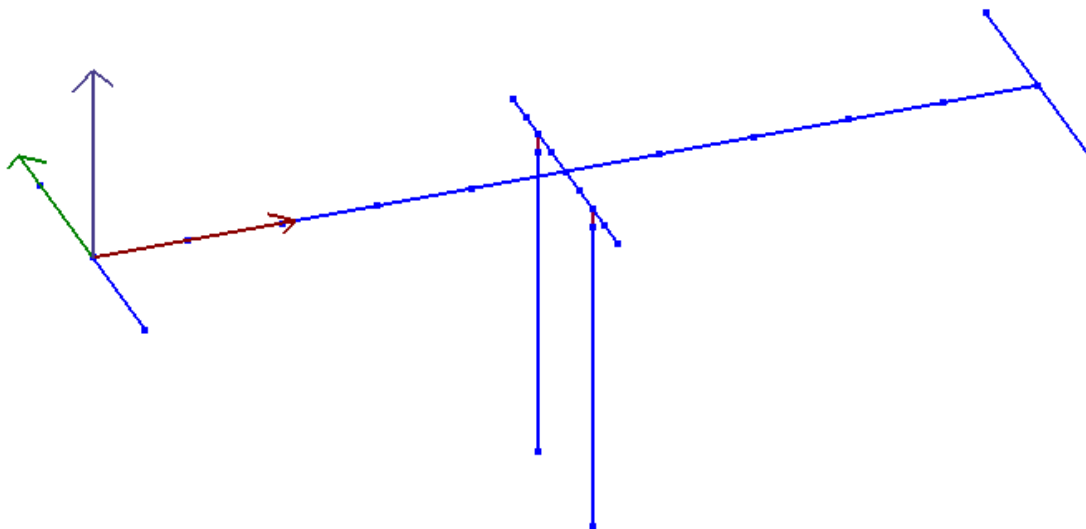


Figure C.7. Single bent model for Case 3 (with rigid base at mudline)

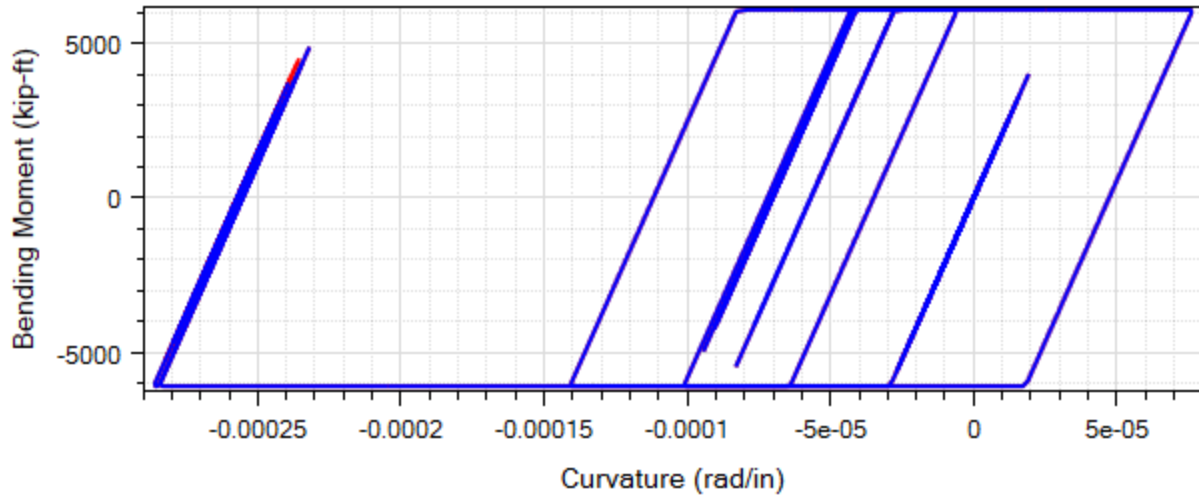


Figure C.8. Moment-curvature response at column top for Motion #1 ROCKS1N1 (Red part shows the end of shaking) for Case 3

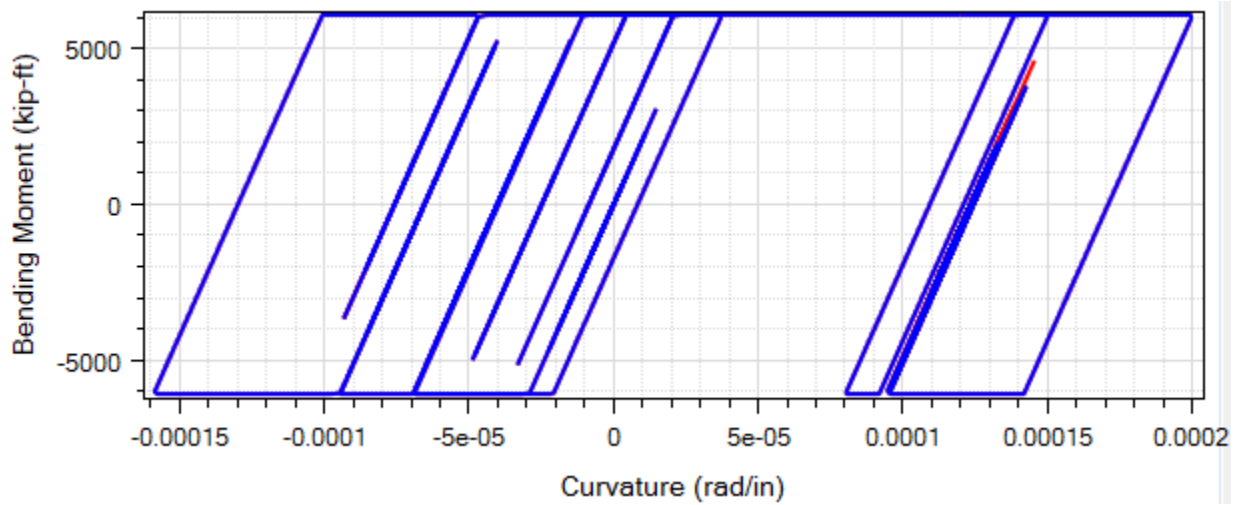


Figure C.9. Moment-curvature response at column top for Motion #2 ROCKS1N2 (Red part shows the end of shaking) for Case 3

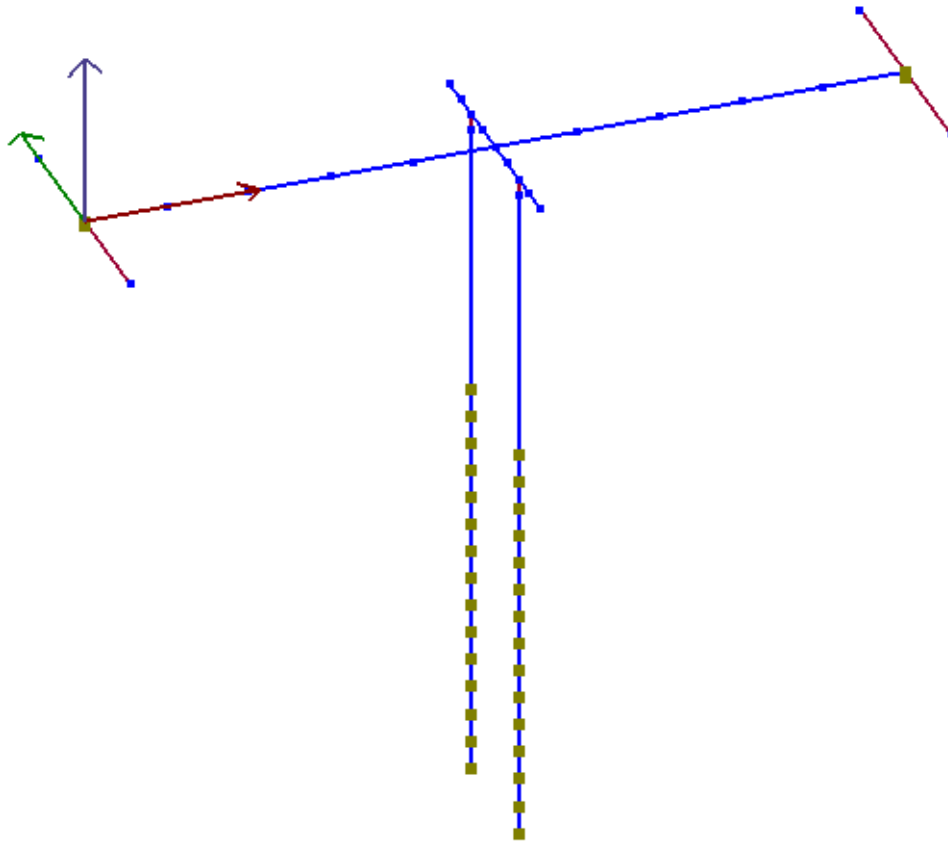


Figure C.10. Single bent model for Case 4

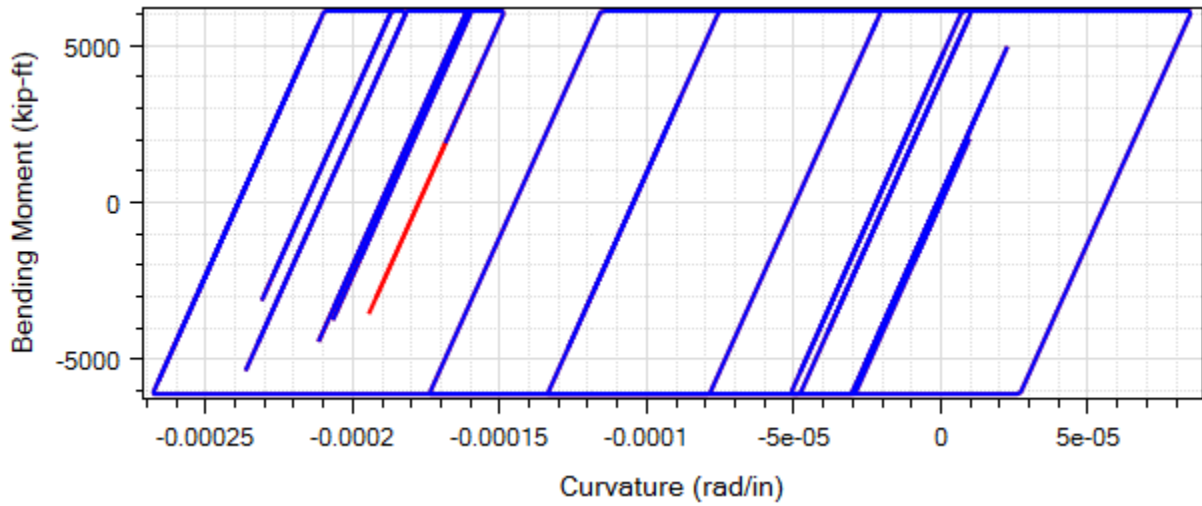


Figure C.11. Moment-curvature response at column top for Motion #1 ROCKS1N1 (Red part shows the end of shaking) for Case 4

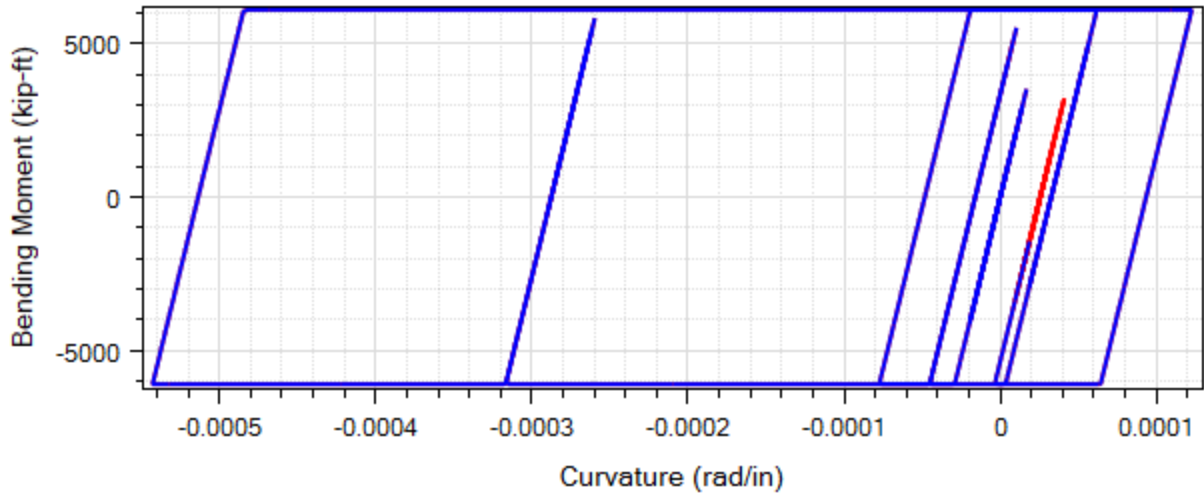


Figure C.12. Moment-curvature response at column top for Motion #2 ROCKS1N2 (Red part shows the end of shaking) for Case 4

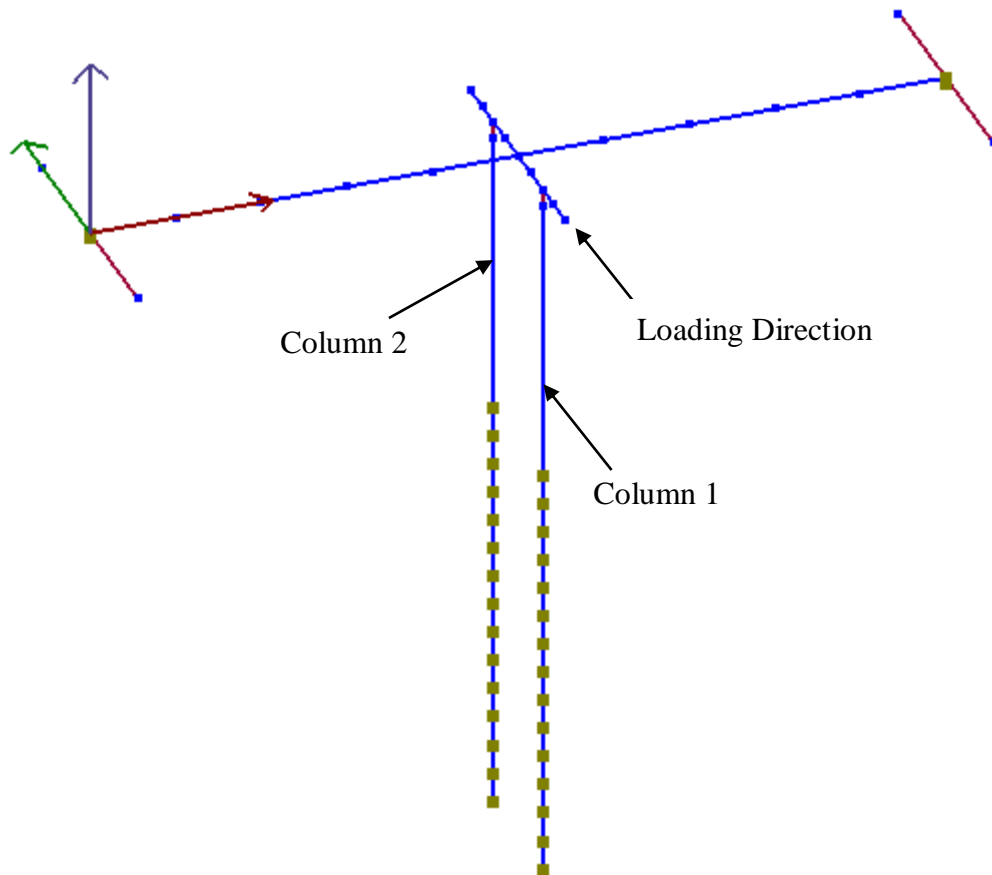


Figure C.13. Single bent model for Case 5

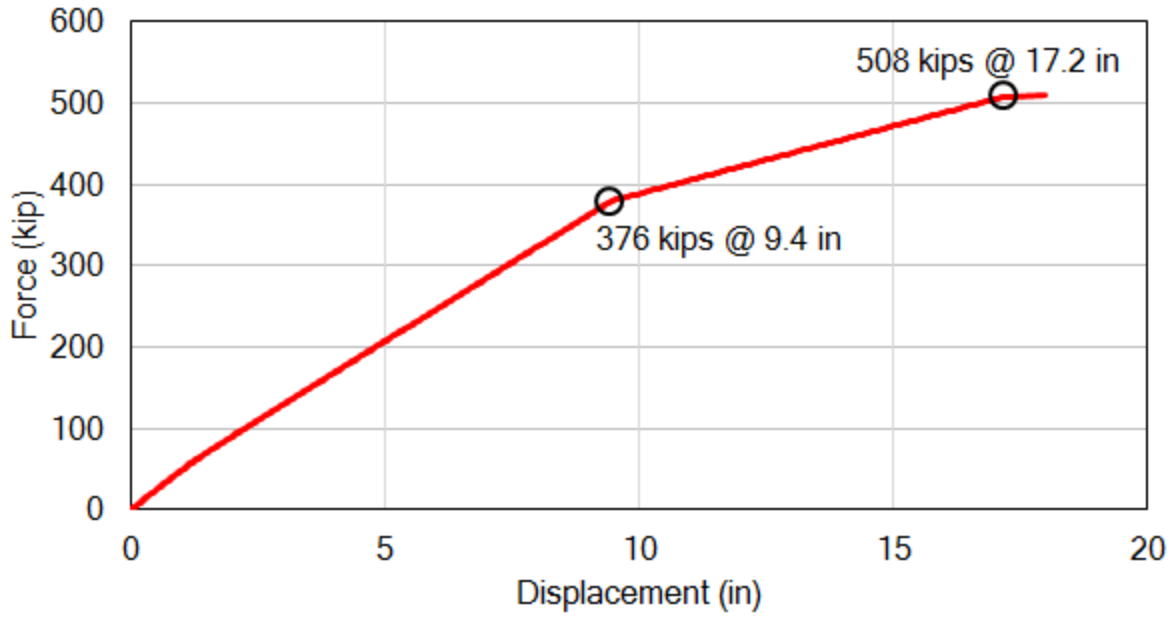


Figure C.14. Pushover load vs. transverse displacement for the transverse ESA

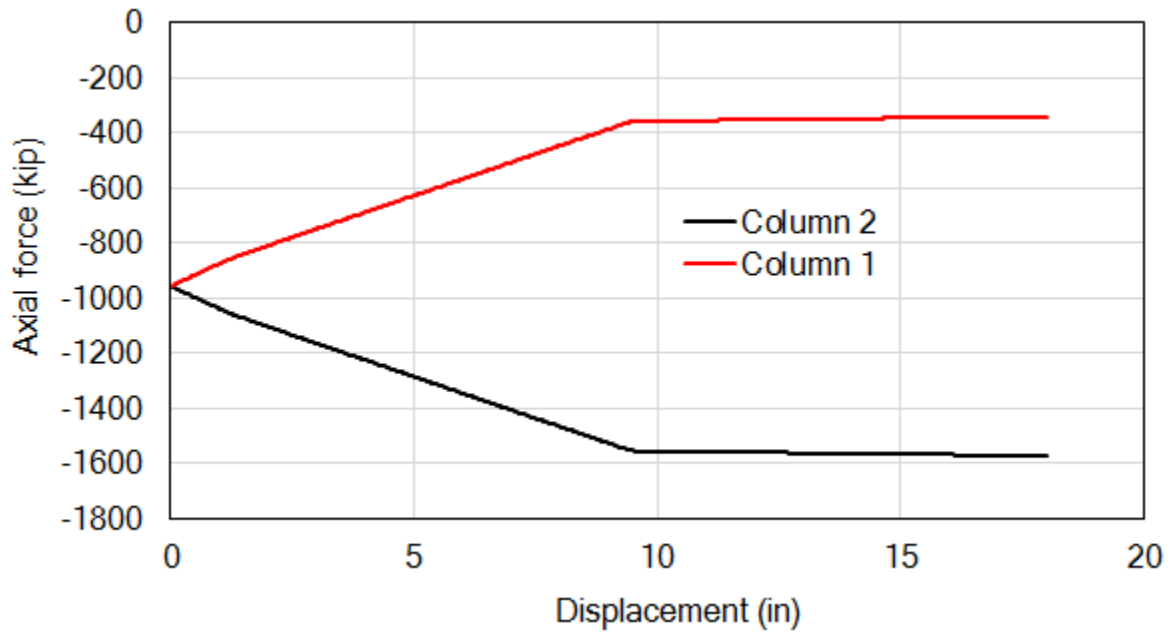


Figure C.15. Axial force vs. transverse displacement for the transverse ESA

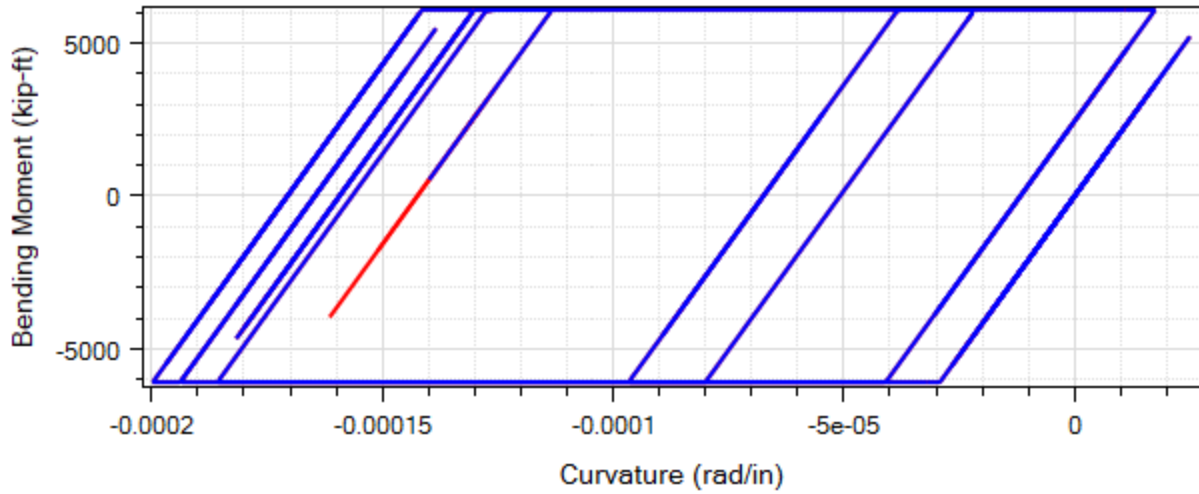


Figure C.16. Moment-curvature response at column top for Motion #1 ROCKS1N1 (Red part shows the end of shaking) for Case 5

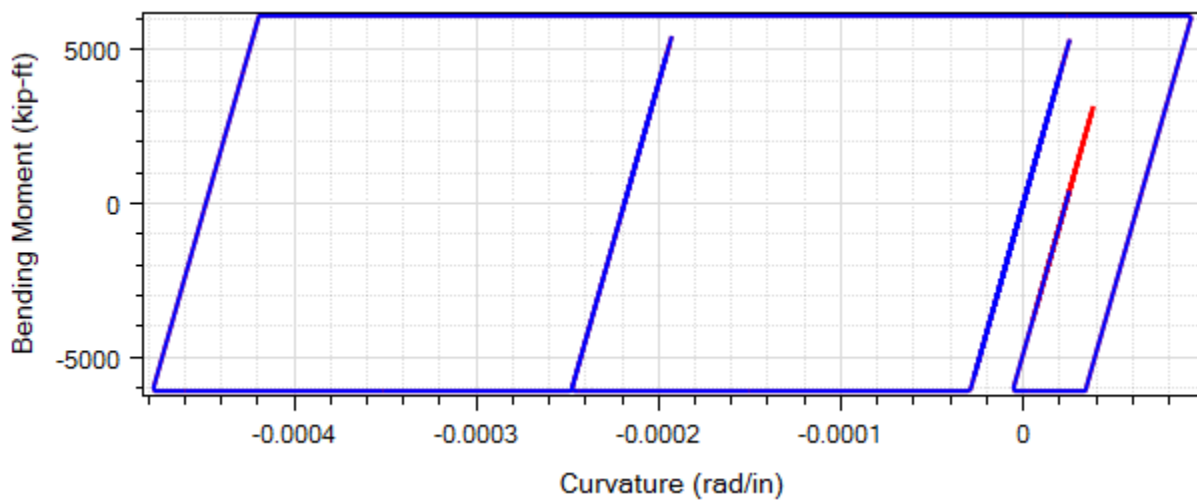


Figure C.17. Moment-curvature response at column top for Motion #2 ROCKS1N2 (Red part shows the end of shaking) for Case 5

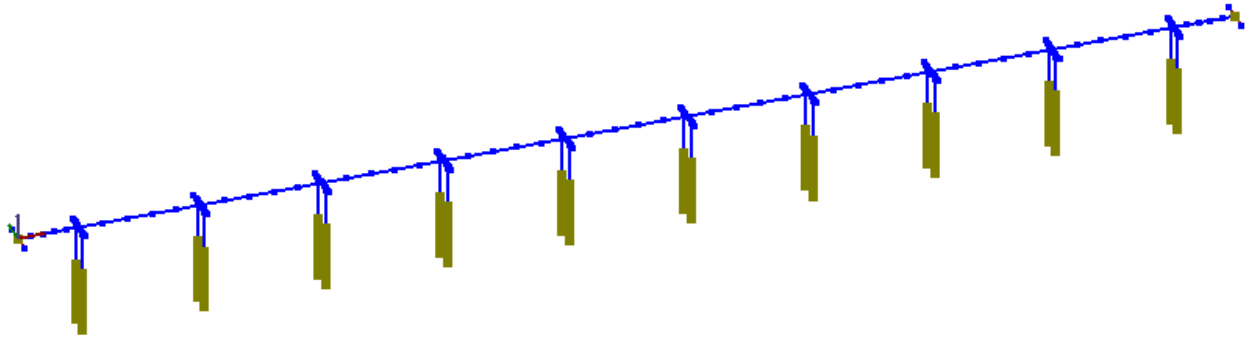
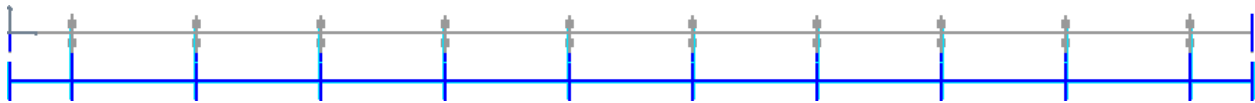
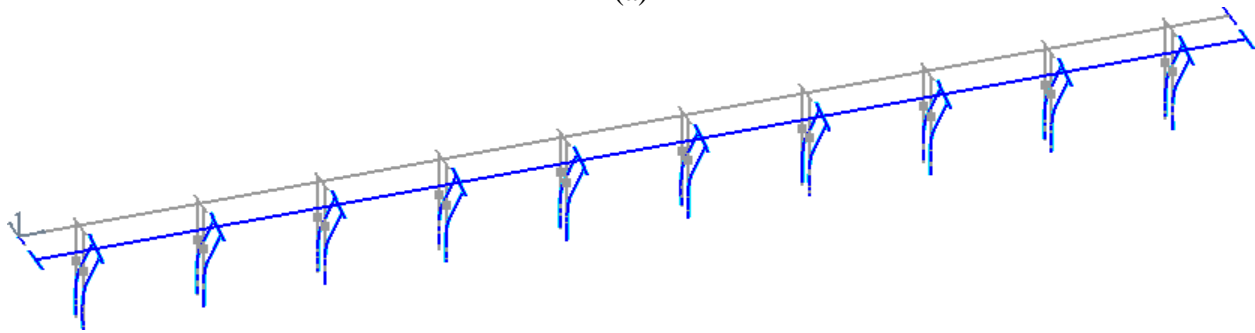


Figure C.18. Multi-bent model for Case 6



(a)



(b)

Figure C.19. First transverse mode of the multi-bent model (period = 2.0 seconds): (a) plan view; (b) 3D view

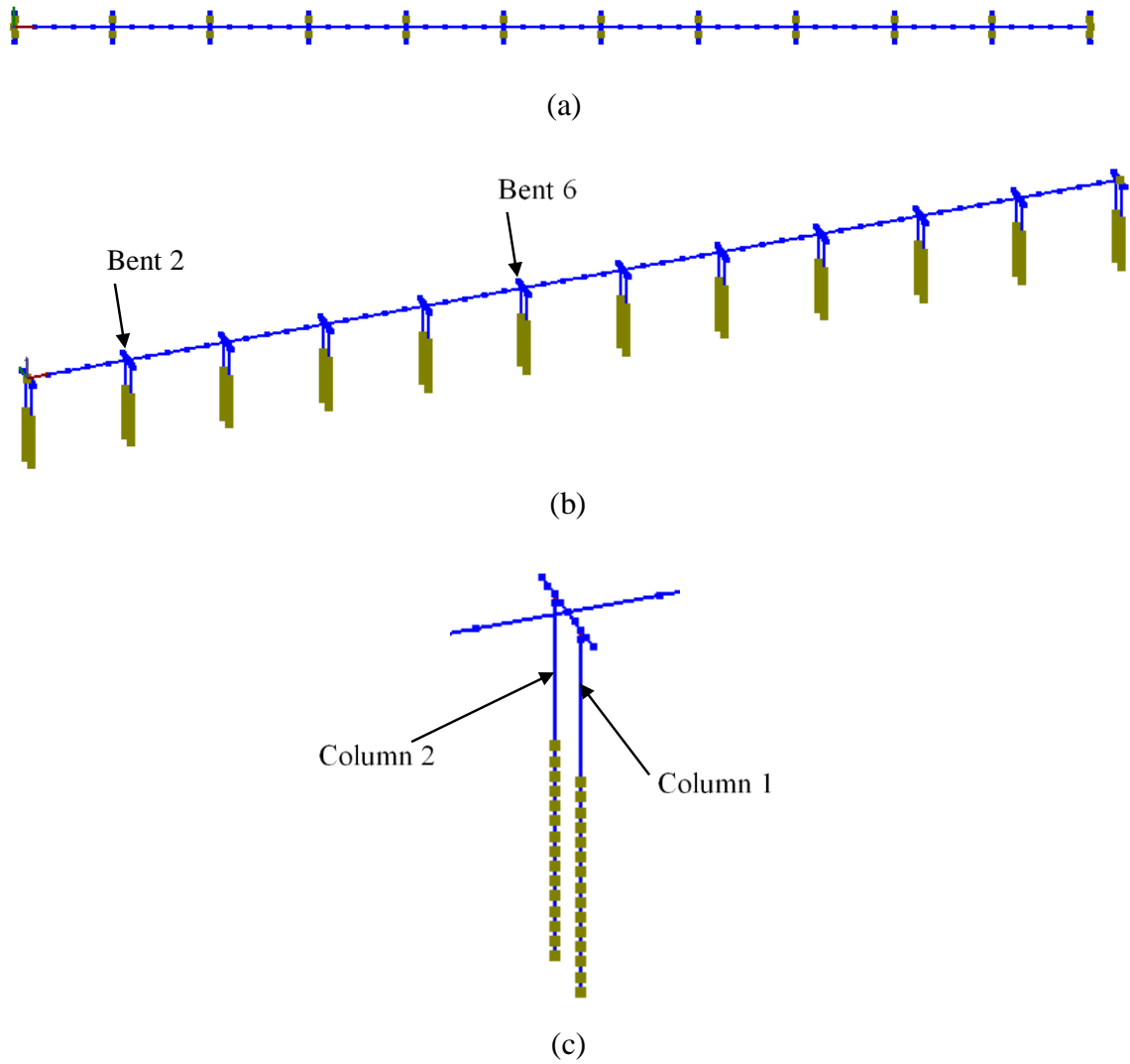


Figure C.20. Multi-bent model with end-bents: (a) plan view; (b) 3D view; (c) bent close-up

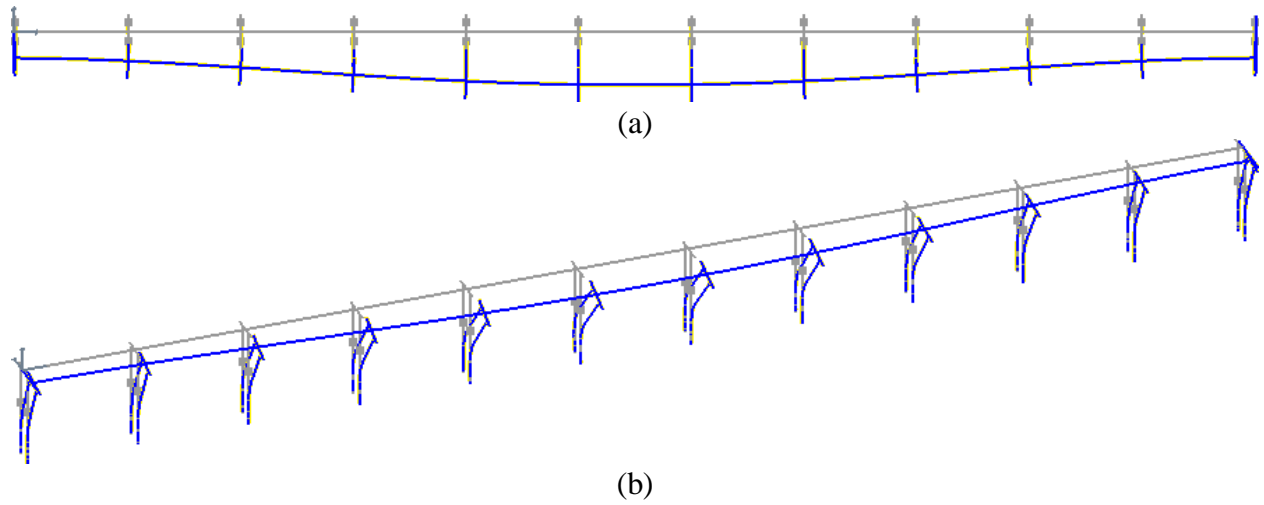


Figure C.21. First transverse mode of the multi-bent model (period = 1.94 seconds)

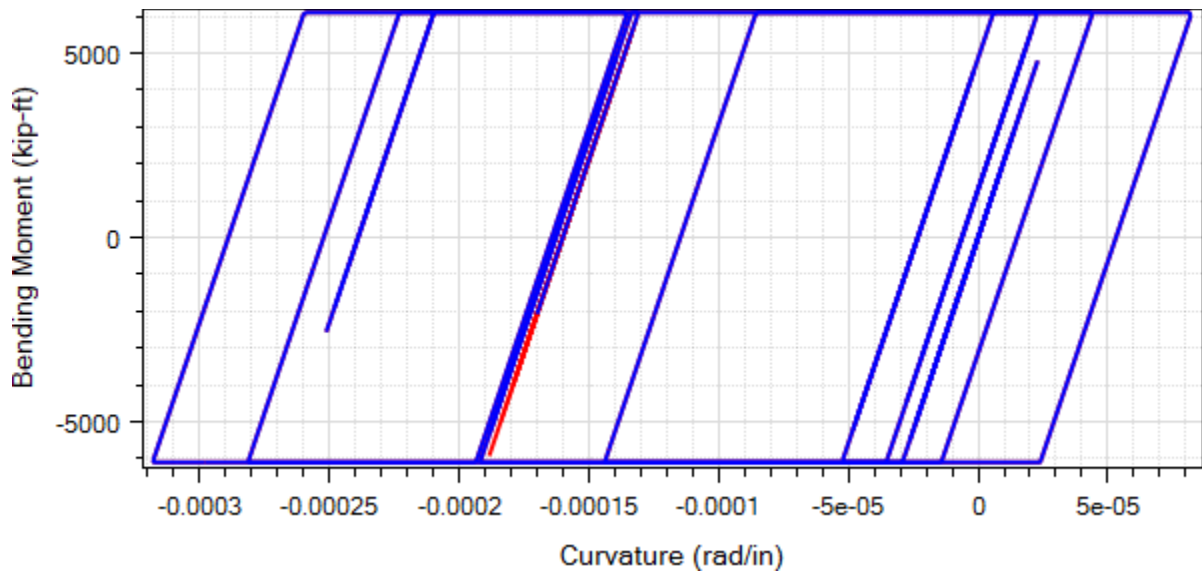


Figure C.22. Moment-curvature response at column top for Column 1 of Bent 6 for Motion #1 ROCKS1N1 (Red part shows the end of shaking) for Case 7

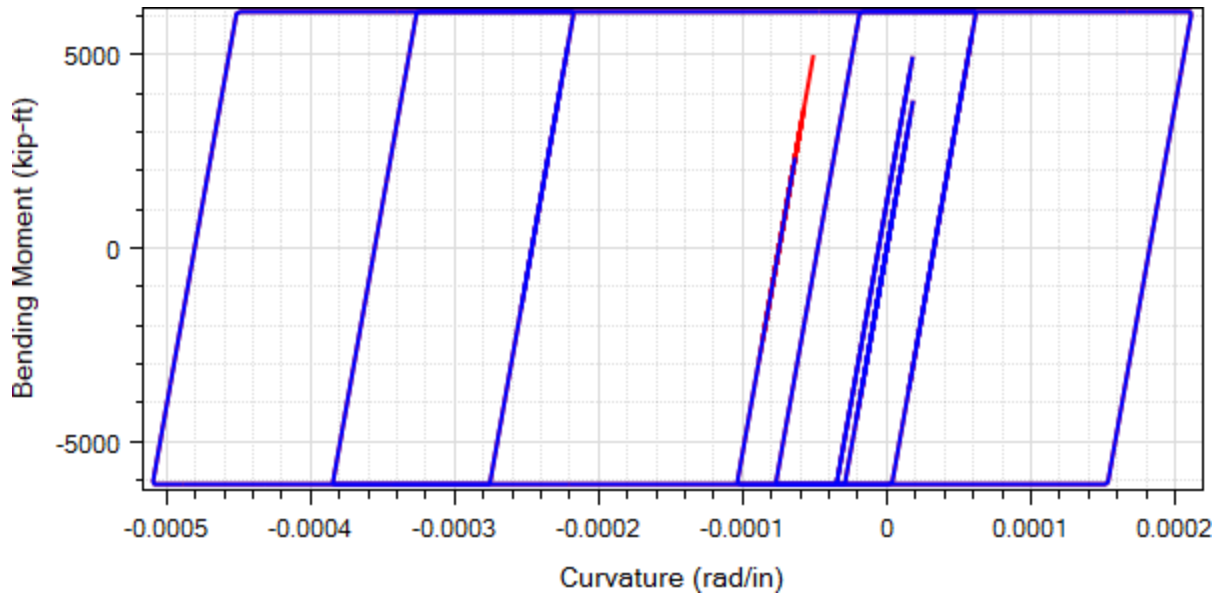


Figure C.23. Moment-curvature response at column top for Column 1 of Bent 6 for Motion #2 ROCKS1N2 (Red part shows the end of shaking) for Case 7

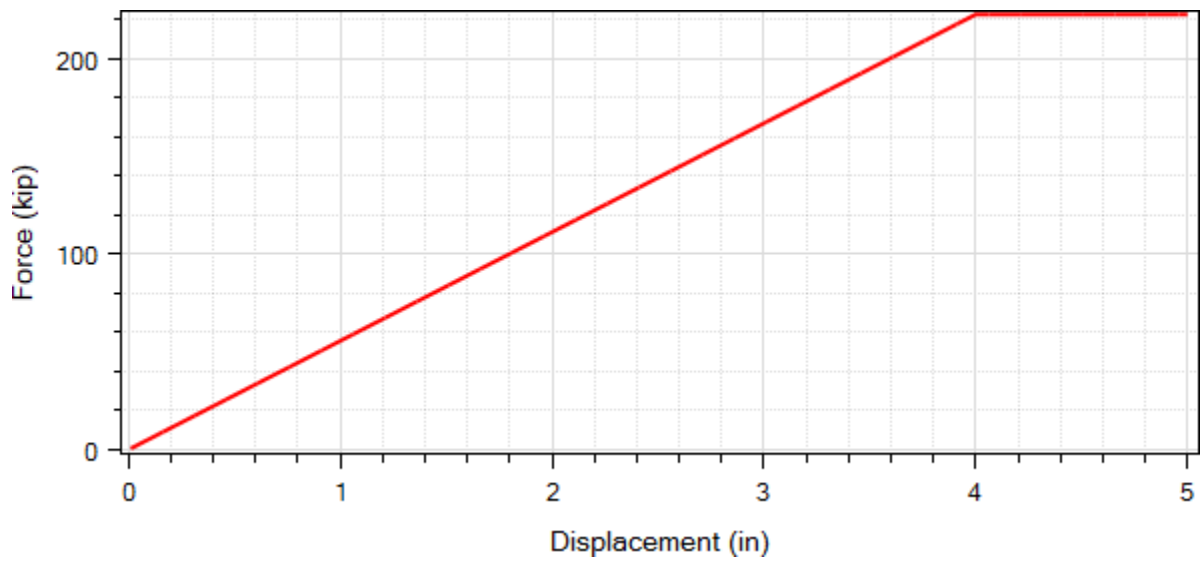


Figure C.24. Idealized bilinear force-displacement relationship employed for the abutment in the transverse direction

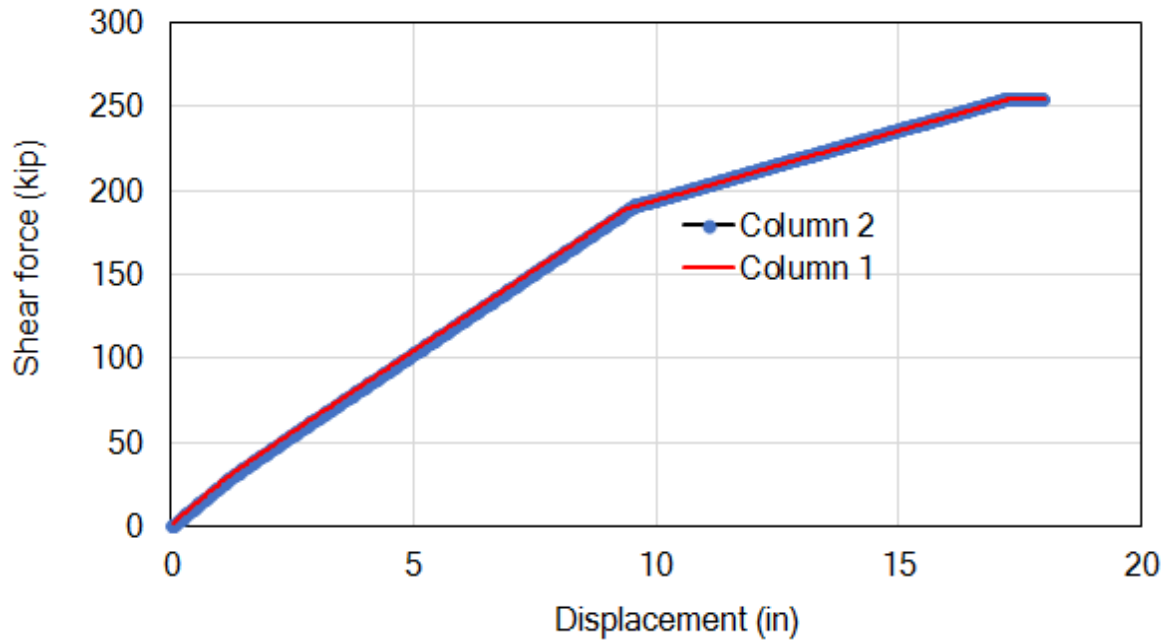


Figure C.25. Column shear force vs. displacement response in pushover analysis

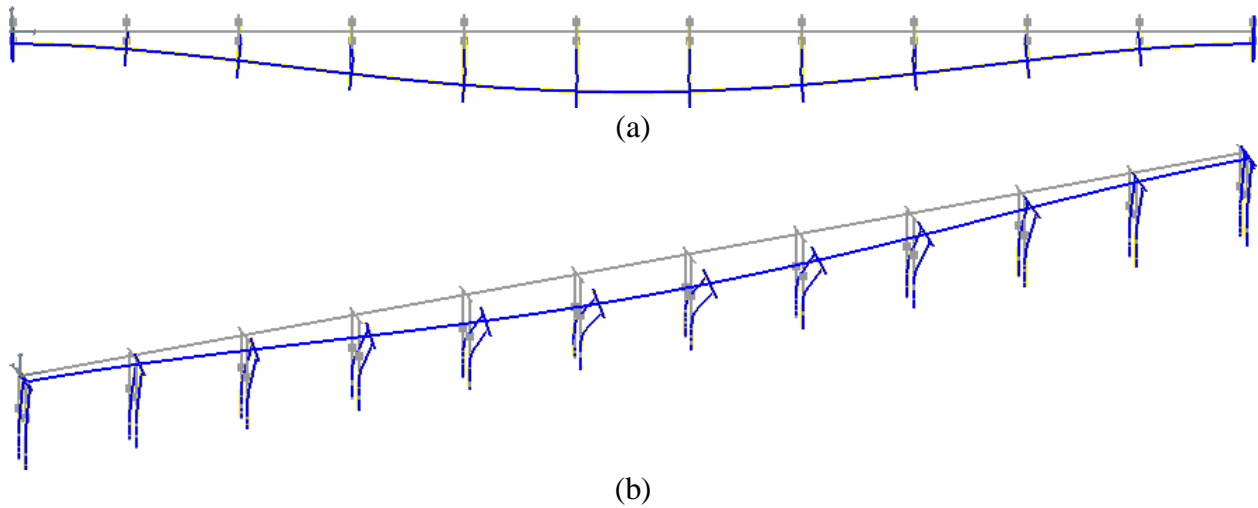


Figure C.26. First transverse mode of Salinas River Bridge (period = 1.91 seconds): (a) plan view; (b) 3D view

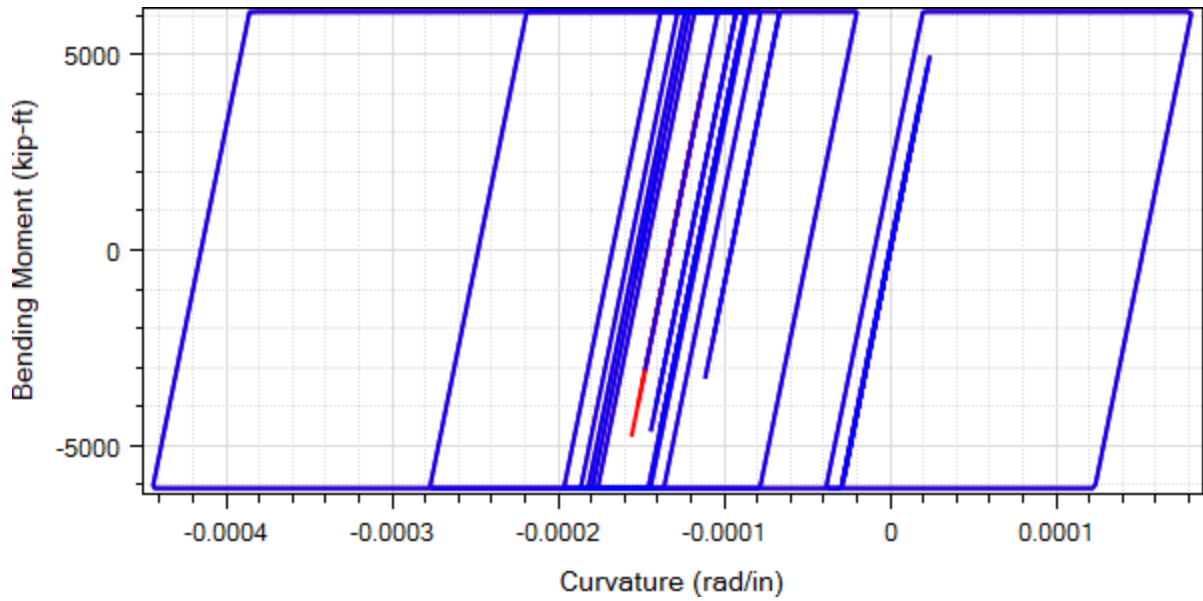


Figure C.27. Moment-curvature response at column top for Column 1 of Bent 6 for Motion #1 ROCKS1N1 (Red part shows the end of shaking) for Case 8

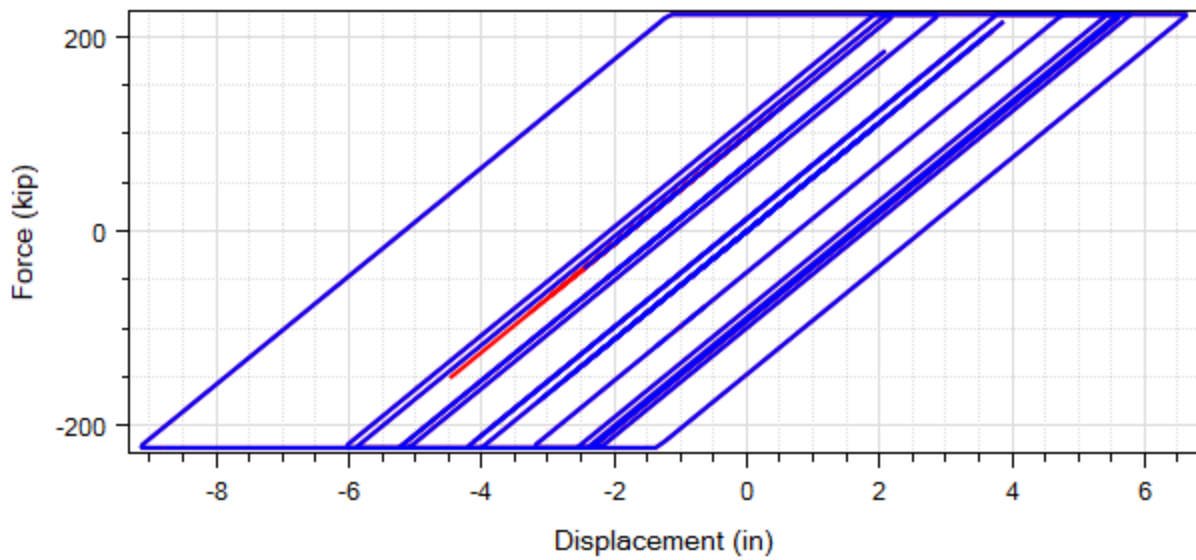


Figure C.28. Abutment (left or right) transverse resisting force-displacement response for Motion #1 ROCKS1N1 (Red part shows the end of shaking) for Case 8

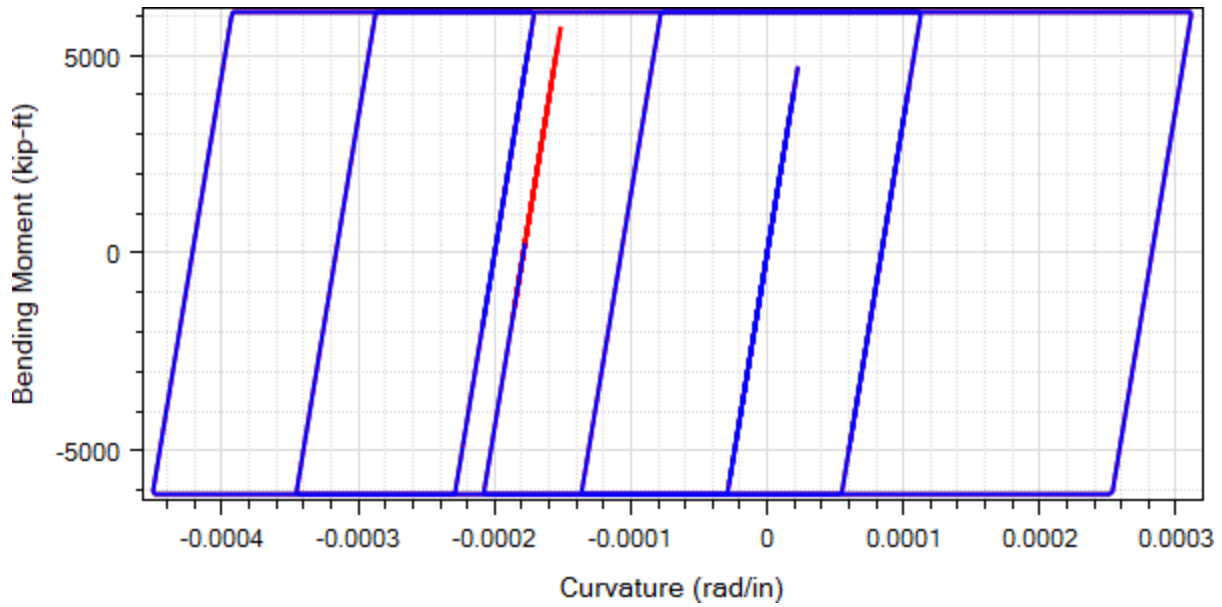


Figure C.29. Moment-curvature response at column top for Column 1 of Bent 6 for Motion #2 ROCKS1N2 (Red part shows the end of shaking) for Case 8

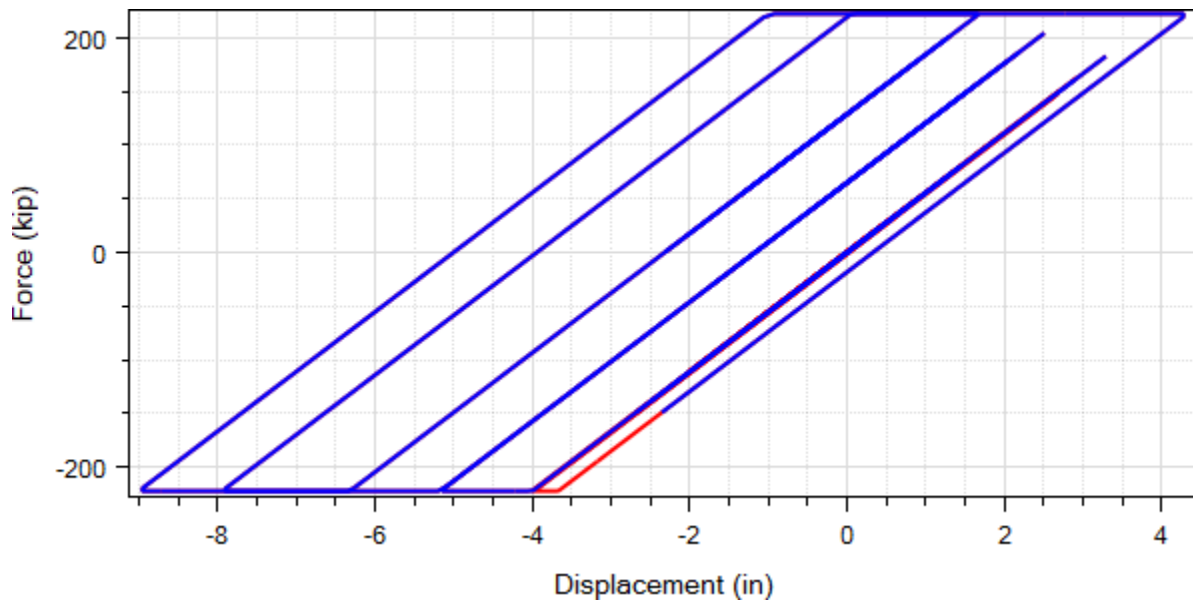


Figure C.30. Abutment (left or right) transverse resisting force-displacement response for Motion #2 ROCKS1N2 (Red part shows the end of shaking) for Case 8

Appendix D. Salinas Bridge Modeling Details

D.1. Column

The Salinas Bridge model created in MSBridge was based on the wFrame model reported in Caltrans (2005). As such, a bi-linear moment-curvature relationship was used to model the columns and pile shafts (Caltrans 2005). Figure D.1 shows the user-defined bi-linear moment-curvature relationships for the columns above the mudline (Figure D.1a) as well as for the pile shafts (Figure D.1b), respectively. An axial compressive load of 1,000 kip was applied in the moment-curvature analysis. For the columns, the plastic moment is 6100 kip-ft (at the curvature of 2.92×10^{-5} rad/in). For the pile shafts, the plastic moment is 19,400 kip-ft (at the curvature of 8.23×10^{-5} rad/in).

D.2. Soil Springs

Figure D.2 to Figure D.5 show the p - y curves used to account for stiffness of the underlying pile foundations and the resulting soil-foundation-structure interaction. The values of these curves were converted to proper soil springs within the push analysis. In addition, Figure D.6 and Figure D.7 show the t - z and Q - z curves, respectively.

D.3. Deck and Bentcap

The material and section properties of the box-girder are listed in Table D.1. The weight of the bridge deck per unit length is 10.445 kip/ft (= $69.64 \text{ ft}^2 \times 0.15 \text{ kcf}$). The material and section properties of the bentcap are listed in Table D.2. The weight of the bridge bentcap per unit length is 5.175 kip/ft (= $34.5 \text{ ft}^2 \times 0.15 \text{ kcf}$).

D.4. Abutment

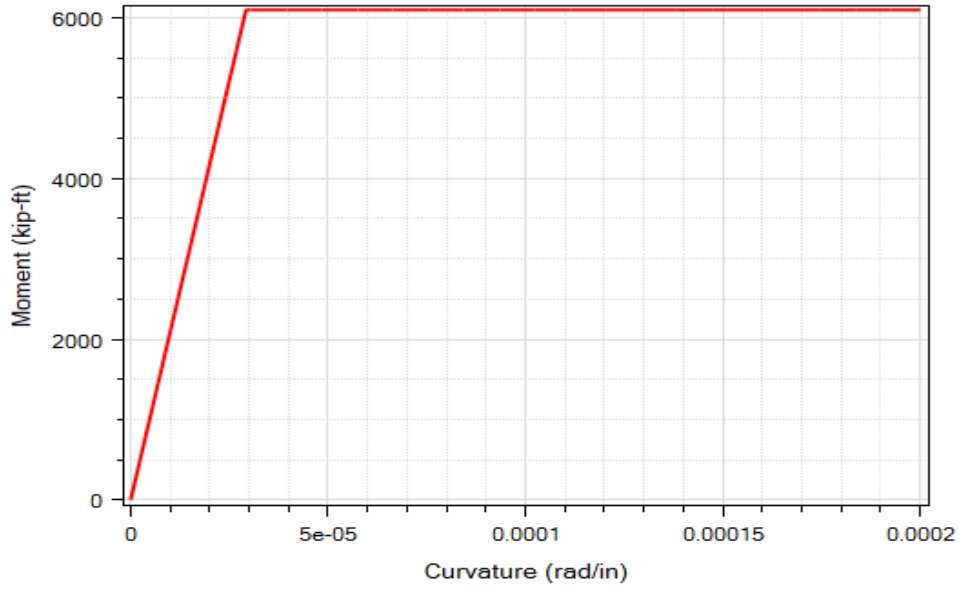
Elastic abutment model with a stiff vertical spring and three stiff rotational springs was employed. In the longitudinal direction, a spring of stiffness $k = 128.25$ kip/in was applied at each of the two abutments (Caltrans 2005). In the transverse direction, a spring of stiffness $k = 55.625$ kip/in was employed (for each of the two abutments). In addition, the abutment was considered to have a pinned connection with the pile foundation.

Table D.1. Salinas Bridge deck material and section properties

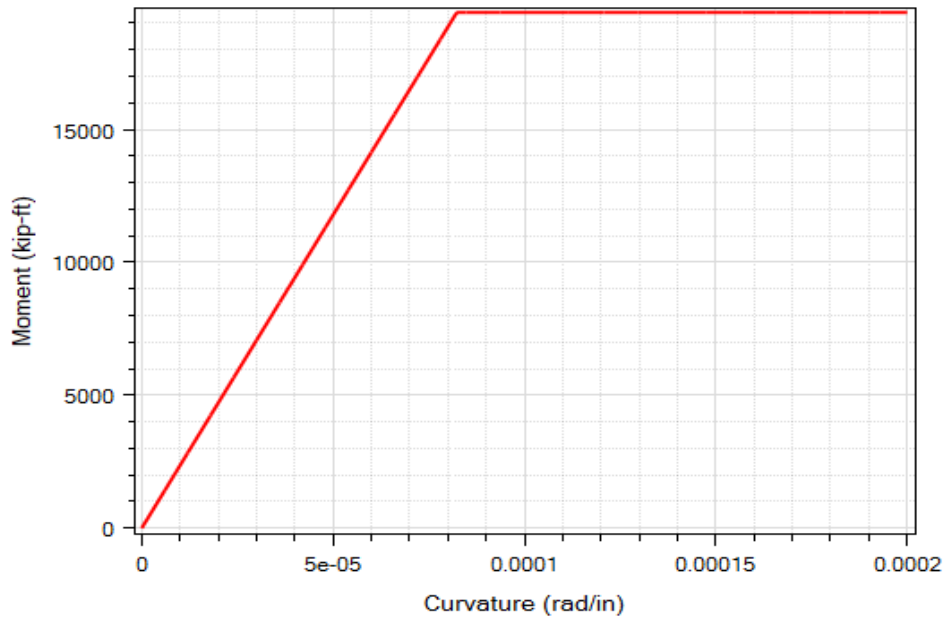
Parameter	Value
Young's modulus (ksi)	4,031
Shear modulus (ksi)	1,668
Unit weight (kcf)	0.15
Area of cross-section (ft ²)	69.64
Moment of inertia @ horizontal axis (ft ⁴)	327.44
Moment of inertia @ vertical axis (ft ⁴)	10105.6
Torsion constant (ft ⁴)	934

Table D.2. Salinas Bridge bentcap properties

Parameter	Value
Young's modulus (ksi)	4,031
Shear modulus (ksi)	1,668
Unit weight (kcf)	0.15
Area of cross-section (ft ²)	34.5
Moment of inertia @ horizontal axis (ft ⁴)	95.1
Moment of inertia @ vertical axis (ft ⁴)	103.5
Torsion constant (ft ⁴)	166.79



(a)



(b)

Figure D.1. Bi-linear moment-curvature relationship: (a) column; (b) pile shaft

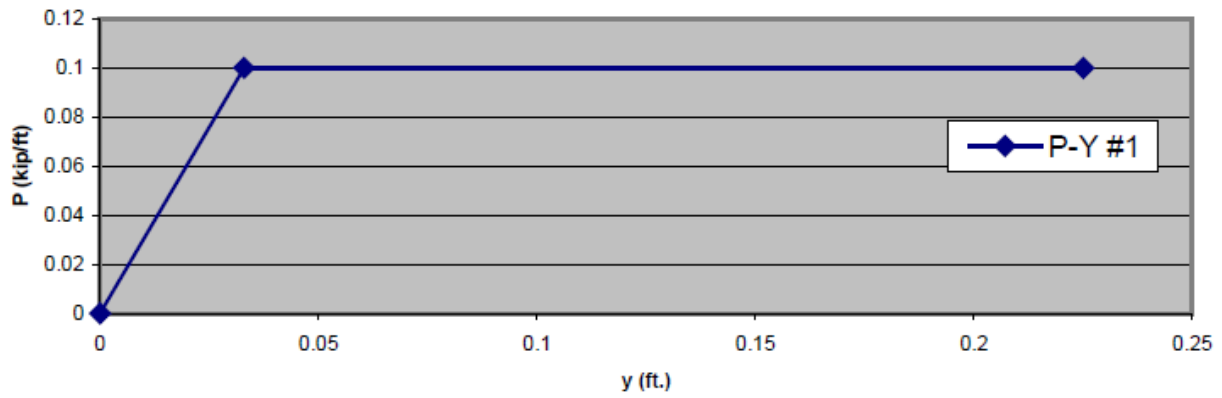


Figure D.2. Idealized soil p - y curve at a depth of 0.5 ft (Caltrans 2005)

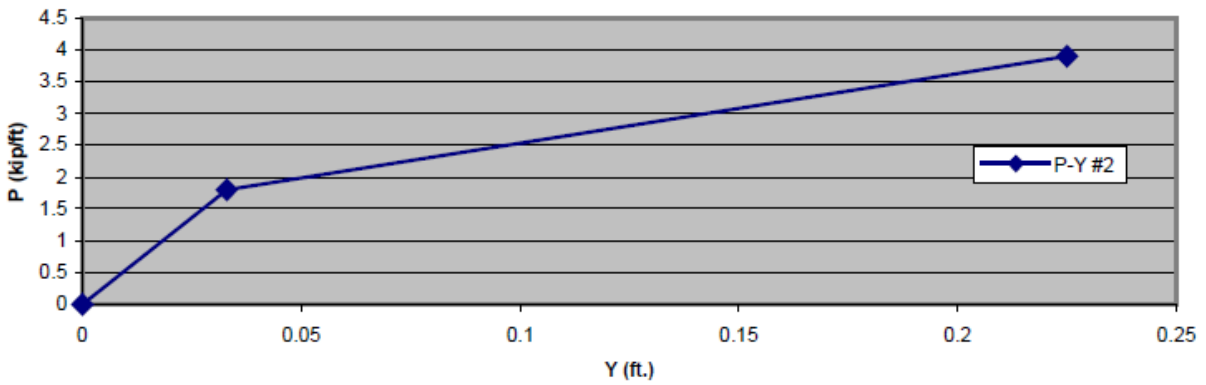


Figure D.3. Idealized soil p - y curve at a depth of 16.5 ft (Caltrans 2005)

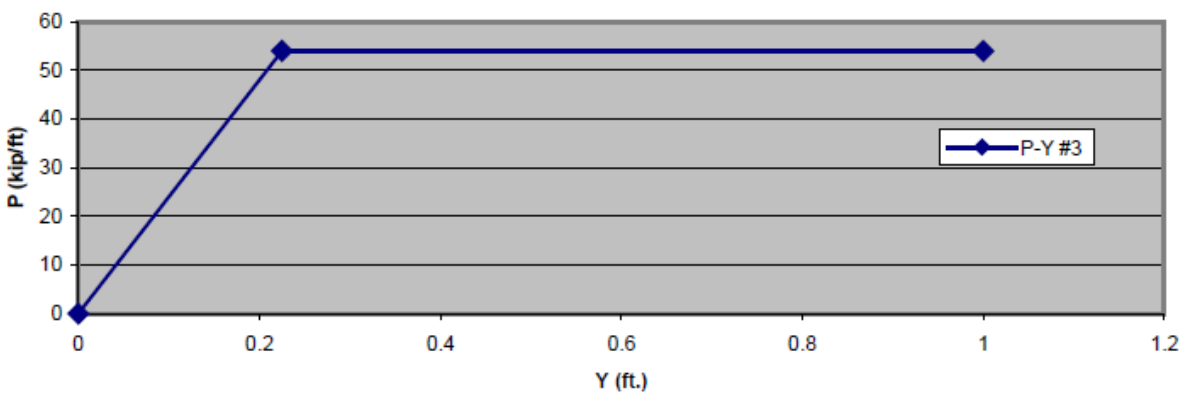


Figure D.4. Idealized soil p - y curve at a depth of 17.5 ft (Caltrans 2005)

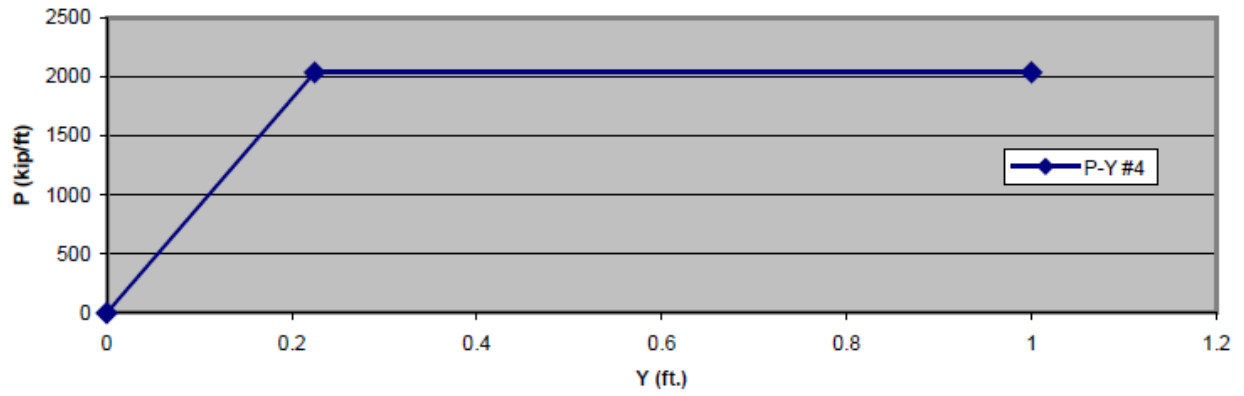


Figure D.5. Idealized soil p - y curve at a depth of 106.5 ft (Caltrans 2005)

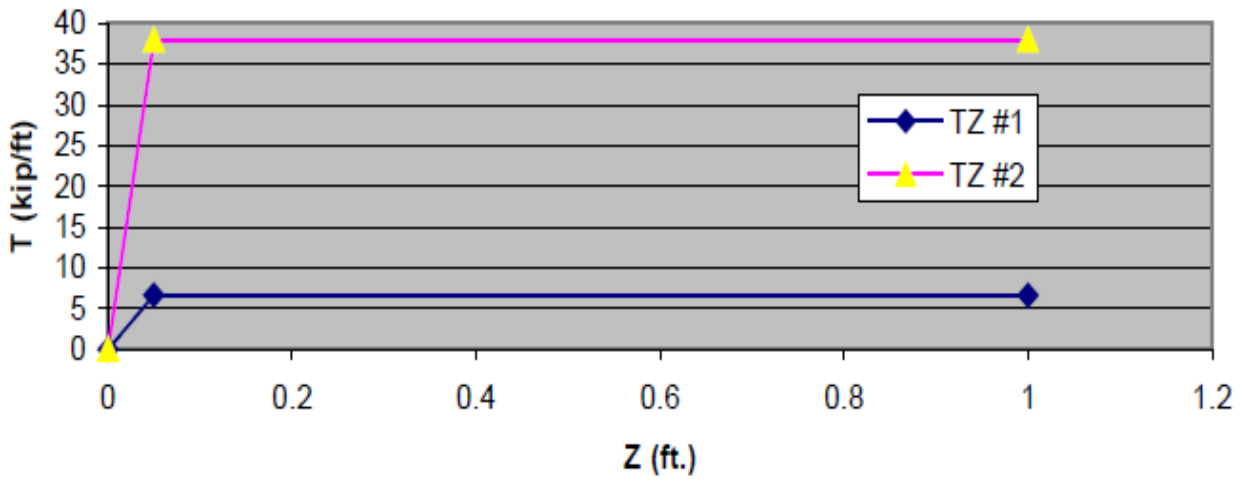


Figure D.6. Idealized soil t - z curves (Caltrans 2005)

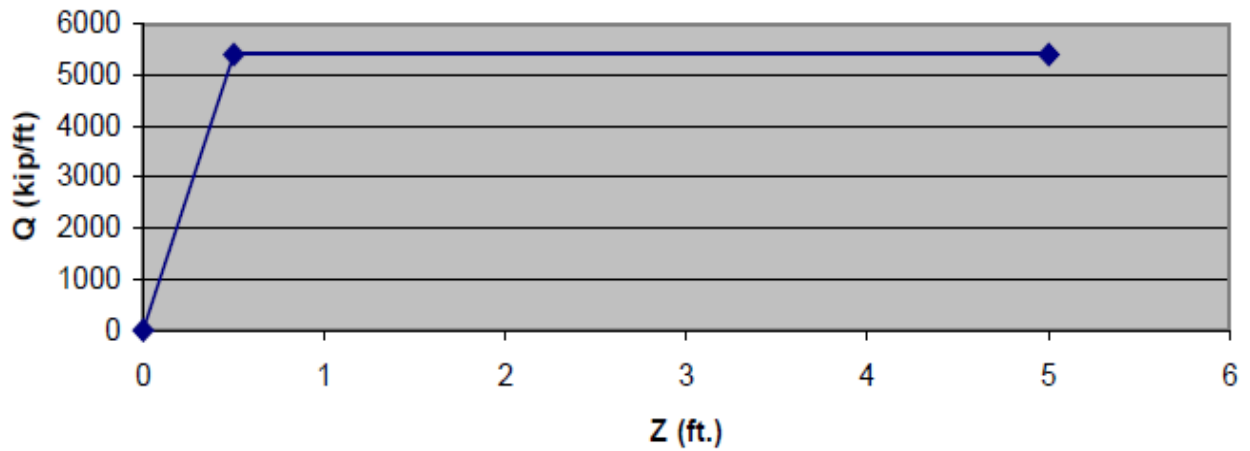


Figure D.7. Idealized soil Q - z curves (Caltrans 2005)

Appendix E. Samoa Channel Bridge Modeling Details

E.1. Column

Nonlinear Fiber section in OpenSees was used to model the columns. Appendix G lists the OpenSees Tcl code snippet for the Fiber section for Piers S-8 and S-9 of Samoa Bridge (Section I) while the Tcl code snippet for other piers (except Piers S-8 and S-9) (Section II)

The moment-curvature response of the column Fiber section for Pier S-8 and S-9 is shown in Figure E.1a. An axial compressive load of 2,000 kip was applied in the moment-curvature analysis in the transverse direction.

For other piers (except Piers S-8 and S-9), the moment-curvature response of the column Fiber section is shown in Figure E.1b. An axial compressive load of 1,300 kip was applied in the moment-curvature analysis in this case for the transverse direction.

Similarly, Figure E.2a shows the moment-curvature response of the column Fiber section in the longitudinal direction with the same applied axial load for Pier S-8 and S-9. Furthermore, Figure E.2b shows the moment-curvature response of the other piers (except Piers S-8 and S-9) in the longitudinal direction.

E.2. Foundation Matrix

The Foundation Matrix model is represented by the coupled foundation stiffness matrix (Lam and Martin 1986). Specifically, the stiffness of a single pile is represented by a 6 x 6 matrix associated with all six degrees of freedom at the pile head (Figure E.3). However, the overall pile-soil stiffness should reflect the soil characteristics and the structural properties of the pile as well. Moreover, Table E.1 and Table E.2 show the foundation matrix coefficients of all bents (Wang 2015).

E.3. Deck

The employed linear elastic material and section properties of the I-girder are listed in Table E.3. The weight of the bridge deck per unit length is 8.687 kip/ft (126.82 kN/m).

E.4. Abutment

Elastic abutment model with a stiff vertical spring and three stiff rotational springs was employed. In the longitudinal direction, a spring of stiffness $k = 102.6$ kip/in (value obtained by scaling the Salinas River Bridge spring stiffness by the ratio of the two bridge deck widths) was applied at each of the two abutments. In the transverse direction, a spring of stiffness $k = 44.5$ kip/in (value obtained also by the scaling scheme similar to the above) was employed (for each of the 2 abutments).

E.5. ESA

The ESA was conducted in the longitudinal and transverse directions. Figure E.4 shows the acceleration response spectrum (ARS) used in the ESA of Samoa and Eureka Bridges.

Table E.1. Samoa Bridge foundation matrix coefficients (Wang 2015)

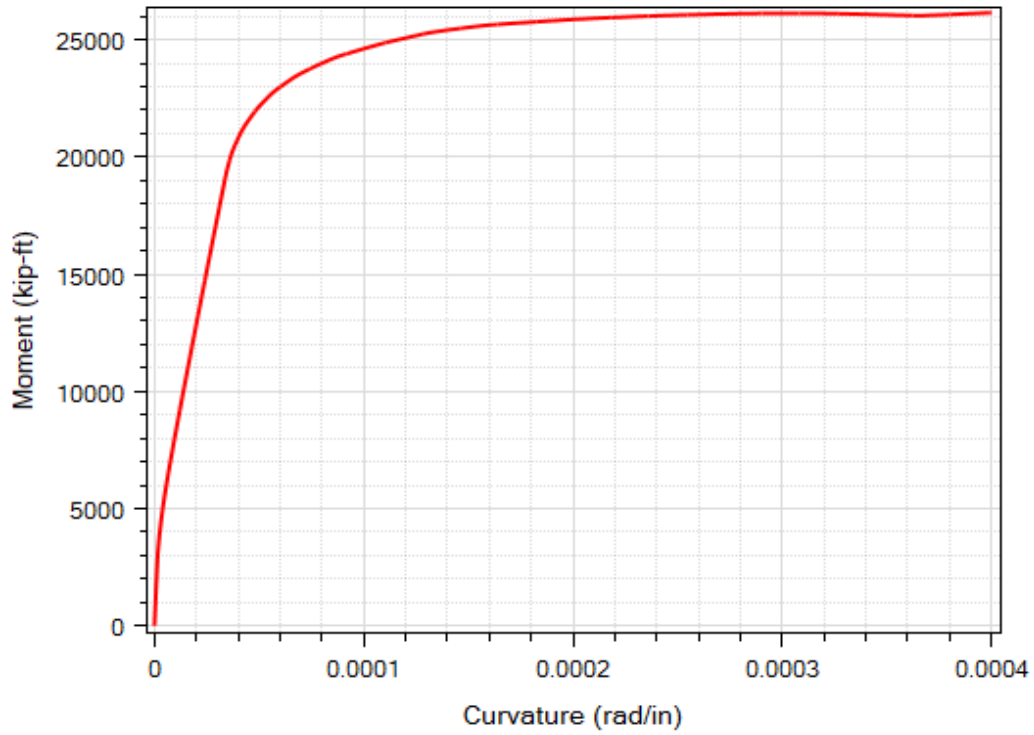
Bent #	k_x or k_y translational stiffness (kip/in)
Bent 2	624.786
Bent 3	78.412
Bent 4	669.903
Bent 5	290.177
Bent 6	151.970
Bent 7	100.286
Bent 8	223.015
Bent 9	289.949
Bent 10	209.081
Bent 11	145.802
Bent 12	230.268
Bent 13	221.359
Bent 14	1,333.52
Bent 15	1,333.52
Bent 16	1,333.52
Bent 17	704.74
Bent 18	704.74
Bent 19	704.74
Bent 20	704.74

Table E.2. Samoa Bridge constant foundation matrix coefficients for all bents (Wang 2015)

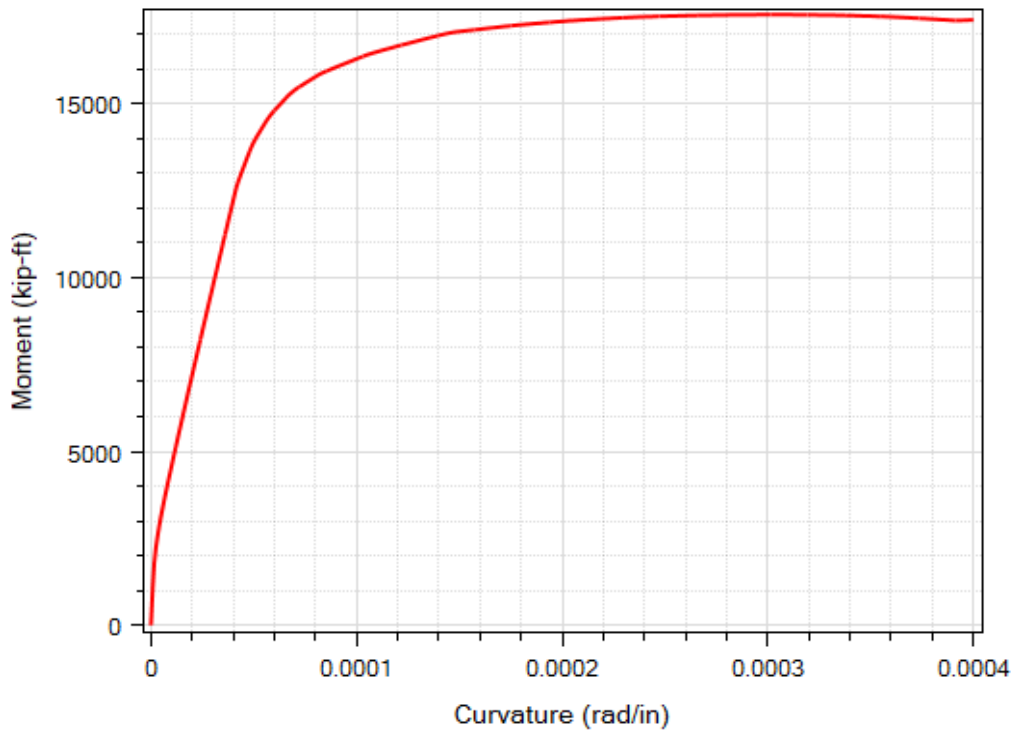
Parameter	Value
k_z (kip/in)	30,000
k_{rx} (kip/in)	20,000,000
k_{ry} (kip/in)	20,000,000
k_t (kip-in/rad)	77,477.88
k_{y-rx} (kip)	10,000
k_{x-ry} (kip)	-10,000

Table E.3. Bridge deck material and section properties for Samoa Bridge (Wang 2015)

Parameter	Value
Young's modulus	3.67×10^3 ksi (2.53×10^7 kPa)
Shear modulus	1.53×10^3 ksi (1.05×10^7 kPa)
Unit weight	160 pcf (25.11 kPa)
Area of cross-section	54.3 ft ² (5.05 m ²)
Moment of inertia @ horizontal axis	783.82 ft ⁴ (6.78 m ⁴)
Moment of inertia @ vertical axis	4.84×10^3 ft ⁴ (41.89 m ⁴)
Torsion constant	113.29 ft ⁴ (0.98 m ⁴)

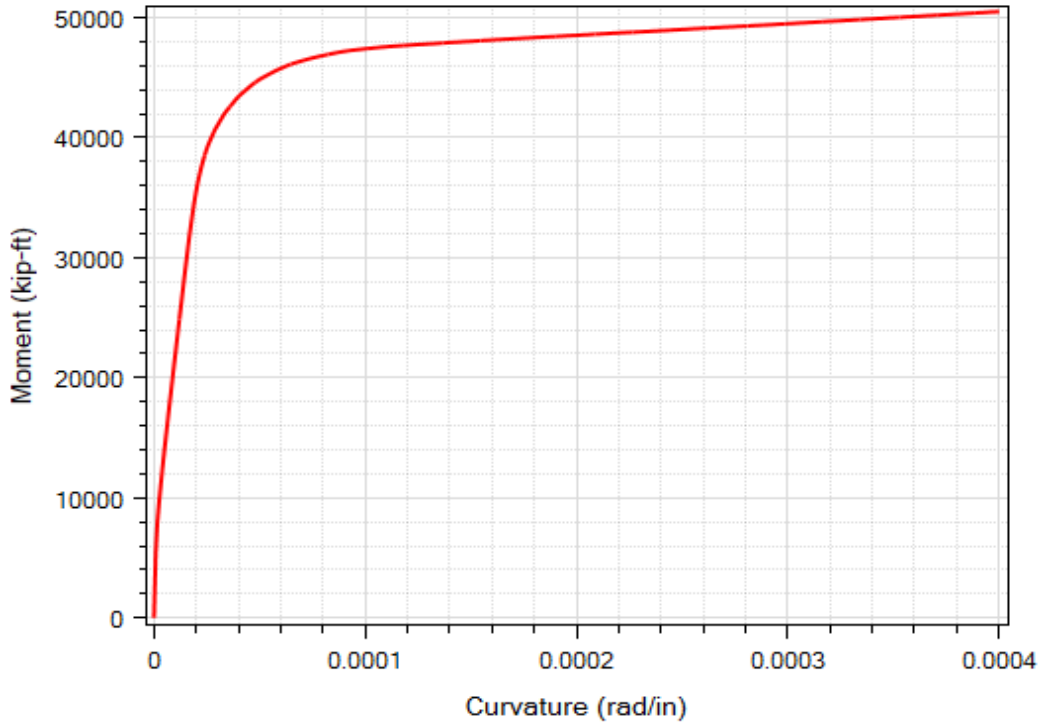


(a)

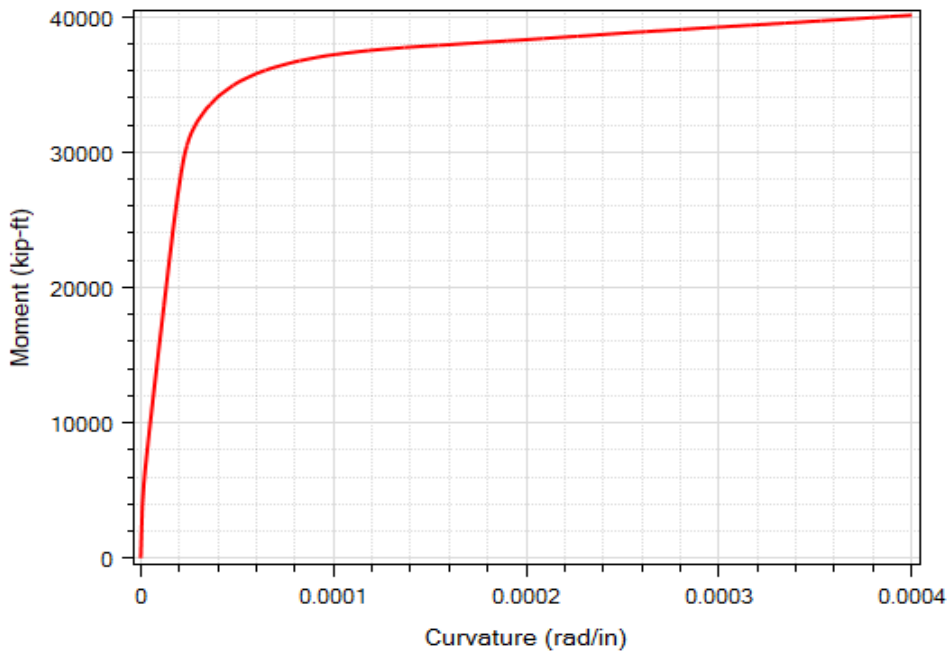


(b)

Figure E.1. Column moment-curvature relationship in the longitudinal direction for: (a) Pier S-8 and Pier S-9; (b) other piers



(a)



(b)

Figure E.2. Column moment-curvature relationship in the transverse direction for: (a) Pier S-8 and Pier S-9; (b) other piers

$$[k] = \begin{bmatrix} k_x & 0 & 0 & 0 & k_{x-ry} & 0 \\ 0 & k_y & 0 & k_{y-rx} & 0 & 0 \\ 0 & 0 & k_z & 0 & 0 & 0 \\ 0 & k_{rx-y} & 0 & k_{rx} & 0 & 0 \\ k_{ry-x} & 0 & 0 & 0 & k_{ry} & 0 \\ 0 & 0 & 0 & 0 & 0 & k_t \end{bmatrix}$$

Figure E.3. Foundation matrix definition

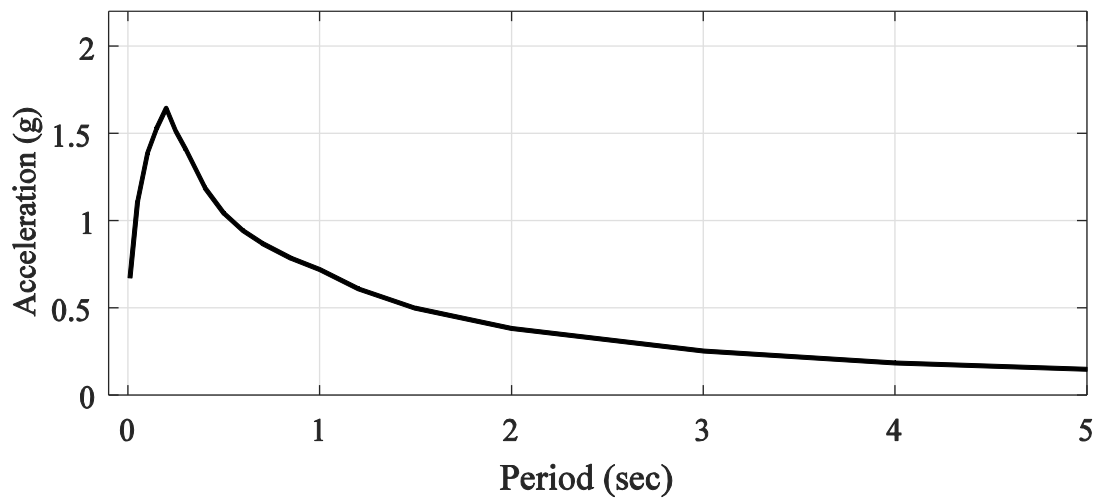


Figure E.4. Acceleration response spectrum employed in the ESA

Appendix F. Eureka Channel Bridge Modeling Details

F.1. Column

Nonlinear Fiber section in OpenSees was used to model the columns. Appendix G lists the OpenSees Tcl code snippet for the Fiber section for Piers E-6 and E-7 of Eureka Bridge (Section I) while the Tcl code snippet for other piers (except Piers E-6 and E-7) (Section II).

The moment-curvature response of the column Fiber section for Pier E-6 and E-7 is shown in Figure E.1a. An axial compressive load of 2,000 kip was applied in the moment-curvature analysis in the transverse direction.

For other piers (except Piers E-6 and E-7), the moment-curvature response of the column Fiber section is shown in Figure E.1b. An axial compressive load of 1,300 kip was applied in the moment-curvature analysis in this case for the transverse direction. In addition, the moment-curvature responses of the column Fiber section in the longitudinal direction are shown in Figure E.2a and Figure E.2b.

F.2. Foundation Matrix

The Foundation Matrix model is represented by the coupled foundation stiffness matrix (Lam and Martin). Moreover, Table F.1 shows the foundation matrix translational coefficients of all bents and Table E.2 shows the other stiffness coefficients (Wang 2015).

F.3. Deck

The employed linear elastic material and section properties of the I-girder are listed in Table F.2. The weight of the bridge deck per unit length is 6.48 kip/ft (94.6783 kN/m).

F.4. Abutment

Elastic abutment model with the same spring stiffness coefficients as those of Samoa Bridge was employed for Eureka Bridge.

Table F.1. Bent foundation matrix coefficients for Eureka Bridge (Wang 2015)

Bent #	K_x or K_y translational stiffness (kip/in)
Bent 2	805.254
Bent 3	885.209
Bent 4	651.057
Bent 5	190.748
Bent 6	725.300
Bent 7	942.319
Bent 8	942.319
Bent 9	560.251
Bent 10	560.251
Bent 11	280.982
Bent 12	190.748
Bent 13	902.342
Bent 14	280.98
Bent 15	205.03

Table F.2. Material and section properties of the bridge deck for Eureka Bridge (Wang 2015)

Parameter	Value
Young's modulus	3.67×10^3 ksi (2.53×10^7 kPa)
Shear modulus	1.53×10^3 ksi (1.05×10^7 kPa)
Unit weight	160 pcf (25.11 kPa)
Area of cross-section	40.53 ft ² (3.77 m ²)
Moment of inertia @ horizontal axis	194.22 ft ⁴ (1.68 m ⁴)
Moment of inertia @ vertical axis	3.80×10^3 ft ⁴ (32.9 m ⁴)
Torsion constant	40.46 ft ⁴ (0.35 m ⁴)

Appendix G. Column nonlinear fiber sections for the Samoa Channel Bridge and the Eureka Channel Bridge

This section lists the Tcl code snippet for the column nonlinear fiber section of Piers S-8 and S-9 for Samoa Bridge (Wang 2015). In addition, the same code snippet was also employed for Piers E-6 and E-7 of Eureka Bridge (Section I). Furthermore, it lists the Tcl code snippet for the column nonlinear fiber section of typical piers (except Piers S-8 and S-9 of Samoa Bridge and Piers E-6 and E-7 of Eureka Bridge) (Section II). SI units were used to write these Tcl codes.

G.1. Section I

```
set in2m 2.54e-2
set kips2Ton 0.4535929
set g 9.81
set kips2KN [expr $kips2Ton*$g]
set pierWidth 2.1336
set pierDepth 1.2192
set triDepth 0.5334
set cover 0.0762
set As [expr 10.06e-004]; # area of longitudinal-reinforcement bars
# Area of no. 11 bar in the columns, in2
set fy 303000.0; # Yield strength of reinforcing steel
set E 20.0e+7; # Young's modulus of reinforcing steel
set np 5; # Number of Gauss-Lobato points per beam-column
element
set fcCore -34700.0;
set fcuCore -30700.0
set fcCover -34000.0; # f'c of cover concrete, ksi
set fcuCover 0.0; # f'cu of cover concrete, ksi
set epscCore -0.0025;
set epscuCore -0.006;
set epscCover -0.002;
set epscuCover -0.005;
set columnSectionArea [expr $pierWidth*$pierDepth+$triDepth*$pierDepth]

#Define materials for nonlinear columns
#Columns material #1/3::Core concrete (confined)
#CONCRETE tag f'c ec0 f'cu ecu
uniaxialMaterial Concrete01 1421 $fcCore $epscCore $fcuCore $epscuCore
#Column Material #2/3::Cover concrete (unconfined)
#CONCRETE tag f'c ec0 f'cu ecu
uniaxialMaterial Concrete01 1422 $fcCover $epscCover $fcuCover $epscuCover
#Column Material #3/3::Reinforcing steel
#STEEL tag fy E0 b
uniaxialMaterial Steel01 1423 $fy $E 0.008
```

```

set columnSectionY1 [expr $pierDepth/2.0-$cover]
set columnSectionZ1 [expr $pierWidth/2.0]

# Define Retrofit
uniaxialMaterial Concrete01 1431 -35700.0 $sepscCore -33200.0 -0.0155;
#Columns material #1/3::Core concrete (confined)
uniaxialMaterial Concrete01 1432 -28000.0 $sepscCover $fcuCover
$sepscCover; #Column Material #2/3::Cover concrete (unconfined)
uniaxialMaterial Steel01 1433 414000.0 $E 0.008;
#Column Material #3/3::Reinforcing steel
set cover2 0.075
set columnSectionY2 [expr 1.83/2.0-$cover2]; #cover
set columnSectionZ2 [expr 1.195]
set triDepth2 [expr 0.915-0.075]; #0.84
set As2 [expr 2.84e-004]; #19
set cover3 0.305;
set columnSectionY3 [expr 1.83/2.0-$cover3]; #Middle
set columnSectionZ3 [expr 1.195]
set triDepth3 [expr 3.355/2-1.195]
set Tricover3 0.4325;
set delta_S [expr (305-75-50)/pow(2,0.5)*0.001]

set pSection 2005
section Fiber $pSection {
  # Create the concrete core fibers (checked)
  patch quad 1421 10 20 -0.5334 -1.0668 0.0 -1.6002 0.0 1.6002 -0.5334
  1.0668
  patch quad 1421 20 10 0.5334 -1.0668 0.5334 1.0668 0.0 1.6002 0.0 -
  1.6002

  #Create the concrete cover fibers (checked)
  patch quad 1422 20 1 -0.6096 1.067 -0.6096 -1.067 -0.533 -1.067 -0.533
  1.0668
  patch quad 1422 20 1 0.533 1.0668 0.5334 -1.0668 0.6096 -1.0668 0.6096
  1.0668
  patch quad 1422 1 10 0.0 -1.6764 0.0 -1.6002 -0.5334 -1.0668 -0.6096 -
  1.0668
  patch quad 1422 1 10 0.0 -1.6002 0.0 -1.6764 0.6096 -1.0668 0.5334 -
  1.0668
  patch quad 1422 1 10 -0.6096 1.0668 -0.5334 1.0668 0.0 1.6002 0.0 1.6764
  patch quad 1422 1 10 0.5334 1.0668 0.6096 1.0668 0.0 1.6764 0.0
  1.6002

  #Create the reinforcing fibers (checked)
  layer straight 1423 1 0.001006 0.0 -1.6002 0.0 -1.6002
  layer straight 1423 2 0.001006 -0.13335 -1.46685 0.13335 -1.46685
  layer straight 1423 2 0.001006 -0.2667 -1.3335 0.2667 -1.3335
  layer straight 1423 2 0.001006 -0.40005 -1.20015 0.40005 -1.20015
  layer straight 1423 2 0.001006 -0.5334 -1.0668 0.5334 -1.0668
  layer straight 1423 2 0.001006 -0.5334 -0.85344 0.5334 -0.85344
  layer straight 1423 2 0.001006 -0.5334 -0.64008 0.5334 -0.64008
  layer straight 1423 2 0.001006 -0.5334 -0.42672 0.5334 -0.42672
  layer straight 1423 2 0.001006 -0.5334 -0.21336 0.5334 -0.21336
  layer straight 1423 2 0.001006 -0.5334 -0.0 0.5334 0.0
  layer straight 1423 2 0.001006 -0.5334 0.21336 0.5334 0.21336
  layer straight 1423 2 0.001006 -0.5334 0.42672 0.5334 0.42672

```



```

layer straight 1423 2 0.001006 -0.5334 0.64008 0.5334 0.64008
layer straight 1423 2 0.001006 -0.5334 0.85344 0.5334 0.85344
layer straight 1423 2 0.001006 -0.5334 1.0668 0.5334 1.0668
layer straight 1423 2 0.001006 -0.40005 1.20015 0.40005 1.20015
layer straight 1423 2 0.001006 -0.2667 1.3335 0.2667 1.3335
layer straight 1423 2 0.001006 -0.13335 1.46685 0.13335 1.46685
layer straight 1423 1 0.001006 0.0 1.6002 0.0 1.6002

# Create concrete core fibers of retrofit (confined) (checked)
patch quad 1431 20 1 -0.84 1.195 -0.84 -1.195 -0.61 -1.0668 -0.61
1.0668
patch quad 1431 20 1 0.61 1.0668 0.61 -1.0668 0.84 -1.195 0.84 1.195
patch quad 1431 1 10 0.0 -2.035 0.0 -1.6775 -0.61 -1.0668 -0.84 -
1.195
patch quad 1431 1 10 0.0 -1.6775 0.0 -2.035 0.84 -1.195 0.61 -
1.0668
patch quad 1431 1 10 -0.84 1.195 -0.61 1.0668 0.0 1.6775 0.0 2.035
patch quad 1431 1 10 0.61 1.0668 0.84 1.195 0.0 2.035 0.0 1.6775

# Create concrete cover3 fibers of retrofit (unconfined) (checked)
patch quad 1432 20 1 -0.915 1.195 -0.915 -1.195 -0.84 -1.195 -0.84
1.195
patch quad 1432 20 1 0.84 1.195 0.84 -1.195 0.915 -1.195 0.915 1.195
patch quad 1432 1 10 0.0 -2.11 0.0 -2.035 -0.84 -1.195 -0.915 -
1.195
patch quad 1432 1 10 0.0 -2.035 0.0 -2.11 0.915 -1.195 0.84 -1.195
patch quad 1432 1 10 -0.915 1.195 -0.84 1.195 0.0 2.035 0.0 2.11
patch quad 1432 1 10 0.84 1.195 0.915 1.195 0.0 2.11 0.0 2.035

#Create the reinforcing fibers of retrofit
layer straight 1433 1 0.000284 0.0 -2.003934 0.0 -2.003934
layer straight 1433 1 0.000284 0.0 -1.7275 0.0 -1.7275
# inner
layer straight 1433 2 0.001006 -0.6596 -1.1168 0.6596 -1.1168
layer straight 1433 2 0.001006 -0.4947 -1.2692 0.4947 -1.2692
layer straight 1433 2 0.001006 -0.3298 -1.4216 0.3298 -1.4216
layer straight 1433 2 0.001006 -0.1649 -1.574 0.1649 -1.574
# outer
layer straight 1433 2 0.001006 -0.621979 -1.396479 0.621979 -
1.396479
layer straight 1433 2 0.001006 -0.457079 -1.548879 0.457079 -
1.548879
layer straight 1433 2 0.001006 -0.292179 -1.701279 0.292179 -
1.701279
# outer
layer straight 1433 2 0.000284 -0.84 -1.195 0.84 -1.195
layer straight 1433 2 0.000284 -0.84 -0.915 0.84 -0.915
layer straight 1433 2 0.000284 -0.84 -0.61 0.84 -0.61
layer straight 1433 2 0.000284 -0.84 -0.305 0.84 -0.305
layer straight 1433 2 0.000284 -0.84 -0.0 0.84 0.0
layer straight 1433 2 0.000284 -0.84 0.915 0.84 0.915
layer straight 1433 2 0.000284 -0.84 0.61 0.84 0.61
layer straight 1433 2 0.000284 -0.84 0.305 0.84 0.305
layer straight 1433 2 0.000284 -0.84 1.195 0.84 1.195
# inner
layer straight 1433 2 0.000284 -0.66 -0.915 0.66 -0.915
layer straight 1433 2 0.000284 -0.66 -0.61 0.66 -0.61

```

```

layer straight 1433 2 0.000284 -0.66 -0.305 0.66 -0.305
layer straight 1433 2 0.000284 -0.66 -0.0 0.66 0.0
layer straight 1433 2 0.000284 -0.66 0.915 0.66 0.915
layer straight 1433 2 0.000284 -0.66 0.61 0.66 0.61
layer straight 1433 2 0.000284 -0.66 0.305 0.66 0.305

# outer
layer straight 1433 2 0.001006 -0.621979 1.396479 0.621979 1.396479
layer straight 1433 2 0.001006 -0.457079 1.548879 0.457079 1.548879
layer straight 1433 2 0.001006 -0.292179 1.701279 0.292179 1.701279

# inner
layer straight 1433 2 0.001006 -0.6596 1.1168 0.6596 1.1168
layer straight 1433 2 0.001006 -0.4947 1.2692 0.4947 1.2692
layer straight 1433 2 0.001006 -0.3298 1.4216 0.3298 1.4216
layer straight 1433 2 0.001006 -0.1649 1.574 0.1649 1.574
layer straight 1433 1 0.000284 0.0 2.003934 0.0 2.003934
layer straight 1433 1 0.000284 0.0 1.7275 0.0 1.7275
}

```

G.2. Section II

```

set in2m 2.54e-2
set kips2Ton 0.4535929
set g 9.81
set kips2KN [expr $kips2Ton*$g]
set pierWidth 2.1336
set pierDepth 1.524
set triDepth 0.6858
set cover 0.0762
set As [expr 10.06e-004]; # area of longitudinal-reinforcement bars
# Area of no. 11 bar in the columns, in2

set fy 303000.0; # Yield strength of reinforcing steel
set E 20.0e+7; # Young's modulus of reinforcing steel
set np 5; # Number of Gauss-Lobato points per beam-column element

set fcCore -34700.0;
set fcuCore -30700.0
set fcCover -34000.0; # f'c of cover concrete, ksi
set fcuCover 0.0; # f'cu of cover concrete, ksi
set epscCore -0.0025;
set epscuCore -0.006;
set epscCover -0.002;
set epscuCover -0.005;
set columnSectionArea [expr $pierWidth*$pierDepth+$triDepth*$pierDepth]

#Define materials for nonlinear columns
#Columns material #1/3::Core concrete (confined)
#CONCRETE tag f'c ec0 f'cu ecu
uniaxialMaterial Concrete01 21 $fcCore $epscCore $fcuCore $epscuCore

#Column Material #2/3::Cover concrete (unconfined)
#CONCRETE tag f'c ec0 f'cu ecu
uniaxialMaterial Concrete01 22 $fcCover $epscCover $fcuCover $epscuCover

#Column Material #3/3::Reinforcing steel

```

```

#STEEL          tag fy  E0 b
uniaxialMaterial Steel01 23 $fy $E 0.008

set columnSectionY1 [expr $pierDepth/2.0-$cover]
set columnSectionZ1 [expr $pierWidth/2.0]

# Define Retrofit
uniaxialMaterial Concrete01 31 -35700.0 $epscCore -33200.0 -0.0155;
#Columns material #1/3::Core concrete (confined)
uniaxialMaterial Concrete01 32 -28000.0 $epscCover $fcuCover $epscuCover;
#Column Material #2/3::Cover concrete (unconfined)
uniaxialMaterial Steel01 33 414000.0 $E 0.008;
#Column Material #3/3::Reinforcing steel

set cover2 0.075
set columnSectionY2 [expr 2.13/2.0-$cover2]; #cover
set columnSectionZ2 [expr 1.195]
set triDepth2 [expr 1.065-0.075]; #0.84
set As2 [expr 2.84e-004]; #19
set As25 [expr 5.1e-004]; #25
set cover3 0.305;
set columnSectionY3 [expr 2.13/2.0-$cover3]; #Middle
set columnSectionZ3 [expr 1.195]
set triDepth3 [expr 3.66/2-1.195]
set Tricover3 [expr (4.52-3.66)/2];
set deltaS [expr 0.305/pow(2, 0.5)]

# User-Defined Fiber Section (Fiber)
set pSection 2015
section Fiber $pSection {

    # Create the concrete core fibers
    patch quad 21 10 20 -0.6858 -1.0668 0.0 -1.7526 0.0 1.7526 -0.6858
1.0668
    patch quad 21 20 10 0.6858 -1.0668 0.6858 1.0668 0.0 1.7526 0.0 -
1.7526

    #Create the concrete cover fibers
    patch quad 22 20 1 -0.762 1.067 -0.762 -1.067 -0.6858 -1.0668 -0.6858
1.067
    patch quad 22 20 1 0.6858 1.067 0.6858 -1.0668 0.762 -1.0668 0.762
1.0668
    patch quad 22 1 10 0.0 -1.8288 0.0 -1.7526 -0.6858 -1.0668 -0.762 -
1.0668
    patch quad 22 1 10 0.0 -1.7526 0.0 -1.8288 0.762 -1.0668 0.6858 -
1.0668
    patch quad 22 1 10 -0.762 1.0668 -0.6858 1.0668 0.0 1.7526 0.0
1.8288
    patch quad 22 1 10 0.6858 1.0668 0.762 1.0668 0.0 1.8288 0.0 1.7526

    #Create the reinforcing fibers
    layer straight 23 1 0.001006 0.0 -1.7526 0.0 -1.7526
    layer straight 23 2 0.001006 -0.13716 -1.61544 0.13716 -1.61544
    layer straight 23 2 0.001006 -0.27432 -1.47828 0.27432 -1.47828
    layer straight 23 2 0.001006 -0.41148 -1.34112 0.41148 -1.34112
    layer straight 23 2 0.001006 -0.54864 -1.20396 0.54864 -1.20396

```

```

layer straight 23 2 0.001006 -0.6858 -1.0668 0.6858 -1.0668
layer straight 23 2 0.001006 -0.6858 -1.0668 0.6858 -1.0668
layer straight 23 2 0.001006 -0.6858 -0.85344 0.6858 -0.85344
layer straight 23 2 0.001006 -0.6858 -0.64008 0.6858 -0.64008
layer straight 23 2 0.001006 -0.6858 -0.42672 0.6858 -0.42672
layer straight 23 2 0.001006 -0.6858 -0.21336 0.6858 -0.21336
layer straight 23 2 0.001006 -0.6858 -0.0 0.6858 0.0
layer straight 23 2 0.001006 -0.6858 0.21336 0.6858 0.21336
layer straight 23 2 0.001006 -0.6858 0.42672 0.6858 0.42672
layer straight 23 2 0.001006 -0.6858 0.64008 0.6858 0.64008
layer straight 23 2 0.001006 -0.6858 0.85344 0.6858 0.85344
layer straight 23 2 0.001006 -0.6858 1.0668 0.6858 1.0668
layer straight 23 2 0.001006 -0.6858 1.0668 0.6858 1.0668

layer straight 23 2 0.001006 -0.54864 1.20396 0.54864 1.20396
layer straight 23 2 0.001006 -0.41148 1.34112 0.41148 1.34112
layer straight 23 2 0.001006 -0.27432 1.47828 0.27432 1.47828
layer straight 23 2 0.001006 -0.13716 1.61544 0.13716 1.61544

layer straight 23 1 0.001006 0.0 1.7526 0.0 1.7526

# Create concrete core fibers of retrofit (confined) (checked)
patch quad 31 20 1 -0.99 1.195 -0.99 -1.195 -0.76 -1.0668 -0.76
1.0668
patch quad 31 20 1 0.76 1.0668 0.76 -1.0668 0.99 -1.195 0.99 1.195
patch quad 31 1 10 0.0 -2.185 0.0 -1.83 -0.76 -1.0668 -0.99 -1.195
patch quad 31 1 10 0.0 -1.83 0.0 -2.185 0.99 -1.195 0.76 -1.0668
patch quad 31 1 10 -0.99 1.195 -0.76 1.0668 0.0 1.83 0.0 2.185
patch quad 31 1 10 0.76 1.0668 0.99 1.195 0.0 2.185 0.0 1.83

# Create concrete cover3 fibers of retrofit (unconfined) (checked)
patch quad 32 20 1 -1.065 1.195 -1.065 -1.195 -0.99 -1.195 -0.99
1.195
patch quad 32 20 1 0.99 1.195 0.99 -1.195 1.065 -1.195 1.065 1.195
patch quad 32 1 10 0.0 -2.26 0.0 -2.185 -0.99 -1.195 -1.065 -1.195
patch quad 32 1 10 0.0 -2.185 0.0 -2.26 1.065 -1.195 0.99 -1.195
patch quad 32 1 10 -1.065 1.195 -0.99 1.195 0.0 2.185 0.0 2.26
patch quad 32 1 10 0.99 1.195 1.065 1.195 0.0 2.26 0.0 2.185

#Create the reinforcing fibers of retrofit
layer straight 33 1 0.000284 0.0 -2.153934 0.0 -2.153934
layer straight 33 1 0.00051 0.0 -2.153934 0.0 -2.153934
layer straight 33 1 0.000284 0.0 2.153934 0.0 2.153934
layer straight 33 1 0.00051 0.0 2.153934 0.0 2.153934

# outer
layer straight 33 2 0.000284 -0.9246 -1.265 0.9246 -1.265
layer straight 33 2 0.000284 -0.7532 -1.429 0.7532 -1.429
layer straight 33 2 0.000284 -0.5817 -1.593 0.5817 -1.593
layer straight 33 2 0.000284 -0.4103 -1.757 0.4103 -1.757
layer straight 33 2 0.000284 -0.2388 -1.921 0.2388 -1.921

layer straight 33 2 0.00051 -0.9246 -1.265 0.9246 -1.265
layer straight 33 2 0.00051 -0.7532 -1.429 0.7532 -1.429
layer straight 33 2 0.00051 -0.5817 -1.593 0.5817 -1.593
layer straight 33 2 0.00051 -0.4103 -1.757 0.4103 -1.757
layer straight 33 2 0.00051 -0.2388 -1.921 0.2388 -1.921

```

```

# inner
layer straight 33 2 0.000284 -0.7974 -1.138 0.7974 -1.138
layer straight 33 2 0.000284 -0.6259 -1.301 0.6259 -1.301
layer straight 33 2 0.000284 -0.4545 -1.465 0.4545 -1.465
layer straight 33 2 0.000284 -0.283 -1.629 0.283 -1.629
layer straight 33 2 0.000284 -0.1116 -1.793 0.1116 -1.793
# width outer
layer straight 33 2 0.000284 -0.99 -1.195 0.99 -1.195
layer straight 33 2 0.000284 -0.99 -0.915 0.99 -0.915
layer straight 33 2 0.000284 -0.99 -0.61 0.99 -0.61
layer straight 33 2 0.000284 -0.99 -0.305 0.99 -0.305
layer straight 33 2 0.000284 -0.99 -0.0 0.99 0.0
layer straight 33 2 0.000284 -0.99 0.915 0.99 0.915
layer straight 33 2 0.000284 -0.99 0.61 0.99 0.61
layer straight 33 2 0.000284 -0.99 0.305 0.99 0.305
layer straight 33 2 0.000284 -0.99 1.195 0.99 1.195

layer straight 33 2 0.00051 -0.99 -1.195 0.99 -1.195
layer straight 33 2 0.00051 -0.99 -0.915 0.99 -0.915
layer straight 33 2 0.00051 -0.99 -0.61 0.99 -0.61
layer straight 33 2 0.00051 -0.99 -0.305 0.99 -0.305
layer straight 33 2 0.00051 -0.99 -0.0 0.99 0.0
layer straight 33 2 0.00051 -0.99 0.915 0.99 0.915
layer straight 33 2 0.00051 -0.99 0.61 0.99 0.61
layer straight 33 2 0.00051 -0.99 0.305 0.99 0.305
layer straight 33 2 0.00051 -0.99 1.195 0.99 1.195

# width inner
layer straight 33 2 0.000284 -0.81 -0.915 0.81 -0.915
layer straight 33 2 0.000284 -0.81 -0.61 0.81 -0.61
layer straight 33 2 0.000284 -0.81 -0.305 0.81 -0.305
layer straight 33 2 0.000284 -0.81 -0.0 0.81 0.0
layer straight 33 2 0.000284 -0.81 0.915 0.81 0.915
layer straight 33 2 0.000284 -0.81 0.61 0.81 0.61
layer straight 33 2 0.000284 -0.81 0.305 0.81 0.305

# outer
layer straight 33 2 0.000284 -0.9246 1.265 0.9246 1.265
layer straight 33 2 0.000284 -0.7532 1.429 0.7532 1.429
layer straight 33 2 0.000284 -0.5817 1.593 0.5817 1.593
layer straight 33 2 0.000284 -0.4103 1.757 0.4103 1.757
layer straight 33 2 0.000284 -0.2388 1.921 0.2388 1.921

layer straight 33 2 0.00051 -0.9246 1.265 0.9246 1.265
layer straight 33 2 0.00051 -0.7532 1.429 0.7532 1.429
layer straight 33 2 0.00051 -0.5817 1.593 0.5817 1.593
layer straight 33 2 0.00051 -0.4103 1.757 0.4103 1.757
layer straight 33 2 0.00051 -0.2388 1.921 0.2388 1.921

# inner
layer straight 33 2 0.000284 -0.7974 1.138 0.7974 1.138
layer straight 33 2 0.000284 -0.6259 1.301 0.6259 1.301
layer straight 33 2 0.000284 -0.4545 1.465 0.4545 1.465
layer straight 33 2 0.000284 -0.283 1.629 0.283 1.629
layer straight 33 2 0.000284 -0.1116 1.793 0.1116 1.793

```

```

}
```

Appendix H. PEER Performance-Based Earthquake Engineering (PBEE) Framework

H.1. Theory and Implementation of PBEE Analysis

The framework consists of four probabilistic models: (1) The hazard model uses earthquake ground motion data to determine an IM, (2) The demand model uses response from dynamic analysis to determine an EDP, (3) The damage model connects the EDP to a DM, and (4) The loss model that links a DM to consequences in terms of repair cost and repair time. Figure H.1 illustrates the PEER PBEE methodology.

The complete analysis is accomplished using the LLRCAT described by Mackie *et al.* (2010) and depicted conceptually in Figure H.2. In the LLRCAT methodology, each bridge system is disaggregated into independent structural defined as PGs that are damaged, assessed, and repaired together using a specific combination of different repair methods. The damage in each of the PGs is characterized according to several discrete DSs that are defined by distributions of critical EDPs.

A total of 11 PGs are considered: PG1: Max column drift ratio; PG2: Residual column drift ratio; PG3: Max relative deck-end/abutment displacement (left); PG4: Max relative deck-end/abutment displacement (right); PG5: Max bridge-abutment bearing displacement (left); PG6: Max bridge-abutment bearing displacement (right); PG7: Approach residual vertical displacement (left); PG8: Approach residual vertical displacement (right); PG9: Abutment residual pile cap displacement (left); PG10: Abutment residual pile top displacement (right); PG11: Column residual pile displacement at ground surface.

Damage states are numbered sequentially in order of increasing severity. The DSs are connected to structural demands obtained from finite element analysis results by way of an EDP specific to each PG. Each PG is linked to a single EDP in this implementation.

The loss model in terms of the repair cost is often presented as normalized costs of repair that are obtained by using the RCR between the cost of repair and the cost of replacement cost. Replacement cost is based on the deck and type of construction, providing a range of cost/SF of deck area according to Caltrans comparative bridge costs (Division of Engineering Services - Cost Estimates Branch, 2014). In addition, Repair time represents the total number of crew-workdays (CWD) required to complete the task.

H.2. Efforts to Expand PBEE Framework

An integrated computational framework was developed to combine nonlinear THA of multi-span bridge systems with an implementation of the PEER PBEE methodology. In addition, the carbon footprint of repair was included as a sustainability metric in this framework. All stages of the involved analyses including the PBEE assessment were executed in a systematic fashion, allowing the end-user to conveniently conduct extensive parametric investigations. For that purpose, the user-interface MSBridge (Elgamal *et al.* 2014) was further developed and employed.

The proposed research will build on previous efforts including a PBEE assessment tool BridgePBEE. The main efforts can be summarized as follow:

- (i) Adapting the PBEE implementation for single-bent/column bridges from BridgePBEE to MSBridge. The work involves conversion of the computer code from Visual C++ (employed for BridgePBEE) to C# (employed for MSBridge).
- (ii) Extending the PBEE implementation to multi-span bridge scenarios. Robust algorithms will be developed for calculating the correlation matrices.

- (iii) Extending the framework to include the carbon footprint of repair as a performance metric. As such, the emission factors from the EIO-LCA model were added to the framework to convert the dollar spent to carbon emissions according to equation H.1 and equation H.2.

$$E [\text{Carbon}_n] = E [\text{EF}_n] \times E [\text{Cost}_n] \quad (\text{H.1})$$

$$\text{Var} [\text{Carbon}_n] = \text{Var} [\text{EF}_n] * E^2 [\text{Cost}_n] + E^2 [\text{EF}_n] * \text{Var} [\text{Cost}_n] \quad (\text{H.2})$$

where $E [\text{Carbon}]$ is the expected value of carbon emission, $E [\text{EF}]$ is the emission factor from EIO-LCA, and $E [\text{Cost}_n]$ is the expected value of cost for each repair item.

H.3. PBEE Quantities

Table H.1 shows the PGs that are used in this framework. Figure H.3 shows the demand model (in log-log space) of a representative PG. For the damage states parameters (Figure H.4), Lambda (λ) is the median EDP that defines the onset of the damage state and is one parameter of the assumed lognormal distribution of damage when conditioned in EDP. It has the same units as the EDP for the selected PG. Beta (β) is the lognormal standard deviation and is the second parameter of the assumed lognormal distribution. In addition, the Repairs, Unit Costs, Production Rates, and Emission Factors are displayed in Figure H.5-Figure H.8, respectively.

H.4. PBEE Outputs

This section displays the probabilistic repair cost, repair time, and carbon footprint along with standard deviation, displayed for each PG (eleven of them) and each repair quantity. The final PBEE results will be displayed against any intensity measure (e.g., PGV) in terms of:

- Contribution to expected repair cost (\$) from each performance group (Figure H.9);
- Total repair cost ratio (%) (Figure H.10);

- Contribution to expected repair cost (\$) from each repair quantity (Figure H.11);
- Contribution to repair cost standard deviation (\$) from each repair quantity (Figure H.12);
- Total repair time (CWD) where CWD stands for Crew Working Day (Figure H.13);
- Contribution to expected repair time (CWD) from each repair quantity (Figure H.14);
- Contribution to expected carbon footprint (Mg CO₂ equivalent) from each performance group (Figure H.15);
- Contribution to expected carbon footprint (Mg CO₂ equivalent) from each repair quantity (Figure H.16).

Table H.1. PBEE performance groups

Performance Group (PG) #	Performance group names
1	Maximum column drift ratio
2	Residual column drift ratio
3	Maximum relative deck-end/abutment displacement (left)
4	Maximum relative deck-end/abutment displacement (right)
5	Maximum bridge-abutment bearing displacement (left)
6	Maximum bridge-abutment bearing displacement (right)
7	Approach residual vertical displacement (left)
8	Approach residual vertical displacement (right)
9	Abutment residual pile cap displacement (left)
10	Abutment residual pile top displacement (right)
11	Column residual pile displacement at ground surface

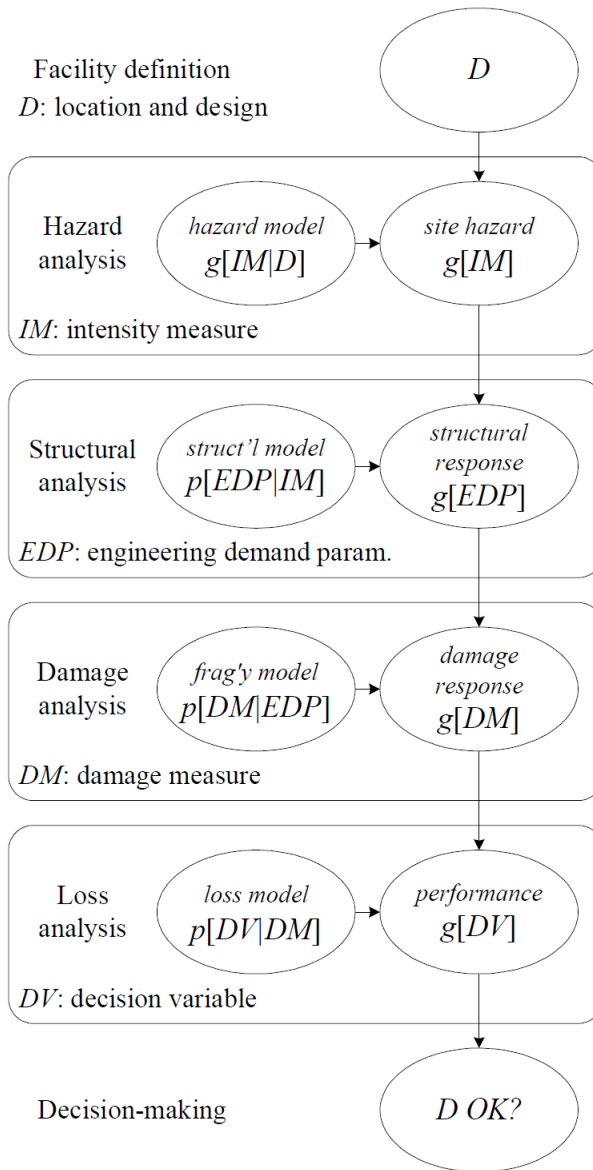


Figure H.1. PEER PBEE methodology (Porter 2003)

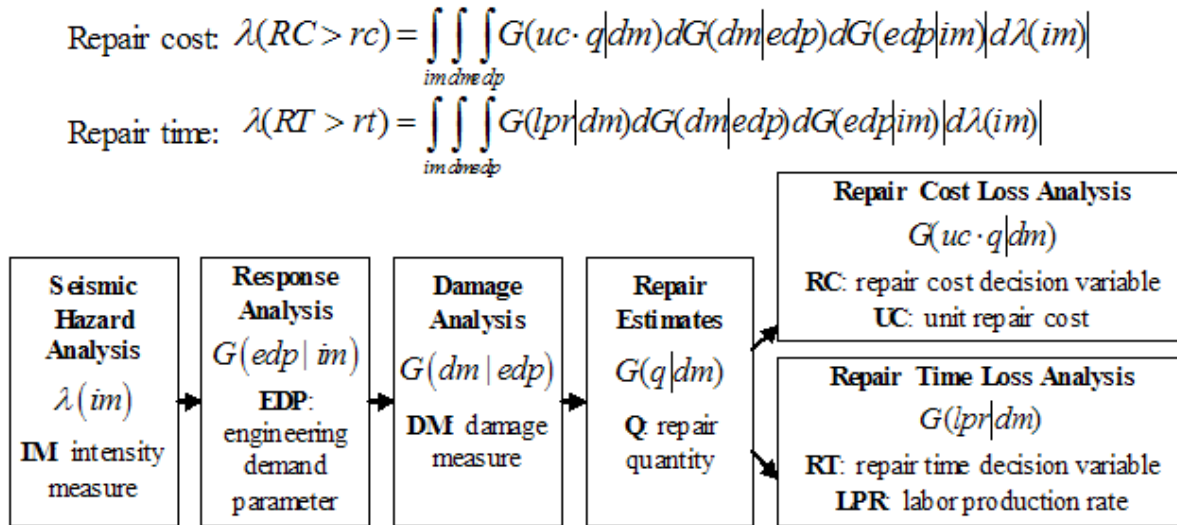


Figure H.2. Schematic procedure of the LLRCAT methodology for a single bridge component Mackie *et al.* (2010)

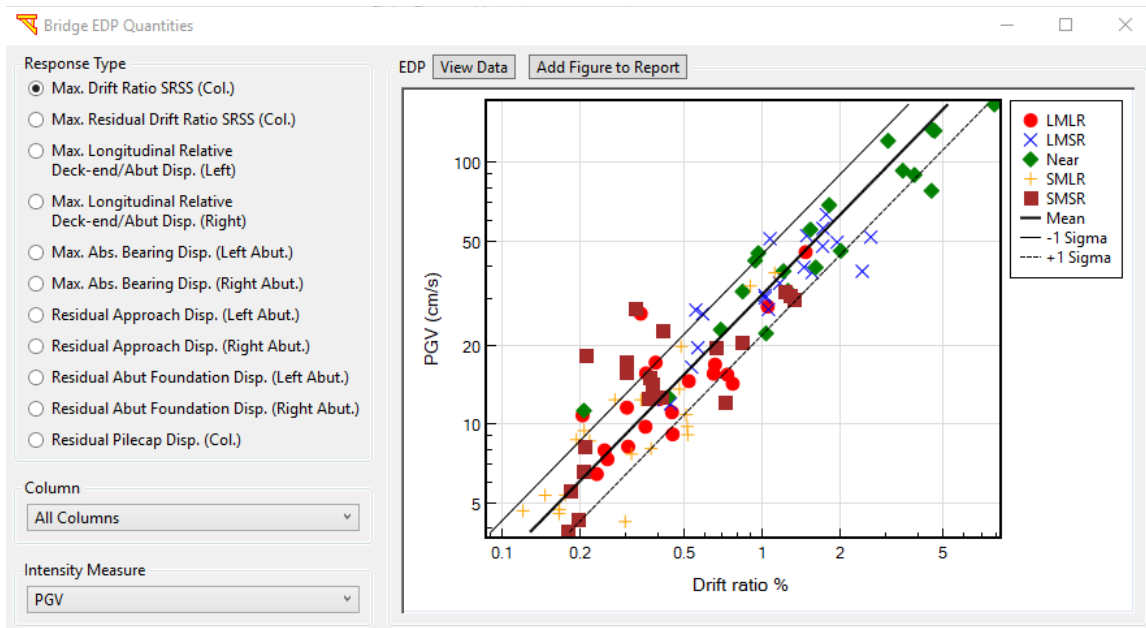


Figure H.3. EDP vs. IM in log-log space

Damage States

Damage States Edit Reset

EDP	DS1 Lamd:	DS1 Beta	DS2 Lamd:	DS2 Beta	DS3 Lamd:	DS3 Beta	DS4 Lamd:	DS4 Beta
PG1-2: Max. Tangent Drift SRSS (%) - Bent 2	0.2406	0.3	1.652	0.33	6.8489	0.25	7.5511	0.35
PG2-2: Residual Tangent Drift SRSS (%) - Bent 2	0.5	0.3	1.25	0.4	2	0.4	7.5511	0.35
PG3: Max. Relative Deck-(Left) Abutment Long. Disp. (m)	0.0508	0.25	0.1016	0.25	0.1108	0.3	0.1382	0.3
PG4: Max. Relative Deck-(Right) Abutment Long. Disp. (m)	0.0508	0.25	0.1016	0.25	0.1108	0.3	0.1382	0.3
PG5: Max. Absolute (Left) Bearing Displacement	0.0765	0.25	0.153	0.25	0	0	0	0
PG6: Max. Absolute (Right) Bearing Displacement	0.0765	0.25	0.153	0.25	0	0	0	0
PG7: Left Approach (Residual) Vertical Displacement	0.0732	0.4	0.1463	0.4	0.3048	0.4	0	0
PG8: Right Approach (Residual) Vertical Displacement	0.0732	0.4	0.1463	0.4	0.3048	0.4	0	0
PG9: Left Abutment Foundation	0.3915	0.4	0.6552	0.4	0	0	0	0
PG10: Right Abutment Foundation	0.3915	0.4	0.6552	0.4	0	0	0	0
PG11-2: Column Foundation - Bent 2	0.5097	0.4	0.8542	0.4	0	0	0	0

OK Cancel

Figure H.4. Damage states window

Repairs

Repairs Edit Reset

Damage States	Item 1	Item 2	Item 3	Item 4	Item 5	Item 6	Item 7	Item 8	Item 9	Item 10	Item 11	Item 12	Item 13	Item 14	Item 1
PG1-2 DS1 (Bent 2)	0	0	0	0	0	0	0	0	0	0	44.0289	27.6823	0	0	0
PG1-2 DS2 (Bent 2)	0	0	0	0	0	0	0	0	0	0	88.0577	69.2058	0	0	0
PG1-2 DS3 (Bent 2)	12.5719	12.5719	5856.299	0	10.2594	0	0	0	4631.519	0	0	0	0	0	0
PG1-2 DS4 (Bent 2)	12.5719	12.5719	5856.299	0	10.2594	0	0	0	4631.519	0	0	0	0	0	0
PG2-2 DS1 (Bent 2)	8.3812	8.3812	2928.15	0	0	0	0	0	231.5759	0	0	0	4429.573	0	0
PG2-2 DS2 (Bent 2)	8.3812	8.3812	2928.15	0	0	0	0	0	231.5759	0	0	0	4429.573	0	0
PG2-2 DS3 (Bent 2)	0	0	2928.15	0	0	0	0	0	0	0	0	0	0	0	0
PG2-2 DS4 (Bent 2)	0	0	0	0	0	0	0	0	0	0	0	0	0	0	0
PG3 DS1	0	0	0	0	2.41	0	0	0	0	0	0	0	0	39.042	0
PG3 DS2	8.6817	8.6817	0	0	2.41	0	0	0	0	0	12.0079	23.4406	0	39.042	0
PG3 DS3	34.7268	34.7268	0	0	8.6817	0	43.3333	0.3022	789.9471	0	0	0	0	39.042	0
PG3 DS4	43.4085	43.4085	0	0	8.6817	0	43.3333	0.64	789.9471	0	0	0	0	39.042	0
PG4 DS1	0	0	0	0	2.41	0	0	0	0	0	0	0	0	39.042	0
PG4 DS2	8.6817	8.6817	0	0	2.41	0	0	0	0	0	12.0079	23.4406	0	39.042	0
PG4 DS3	34.7268	34.7268	0	0	8.6817	0	43.3333	0.3022	789.9471	0	0	0	0	39.042	0
PG4 DS4	43.4085	43.4085	0	0	8.6817	0	43.3333	0.64	789.9471	0	0	0	0	39.042	0
PG5 DS1	0	0	0	2928.15	0	0	0	0	0	0	0	0	0	0	3
PG5 DS2	0	0	0	2928.15	0	0	0	0	0	0	0	0	0	0	3
PG5 DS3	0	0	0	0	0	0	0	0	0	0	0	0	0	0	0
PG5 DS4	0	0	0	0	0	0	0	0	0	0	0	0	0	0	0
PG6 DS1	0	0	0	2928.15	0	0	0	0	0	0	0	0	0	0	3
PG6 DS2	0	0	0	2928.15	0	0	0	0	0	0	0	0	0	0	3

OK Cancel

Figure H.5. Repair quantities window

Unit Costs

Unit Costs Edit Reset

Item#	Item Name	Unit	UC mean	UC std dev
1	Structure excavation	Cubic Yard (CY)	165	33
2	Structure backfill	Cubic Yard (CY)	220	44
3	Temporary support (superstruc	Squire Foot (SF)	38	7.6
4	Temporary support (abutment	Squire Foot (SF)	38	7.6
5	Structural concrete (bridge)	Cubic Yard (CY)	2225	445
6	Structural concrete (footing)	Cubic Yard (CY)	520	104
7	Structural concrete (approach	Cubic Yard (CY)	1625	325
8	Aggregate base (approach slab	Cubic Yard (CY)	325	65
9	Bar reinforcing steel (bridge)	Pound (LB)	1.35	0.27
10	Bar reinforcing steel (footing, r	Pound (LB)	1.2	0.24
11	Epoxy inject cracks	Linear Foot (LF)	215	43
12	Repair minor spalls	Squire Foot (SF)	300	60
13	Column steel casing	Pound (LB)	10	2
14	Joint seal assembly	Linear Foot (LF)	275	55
15	Elastomeric bearings	Each (EA)	1500	300
16	Drill and bond dowel	Linear Foot (LF)	55	11
17	Furnish steel pipe pile	Linear Foot (LF)	55	11
18	Drive steel pipe pile	Each (EA)	2050	410
19	Drive abutment pipe pile	Each (EA)	9000	1800
20	Asphalt concrete	TON	265	53
21	Mud jacking	Cubic Yard (CY)	380	76
22	Bridge removal (column)	Cubic Yard (CY)	3405	681
23	Bridae removal (portion)	Cubic Yard (CY)	2355	471

OK Cancel

Figure H.6. Unit costs window

The image shows a software window titled "Production Rates" with a standard Windows-style title bar (minimize, maximize, close buttons). Inside the window, there are "Edit" and "Reset" buttons. The main content is a table with 5 columns: "Item#", "Item Name", "Unit", "PR mean", and "PR std dev". The table lists 23 items, all with "CWD" as the unit. At the bottom of the window are "OK" and "Cancel" buttons.

Item#	Item Name	Unit	PR mean	PR std dev
1	Structure excavation	CWD	1.2	0.2
2	Structure backfill	CWD	2.2	0.5
3	Temporary support (superstructure)	CWD	34.2	3.8
4	Temporary support (abutment)	CWD	33.2	3.8
5	Structural concrete (bridge)	CWD	10	0.7
6	Structural concrete (footing)	CWD	10	0.7
7	Structural concrete (approach slab)	CWD	2	0.3
8	Aggregate base (approach slab)	CWD	1.2	0.2
9	Bar reinforcing steel (bridge)	CWD	1.8	0.2
10	Bar reinforcing steel (footing, retaining wa	CWD	1.8	0.2
11	Epoxy inject cracks	CWD	2	0.3
12	Repair minor spalls	CWD	2	0.3
13	Column steel casing	CWD	70	7.7
14	Joint seal assembly	CWD	2	0.3
15	Elastomeric bearings	CWD	1.2	0.2
16	Drill and bond dowel	CWD	1.2	0.2
17	Furnish steel pipe pile	CWD	35	1.7
18	Drive steel pipe pile	CWD	2	0.3
19	Drive abutment pipe pile	CWD	3	0.3
20	Asphalt concrete	CWD	2	0.3
21	Mud jacking	CWD	2	0.3
22	Bridge removal (column)	CWD	16.2	1.8
23	Bridae removal (portion)	CWD	2	0.3

Figure H.7. Production rates window

Emission Factors

Emission Factors (EF) Edit Reset

Item#	Item Name	Unit	EF mean	EF std dev
1	Structure excavation	t-CO2/Million\$	457.1	137.1
2	Structure backfill	t-CO2/Million\$	457.1	137.1
3	Temporary support (superstructu	t-CO2/Million\$	1000	300
4	Temporary support (abutment)	t-CO2/Million\$	1000	300
5	Structural concrete (bridge)	t-CO2/Million\$	333.33	1000
6	Structural concrete (footing)	t-CO2/Million\$	3571.4	1071.4
7	Structural concrete (approach sla	t-CO2/Million\$	3285.7	985.7
8	Aggregate base (approach slab)	t-CO2/Million\$	3000	900
9	Bar reinforcing steel (bridge)	t-CO2/Million\$	4000	1200
10	Bar reinforcing steel (footing, ret	t-CO2/Million\$	4363.6	1309.1
11	Epoxy inject cracks	t-CO2/Million\$	2500	750
12	Repair minor spalls	t-CO2/Million\$	1000	300
13	Column steel casing	t-CO2/Million\$	1000	300
14	Joint seal assembly	t-CO2/Million\$	2000	600
15	Elastomeric bearings	t-CO2/Million\$	2500	750
16	Drill and bond dowel	t-CO2/Million\$	3500	1050
17	Furnish steel pipe pile	t-CO2/Million\$	2666.7	800
18	Drive steel pipe pile	t-CO2/Million\$	444.4	133.3
19	Drive abutment pipe pile	t-CO2/Million\$	444.4	133.3
20	Asphalt concrete	t-CO2/Million\$	1000	300
21	Mud jacking	t-CO2/Million\$	500	150
22	Bridge removal (column)	t-CO2/Million\$	500	150
23	Bridae removal (portion)	t-CO2/Million\$	500	150

OK Cancel

Figure H.8. Emission factors window

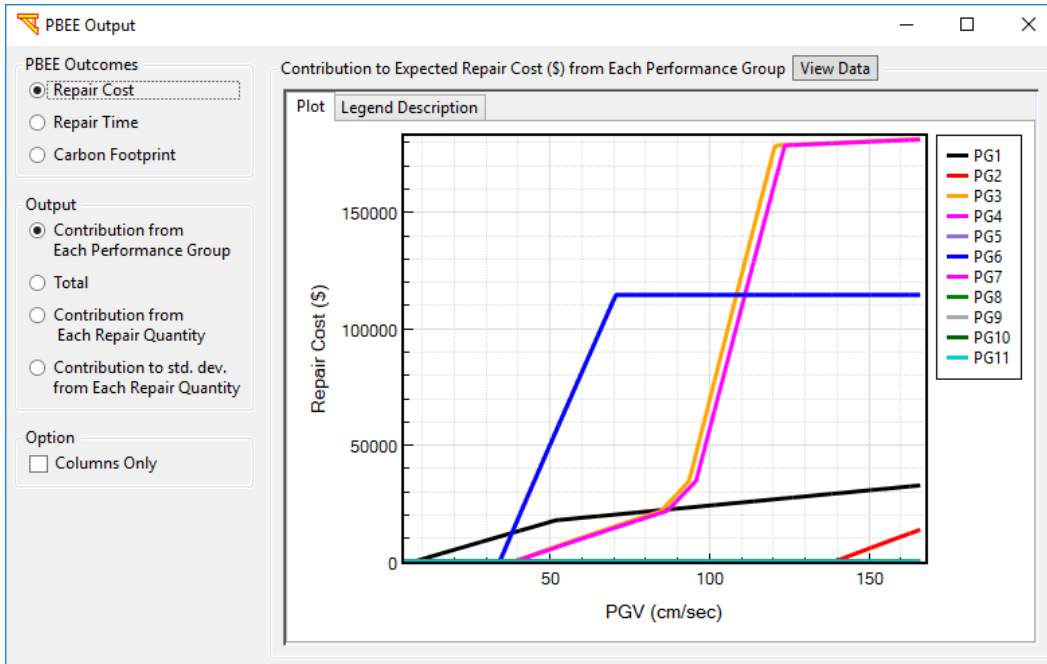


Figure H.9. Contribution to expected repair cost (\$) from each performance group

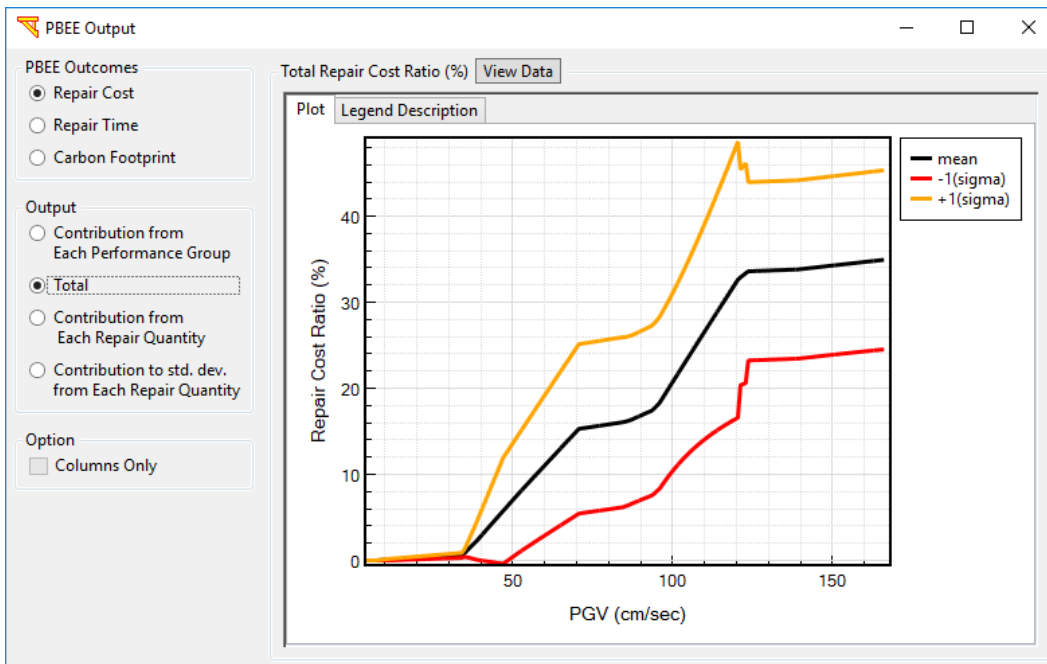


Figure H.10. Total repair cost ratio (%) as a function of intensity

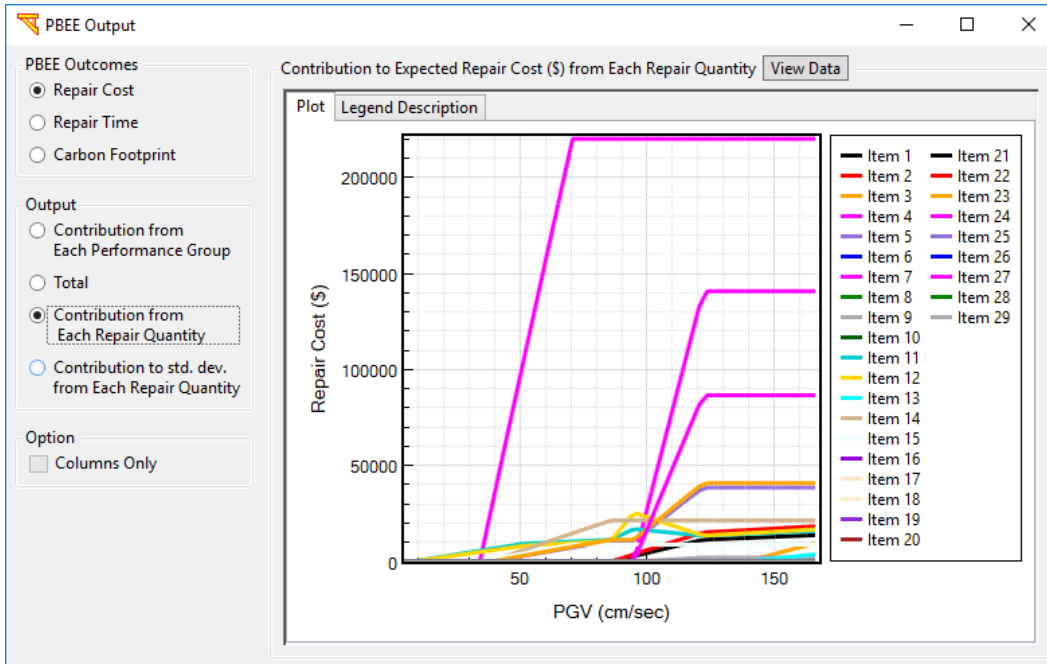


Figure H.11. Contribution to expected repair cost (\$) from each repair quantity

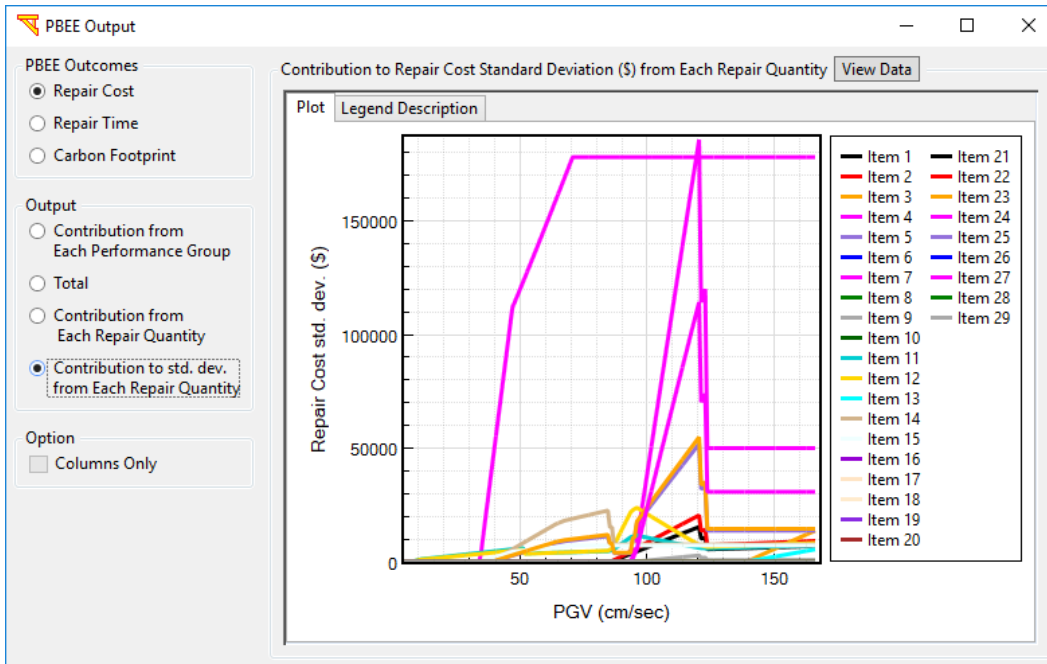


Figure H.12. Contribution to repair cost standard deviation (\$) from each repair quantity

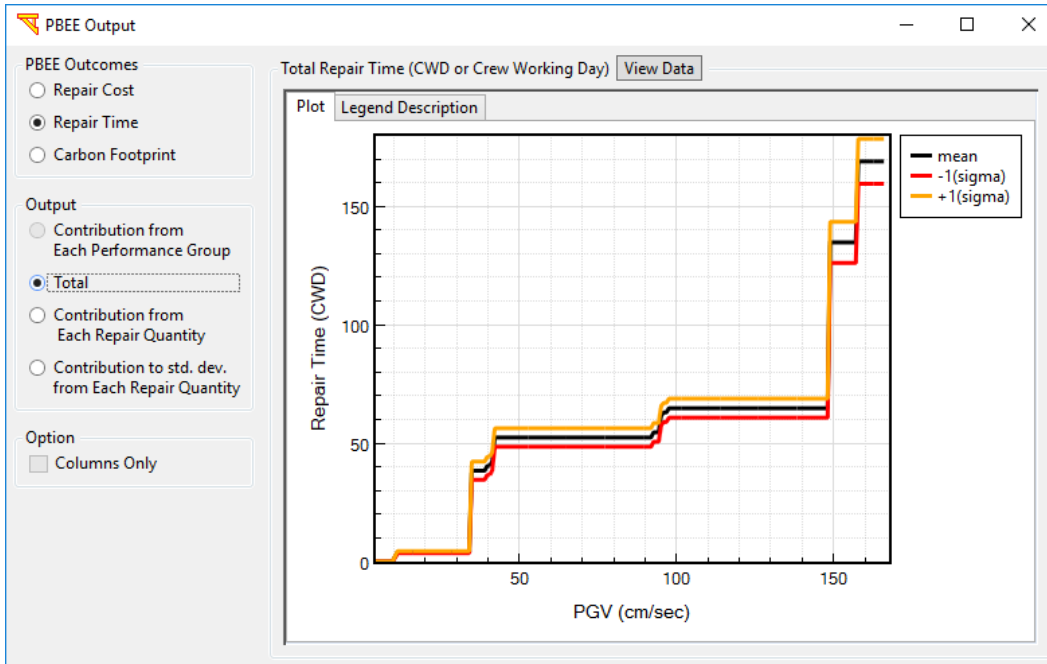


Figure H.13. Total repair time (CWD) as a function of intensity

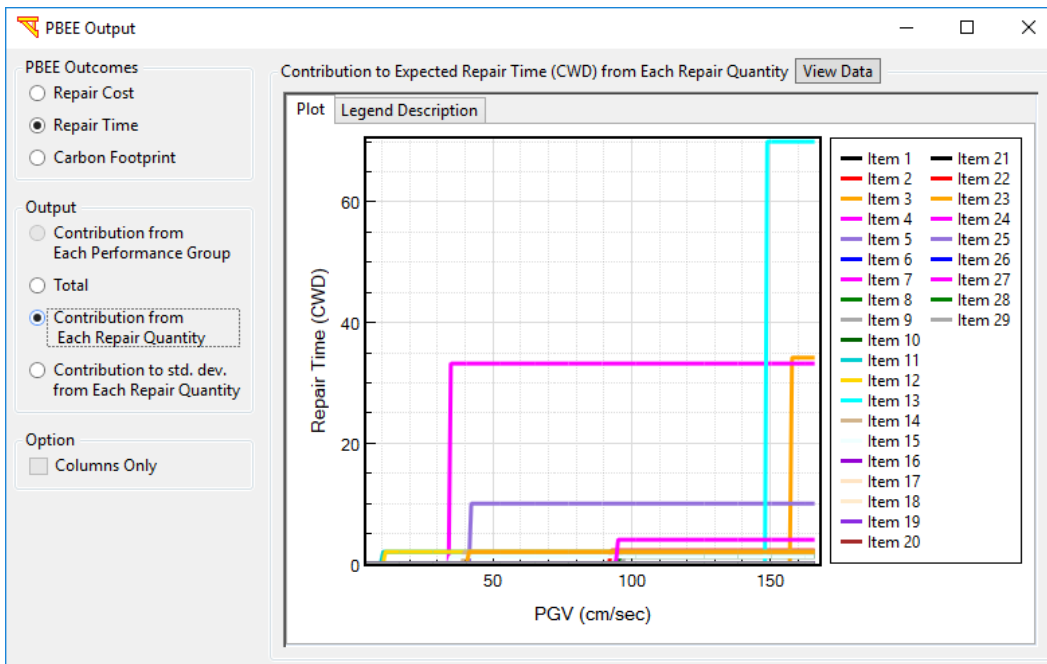


Figure H.14. Contribution to expected repair time (CWD) from each repair quantity

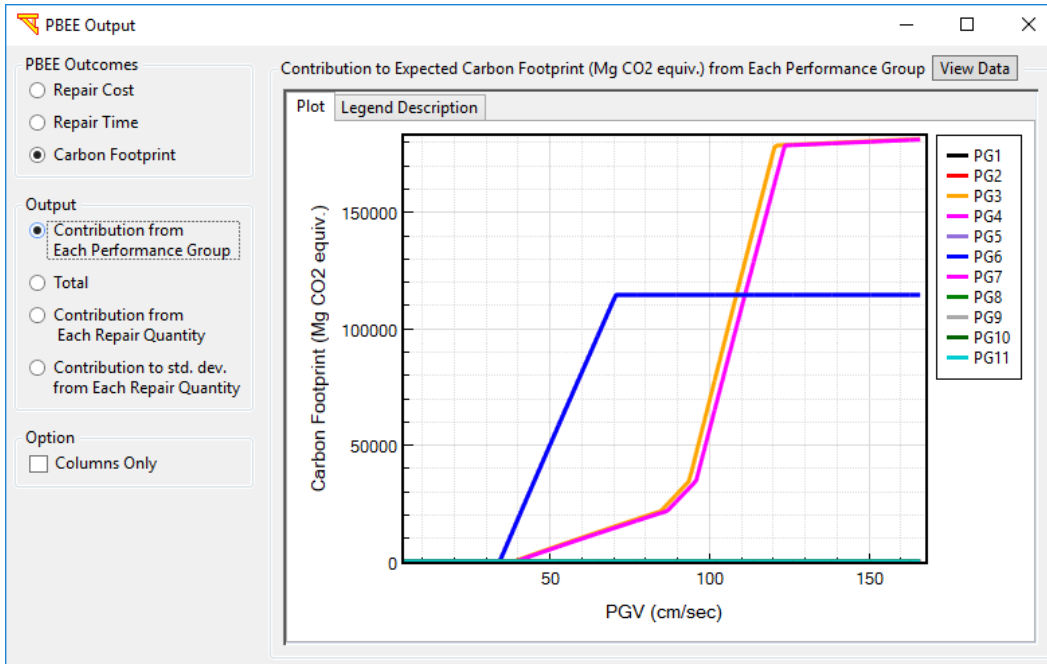


Figure H.15. Contribution to expected carbon footprint (Mg CO₂ equivalent) from each repair quantity

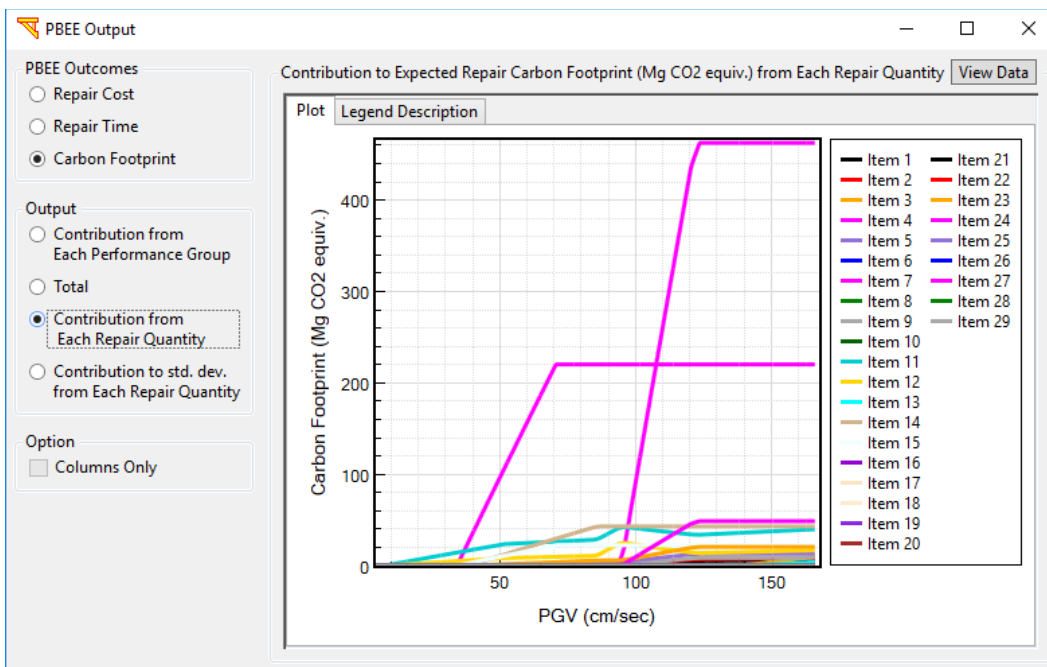


Figure H.16. Contribution to expected carbon footprint (Mg CO₂ equivalent) from each repair quantity

Appendix I. PBEE for Pile-Supported Wharves

This appendix presents a preliminary undertaken effort to apply the PEER PBEE framework steps to evaluate the performance of wharves using results from Yang *et al.* (2012). Previous studies show that the connection between the pile and the deck can experience most of the damage. Therefore, the curvature of the pile-to-deck connection was selected to be the engineering demand parameter (EDP). Three experiment-based damage states were defined by Lehman *et al.* (2009), and their fragility curves were developed. In addition, the probabilities of exceeding slight, moderate, and extensive damage states were calculated for a wide range of input shaking scenarios.

I.1. Introduction

Seaports play a vital role to a country's economic stability through the import and export activities. For that purpose, preventing the seismic damage to these large-scale constructed facilities has attracted attention to study and mitigate the negative economic consequences. Previous studies showed that the seaports are susceptible to damage caused by earthquakes, especially those located along the western coast of the United States of America (Roeder *et al.* 2005; Jellin 2008; Lehman *et al.* 2009; Yang *et al.* 2012).

A two-dimensional (2D) modeling approach was adopted to study the seismic response mechanisms of wharves (Arulmoli *et al.* 2004; Yan *et al.* 2004; and Na *et al.* 2009). However, the results showed that the 2D modeling approach may not fully capture the actual response. Therefore, other studies were more concerned with the three-dimensional (3D) modeling approach (Shafieezadeh *et al.* 2012; Doran *et al.* 2015; and Su *et al.* 2017).

A significant number of studies aimed to evaluate the seismic performance of port facilities under alternative levels of seismic loading. However, less effort was made in probabilistic assessment of wharves (Lehman *et al.* 2009; Torkamani *et al.* 2014; and Yang *et al.* 2012).

In this study, the PBEE steps were carried out to evaluate the response of pile-supported wharves under different hazard levels and to estimate the post-earthquake repair cost. Using a set of appropriate experimentally-based limit states, seismic fragility curves for wharf structures common in the western U.S. were developed.

Pile-supported wharves share components similar to the bridge. Therefore, the user-interface (MSBridge) can be used to model and perform the THA and PBEE framework for this important class of structures.

I.2. Characteristics of the Vertical-Pile-Supported Wharf

Seismic performance of a vertical-pile-supported wharf (Figure I.1) was studied by Yang *et al.* (2012). This class of wharves was constructed of continuous reinforced concrete decks, supported on 0.60 m (24 in) octagonal vertical prestressed concrete piles (Figure I.1c). Shorter piles on rows G and H are major lateral force resisting components and referred to as seismic piles. The depth of the concrete deck is 0.6 m (2 ft) between pile rows A and G, and increases to 0.9 m (3 ft) between pile rows G and H. More details about the characteristics of the studied wharf can be found in Yang *et al.* (2012).

I.3. Numerical Modeling of the Wharf

OpenSees was utilized by Yang *et al.* (2012) to model and investigate the transverse seismic response of the wharf using the 2D approach (Figure I.2). SSI was conveniently handled by soil springs (p - y curves).

I.4. Experimental-Based Damage States

According to information from the tests on T-headed dowel connections (Jellin 2008; and Brackmann 2009), the curvature of the pile-to-deck connection was selected to be the EDP that is used to measure the level of damage. The proposed damage states by Lehman *et al.* (2009) are shown in Table I.1. Lehman *et al.* (2009) describes the damage states as follow:

Damage state 1 (DS 1) is the lowest level of damage and includes incipient spalling of the concrete cover of the pile, deck, or both. The required repair method would include removal of the loose concrete cover, patching the concrete and epoxy inject of open cracks.

For DS2, spalling and cracking damage is significantly more severe. Spalling may expose reinforcement and leave the connection susceptible to corrosion and further deterioration. Since cover concrete may be completely lost, there is a clear loss of resistance of the connection, but the basic integrity of the connection is still intact.

For DS3, severe permanent damage requiring significant repair or replacement was noted. Several different types of deterioration could cause this damage state including concrete spalling and loss of concrete in the core of the pile; or fractured dowels.

Table I.2 shows the fragility curves parameters (λ and β) for each damage state. In creating the fragility curves, Method A from the ATC-58 Project (Porter 2007) was used and idealized by a lognormal distribution (equation I.1).

$$P[DS \geq ds | EDP = edp] = \Phi\left(\frac{\ln(edp/\lambda)}{\beta}\right) \quad (I.1)$$

where Φ denotes the standard normal (Gaussian) cumulative distribution function, λ denotes the median value of the distribution, and β denotes the logarithmic standard deviation. Figure I.3 shows the fragility curves for the three damage states.

I.5. Probabilities of Exceeding the Damage States

Yang *et al.* (2012) performed the Nonlinear time-history analysis using two suites of ground motion records. A total of three bins of 20 records for the Los Angeles (LA) area were utilized (LA ground motions) (Somerville *et al.* 1997). Figure I.4 shows the demand model for the wharf with crane under LA ground motions in terms of PGA.

From the demand model shown in Figure I.4, the probabilities of exceeding slight, moderate, and extensive damage states were calculated using equation I.2 (Porter 2007). In addition, Figure I.5 shows the probabilities of occurrence for each damage state for the wharf with cranes under the LA ground motion suite. From Figure I.5, at a PGA of 0.50 g, the probabilities of exceeding slight, moderate, extensive, and complete damage states are approximately 23.0%, 7.0%, and 4.0%, respectively.

$$P[\text{EDP} \geq \text{DS}|\text{IM}] = 1 - \Phi\left(\frac{\ln(\text{DS}) - \mu[\ln(\text{EDP})]}{\sqrt{\beta_{\text{EDP}}^2 + \beta_{\text{DS}}^2}}\right) \quad (\text{I.2})$$

where $\mu[\ln(\text{EDP})]$ denotes the mean of the $\ln(\text{EDP})$, β_{EDP} and β_{DS} denote the logarithmic standard deviation for the EDP and the DS, respectively.

I.6. Repair Methods

The repair quantities and repair method descriptions for the damage states are summarized in Table I.3 after Mackie *et al.* (2007). In addition, Table I.4 shows the expected repair quantities and associated costs. Furthermore, Figure I.6 shows the repair costs for one pile vs. PGA. The results from Figure I.5 shows that only the first two DSs were triggered. As such, the associated cost started to accumulate at a PGA of 0.7 g and 1.3 g for DS1 and DS2, respectively.

Table I.1. Damage states for wharf piles from Lehman *et al.* (2009)

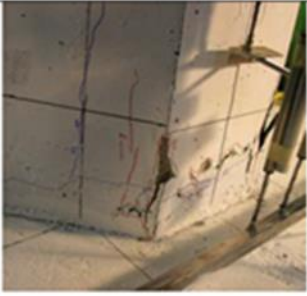

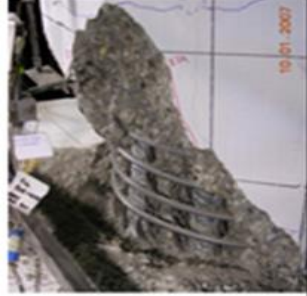
DS1	DS2	DS3
		
Initial cracking and spalling of the pile and/or deck.	Substantial spalling of the pile or the deck to a depth exposes the spiral or deck reinforcement.	Broken connection from either spalling into the core, fractured bars or buckled strands.

Table I.2. Fragility curve parameters from Yang *et al.* (2012)

	DS1	DS2	DS3
Log Median (λ)	0.05	0.166	0.235
Log Std. Dev. β	0.28	0.46	0.29

Table I.3. Repair items: pile damage states after Mackie *et al.* (2007)

Damage State	Repair Item	Unit Computation
DS1 <i>Initial cracking and spalling of the pile</i>	Epoxy inject cracks (LF)	$2 \times \text{pile height}$
	Repair minor spalls (CY)	$10\% \times (\text{surface area}) \times (\text{cover} + 1'')$
DS2 <i>Substantial spalling of the pile</i>	Epoxy inject cracks (LF)	$4 \times \text{pile height}$
	Repair minor spalls (CY)	$25\% \times (\text{surface area}) \times (\text{cover} + 1'')$
DS3 <i>Replace pile</i>	Structural concrete, wharf (CY)	Gross pile volume
	Wharf removal, pile (CY)	Same as structural concrete
	Bar reinforcing steel, wharf (LB)	$(\text{column gross volume}) \times (\text{rebar weight})$
	Temporary support, wharf (SF)	$\text{Tributary length} \times (\text{deck width})$
	Structure excavation (CY)	3 ft embedment plus 4 ft concentric circle around column
	Structure backfill (CY)	Same as structure excavation

Table I.4. Repair cost estimates after Mackie *et al.* (2007)

Damage State	Repair Item	Quantity	Price	Amount
DS1 <i>Initial cracking and spalling of the pile</i>	Epoxy inject cracks (LF)	44.03	\$215.00	\$9,466.45
	Repair minor spalls (CY)	27.68	\$300.00	\$8,304.00
DS2 <i>Substantial spalling of the pile</i>	Epoxy inject cracks (LF)	88.06	\$215.00	\$18,932.90
	Repair minor spalls (CY)	69.21	\$300.00	\$20,763.00
DS3 <i>Replace pile</i>	Structural concrete, wharf (CY)	15.99	\$2,225.00	\$35,577.75
	Wharf removal, pile (CY)	15.99	\$3,405.00	\$54,445.95
	Bar reinforcing steel, wharf (LB)	7222.52	\$1.35	\$9,750.40
	Temporary support, wharf (SF)	419.25	\$38.00	\$15,931.50
	Structure excavation (CY)	14.75	\$165.00	\$2,433.75
	Structure backfill (CY)	14.75	\$220.00	\$3,245.00

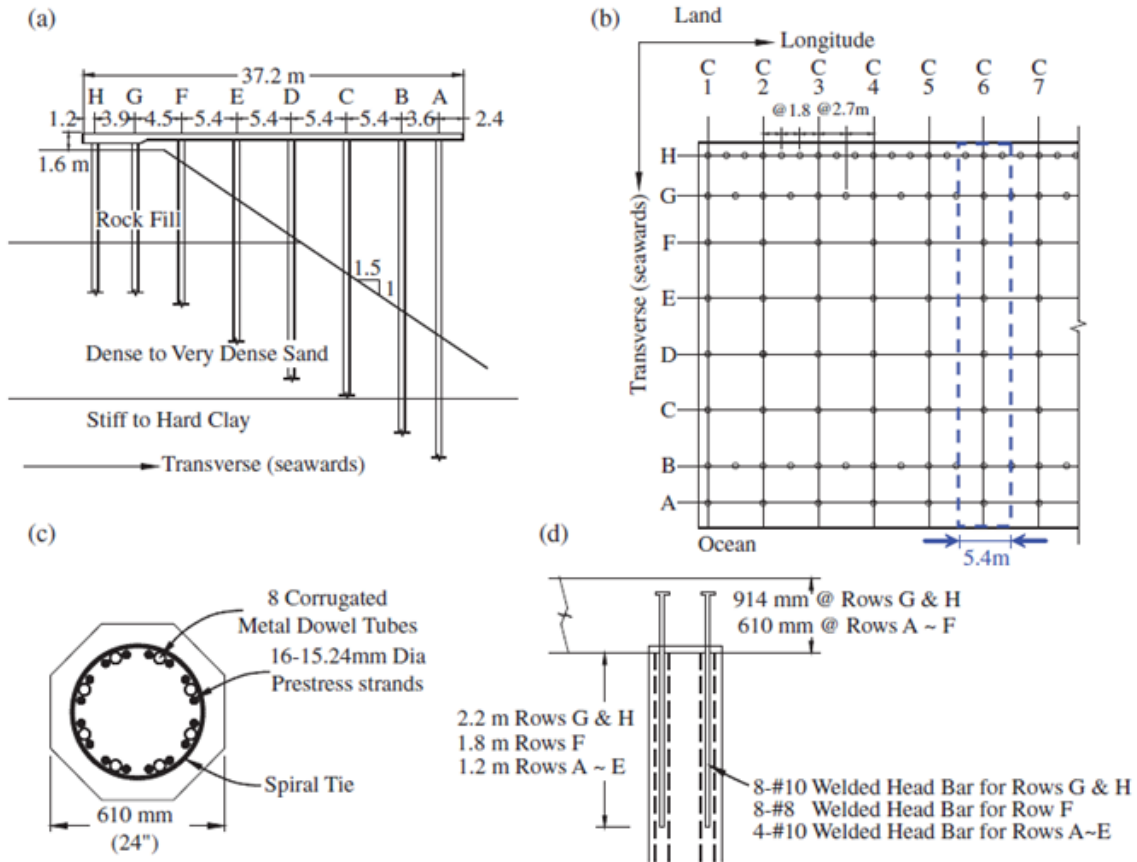


Figure I.1. Vertical-pile-supported wharf: (a) schematic of wharf transverse section; (b) wharf pile plan; (c) prestressed pile details; and (d) pile-to-deck connections from Yang *et al.* (2012)

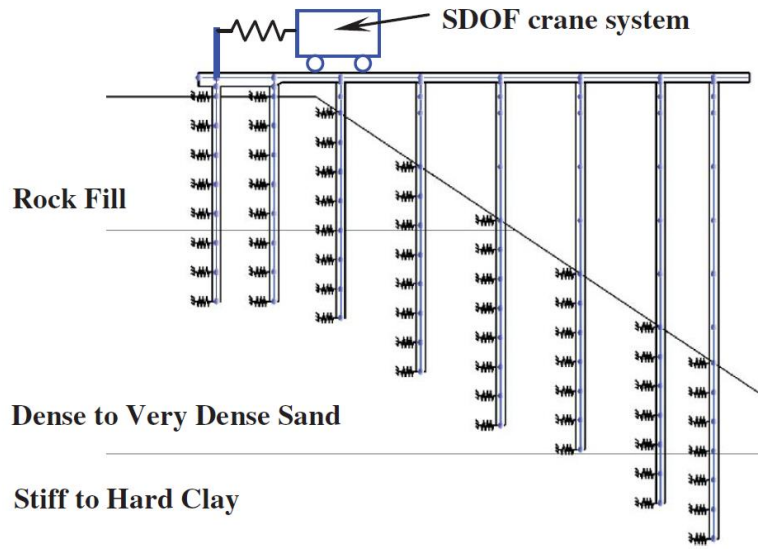


Figure I.2. Numerical wharf model with soil profile from Yang *et al.* (2012)

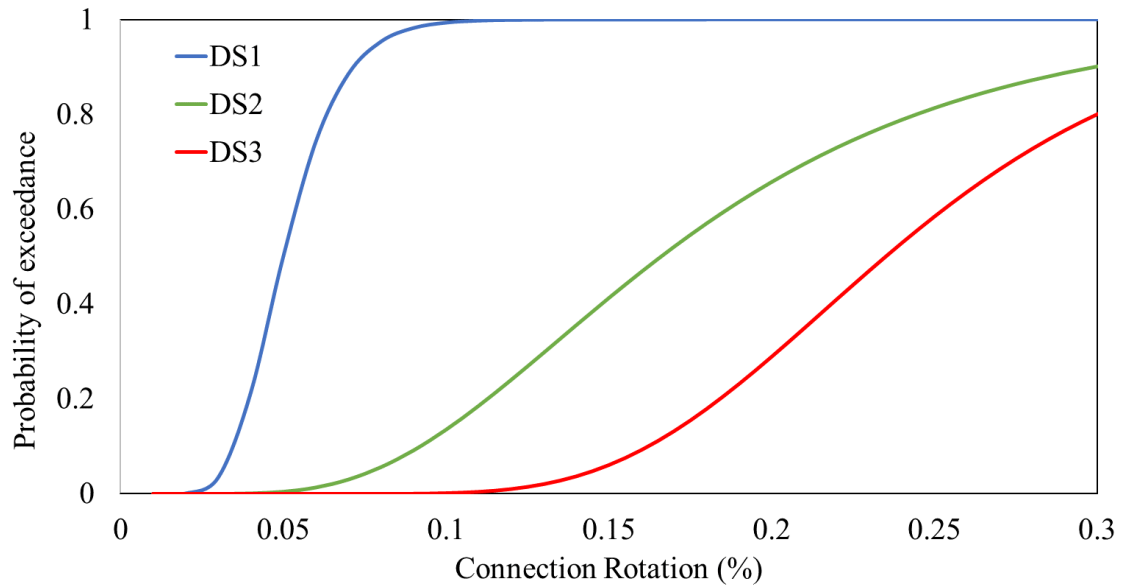


Figure I.3. Fragility curves for the pile-to-deck connection

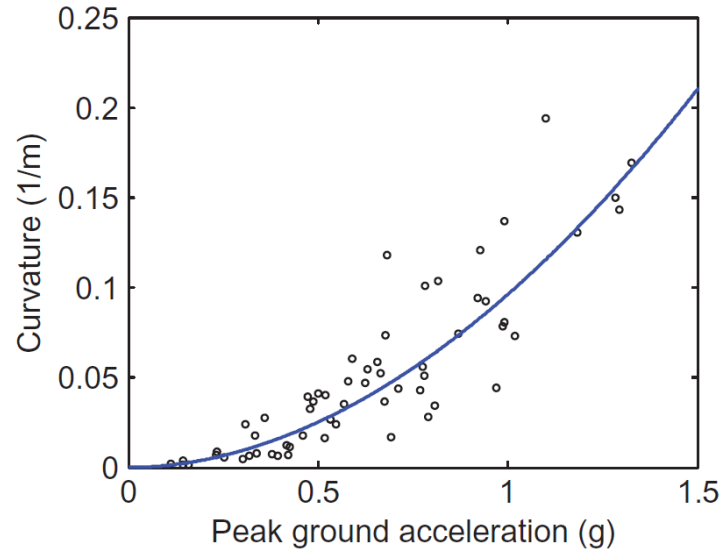


Figure I.4. Demand model of the wharf under LA motions in terms of PGA (Yang *et al.* 2012)

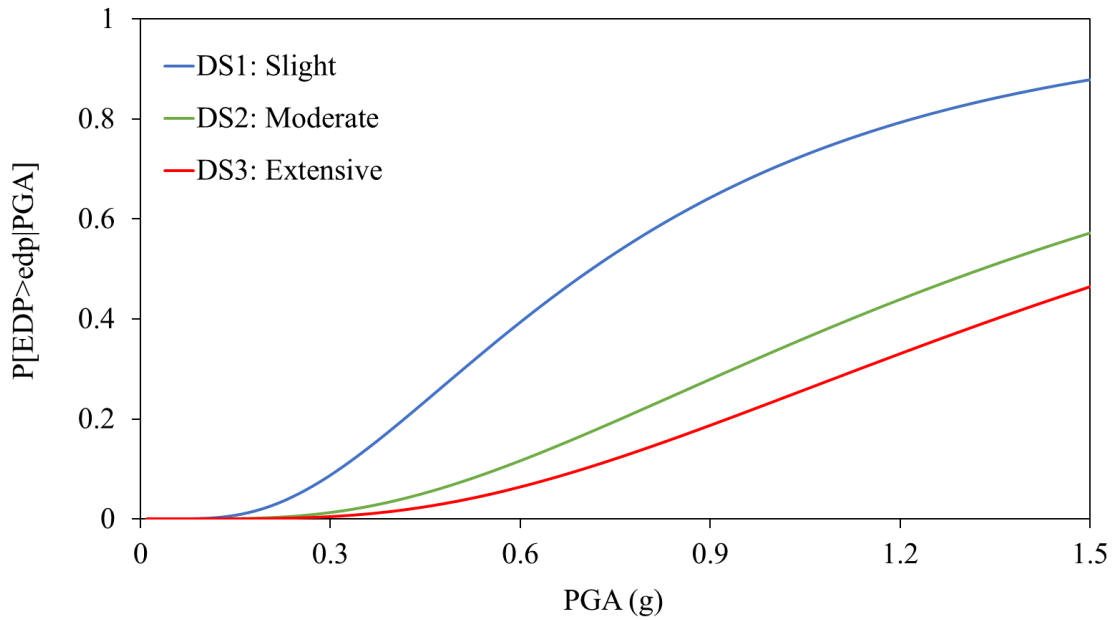


Figure I.5. Probabilities of occurrence for each damage state for the wharf with cranes under the LA ground motion suite

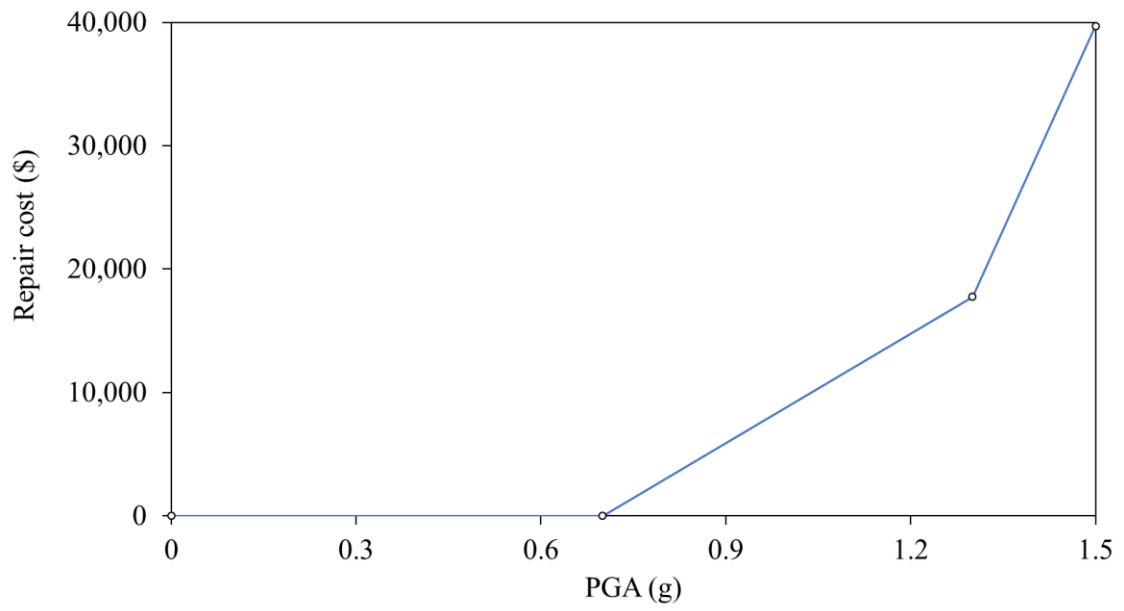


Figure I.6. Expected repair cost vs. PGA for one pile

Appendix J. Simplified Method for Lateral Spreading Load on Bridge Foundation

The simplified method MTD 20-15 (Caltrans 2017) combines two procedures to calculate the slope displacement demand and forces acting on the pile foundation. The first procedure is a slope stability analysis towards the evaluation of lateral ground movement (using an empirical estimation equation) and the second is to impose this displacement via a simplified ground displacement profile on the pile foundation via a p - y spring lateral analysis. Figure J.1 presents a typical abutment model where this type of analysis is employed.

J.1. Step-by-step Procedures

The simplified procedure employed in this study involves the following steps to define the demand lateral ground displacement:

1. Identify stratum with a factor of safety that denotes the triggering of liquefaction, based on PGA and the soil properties.
2. Assign residual shear strength to the liquefiable soil layer (Kramer and Wang 2015, equation J.1):

$$S_r = \exp[-8.444 + 0.109(N_1)_{60} + 5.379\sigma_v'^{0.1}] \quad (\text{J.1})$$

where S_r is the residual strength in units of atm, $(N_1)_{60}$ is the corrected SPT blow count, and σ_v' is the effective vertical stress in units of atm.

3. On this basis, perform a slope stability analysis to determine the critical failure surface without the presence of foundation restraining forces to determine the affected region (Caltrans

2017 using the software Slide v.8.023 (<https://www.rocscience.com/rocscience/products/slide>).

Piles within that region are affected by lateral deformations.

4. Using SLIDE, with a force that represents the restraining action of the superstructure, define the soil response curve (Figure J.1) by applying a range of pile restraining forces (Caltrans 2017). For each applied force, the corresponding yield acceleration (k_y) required to achieve a factor of safety of unity is used to estimate the corresponding slope displacement (Bray and Travasarou 2007, equation J.2):

$$D(\text{cm}) = \exp[-0.22 - 2.83 \ln(k_y) - 0.333 \ln(k_y)^2 + 0.566 \ln(k_y)\ln(\text{PGA}) + 3.04 \ln(\text{PGA}) - 0.244 \ln(\text{PGA})^2 + 0.278 (M_w - 7)] \quad (\text{J.2})$$

where, PGA is the peak ground acceleration, M_w is the moment magnitude of the design event. As such, the soil response curve is represented by displacement vs. restraining force multiplied by the effective embankment width.

5. Define the pile response curve (Figure J.1) by:

5.1. Using the global bridge finite element model, impose a series of increasing soil displacement profiles (Figure J.1) on the foundation model via soil p - y curves. The profile is developed by applying constant displacement in the crust and linearly decreasing in the liquefied layer, with zero displacement below.

5.2. As such, the pile response curve is represented by the top profile displacement against the shear force in the pile developed at the center of the liquefiable layer (critical failure surface location).

6. Determine the design displacement demand from the intersection of the pile response and soil response curves.

7. Load the global bridge finite element model with the calculated design displacement to evaluate the corresponding pile foundation displacement and structural demands.

8. For the parametric studies, the equation to estimate the variation of the residual shear strength (in atm) is shown in equation J.3 (Kramer and Wang 2015).

$$\text{Var}[S_r] = 1.627 + 0.00073 (N_1)_{60}^2 + 0.0194 - 0.027 (N_1)_{60} \sigma_v'^{0.1} - 3.099 \sigma_v'^{0.1} + 1.621 \sigma_v'^{0.2} \quad (\text{J.3})$$

9. In addition, the empirical equation proposed by Martin and Qiu (1994) is shown in equation J.4.

$$\log(d) = -1.56 - 0.72 \log\left(\frac{k_y}{k_{\max}}\right) + 3.21 \log\left(1 - \frac{k_y}{k_{\max}}\right) - 0.87 \log(k_{\max}) + 1.62 \log(\text{PGV}) \quad (\text{J.4})$$

where, k_{\max} is the peak ground acceleration (PGA) modified by a site class factor F_{pga} (Table J.1). PGV is the peak ground velocity (in/sec). The equation yields displacement d in inches.

J.2. Worked Example

The step-by-step procedures concern the evaluation of the abutment. Figure J.2 shows the abutment configuration and soil properties and Figure J.3 shows the abutment elevation view. The soil properties are shown in Table 7.1.

The estimated displacement demand of the potential sliding mass can be reduced when the lateral stiffness of the foundation is included as a restraining force (pile-pinning effect). In addition, the restraining force itself depends on the amount of slope movement. To account for the interdependency between the restraining force and the slope movement, the step-by-step procedures required to evaluate the restrained soil displacement are presented in this section as a worked example of the bridge configuration shown in Chapter 7 and Chapter 8.

Step 1: Assess liquefaction potential for each layer

Previous evaluation of the Salinas site condition has shown that only the top loose sand layer with a thickness of 17 ft was considered liquefiable. While the dense sand layer is not susceptible to liquefaction. However, the Factor of Safety for liquefaction potential (FS_{liq}) is calculated for both layers.

Following Youd (2001), the cyclic resistance ratio (CRR) can be estimated using equation (J.5)

$$CRR = CRR_{\sigma'_v=1, \alpha=0} \cdot K_\sigma \cdot K_\alpha \quad (J.5)$$

where $CRR_{\sigma'_v=1, \alpha=0}$ is estimated to be 0.16 g (for $(N_1)_{60CS} = 14$), $K_\sigma=1$, and $K_\alpha=1.2$. Therefore,

$$CRR = 0.19$$

The cyclic stress ratio (CSR) can be estimated using equation (J.6)

$$CSR = 0.65 \frac{\sigma_v}{\sigma'_v} \cdot \frac{A_{max}}{g} \cdot r_d \quad (J.6)$$

where $\frac{A_{max}}{g}$ is 0.5, r_d is 0.9. the vertical stresses are calculated using an average embankment height.

$$\sigma_v = 28.9 \text{ ft} \times 135 \text{ pcf} + 8.5 \text{ ft} \times 127 \text{ pcf} = 4981 \text{ psf}$$

$$\sigma'_v = 28.9 \text{ ft} \times 135 \text{ pcf} + 8.5 \text{ ft} \times (127 - 62.4) \text{ pcf} = 4451 \text{ psf}$$

Thus, CSR = 0.33

$FS_{liq} = 0.19/0.33 = 0.58 < 1$, susceptible to liquefaction.

On the other hand, using the same method for the dense sand, $FS_{liq} = 1.43 > 1$, not susceptible to liquefaction.

Step 2: Determine residual strengths for the center of the loose sand layer

For the liquefied sand that has an FS_{liq} less than 1.05, reduced strength should be assigned as soft clay. As according to MTD 20-15, Kramer and Wang (2015) equation is used to estimate the residual shear strength. The results of the residual strengths by location can be found in Table J.2.

Step 3: Develop Crust p - y curves

The interaction between the foundation and soil crust can be modeled using user-defined trilinear p - y curves. Figure J.4 show the trilinear force-deflection model defined by parameters F_{ult} and Δ_{max} .

Step 3.1: F_{ult}

For the calculation of the ultimate passive load due to the soil crust, two design cases are considered as shown in Figure J.5. However, for most practical problems, Case B will govern. For simplicity only the calculation of Case B is presented in this section. Equation (J.7) shows that the

F_{ult} consists of two loads, $F_{passive}$ and F_{sides} . In addition, equations (J.8) and (J.9) show how to calculate $F_{passive}$ and F_{sides} , respectively.

$$F_{ult} = F_{passive} + F_{sides} \quad (J.7)$$

$$F_{passive} = (\overline{\sigma'_v} \cdot K_p) \cdot (H) \cdot W_T \cdot k_w \quad (J.8)$$

where $\overline{\sigma'_v}$ is the mean vertical effective stress along the crust height, K_p is the passive pressure coefficient, H is the crust height, and k_w is an adjustment factor for a wedge-shaped failure surface.

$$F_{passive} = 3635 \text{ psf} \times 5.83 + 52 \text{ ft} \times 42.5 \text{ ft} \times 1.59 = 99,562 \text{ kips.}$$

Similarly, F_{sides} is calculated using equation (I.9).

$$F_{sides} = 2 \cdot \overline{\sigma'_v} \cdot \tan(\delta) \cdot W_L \cdot H \quad (J.9)$$

where δ is the pile-soil interface friction angle (recommended as $\phi/3$ for cases of liquefaction [ϕ is the friction angle]) and W_L is the longitudinal abutment width.

$$F_{sides} = 694 \text{ kips.}$$

From equation (4), $F_{ult} = 100,256$ kips. To construct p_{ult} (kip/in), F_{ult} should be divided by the crust height, $p_{ult} = 100,256 \text{ kips} / 52 \text{ ft} \times 12 \text{ in/ft} = 160.7 \text{ kips/in.}$

Step 3.2: Δ_{max}

The maximum relative displacement (Δ_{max}) is required to mobilize the full passive force. It can be calculated using equation (I.10) with two adjustment factors that account for the depth and width (Figure J.6). The p - y trilinear curve for the crust consists of the following points: (0,0), (11.25,80350), (45,160,700), (100,79300) as shown in Figure J.7.

$$\Delta_{max} = H(0.05 + 0.45 \cdot f_{depth} \cdot f_{width}) \quad (J.10)$$

where H is the crust height, f_{depth} and f_{width} are depth and width adjustment factors, respectively.

$$\Delta_{max} = 45 \text{ in.}$$

Step 4: Modification to p - y curves near liquefaction boundary

The liquefaction layer has a weakening effect on the neighboring nonliquefied layers. Therefore, p_{u-1} is assumed to vary linearly from the liquefied resistance to the full resistance of the nonliquefied strata over a length shown in Figure J.8. For Salinas example, the pile diameter is 5 ft, therefore S_b is 1 that means the length of the affected nonliquefied layer is 5 ft above and below the liquefied layer. However, since the design Case B controls, then the soil above the liquefied layer is part of the crust that will not be affected by this modification. Table J.3 shows the adjustments of the p-multiplier (m_p , equation J.11) over a length of 5 ft below the liquefied layer.

$$m_p = \frac{p_{u-1}}{p_{u-nl}} + \left(1 - \frac{p_{u-1}}{p_{u-nl}}\right) \cdot \left(\frac{z}{S_b B}\right) \quad (J.11)$$

Where z is the depth in ft, B is pile diameter in ft, S_b is diameter factor, p_{u-1} and p_{u-nl} are the ultimate subgrade reaction of the liquefied and nonliquefied layers, respectively.

Step 5: Calculate F_{DECK}

To consider the superstructure restrain, a force at top of the slope should be added assuming that the superstructure is stiff enough to resist the sliding of the abutment. However, the superstructure restraining is limited by the ultimate passive force of the soil behind the back wall. This force is calculated using equation J.12 with K_p (log-spiral).

$$F_{DECK} = (\overline{\sigma'_v} \cdot K_p) \cdot (T_{DECK}) \cdot W_T \quad (J.12)$$

where $\overline{\sigma'_v}$ is the mean vertical effective stress along the deck thickness, K_p is the passive pressure coefficient, T_{DECK} is the deck thickness, and W_T is the deck width.

Step 6: Perform slope stability analysis

The slope stability analysis was performed using the software Slide v.8.023 (<https://www.rocscience.com/rocscience/products/slide>). As according to MTD 20-15, some constraints are placed on the failure surface as follow:

- (1) constrained laterally to less than $4H$ as measured from the slope crest;
- (2) placed in the center of the liquefied stratum;
- (3) constrained to a maximum depth of $1.2H$; and
- (4) Have a wedge type shape.

Figure 7.5 shows the slope stability model that satisfies the previous mentioned constraints. It worth noting that the liquefied layer was divided into three segments since the properties of the liquefied layer depend on the vertical stress as shown in Table J.2.

Table J.1. Values of site factors, F_{pga}

Site Class	Peak Ground Acceleration Coefficient (PGA)				
	PGA < 0.10	PGA = 0.20	PGA = 0.30	PGA = 0.40	PGA > 0.50
A	0.8	0.8	0.8	0.8	0.8
B	1.0	1.0	1.0	1.0	1.0
C	1.2	1.2	1.1	1.0	1.0
D	1.6	1.4	1.2	1.1	1.0
E	2.5	1.7	1.2	0.9	0.9

Table J.2. Residual strengths by location

Embankment zone	σ'_v (psf)	S_r (psf)
Bottom	658	251
midslope	2026	444
top	3394	589

Table J.3. Adjustments for p-multiplier at the boundary of the liquefied layer

Depth (ft)	m_p
0	0.11
1	0.29
2	0.47
3	0.64
4	0.82
5	1

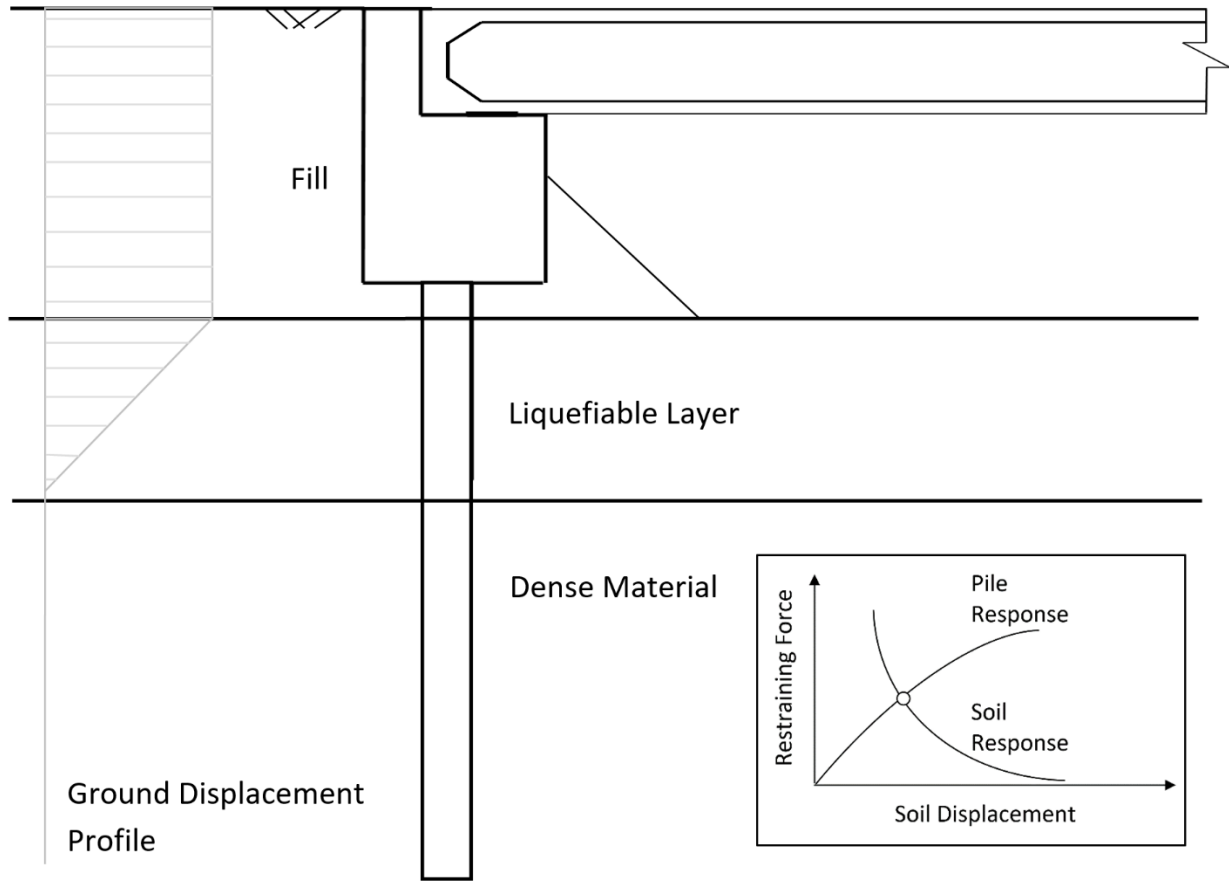


Figure J.1. Schematic abutment configuration and soil properties (not to scale)

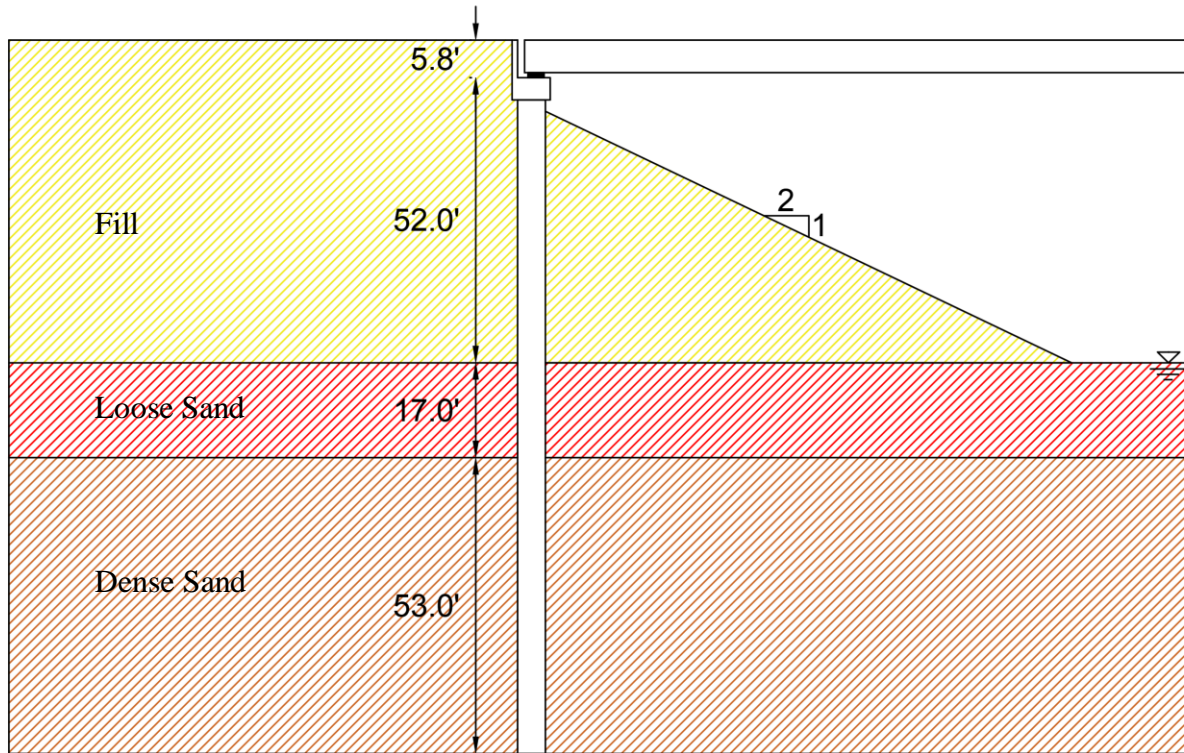


Figure J.2. Abutment configuration and soil properties.

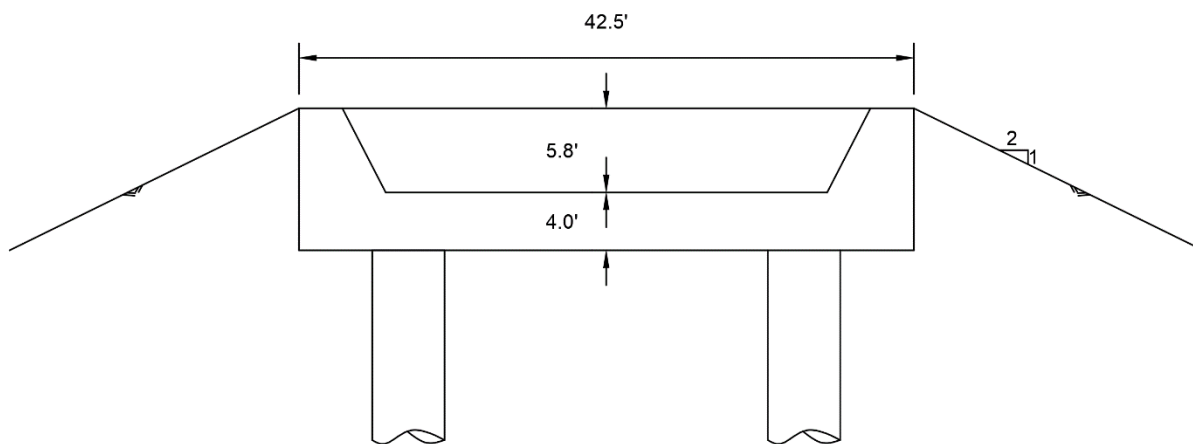


Figure J.3. Abutment elevation view.

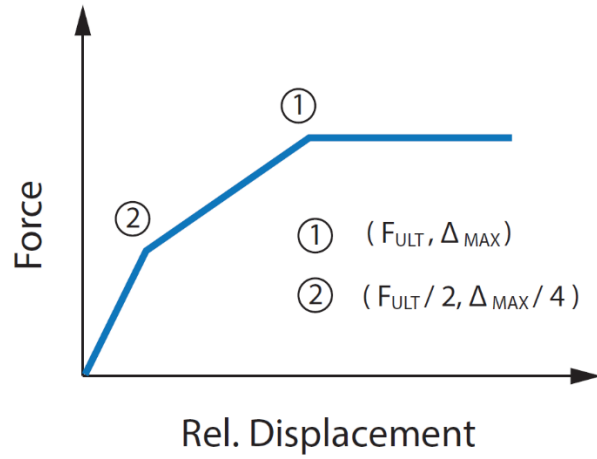


Figure J.4. A crust trilinear force-deflection behavior (Caltrans 2017).

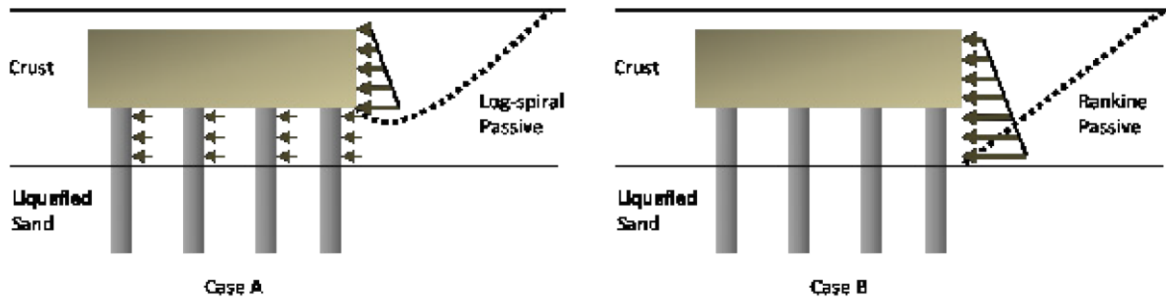
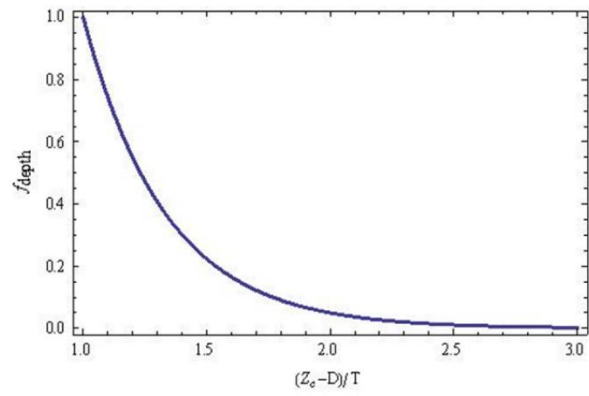
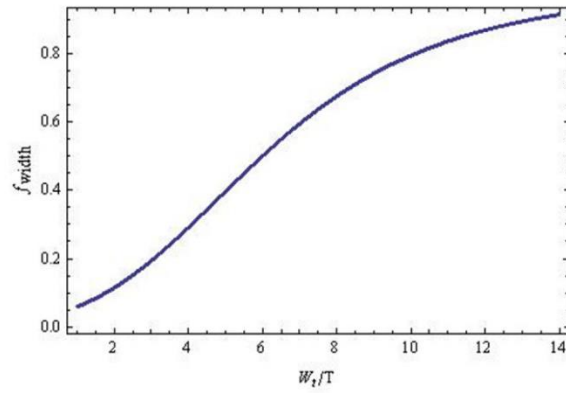


Figure J.5. Two possible design cases to calculate the crust ultimate passive force (Caltrans 2017).



(a)



(b)

Figure J.6. Adjustment factors used in calculation of Δ_{max} : (a) depth factor, and (b) width factor (Caltrans 2017).

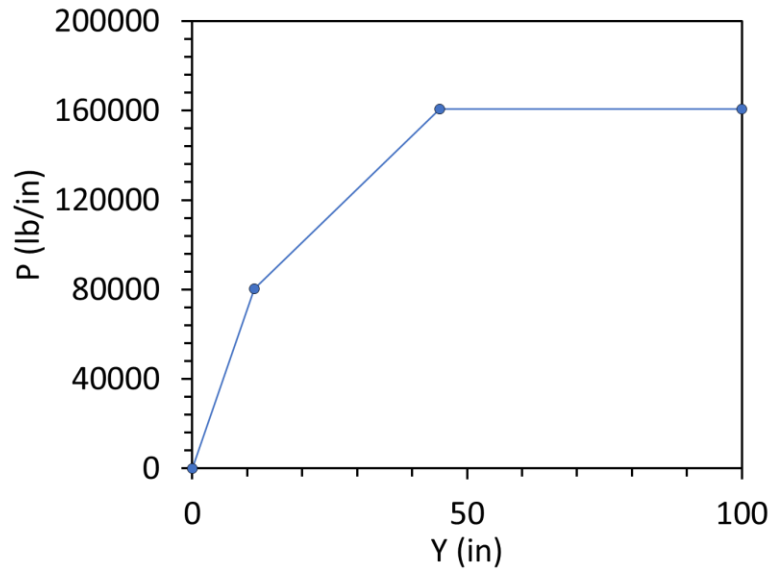


Figure J.7. Crust trilinear p - y curve

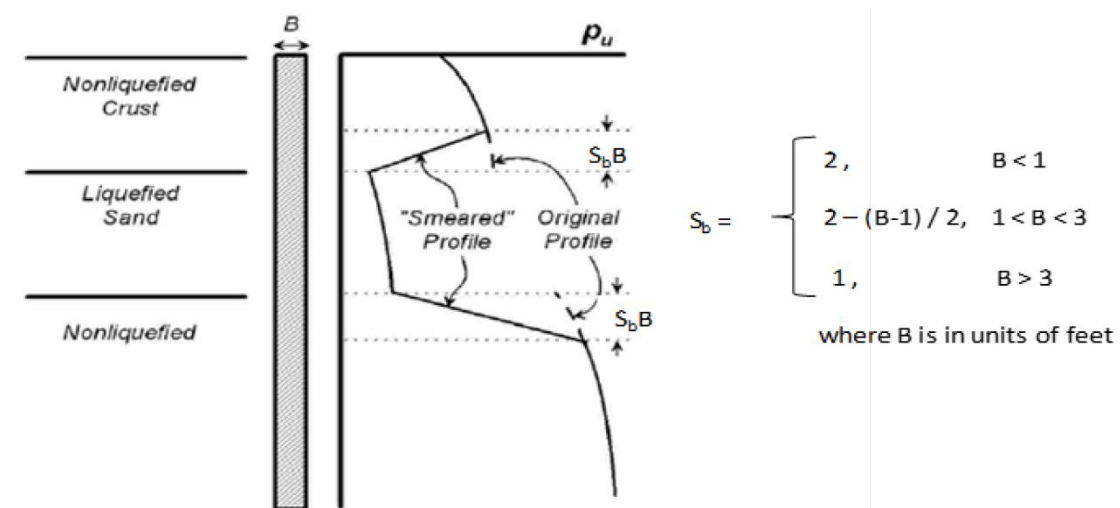


Figure J.8. Modification of p_{ult} near liquefaction boundary (Caltrans 2017)